NASA CONTRACTOR REPORT

NASA CR-66662

NASA CR-66662

FINAL REPORT

STUDY OF DIRECT VERSUS ORBITAL ENTRY FOR MARS MISSIONS

Volume IV - Appendix B - Entry and Terminal Phase Performance Analysis

Prepared by

MARTIN MARIETTA CORPORATION
DENVER, COLORADO

for

Langley Research Center

NATIONAL AERONATUICS AND SPACE ADMINISTRATION • WASHINGTON, D.C. • AUGUST 1968

NASA CR-66662

FINAL REPORT

STUDY OF DIRECT VERSUS ORBITAL ENTRY FOR MARS MISSIONS

VOLUME IV: APPENDIX B - ENTRY AND TERMINAL PHASE PERFORMANCE ANALYSIS

By Charles E. French and Duane A. Howard

Distribution of this report is provided in the interest of information exchange. Responsibility for the contents resides in the author or organization that prepared it.

Prepared under Contract No. NAS1-7976 by
MARTIN MARIETTA CORPORATION
Denver, Colorado

for

NATIONAL AERONAUTICS AND SPACE ADMINISTRATION

FOREWORD

This Final Report for the "Study of Direct Versus Orbital Entry for Mars Missions" (NASA Contract NAS1-7976) is provided in accordance with Part III A.4 of the contract schedule as amended. The report is in six volumes as follows:

NASA CR-66659 - Volume I - Summary;

NASA CR-66660 - Volume II - Parametric Studies, Final Analyses, and Conceptual Designs;

NASA CR-66661 - Volume III - Appendix A - Launch Vehicle Performance and Flight Mechanics;

NASA CR-66662 - Volume IV - Appendix B - Entry and Terminal Phase Performance Analysis;

NASA CR-66663 - Volume V - Appendix C - Entry Configuration Analysis;

NASA CR-66664 - Volume VI - Appendix D - Subsystem Studies and Parametric Data.

APPENDIX B

CONTENTS

APPENDIX B

APPENDIX B

APPENDIX B

ENTRY AND TERMINAL PERFORMANCE ANALYSIS

APPENDIX B

The entry trajectory includes that portion of the mission from atmospheric entry (800 000 ft altitude) to terminal phase initiation, occurring in the vicinity of 20 000 ft altitude. The terminal phase is that portion of the trajectory from entry trajectory termination to touchdown on the surface. The objectives of the entry and terminal phase performance analysis are:

1) Determine entry trajectory characteristics to define the entry environment and terminal phase initial conditions for the two mission modes;

2) Compare mission modes for several terminal phase deceleration systems;

3) Compare terminal phase deceleration system performance for each mission mode.

The entry trajectory analysis assumes a 70° half-angle cone aeroshell $C_D = 1.64$ and the VM-1 thru VM-8 range of Martian atmosphere models. Entry variables include velocity, ballistic coefficient, and flightpath angle. The environmental characteristics during entry (dynamic pressure, acceleration, etc.) provide data for aeroshell and subsystem analysis and design. The trajectory characteristics (velocity, dynamic pressure, Mach number, flightpath angle, altitude) provide initial conditions for the terminal phase analysis.

The terminal phase system provides deceleration from velocities at the end of the entry phase to zero velocity at the Martian surface. The types of decelerator systems studied generally include two basic types -- aerodynamic with retro-vernier and all-retro. Performance is measured by variables such as aeroshell diameter required, flightpath angle that can be tolerated, landed weight, and entry weight. A number of constraints are imposed; these will be discussed in the appropriate section. Required entry weights are compared with launch vehicle capability (Appendix A). Limiting entry flightpath angles are correlated with the entry corridors resulting from the error analysis (also from Appendix A).

1. ENTRY TRAJECTORY ANALYSIS

Parametric Mars entry trajectory data are presented in this section of Appendix B. Entry data are presented in the form of carpet plots at a constant value of entry velocity with the

dependent variable a function of entry flightpath angle and entry ballistic coefficient. A range of entry velocities covering the orbital and direct entry modes is presented. These summary plots are derived from a parametric matrix of entry trajectory calculations performed on the CDC 6400 computer. The simulation model is a point mass program and, therefore, does not include the effects of vehicle dynamics. For the small angles of attack at entry achieved with an active attitude control system, the point mass simulation provides entirely satisfactory data for the entry environment parameters presented herein.

Entry vehicle drag coefficient used in the trajectory calculations is a function of Mach number. The normalized drag coefficient as a function of Mach number is shown in figure B1. Indicated on the curve is the hypersonic drag coefficient level for a 60 and 70° half-angle cone.

V_E = entry velocity (inertial) at entry altitude (800 000 ft);

γ_E = entry flightpath angle (inertial) at entry altitude (negative downward);

B_E = entry vehicle hypersonic ballistic coefficient, $m/C_D A$, slug/ft^2;

C_A = axial force coefficient of entry vehicle;

A = reference area, plan area of entry vehicle.

Velocity and flightpath angles at initial entry conditions are defined in an inertial system with the coordinate system origin at the center of Mars. Entry trajectories consider the rotation of the planet and are computed in a coordinate system that rotates with the planet. Velocities and angles during the entry trajectories are therefore relative to the atmosphere, which is considered to rotate with the planet. The trajectories from which the data presented in this report are taken, enter in the equatorial plane with an east (posigrade) heading.

The following planetary characteristics are used in the entry trajectory calculations:

1) Planet radius, 3393 km (11 131 754 ft);
2) Gravitational constant, 1.51254×10^{15} ft^3/sec^2;
3) Rotation rate, 7.088133×10^{-5} rad/sec;
4) Atmosphere models, VM-1, -2, -3, -4, -7, and -8.

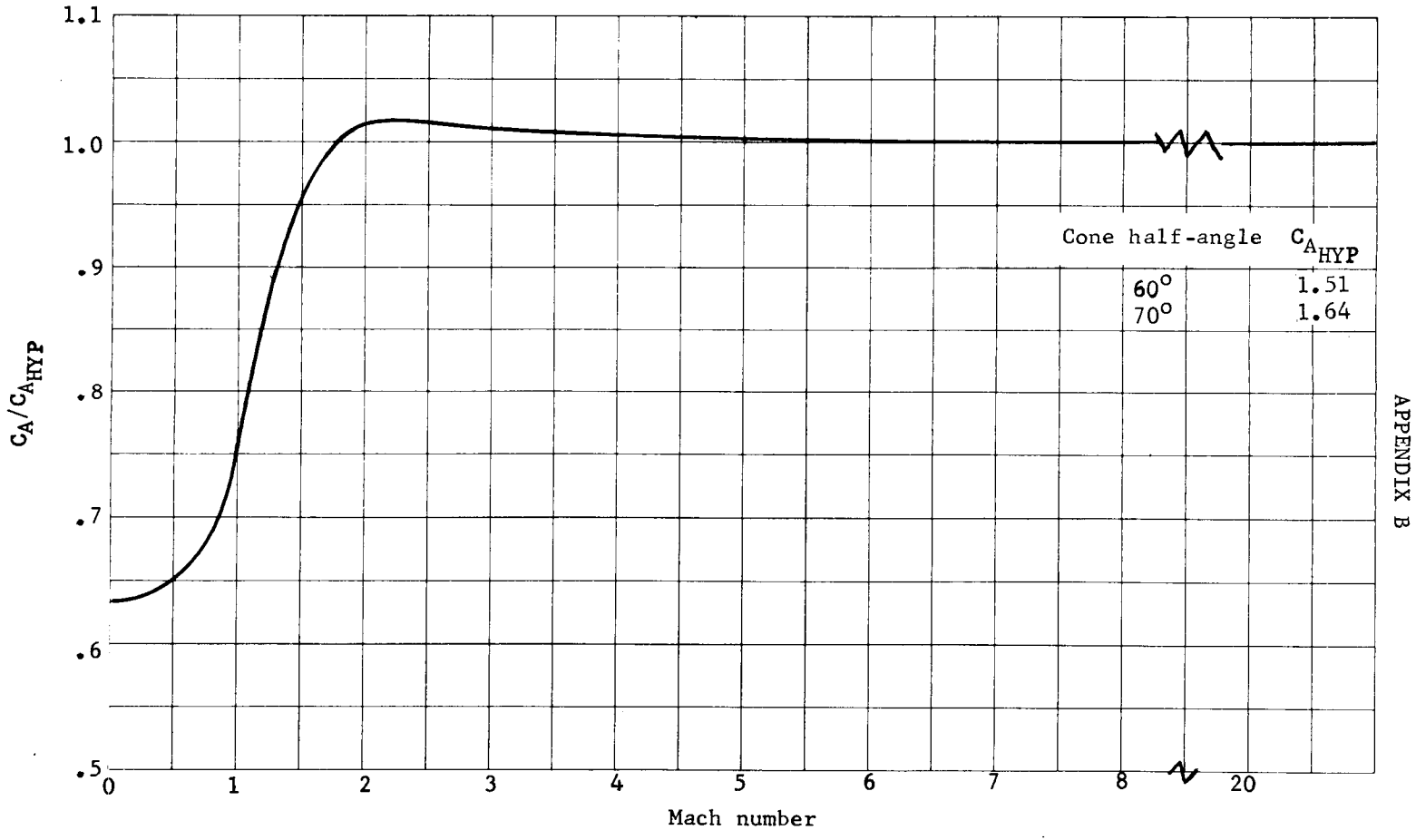

Figure B1.- Normalized Axial Force Coefficient versus Mach Number

APPENDIX B

The atmosphere models are the VM atmosphere as specified in RFP-VO-6-4509. Important characteristics are tabulated below.

Model	VM-1	VM-2	VM-3	VM-4	VM-7	VM-8
Surface pressure, mb	7.0	7.0	10.0	10.0	5.0	5.0
Surface density, slug/ft^3 x 10^5	1.85	3.59	2.65	4.98	1.32	2.56
Surface temperature, °R	495	360	495	360	495	360
Tropopause altitude, ft x 10^{-3}	63.3	61.0	63.3	56.1	63.3	61.0
Stratosphere temperature, °R	360	180	360	180	360	180
Composition, % (by mass)						
CO_2	28.2	100.0	28.2	70.0	28.2	100.0
N_2	71.8	0	71.8	0	71.8	0
A	0	0	0	30.0	0	0
Molecular weight	31.2	44.0	31.2	42.7	31.2	44.0
Specific heat ratio	1.38	1.37	1.38	1.43	1.38	1.37
Inverse scale height, 10^{-5}/ft	2.15	6.07	2.15	5.89	2.15	6.07

Figures B2 and B3 present density versus altitude and temperature and speed of sound versus altitude for the six model atmospheres. Reference to figure B2 shows that VM-8, VM-7, and VM-3 bracket the range of atmospheric densities and upper atmosphere density scale heights for the six models described above. VM-8 bounds the low scale height for the upper atmosphere and has the lowest density down to approximately 45 000 ft where VM-7 represents the minimum density down to mean surface level. VM-3 provides the highest stratosphere density as well as the highest density scale height. This reasoning, together with a limited number of entry trajectory runs in all six atmospheres, has indicated that over the range of ballistic coefficients and entry flightpath angles studied in the report, atmosphere VM-8, -7, and -3 represent limiting entry environment and provide terminal phase critical design conditions. Parametric data presented in this report are therefore limited to VM-3, -7, and -8. Speed of sound in VM-8, figure B3, is lowest of all models. This characteristic, in combination with the low stratosphere density and low density scale height, makes VM-8 critical for Mach number-dependent functions for terminal phase system design. For this reason, parametric data presenting altitude for Mach 2, 3, and 5 are shown only for the critical VM-8 atmosphere.

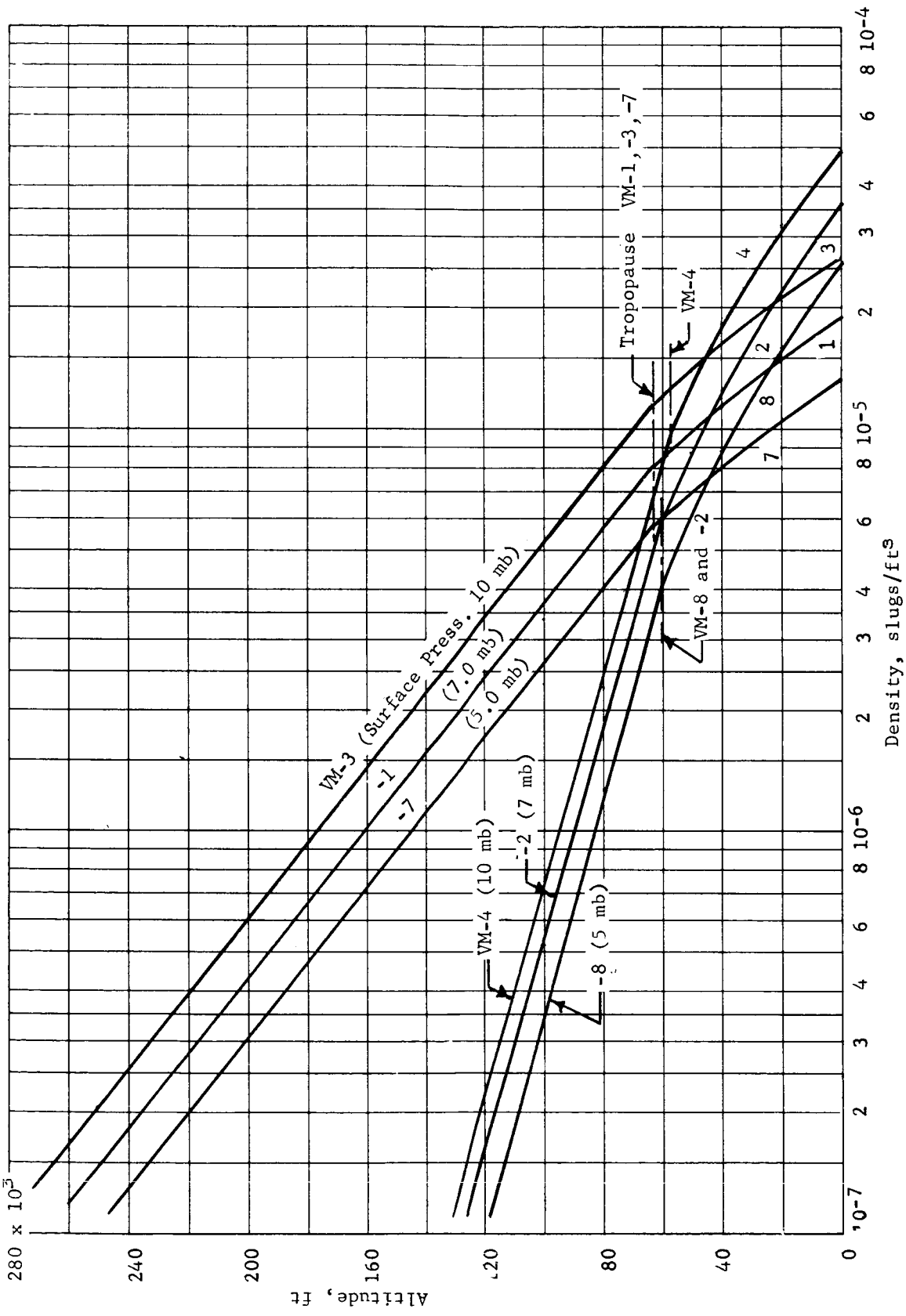

Figure B2.- Mars Model Atmospheres

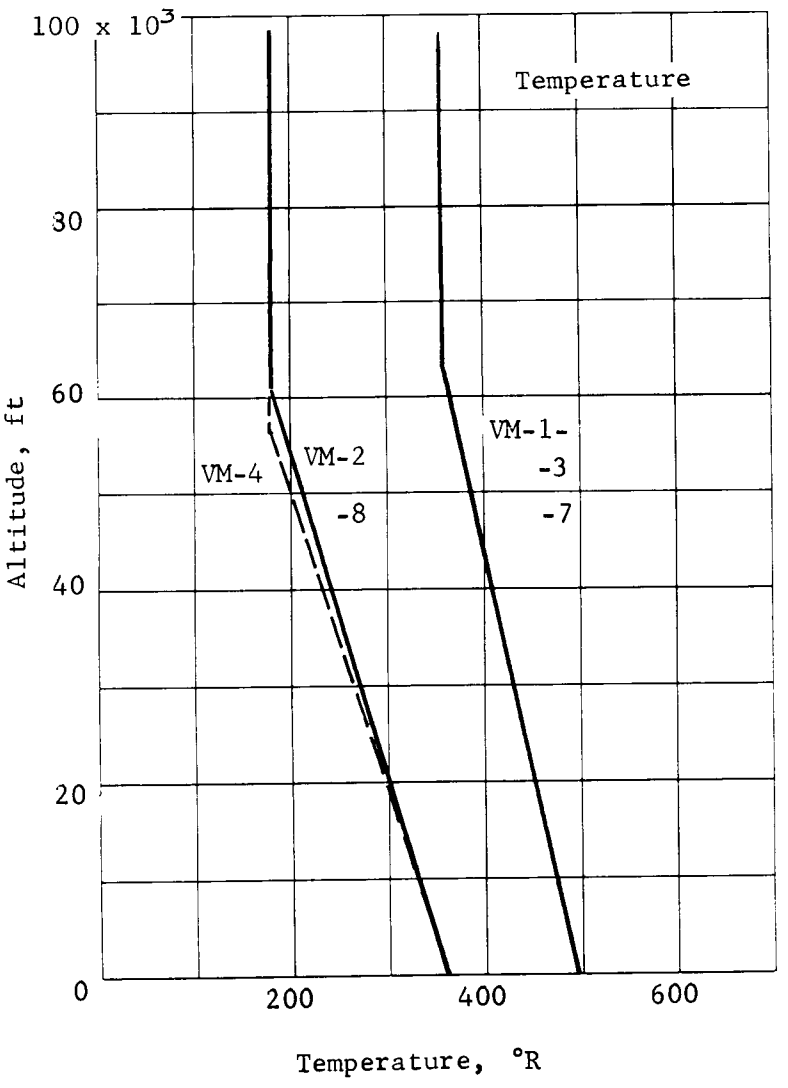

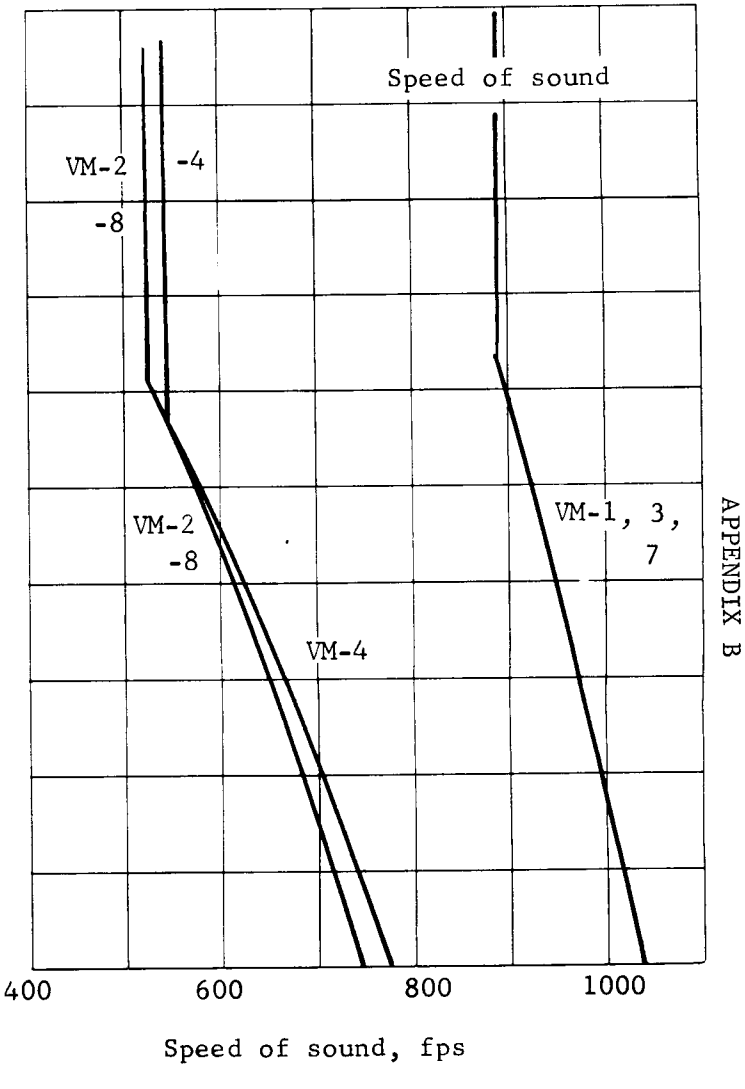

Figure B3.- Ambient Temperature and Speed of Sound versus Altitude

APPENDIX B

Parametric data presented are for the conditions tabulated below.

V_E, fps	B_E, slug/ft^2	$-\gamma_E$, deg	Atmospheric model
14 000	0.1, 0.2, 0.3, 0.4, 0.6	14, 16, 20, 24	VM-3, -7, -8
16 000	0.1, 0.2, 0.3, 0.4, 0.6	16, 20, 24	VM-3, -7, -8
18 000	0.1, 0.2, 0.3, 0.4, 0.6	20, 30, 40	VM-3, -7, -8
21 000	0.1, 0.2, 0.3, 0.4, 0.6	20, 30, 40	VM-3, -7, -8
24 000	0.1, 0.2, 0.3, 0.4, 0.6	20, 30, 40	VM-3, -7, -8

Time from entry altitude (800 000 ft) to 20 000 ft altitude is shown as a function of ballistic coefficient, entry flightpath angle, and entry velocity for VM-3, -7, and -8 in figures B4 thru B18. The terminal condition for the entry trajectory is taken as 20 000 ft as it is a representative altitude for initiation of the terminal phase decelerator system.

Figures B19 thru B33 present downrange angle as a function of ballistic coefficient, entry flightpath angle, and entry velocity for VM-3, -7, and -8. The downrange angle is the central angle covered from entry to 20 000 ft altitude, the termination of the basic entry trajectory. The downrange angle shown is calculated for an equitorial posigrade trajectory (east heading) and includes the effect of planet rotation.

Figures B34 thru B43 present peak drag deceleration as a function of ballistic coefficient (where applicable), entry flightpath angle, and entry velocity for VM-3, -7, and -8. In accordance with the approximate expression,

$$g_{max.} = -\frac{V^2 \sin \gamma_E}{2\, e\, g_{\oplus}\, h_S}$$ where h_S is the scale height (shown in atmoshpere table above),

peak g is not a function of ballistic coefficient for constant values of scale height. For VM-3 and VM-7 atmospheres, peak g occurs along the constant scale height region, (i.e., in the stratosphere). In the case of VM-8, peak deceleration occurs at altitudes below the tropopause altitude (fig. B2) for the higher ballistic coefficients and steep entry angles. This leads to peak drag deceleration with nonlinear characteristics as a function of ballistic coefficient, as shown in figures B35, B37, B39, B41, and B43. The increase in scale height below the tropopause accounts for the reduction in peak G at the higher ballistic coefficients and steeper entry flightpath angles.

APPENDIX B

Velocity (relative) at the terminal decelerator system initiation altitude of 20 000 ft is presented as a function of ballistic coefficient, entry flightpath angle and entry velocity for VM-3, -7, and -8 in figures B44 thru B58.

Figures B59 thru B70 present the altitude at which Mach 2.0, 3.0, and 5.0 occur as a function of ballistic coefficient, entry flightpath angle, and entry velocity in VM-8. As discussed earlier, Mach number at a given altitude for the same entry condition will always be highest in VM-8. Mach number sensitive functions for terminal phase deceleration systems such as parachute deployment will occur at the lowest altitude (critical) in VM-8. Representative data showing this are tabulated below.

Entry condition	Altitude for Mach 2.0, ft		
	VM-3	VM-7	VM-8
V_E = 14 000 fps, B_E = 0.30, γ_E = -20°	73 250	41 580	19 000
V_E = 21 000 fps, B_E = 0.30, γ_E = -20°	78 600	48 000	24 000

As mentioned above, the entry trajectory data are used to define terminal phase initial conditions. In addition, the entry environment data (peak g, time, etc.) are factored into subsystem design studies.

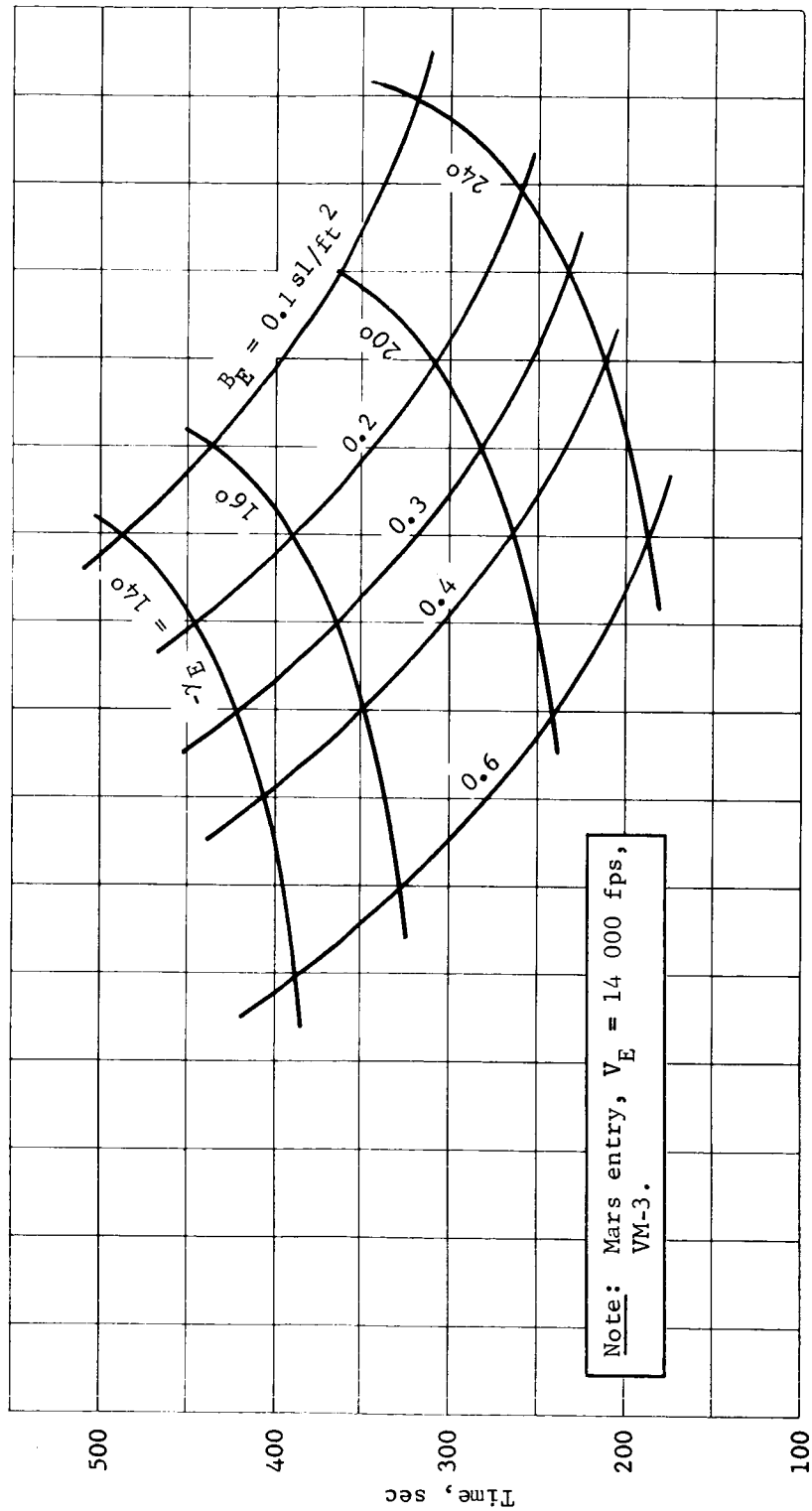

Figure B4.- Time from Entry to 20 000-ft Altitude

APPENDIX B

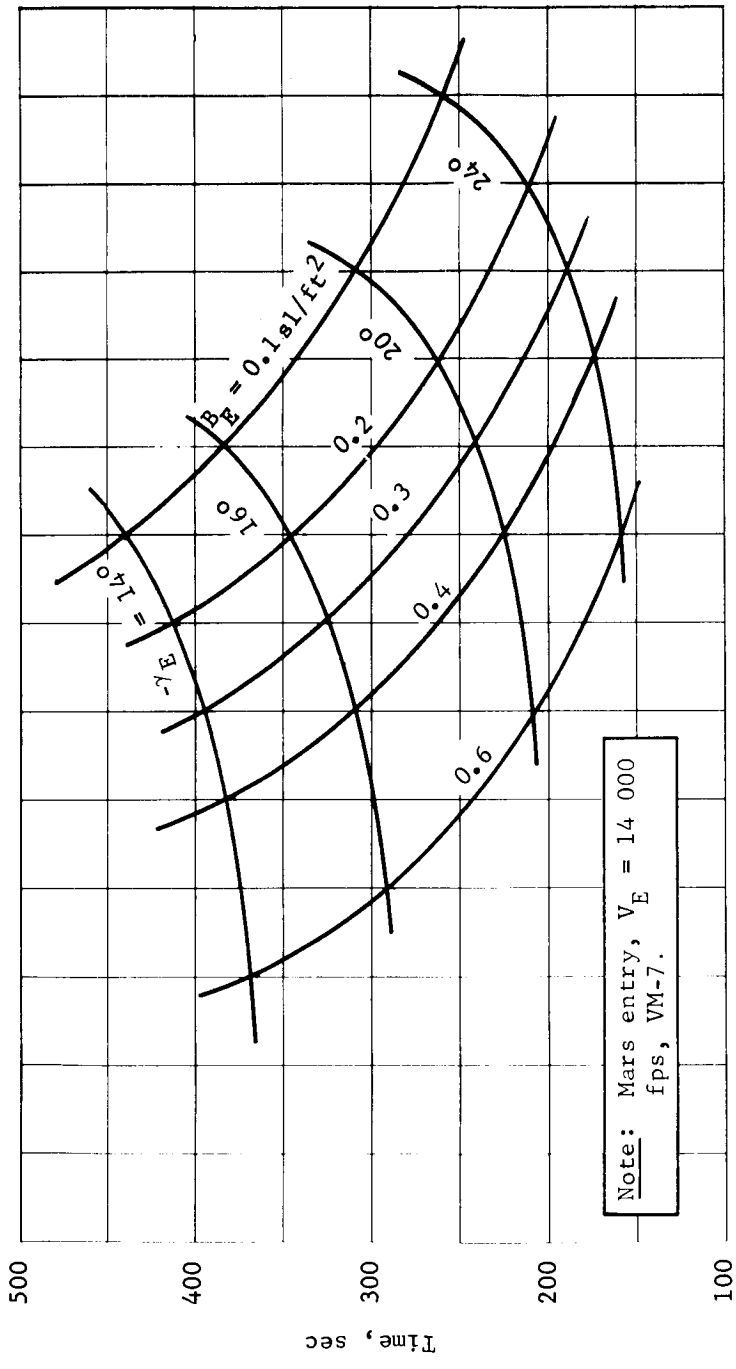

Figure B5.- Time from Entry to 20 000-ft Altitude

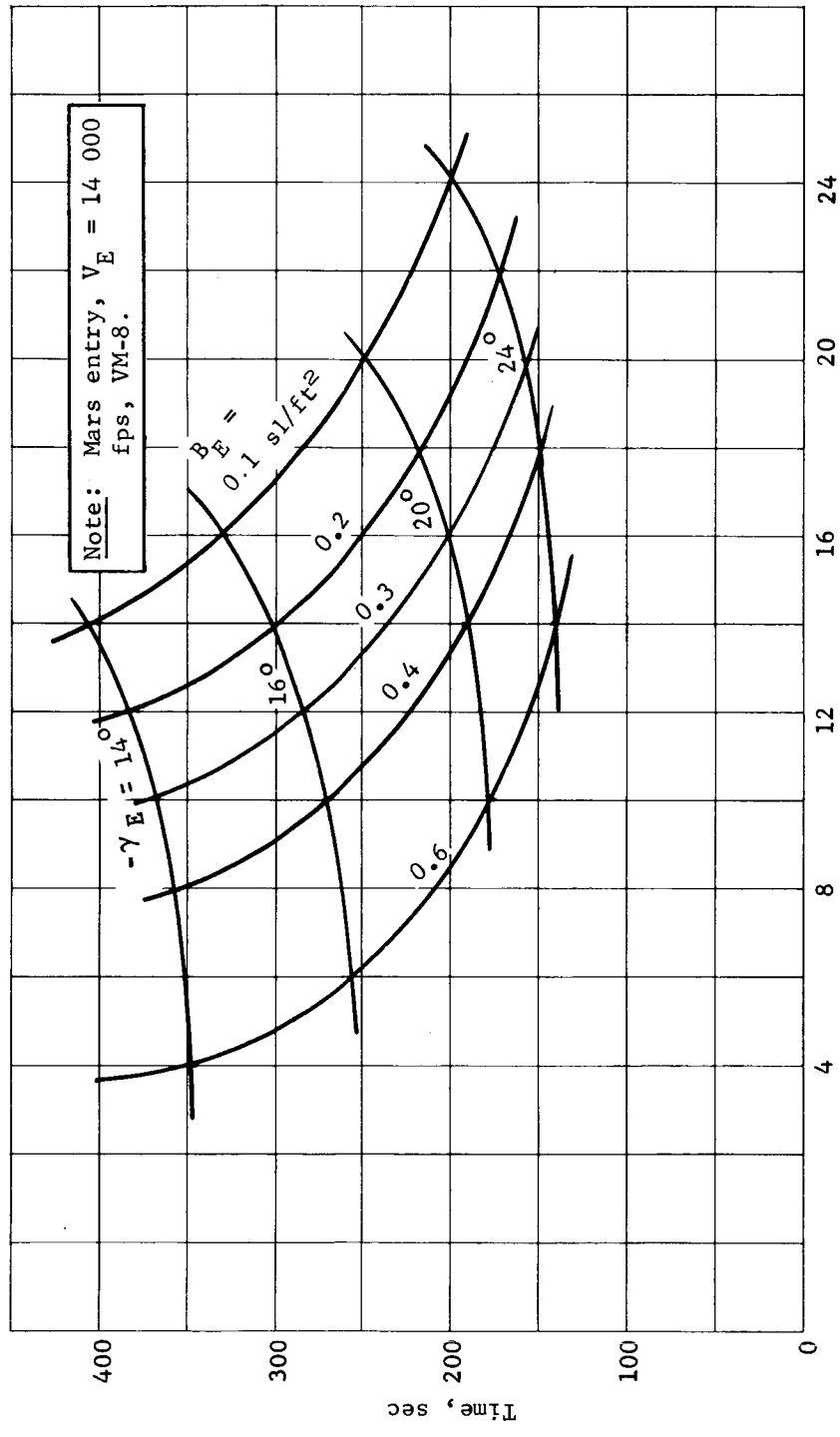

Figure B6.- Time from Entry to 20 000-ft Altitude

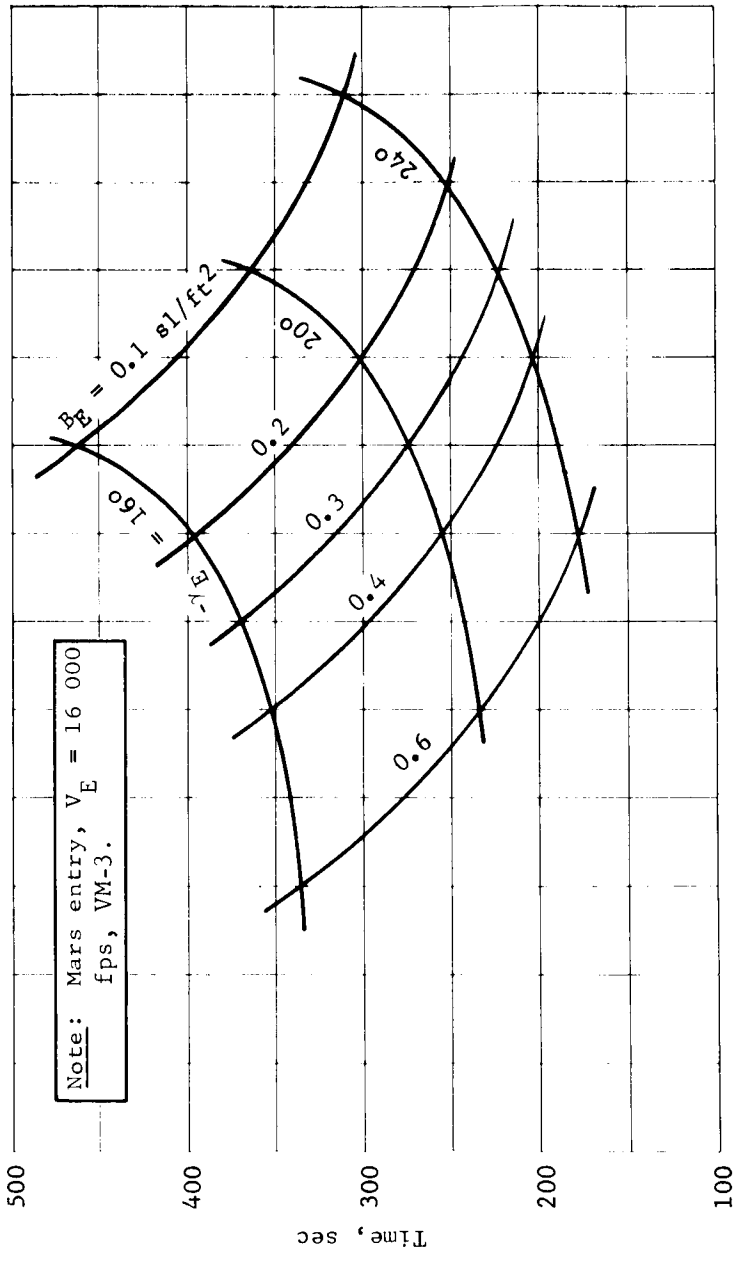

Figure B7.- Time from Entry to 20 000-ft Altitude

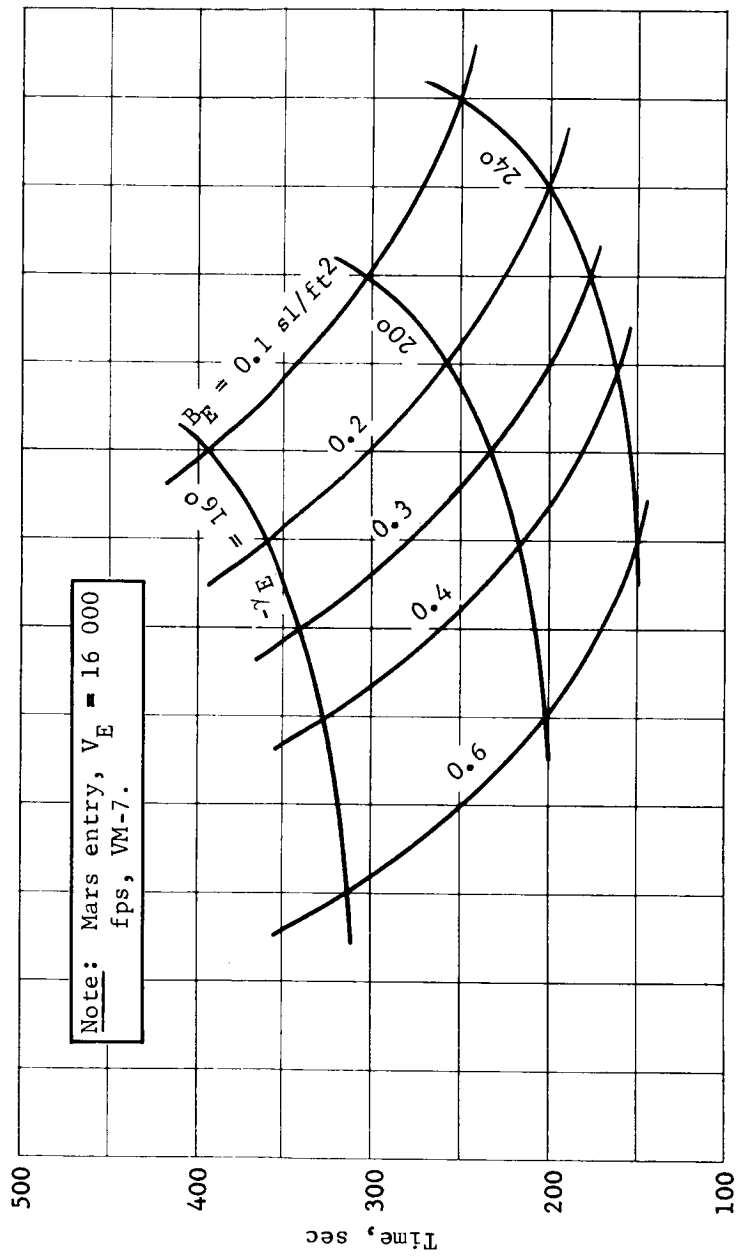

Figure B8.- Time from Entry to 20 000-ft Altitude

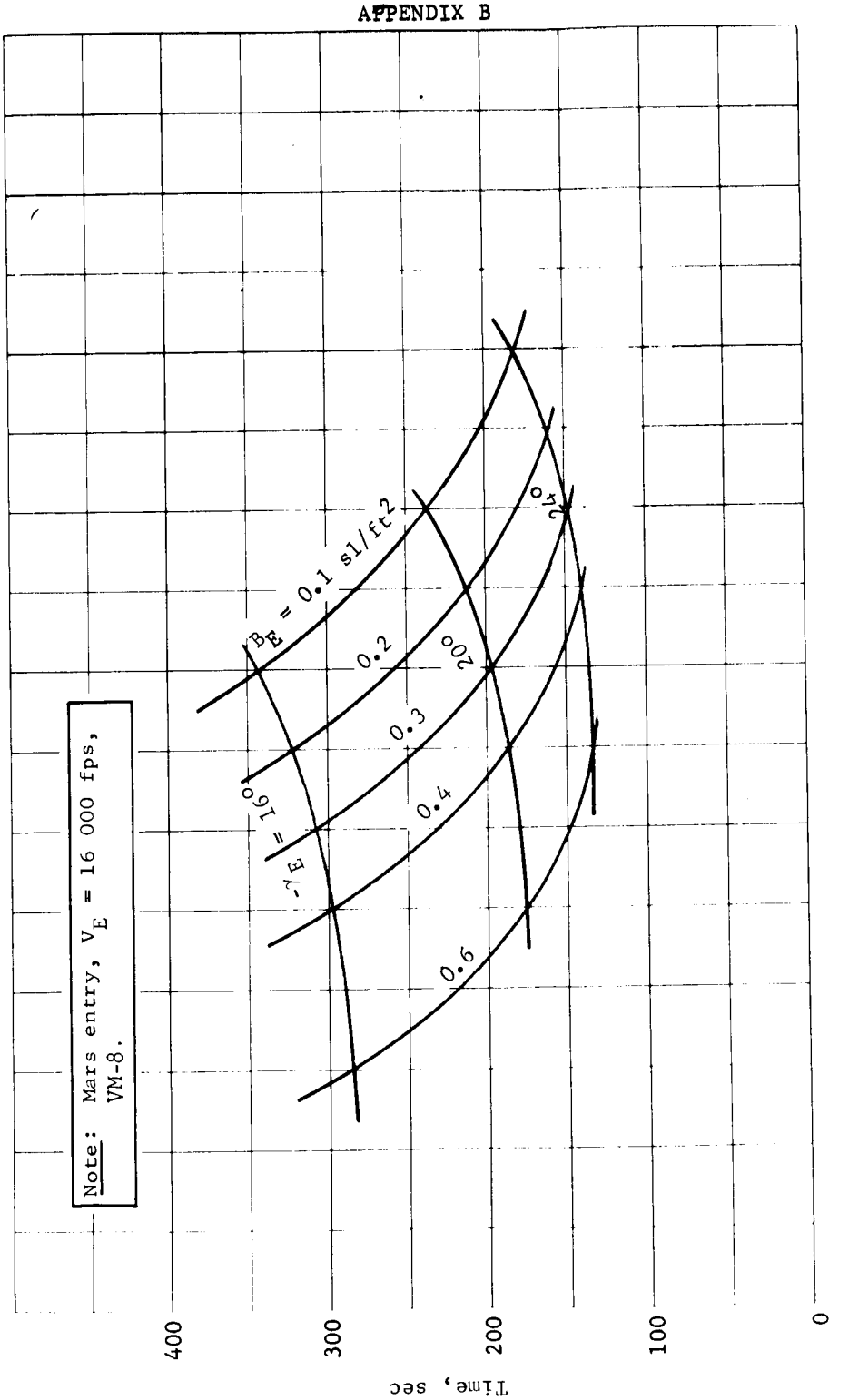

Figure B9.- Time from Entry to 20 000-ft Altitude

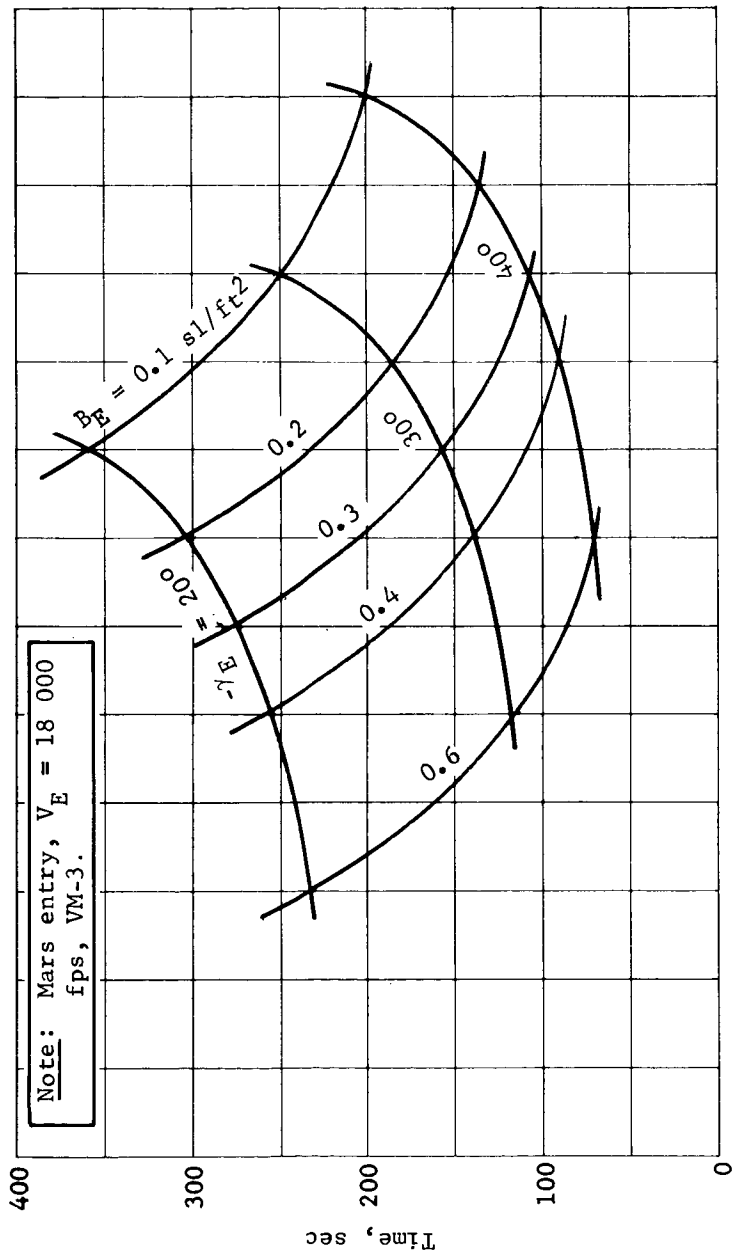

Figure B10.- Time from Entry to 20 000-ft Altitude

APPENDIX B

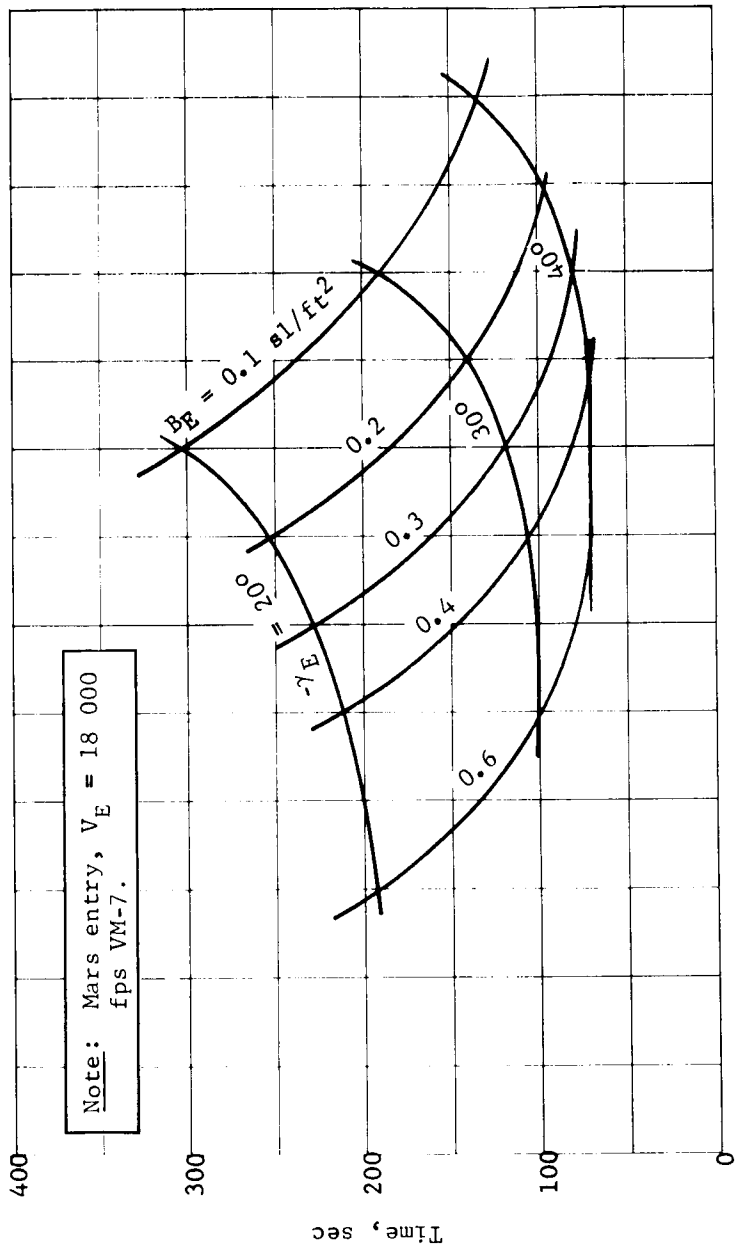

Figure B11.- Time from Entry to 20 000-ft Altitude

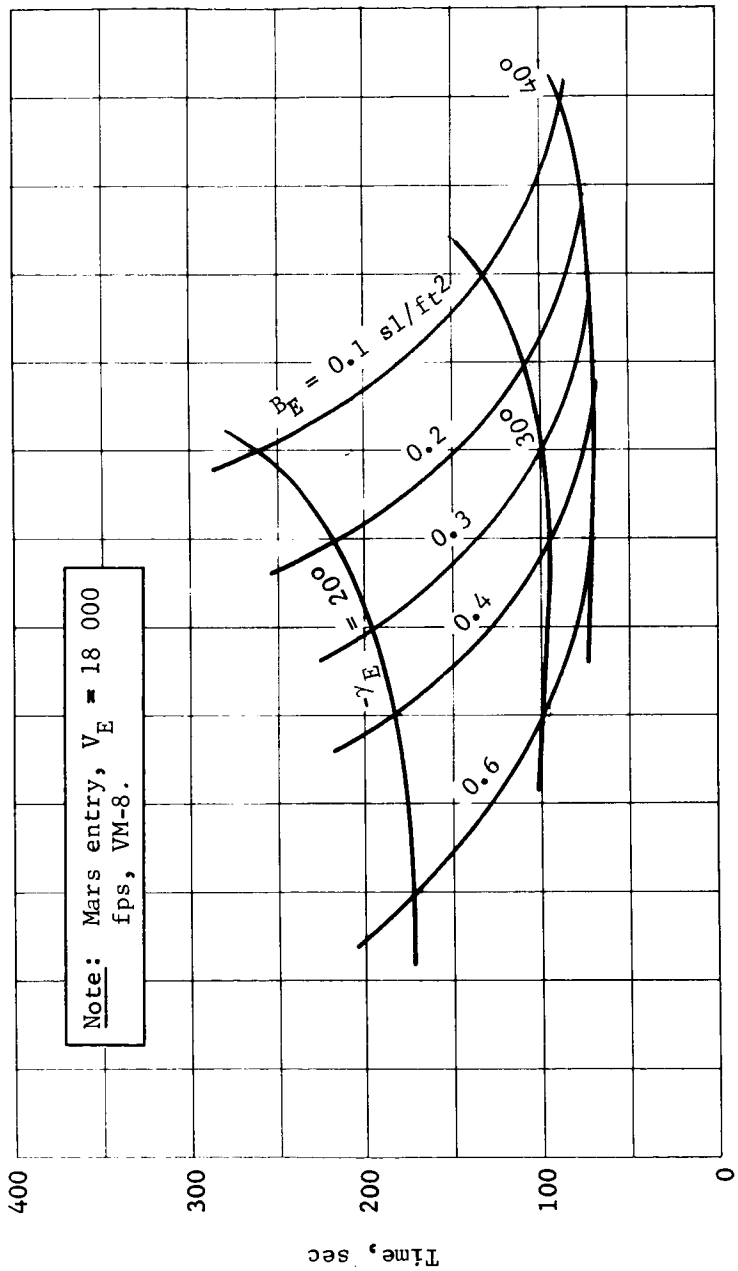

Figure B12.- Time from Entry to 20 000-ft Altitude

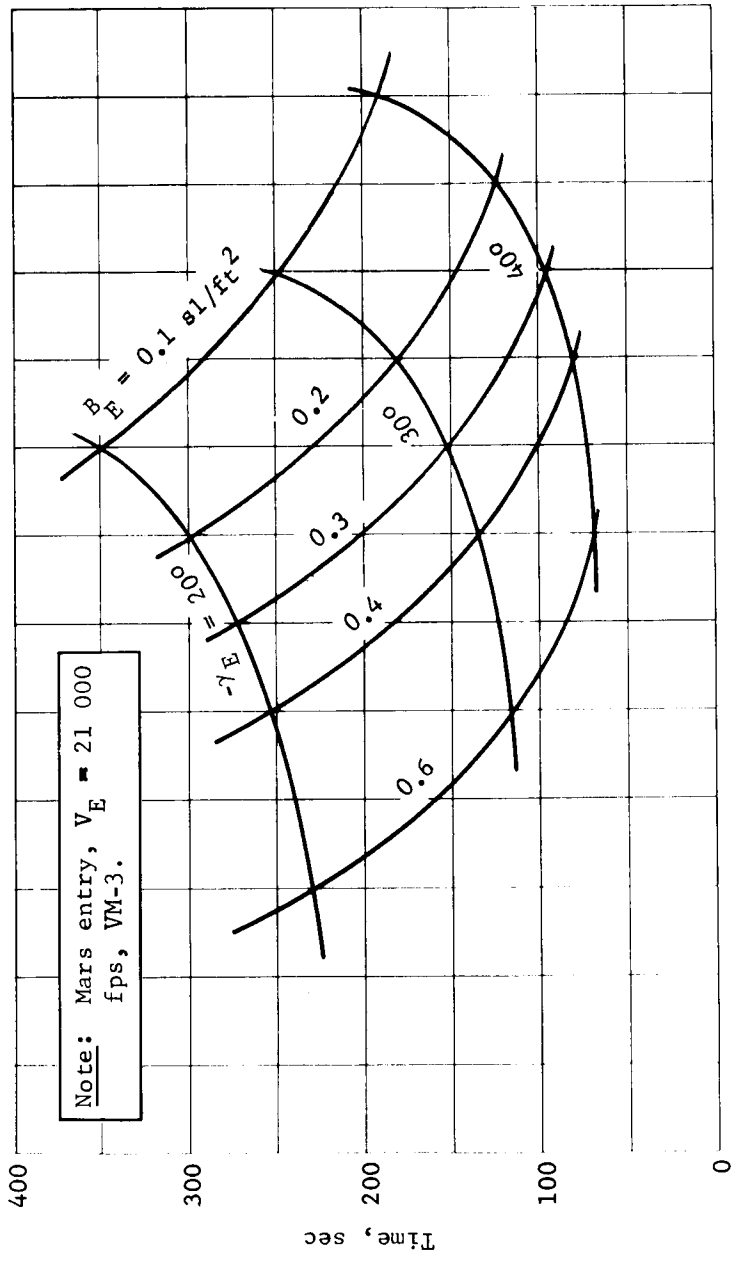

Figure B13.- Time from Entry to 20 000-ft Altitude

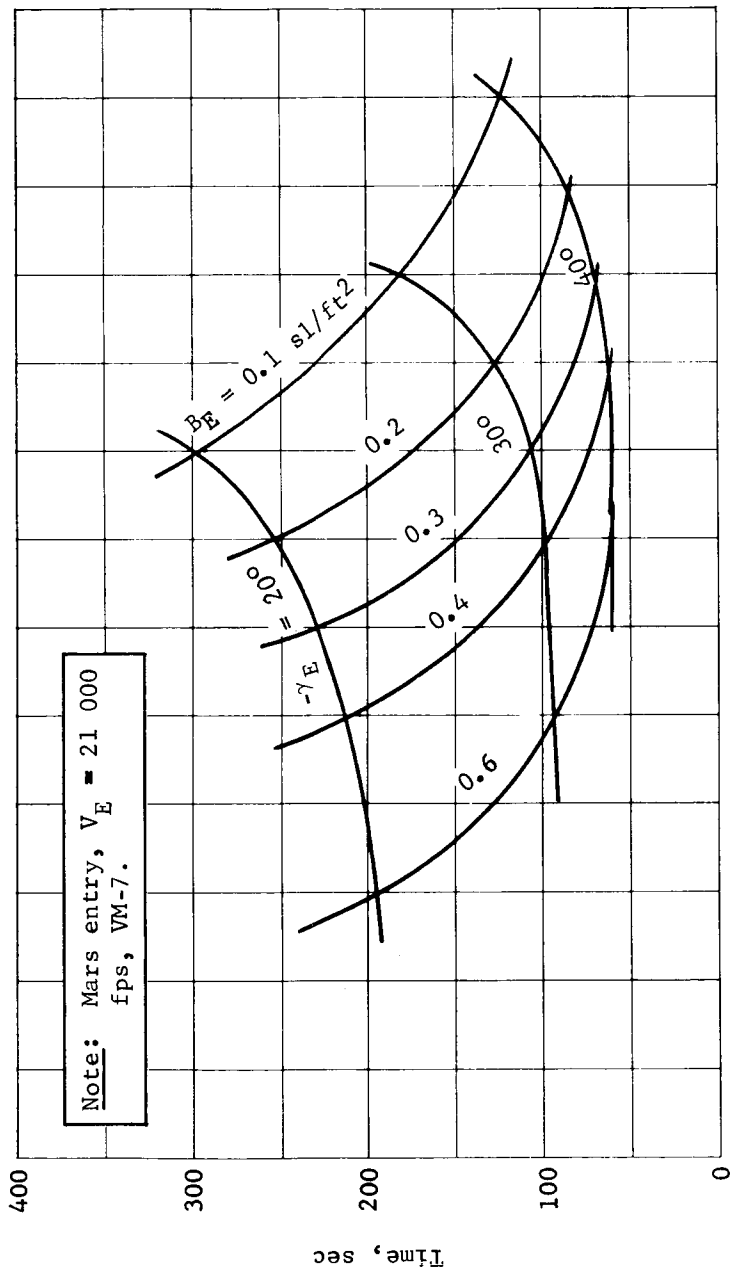

Figure B14.- Time from Entry to 20 000-ft Altitude

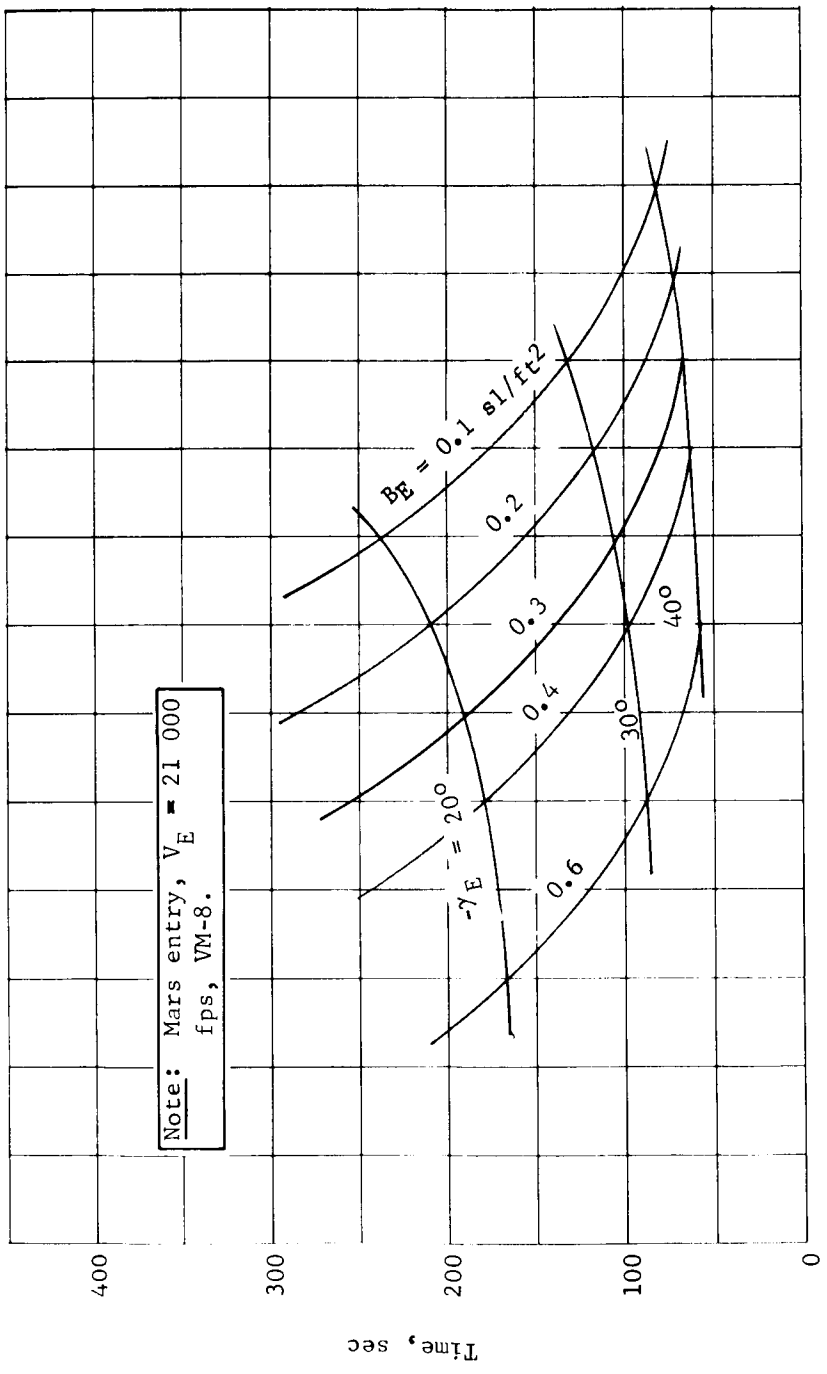

Figure B15.- Time from Entry to 20 000-ft altitude

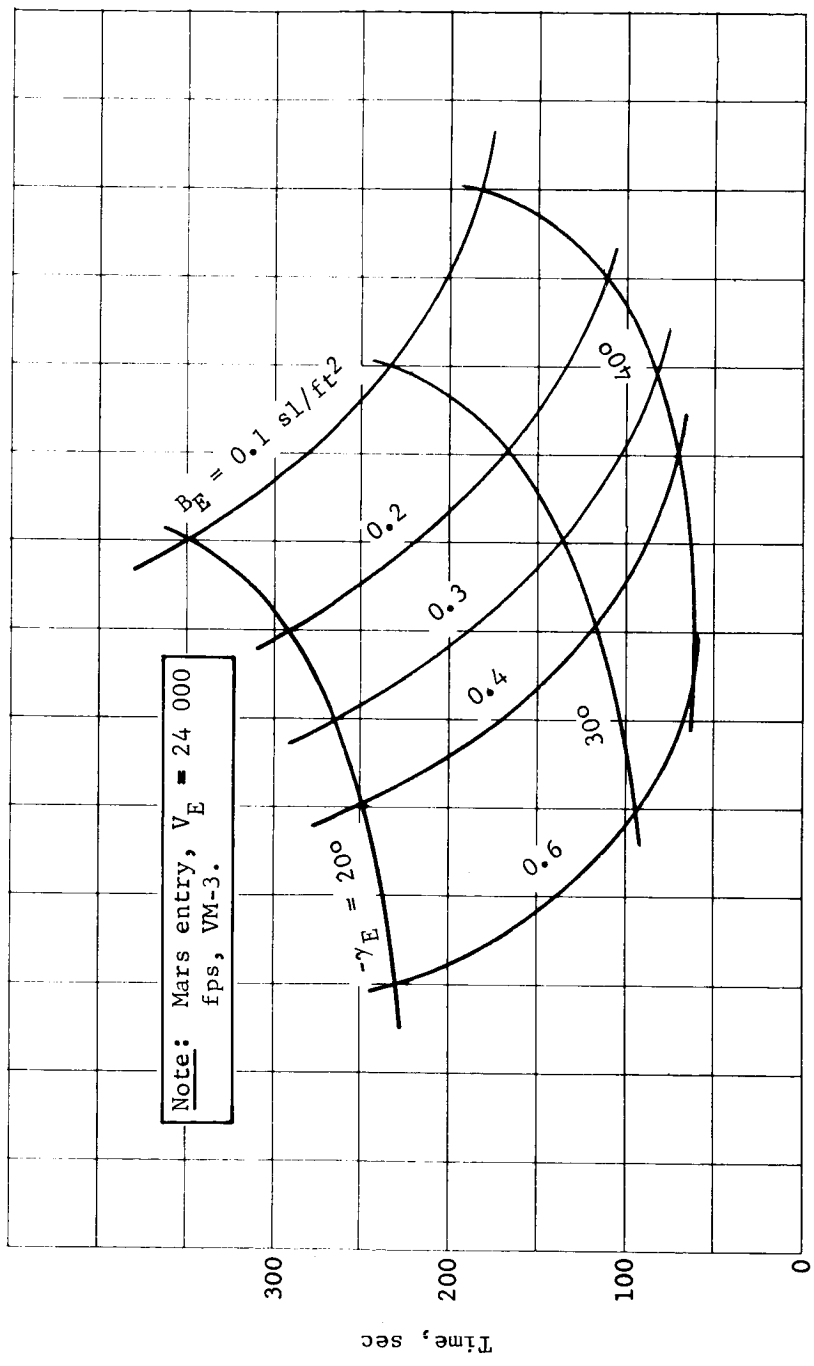

Figure B16.- Time from Entry to 20 000-ft Altitude

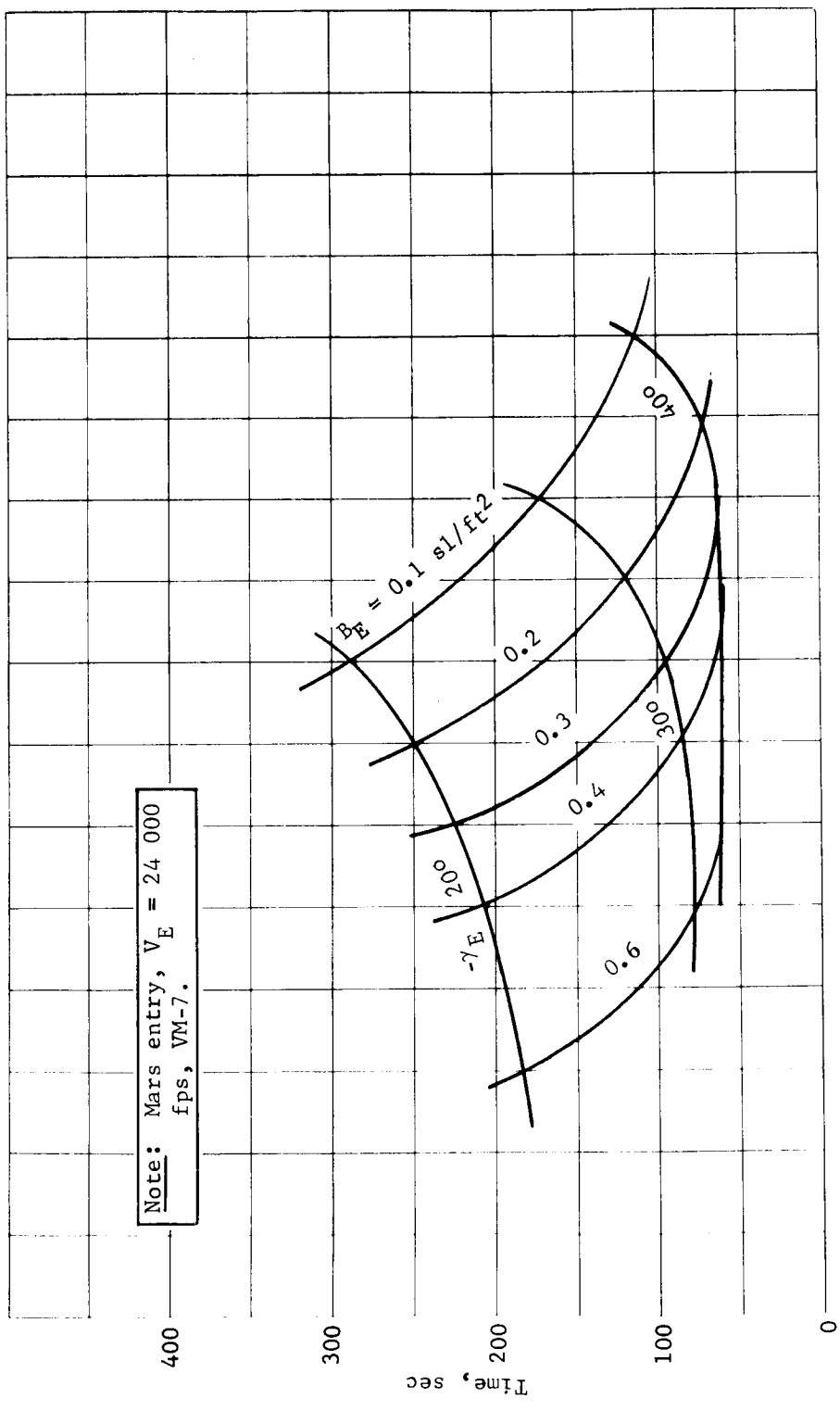

Figure B17.- Time from Entry to 20 000-ft Altitude

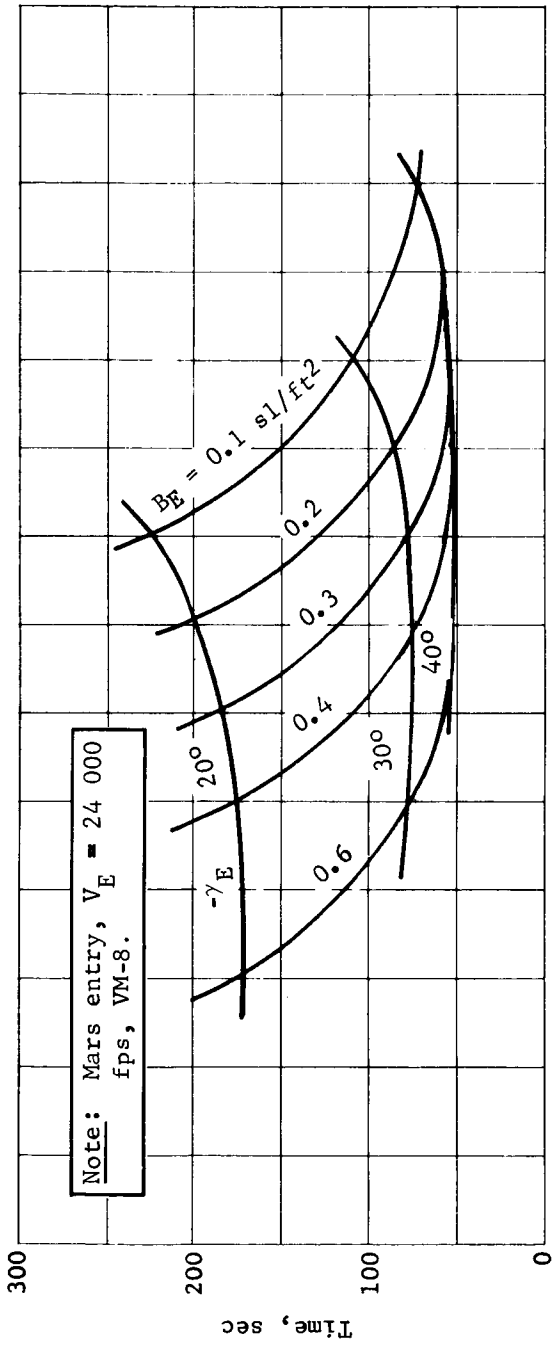

Figure B18.- Time from Entry to 20 000-ft Altitude

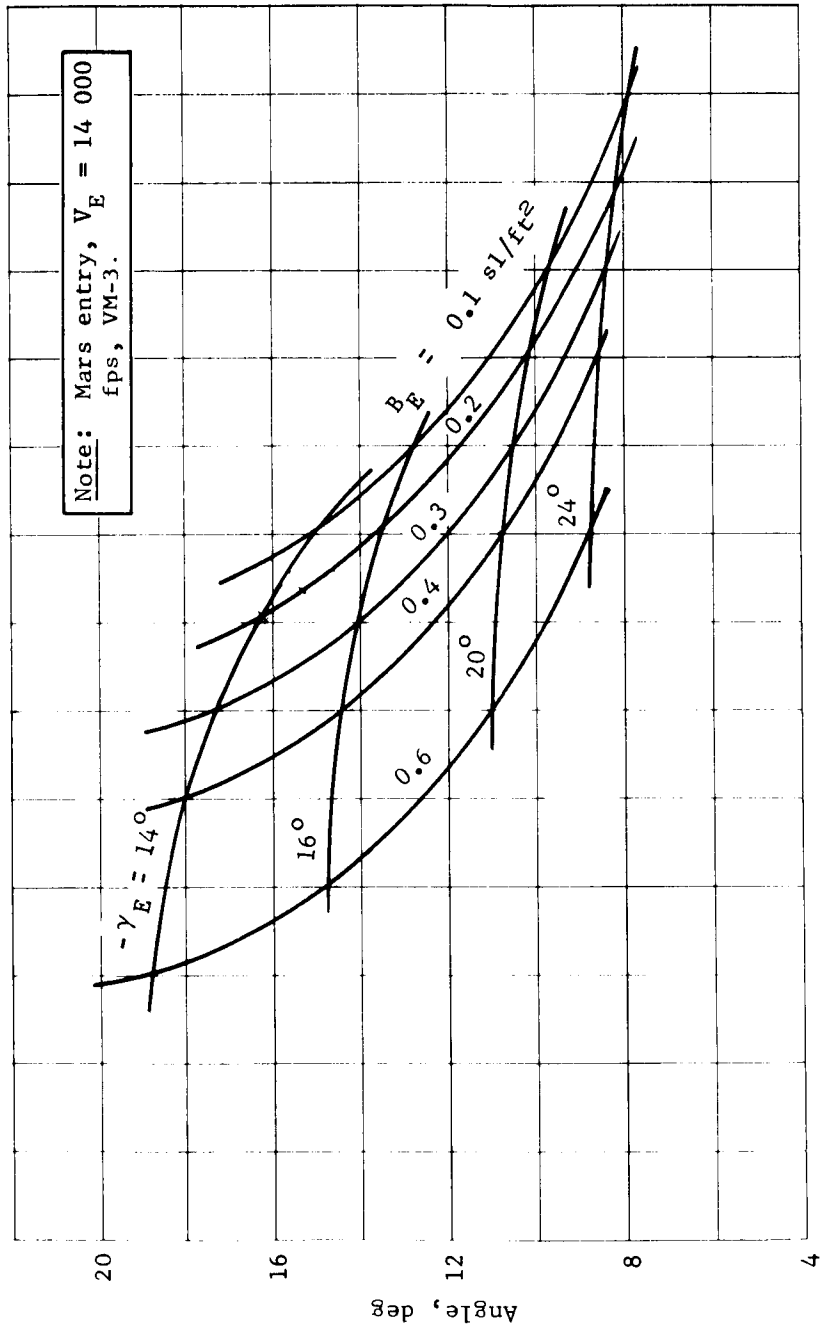

Figure B19.- Downrange Angle Entry to 20 000-ft Altitude

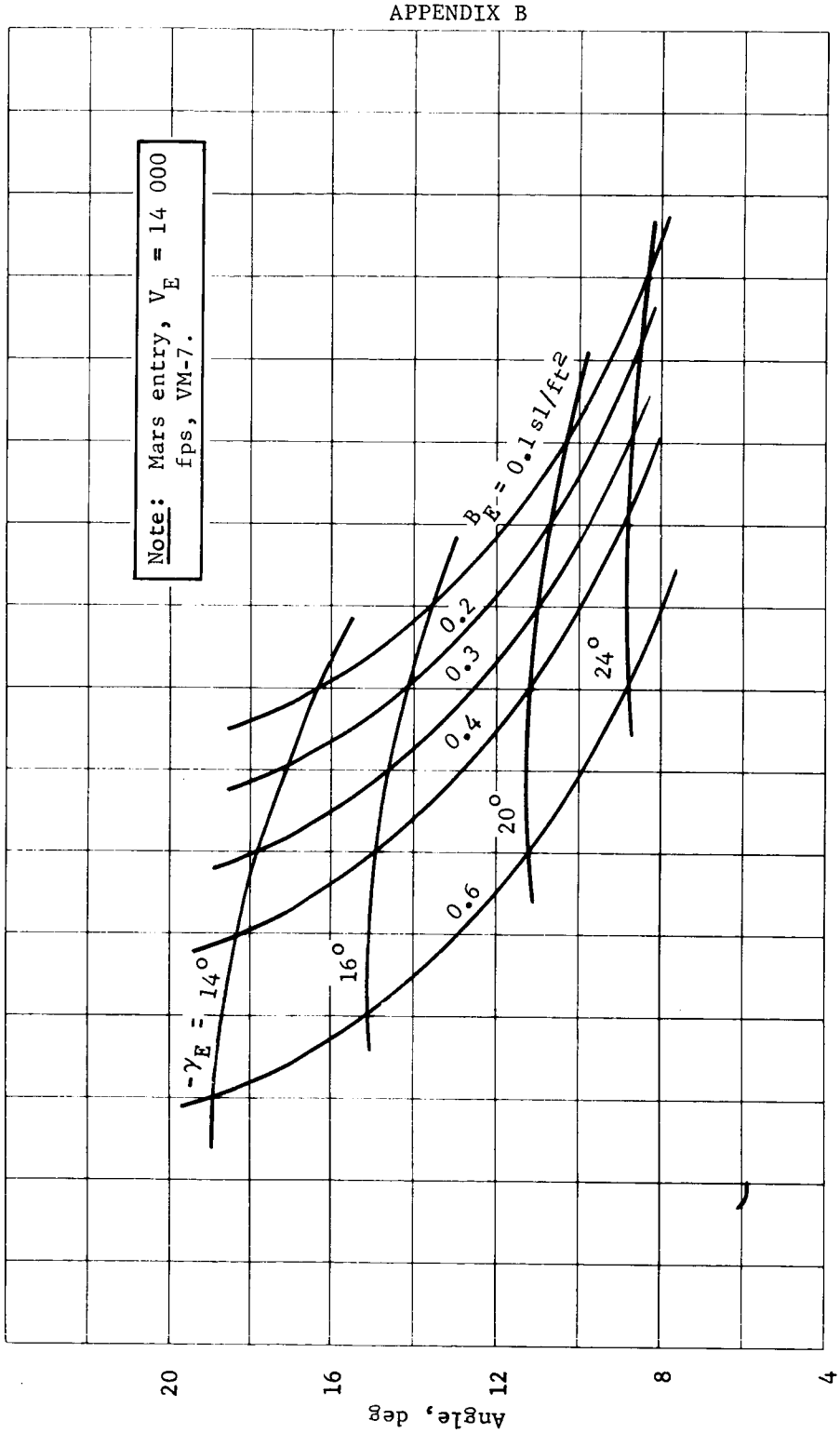

Figure B20.- Downrange Angle Entry to 20 000-ft Altitude

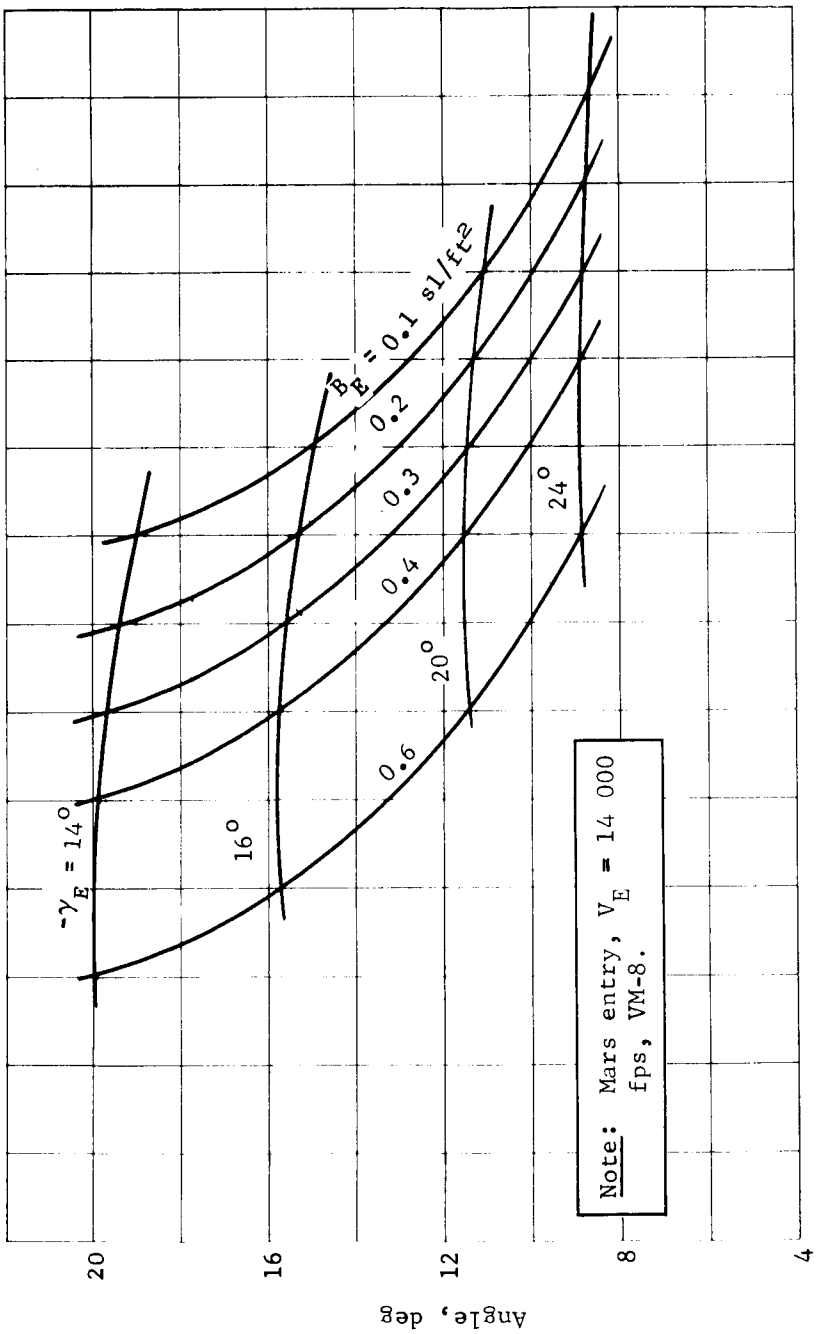

Figure B21.- Downrange Angle Entry to 20 000-ft Altitude

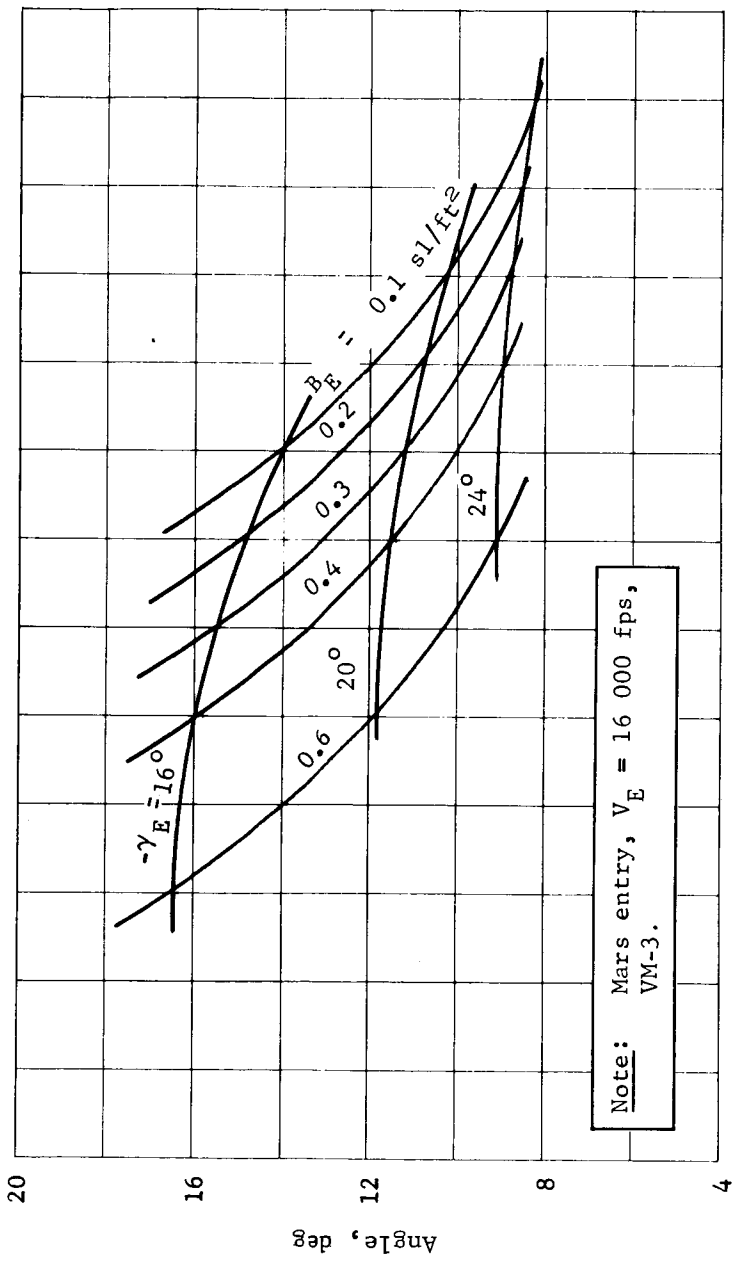

Figure B22.- Downrange Angle Entry to 20 000-ft Altitude

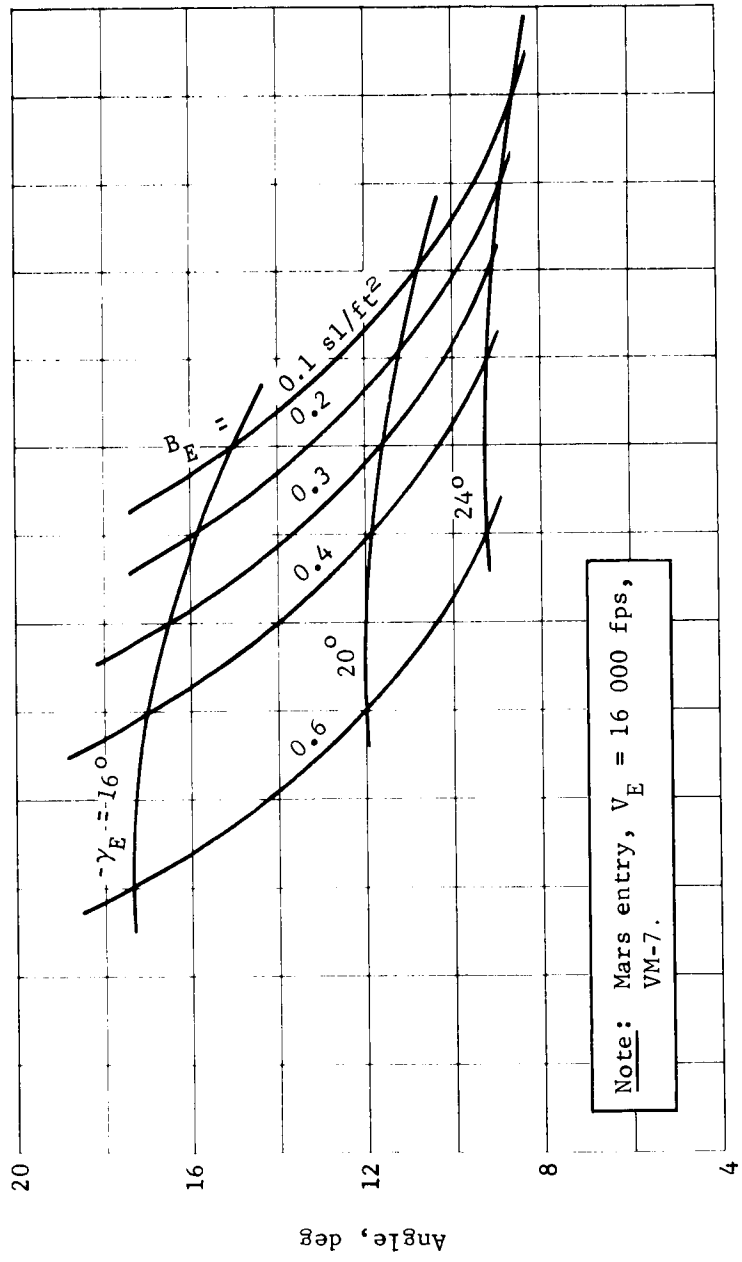

Figure B23.- Downrange Angle Entry to 20 000-ft Altitude

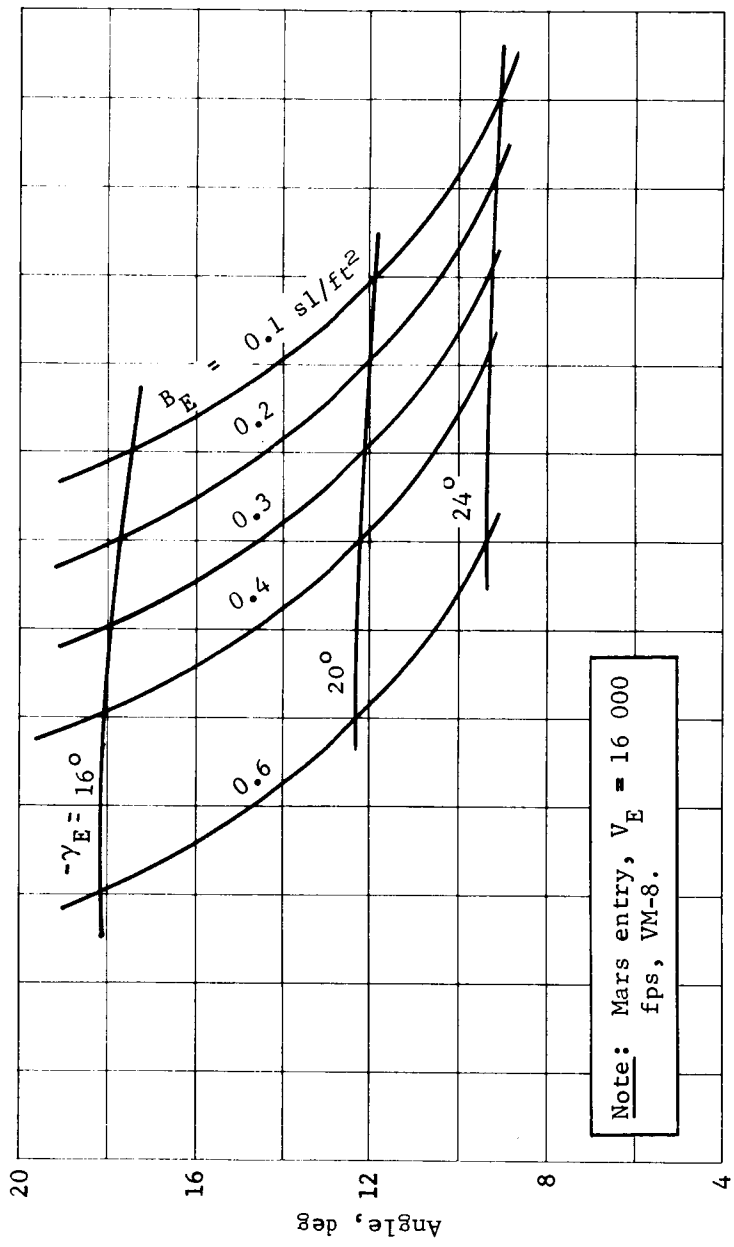

Figure B24.- Downrange Angle Entry to 20 000-ft Altitude

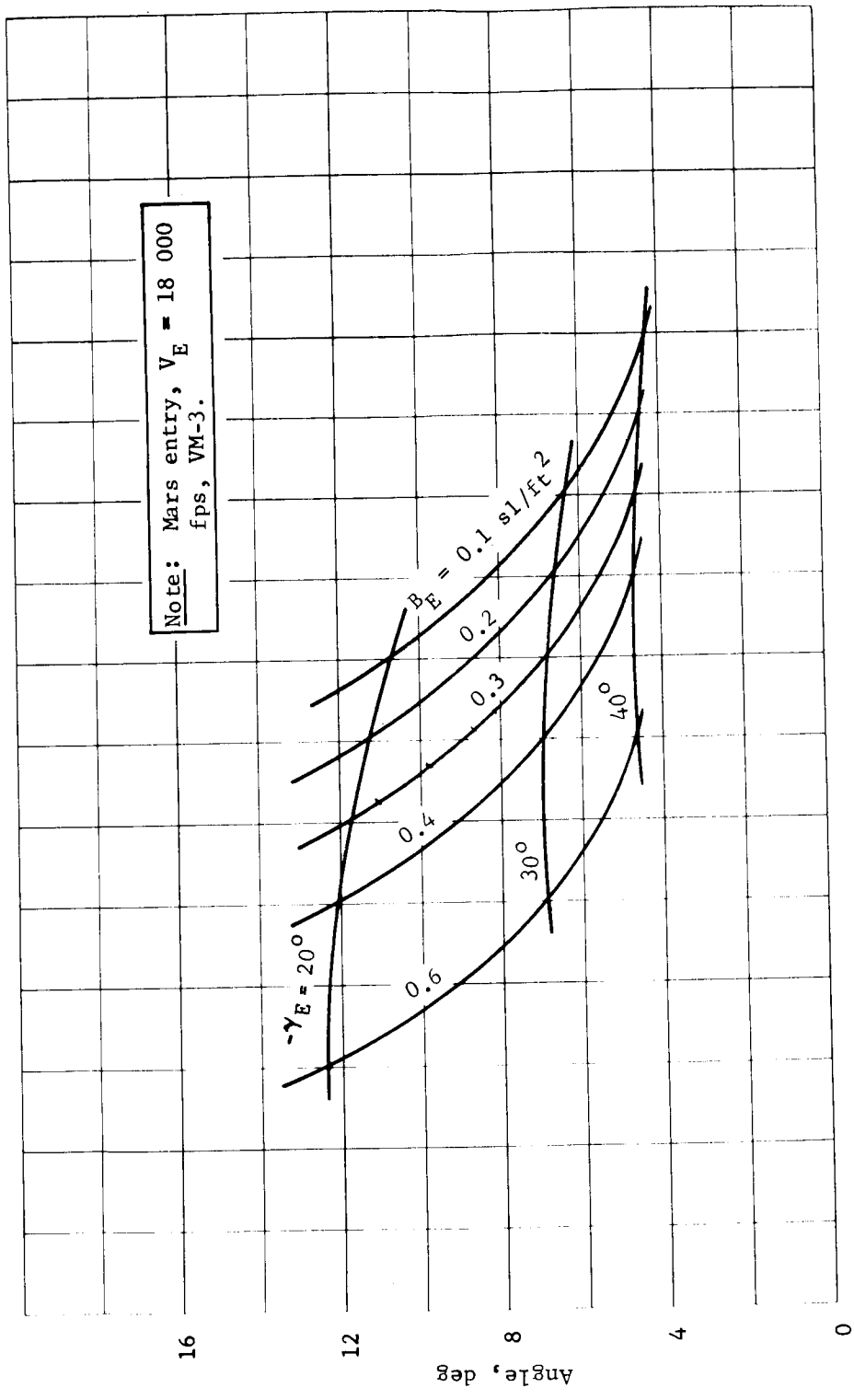

Figure B25.- Downrange Angle Entry to 20 000-ft Altitude

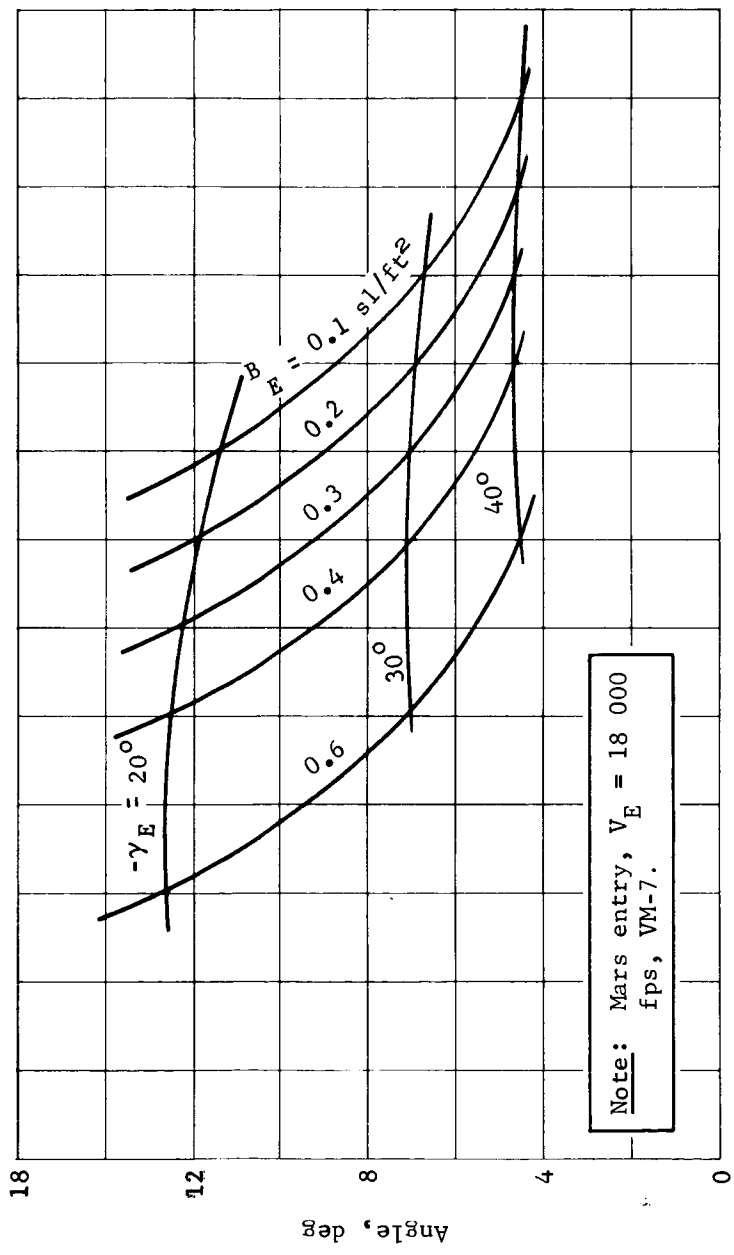

Figure B26.- Downrange Angle Entry to 20 000-ft Altitude

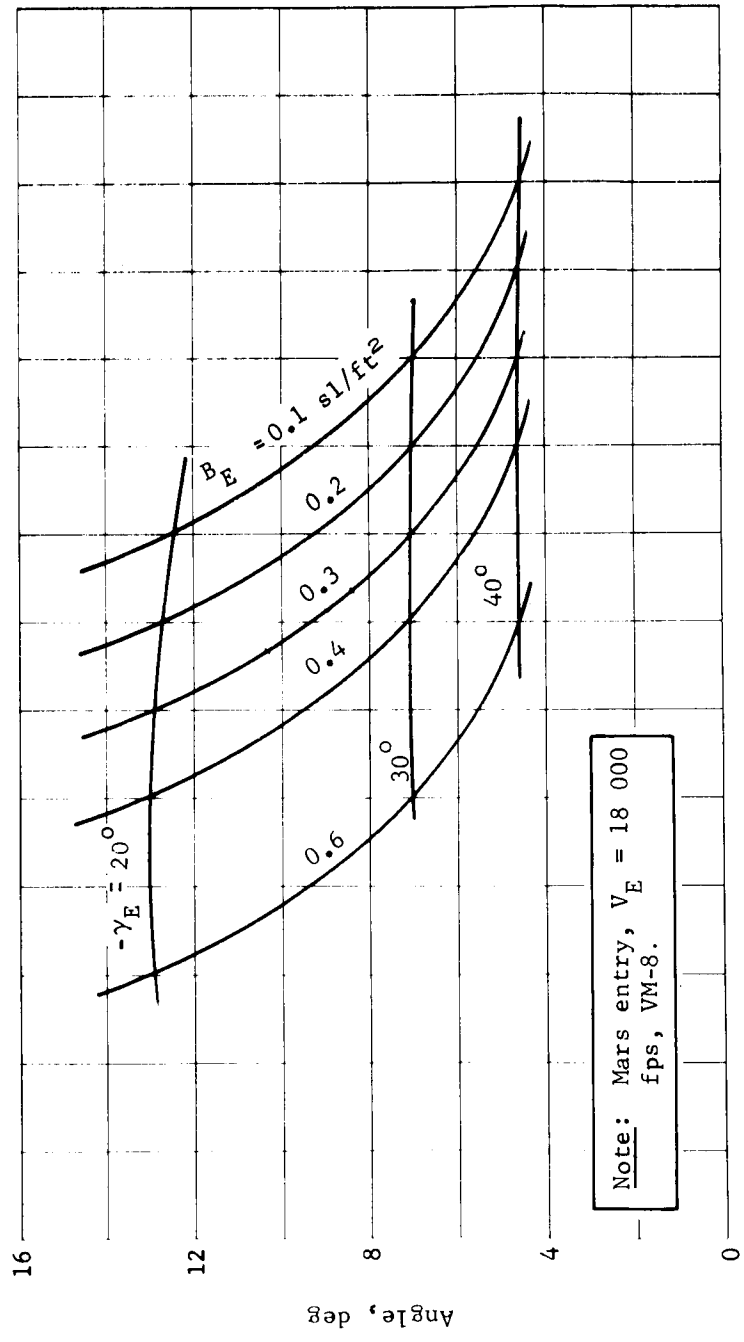

Figure B27.- Downrange Angle Entry to 20 000-ft Altitude

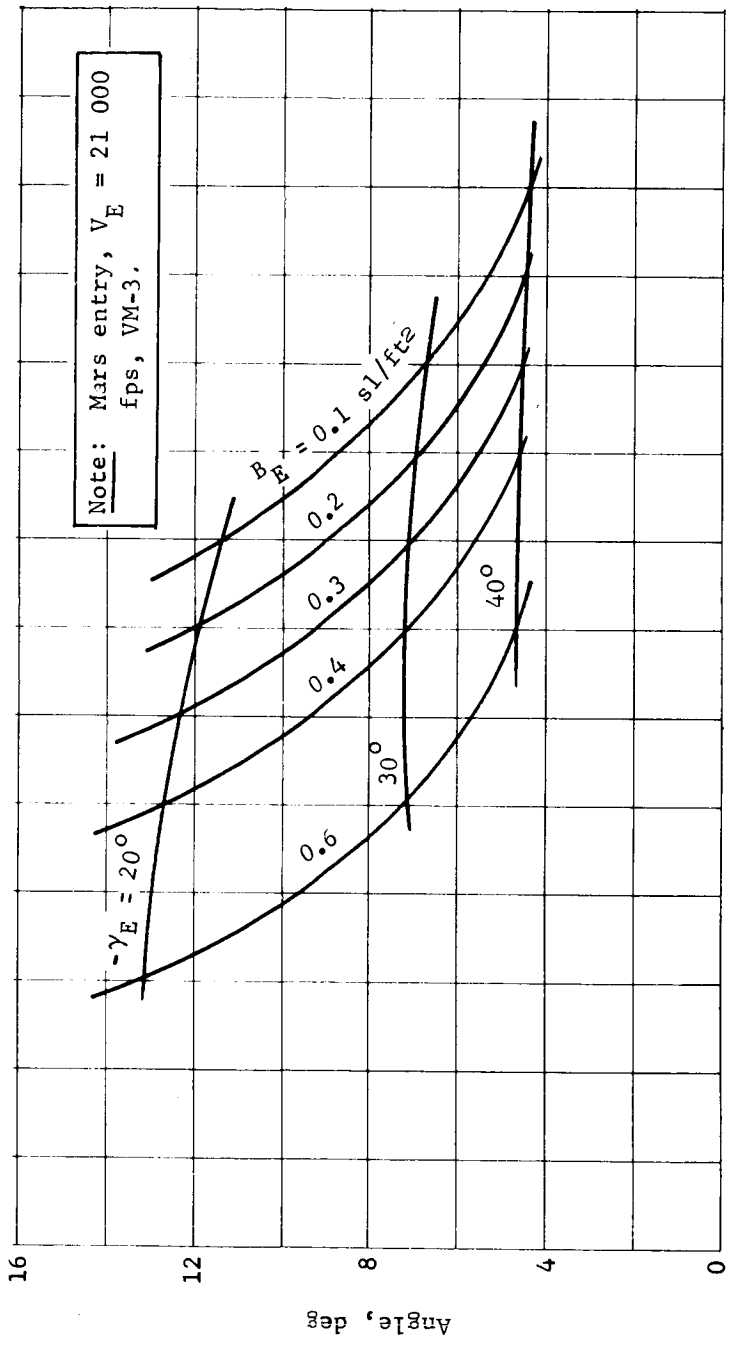

Figure B28.- Downrange Angle Entry to 20 000-ft Altitude

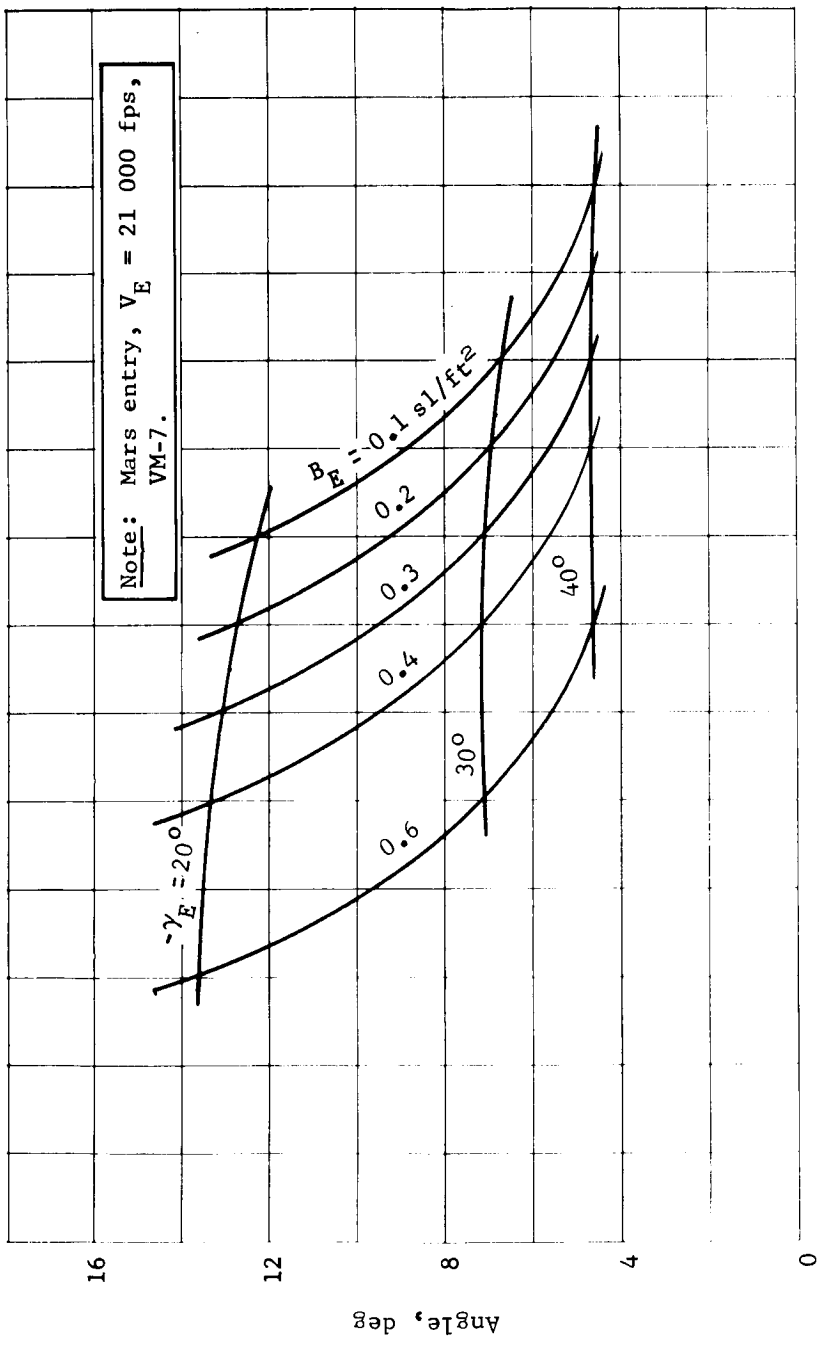

Figure B29.- Downrange Angle Entry to 20 000-ft Altitude

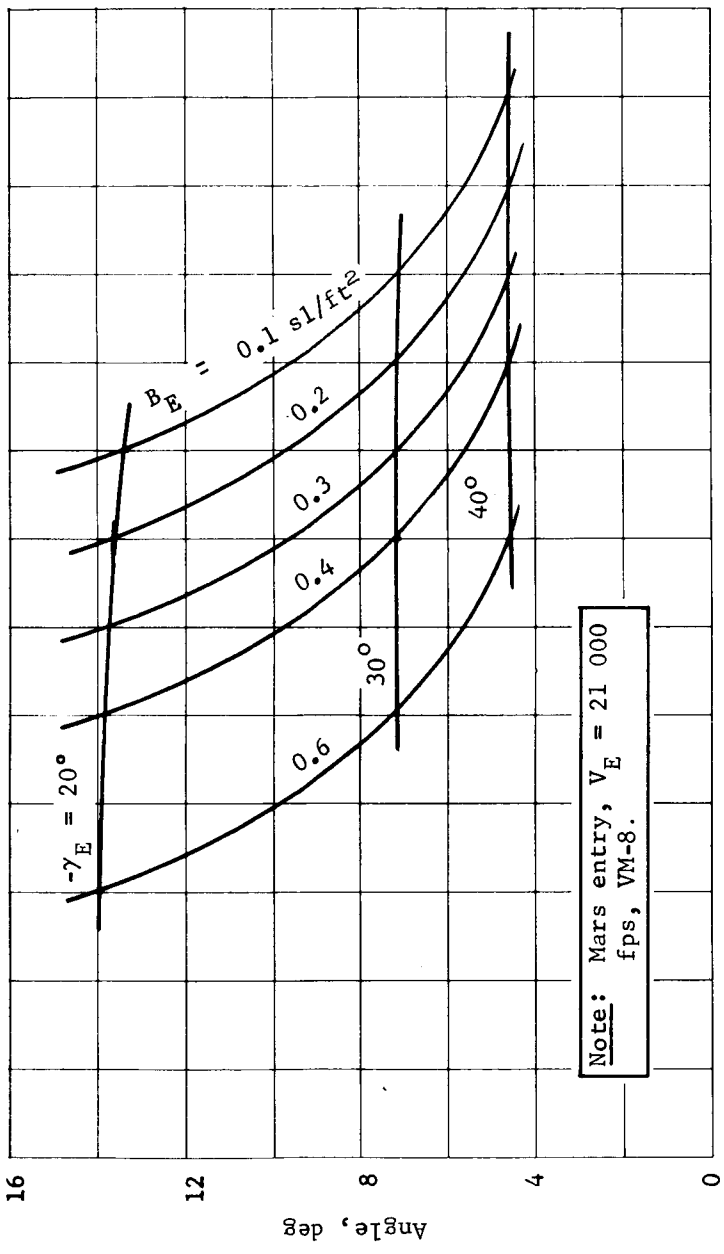

Figure B30.- Downrange Angle Entry to 20 000-ft Altitude

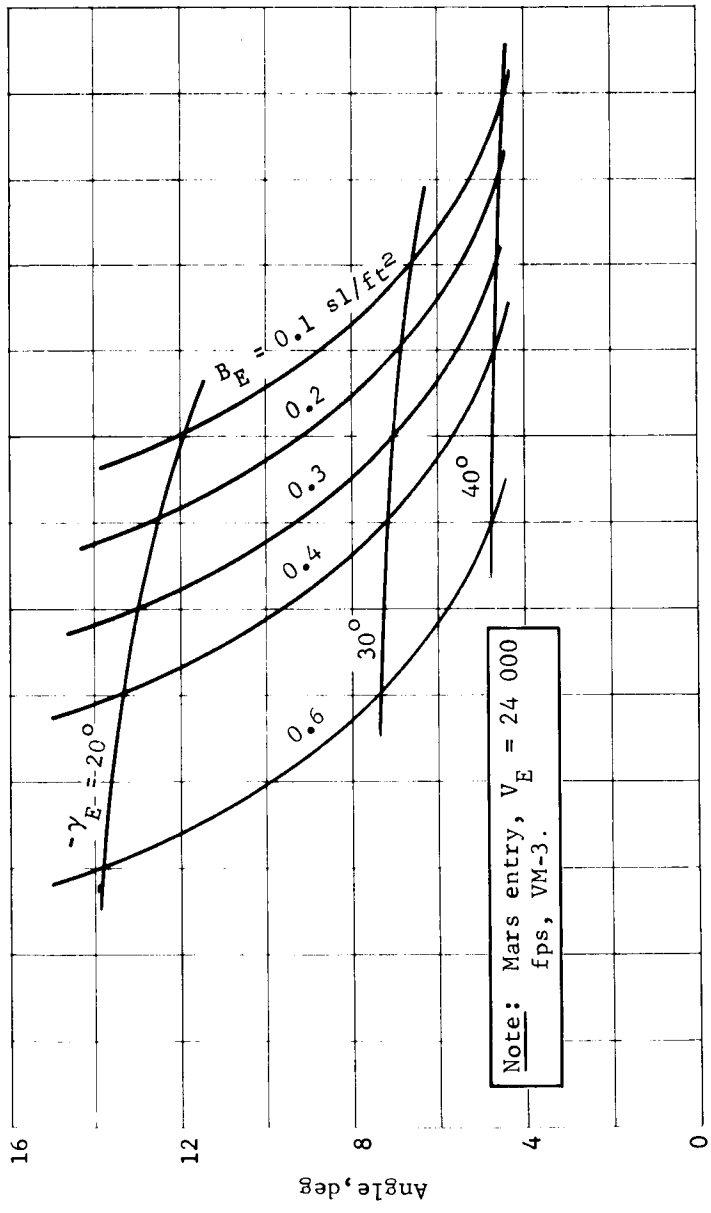

Figure B31. - Downrange Angle Entry to 20 000-ft Altitude

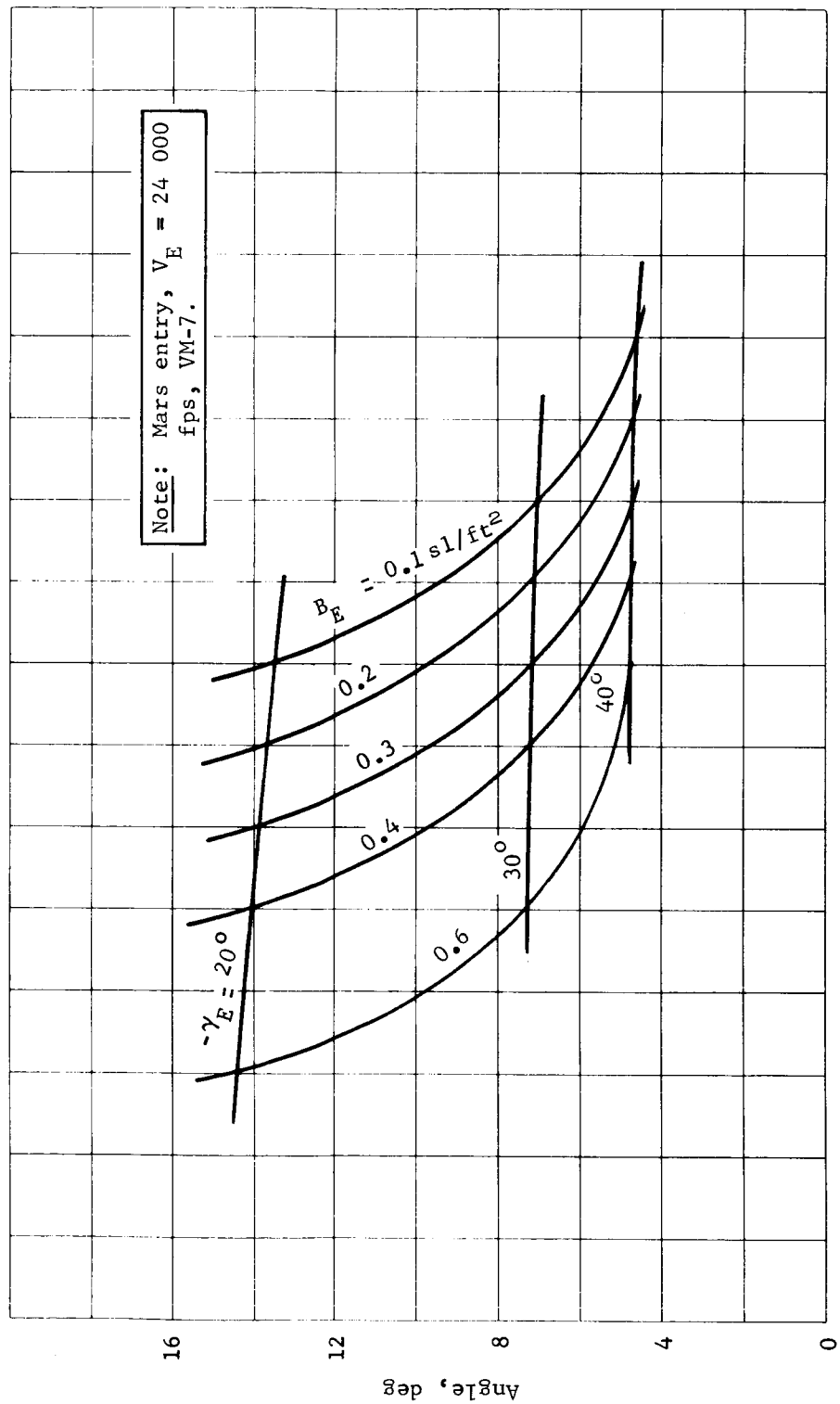

Figure B32.- Downrange Angle Entry to 20 000-ft Altitude

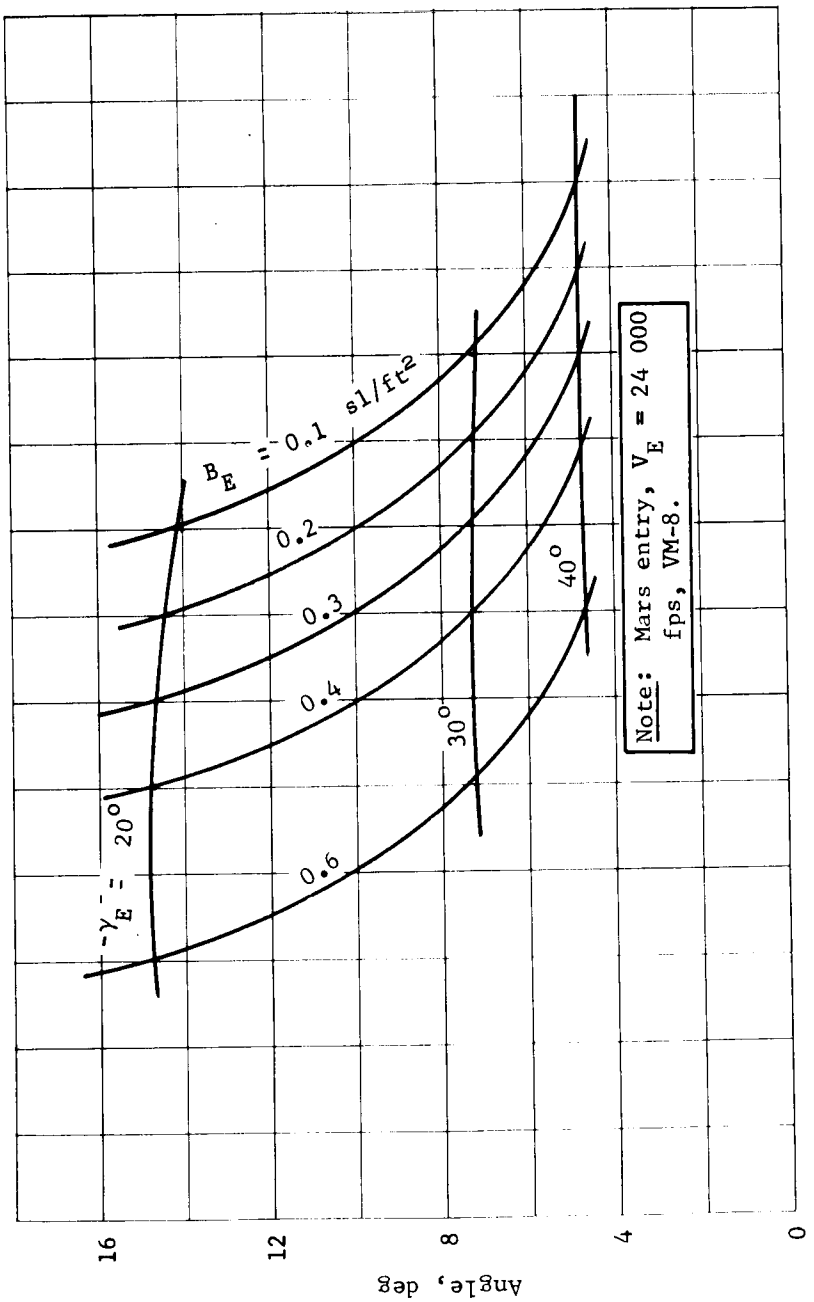

Figure B33.- Downrange Angle Entry to 20 000-ft Altitude

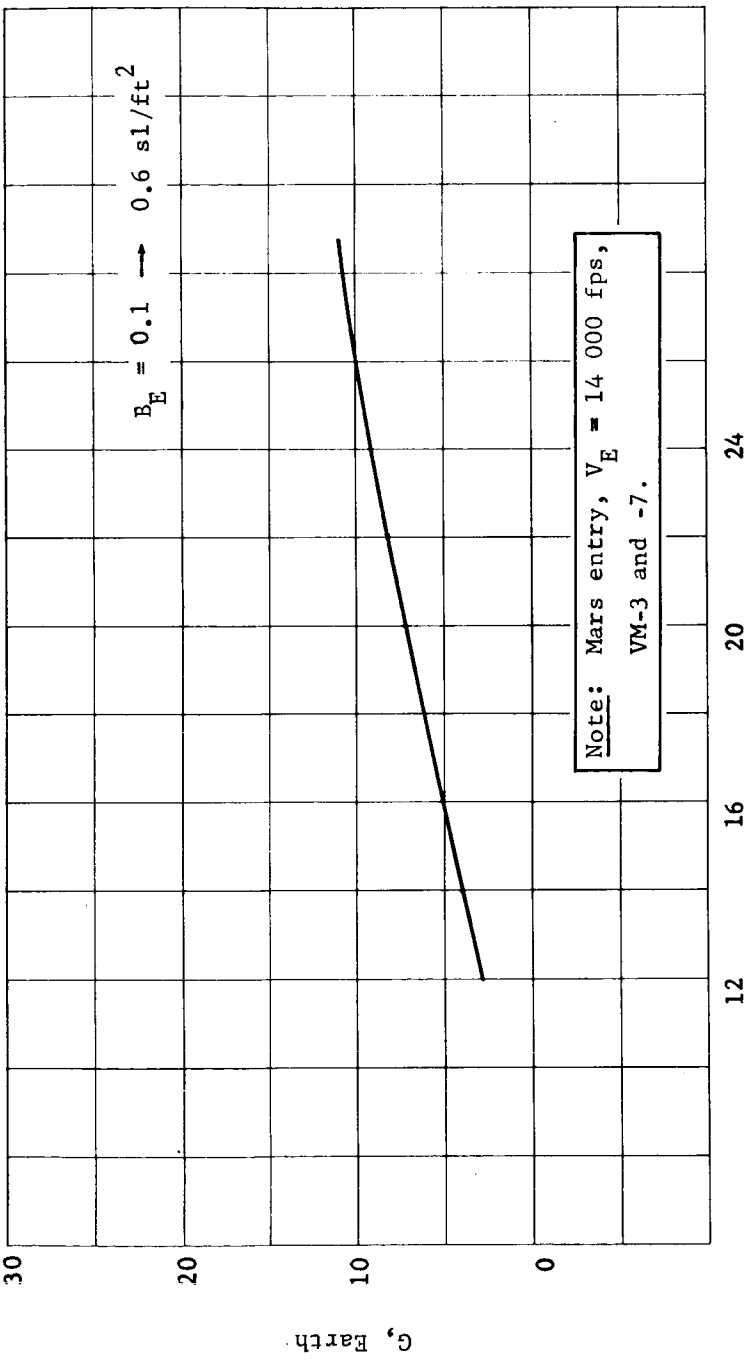

Figure B34.- Peak Drag Deceleration

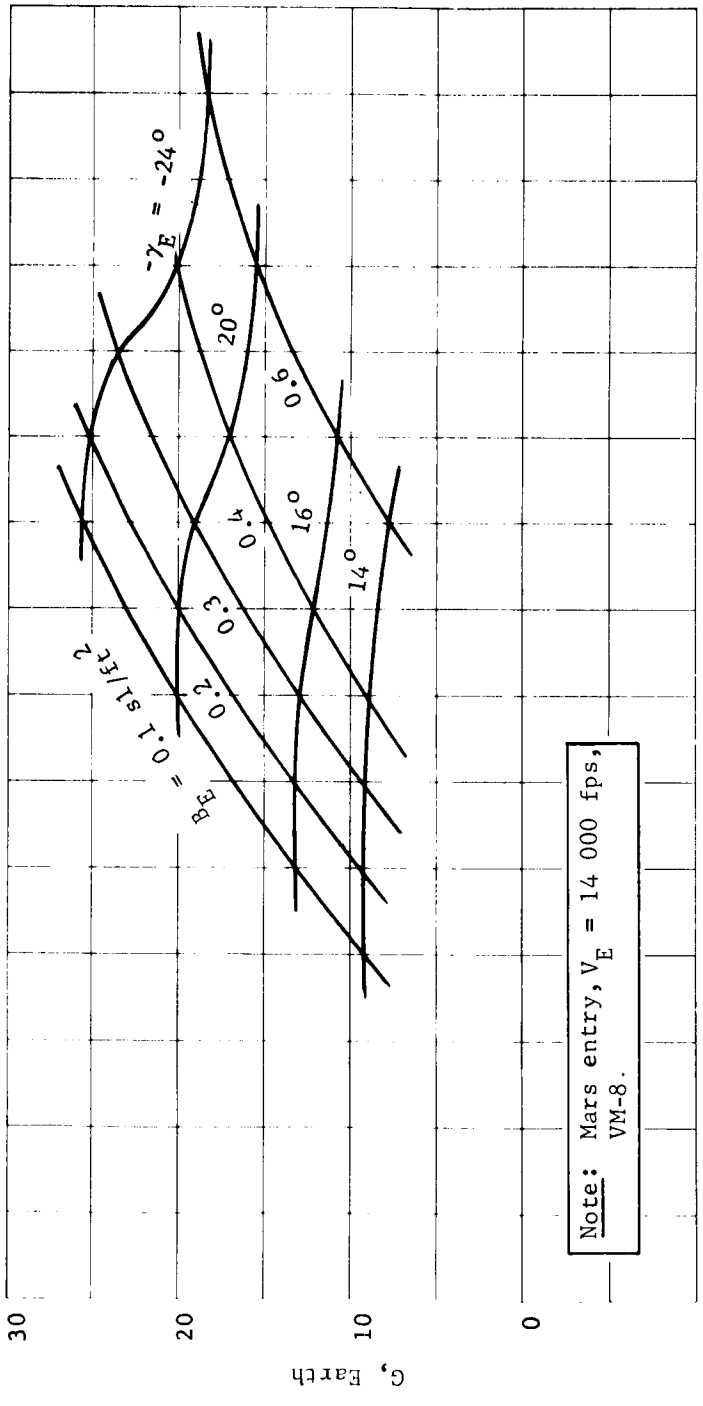

Figure B35.- Peak Drag Deceleration

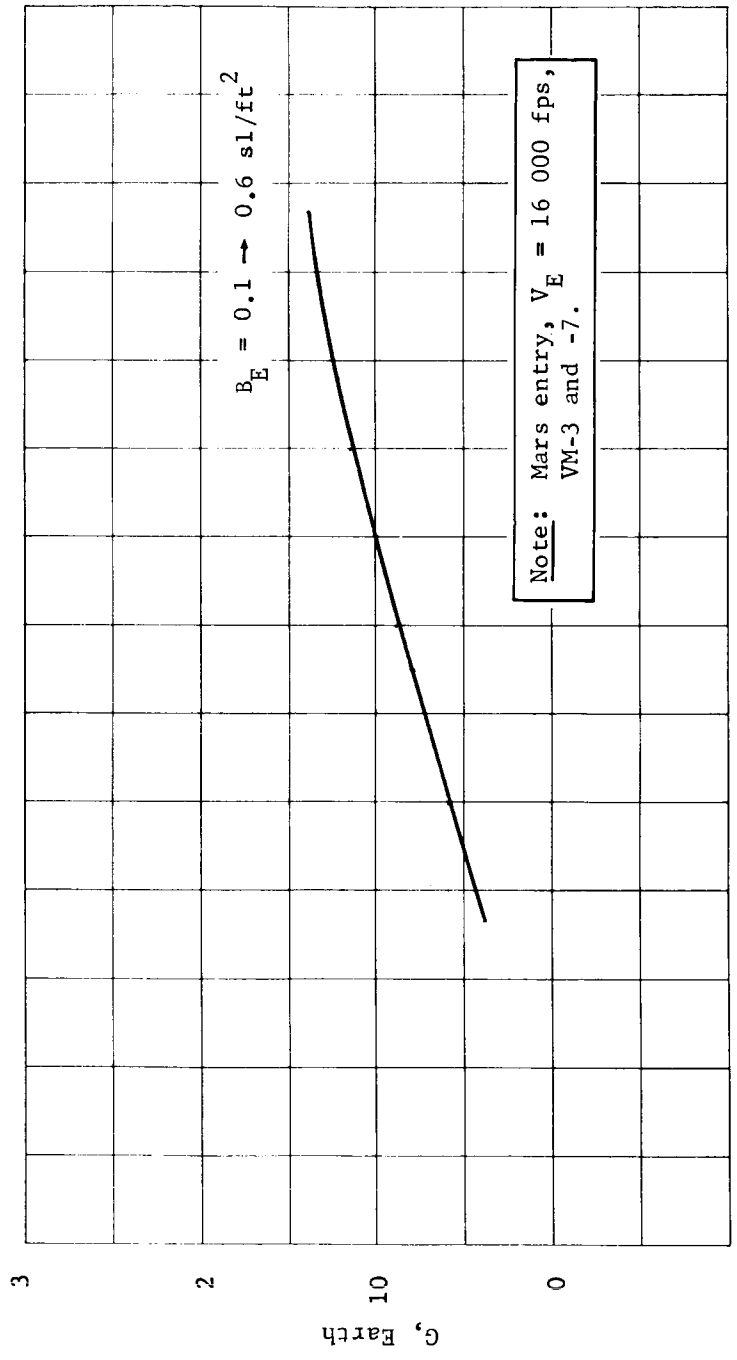

Figure B36.- Peak Drag Deceleration

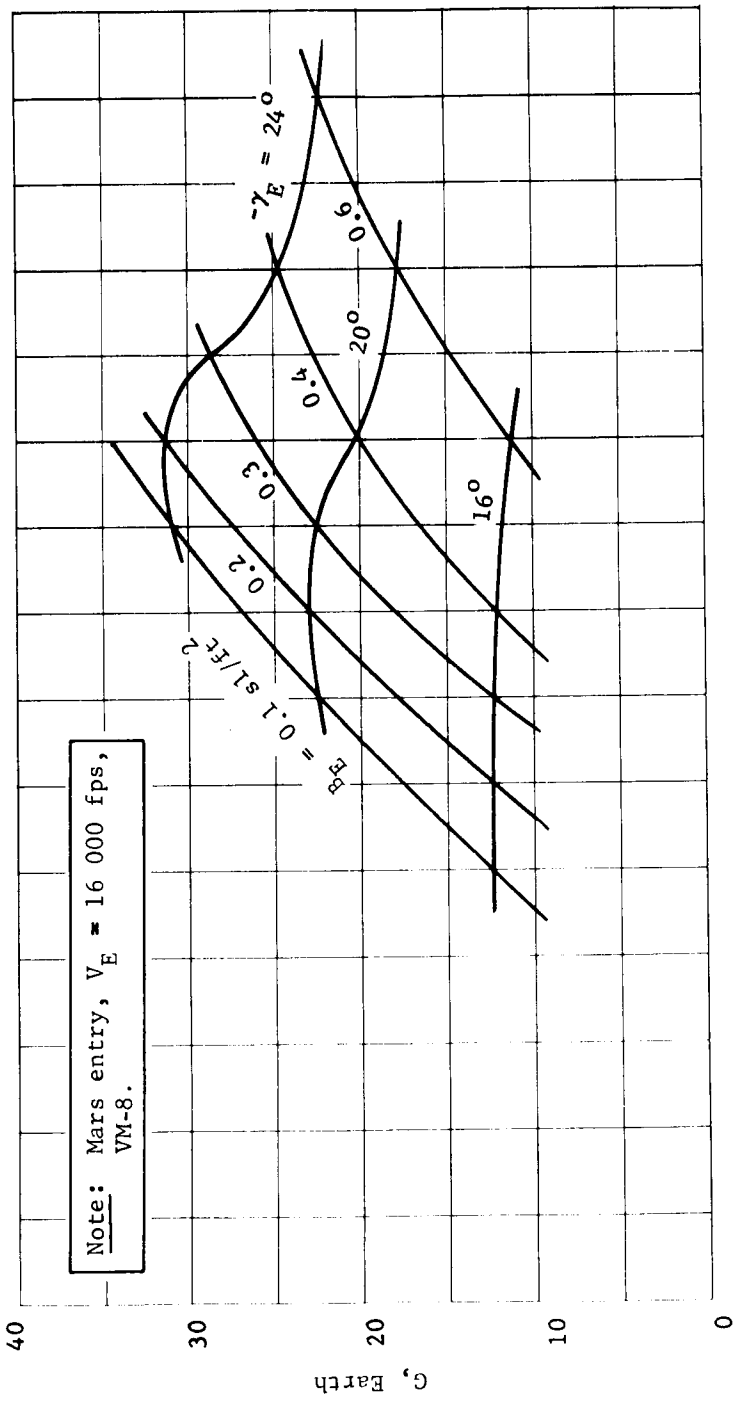

Figure B37.- Peak Drag Deceleration

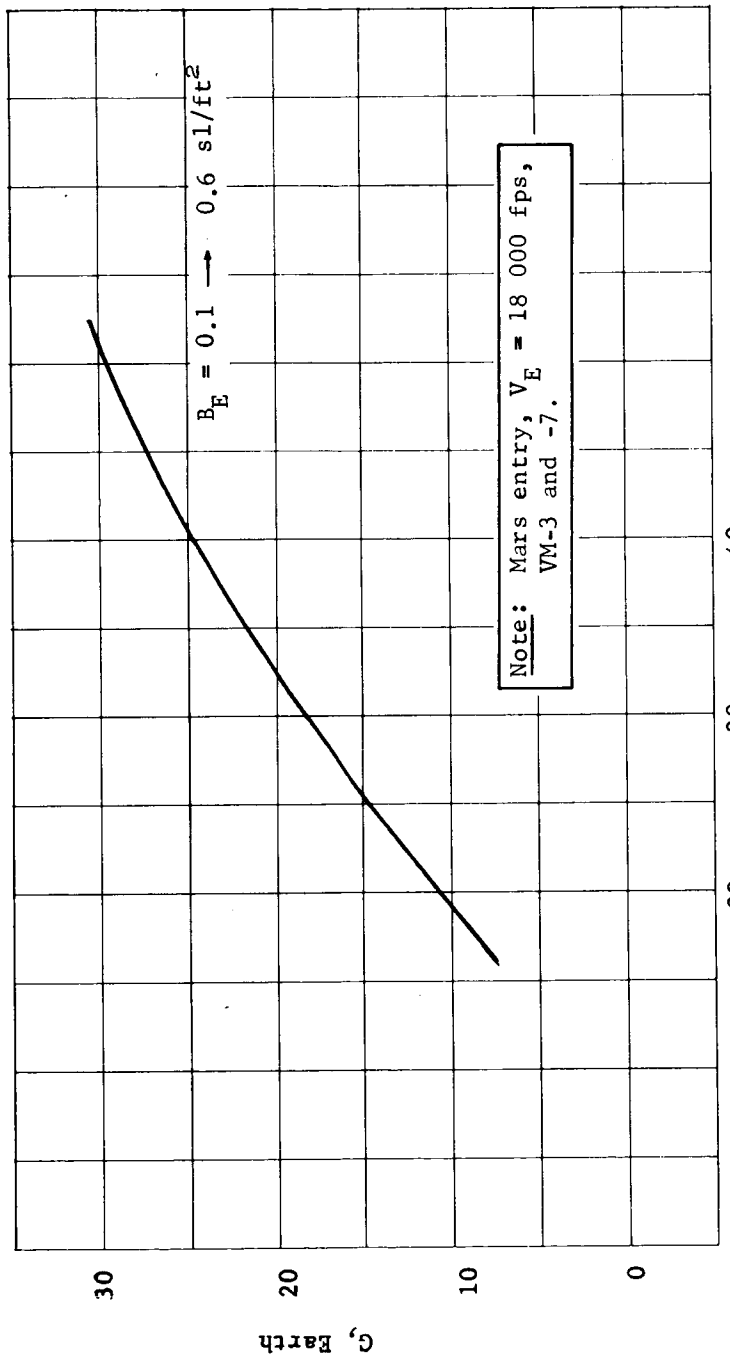

Figure B38.- Peak Drag Deceleration

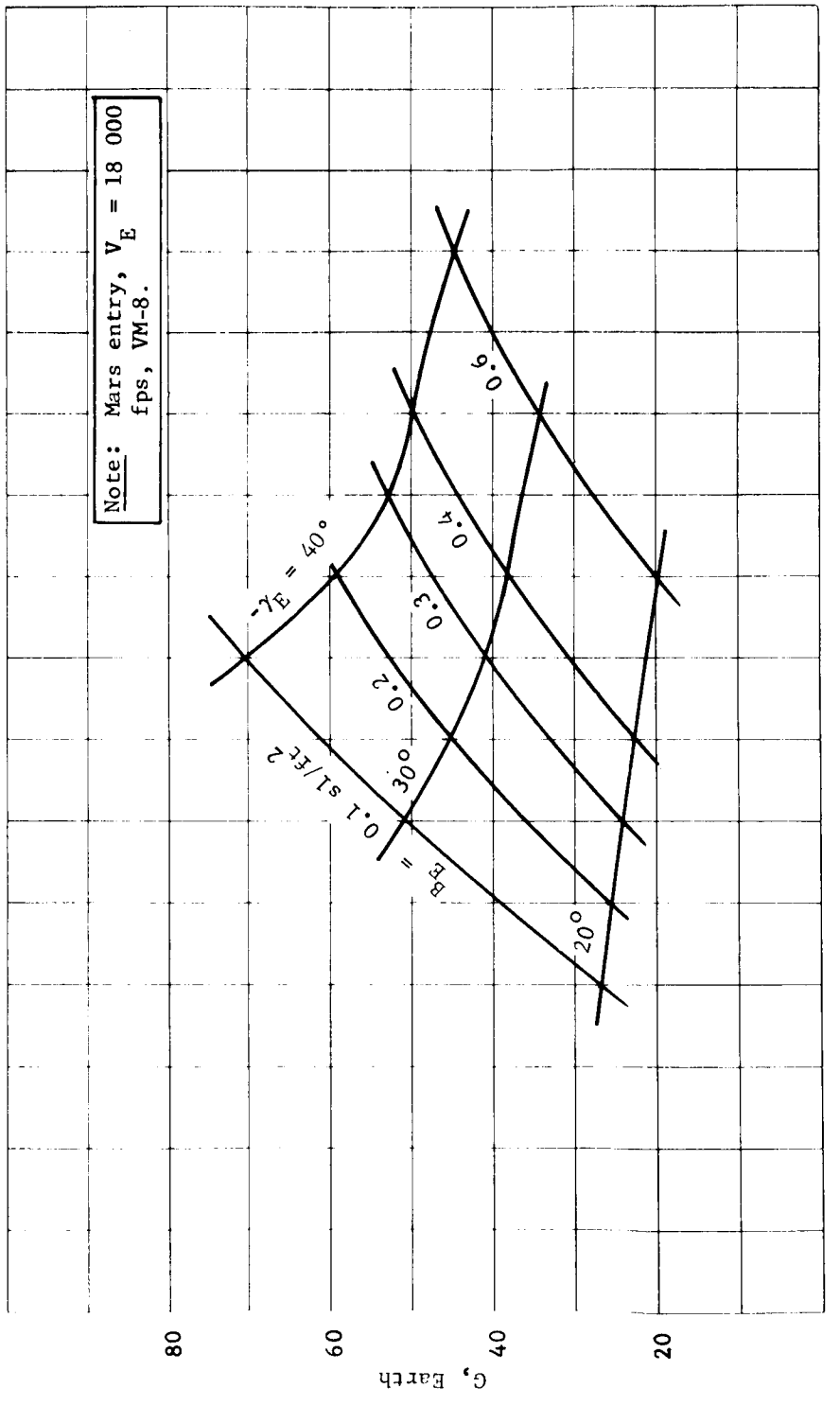

Figure B39.- Peak Drag Deceleration

APPENDIX B

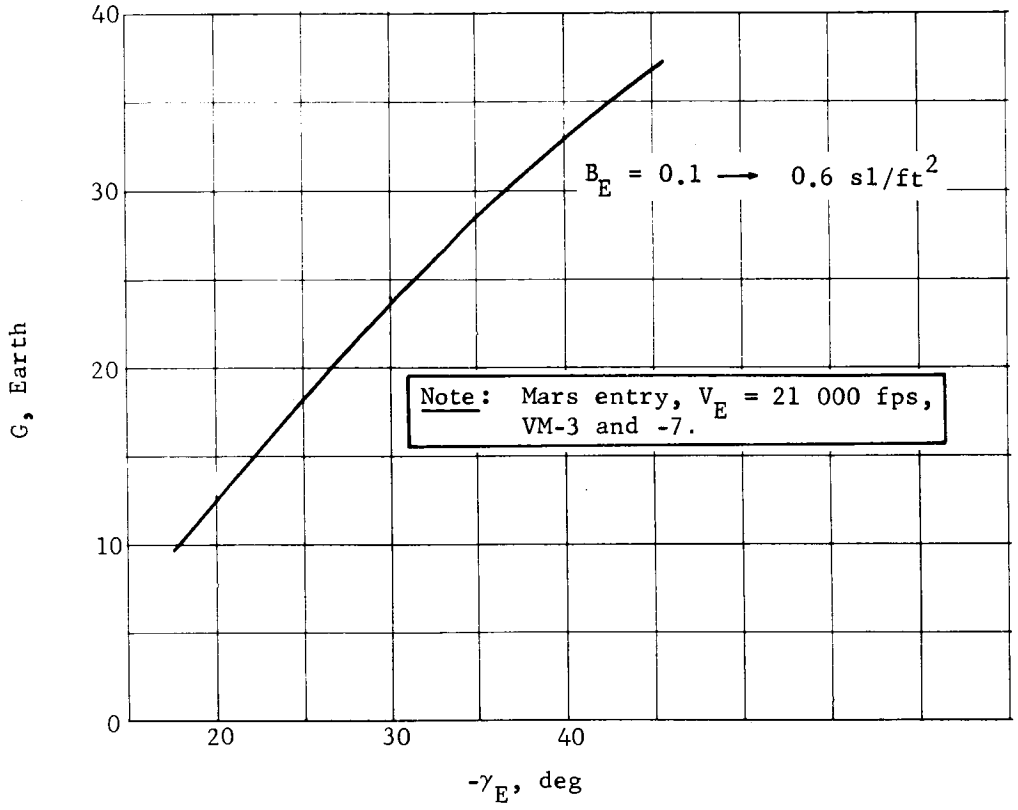

Figure B40.- Peak Drag Deceleration

APPENDIX B

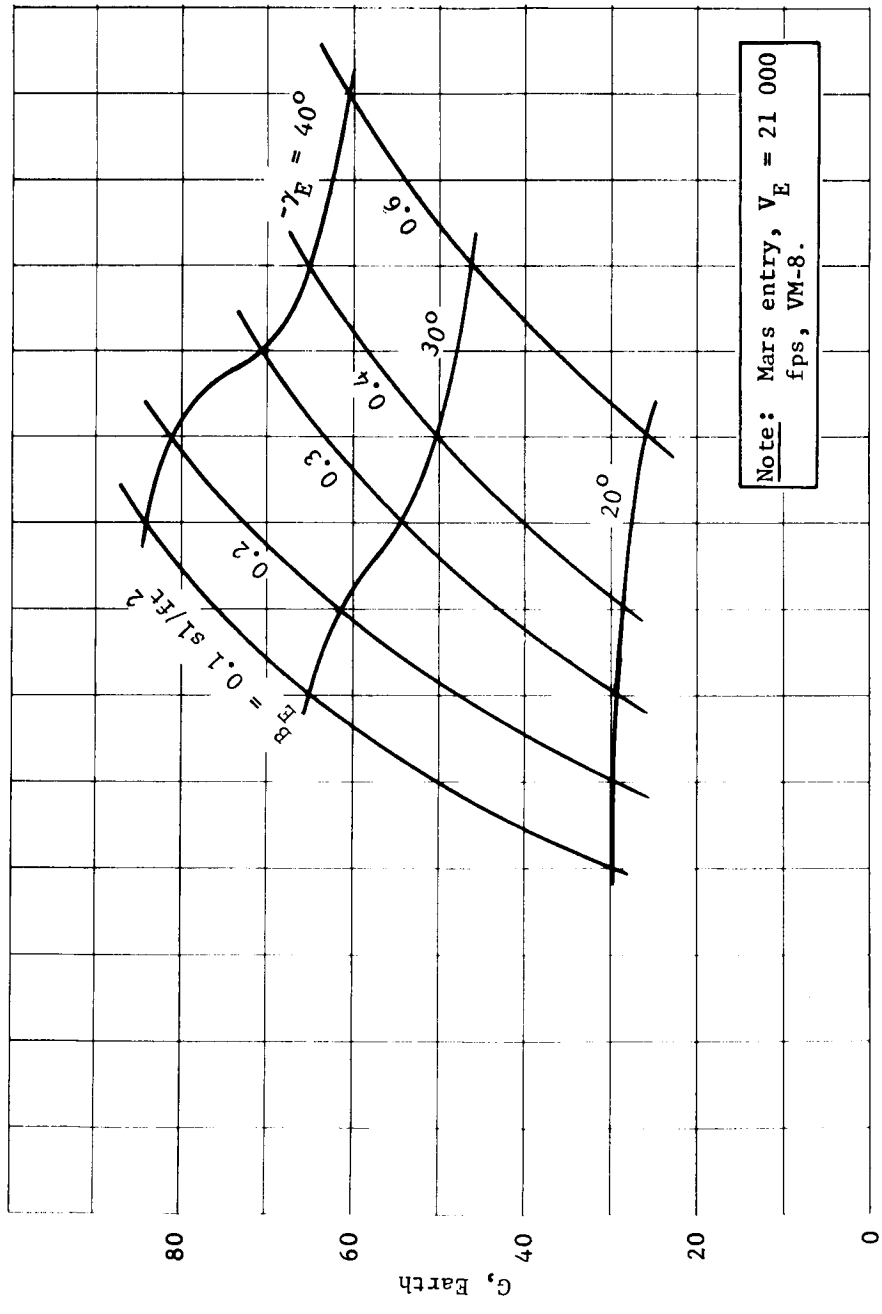

Figure B41.- Peak Drag Deceleration

APPENDIX B

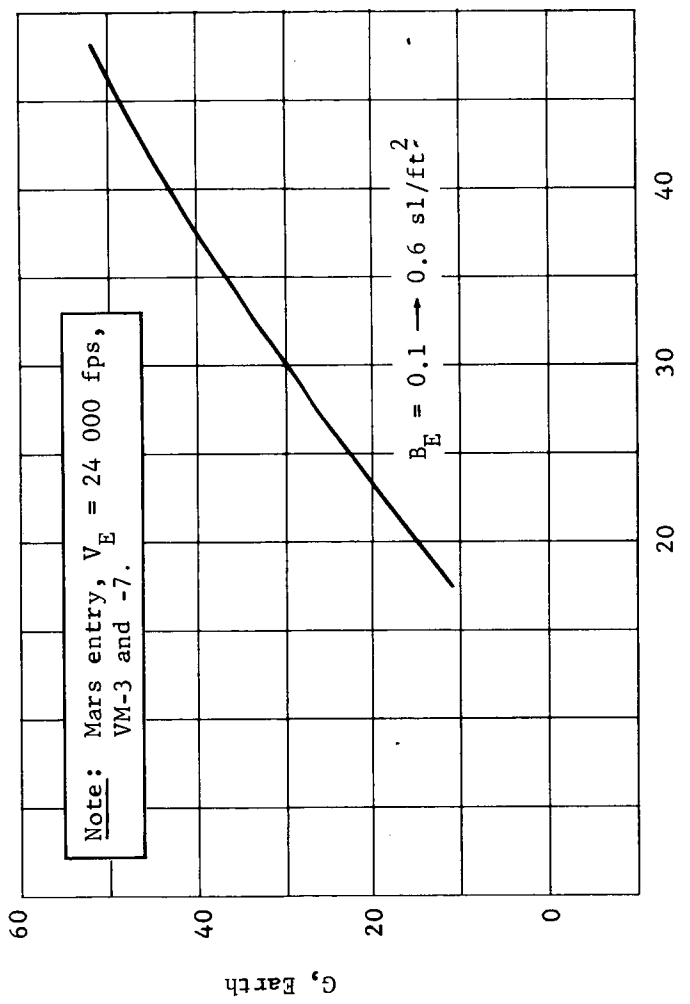

Figure B42.- Peak Drag Deceleration

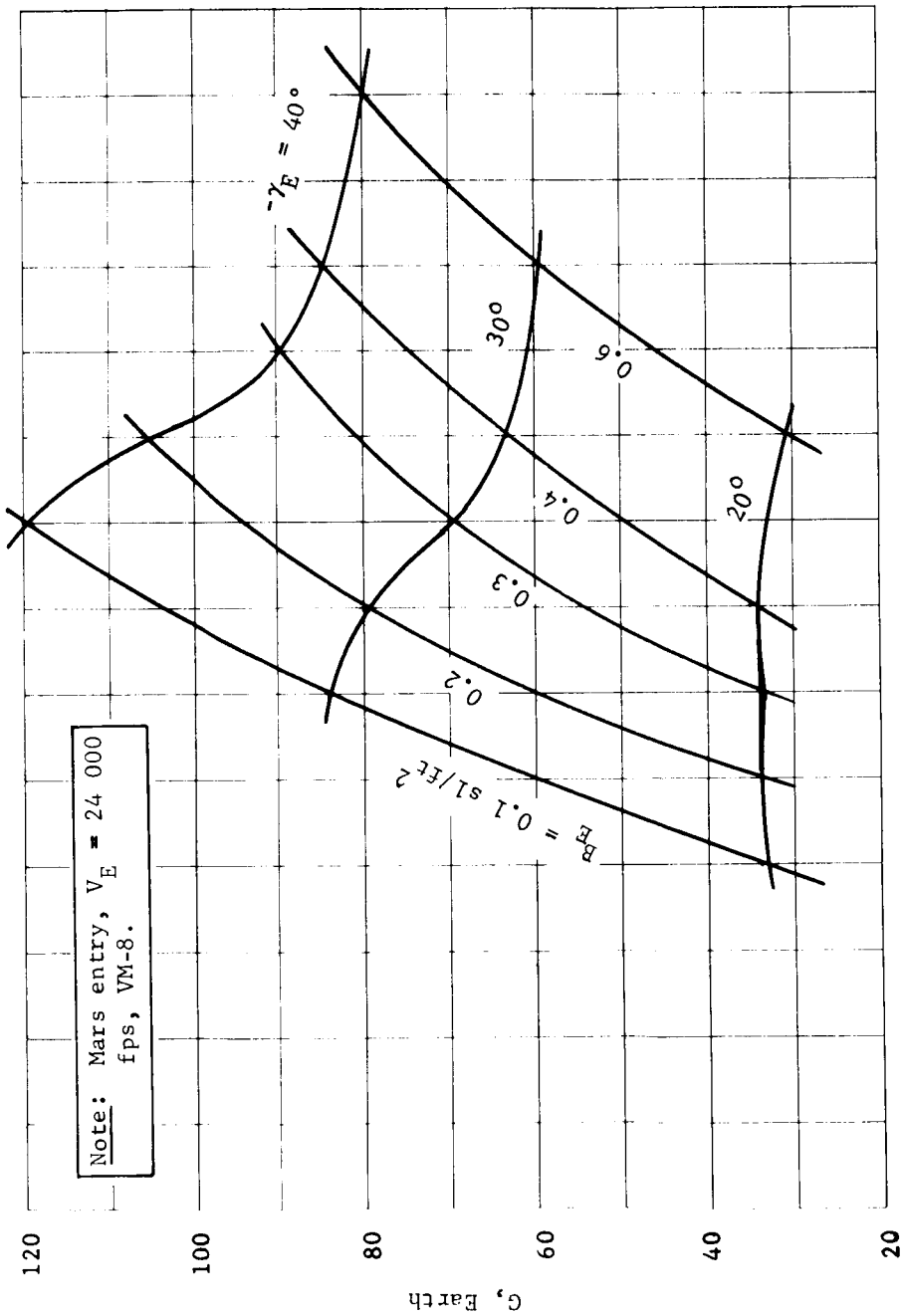

Figure B43.- Peak Drag Deceleration

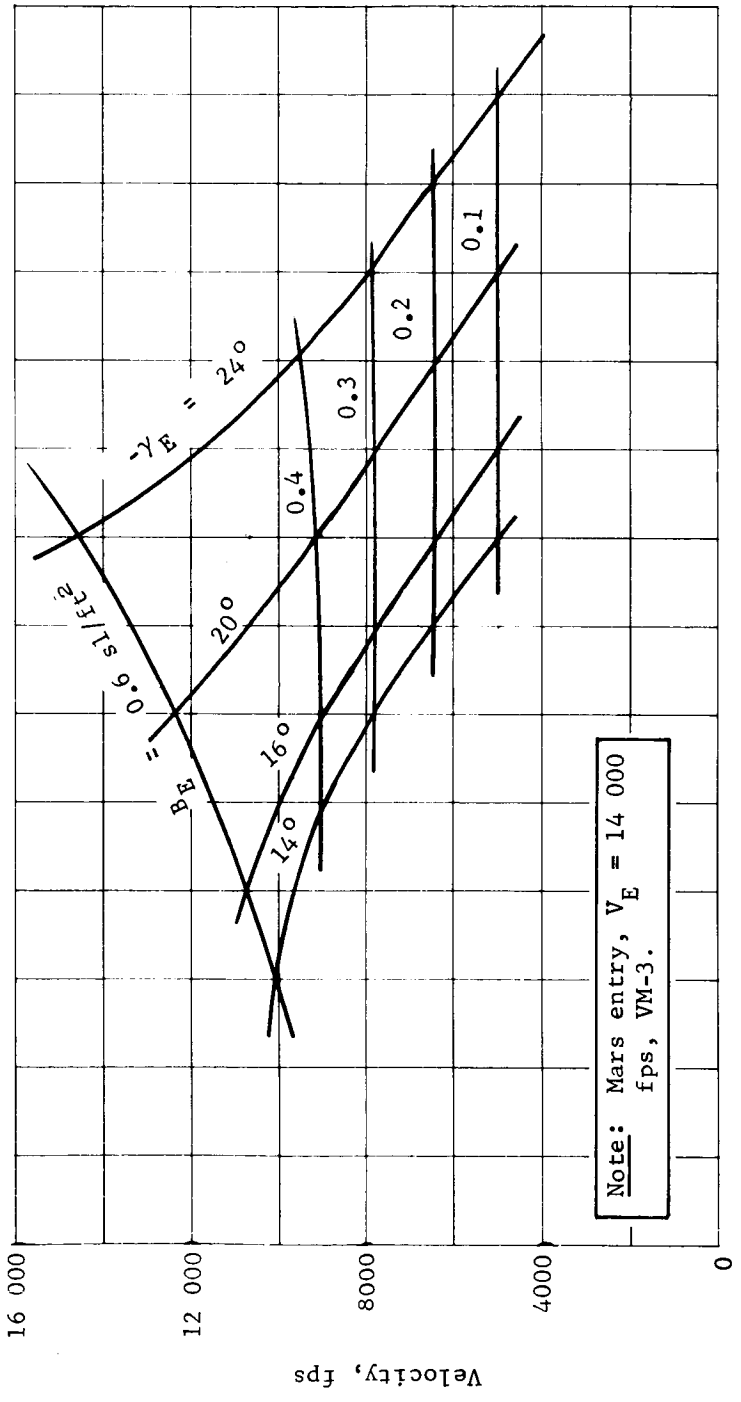

Figure B44.- Velocity at 20 000-ft Altitude

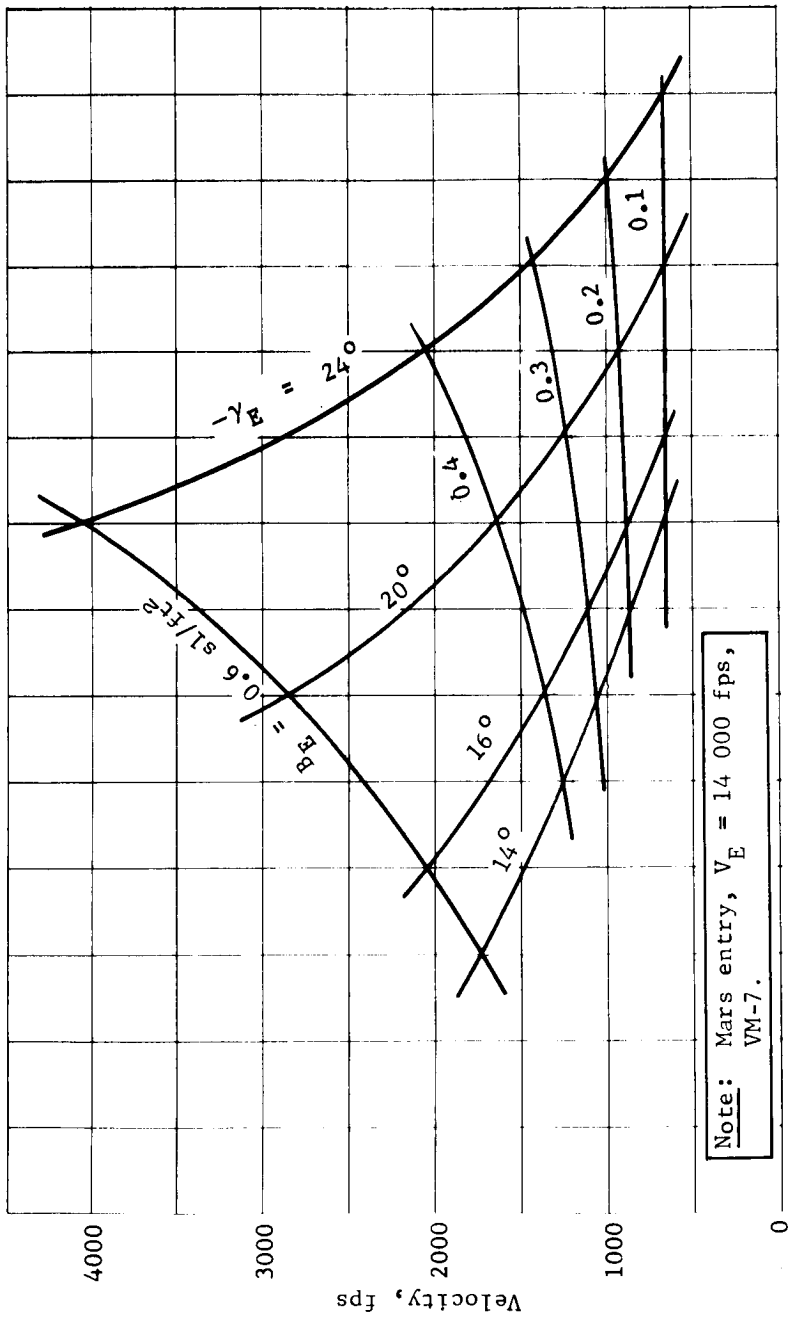

Figure B45.- Velocity at 20 000-ft Altitude

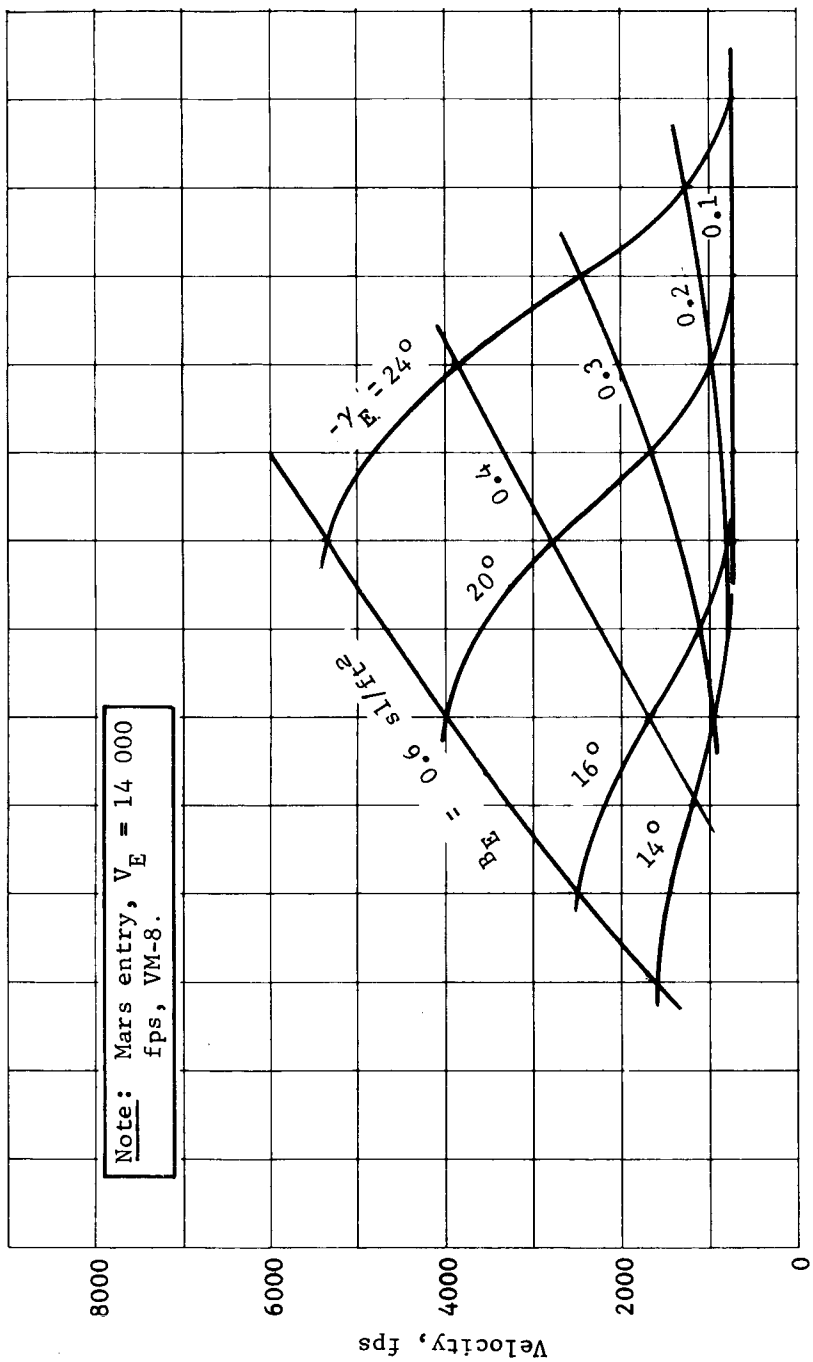

Figure B46.- Velocity at 20 000-ft Altitude

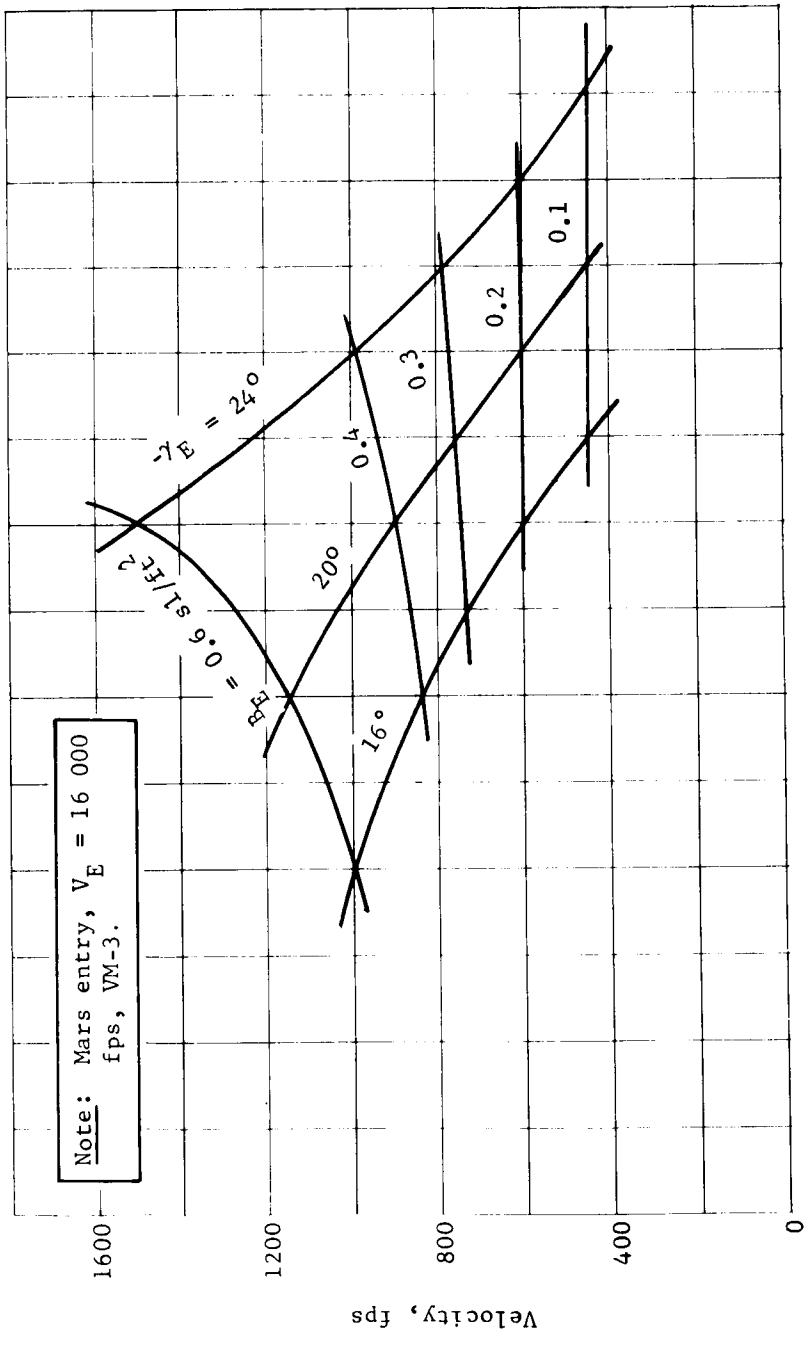

Figure B47.- Velocity at 20 000-ft Altitude

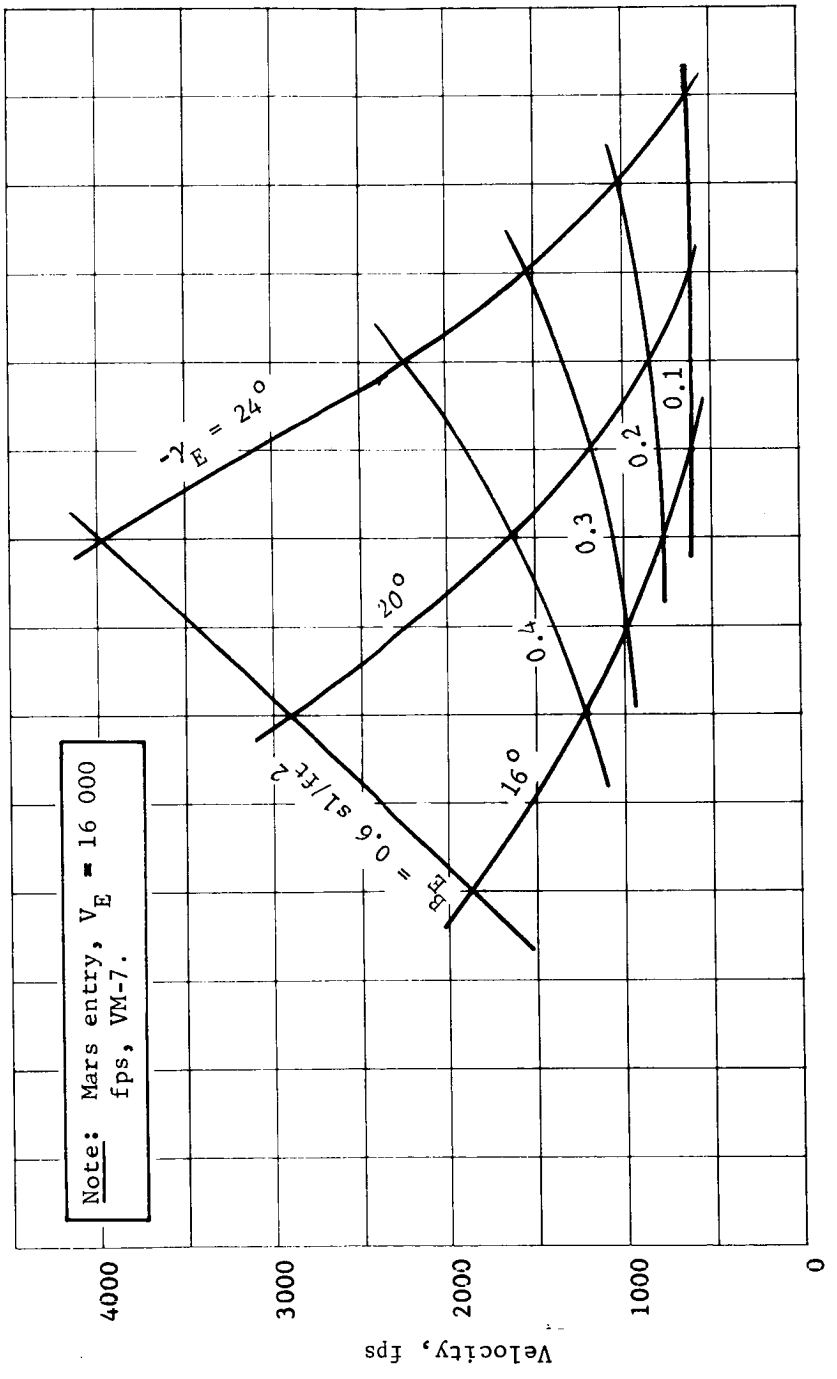

Figure B48.- Velocity at 20 000-ft Altitude

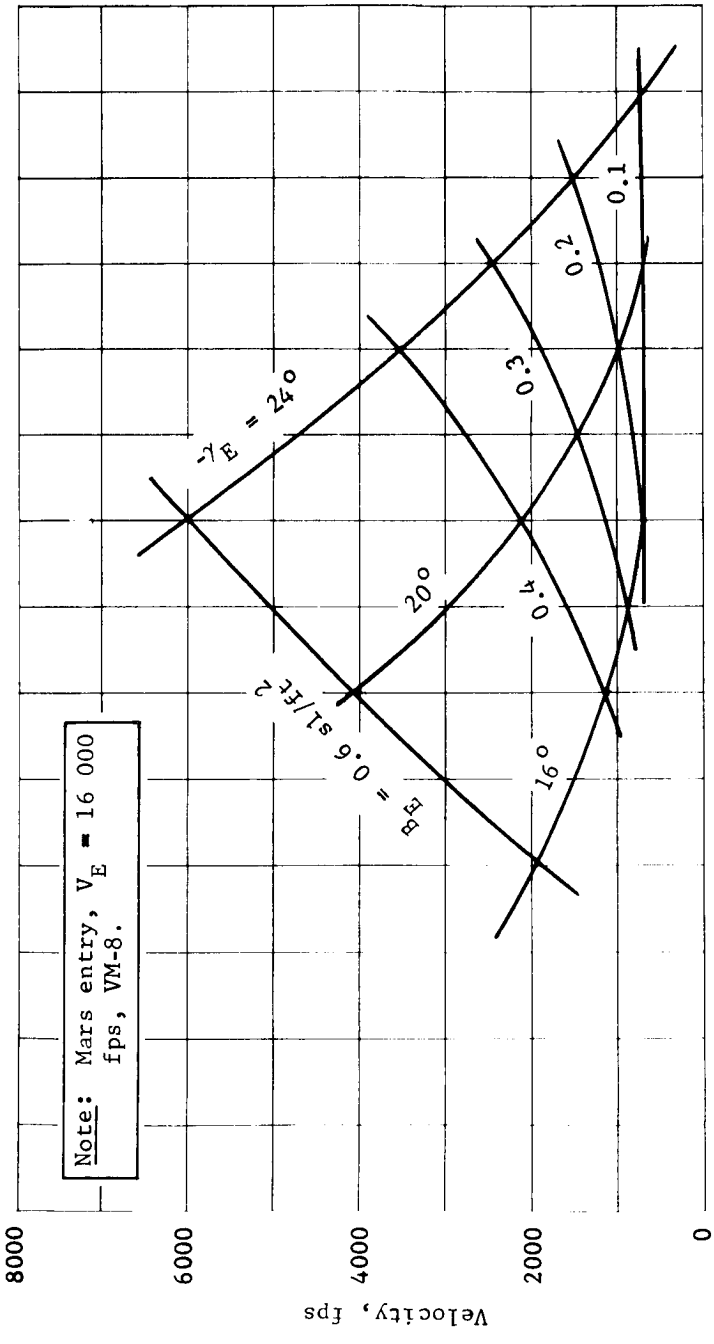

Figure B49.- Velocity at 20 000-ft Altitude

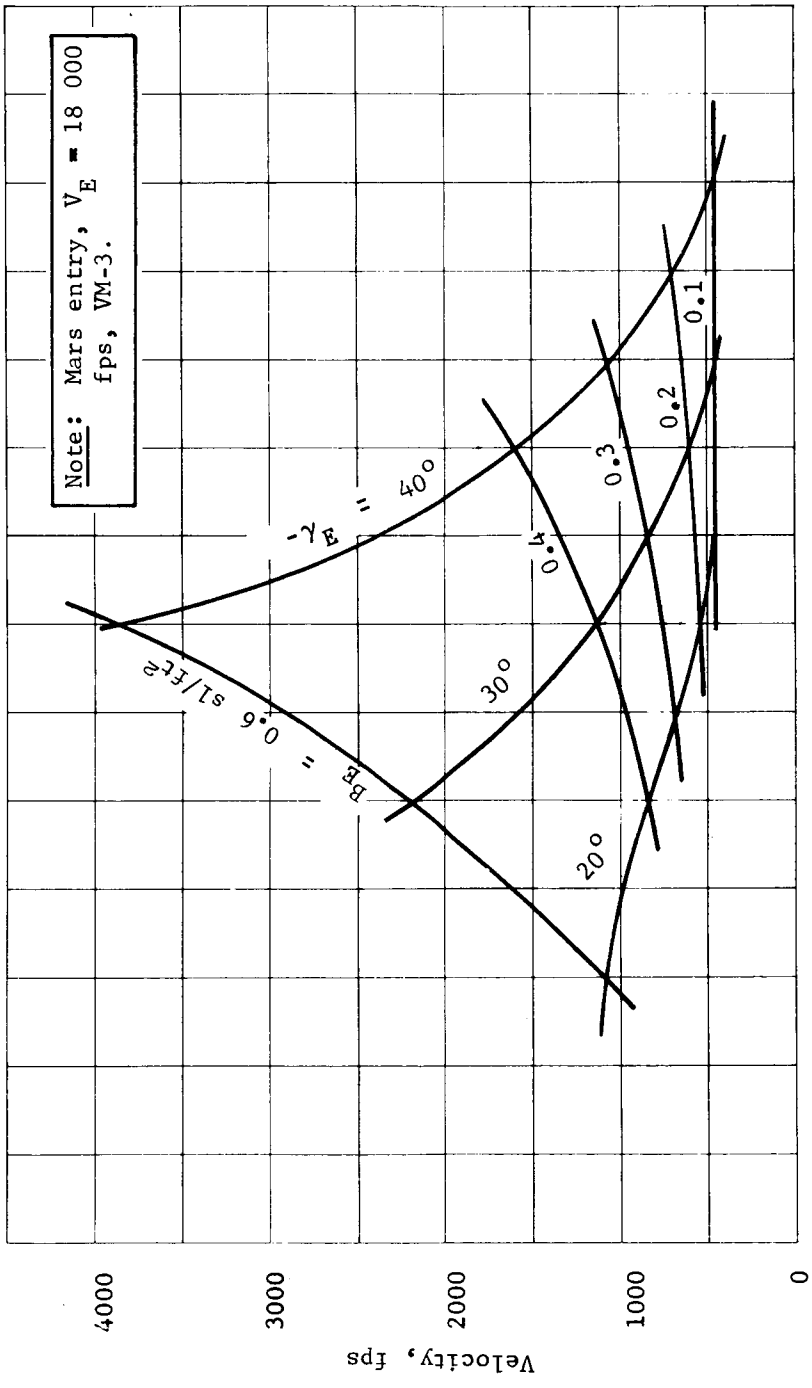

Figure B50.- Velocity at 20 000-ft Altitude

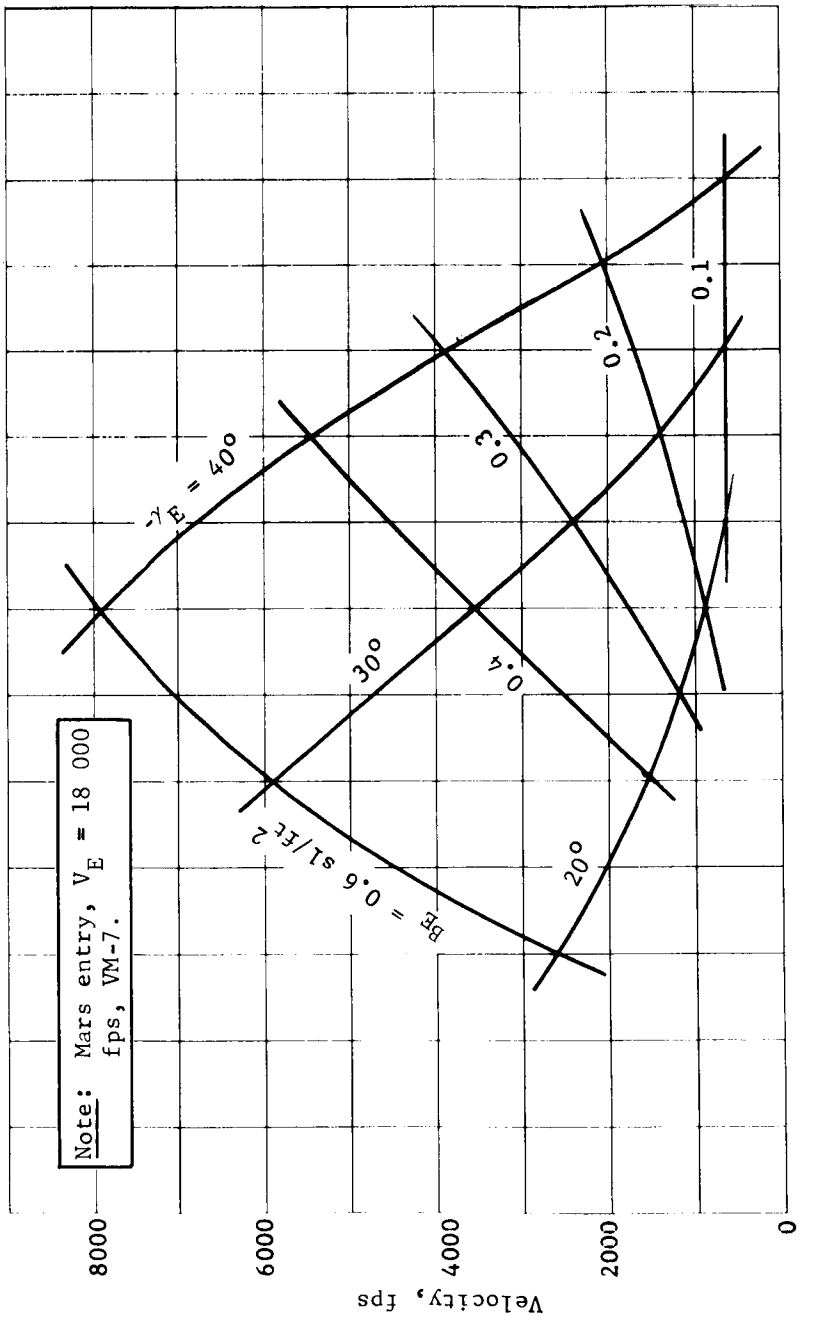

Figure B51.- Velocity at 20 000-ft Altitude

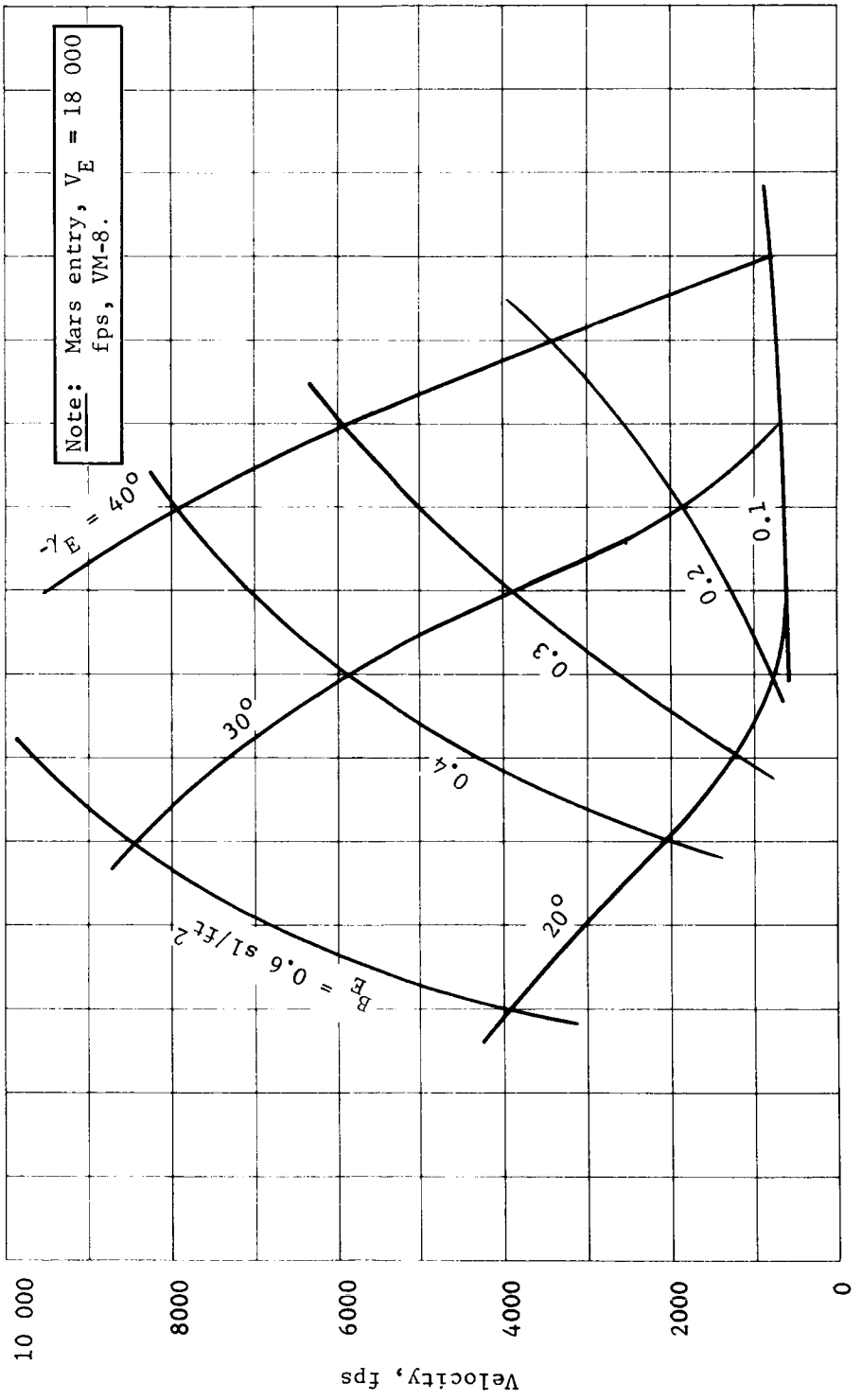

Figure B52.- Velocity at 20 000-ft Altitude

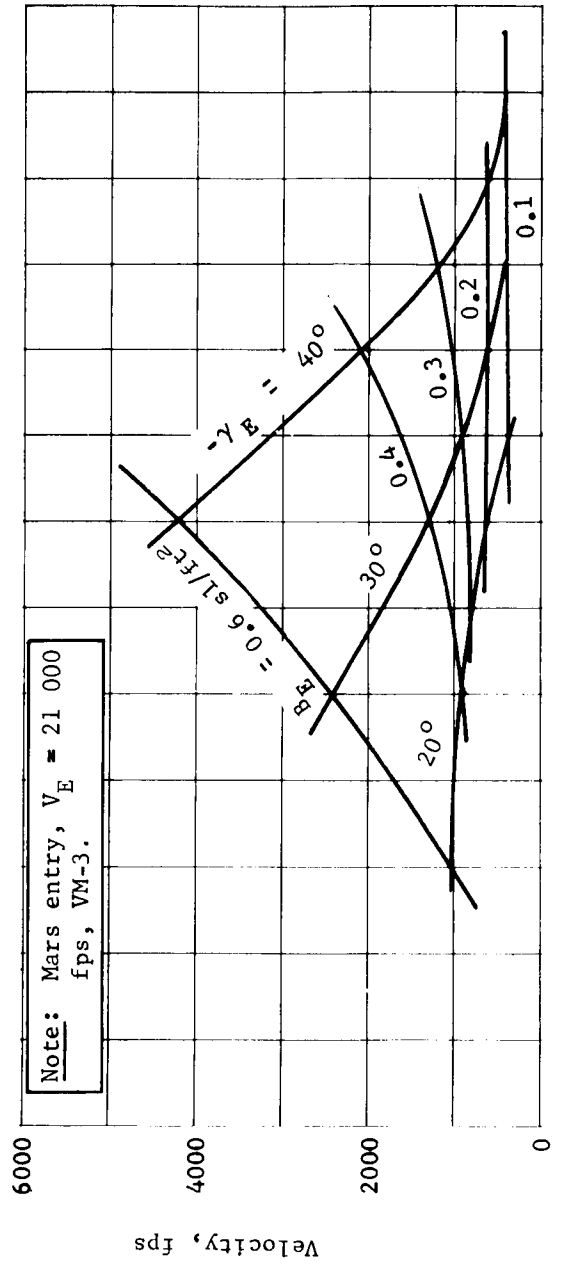

Figure B53.- Velocity at 20 000-ft Altitude

APPENDIX B

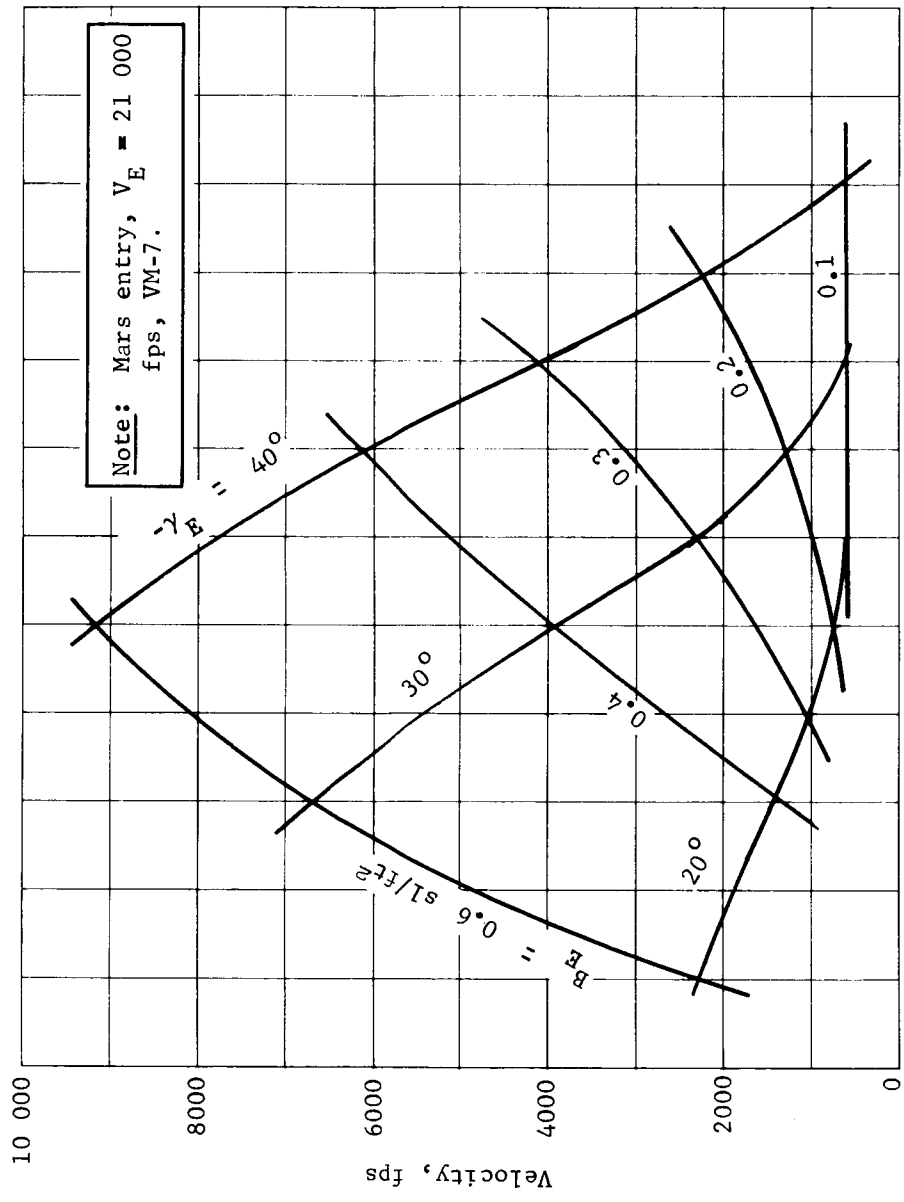

Figure B54.- Velocity at 20 000-ft Altitude

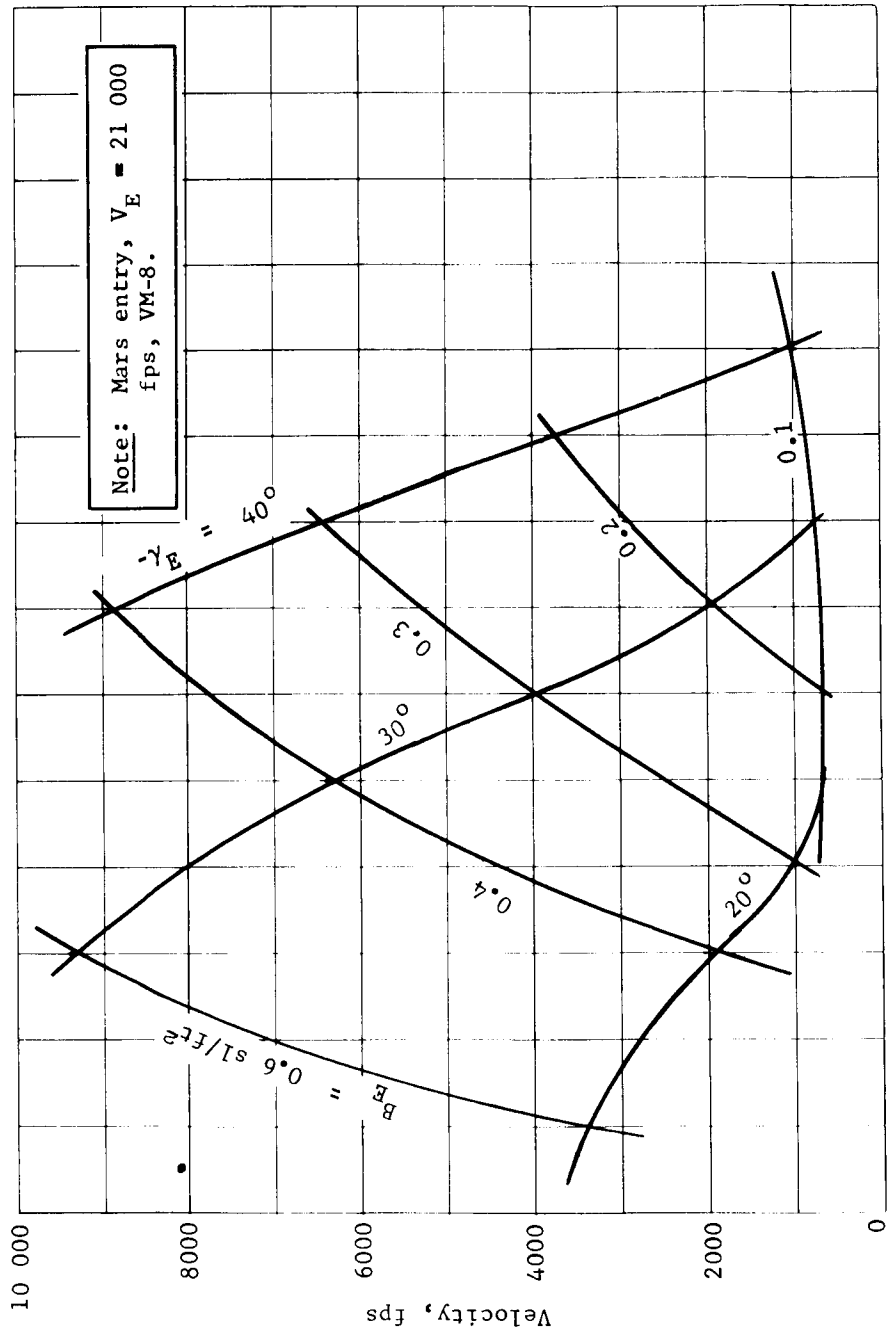

Figure B55.- Velocity at 20 000-ft Altitude

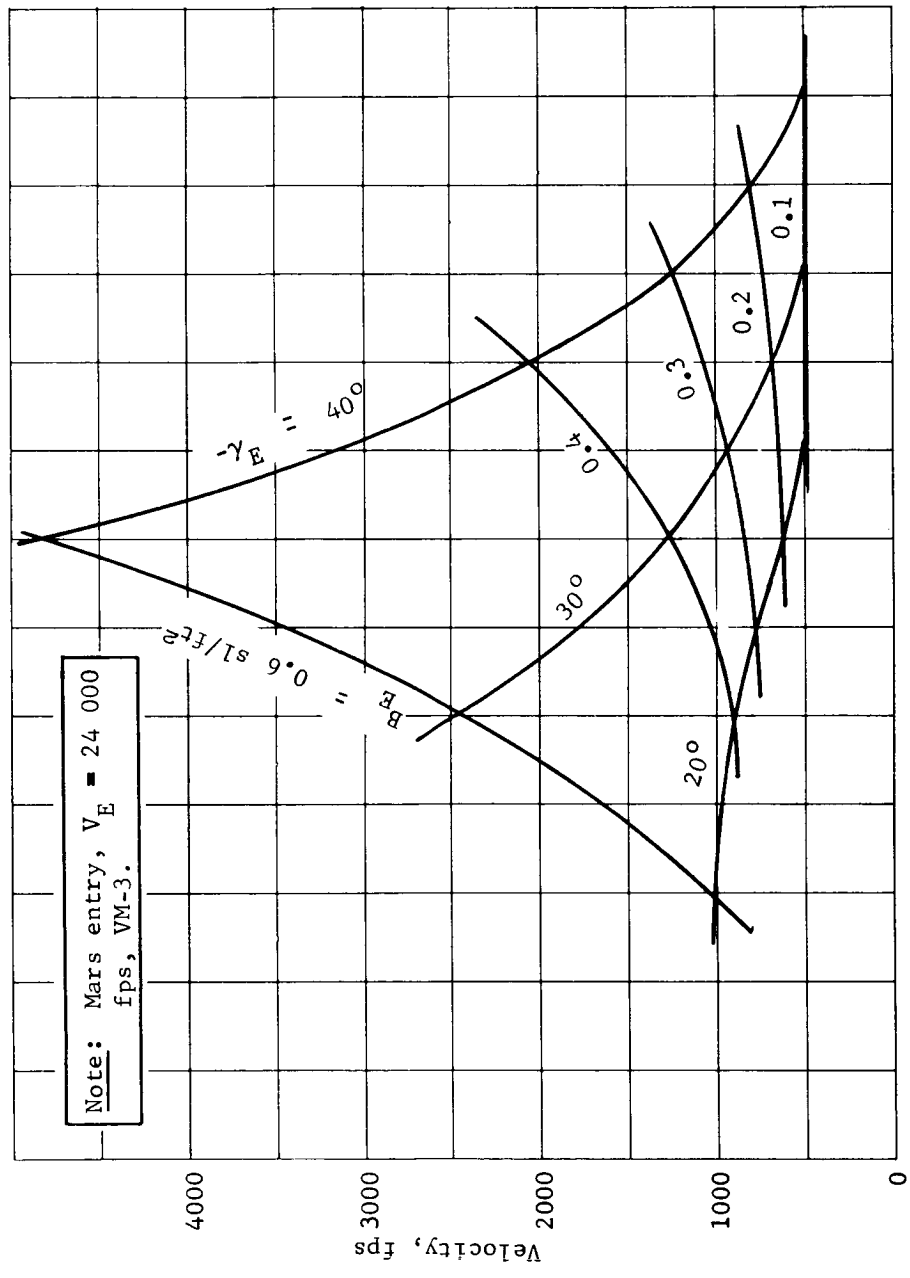

Figure B56.- Velocity at 20 000-ft Altitude

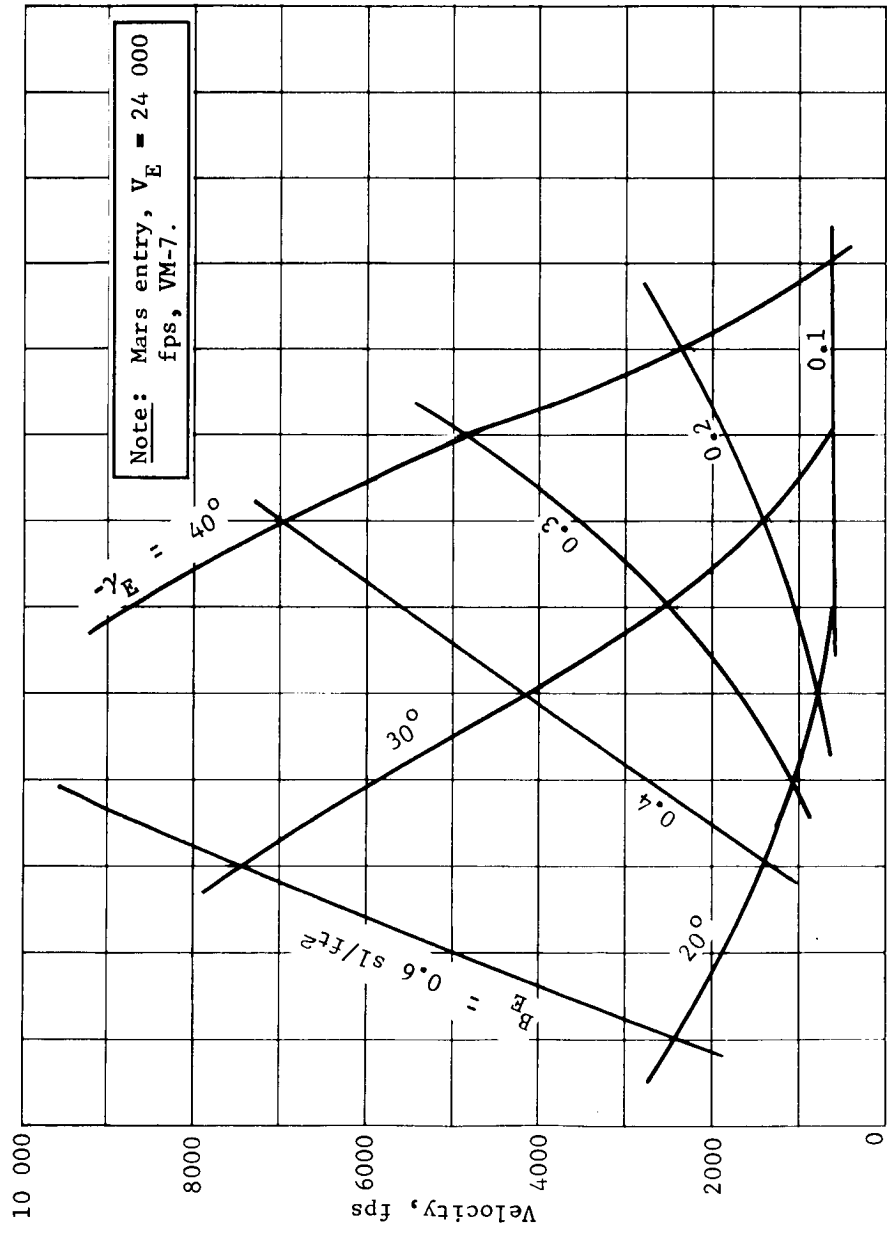

Figure B57.- Velocity at 20 000-ft Altitude

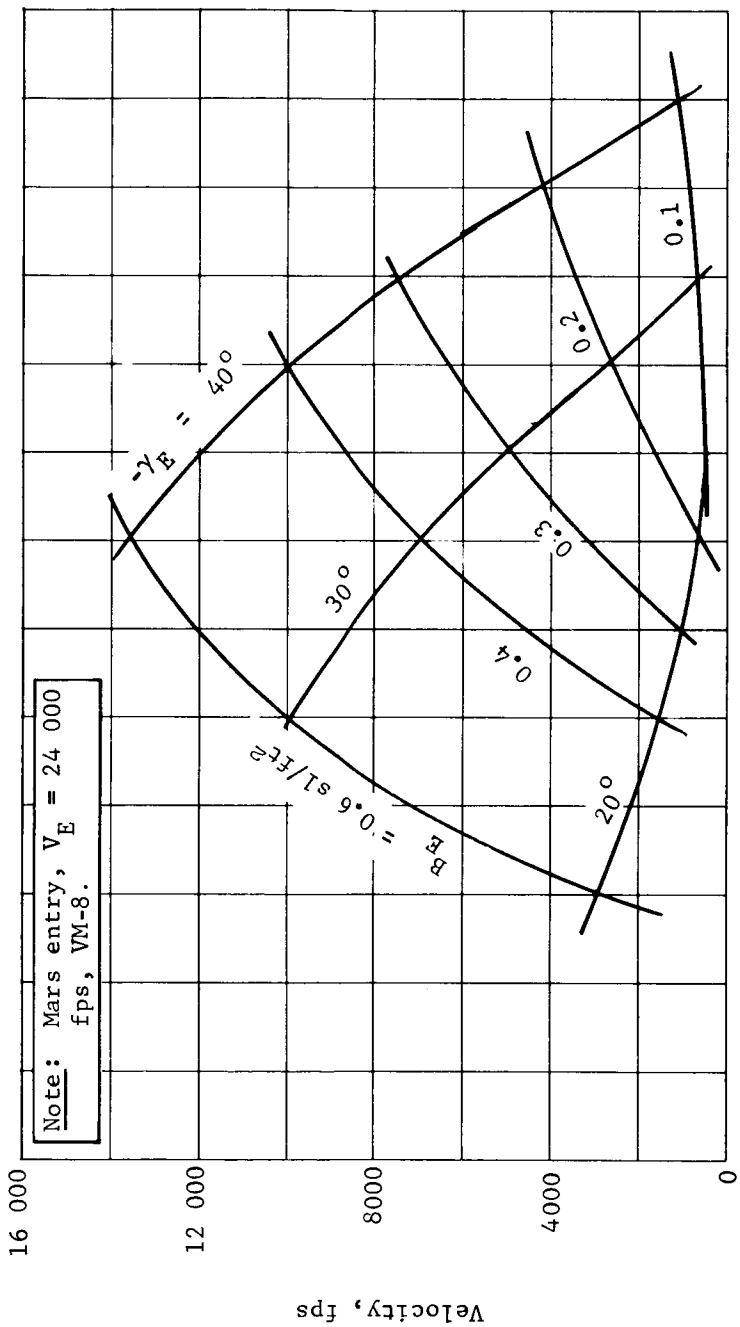

Figure B58.- Velocity at 20 000-ft Altitude

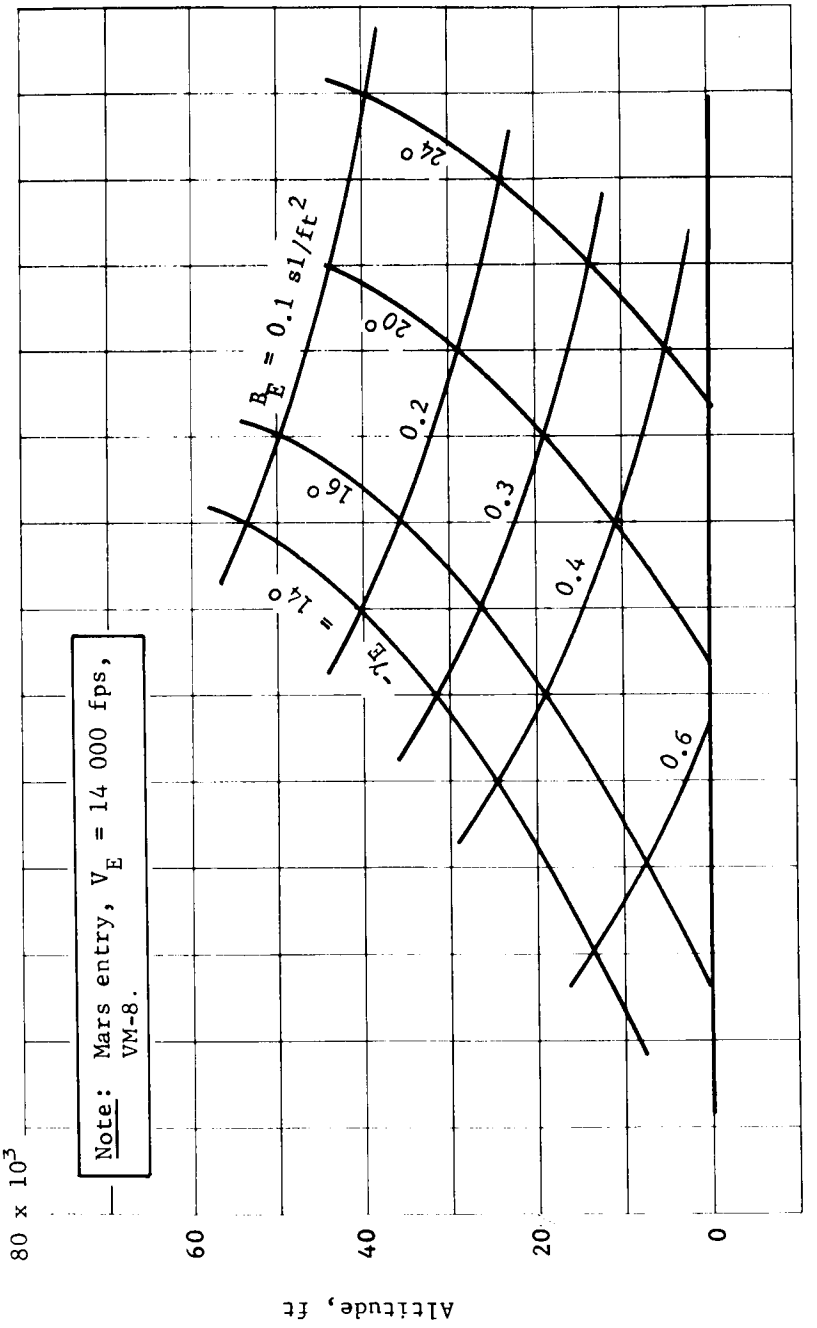

Figure B59.- Altitude at Mach 2.0

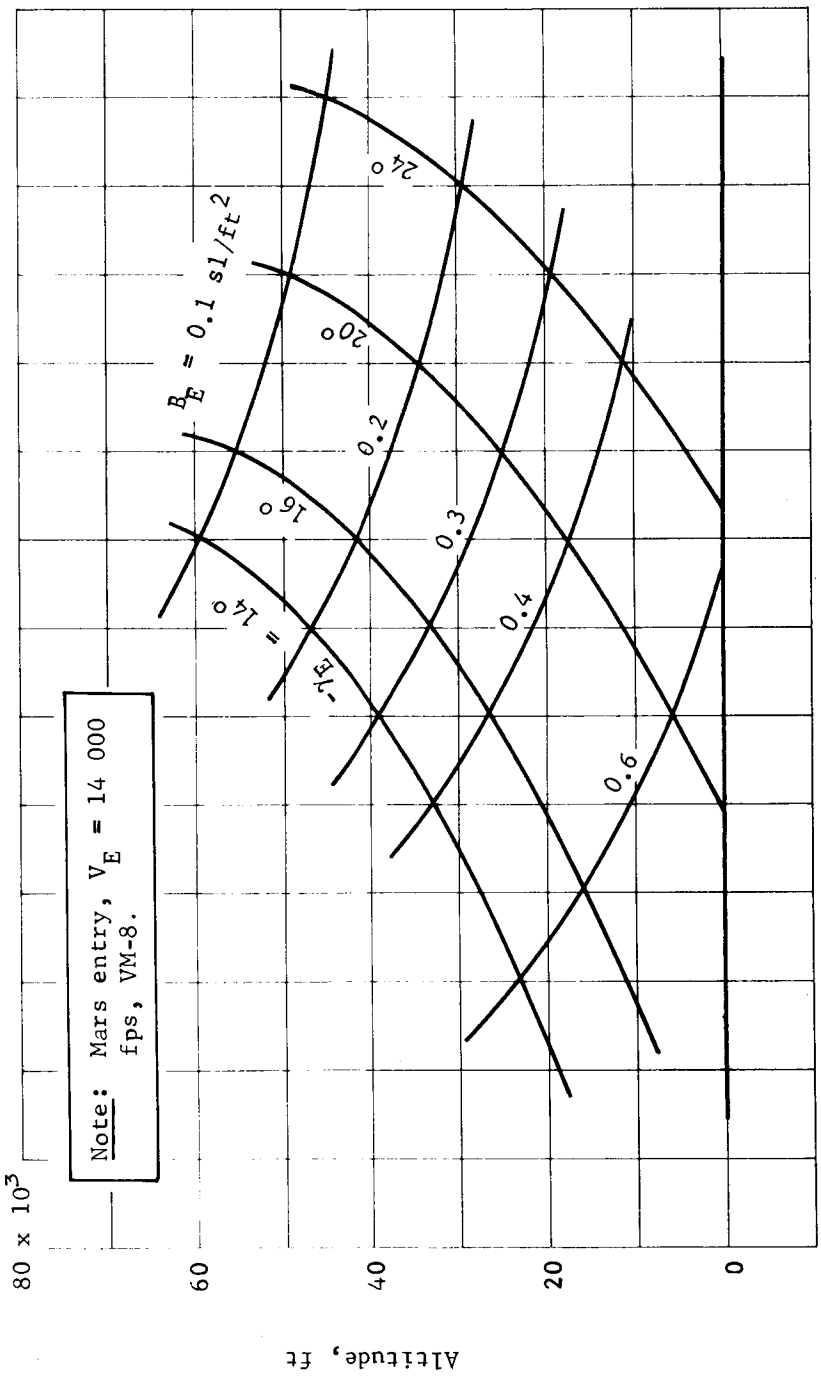

Figure B60.- Altitude at Mach 3.0

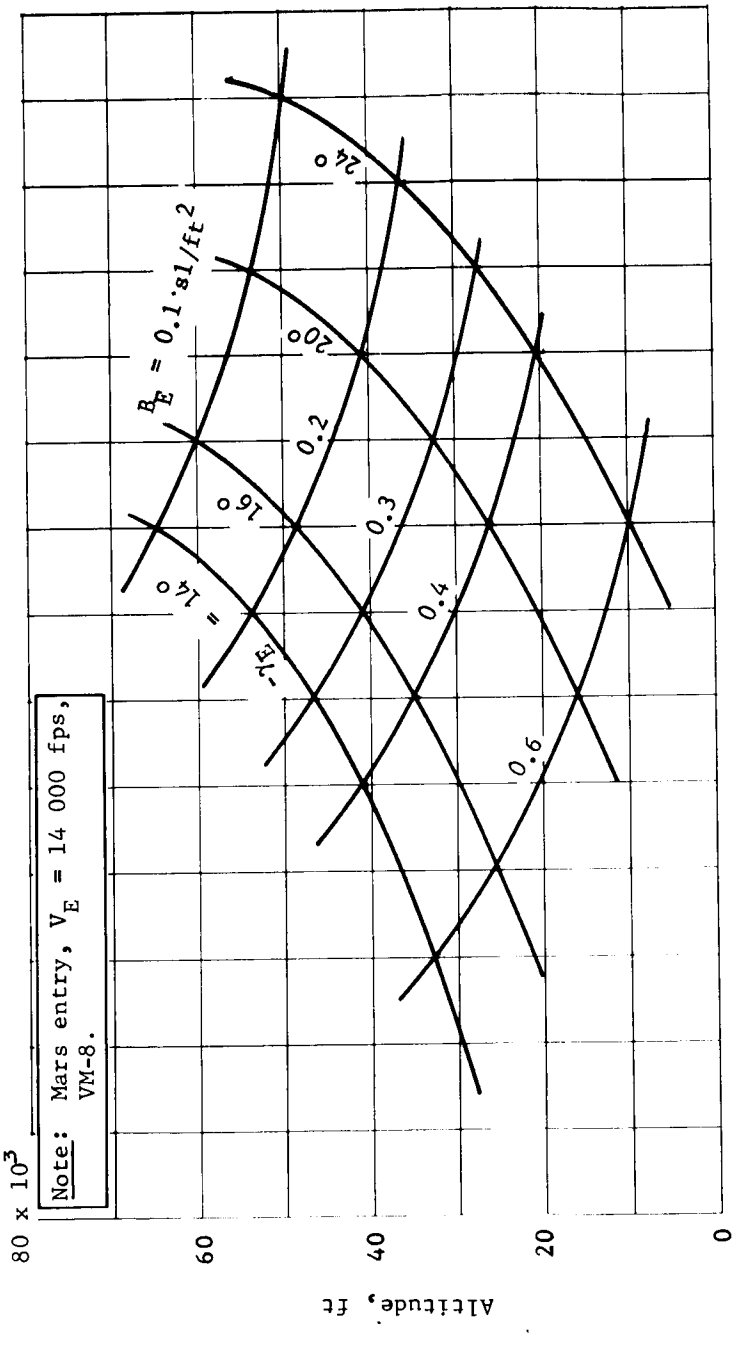

Figure B61.- Altitude at Mach 5.0

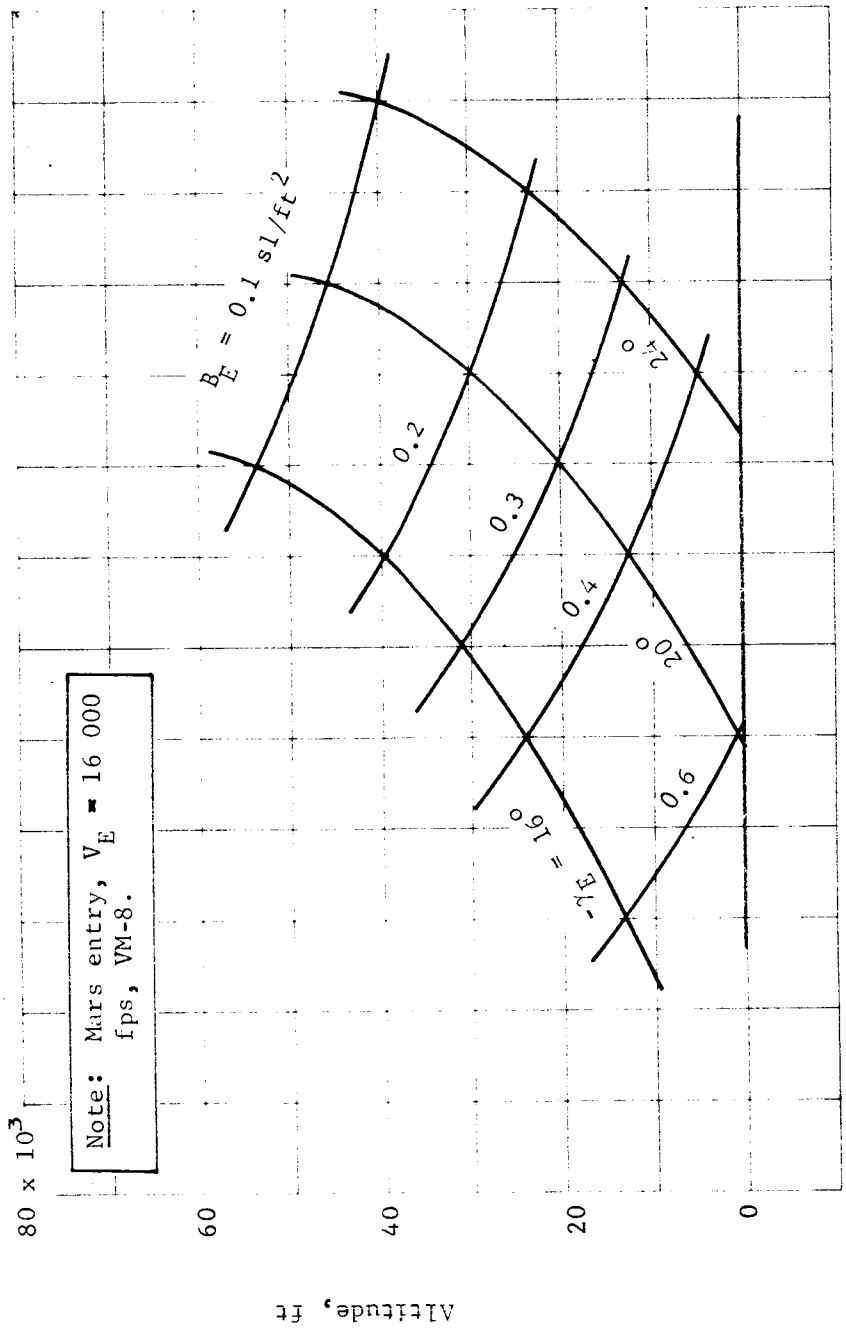

Figure B62.- Altitude at Mach 2.0

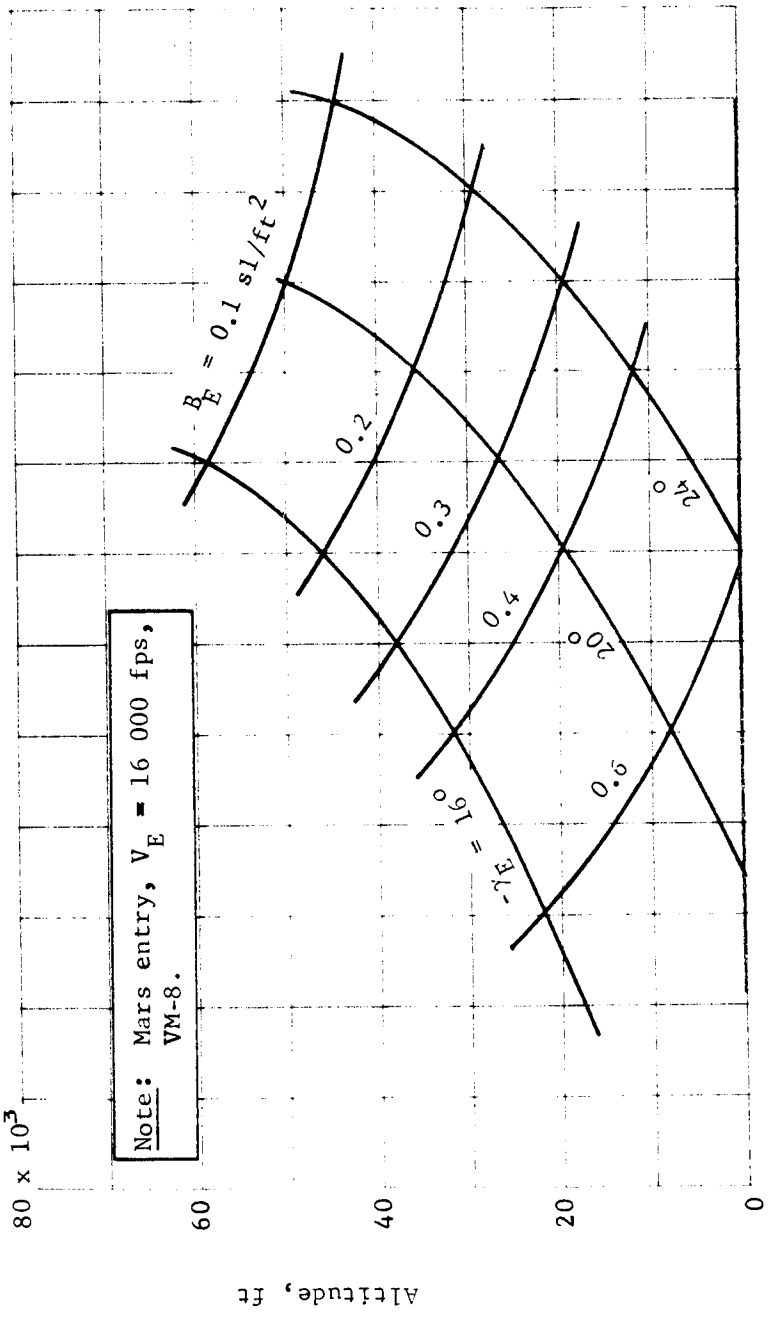

Figure B63.- Altitude at Mach 3.0

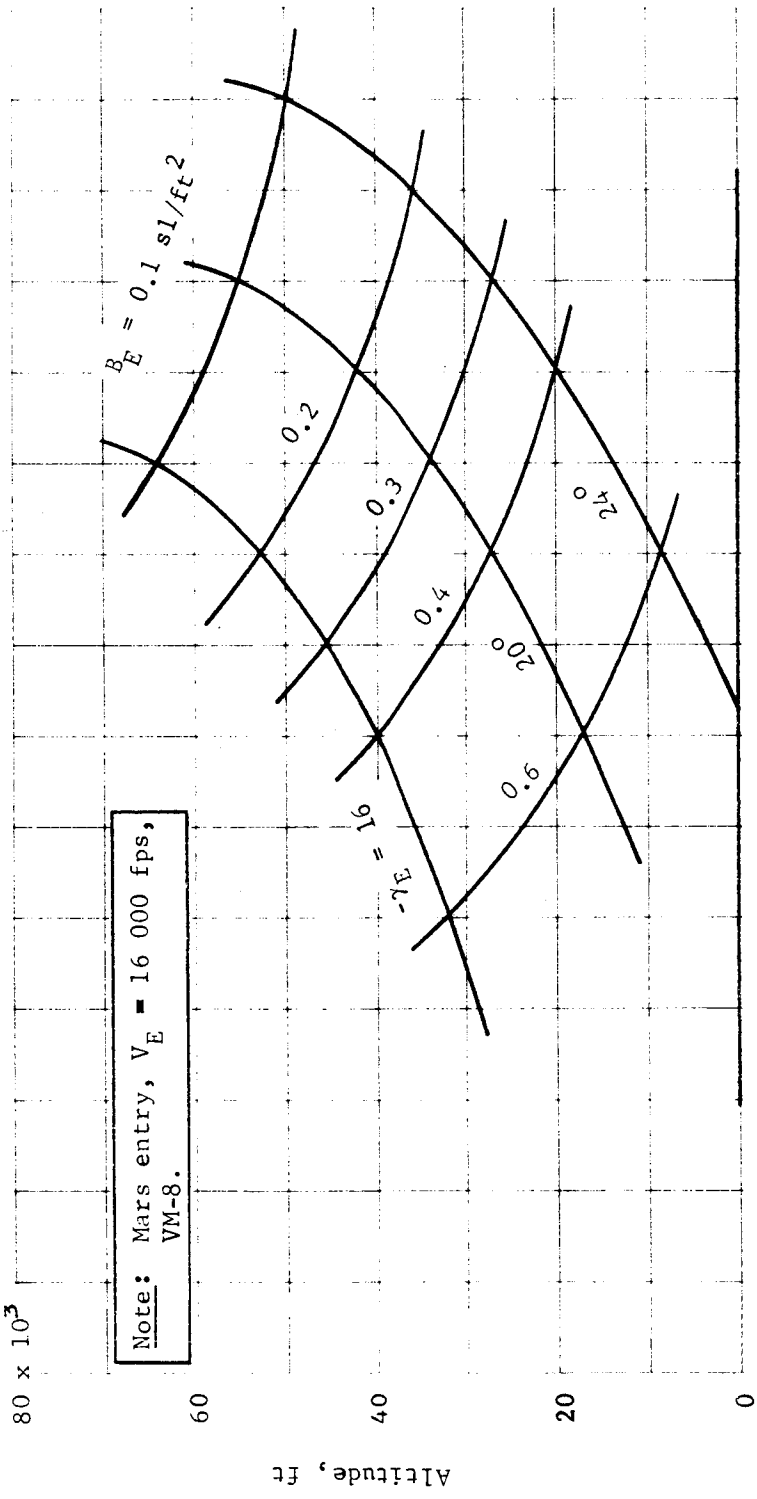

Figure B64.- Altitude at Mach 5.0

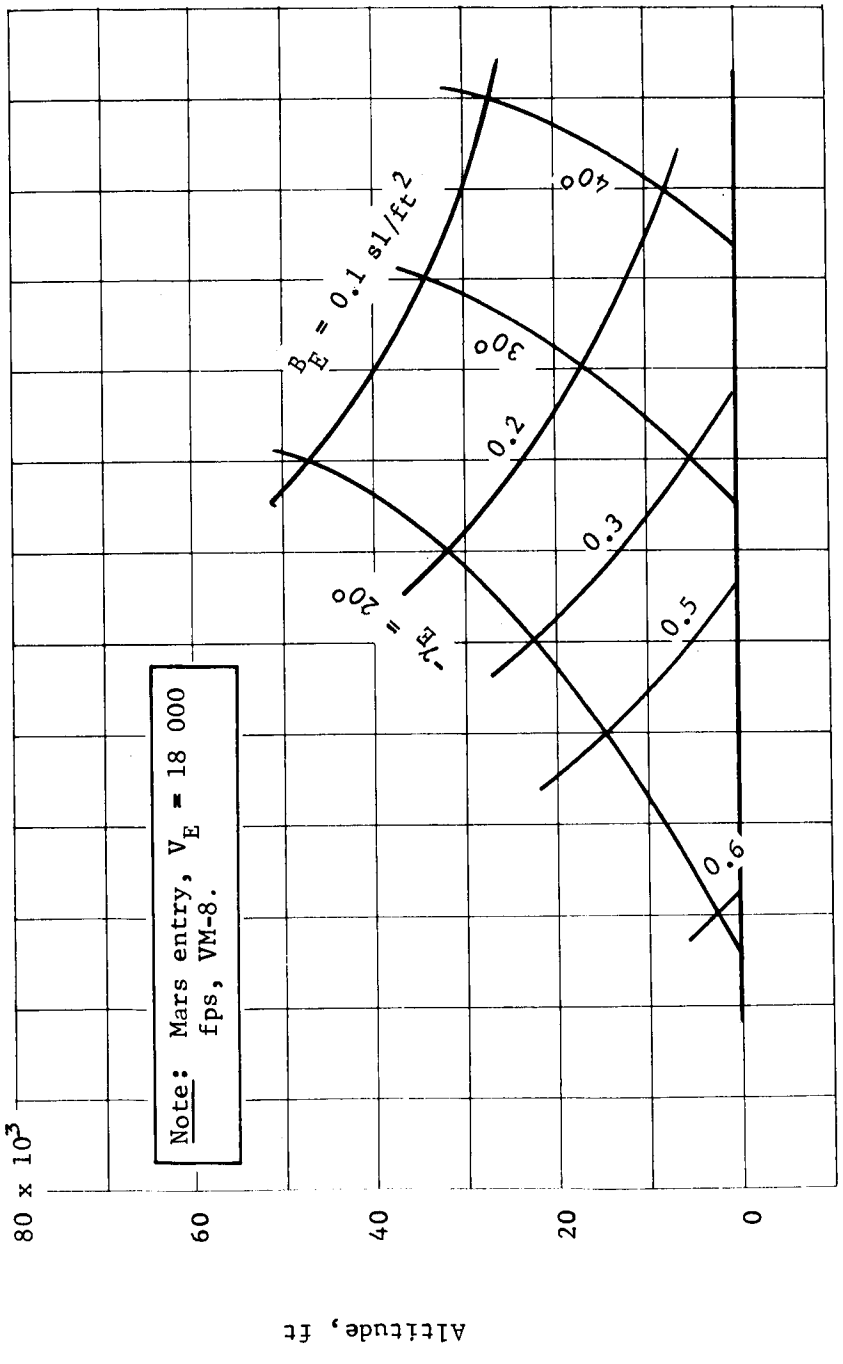

Figure B65.- Altitude at Mach 2.0

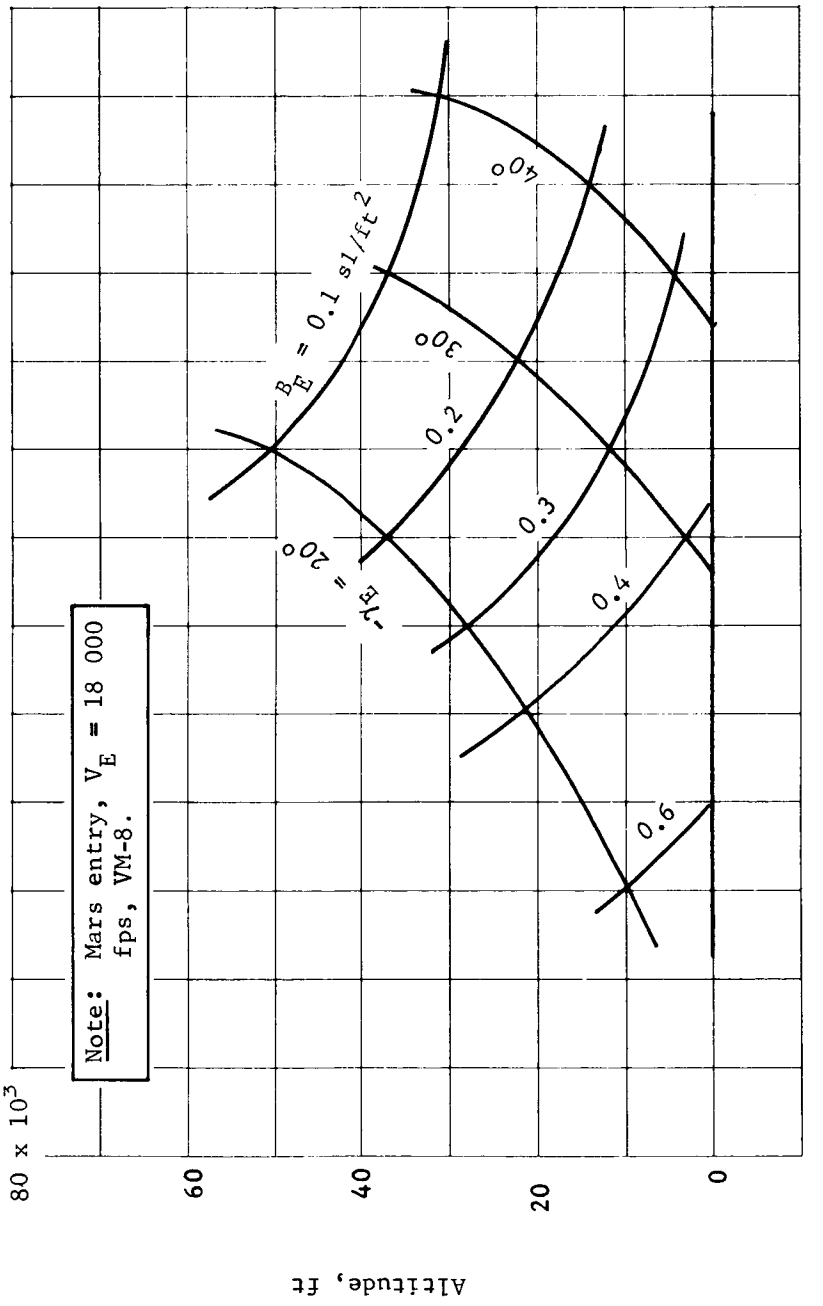

Figure B66.- Altitude at Mach 3.0

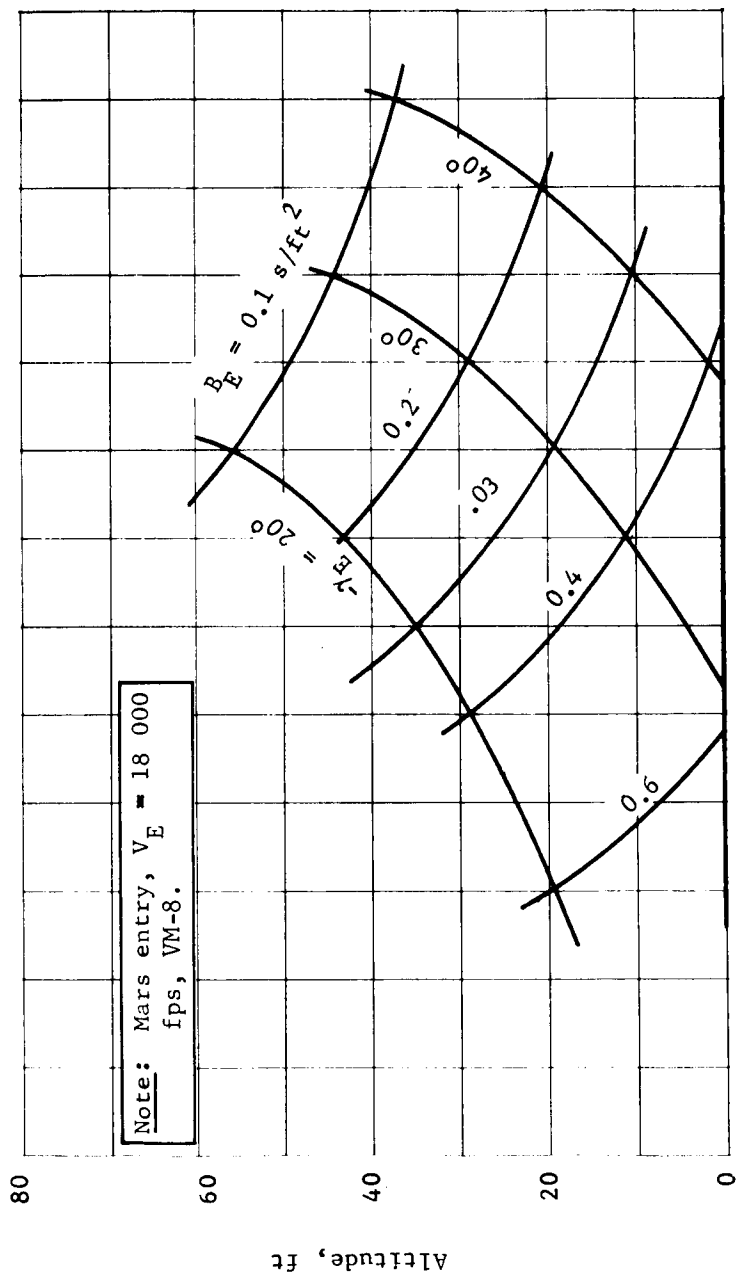

Figure B67.- Altitude at Mach 5.0

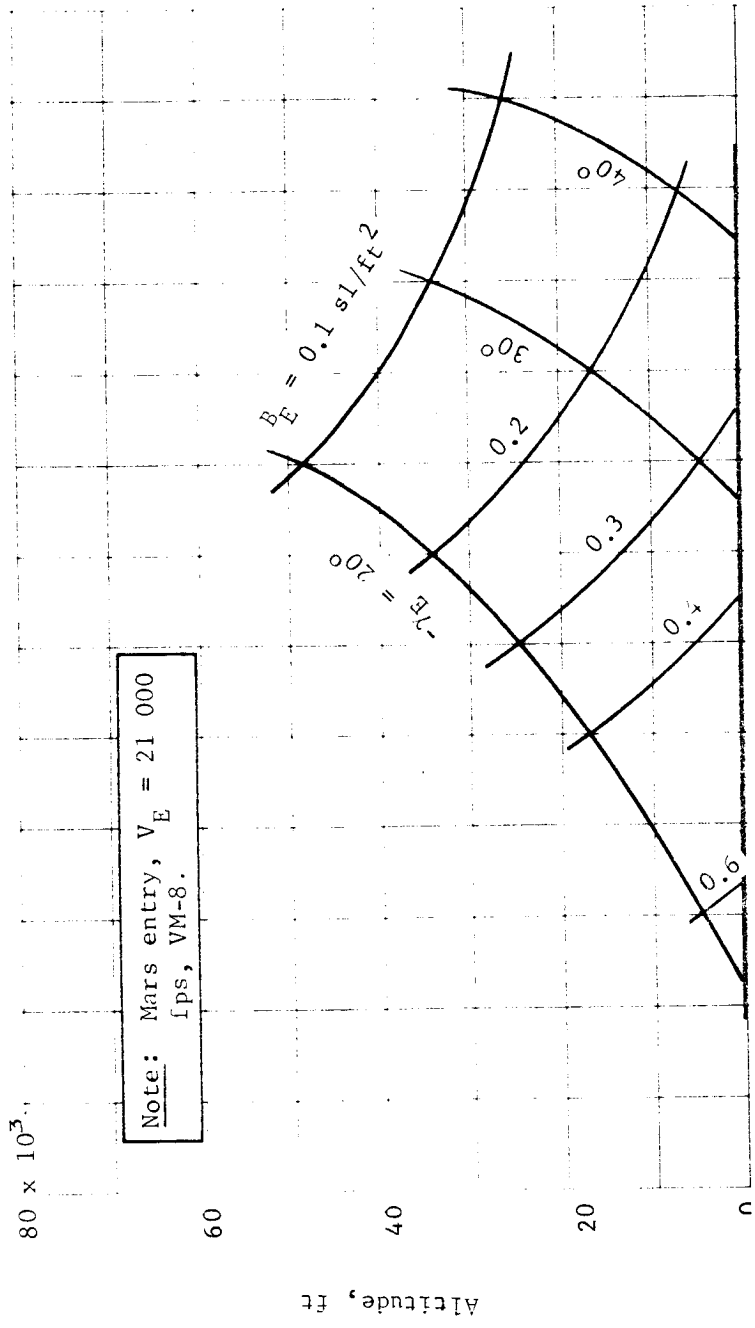

Figure B68.- Altitude at Mach 2.0

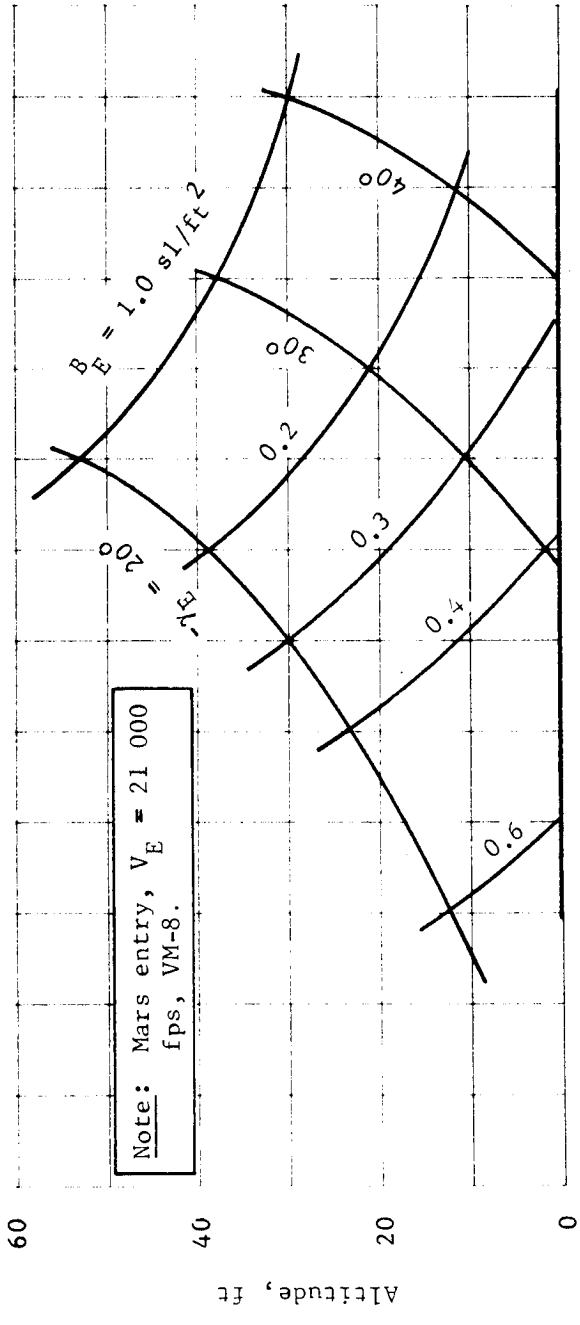

Figure B69.- Altitude at Mach 3.0

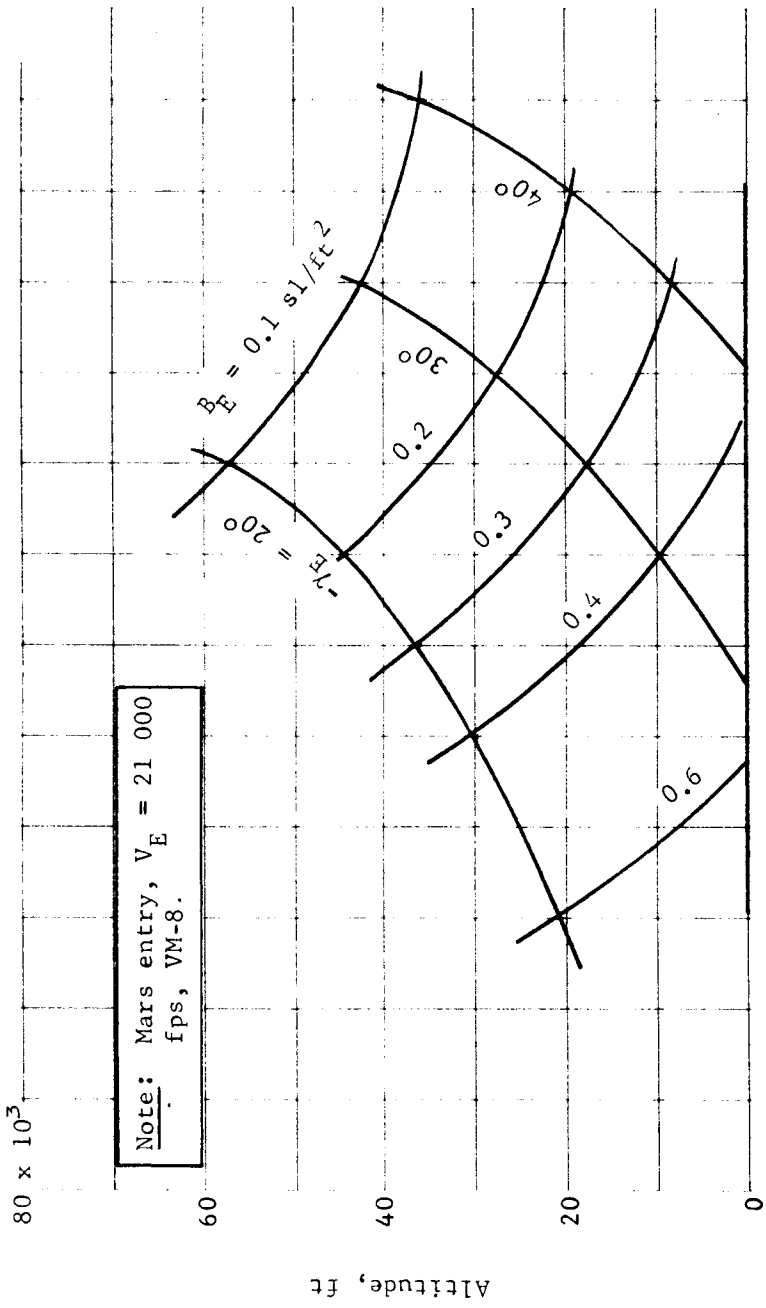

Figure B70.- Altitude at Mach 5.0

APPENDIX B

This page intentionally left blank.

APPENDIX B

2. TERMINAL PHASE SYSTEM ANALYSIS

Objectives

The terminal phase system decelerates the capsule from velocities at the end of the entry phase (approximately 20 000-ft altitude) to zero velocity at the Martian surface. The objectives of the terminal phase analysis are to evaluate the effect of mission mode (i.e., direct mode, entry from the approach trajectory; and orbit mode, entry from orbit) on terminal phase performance and to compare several candidate systems for each mission mode. The terminal phase systems considered include subsonic-type parachute plus vernier, tuckback ballute plus vernier, all-retro propulsion landing system, and two-burn systems, making use of a solid rocket motor for braking before parachute or all-retro system deployment.

Terminal phase initial conditions are determined by entry trajectory characteristics and are related directly to entry conditions (velocity, flightpath angle, and ballistic coefficient). Entry corridors (flightpath angle vs. velocity at entry) result from the targeting and error analysis (Appendix A). Correlation with these values defines the required values over the parametric range used in the terminal phase analysis. Terminal phase performance is measured in terms of entry weight, aeroshell diameter, and useful landed weight. Entry weight, converted to capsule system weight, allows correlation with launch vehicle capability (Appendix A). Thus, the end point of the terminal phase analysis defines useful landed weight as a function of aeroshell diameter, entry conditions and dispersions, and required launch vehicle. Sensitivity to design parameters such as landed terrain height and decelerator size is also factored into the analysis along with the constraints under which the system is assumed to perform.

System Description, Ground Rules and Constraints

The terminal phase systems considered in this study are:

1) Mach 2.0 deployed subsonic-type parachute with monopropellant or bipropellant vernier landing rocket motors;

2) Mach 3.0 and 5.0 deployed tuckback ballutes with monopropellant vernier motors;

3) All-retro propulsion bipropellant decelerator and vernier system (three-engine arrangement);

4) Two-burn system employing a high-thrust solid rocket motor in front of either the $M_D = 2.0$ parachute or all-retro system.

The two-burn system concept is investigated for the direct mode only; the other systems are investigated for both direct and orbit modes.

Ground rules and constraints related to the entry trajectory analysis are as follows:

1) Entry velocities of 4.5 km/sec (14 800 fps, orbit mode) and 18 000 to 24 000 fps (direct mode);

2) Entry flightpath angles of -16 to -20° (orbit mode) and -26 to -38° (direct mode).

Entry ballistic coefficients are determined as a function of terminal phase system limitations and are discussed separately below. The entry trajectory analysis also defines the attitude of deployment of the aerodecelerator terminal phase systems. The VM-8 atmosphere is critical in defining the Mach number-sensitive deployment conditions because of its lowest upper altitude density (above 44 000 ft results in highest velocities) and its low speed of sound.

Before discussing terminal phase, a word of explanation is required relative to the philosophy adopted for defining the entry flightpath angle versus entry velocity profile to be used for the deorbit/ejection maneuver strategy. The analysis performed during our Voyager Phase B effort indicated the sensitivity of landed payload to entry flightpath angle. To avoid the problem of analyzing terminal phase system performance as a function of entry velocity and entry flightpath angle as well as system parameters, the maneuver strategy was devised, which desensitized the terminal phase system initial conditions to V_E and γ_E. An example is shown in figure B71, which shows that there are V_E, γ_E contours that result in essentially identical flight conditions below 30 000 ft. All of the targeting analysis discussed in Appendix A are based on V-γ contours that have these characteristics.

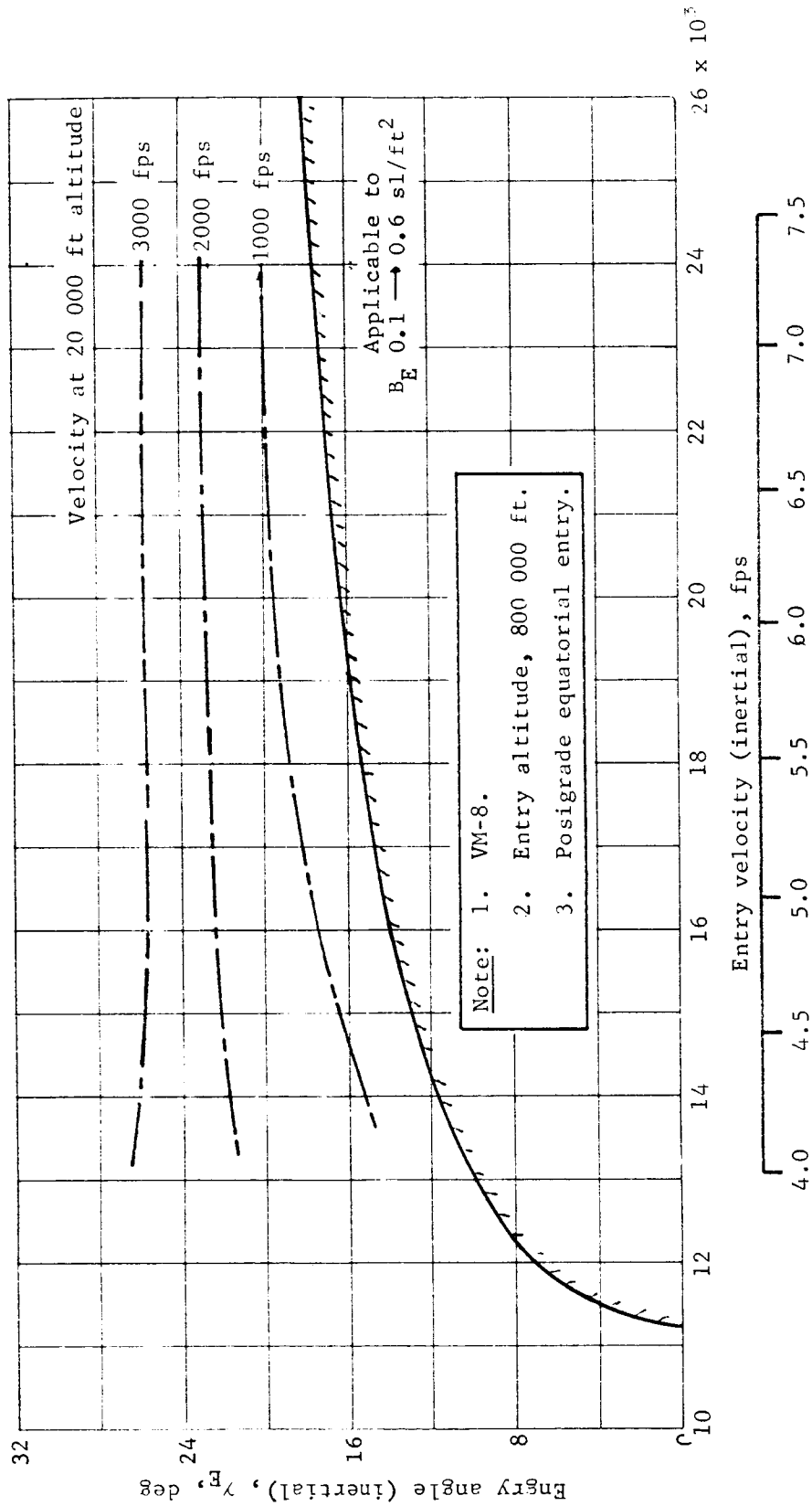

Figure B71.- Mars Skipout Boundary

APPENDIX B

The point is essential here to relate quoted entry flightpath angles in preceding sections to those that appear below. For example, the entry corridors defined above for the two orbits considered defined the maximum $\gamma_E = 16.2°$ and 18.1° for the 1000x15 000- and 1000x33 070-km orbits, respectively. These γ_E occur at entry velocities of approximately 14 400 and 15 100 fps, respectively. The terminal phase system analysis was based on an entry velocity of 4.5 km/sec (14 764 fps). The γ_E to be used in the terminal phase system comparison is obtained by taking the above values and following the trend shown in figure B71 from the actual V_E to 4.5 km/sec. Thus, the entry corridor limits for the two orbits change from -16.2 and -18.1° to -16.6 and -17.8° as far as the discussion below is concerned.

The analysis is performed for a range of aeroshell diameters as follows:

1) Orbit mode - 6.5, 8.5, 12, and 15 ft;
2) Direct mode - 6.5, 8.5, 12, 15, 20, 25, and 30 ft.

The launch vehicle shroud size limitation (16 ft diam) has been interpreted in this parametric analysis to limit the aeroshell diameter to approximately 15 ft. Aeroshell diameters greater than 15 ft are obtained by deploying flaps or extendible afterbodies.

Additional ground rules common to both orbit and direct mode analyses are:

1) VM-7 and VM-8 atmospheres;
2) Terrain heights at 0 and 6000 ft above the mean planet surface;
3) Wind velocity of 220 fps at aerodecelerator separation or retrosystem ignition.

The VM-7 and VM-8 atmospheres are critical for the terminal phase analysis. The VM-8 atmosphere determines the critical deployment altitude (Mach number sensitive) for the aerodecelerators. Either VM-7 or VM-8 atmosphere is critical for aerodecelerator altitude loss (they size the aerodecelerators). In addition, the VM-7 and VM-8 atmospheres result in the maximum velocity entering the terminal phase region. Terrain heights of both zero and some positive value (6000 ft) are studied because an altitude initiation trigger must be designed on some altitude other than zero. It is therefore necessary to know terminal phase performance sensitivity to terrain height.

APPENDIX B

Additional ground rules and constraints related to the terminal phase decelerator types are described in the following paragraphs.

Aerodecelerator system. - Ground rules and constraints include:

1) Aerodecelerator completes its job at 4000 ft above terrain;
2) Flightpath angle at aerodecelerator separation must be steeper than -60°;
3) Time on aerodecelerator must be at least 16 sec or longer;
4) The $M_D = 2.0$ system must be sized to accomplish 2) and 3) above or separate aeroshell, whichever is larger.

All-retro system. - Ground rules and constraints include:

1) High thrust braking phase to zero horizontal velocity with thrust vector aligned along velocity vector at initiation;
2) Vertical drop at one Mars G for 3 sec followed by 3 Mars G braking to zero velocity;
3) Initial thrust for high thrust braking phase provides an acceleration equal to the drag acceleration (i.e., minimum allowable thrust-to-weight ratio).

An introductory system description was given at the beginning of this section. A more comprehensive description is presented below.

Vernier System

The aerodynamic decelerators (parachute, ballute) use a retro propulsion vernier for final deceleration to touchdown at zero velocity on the surface. Vernier system performance is based on the following ground rules and assumptions:

1) Ignition at 4000 ft above the surface;
2) Velocity at ignition is 1.25 times parachute terminal velocity;
3) Flightpath angle at ignition is -60°;

4) A 220-fps horizontal velocity due to wind at ignition;

5) Aerodecelerator separation at vernier ignition.

A monopropellant three-engine system is assumed for the majority of the terminal phase analyses. The propellant weight is determined from the normalized propellant shown in figure B72 and the equation:

$$W_p = \frac{F_{norm} W_{v_o}}{I_{sp}}$$

The thrust-to-weight ratio (T/W) is also shown in figure B72 as a function of parachute terminal velocity,

$$V_T^2 = \frac{2g_\sigma B_{DEC}}{\rho}$$

Vernier system engine and tankage weights are determined from data that appear in Appendix D. A bipropellant system is also used to compare with monopropellant performance for the parachute/orbit case. The equations and curves discussed above and the data in Appendix D are also applicable to that configuration. Specific impulse is 225 sec for the monopropellant system and 285 sec for the bipropellant.

Parachute/Vernier System

The parachute is deployed either at $M = 2.0$ in VM-8 or at the same altitude in VM-7. The parachute is assumed to have accomplished its purpose when a relative flightpath angle of -60° is reached in the most critical atmosphere. Figures B73 thru B78 show B_{DEC} or parachute size required to reach these final conditions for various γ_E and B_E. For example, in figure B73 an entry ballistic coefficient, $B_E = 0.4$ slug/ft^2 at $\gamma_E = -18°$ and $h_T = 0$ requires a B_{DEC} size of 0.045 slug/ft^2. Any larger B_{DEC} will fail to reach $\gamma = -60°$ at 4000 ft above terrain.

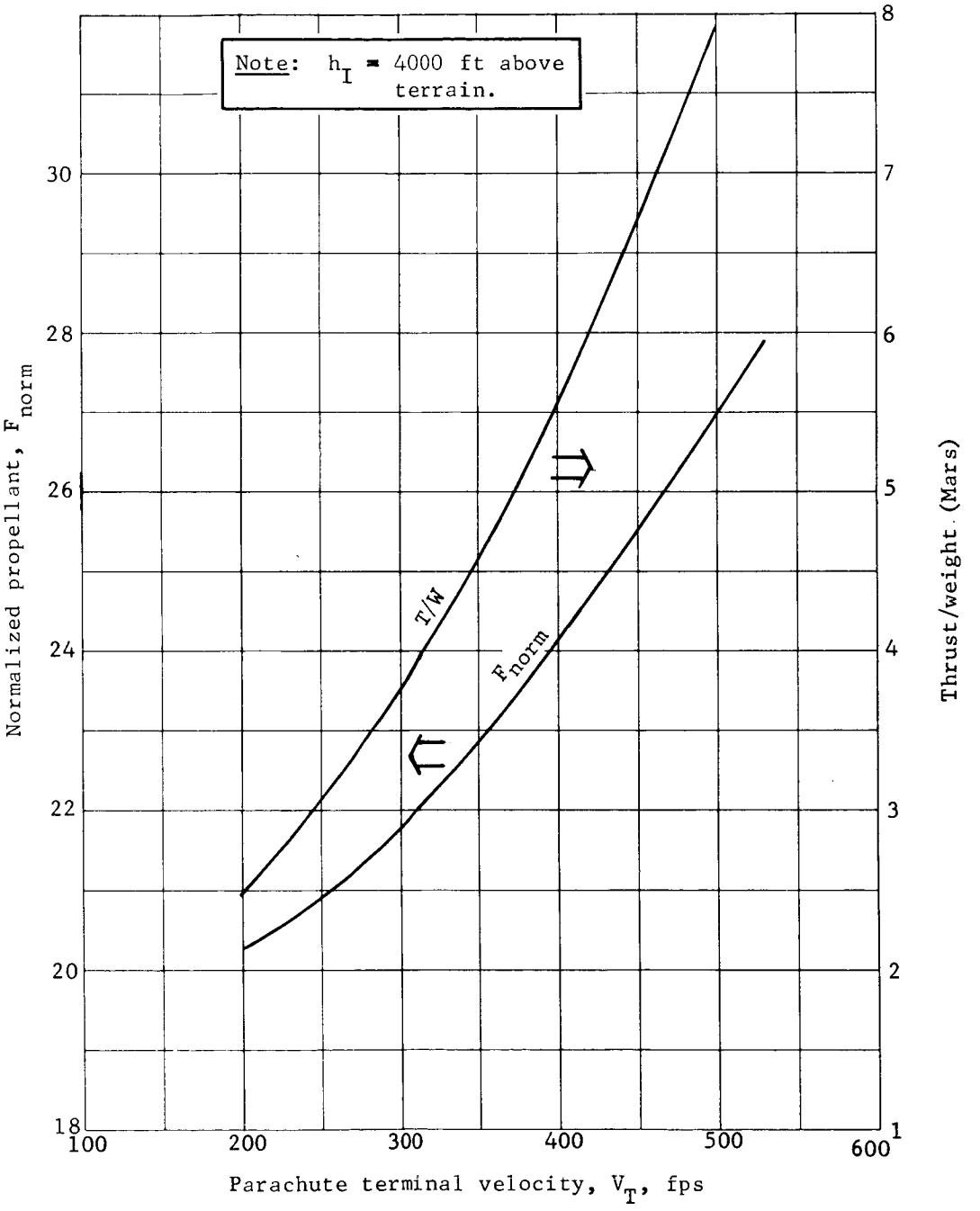

Figure B72.- Propellant and Thrust/Weight as a Function of Parachute Terminal Velocity

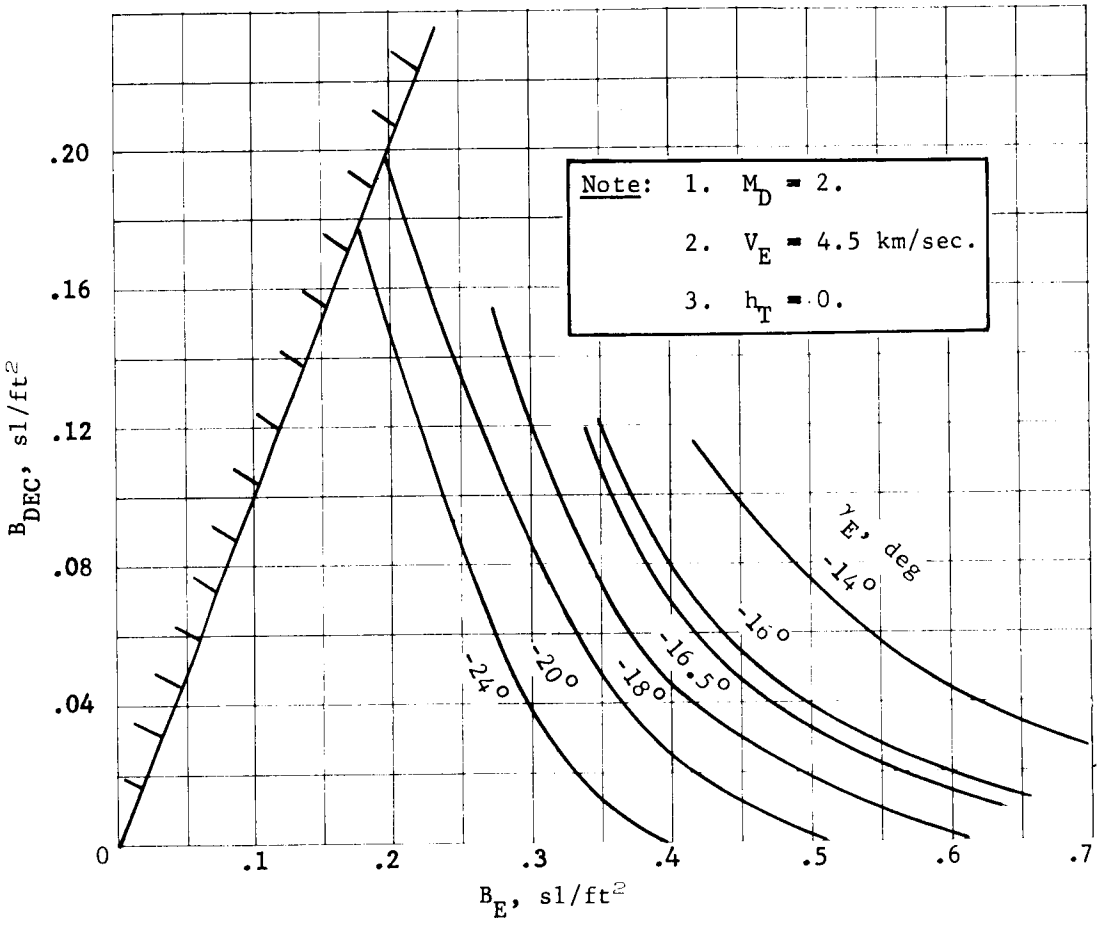

Figure B73.- Aerodecelerator Size Limit

APPENDIX B

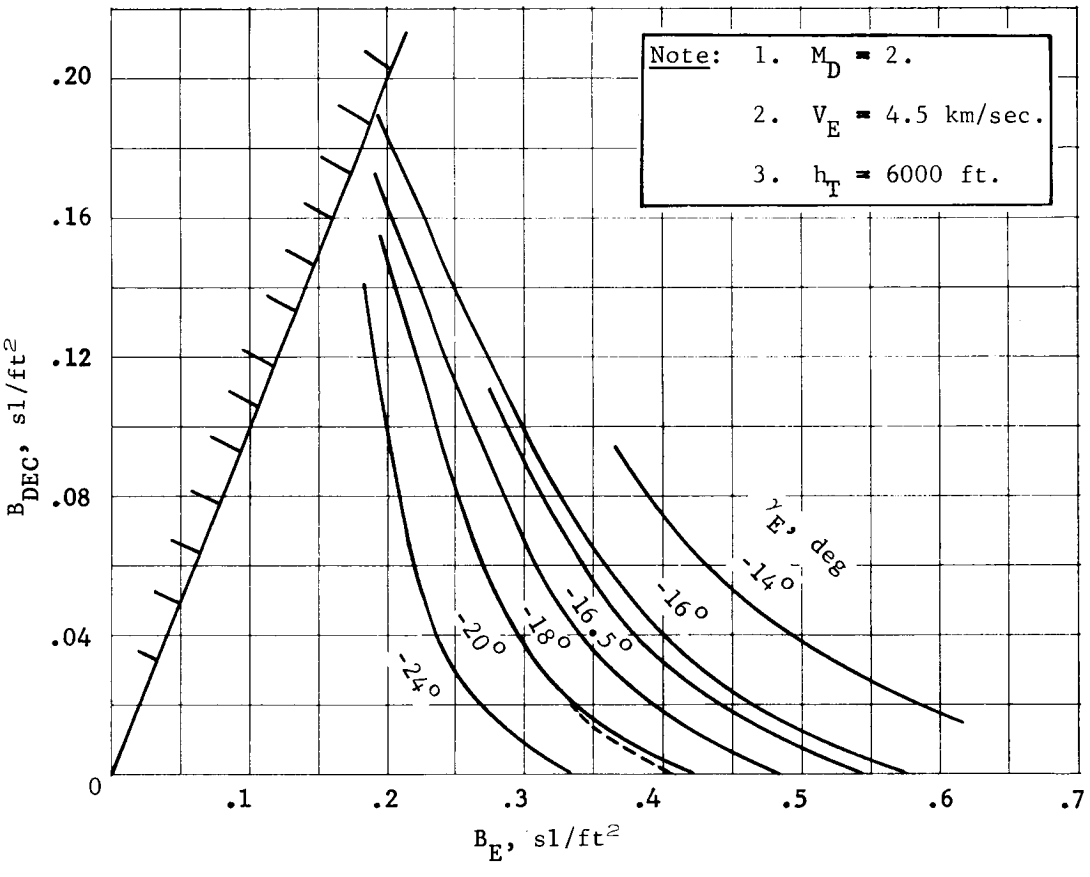

Figure B74.- Aerodecelerator Size Limit

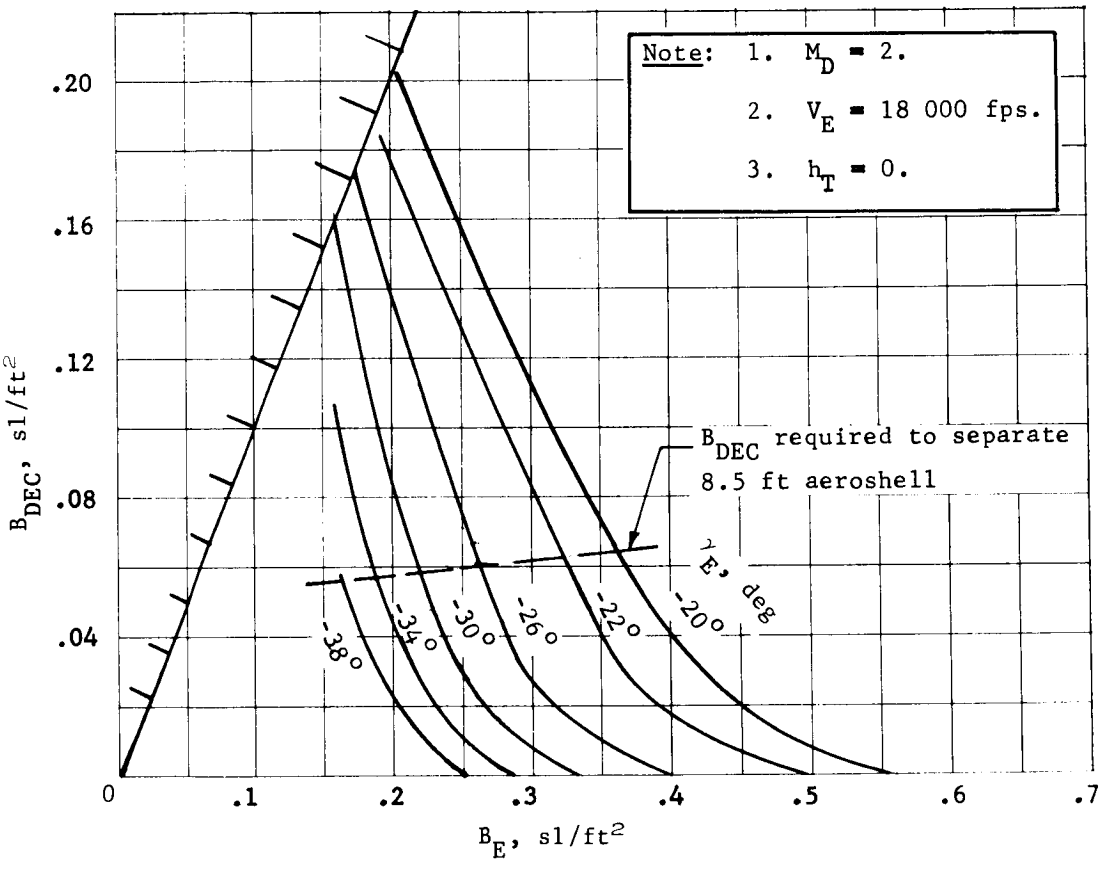

Figure B75.- Aerodecelerator Size Limit

APPENDIX B

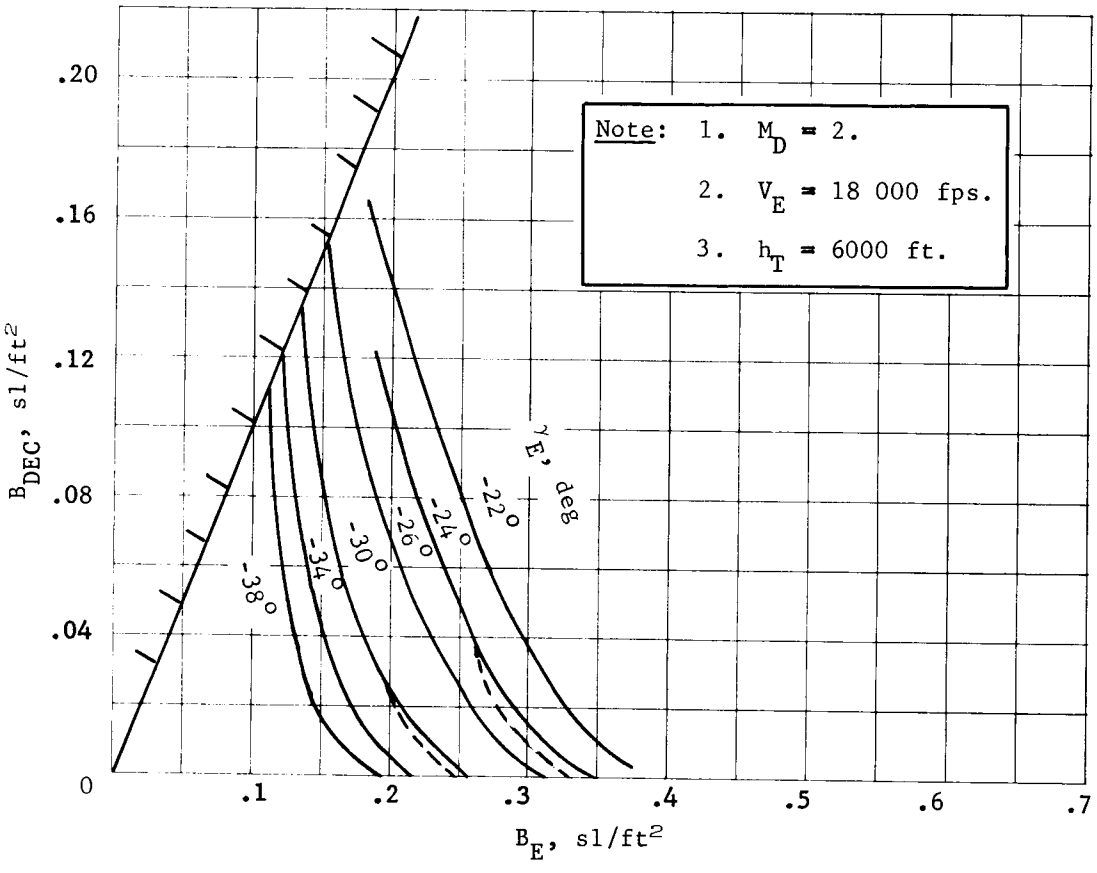

Figure B76.- Aerodecelerator Size Limit

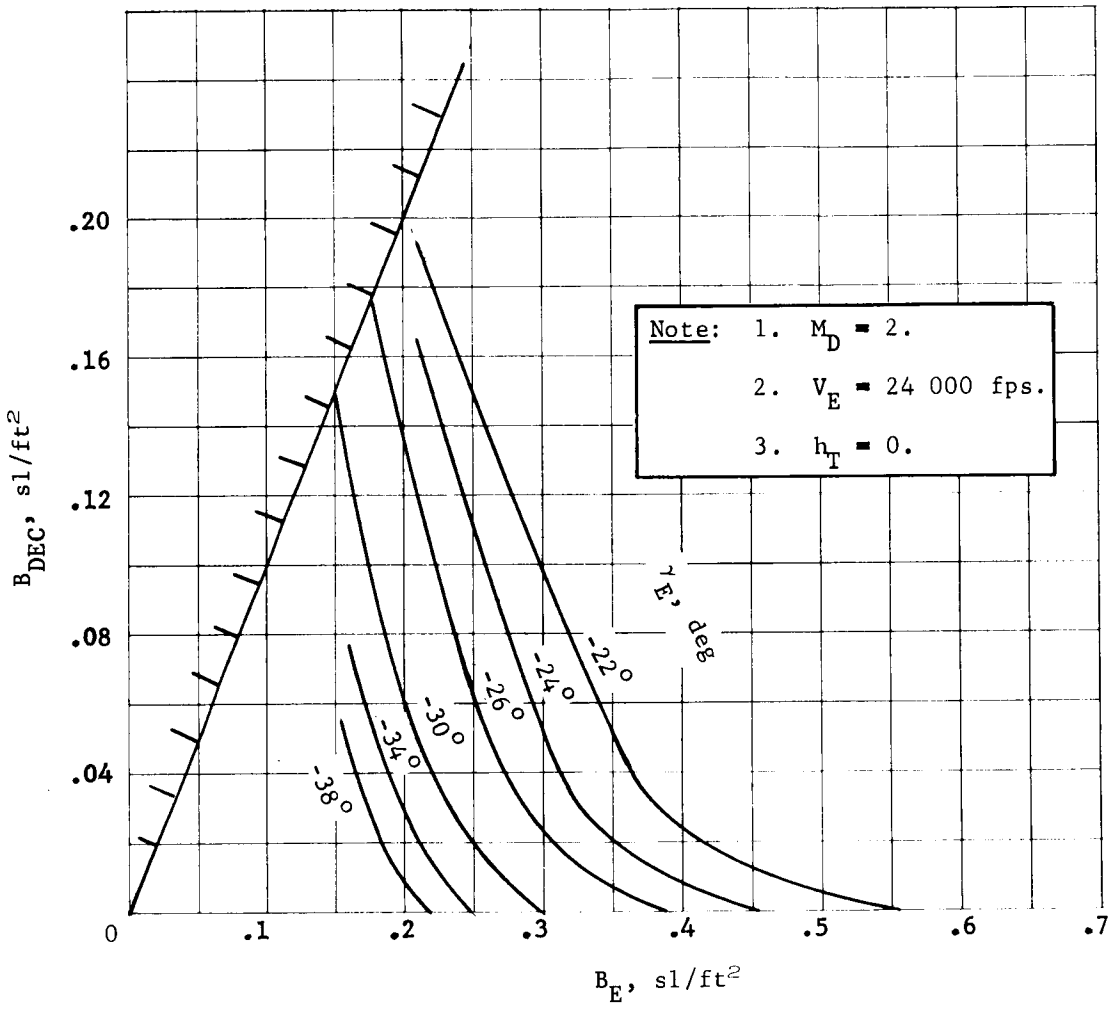

Figure B77.- Aerodecelerator Size Limit

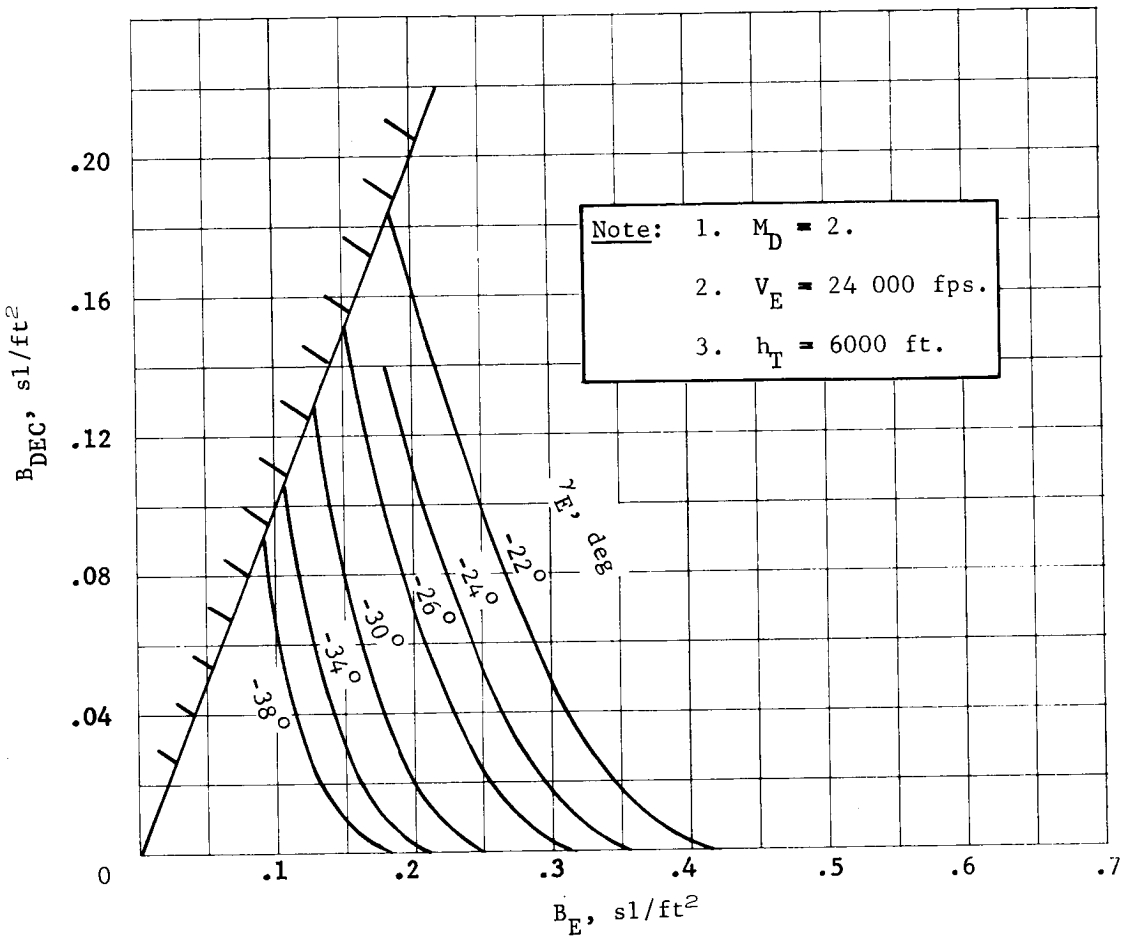

Figure B78.- Aerodecelerator Size Limit

APPENDIX B

In landed equipment weight calculations, the parachute size used is always sufficient to separate the system from the aeroshell at M = 0.8. Therefore, in those cases where the parachute size required for separation is larger than shown in figures B73 thru B78, the size required for separation is used. The relative acceleration required to separate from the aeroshell is assumed to be 30 ft/sec^2. The required parachute size is determined from:

$$q_D \left[\frac{(C_D A)_{DEC}}{m_{DEC}} - \frac{(C_D A)_{A/S}}{m_{A/S}} \right] = 30 \text{ ft/sec}^2$$

$$30 = q_D \left[\frac{1}{B_{DEC}} - \frac{1}{B_{A/S}} \right]$$

$B_{A/S}$ is shown in figure B79 as a function of aeroshell weight. The dotted line in figure B75 shows B_{DEC} required for separation. Larger B_{DEC} will not separate the aeroshell.

A minimum time on the parachute criterion is also assumed. There must be 16 sec on the parachute to allow for four operations. Deployment to aeroshell separation requires 5 to 7 sec. Three seconds is required to separate the system 100 ft from the aeroshell, assuring that no more than one radar beam is blocked. It is planned to have an offset load in the aeroshell to allow the aeroshell to clear the path of the radar beams. Three seconds is allowed for TDLR lockup. Another 2 to 3 sec is allowed for vernier ignition and verification. Figure B80 shows altitude loss on the parachute versus B_{DEC}. The boundaries shown are for 16, 30, and 50 sec on the parachute. These boundaries were formed from all the trajectories calculated in this study, both orbit and direct. An example of the data variation of these points is shown for the 30-sec boundary. Any point above a boundary will have times that are equal to or greater than the minimum time indicated. Three typical contours taken from the B_E versus B_{DEC} (figs. B74 and B76) are superimposed. These contours intersect the t = 16 sec boundary. At that point, the B_E versus B_{DEC} boundary must be modified to follow the t = 16 sec boundary as shown in figures B74 and B76. These show that for a particular γ_E a larger size parachute must be used for a given B_E to obtain at least 16 sec on the parachute.

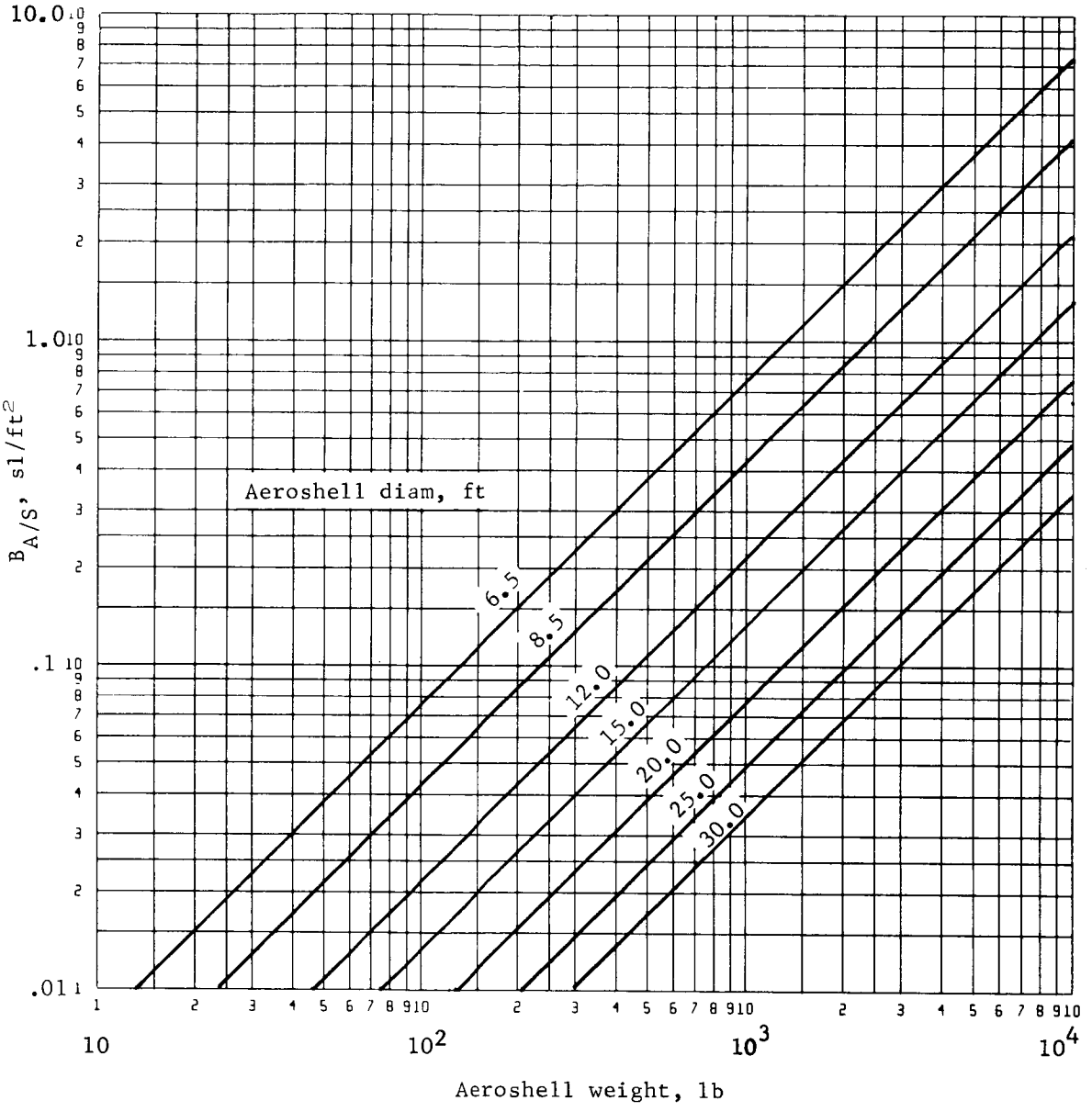

Figure B79.- Aeroshell Ballistic Coefficient

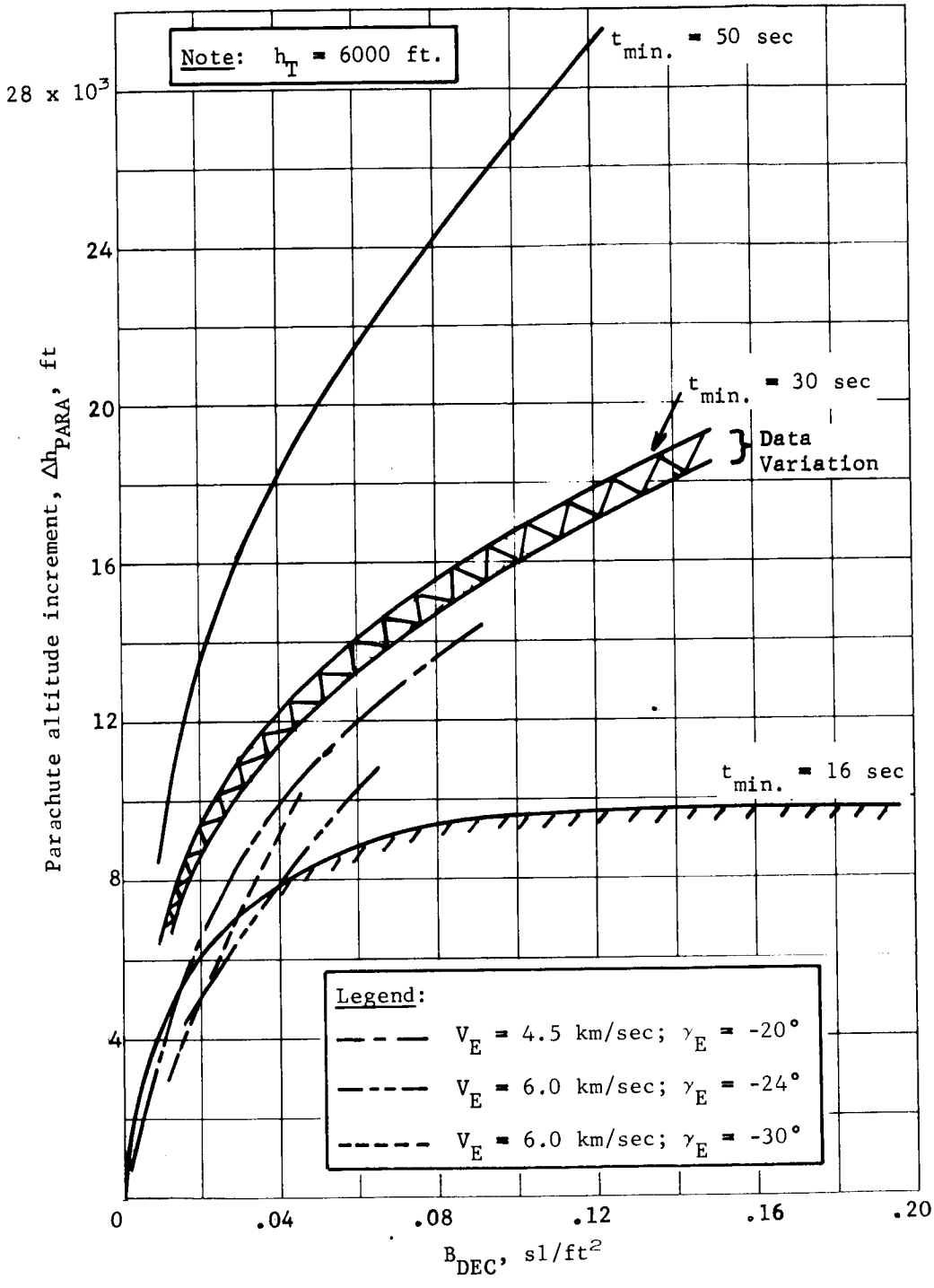

Figure B80.- Minimum Time on Parachute versus Altitude Change

APPENDIX B

Although a complete determination of minimum time limits was not calculated for all conditions, a check of the study results indicates that all cases of interest meet the time requirement.

Ballute/Vernier System

Ballute deployment Mach numbers investigated are $M = 3$ and $M = 5$ in VM-8 and at the same altitudes in VM-7. A tucked-back ballute with a 10% burble fence is used in the study. No provision is made to size the ballute to separate from the aeroshell as in the parachute system. Plots of B_{DEC} versus B_E, similar to those for the parachute system, are shown in figures B81 thru B92. Final conditions are the same as for the parachute (at least $\gamma = -60°$ at 4000 ft above terrain).

It may be seen in comparing Mach numbers of 2, 3, and 5 that with increasing deployment Mach numbers, larger B_E and smaller decelerator sizes are required at the same entry angle. In general, the orbit mode requires smaller decelerators than the direct mode. For the direct mode at high γ_E, the limiting entry velocity is 24 000 fps. For lower γ_E, the limiting entry velocity is 18 000 fps.

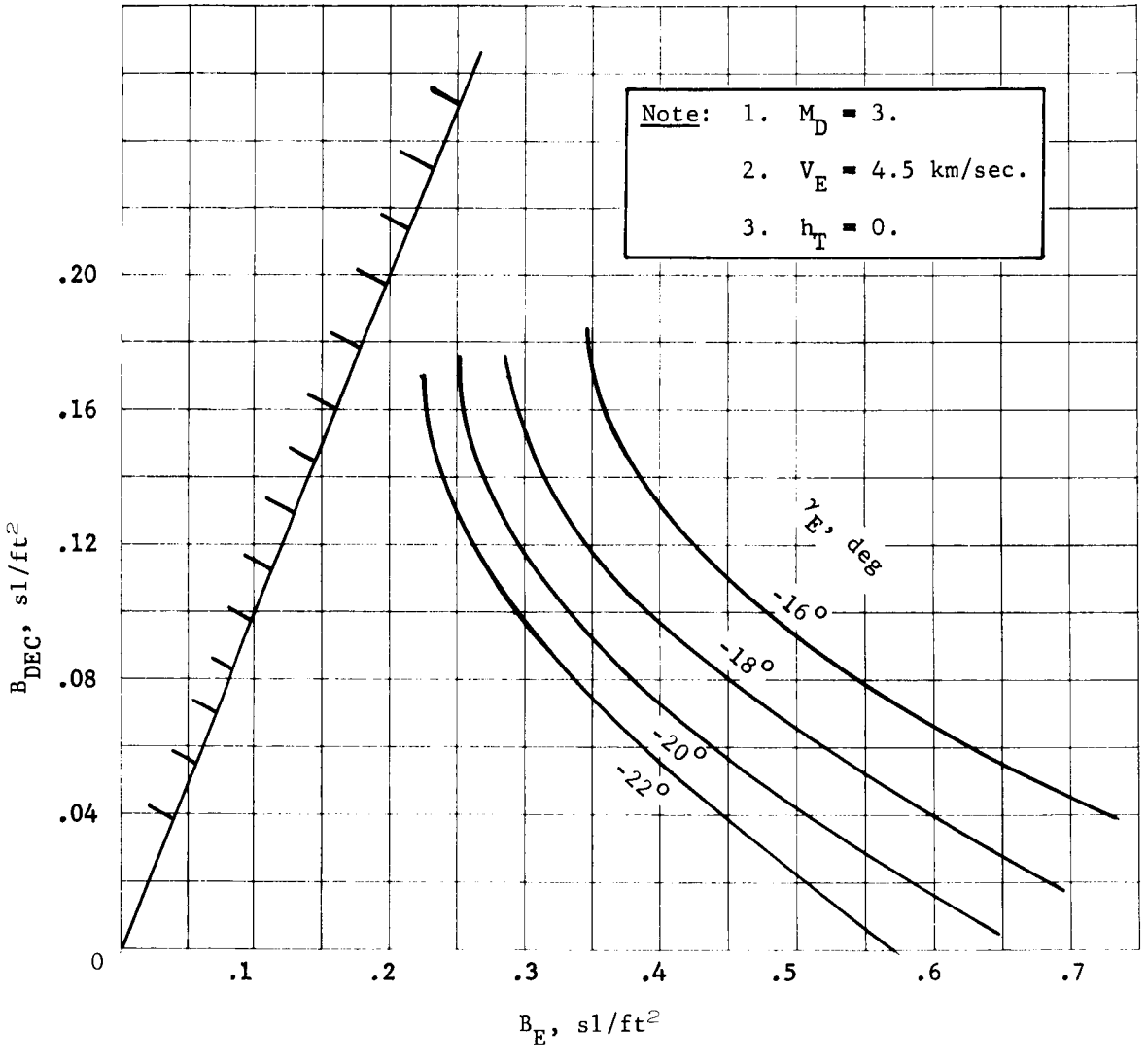

Figure B81.- Aerodecelerator Size Limit

APPENDIX B

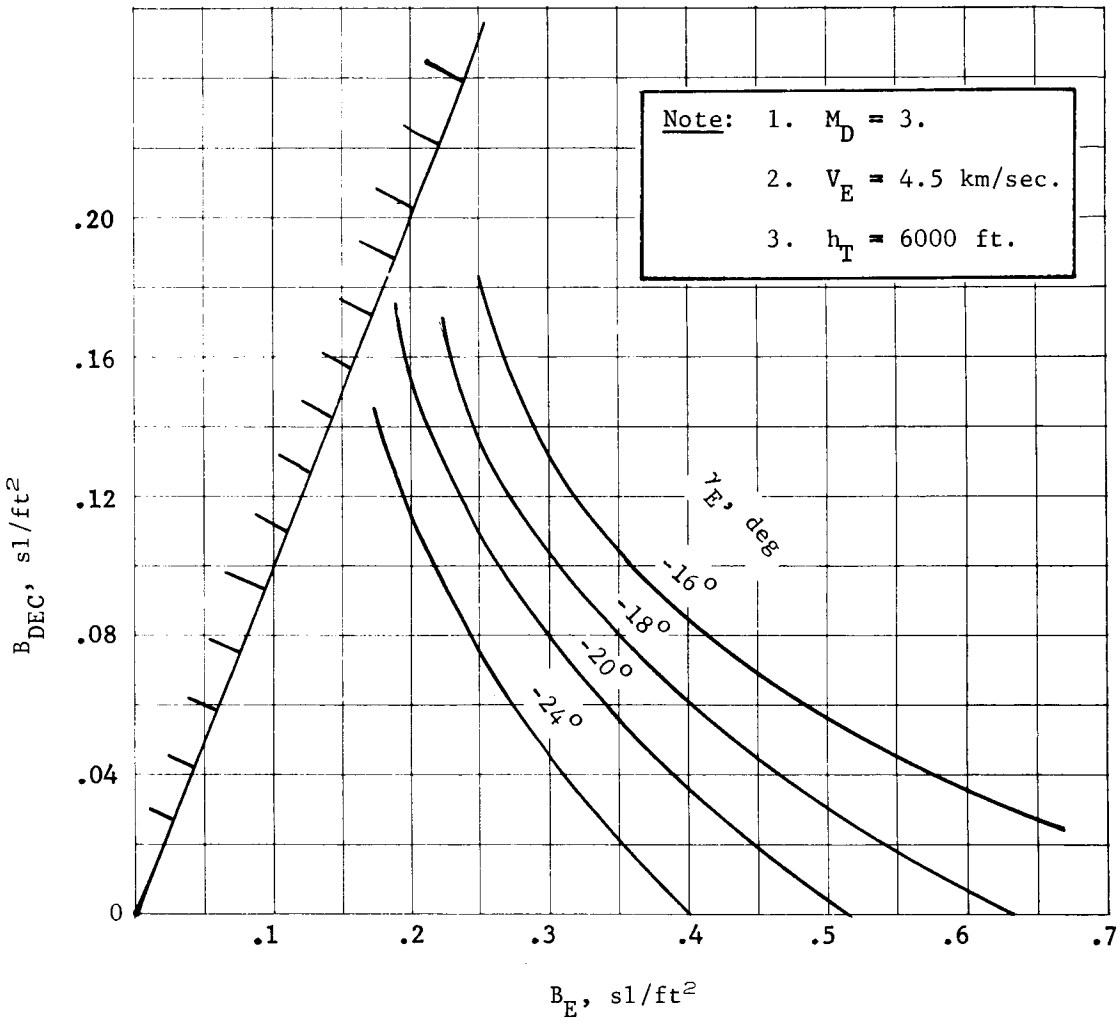

Figure B82.- Aerodecelerator Size Limit

APPENDIX B

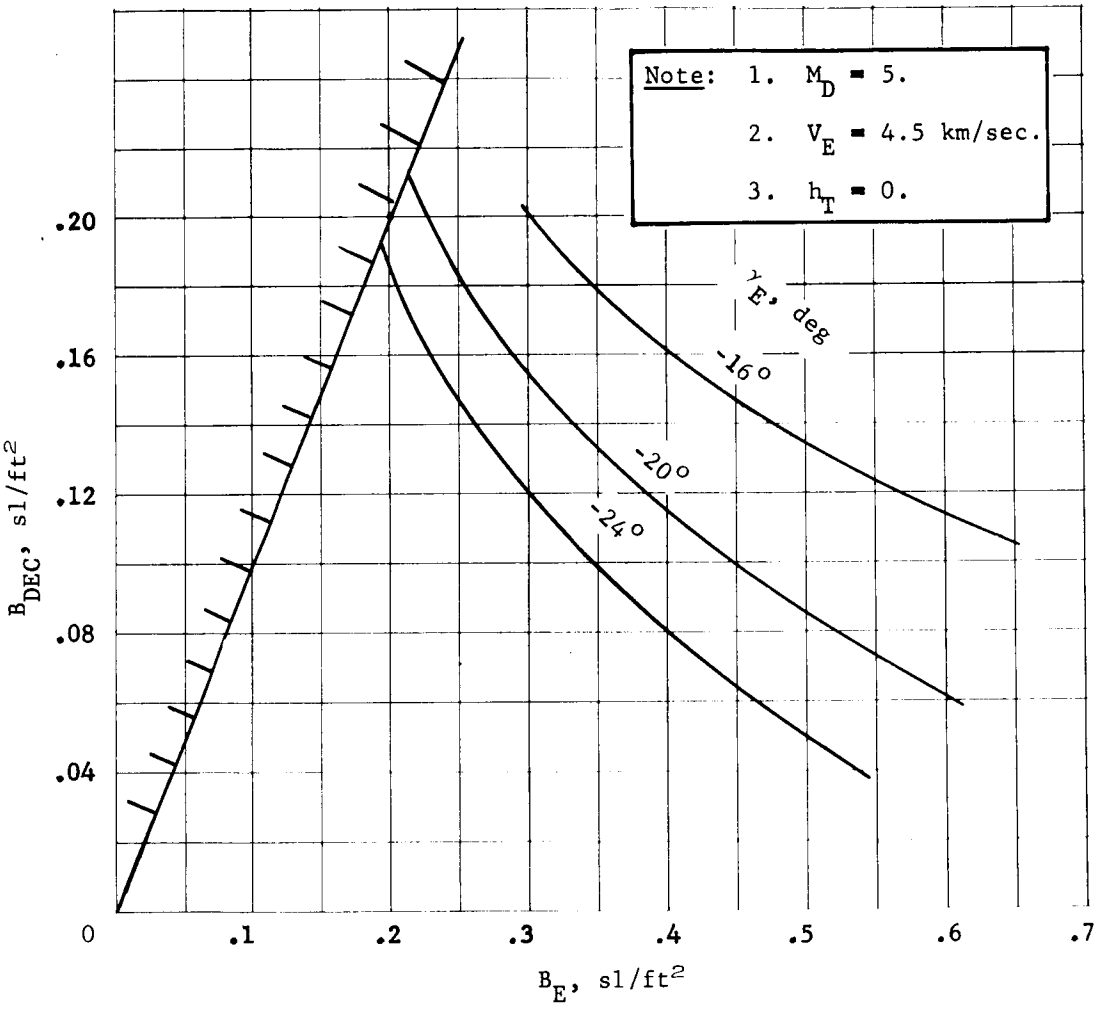

Figure B83.- Aerodecelerator Size Limit

APPENDIX B

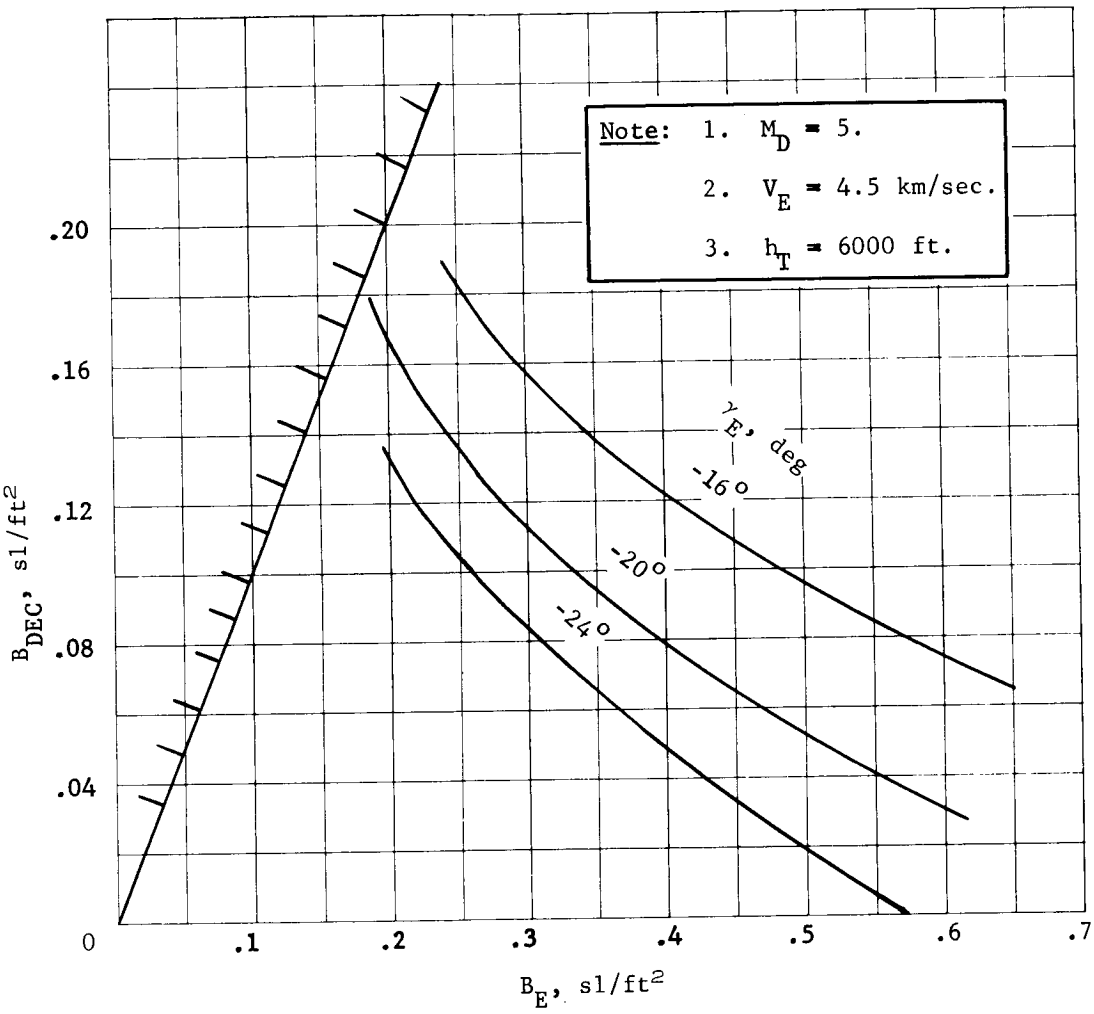

Figure B84.- Aerodecelerator Size Limit

APPENDIX B

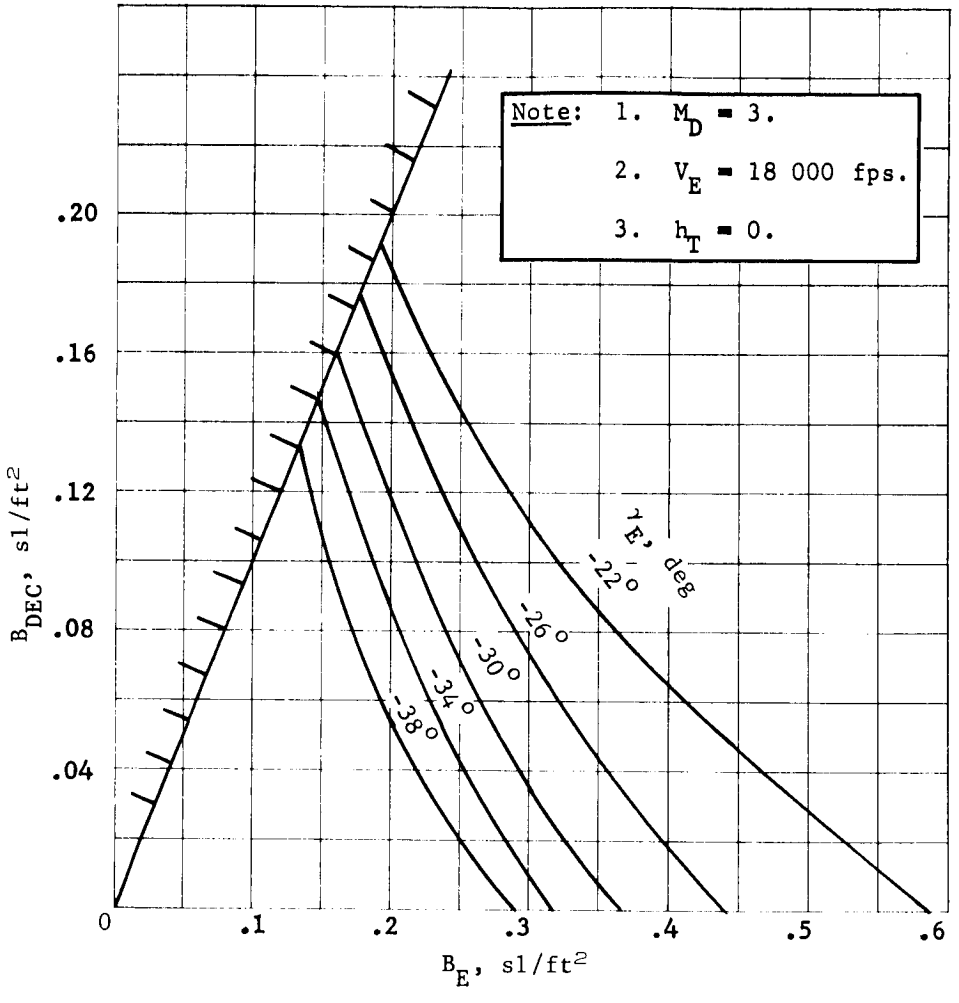

Figure B85.- Aerodecelerator Size Limit

APPENDIX B

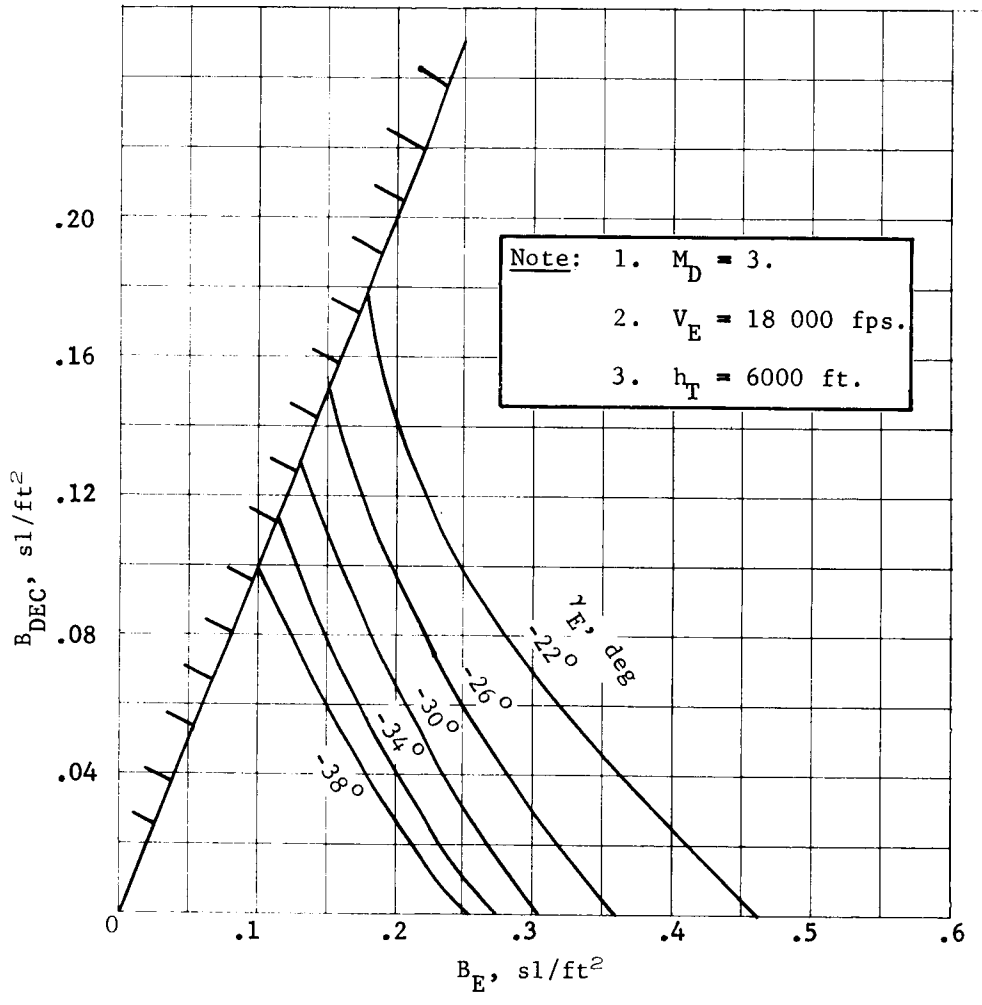

Figure B86.- Aerodecelerator Size Limit

APPENDIX B

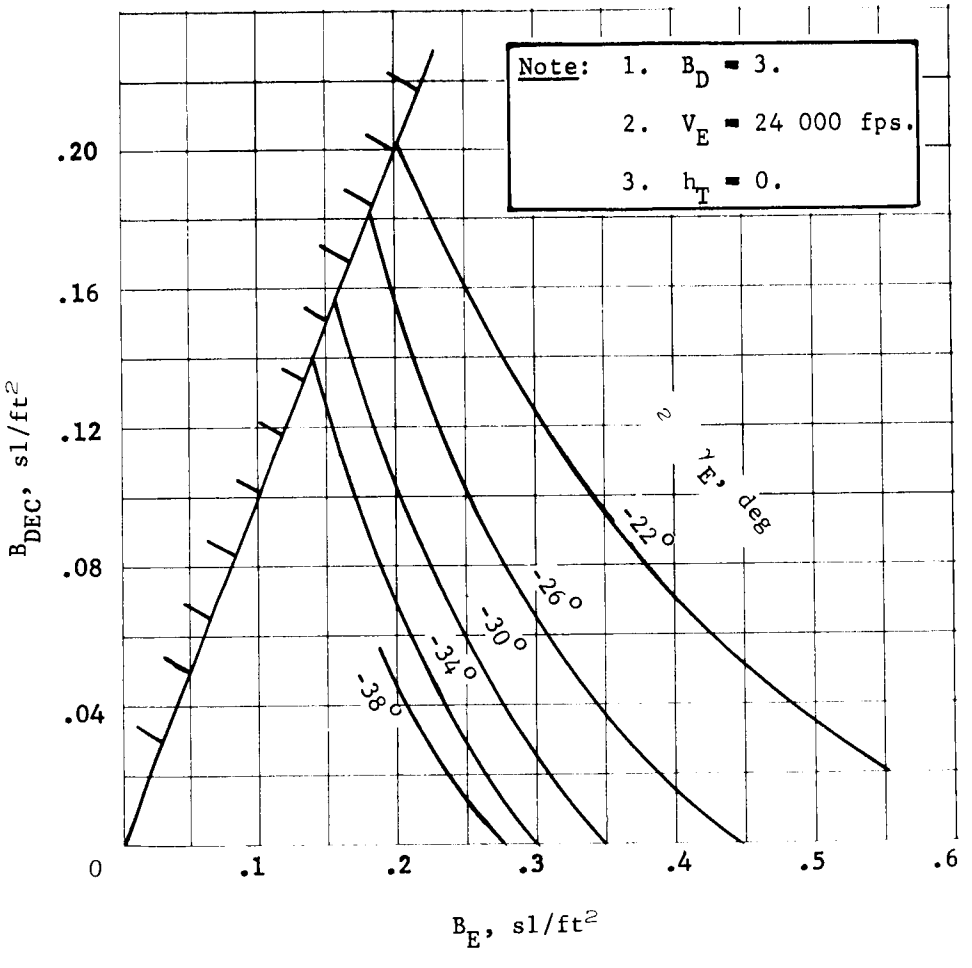

Figure B87.- Aerodecelerator Size Limit

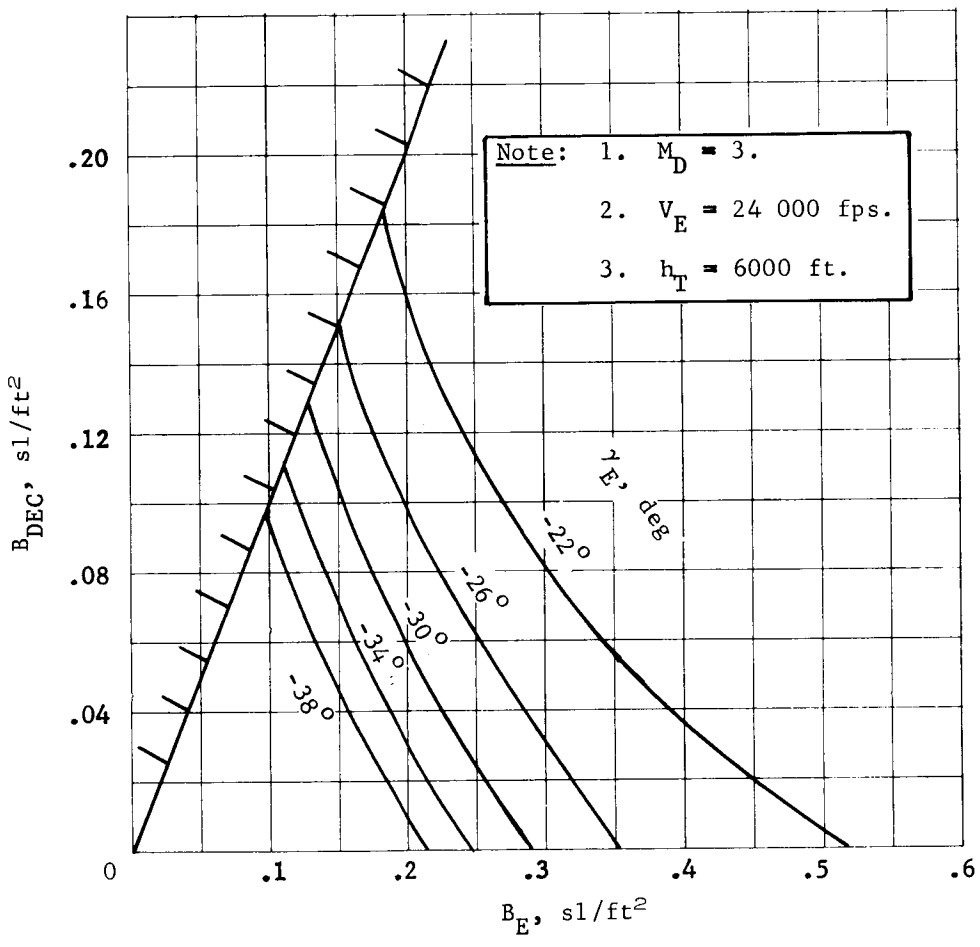

Figure B88.- Aerodecelerator Size Limit

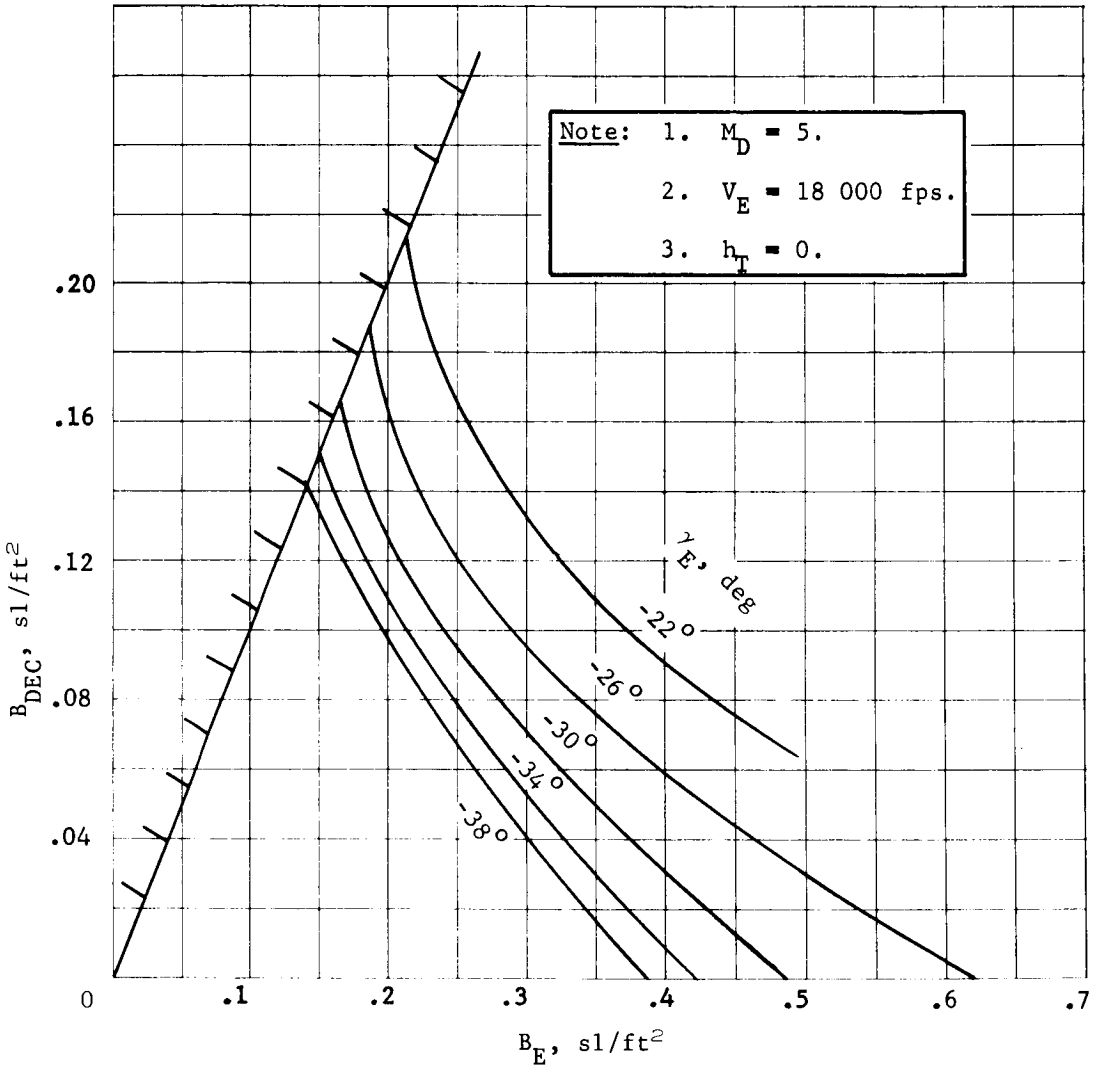

Figure B89.- Aerodecelerator Size Limit

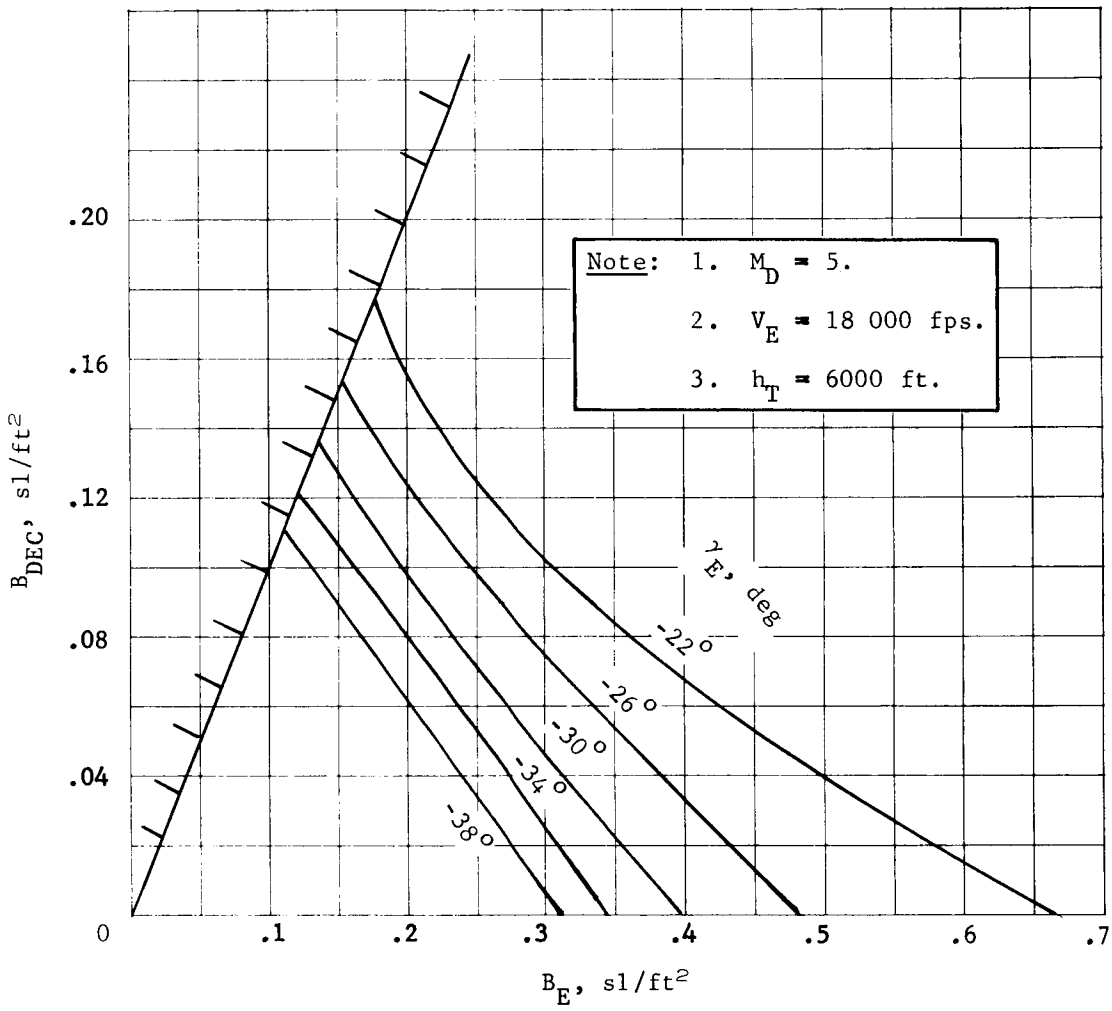

Figure B90.- Aerodecelerator Size Limit

APPENDIX B

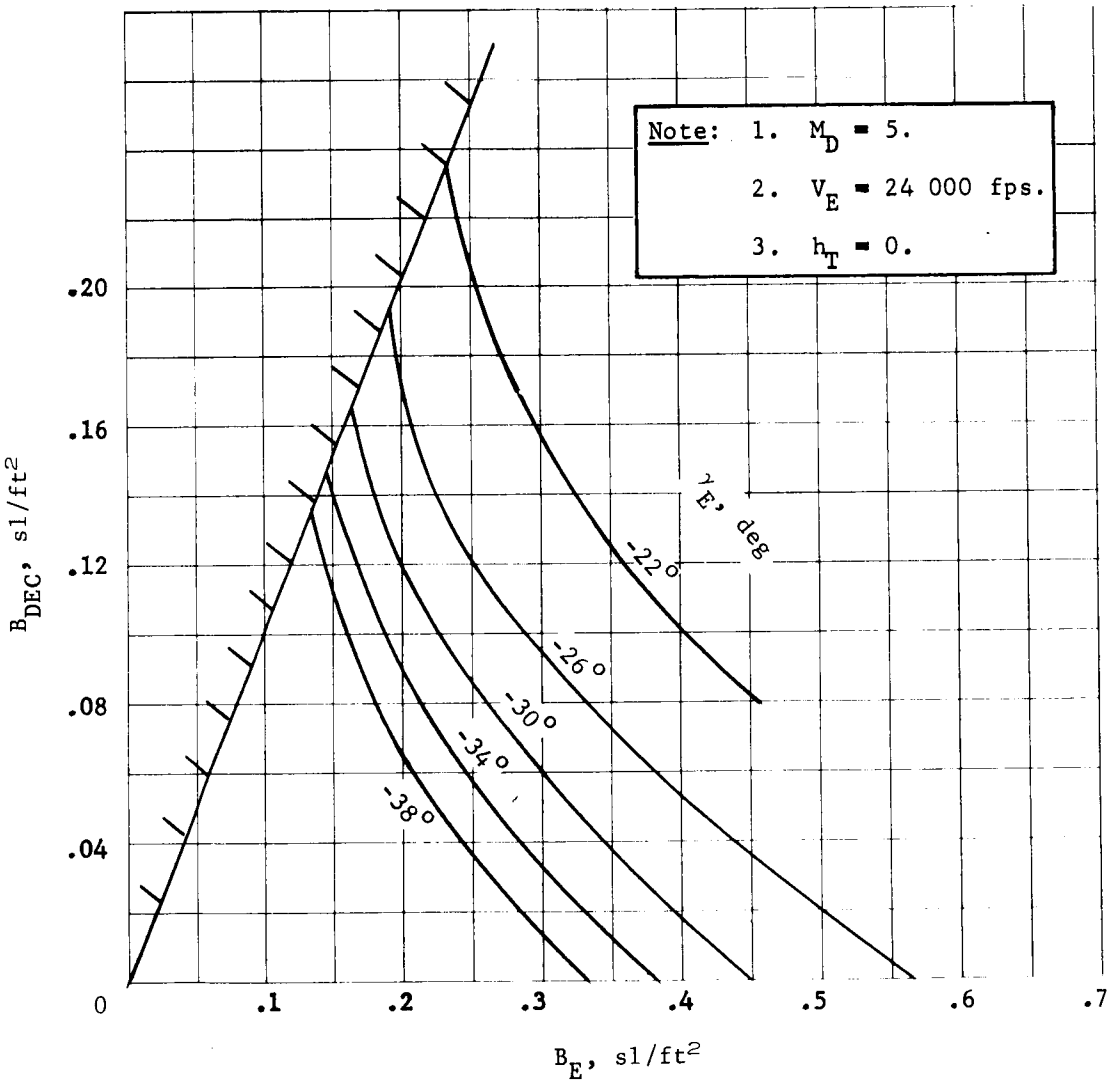

Figure B91.- Aerodecelerator Size Limit

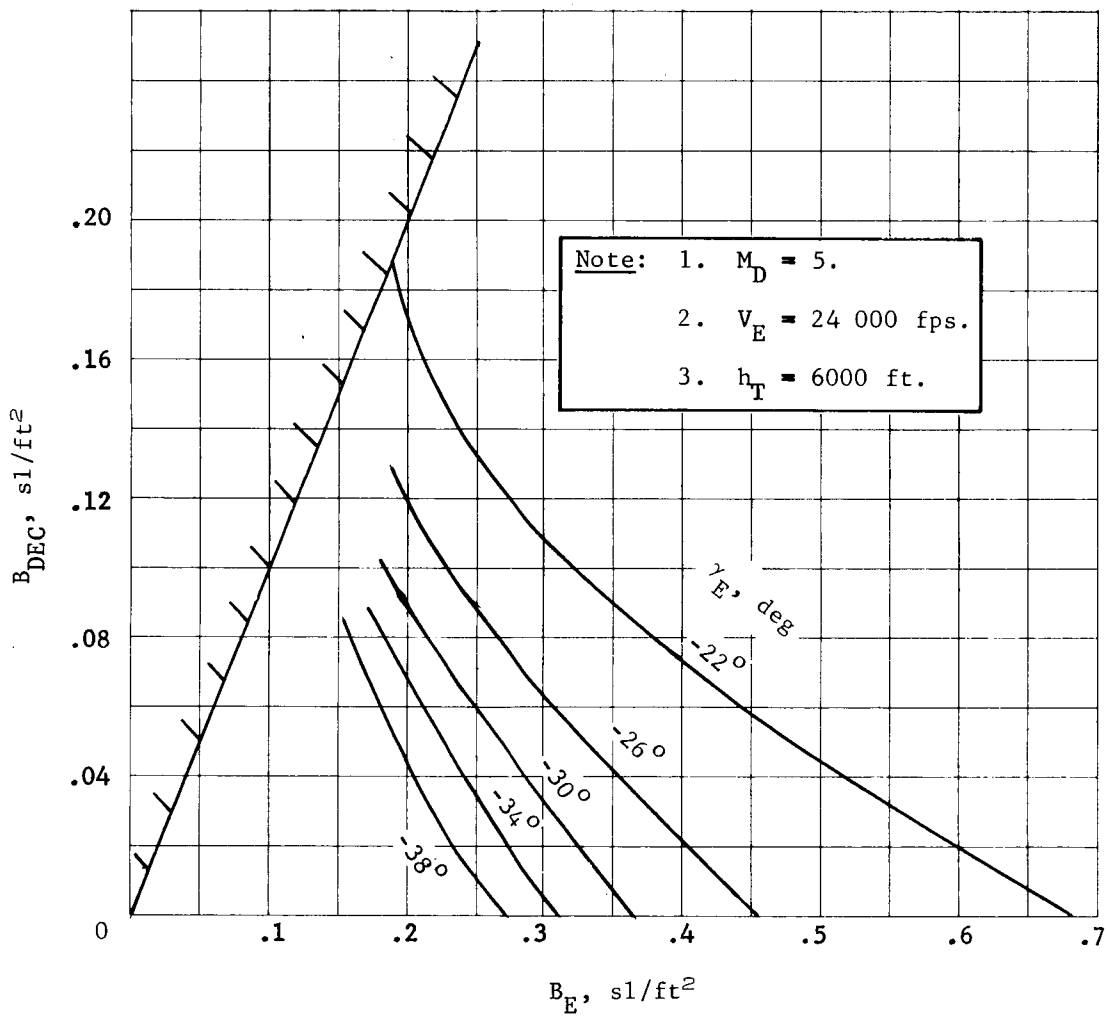

Figure B92.- Aerodecelerator Size Limit

APPENDIX B

Single-Stage Retro

The single-stage retro system assumes a three-engine liquid bipropellant system with a specific impulse of 300 sec. The aeroshell is assumed to separate at retro initiation, though no attempt was made to size the thrust to ensure this. The thrust to initial mass is set equal to the drag acceleration at retro initiation. This represents the minimum allowable thrust-to-weight ratio. An initiation altitude based on this thrust level is found by iteration, which results in zero velocity at the terrain surface.

The flight sequence used in the calculations consist of three phases -- a braking phase to remove the horizontal velocity component, a vertical descent at 1.0 g_σ for 3 sec, and a final vertical braking at 3.0 g_σ. Though this sequence would not be used in an operational design, it gives performance values very close to a real design.

Two-Stage Retro

The two-stage retro system consists of a first stage solid rocket motor (SRM) and a second stage liquid rocket motor (LRM). The aeroshell is assumed to separate at SRM ignition. At LRM ignition, the SRM assembly separated. The second stage reaches zero velocity at the terrain surface. The solid motor thrust to initial mass is assumed equal to the drag acceleration at ignition. However, the burntime and solid propellant used must be found in combination with the liquid rocket motor size in order to find the maximum landed equipment.

Retro/Parachute/Vernier

This system consists of a solid stage retro, a parachute, and a monopropellant vernier. The parachute deployment altitude is chosen sufficiently high to ensure at least $\gamma = -60°$ at 4000 ft above terrain (vernier ignition altitude). The retro maneuver is similar to the solid phase of the two-stage retro. Thrust to initial mass is equal to drag acceleration at ignition. For this study a $B_{DEC} = 0.30$ slug/ft^2 deployed at 20 700 ft above terrain is assumed. Retro specific impulse is 280 sec.

APPENDIX B

Extendible Flaps

Extendible flaps are investigated as a means of increasing the aeroshell diameter. They are deployed before entry. Their purpose is the same as the inflatable afterbody. Flap sizes with drag areas equal to 20-, 25-, and 30-ft aeroshell diameters are investigated. They are studied with the parachute, ballute, and single-stage retro systems for the direct mode only.

Inflatable Afterbody/Retro

The inflatable afterbody/retro system consists of a tucked-back ballute without burble fence deployed before entry and a single-stage liquid retro identical to that described above. The aeroshell and ballute are assumed to separate from the lander at retro ignition. The retro thrust to initial mass is equal to the drag acceleration at ignition. The ballute is sized for drag areas equivalent to 20-, 25-, and 30-ft diameter aeroshells. The ballute weight is based on the maximum dynamic pressure encountered during the trajectory.

Techniques and Equations

Single-stage retro. - The ground rules and assumptions are as follows:

1) Flat planet;
2) Constant gravitational acceleration;
3) Constant thrust;
4) Constant thrust direction;
5) Zero aerodynamic forces.

The diagram below shows directions of forces

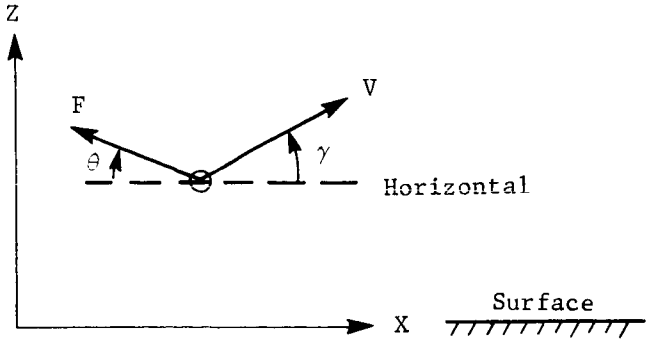

APPENDIX B

The single-stage retro system flight sequence consists of three phases:

1) Phase 1 - A braking phase, $\theta = -\gamma$, F/m_o = system drag acceleration at retro initiation, final condition $\dot{X}_f = o$;

2) Phase 2 - Vertical descent at 1.0 g_σ for 3 sec;

3) Phase 3 - Final vertical braking at 3.0 g_σ.

Phase 1 equations are as follows

$$\dot{X}_o = V_o \cos \gamma_o + V_w \qquad X_o = 0$$

$$\dot{Z}_o = V_o \sin \gamma_o$$

$$C_j = g\, I_{sp}$$

$$\dot{X}_f = 0 = \dot{X}_o + \cos \theta \ln \left(1 - \frac{F}{m_o} \frac{t}{C_j}\right)$$

$$\ln = \left(1 - \frac{F}{m_o} \frac{t}{C_j}\right) = - \frac{V_o}{C_j}$$

$$\left(\frac{m_p}{m_o}\right) = 1 - e^{-V_o/C_j} = \text{mass of propellant used for Phase 1}$$

then with

$$\dot{Z}_f = \dot{Z}_o - gt - C_j \sin \theta \ln \left(1 - \frac{F}{m_o} \frac{t}{C_j}\right) = g_\sigma t$$

or

$$\dot{Z}_f = \frac{-C_j\, g_\sigma}{(F/m_o)} \left(1 - e^{-V_o/C_j}\right) = \text{Vertical velocity at end of Phase 1}$$

Finally:

$$h_{f_1} = h_o + \left(\frac{\dot{Z}_{f_1}}{g_\sigma}\right) \left\{C_j \sin \gamma_o \left[1 - \frac{V_o/C_j}{1 - e^{-V_o/C_j}}\right] - \tfrac{1}{2} \dot{Z}_{f_1}\right\} =$$

$$= \text{altitude at end of Phase 1}$$

APPENDIX B

Phase 2 equations:

$$\dot{Z}_{f_2} = \dot{Z}_{f_1}$$

$$h_{f_2} = h_{f_1} + \dot{Z}_{f_1} t_2 = h_{f_1} + \dot{Z}_{f_1} \quad (3.0) = \text{altitude at end of Phase 2}$$

To get the propellant used in both Phases 2 and 3, consider general equations for vertical descent at constant acceleration.

$$m\ddot{Z} = F - gm$$

$$\ddot{Z} = \frac{F}{m} - g_{\sigma} = g_{\sigma} (n - 1)$$

Integrating

$$\dot{Z}_f = g_{\sigma} (n - 1)\ t + \dot{Z}_o$$

and, from

$$\dot{m} = \frac{-F}{g\ I_{sp}} = \frac{-F}{C_j} = \frac{dm}{dt}$$

$$\frac{dm}{m} = \frac{-F/M}{C_j}\ dt = \frac{-n\ g_{\sigma}}{C_j}\ dt$$

Integrating

$$\ln\left(\frac{m}{m_o}\right) = \frac{-n\ g_{\sigma}\ t}{C_j}$$

$$\frac{m_p}{m_o} = 1 - \frac{m}{m_o} = 1 - e^{\frac{-n\ g_{\sigma}\ t}{C_j}}$$

$$\left(\frac{m_p}{m_o}\right)_2 = 1 - e^{\frac{-3\ g_{\sigma}}{C_j}} = \text{propellant used during Phase 2}$$

APPENDIX B

Phase 3 equations:

$$\dot{Z}_{f_3} = g_{\sigma'} (n - 1)\, t_3 + \dot{Z}_{o_3} = g_{\sigma'} (n - 1)\, t_3 + \dot{Z}_{f_1}$$

$$t_3 = \frac{-\dot{Z}_{f_1}}{g_{\sigma'} (n - 1)} = \frac{-\dot{Z}_{f_1}}{2g_{\sigma'}} = \text{burning time for Phase 3}$$

Then, with

$$\dot{Z}_{f_3} = g_{\sigma'} (n - 1)\, t_3 + \dot{Z}_o$$

Integrating:

$$Z_f = \tfrac{1}{2}\, g_{\sigma'} (n - 1)\, t_3^2 + \dot{Z}_o t_3 + h_o$$

or

$$h_{f_3} = h_{o_3} + \tfrac{1}{2}\, g_{\sigma'} (n - 1)\, t_3^2 + \dot{Z}_{f_1} t_3$$

$$h_{f_3} = h_{f_2} - \frac{\dot{Z}_{f_1}^2}{4g} = \text{altitude at end of Phase 3 with } n = 3$$

The altitude at the end of the retro maneuver is:

$$h_{f_3} = h_o + \dot{Z}_{f_1} \left\{ \frac{C_j}{g_{\sigma'}} \sin \gamma_o \left[1 - \frac{\nu}{1 - e^{-\nu}} \right] + 3 \right\} - \frac{3\dot{Z}_{f_1}^2}{4g_{\sigma'}}$$

where

$$\nu = \frac{V_o}{C_j}$$

The h_o is found by iteration as is noted on the figures described below.

APPENDIX B

$$\left(\frac{m_p}{m_o}\right)_3 = 1 - \exp\left\{\frac{-n\, g_\sigma\, t_3}{C_j}\right\} = 1 - \exp\left\{\frac{3g\, \dot{Z}_{f_1}}{2C_j\, g_\sigma}\right\}$$

= propellant used during Phase 3

Note: the m_o in the previous equations are masses at the beginning of the particular phase. Correcting to the mass at retro igntiion, the total propellant used is:

$$\frac{m_{p_{TOT}}}{m_{o_1}} = 1.0 - e^{-\nu} \exp\left\{\frac{3g_\sigma}{C_j}\left(\frac{\dot{Z}_{f_1}}{2g_\sigma} - 1\right)\right\}$$

Two-stage retro. - The solid rocket motor phase is similar to the first phase of the single-state retro. Thrust equals drag acceleration at ignition and $\theta = -\gamma_o$. The three phases of the LRM are the same as the single-stage retro.

The final altitude for the SRM is:

$$Z_{f_s} = Z_o + \dot{Z}_o t - \tfrac{1}{2} g_\sigma t^2 - \left(C_j t \sin \gamma_o\right)\left[1 - \ln\left(1 - \frac{m_{p_s}}{m_o}\right) + \frac{\ln\left(1 - \frac{m_{p_s}}{m_o}\right)}{\left(m_{p_s}/m_o\right)}\right]$$

For the LRM (first phase):

$$Z_{f_{L_1}} = Z_{f_s} + \dot{Z}_{f_s} t - \tfrac{1}{2} g_\sigma t^2 - \left(C_j t \sin \gamma_o\right)\left[1 - \ln\left(1 - \frac{m_{p_L}}{m_{o_L}}\right) + \frac{\ln\left(1 - \frac{m_{p_L}}{m_{o_L}}\right)}{\left(m_{p_L}/m_{o_L}\right)}\right]$$

APPENDIX B

The final altitude is:

$$h_f = Z_{f_{L_1}} + 3\dot{Z}_f + \frac{\dot{Z}_f^2}{4g_\delta}$$

The liquid propellant weight will now be found.

$$\dot{X}_{f_L} = 0 = \dot{X}_{f_s} + C_{j_L} \cos \gamma_o \ln \left(1 - \frac{m_{p_L}}{m_{o_L}}\right) = \dot{X}_o$$

$$+ C_{j_s} \cos \gamma_o \ln \left(1 - \frac{m_{p_s}}{m_{o_s}}\right) + C_{j_L} \cos \gamma_o \ln \left(1 - \frac{m_{p_L}}{m_{o_L}}\right)$$

$$\frac{-\dot{X}_o}{C_{j_L} \cos \gamma_o} = \frac{-V_o}{C_{j_L}} = \ln \left(1 - \frac{m_{p_s}}{m_{o_s}}\right)^{C_o} + \ln \left(1 - \frac{m_{p_L}}{m_{o_s} - \frac{m_{p_s}}{\lambda_s}}\right)$$

where

$$C_o = \left(I_{sp_S} / I_{sp_L}\right)$$

Solving for M_{PL}, the liquid propellant weight,

$$m_{p_L} = \left(m_o - \frac{m_{p_s}}{\lambda_s}\right) \left[1 - \frac{e^{-V_o/C_j}}{\left(1 - \frac{m_{p_s}}{m_o}\right)^{C_o}}\right]$$

The liquid propellant weight depends on M_{PS}, the solid propellant weight. Therefore, the optimum combination of solid and liquid systems is found by varying the solid system and finding the liquid system size that gives the maximum landed weight.

The initiation altitude must be found by an iteration procedure as mentioned in the previous section.

APPENDIX B

Retro/parachute/vernier.- The Mach number at parachute deployment is assumed to be 2.0 in VM-8. The altitude at the end of the retro maneuver is found from:

$$V_f = 2V_c = 2X \text{ speed of sound}$$

$$m\dot{dV} = - F - m\, g_{\sigma'} \sin \gamma_o$$

$$\dot{dV} = (- n - \sin \gamma_o)\, g_{\sigma'}$$

$$2V_c = V = V_o - (n + \sin \gamma_o)\, g_{\sigma'} t$$

$$t_b = \frac{(V_o - 2V_c)}{g_{\sigma'} (n + \sin \gamma_o)}$$

$$h_f = h_o + \frac{V_o (V_o - 2V_c) \sin \gamma_o}{g_{\sigma'} (n + \sin \gamma_o)} - \frac{\frac{1}{2}(V_o - 2V_c)^2 \sin \gamma_o}{g_{\sigma'} (n + \sin \gamma_o)}$$

or

$$h_f = h_o + \frac{(V_o - 2V_c) \sin \gamma_o}{g_{\sigma'} (n + \sin \gamma_o)} \left[\frac{1}{2} V_o + V_c\right] = \text{altitude at end of retro}$$

with

$$\frac{F}{-\dot{m}} = g\, I_{sp} = C_j$$

$$\frac{dm}{m} = - \left(\frac{F}{m}\right) \frac{1}{C_j} dt$$

Integrating

$$\ln \left(\frac{m_f}{m_o}\right) = \frac{n\, g_{\sigma'}\, t}{C_j}$$

where

$$\frac{F}{m} = n\, g_{\sigma'} = \text{constant}$$

Finally

$$m_f = m_o \exp\left\{\frac{-n\,(V_o - 2V_c)}{C_j\,(n + \sin\gamma_o)}\right\}$$

Basic Parametric Data

The approach used in this analysis is to compare the useful payload on the ground for the various systems on the basis of entry weight and aeroshell diameter. The parameter used to compare the systems is landed equipment weight, W_{LE}. This parameter is defined as entry weight, W_E, minus the following:

1) Aeroshell weight - Function of diameter, ballistic coefficient, γ_E;
2) Total aerodecelerator system - Function of size and deployment dynamic pressure, Mach number, etc.;
3) Vernier or retro system - Function of thrust level and propellant loading;
4) Entry thermal control and ACS - Function of diameter and weight;
5) Landed structure and legs - Function of landed weight;
6) Pyro subsystem, cabling, etc. - Constant plus function of diameter.

Thus, W_{LE} is the effective usable weight on the ground comprised of entry G&C, all communications and data handling subsystems, power subsystems, surface thermal control, and surface science subsystems. The parametric weight equations used for the delivery system weights (i.e., $W_E - W_{LE}$) are given in section 1 of Appendix D.

Data are presented for fixed aeroshell diameters of 6.5, 8.5, 12, and 15 ft. Direct mode analysis also includes aeroshells with effective diameters of 20, 25, and 30 ft obtained by flaps or inflatable afterbodies on a 15-ft basic aeroshell. The analysis uses entry weight as the independent variable. The relationship between entry weight and B_E is shown in figure B93 for reference.

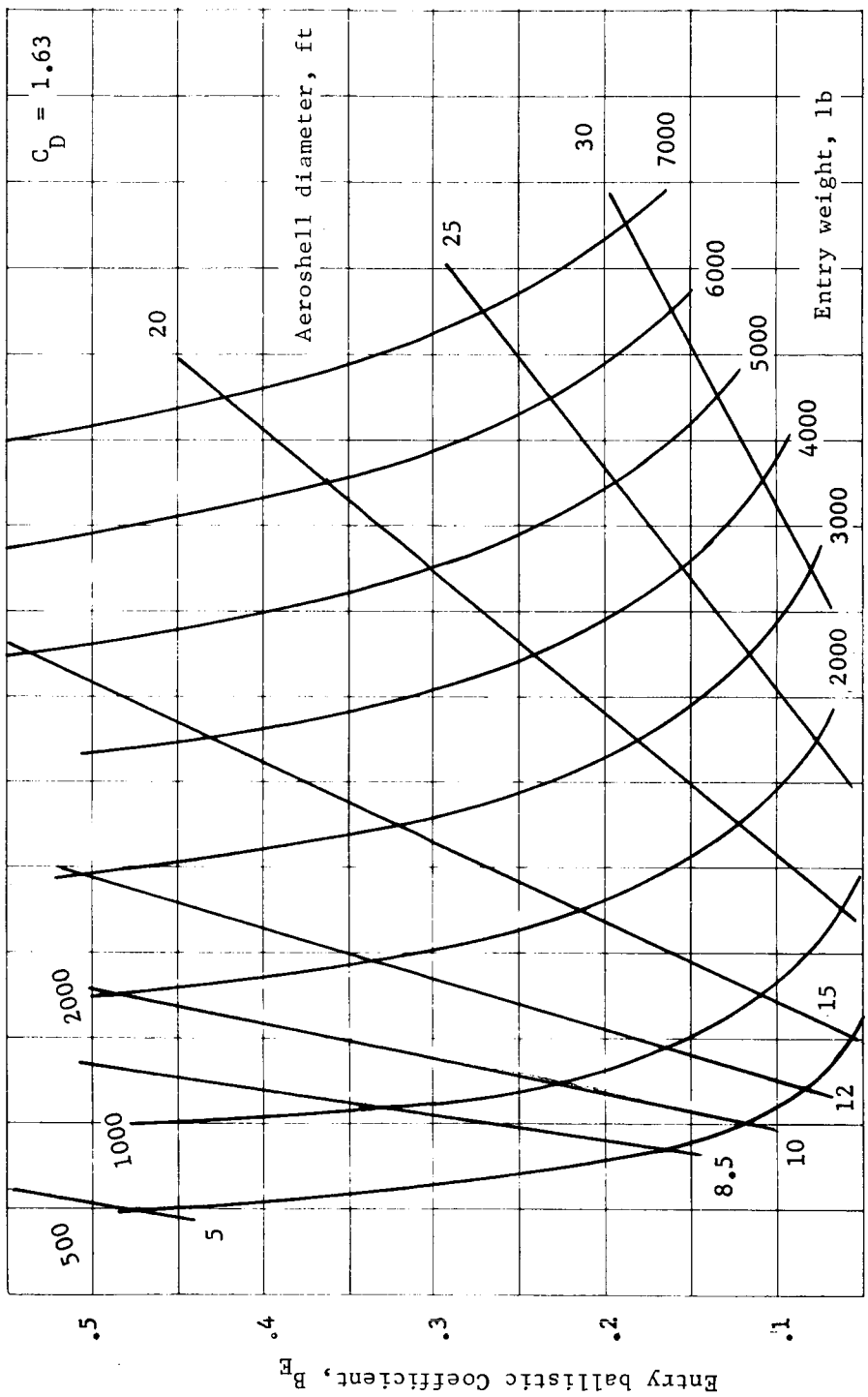

Figure B93.- Entry Ballistic Coefficient

APPENDIX B

Basic data are presented in figures B94 thru B154 for all of the systems. The data are presented as landed weight ratios (W_{LE}/W_E) so that a consistant set of scales could be used for all figures.

Symbols used to define the aeroshell diameters on the machine plotted figures (figs. B94 thru B154) are defined below.

Symbol	Aeroshell diameter, ft
+	6.5
×	8.5
▷	12
▽	15
◁	20
△	25
+	30

An example is shown in figure B113.

The landed equipment weight may be found by using the overlay supplied inside the back cover of this report. Of most interest on these plots is the point of maximum landed weight ratio and the point of maximum landed equipment weight. It should be noted that maximum landed equipment weight always occurs at a higher entry weight than maximum landed weight ratio. The ballistic coefficients used in these figures were obtained from the B_E versus B_{DEC} curves shown earlier. Therefore, all points on the weight curves represent systems with the smallest aerodecelerators that will reach final conditions at $\gamma = -60°$ at 4000 ft above terrain. For the parachute cases, the parachute size used is always sufficient to separate from the aeroshell. For ballute cases, the aeroshell remains with the ballute during the aerodecelerator phase. However, ballute size required for aeroshell separation has been calculated for the $h_T = 6000$ ft cases. The boundary where the ballute will not separate is illustrated by fences beginning with figure B107. If no boundary is shown in these figures, the ballute will separate from the aeroshell for all points.

APPENDIX B

For direct entry, a heat shield on the backface of the aeroshell was employed. This separates at aerodecelerator deployment. In the figures for the parachute/vernier, direct mode only, the landed equipment weights must be corrected by subtracting the backface weights. The backface weights are as follows:

1) $D = 6.5$ ft $\Delta W_{BF} = 15$ lb;

2) $D = 8.5$ ft $\Delta W_{BF} = 26$ lb;

3) $D = 12$ ft $\Delta W_{BF} = 52$ lb;

4) $D \geq 15$ ft $\Delta W_{BF} = 81$ lb.

For aerodecelerator cases, the verniered weight is the entry weight less the following:

1) Weight of aeroshell (see Appendix D);

2) Weight of aerodecelerator, expendable (see Appendix D);

3) Weight of ACS propellant

$$W_{ACS_E} = 0.00007\ W_E\ D_{A/S} + 0.00085\ W_E;$$

4) Weight of science in aeroshell (13 lb).

The landed weight is the verniered weight less the vernier propellant. The landed equipment weight is the landed weight less the following:

1) Weight of lander structure

$$W_{STR} = \begin{matrix} 20 + K\ (\text{landed wt})^{0.7} \text{ where } K = 1.1 \text{ (orbit)}; \\ 1.57 \text{ (direct)} \end{matrix}$$

2) Weight of aerodecelerator, fixed,

   a) Parachute (see Appendix D),

   b) Ballute (see Appendix D);

3) Weight of ACS, fixed

$$W_{ACS_F} = 23.5 + 0.00022\ W_E\ D_{A/S} + 0.0027\ W_E$$

4) Weight of telecommunications cabling

$$W_{TE} = 0.7\ D_{A/S}\ (D_{A/S} = 15\ \text{ft max.})$$

5) Weight of entry thermal control

$$W_{TH} = 13 + K\ (D_{A/S})^2;\ (D_{A/S} = 15\ \text{ft max.})\ K = 0.1\ \text{(orbit)},\ 0.02\ \text{(direct)}$$

6) Weight of pyrotechnic control

$$W_{PY} = 25 + 2\ D_{A/S}\ (D_{A/S} = 15\ \text{ft max.})$$

Figures B155 thru B186 show retro system weights for both orbit and direct modes. Ballistic coefficients of 0.1, 0.2, 0.3, 0.4, and 0.6 slug/ft^2 are used. The retro initiation altitude for each B_E is printed out below the B_E. The F/M_o of the retro is equal to drag acceleration at initiation altitude and is constant for all diameters at a given B_E. The weight breakdown is the same as outlined above for the aerodecelerators except for deletion of the aerodeceleration system and substitution of bipropellant motors for monopropellant motors. The ACS weights are not included in the retro figures, and they should be subtracted from the landed equipment weight for a correct value. Equations for ACS weight are shown in the above parachute breakdown. Landed weight ratios for the inflatable afterbody/retro system are shown in figures B187 thru B194.

The ablator thickness is based on the design condition of minimum flightpath angle (Appendix C). The weight equations reflect an abrubpt change in ablator thickness at $B_E = 0.3$ due to flow transition. This is illustrated in figure B195. Curves were arbitrarily faired to create a smooth curve as shown in the figure.

Much of the data presented herein is in terms of W_{LE}, landed equipment weight. This is defined with the aid of figures B196 thru B200, which illustrate the components subtracted from entry weight, W_E, to arrive at W_{LE}. Weight breakdowns are shown for aerodecelerators with 8.5-, 15-, and 25-ft diameter aeroshells, and a retro system with a 8.5-ft aeroshell. It may be observed that the largest differences between configurations is in aeroshell weight. For the aerodecelerators, the large increase in aerodecelerator weight determines the peak landed equipment weight.

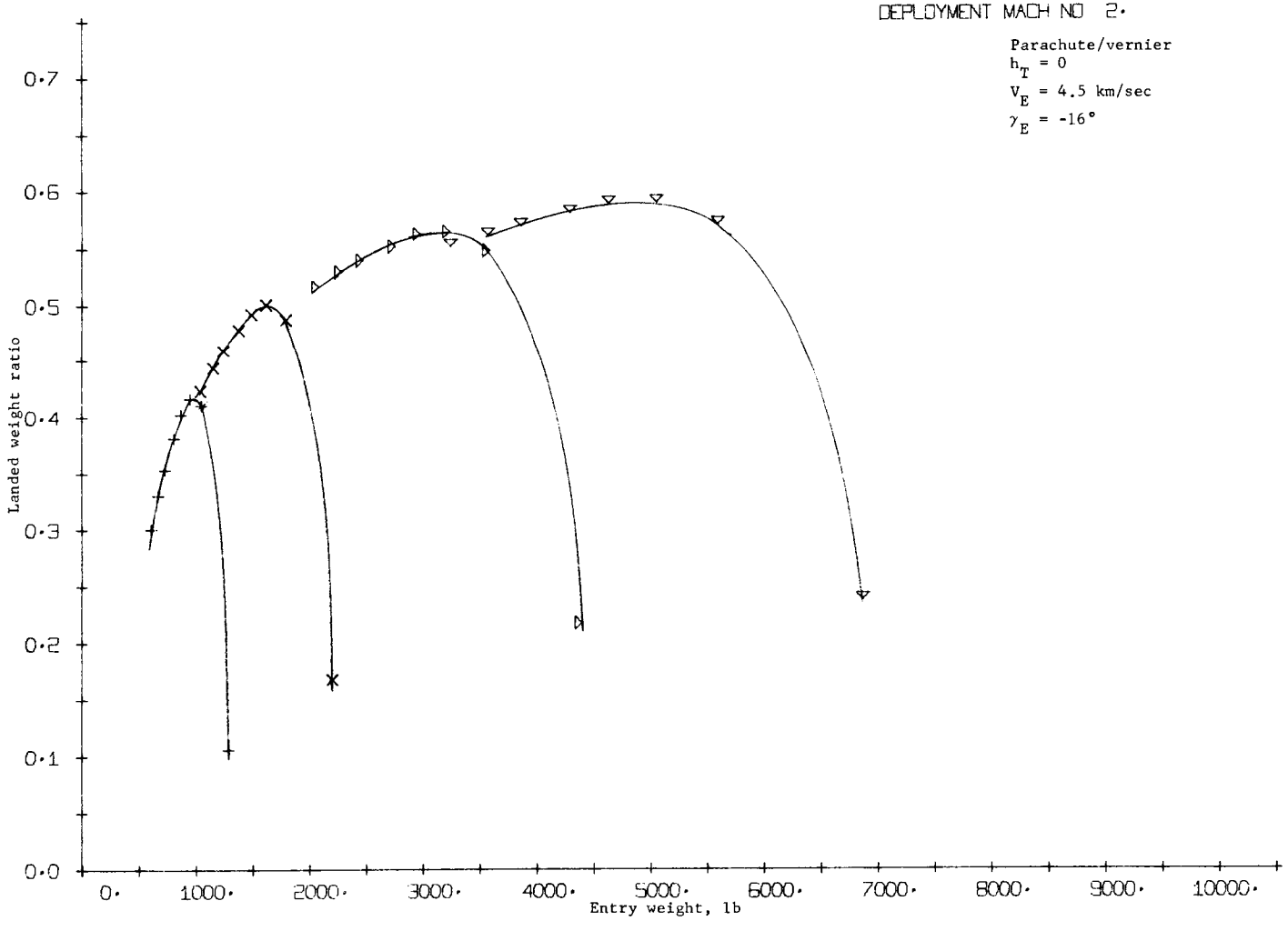

Figure B94.- Terminal Phase System Performance

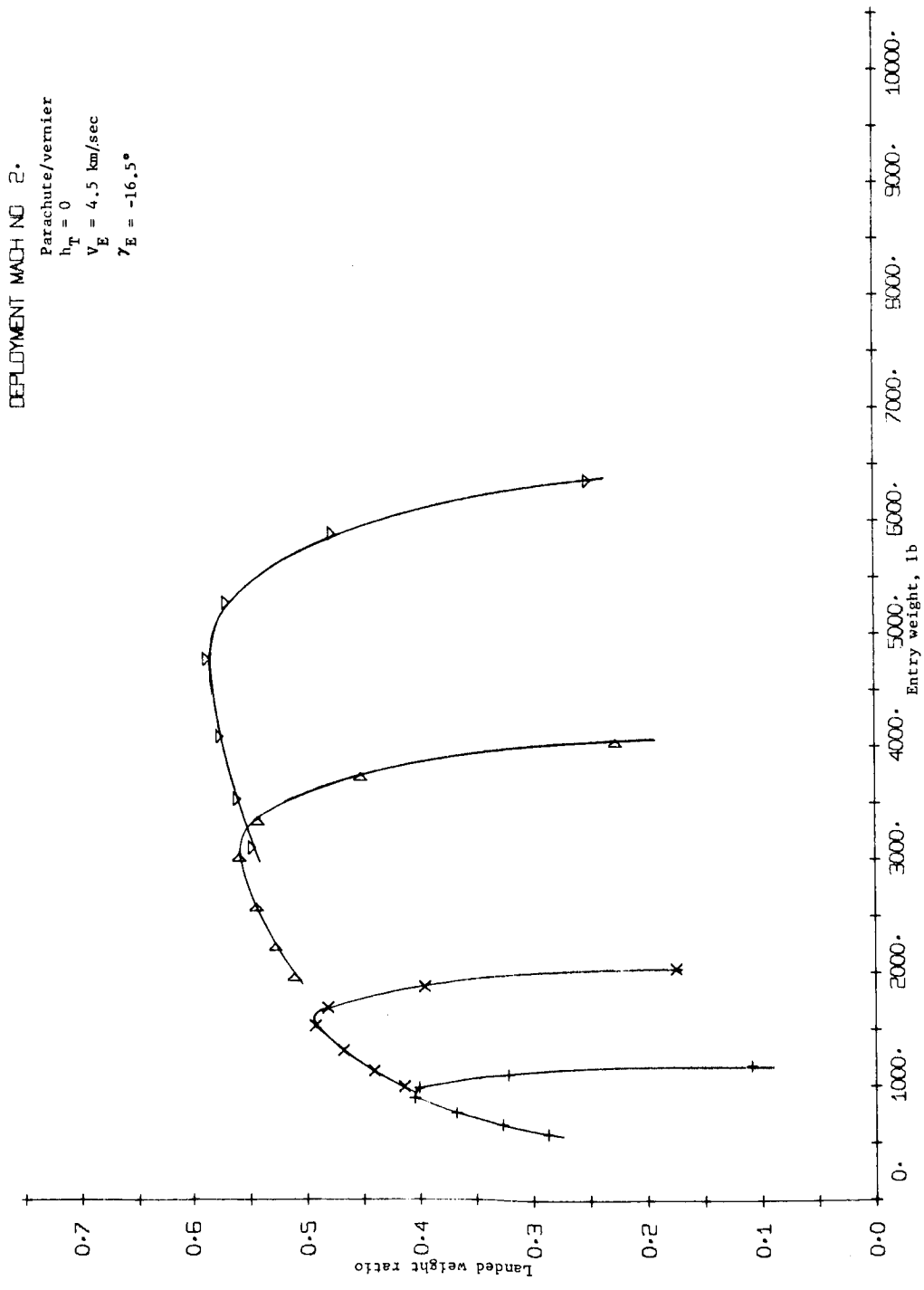

Figure B95.- Terminal Phase System Performance

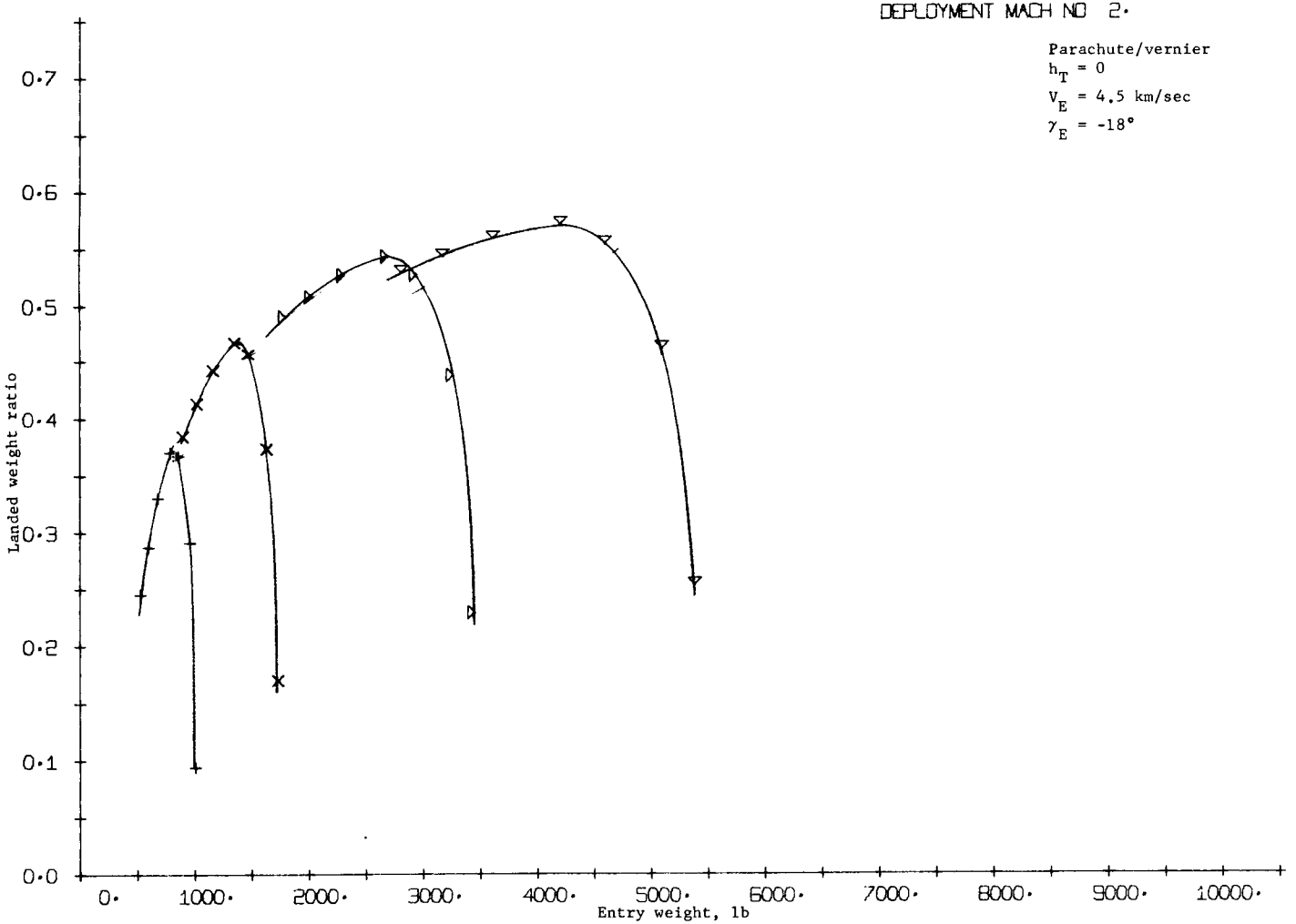

Figure B96.- Terminal Phase System Performance

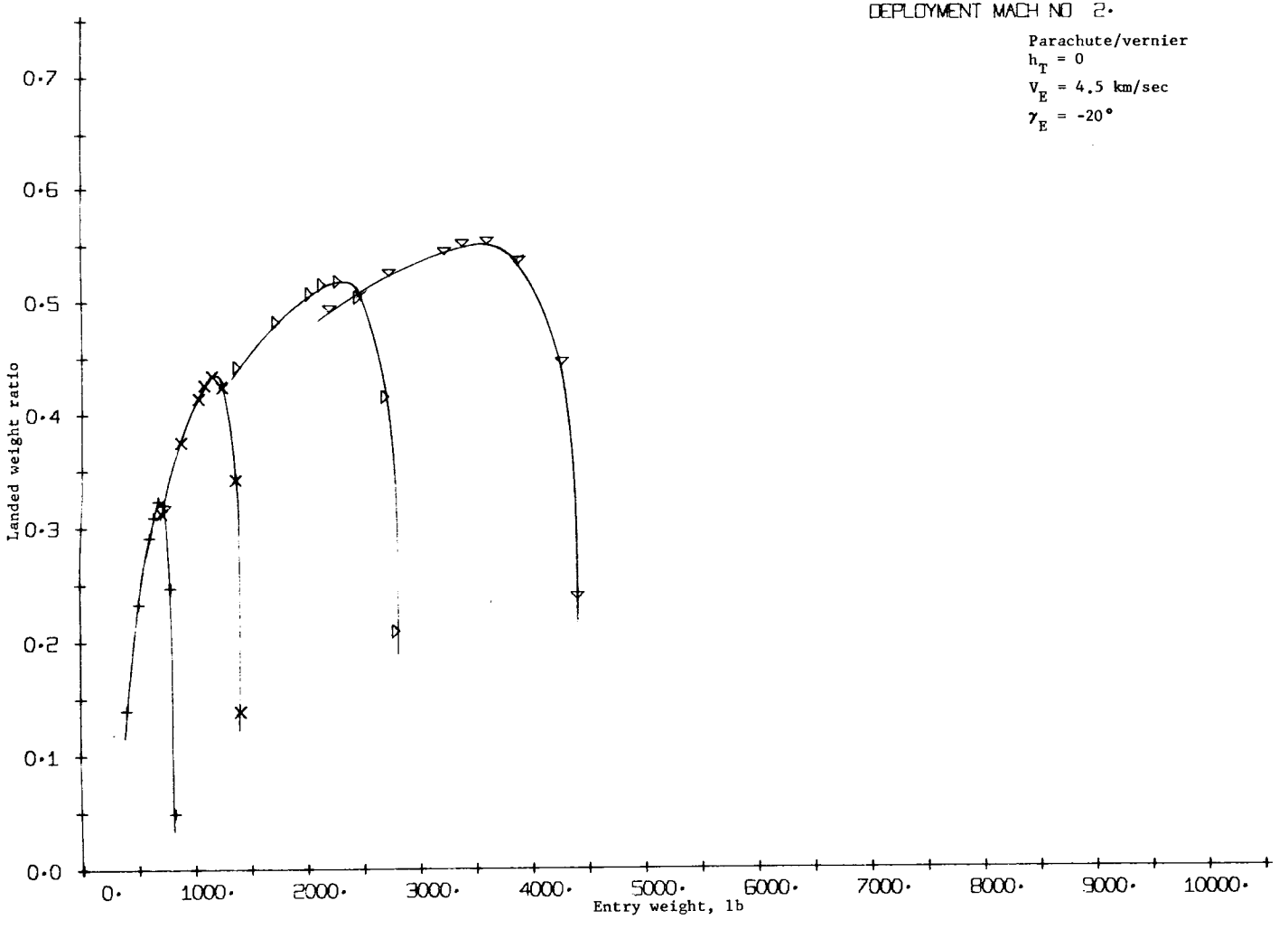

Figure B97.- Terminal Phase System Performance

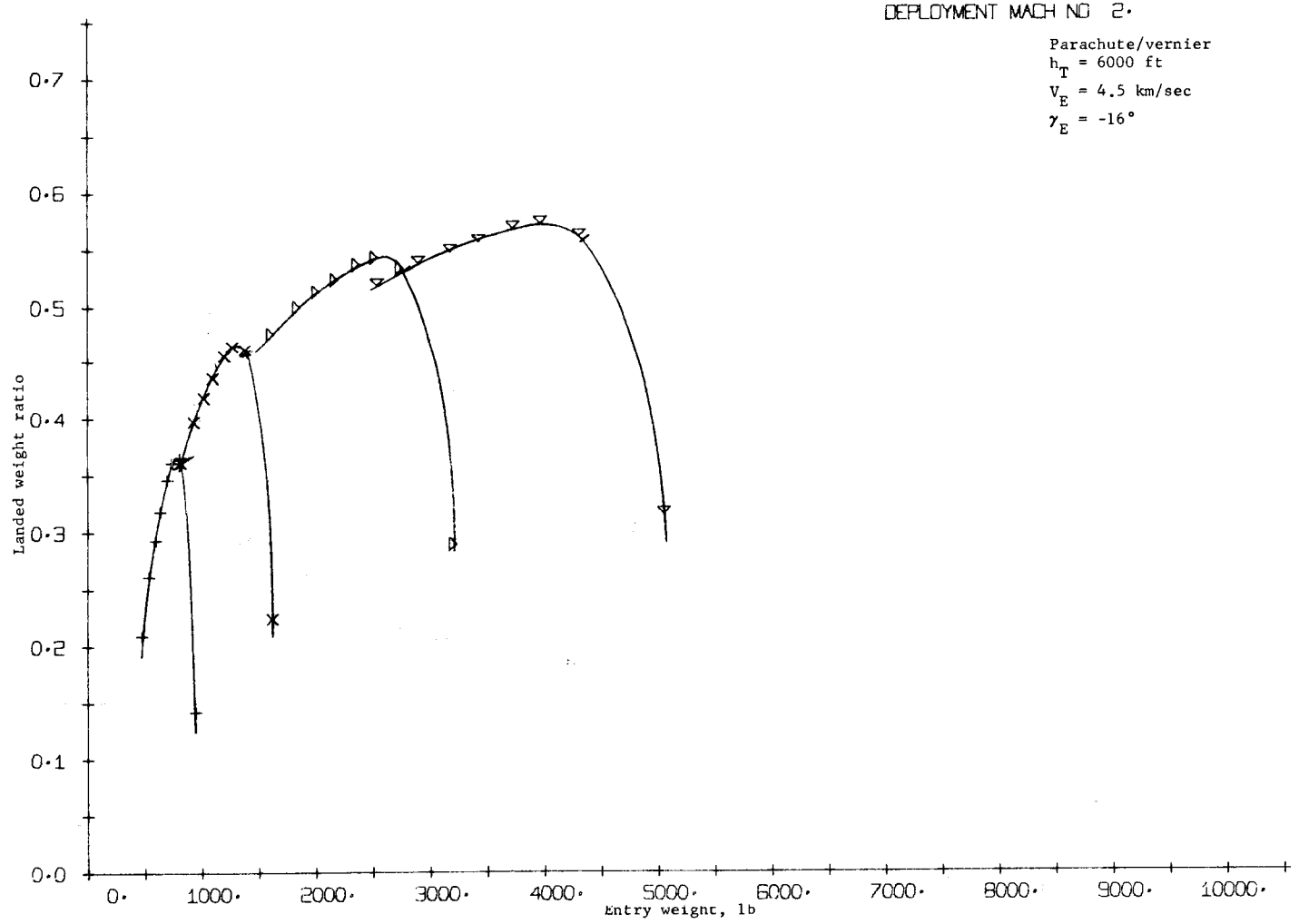

Figure B98.- Terminal Phase System Performance

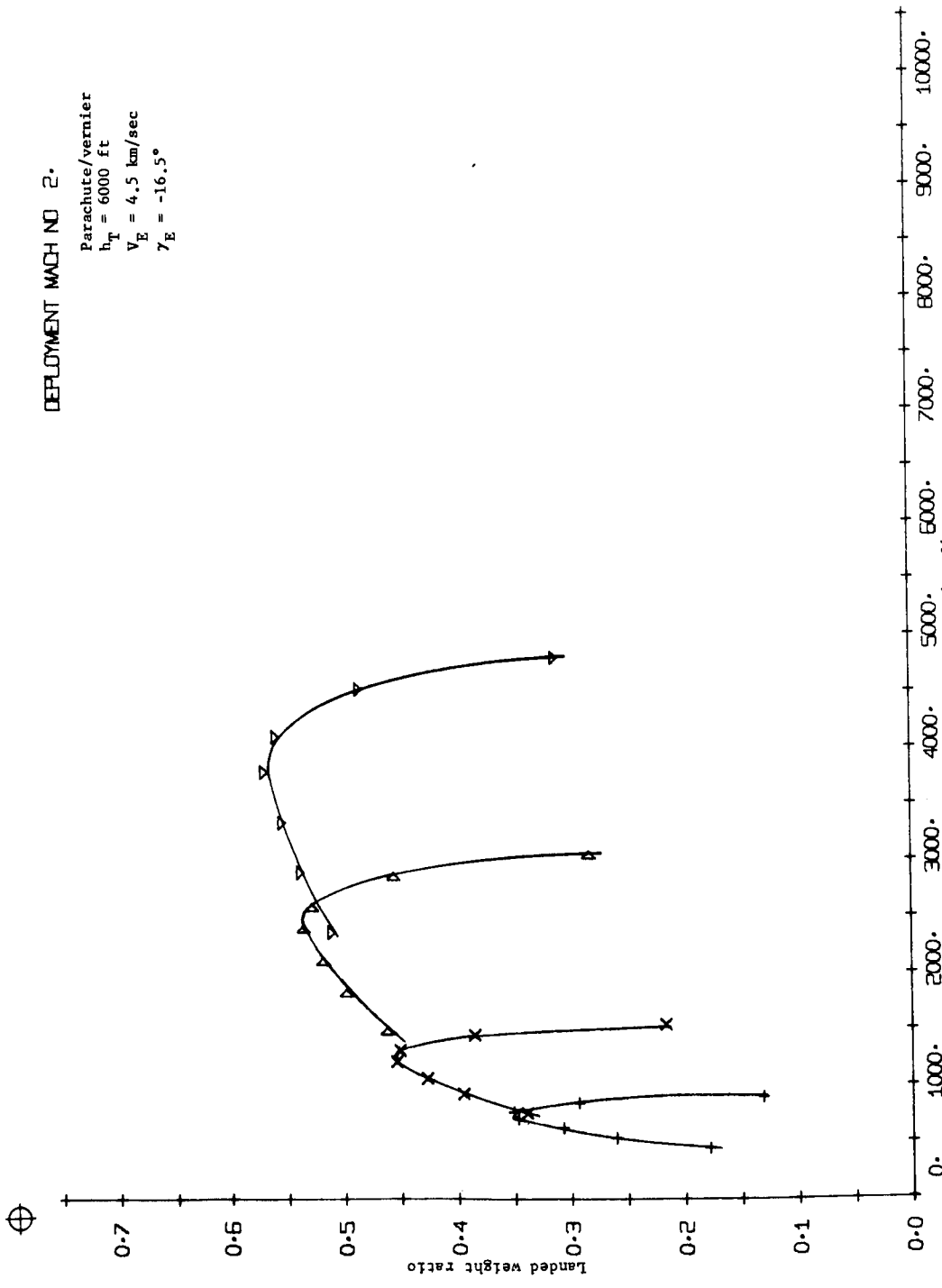

Figure B99.- Terminal Phase System Performance

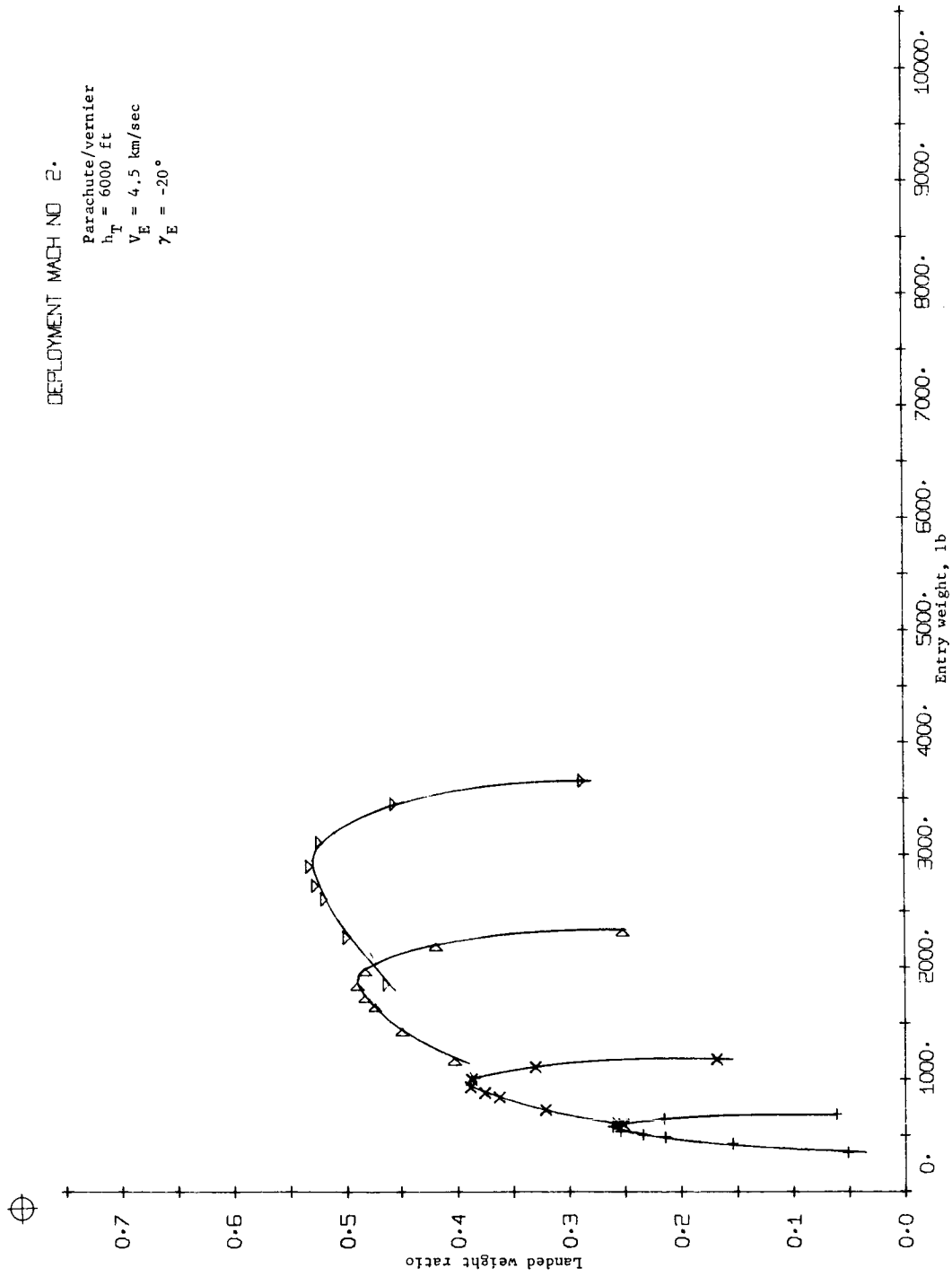

Figure B100.- Terminal Phase System Performance

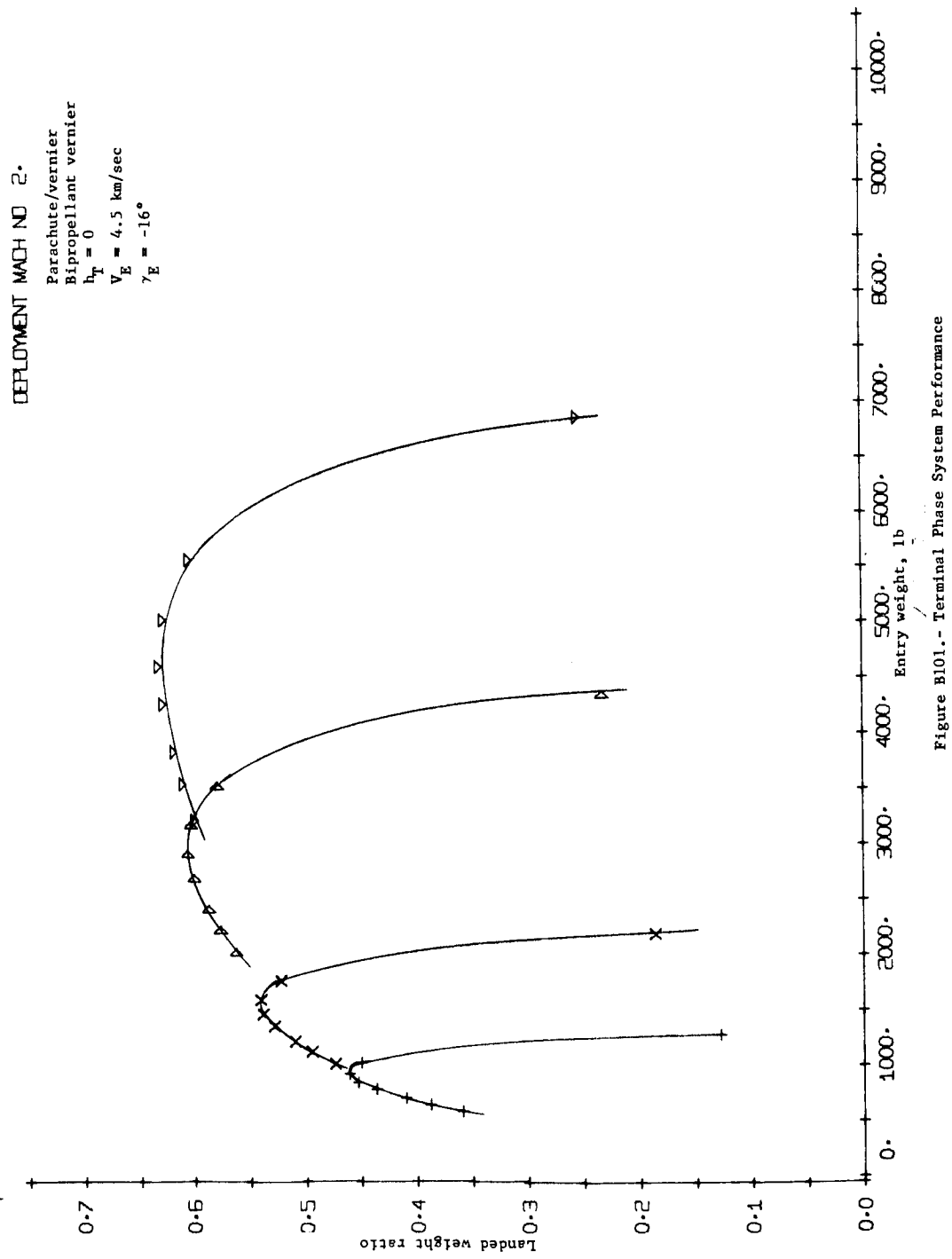

Figure B101.- Terminal Phase System Performance

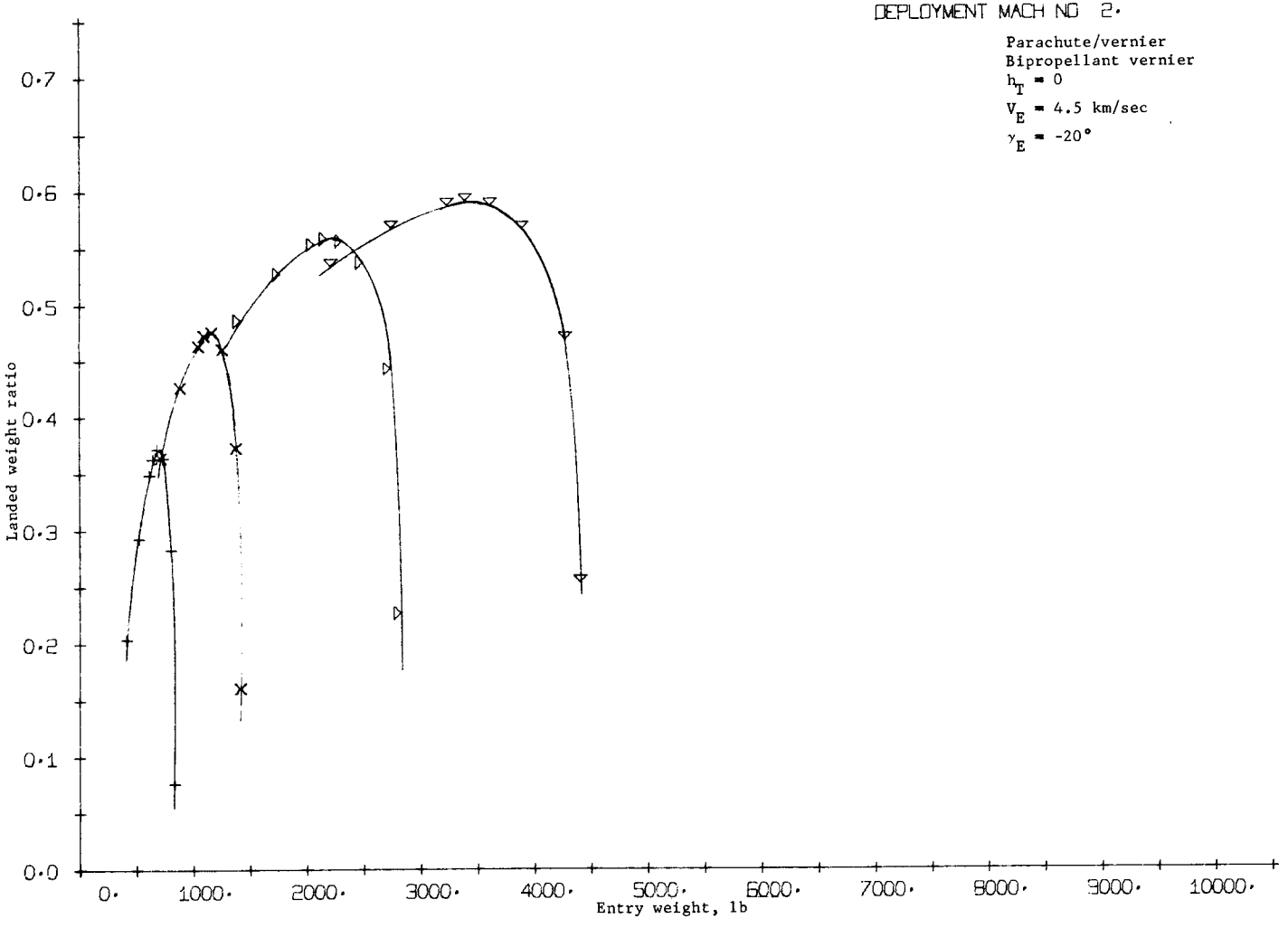

Figure B102.- Terminal Phase System Performance

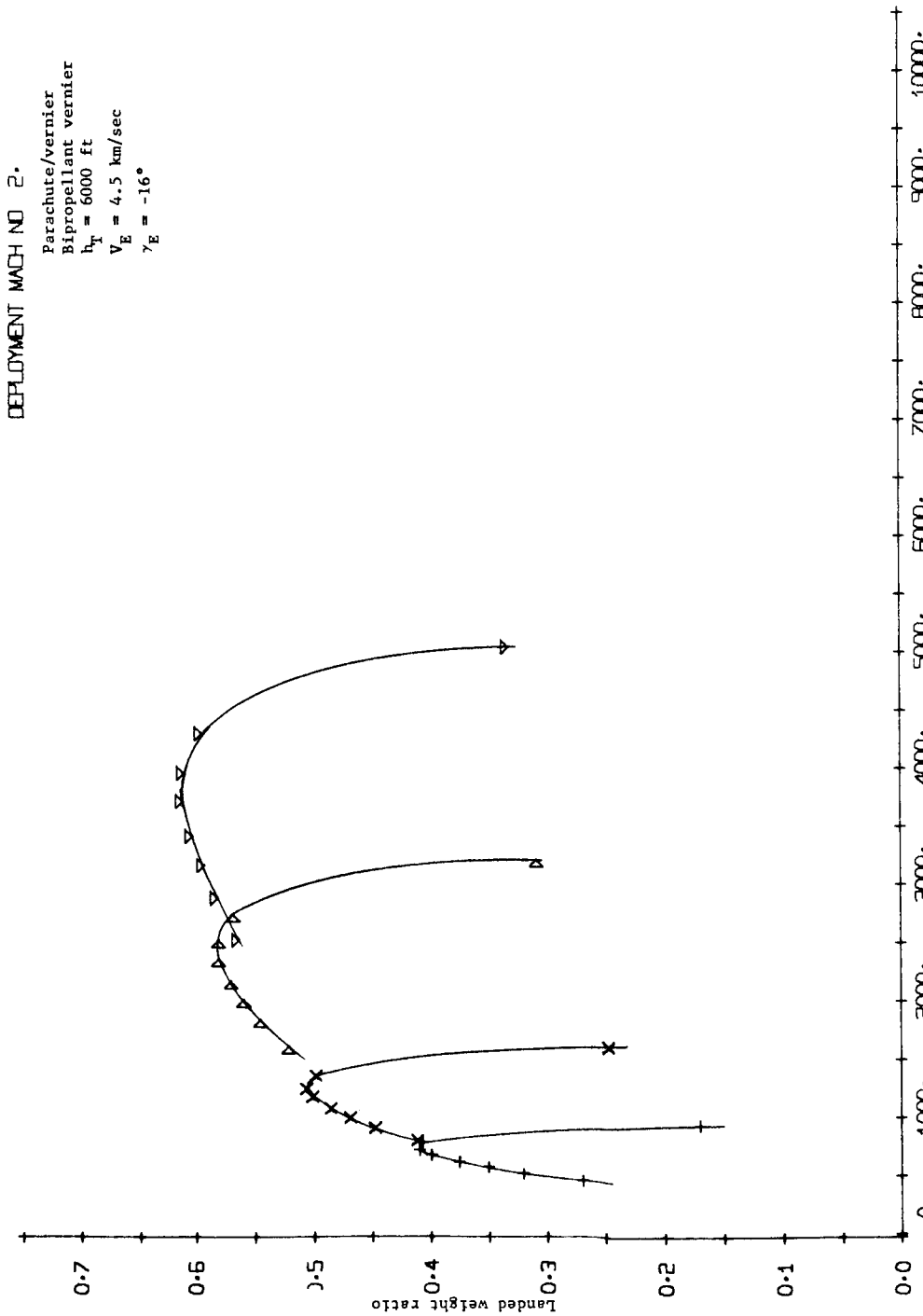

Figure B103.- Terminal Phase System Performance

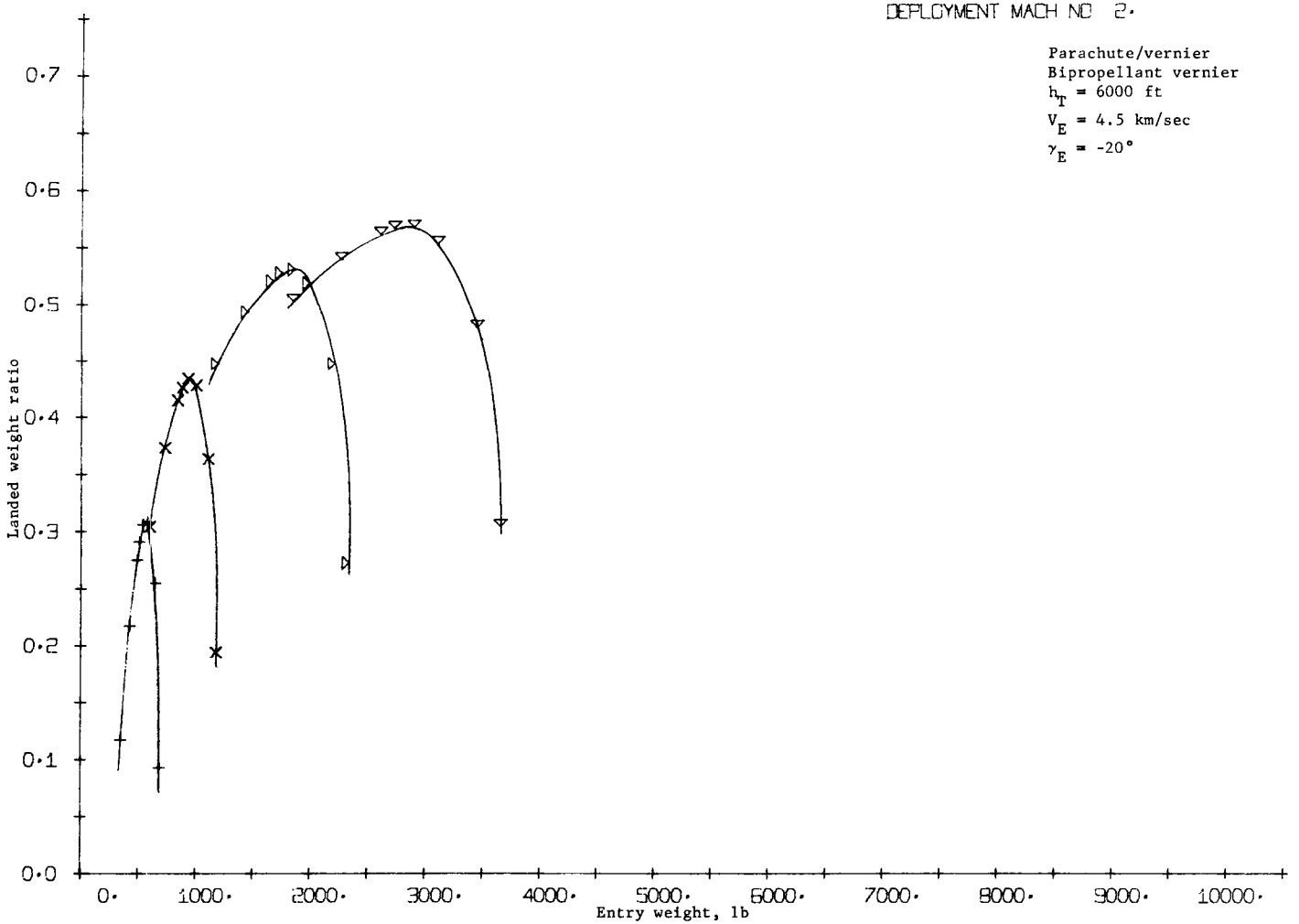

Figure B104.- Terminal Phase System Performance

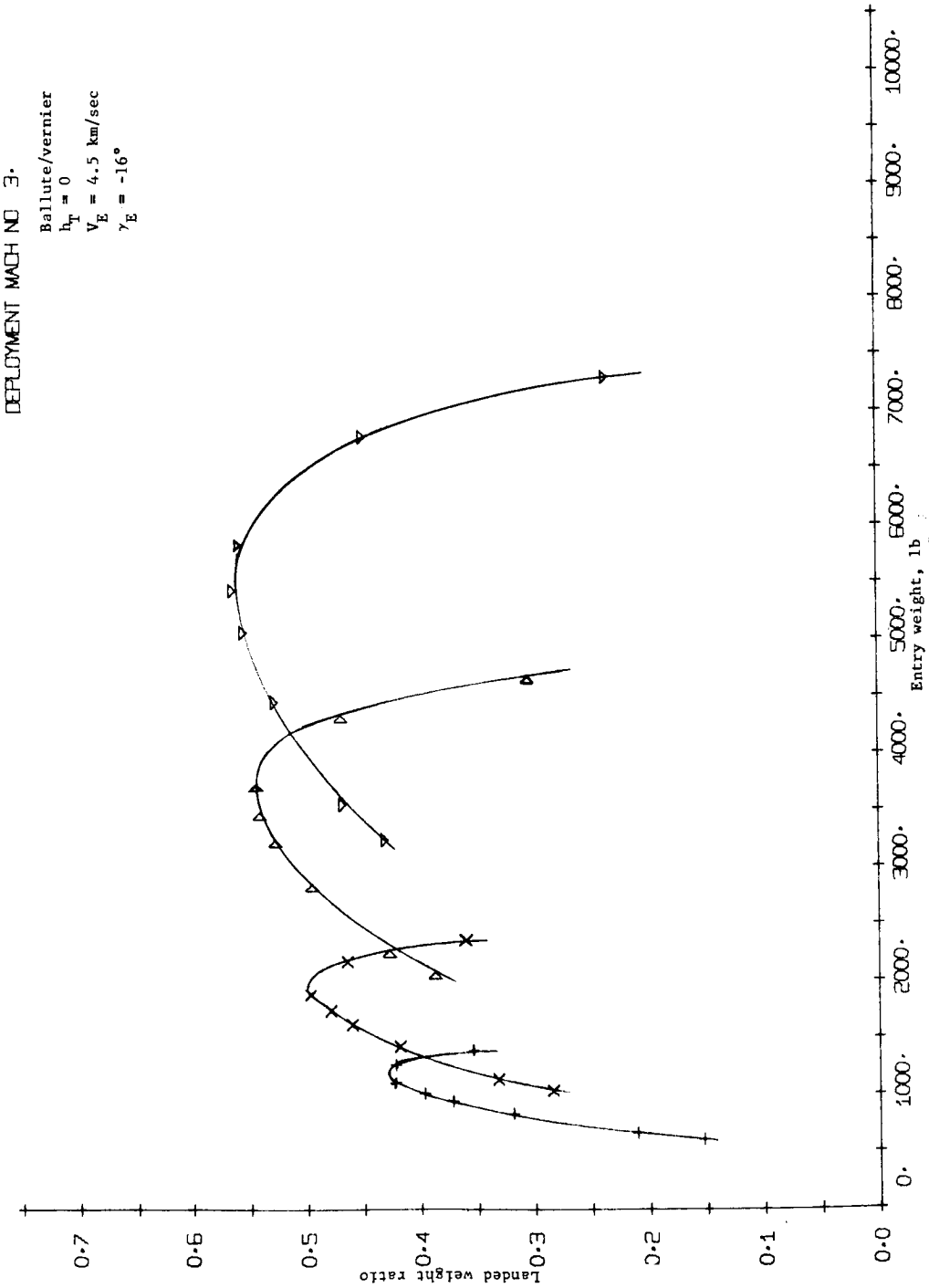

Figure B105.- Terminal Phase System Performance

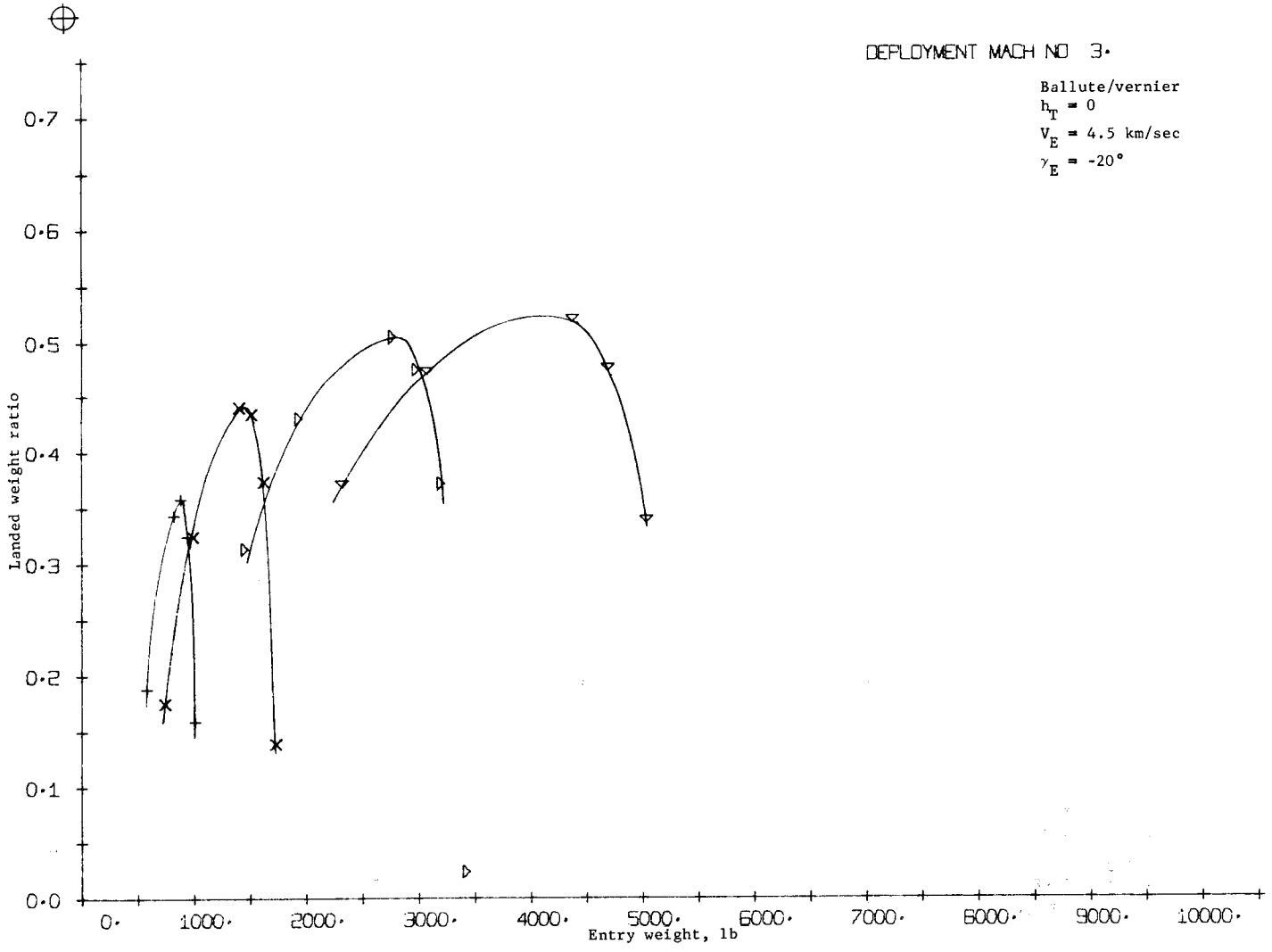

Figure B106.- Terminal Phase System Performance

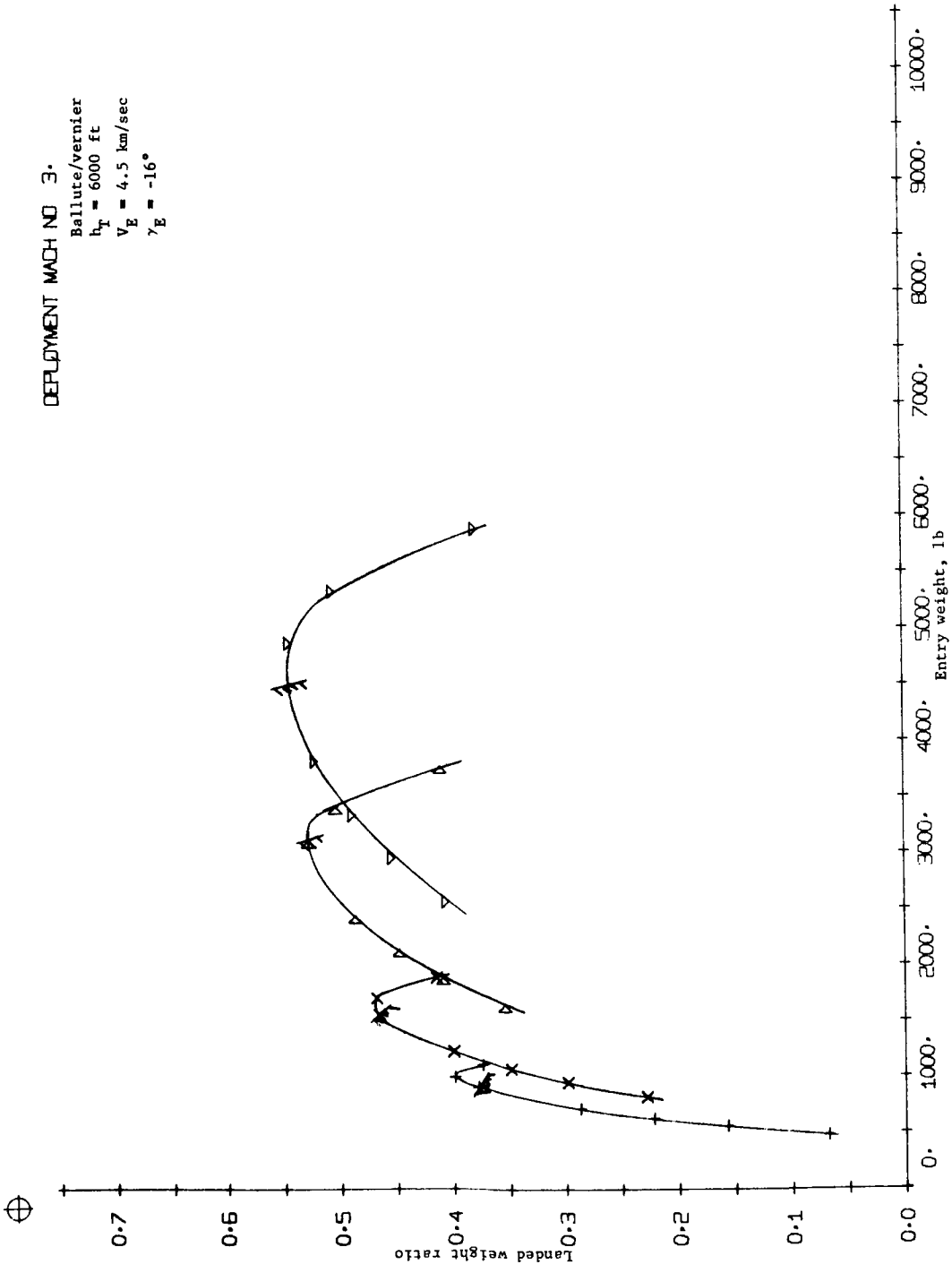

Figure B107.- Terminal Phase System Performance

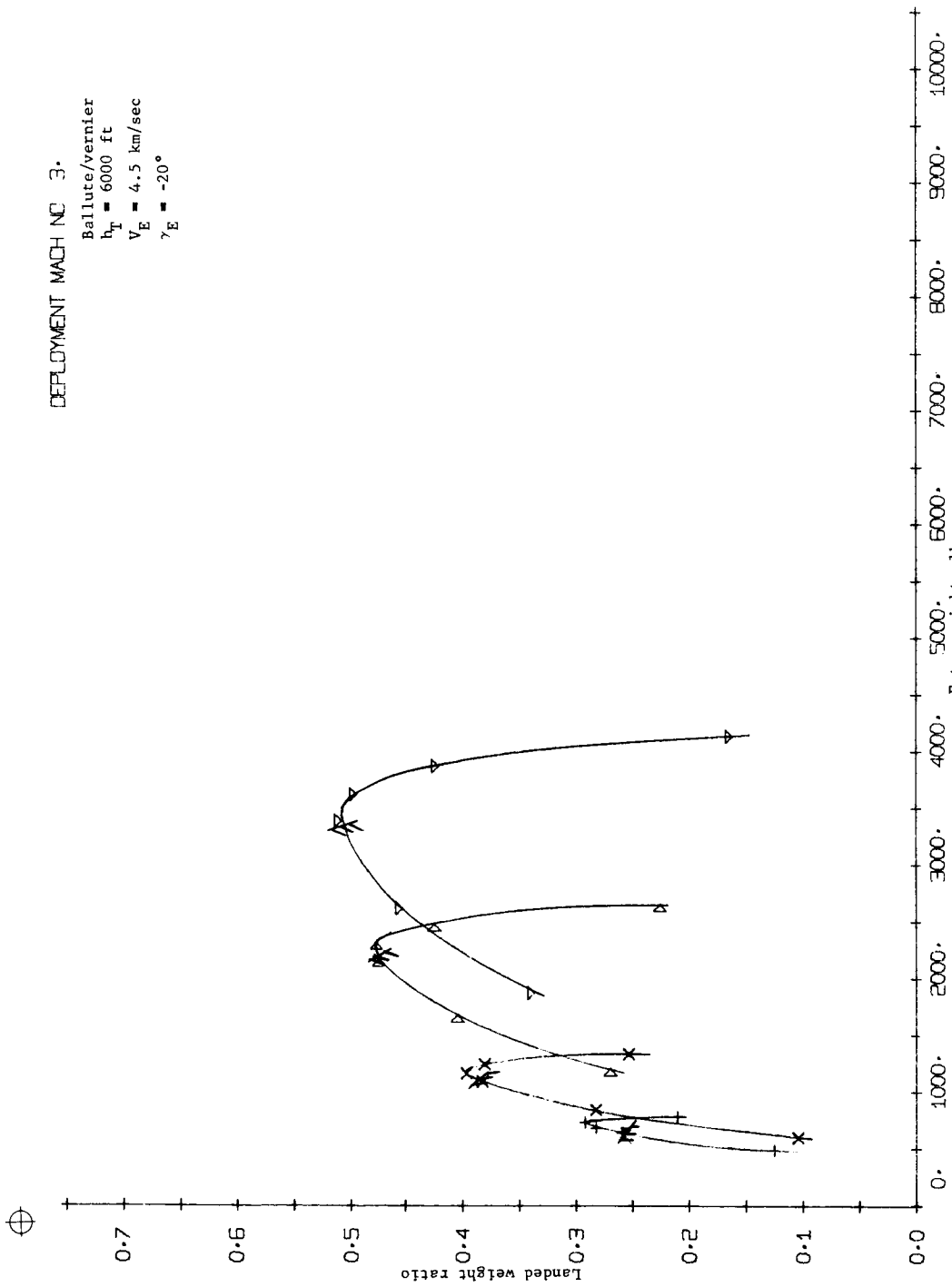

Figure B108.- Terminal Phase System Performance

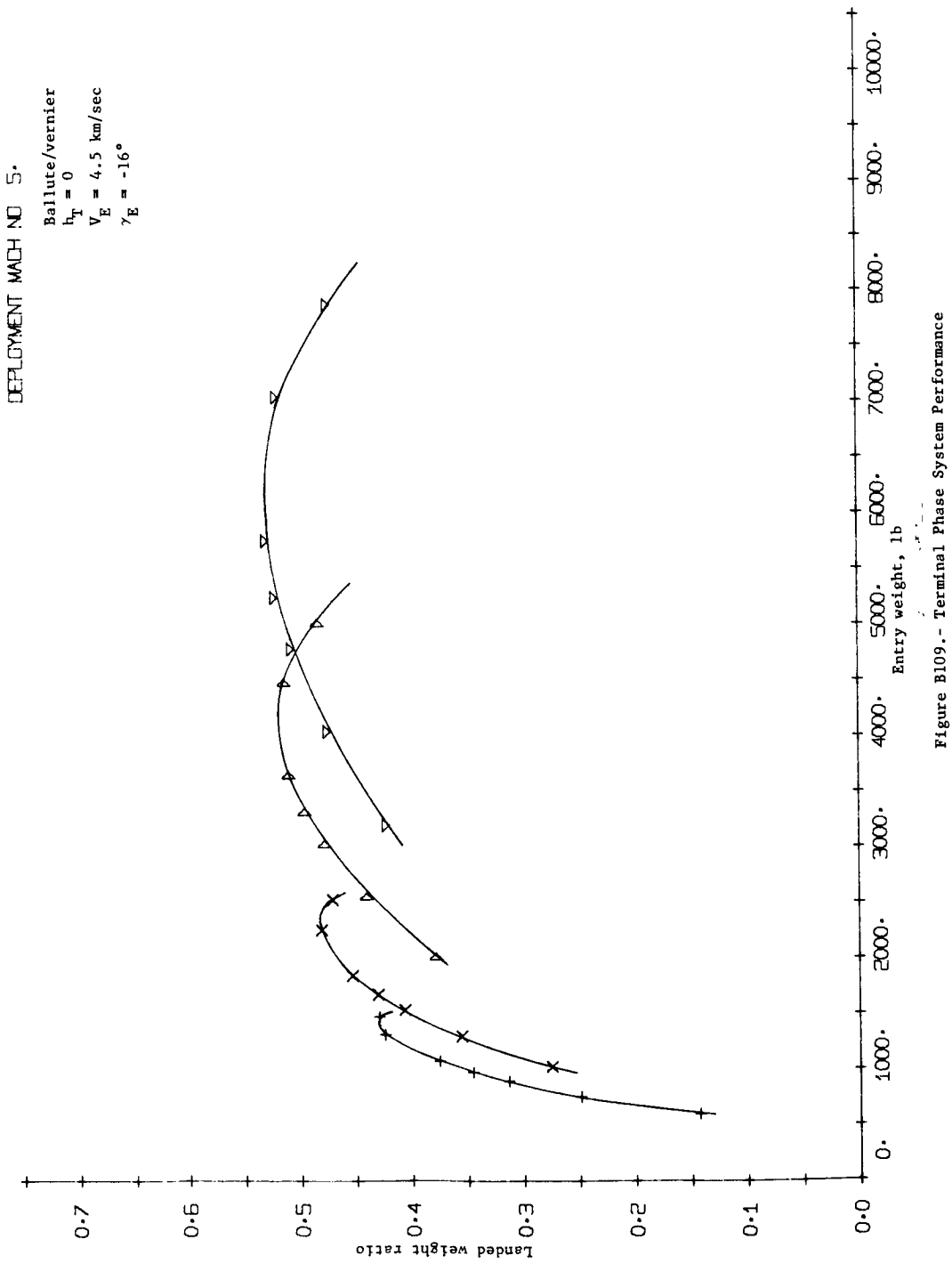

Figure B109.- Terminal Phase System Performance

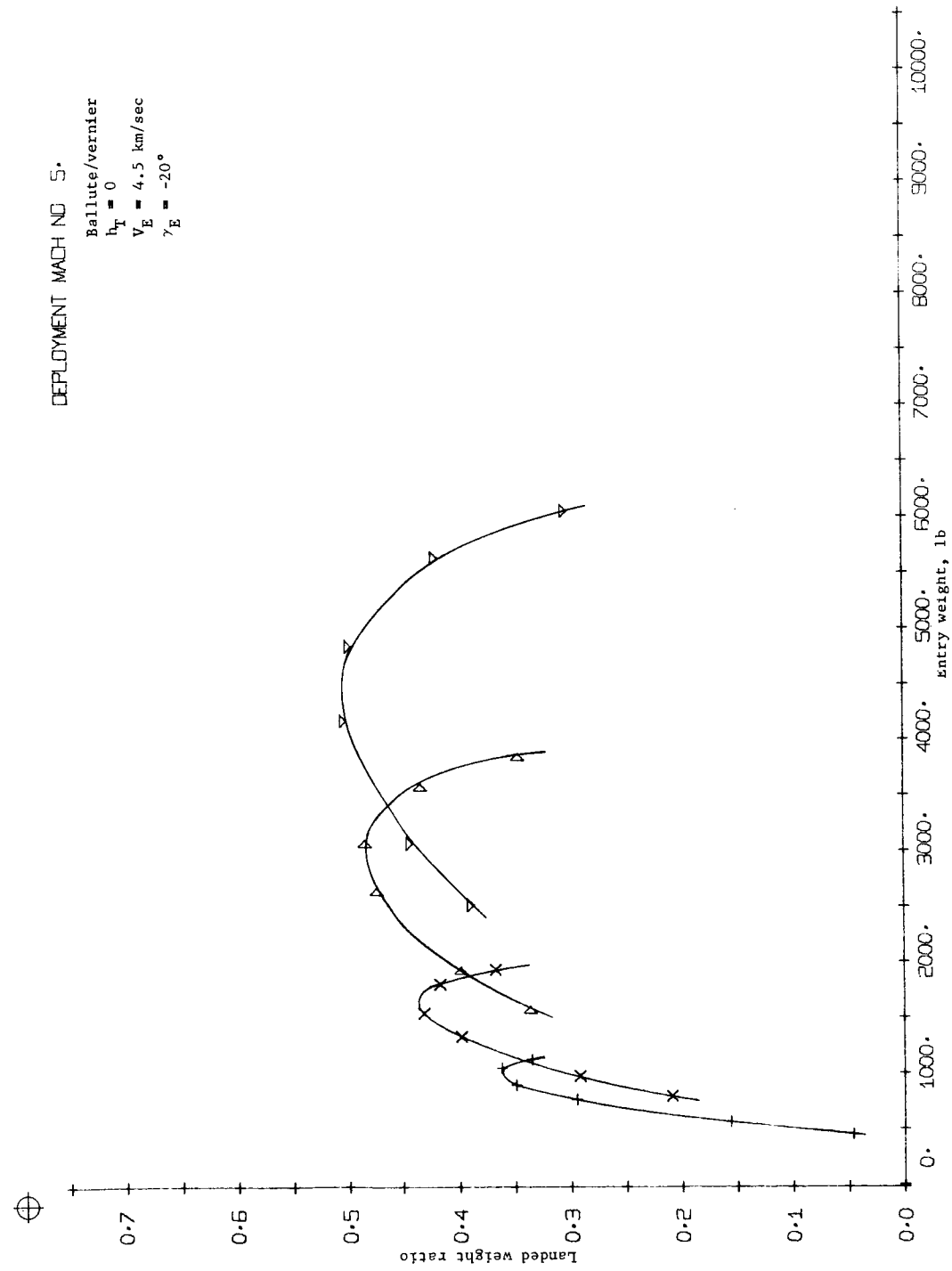

Figure B110.- Terminal Phase System Performance

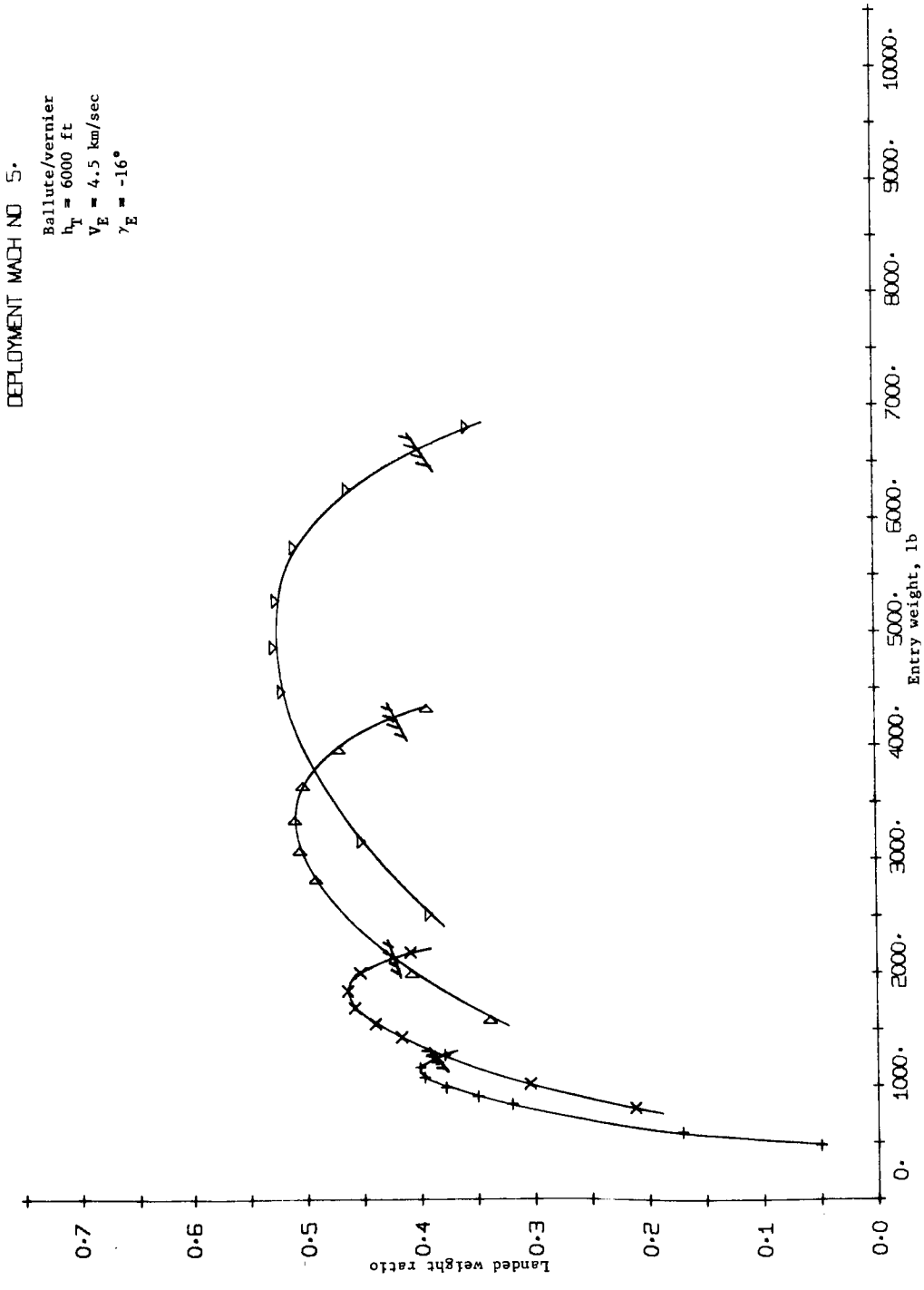

Figure B111.- Terminal Phase System Performance

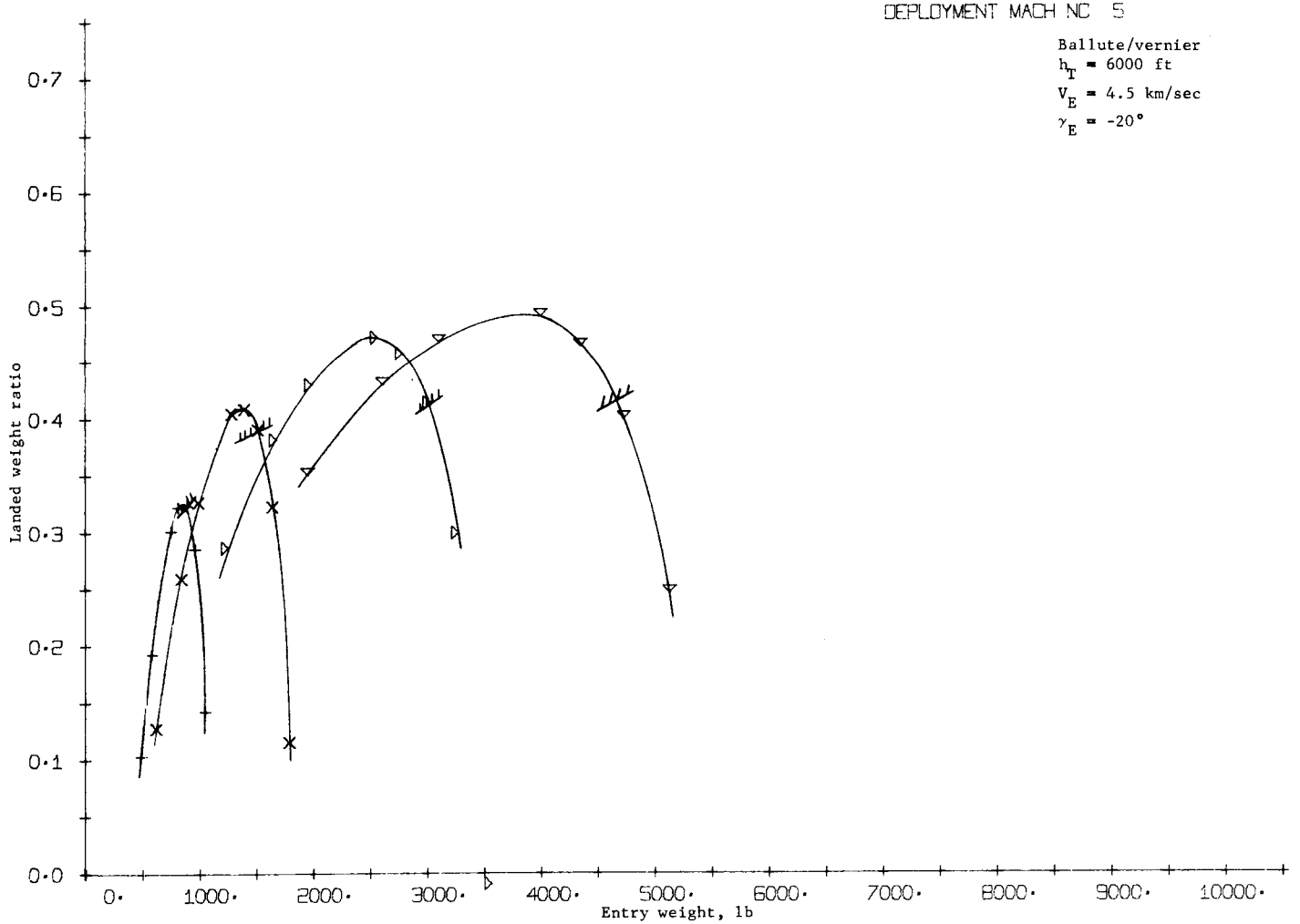

Figure B112.- Terminal Phase System Performance

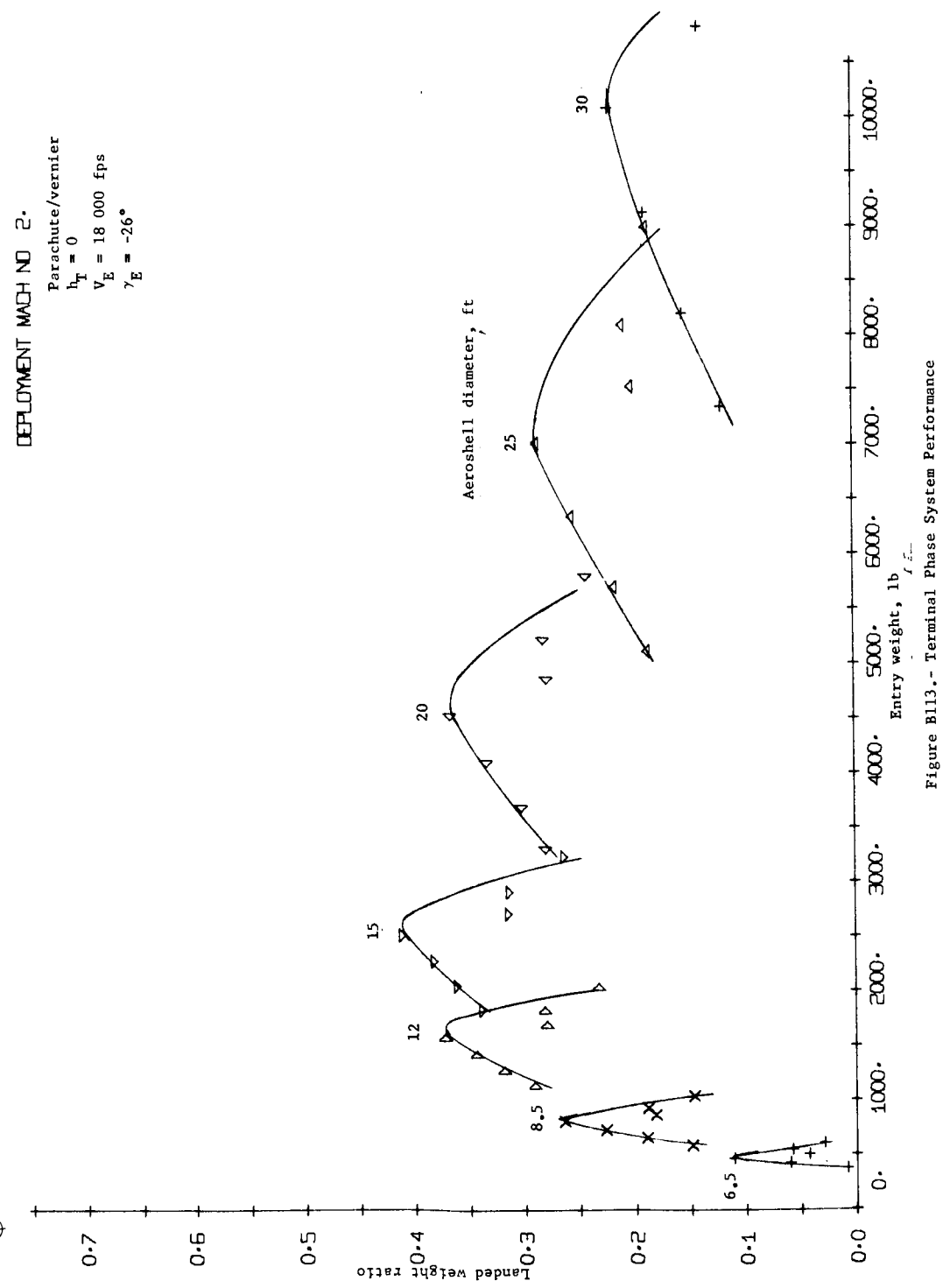

Figure B113.- Terminal Phase System Performance

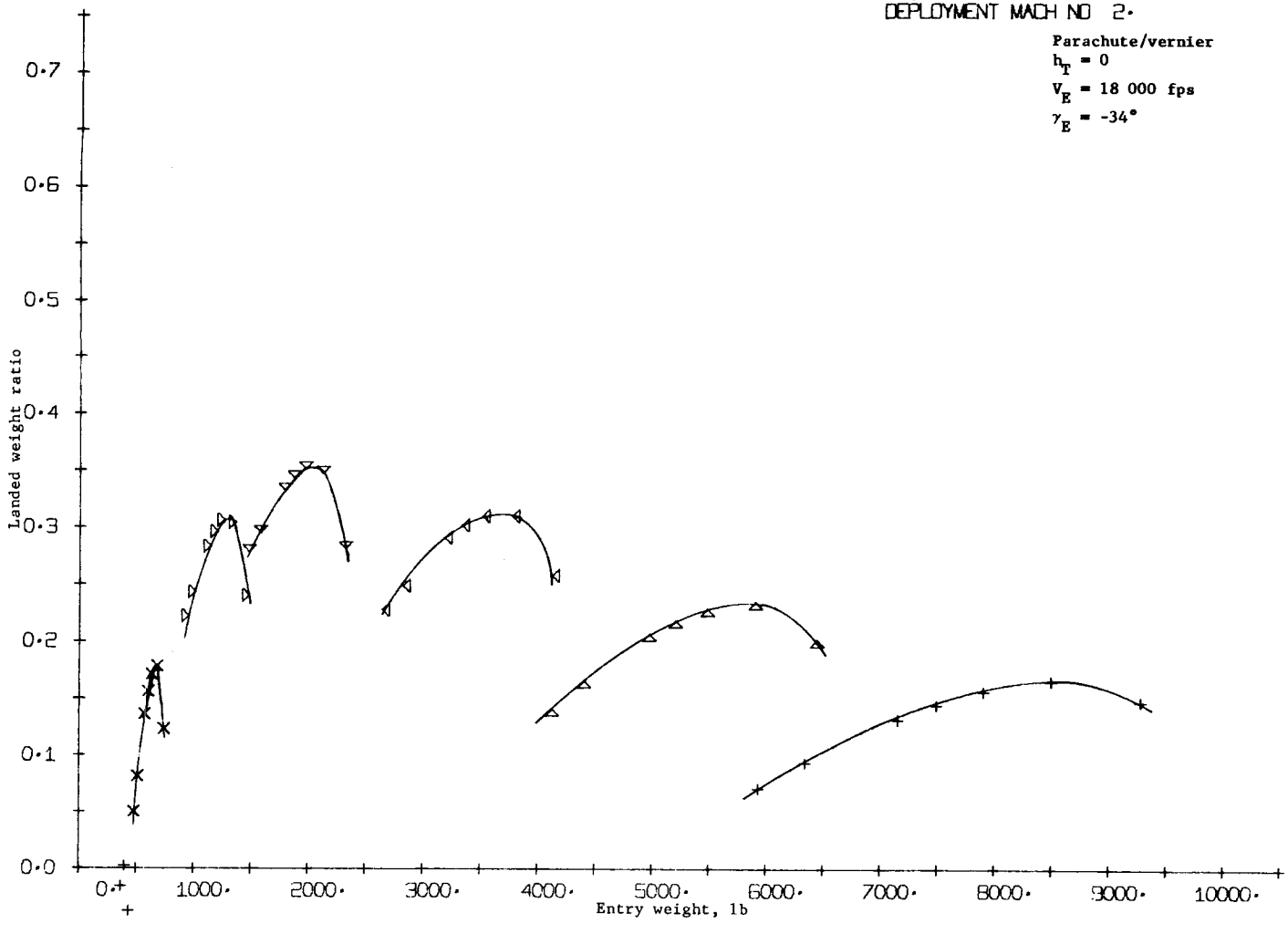

Figure B114.- Terminal Phase System Performance

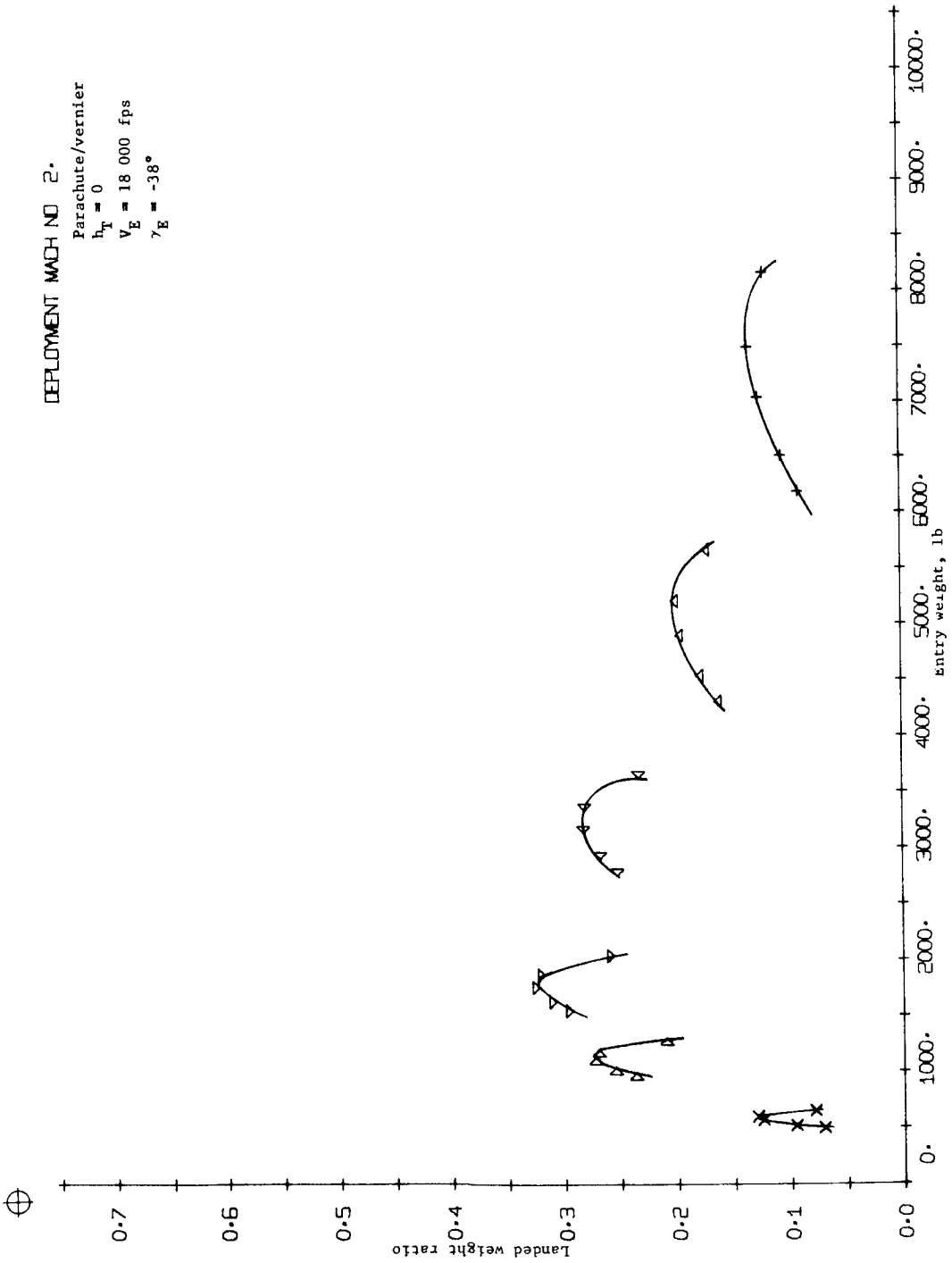

Figure B115.- Terminal Phase System Performance

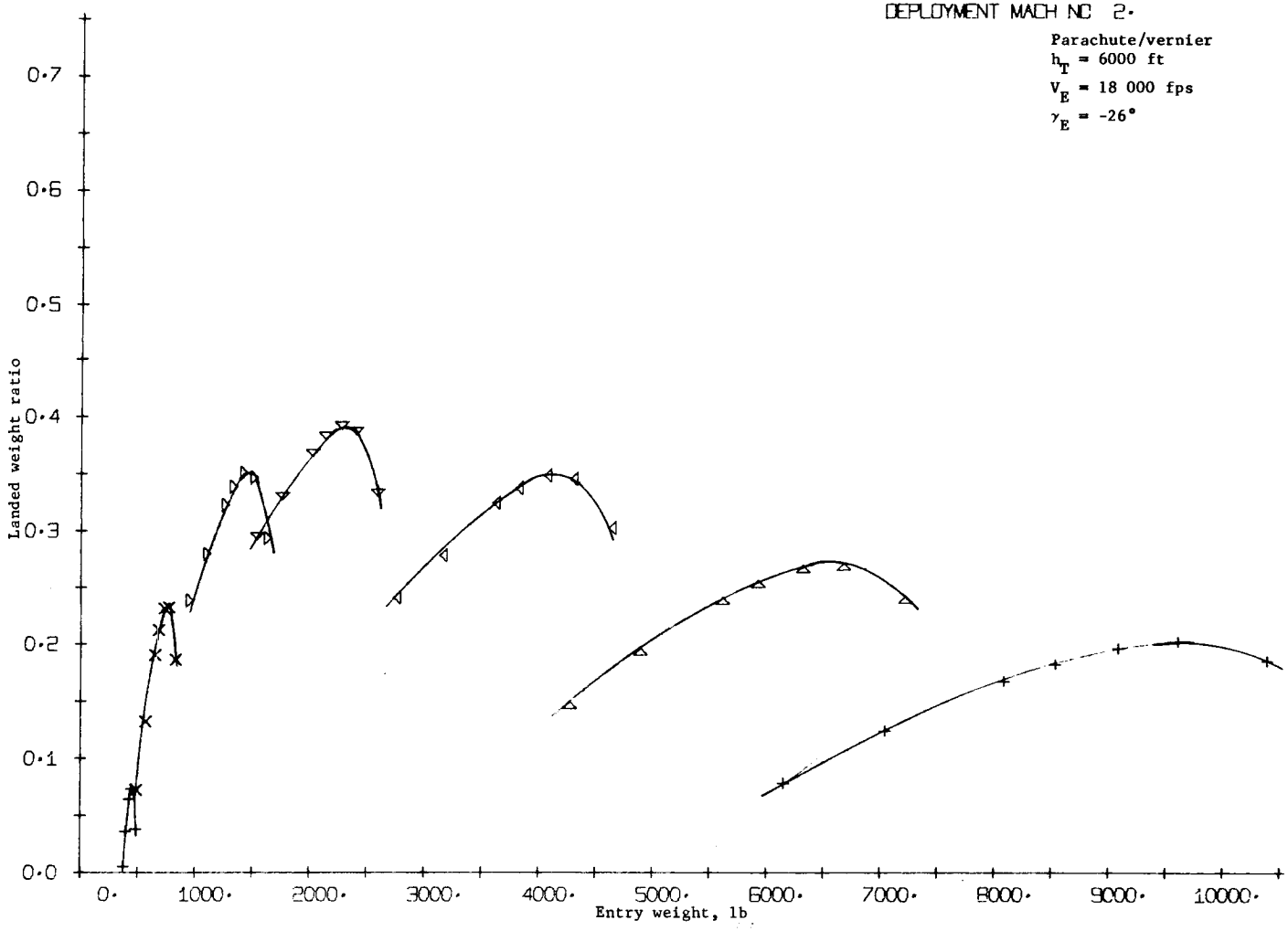

Figure B116.- Terminal Phase System Performance

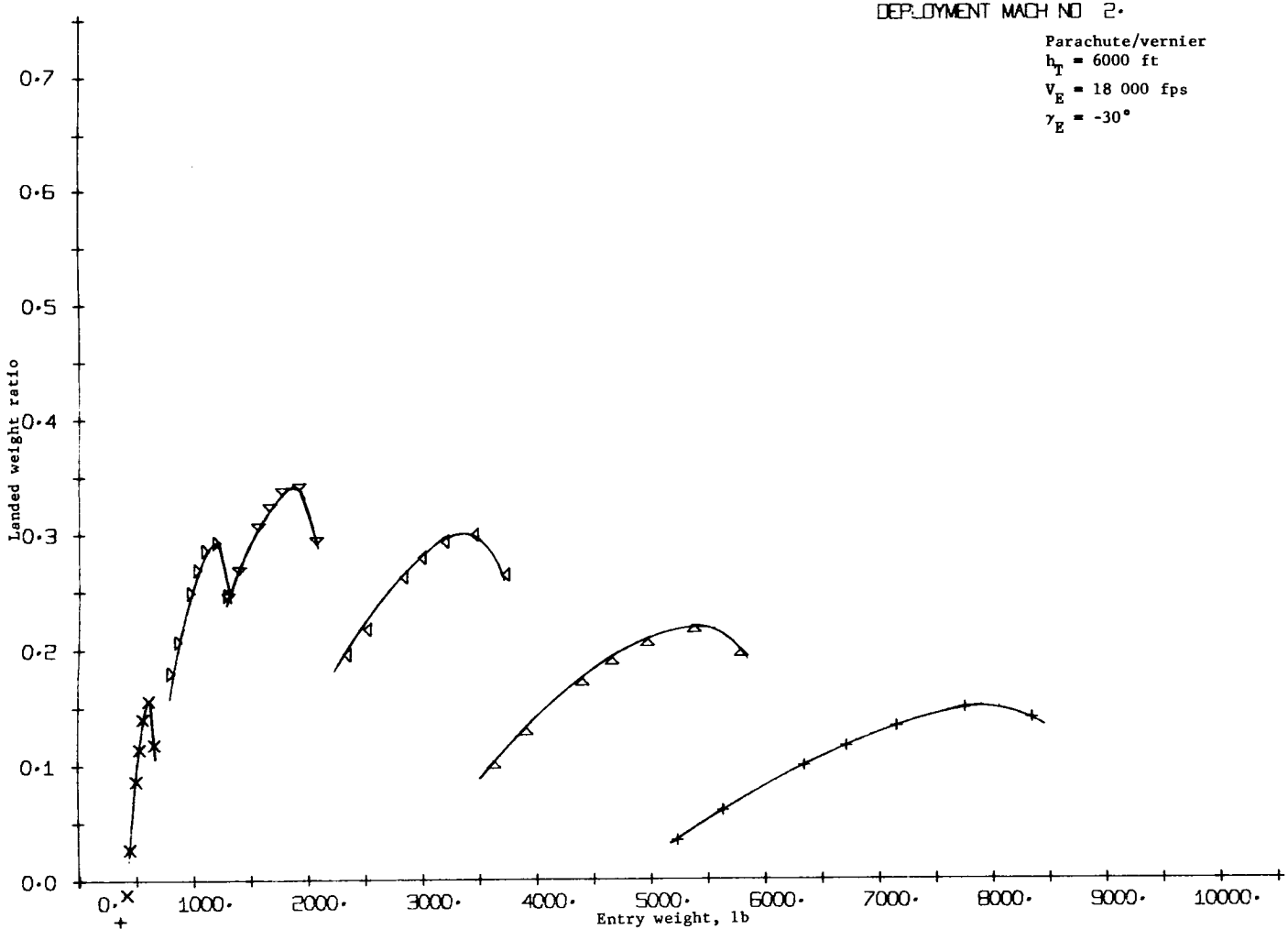

Figure B117.- Terminal Phase System Performance

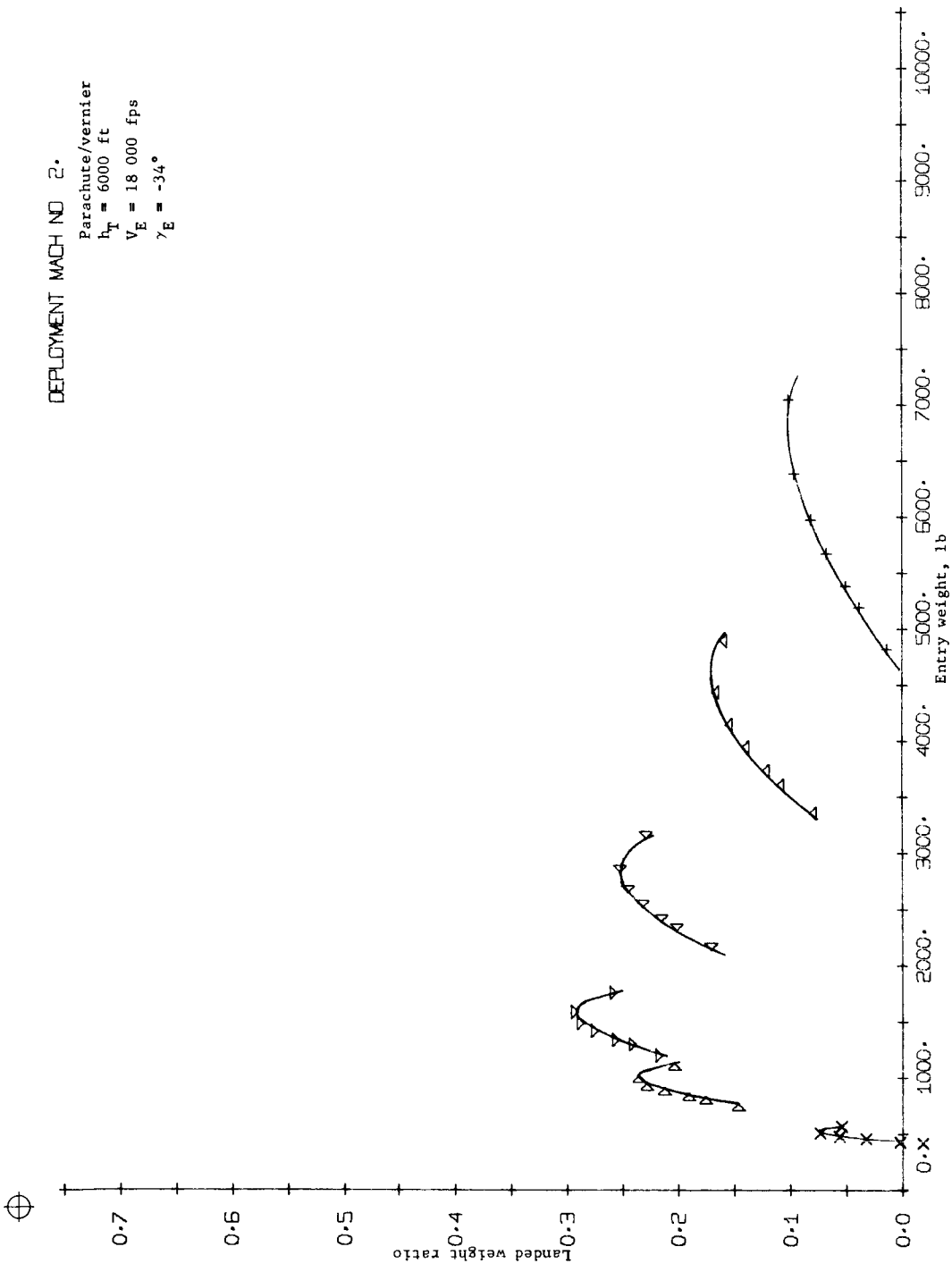

Figure B118.- Terminal Phase System Performance

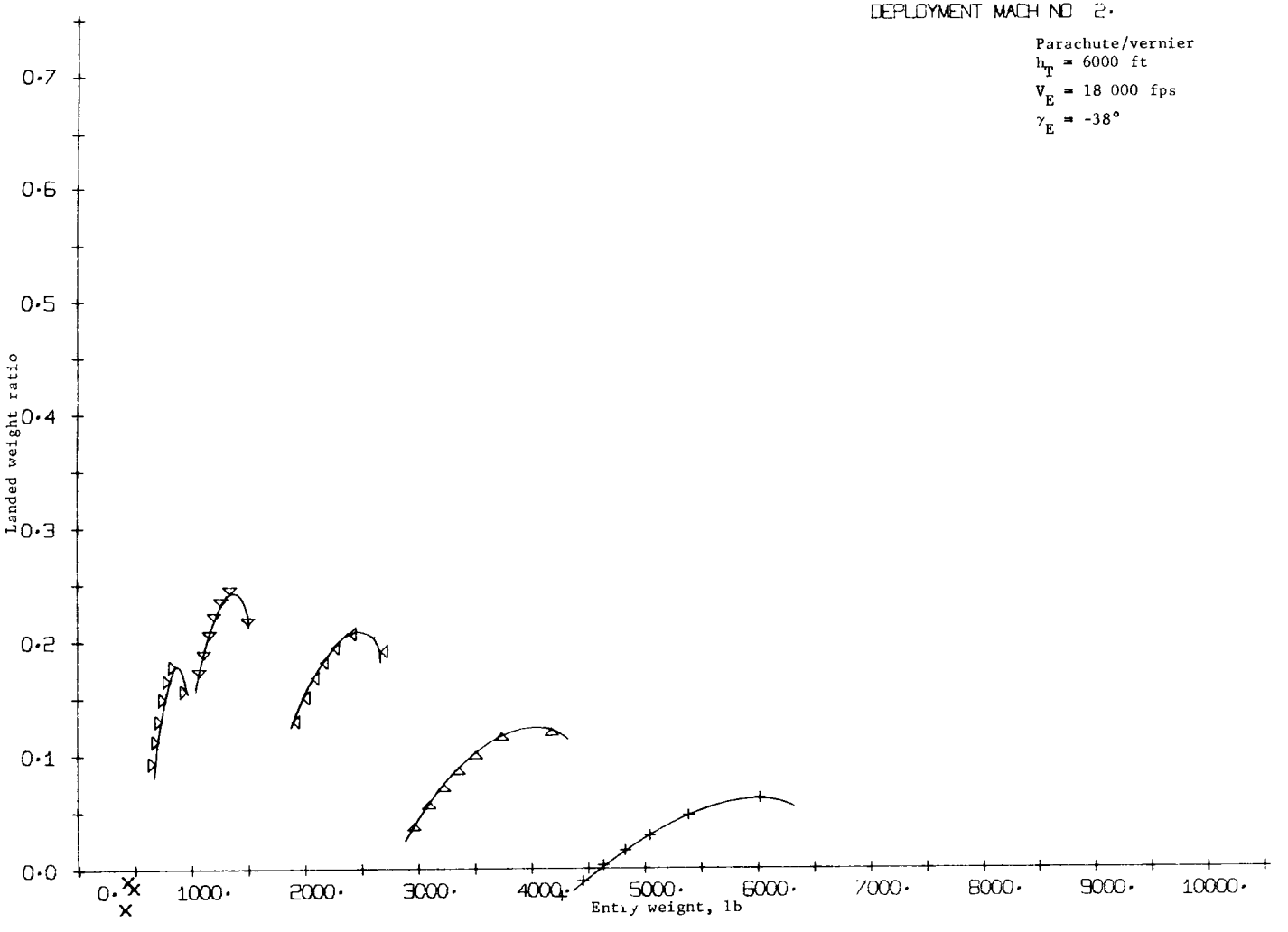

Figure B119.- Terminal Phase System Performance

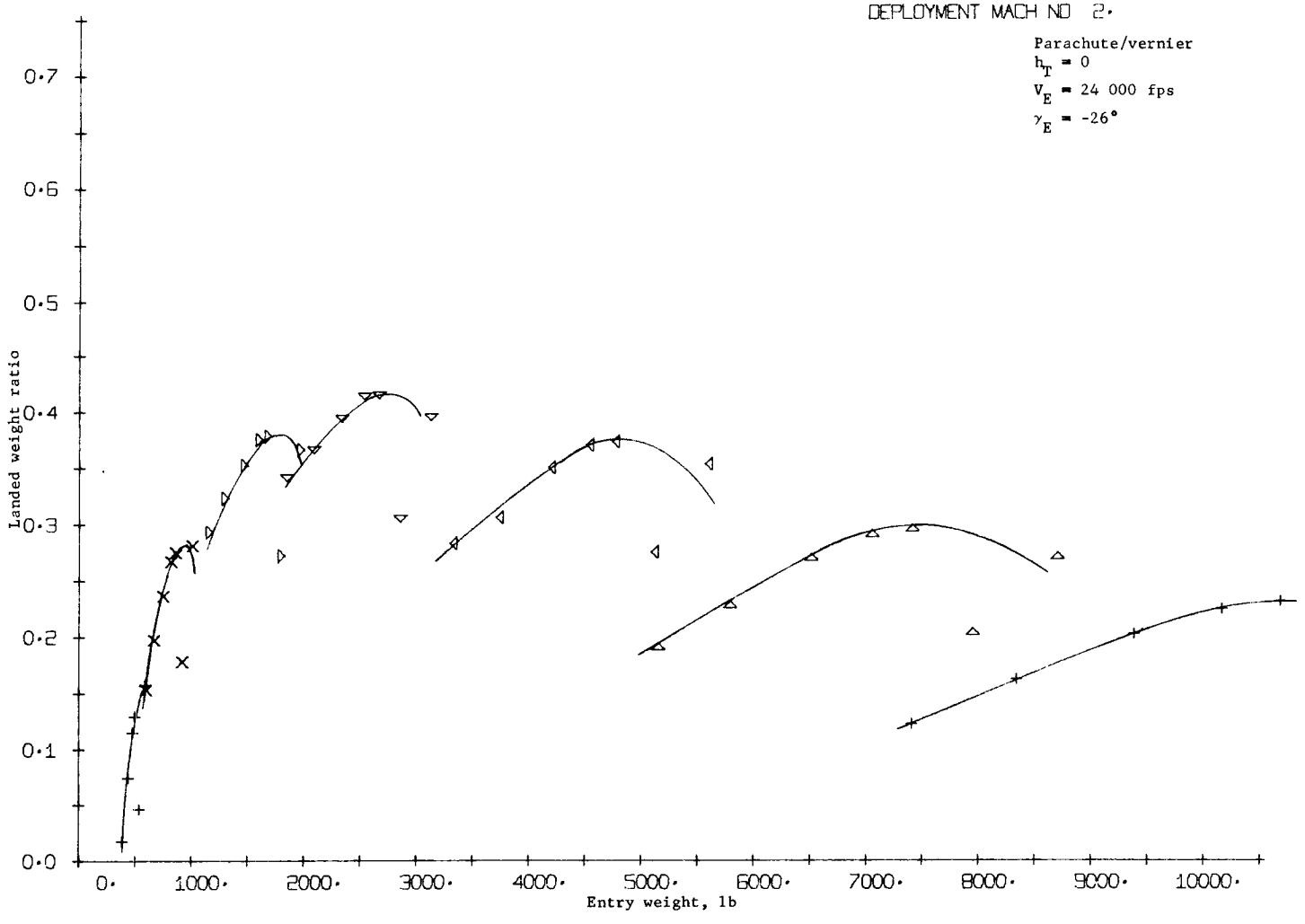

Figure B120.- Terminal Phase System Performance

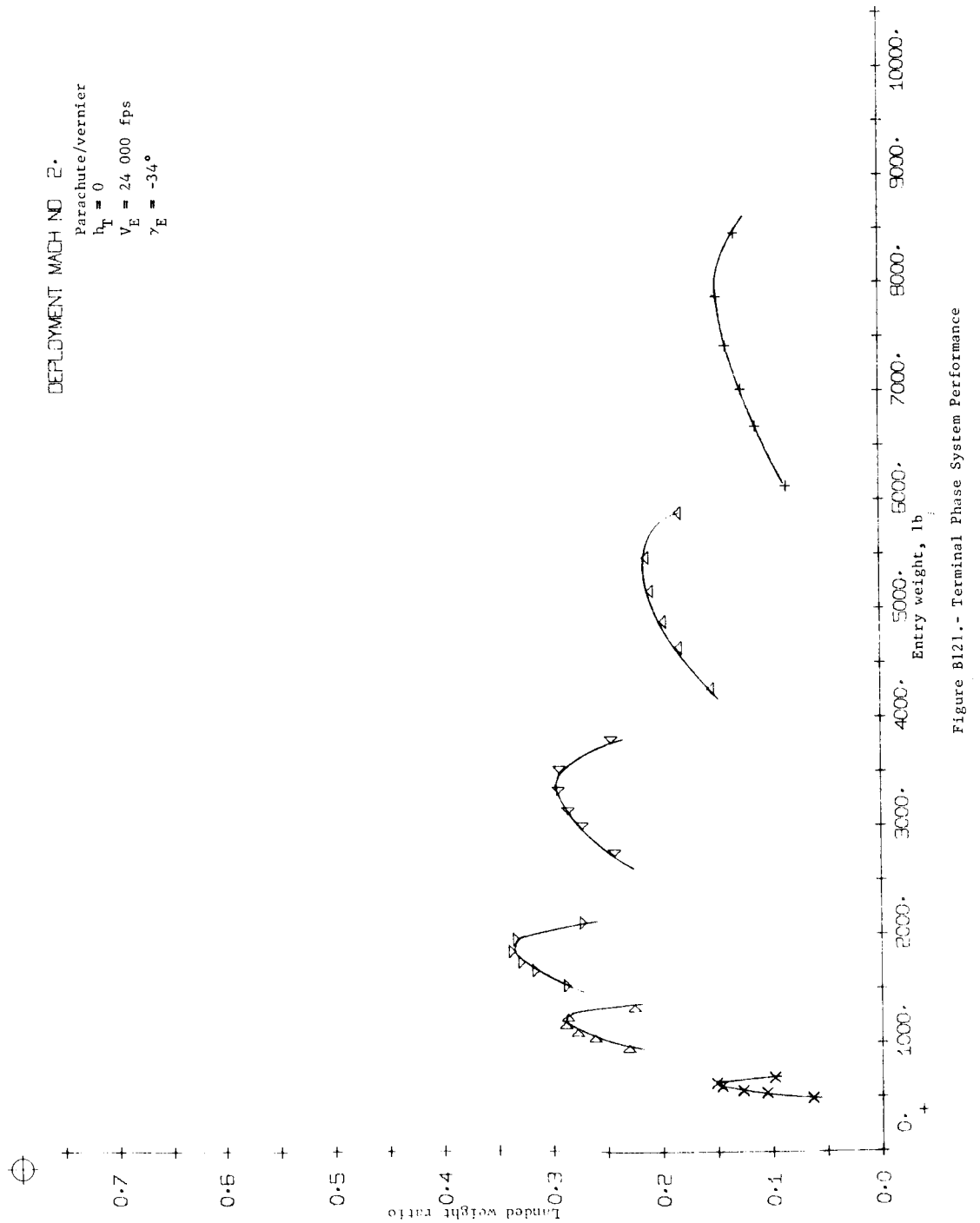

Figure B121.- Terminal Phase System Performance

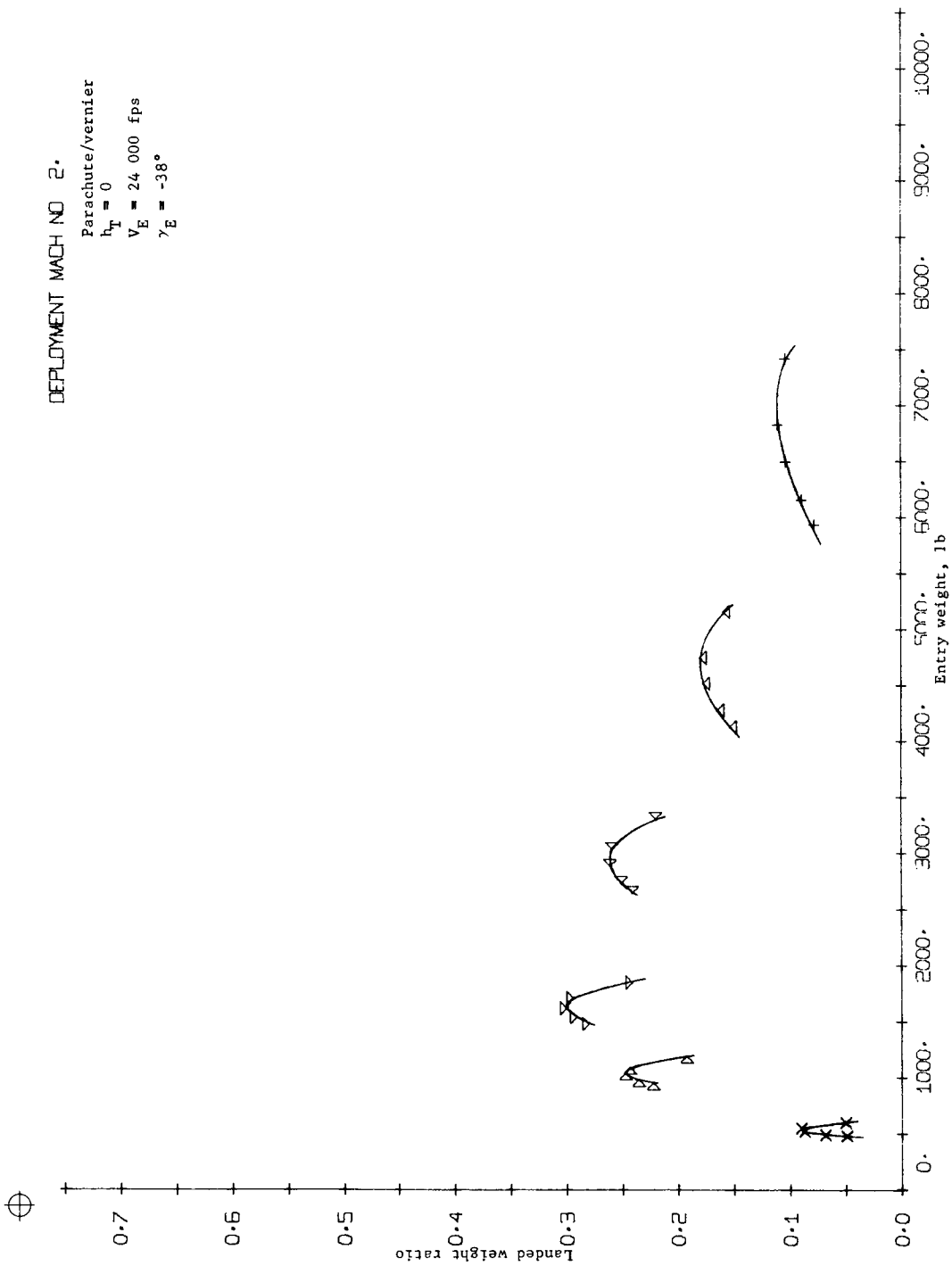

Figure B122.- Terminal Phase System Performance

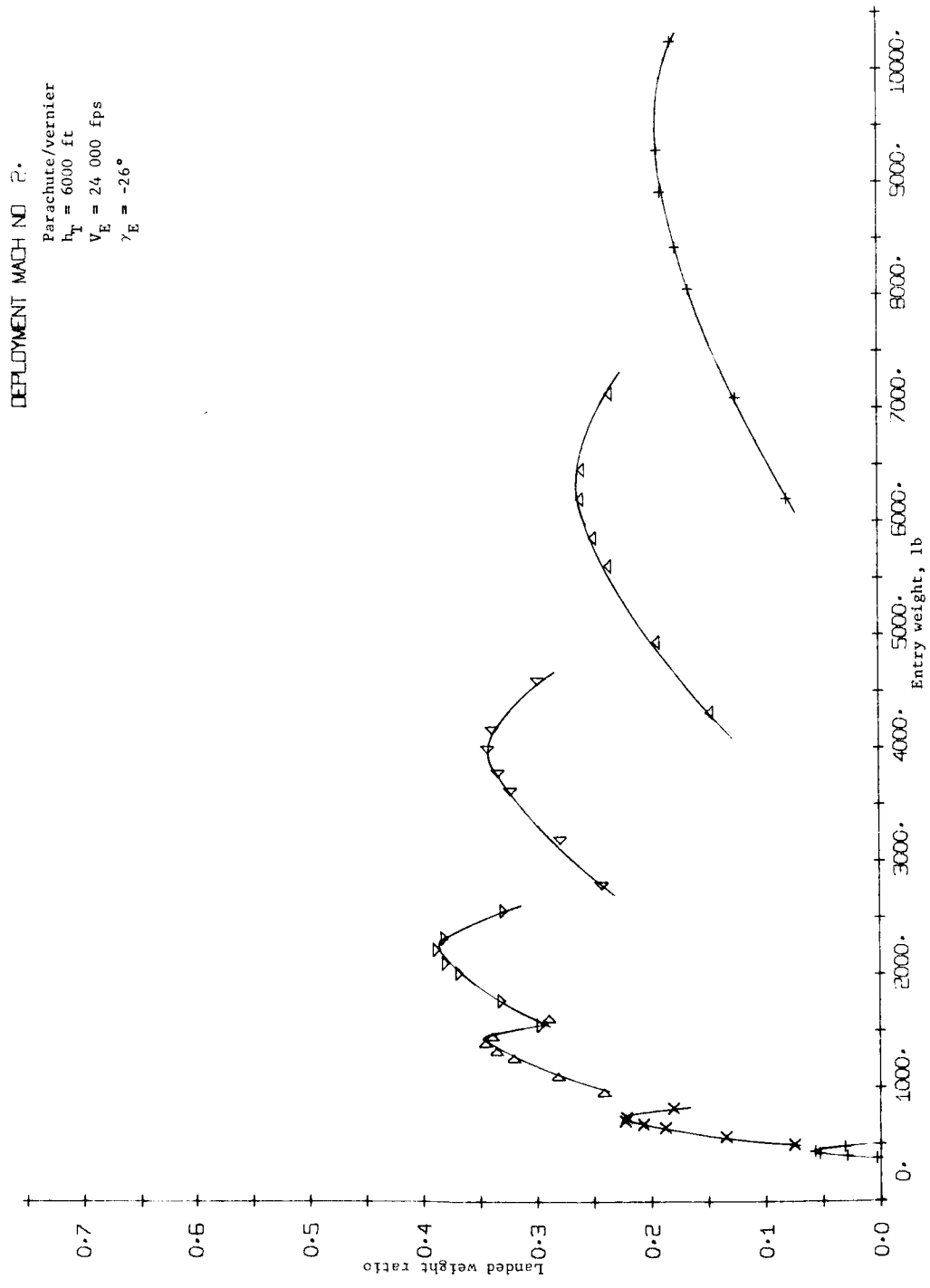

Figure B123.- Terminal Phase System Performance

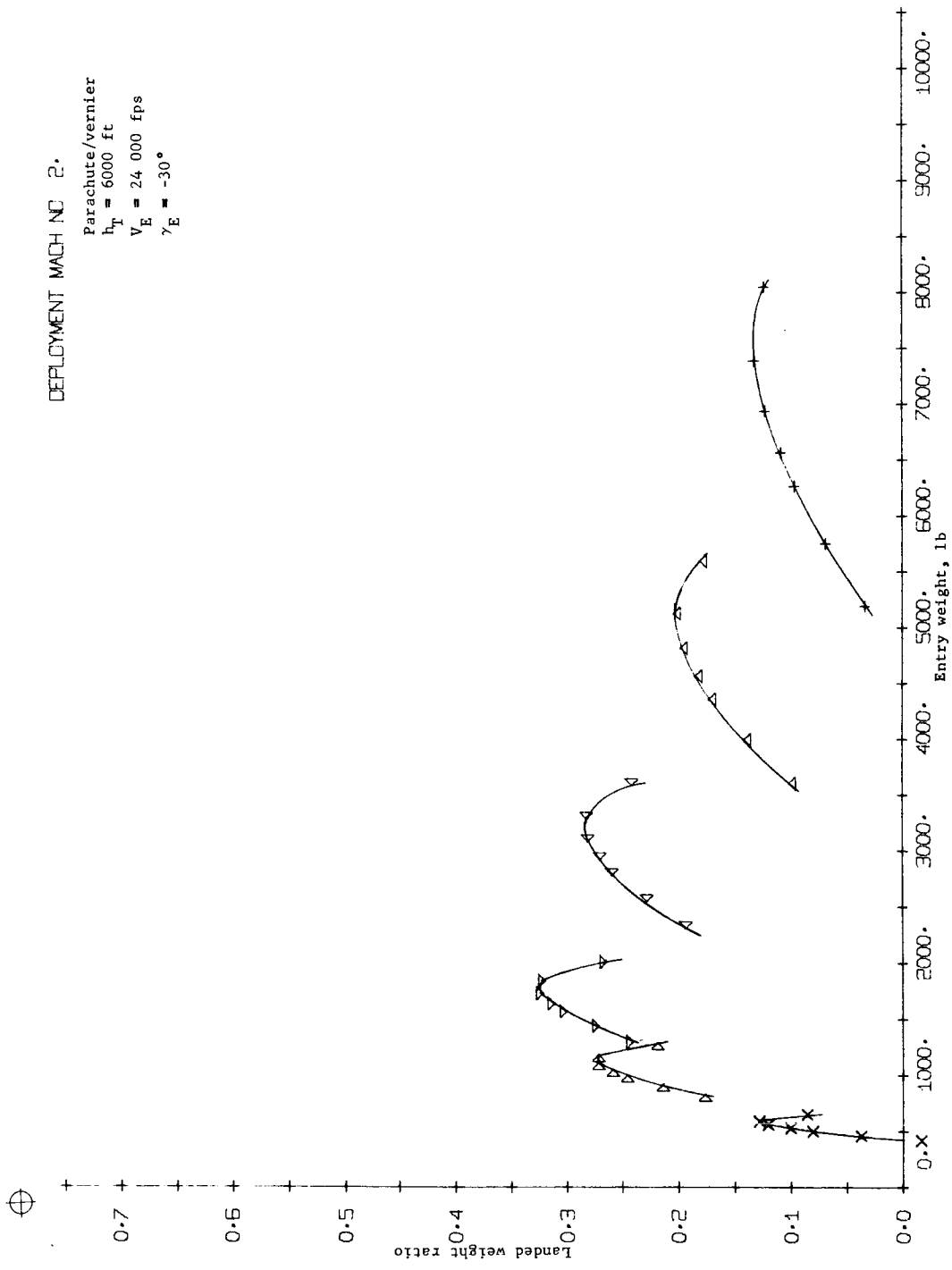

Figure B124.- Terminal Phase System Performance

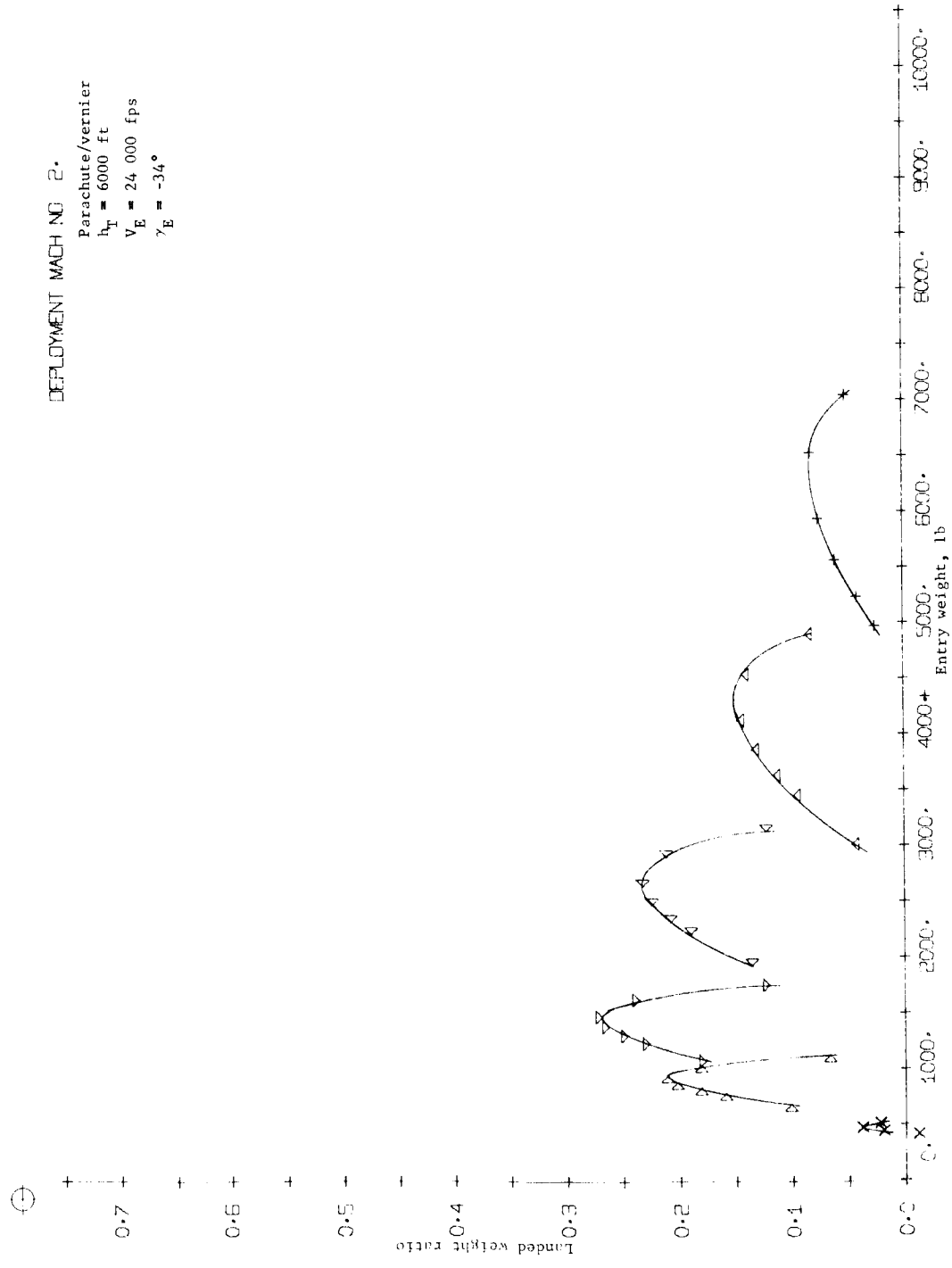

Figure B125.- Terminal Phase System Performance

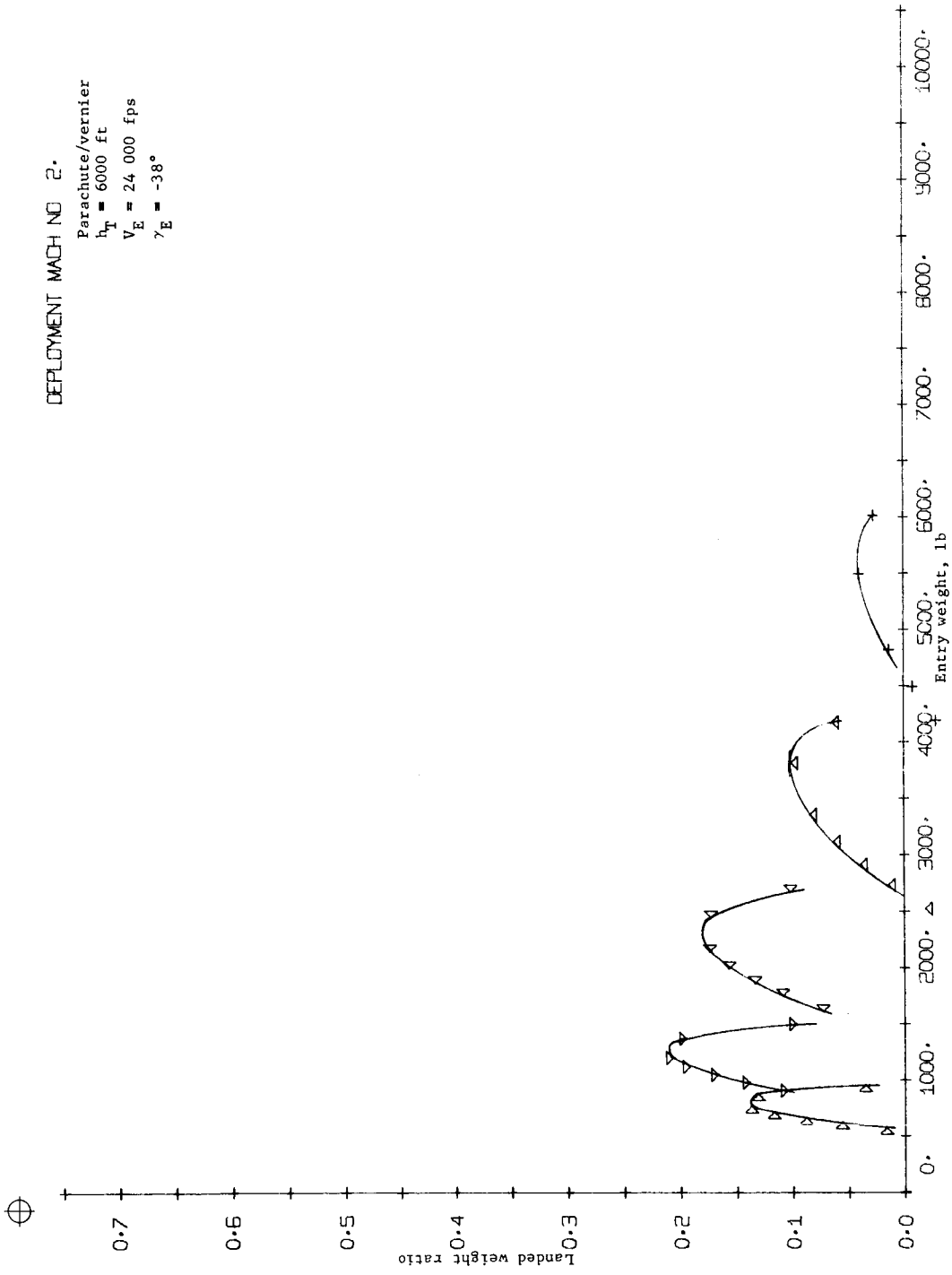

Figure B126.- Terminal Phase System Performance

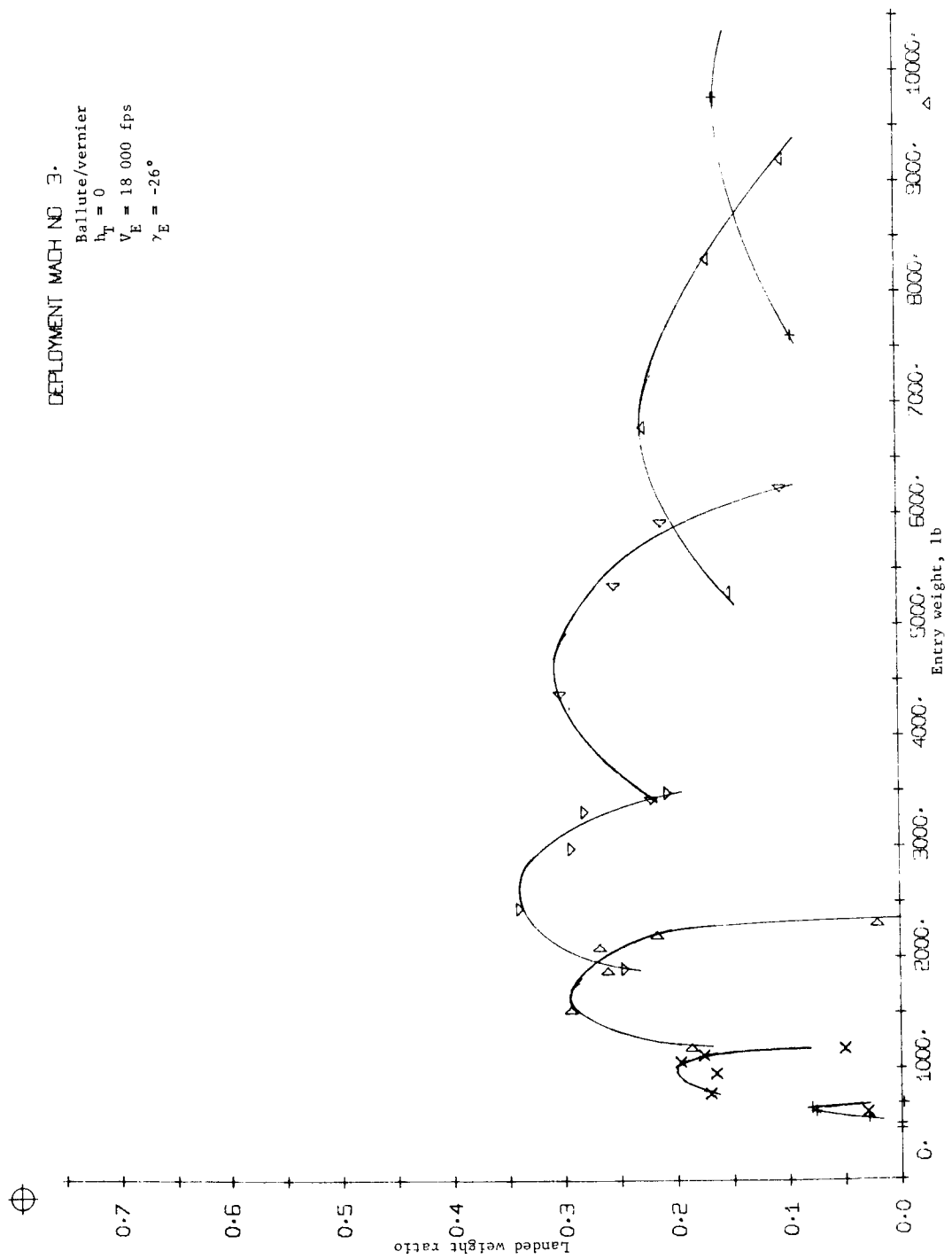

Figure B127.- Terminal Phase System Performance

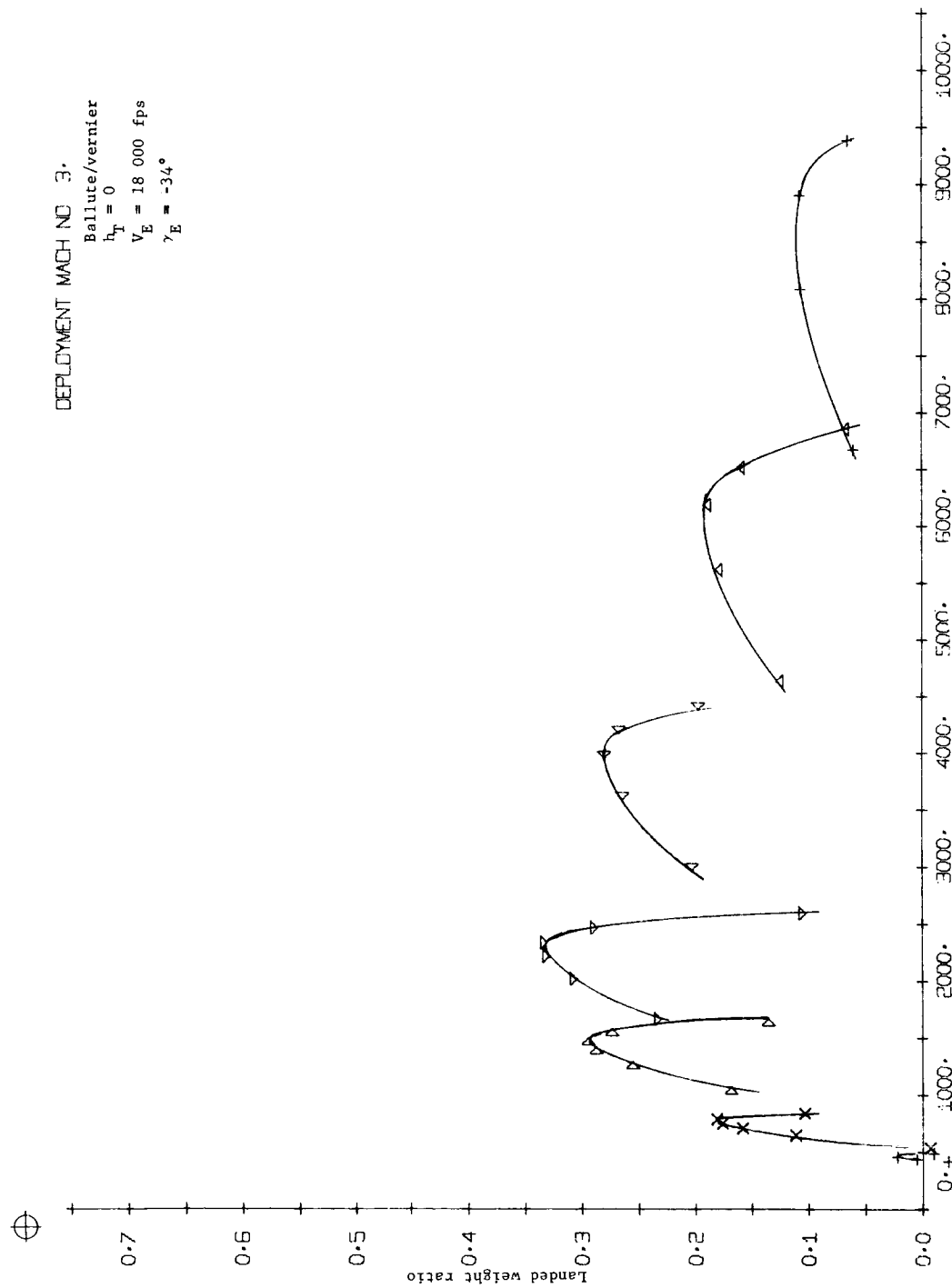

Figure B128.- Terminal Phase System Performance

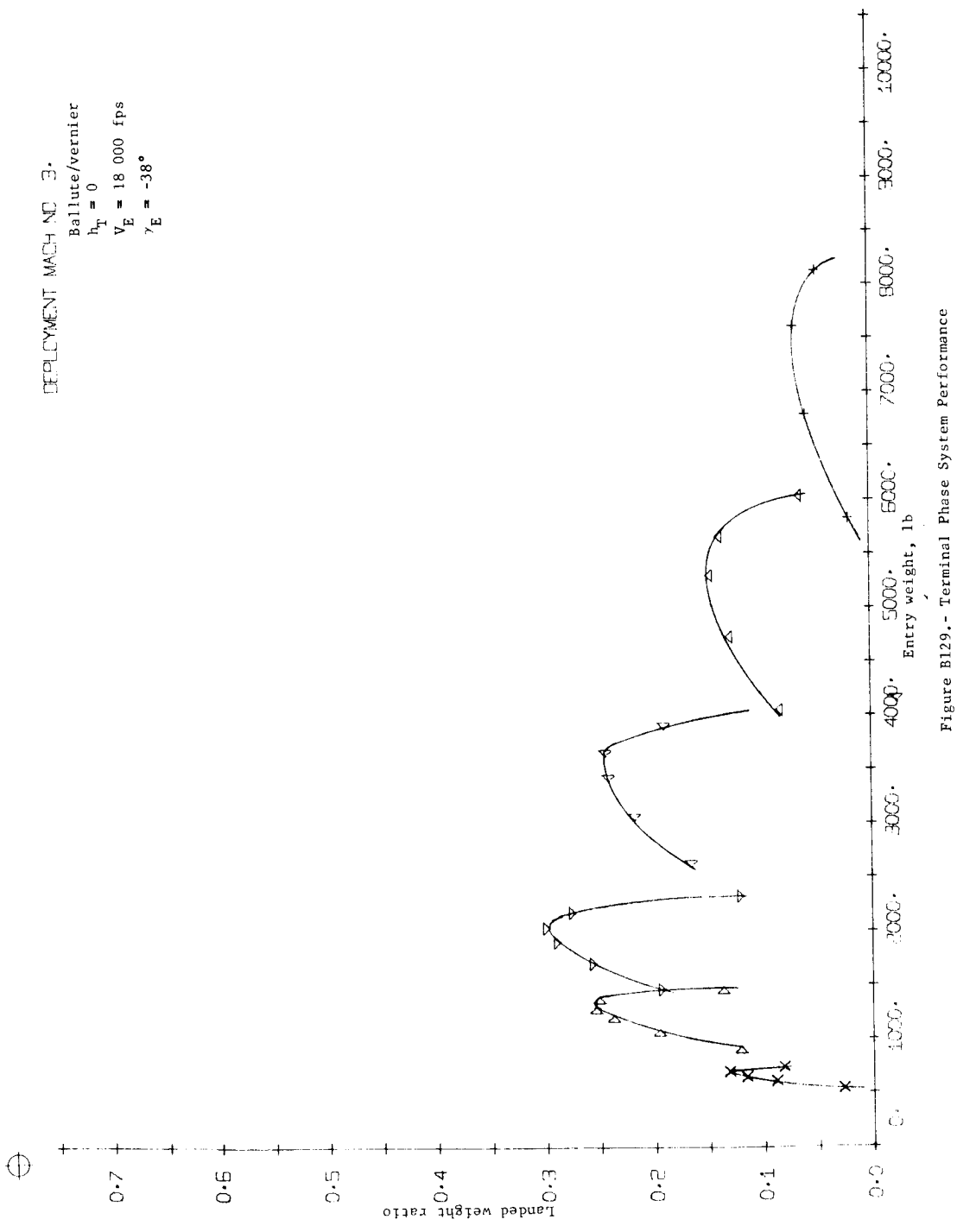

Figure B129.- Terminal Phase System Performance

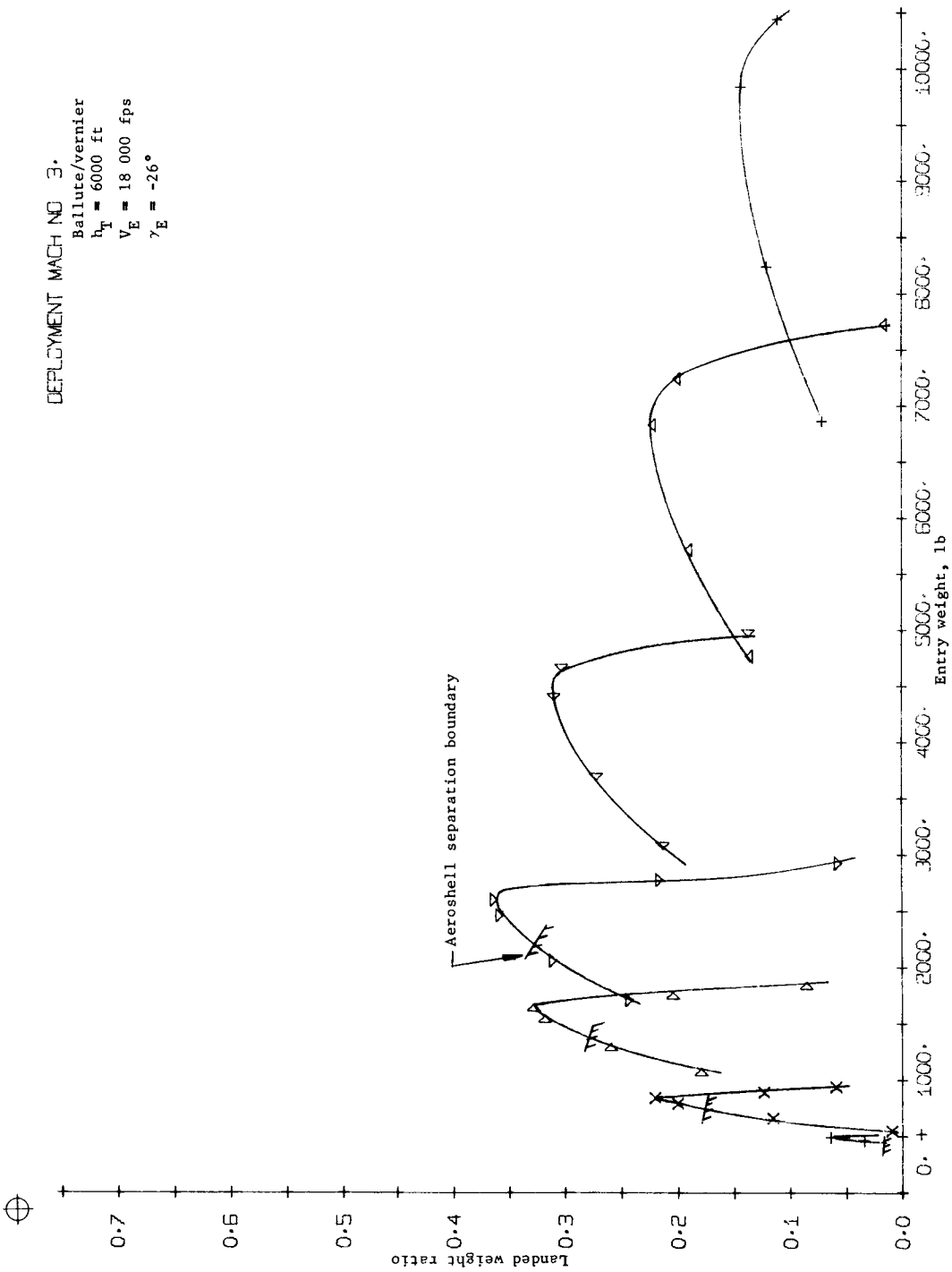

Figure B130.- Terminal Phase System Performance

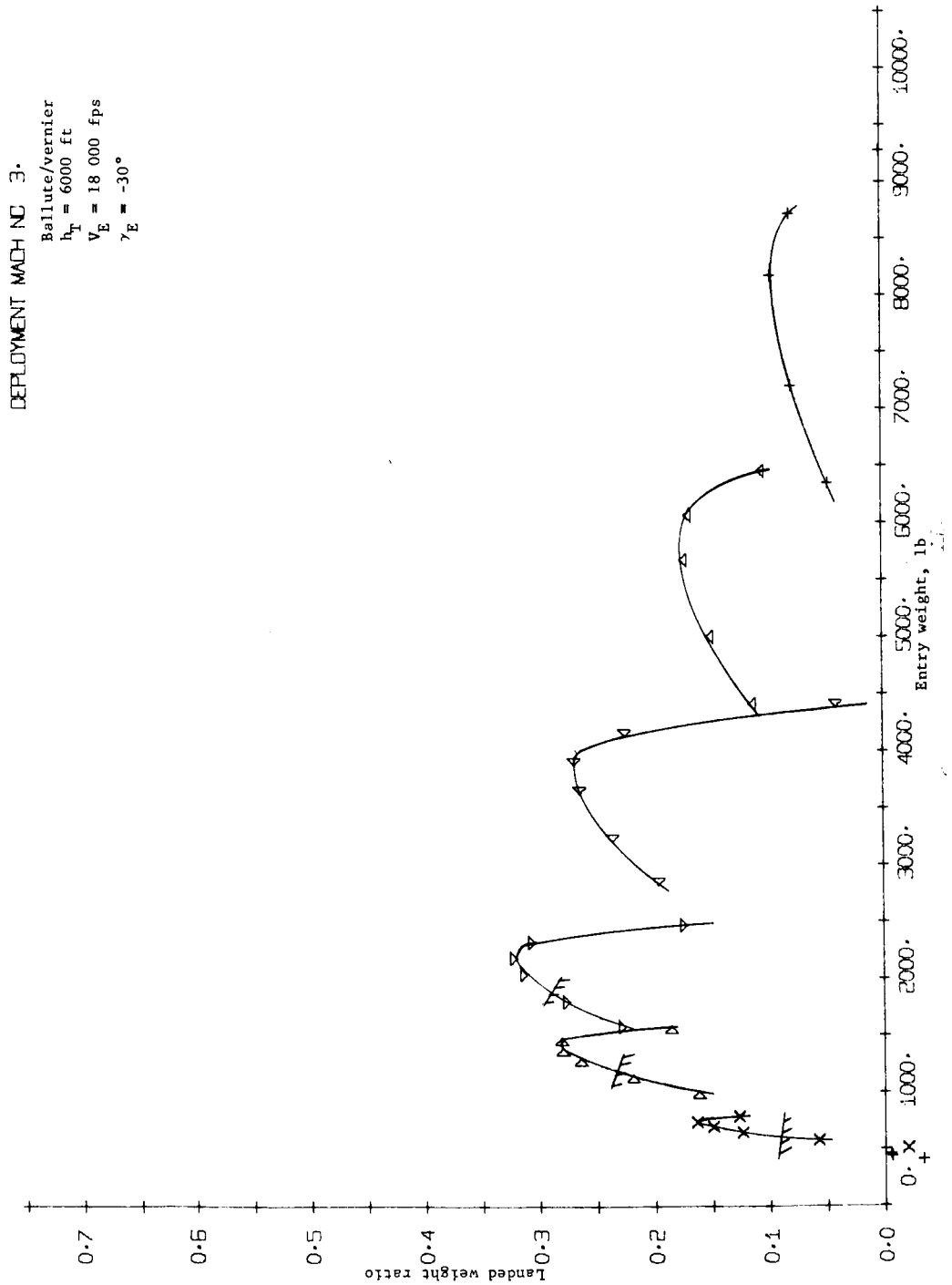

Figure B131.- Terminal Phase System Performance

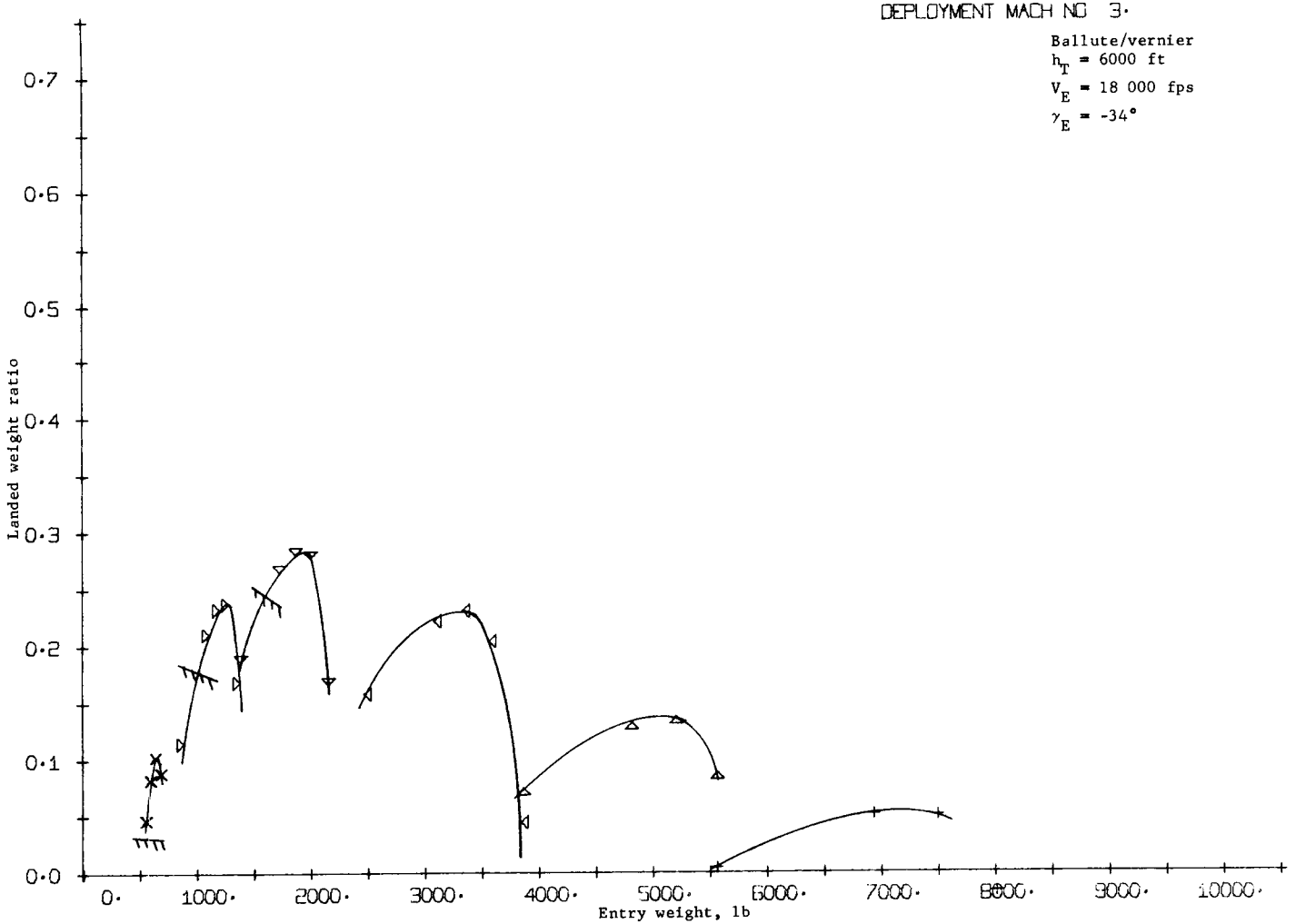

Figure B132.- Terminal Phase System Performance

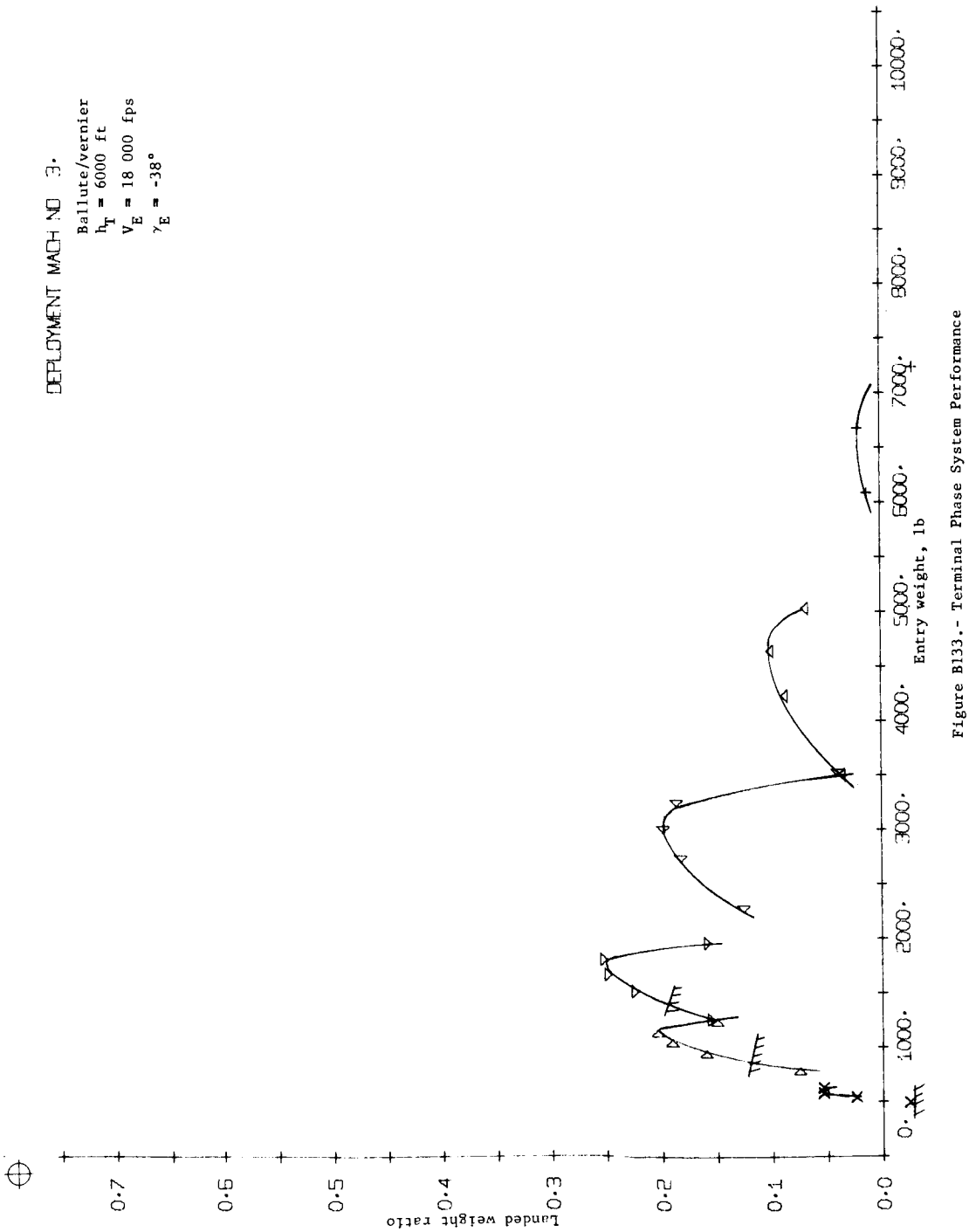

Figure B133.- Terminal Phase System Performance

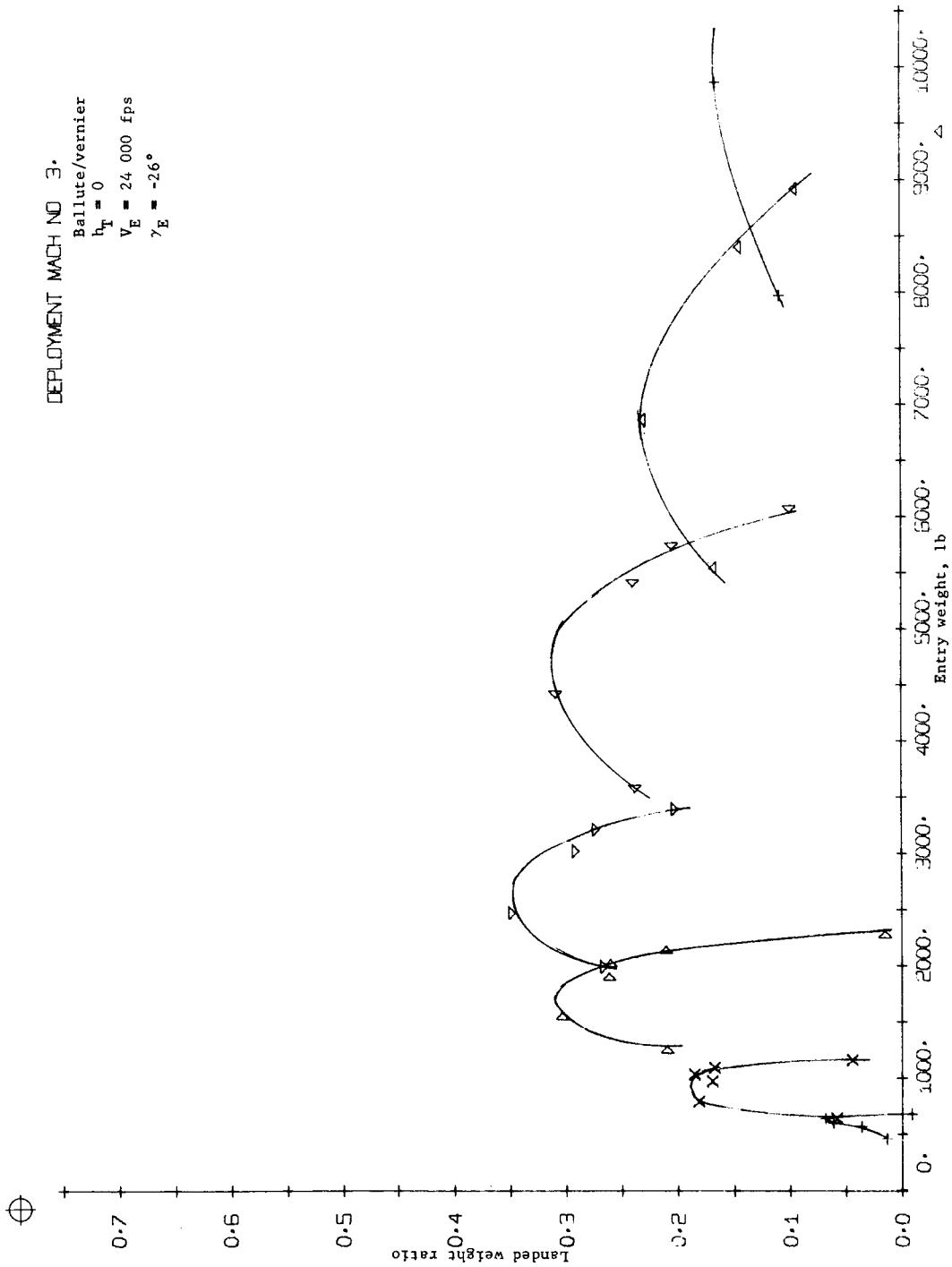

Figure B134.- Terminal Phase System Performance

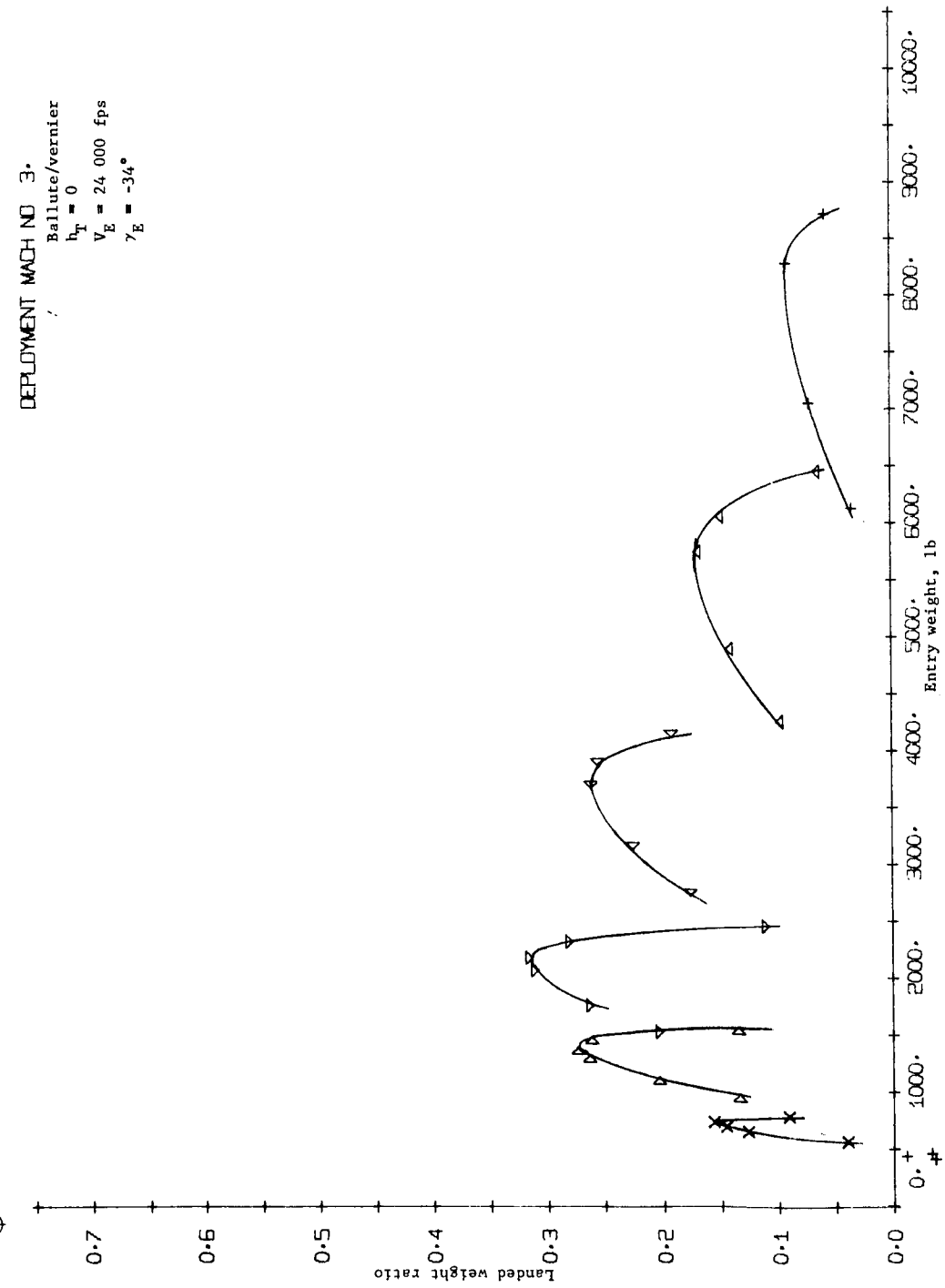

Figure B135.- Terminal Phase System Performance

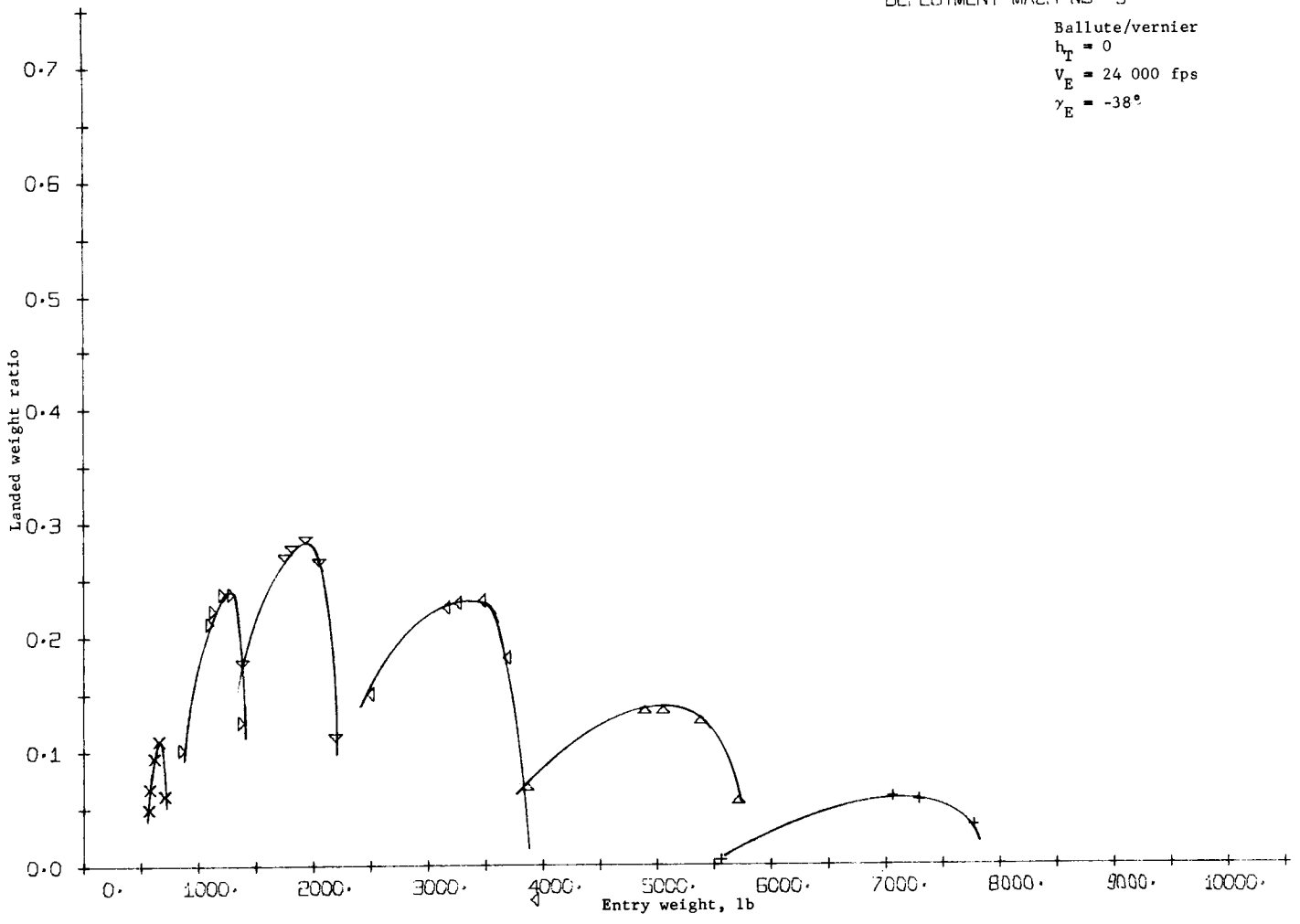

Figure B136.- Terminal Phase System Performance

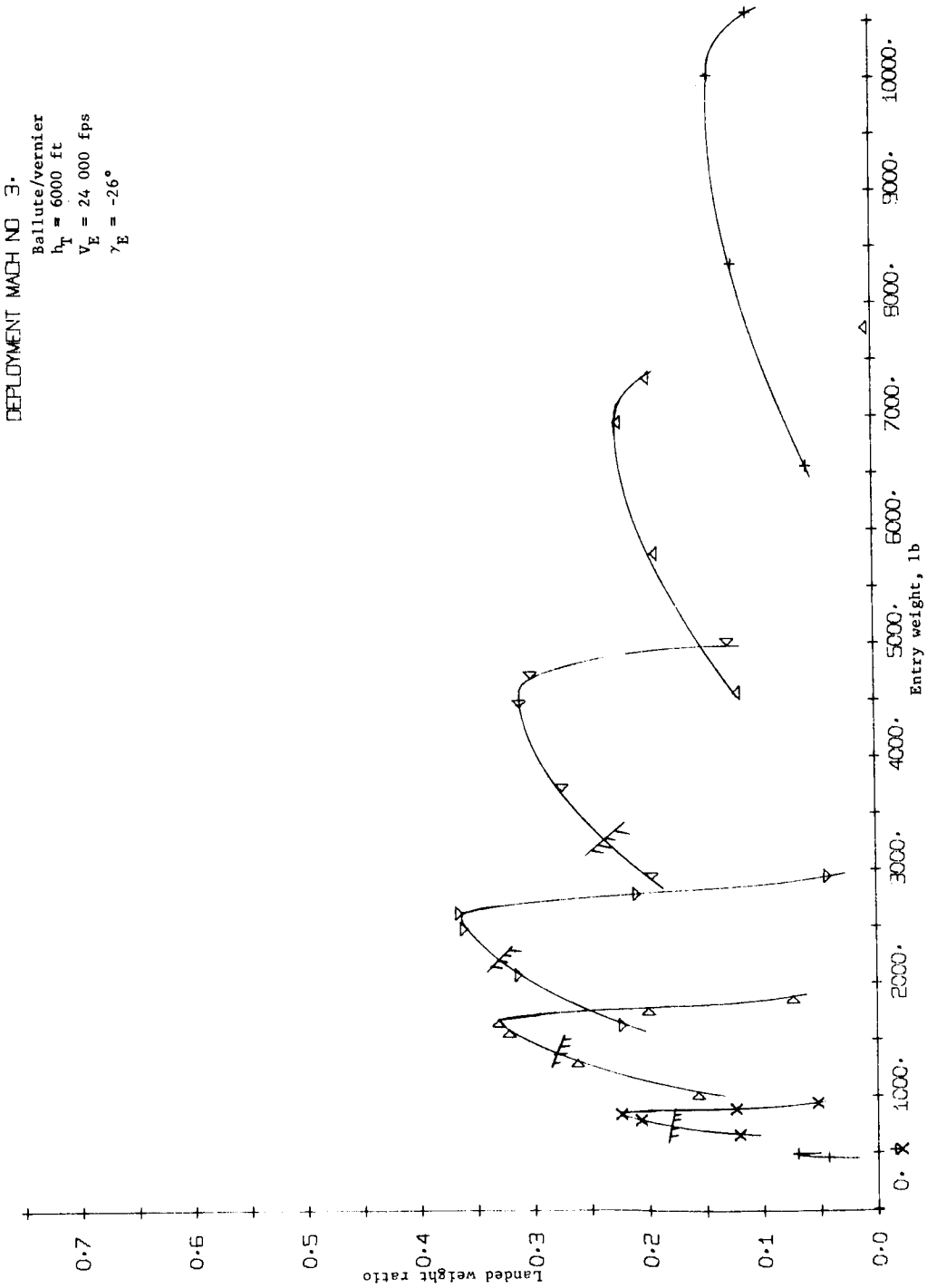

Figure B137.- Terminal Phase System Performance

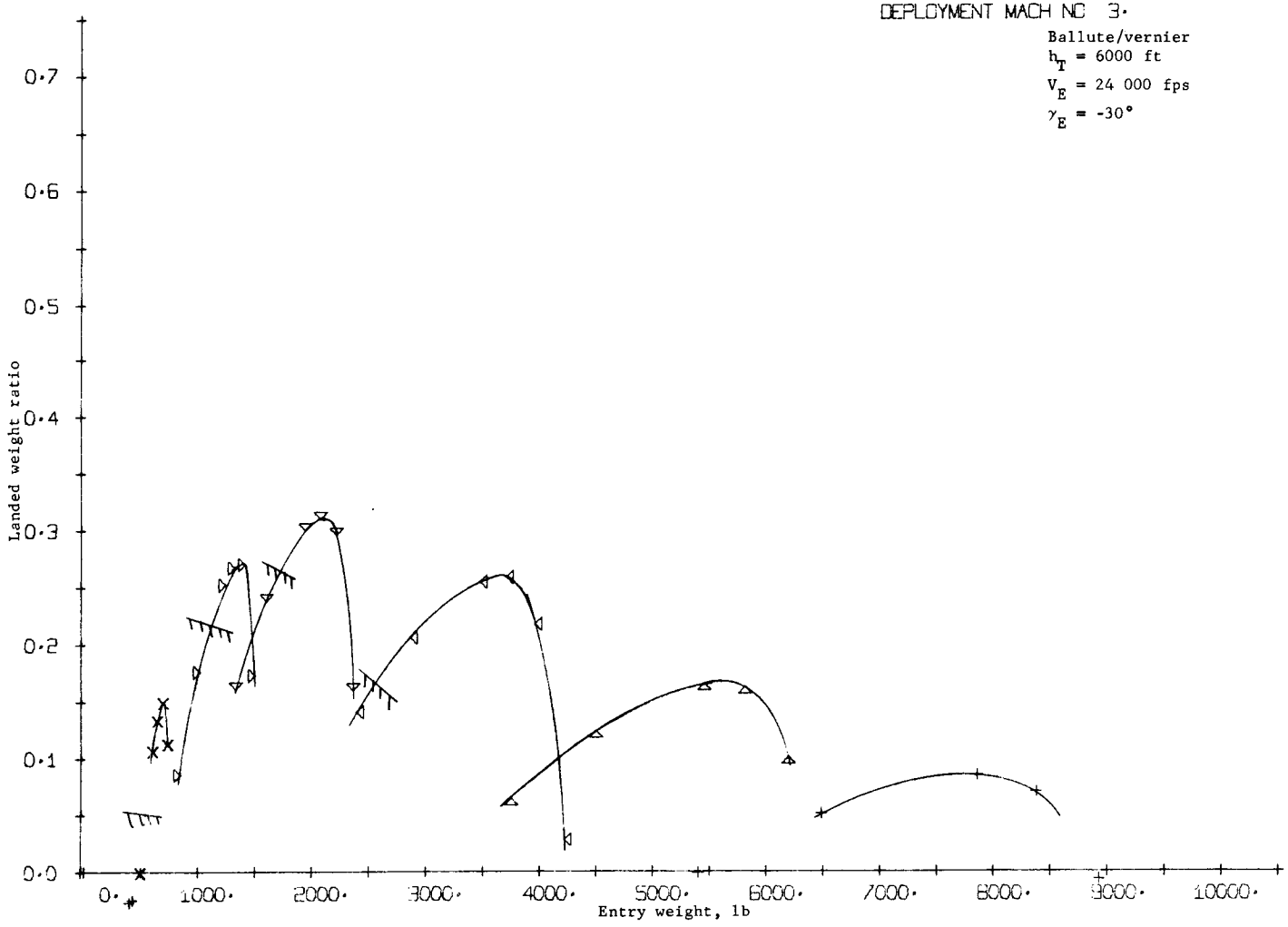

Figure B138.- Terminal Phase System Performance

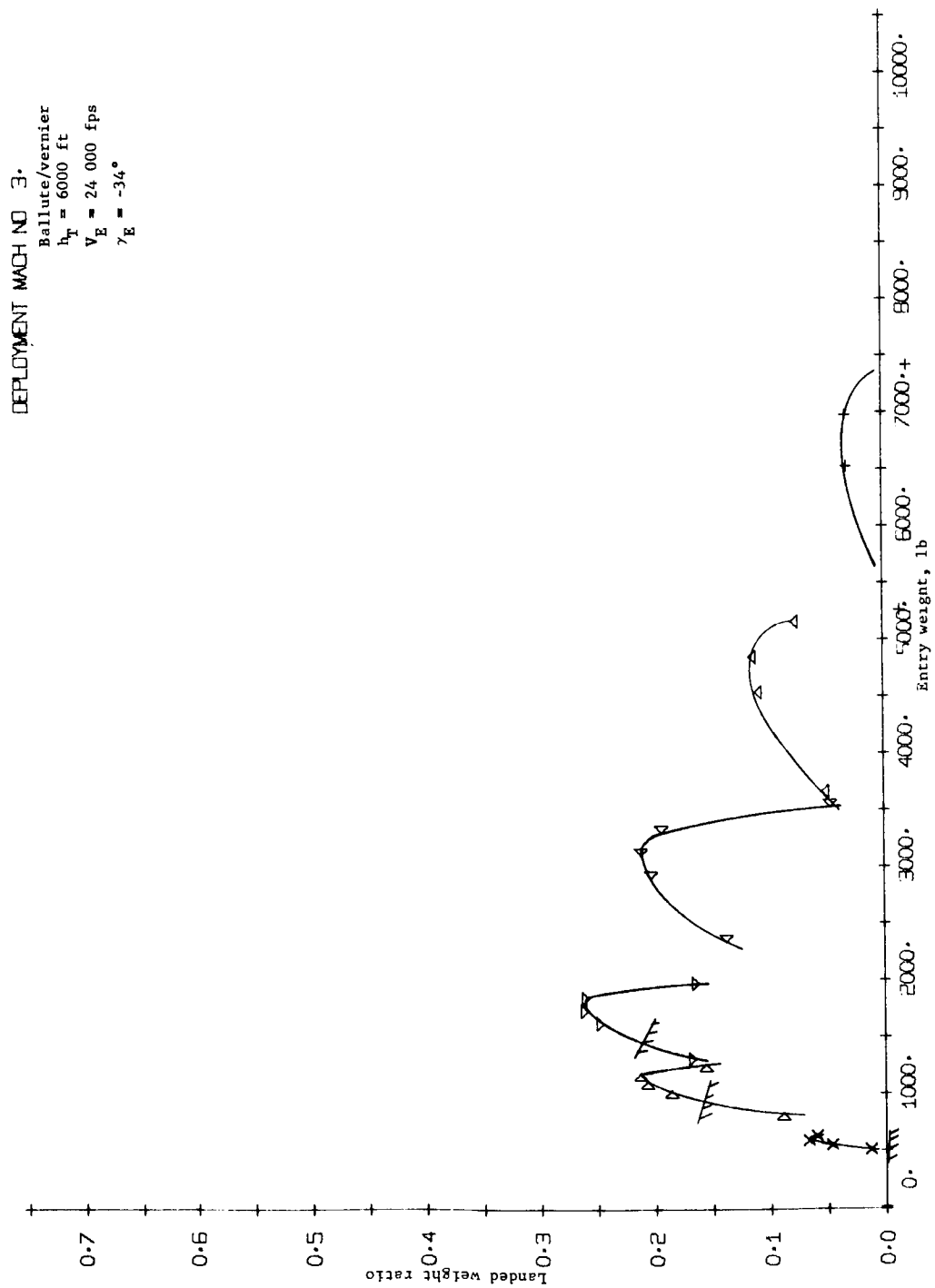

Figure B139.- Terminal Phase System Performance

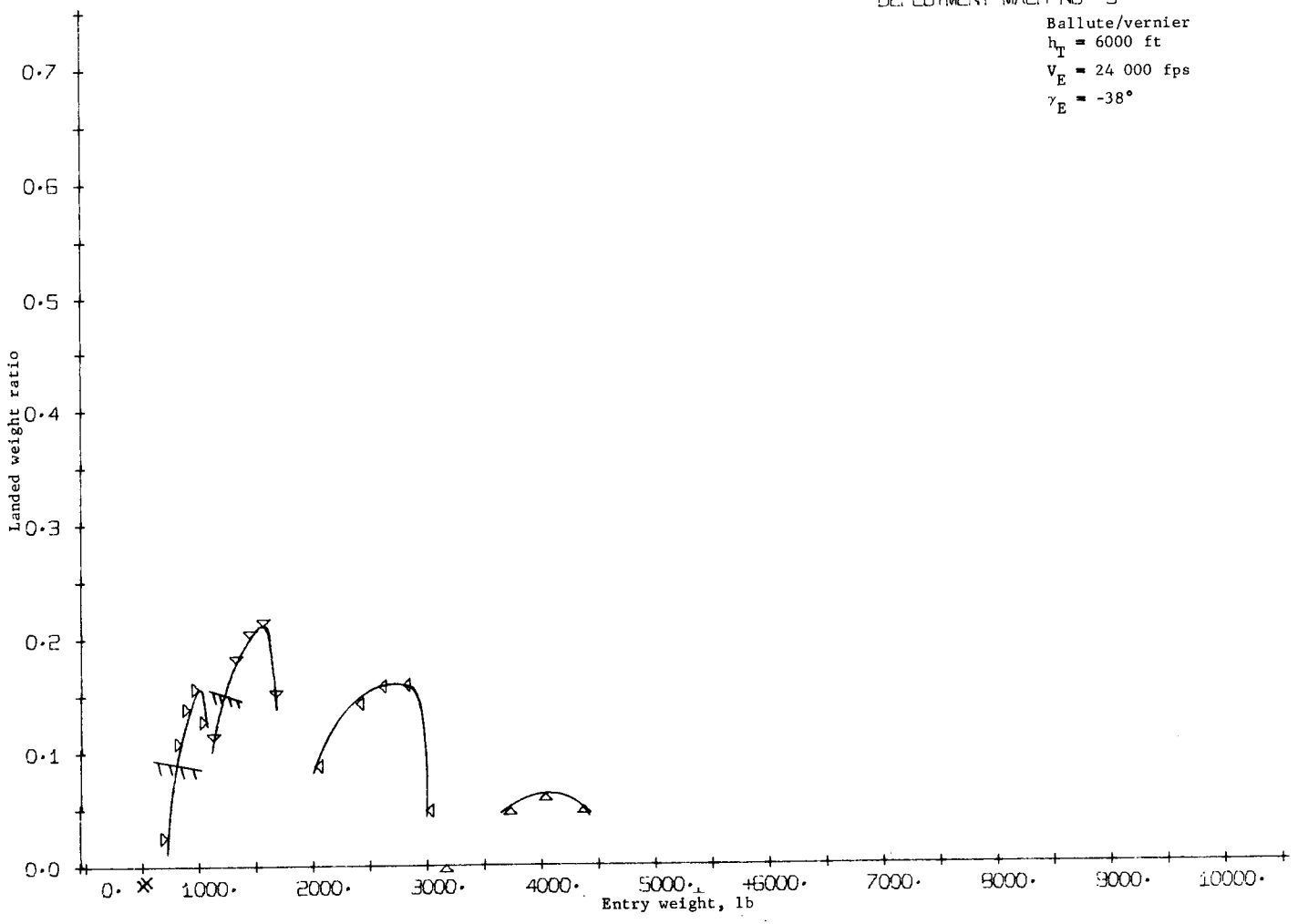

Figure B140.- Terminal Phase System Performance

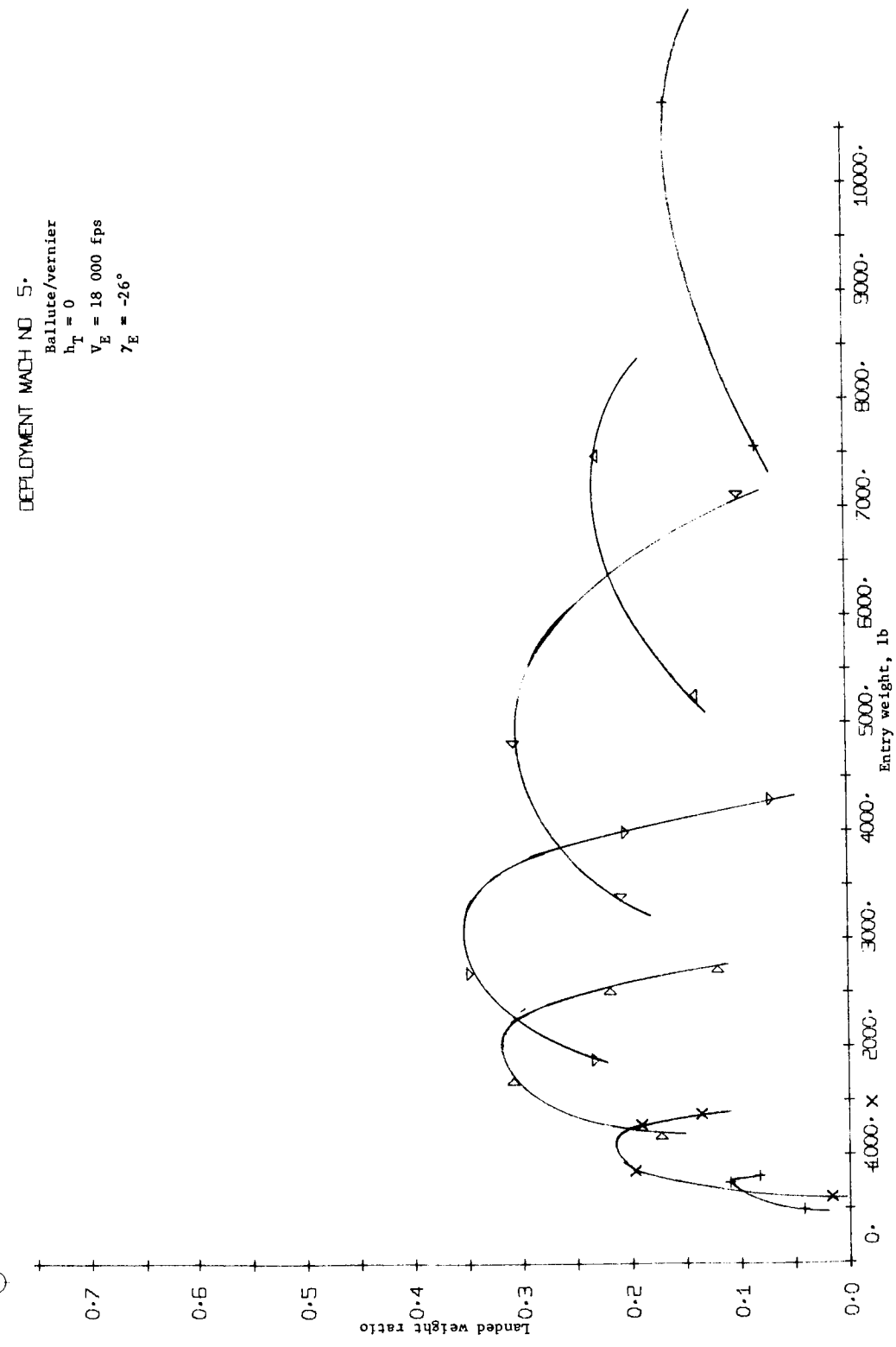

Figure B141.- Terminal Phase System Performance

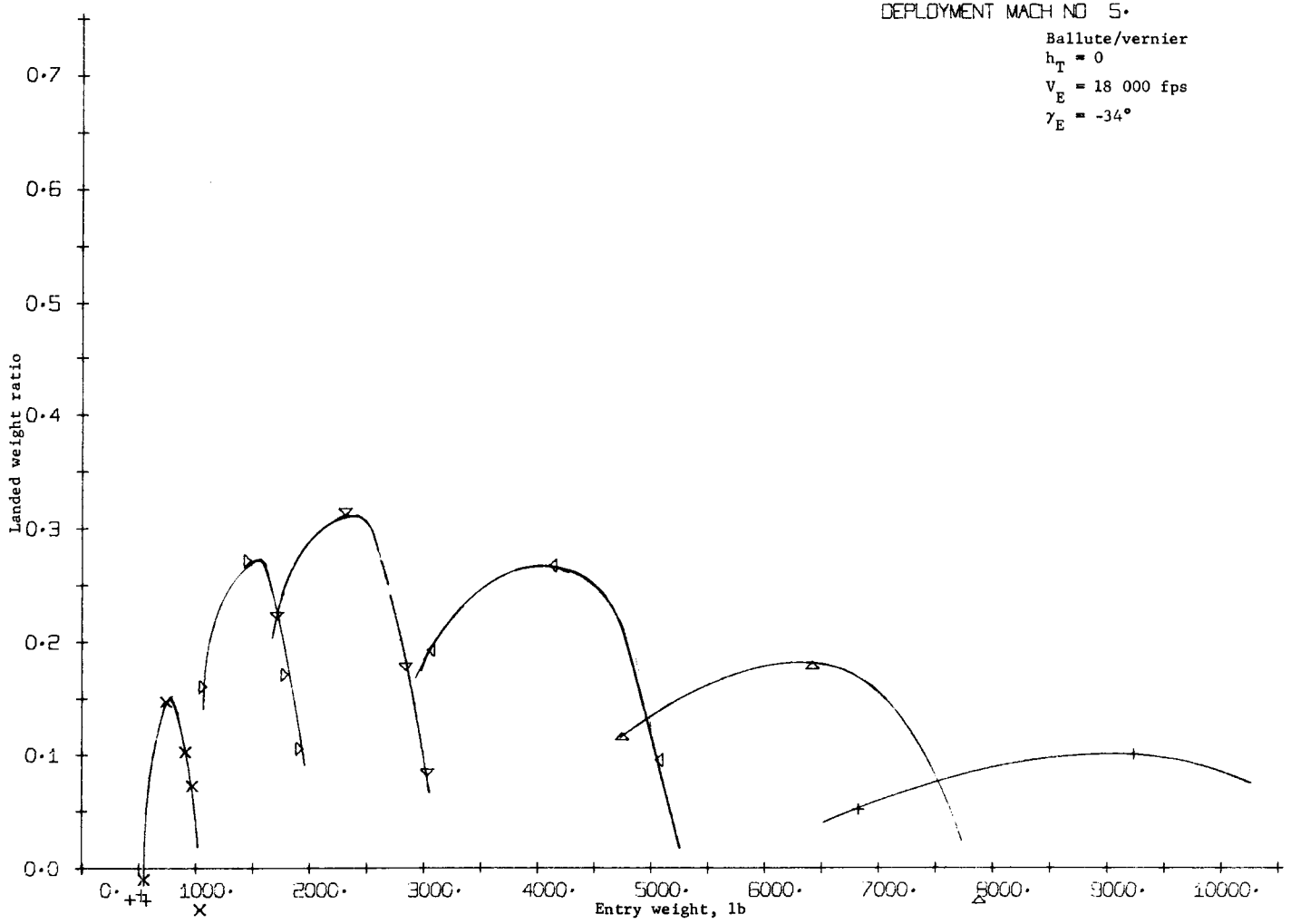

Figure B142.- Terminal Phase System Performance

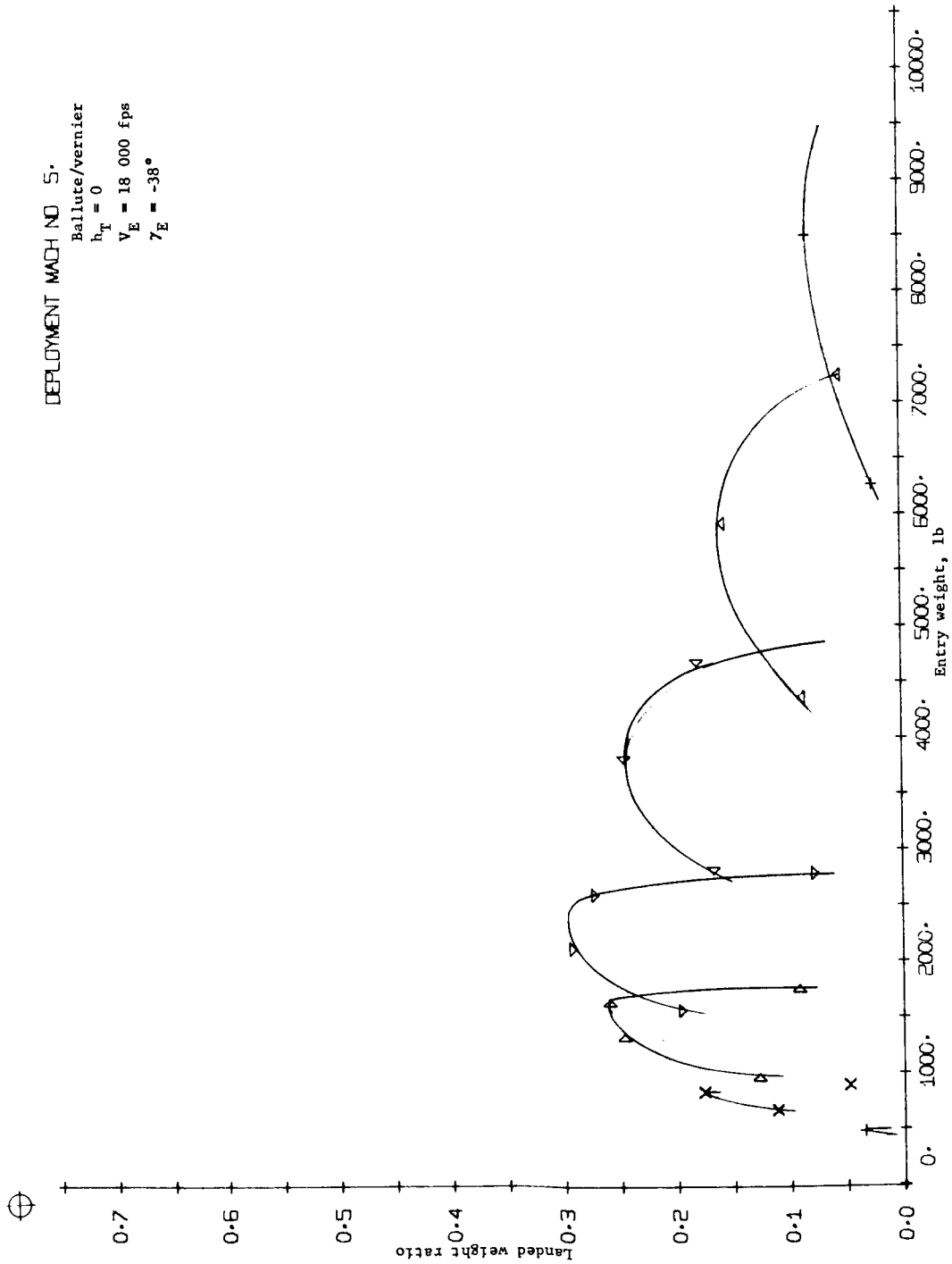

Figure B143.- Terminal Phase System Performance

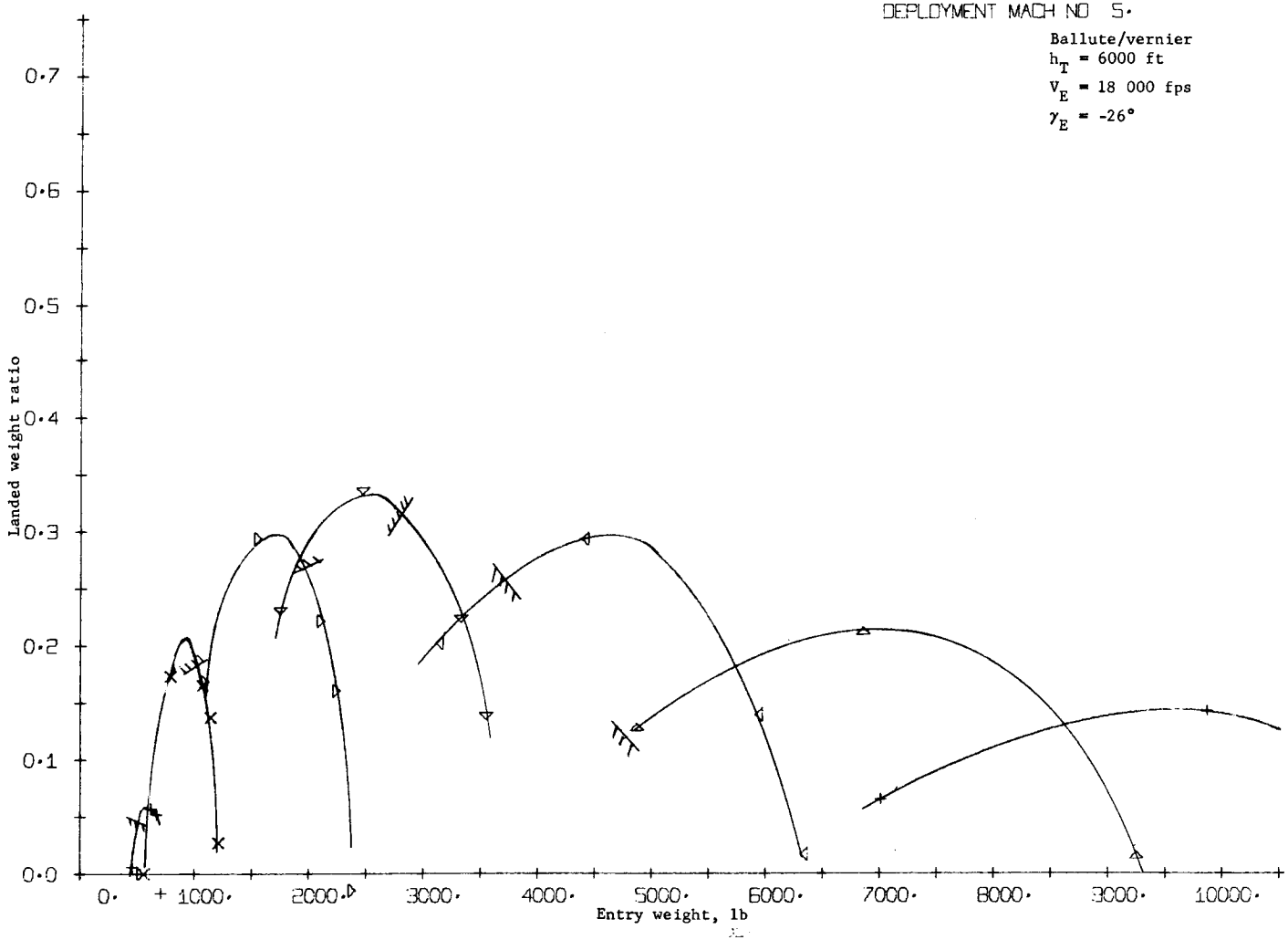

Figure B144.- Terminal Phase System Performance

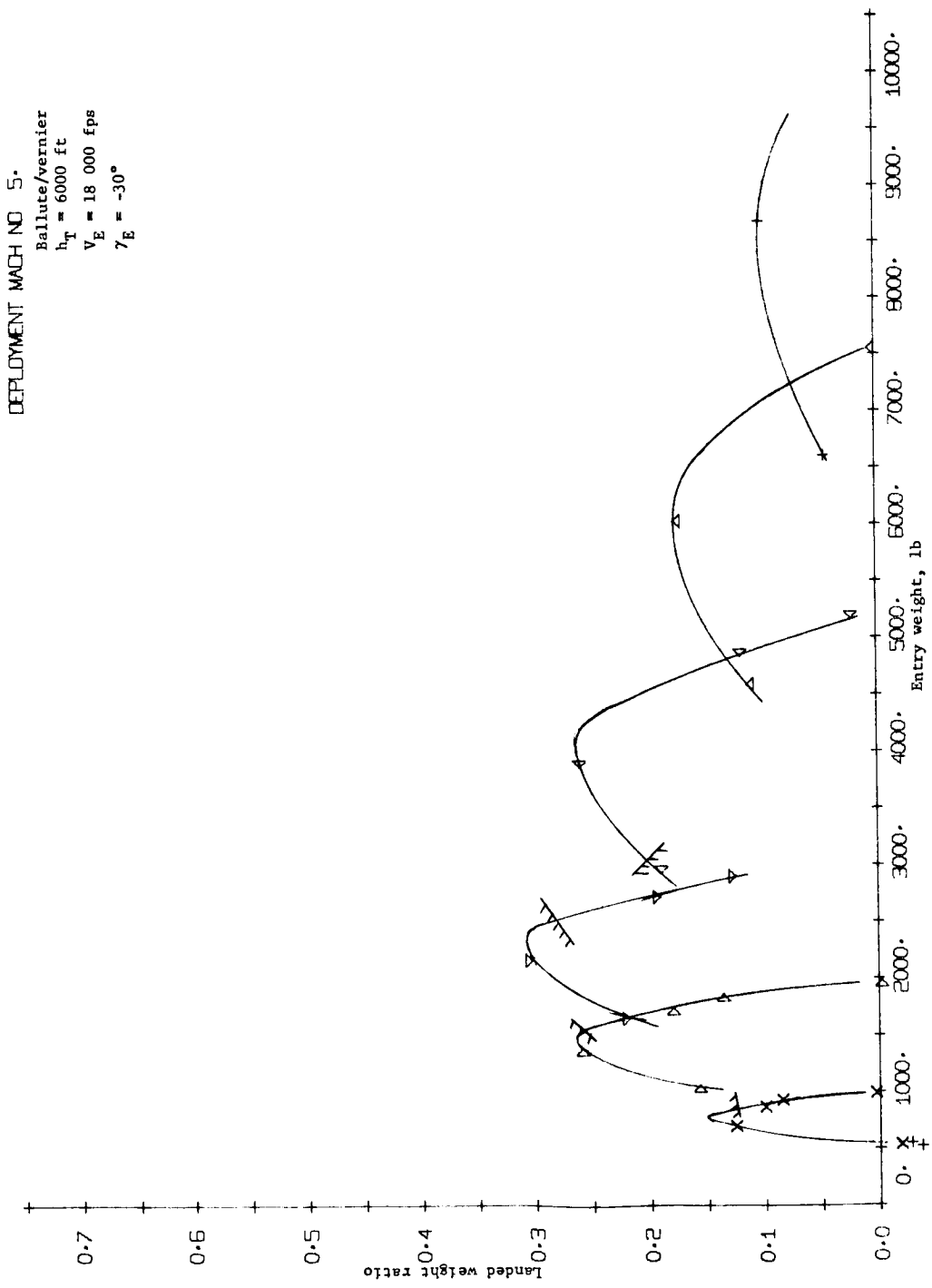

Figure B145.- Terminal Phase System Performance

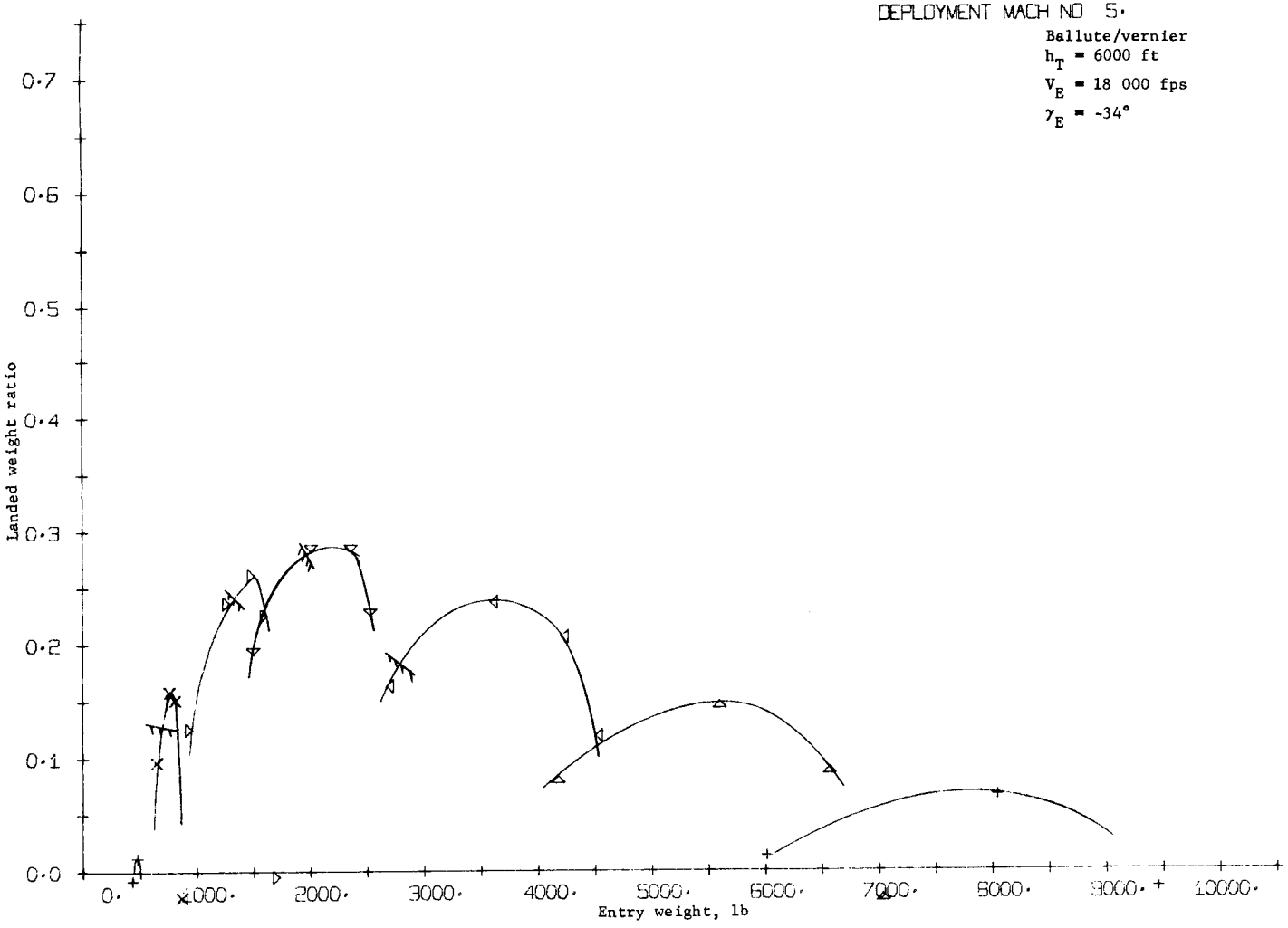

Figure B146.- Terminal Phase System Performance

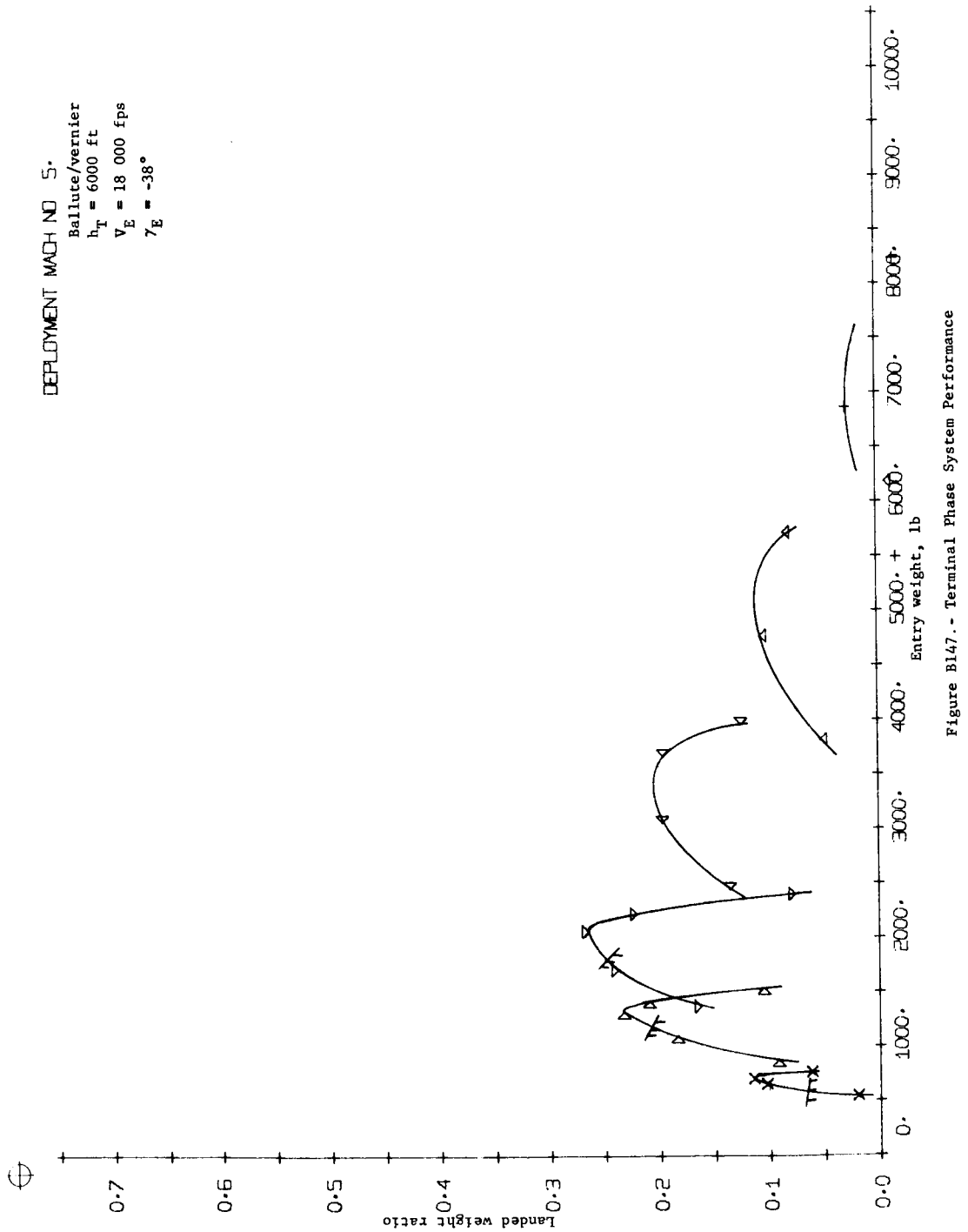

Figure B147.- Terminal Phase System Performance

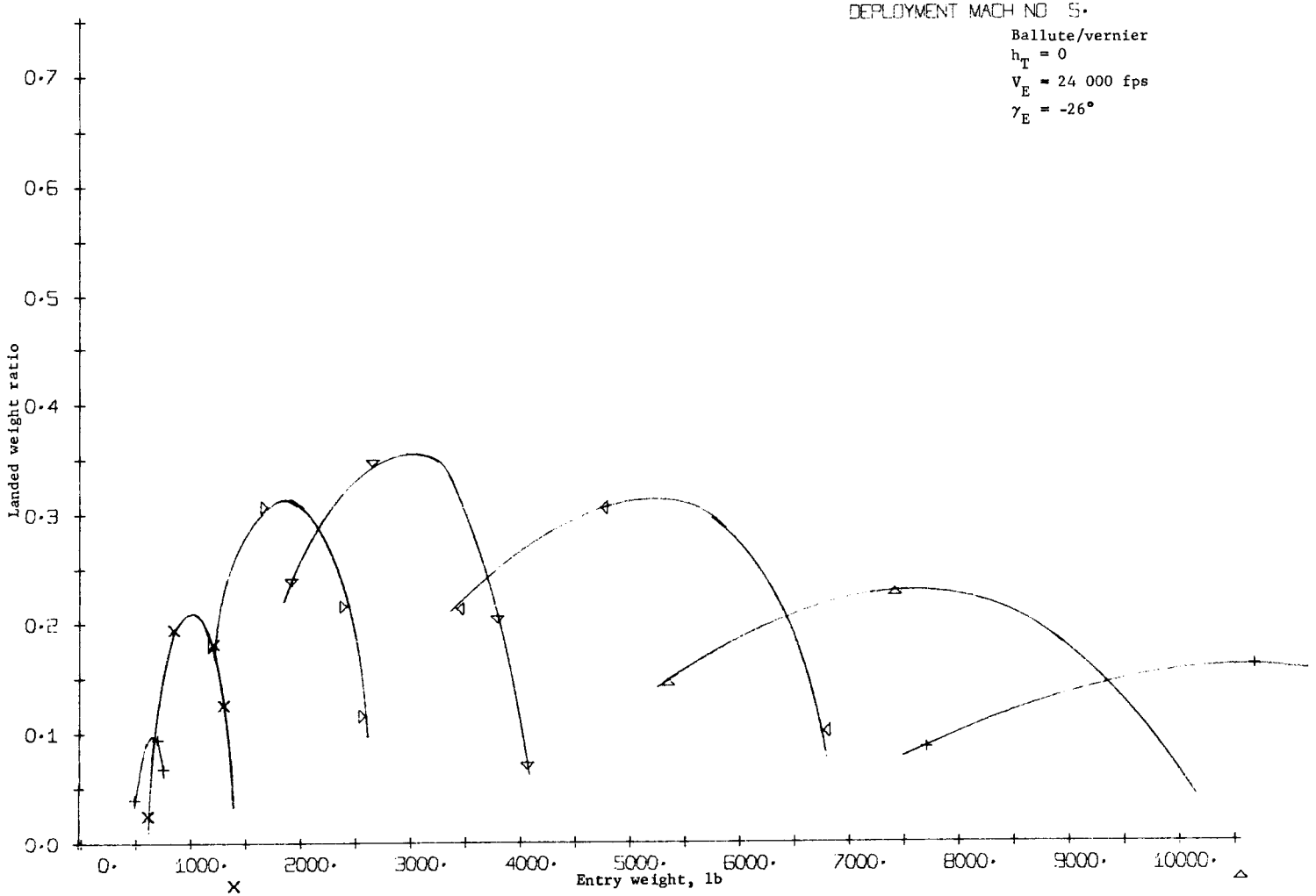

Figure B148.- Terminal Phase System Performance

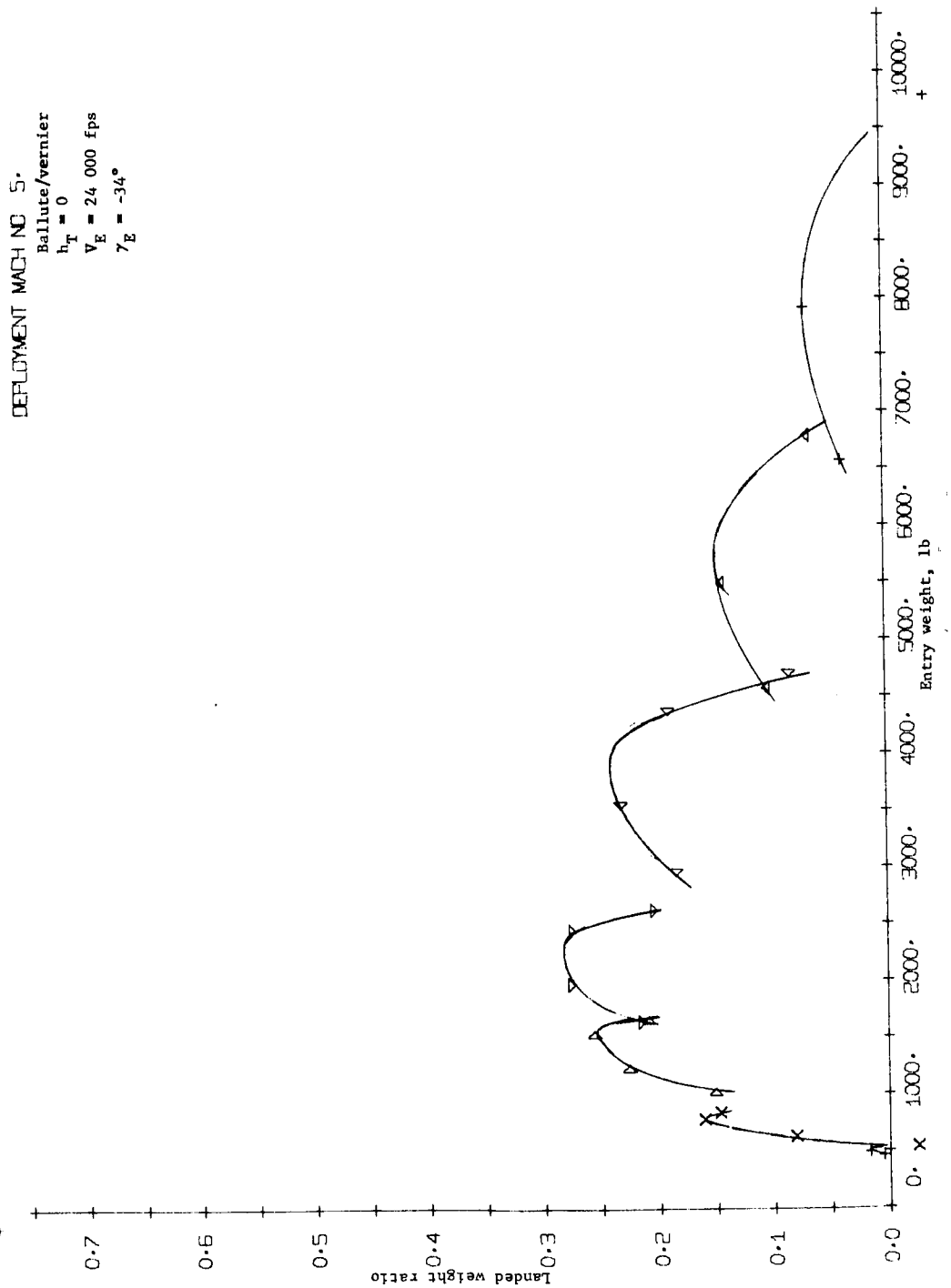

Figure B149.- Terminal Phase System Performance

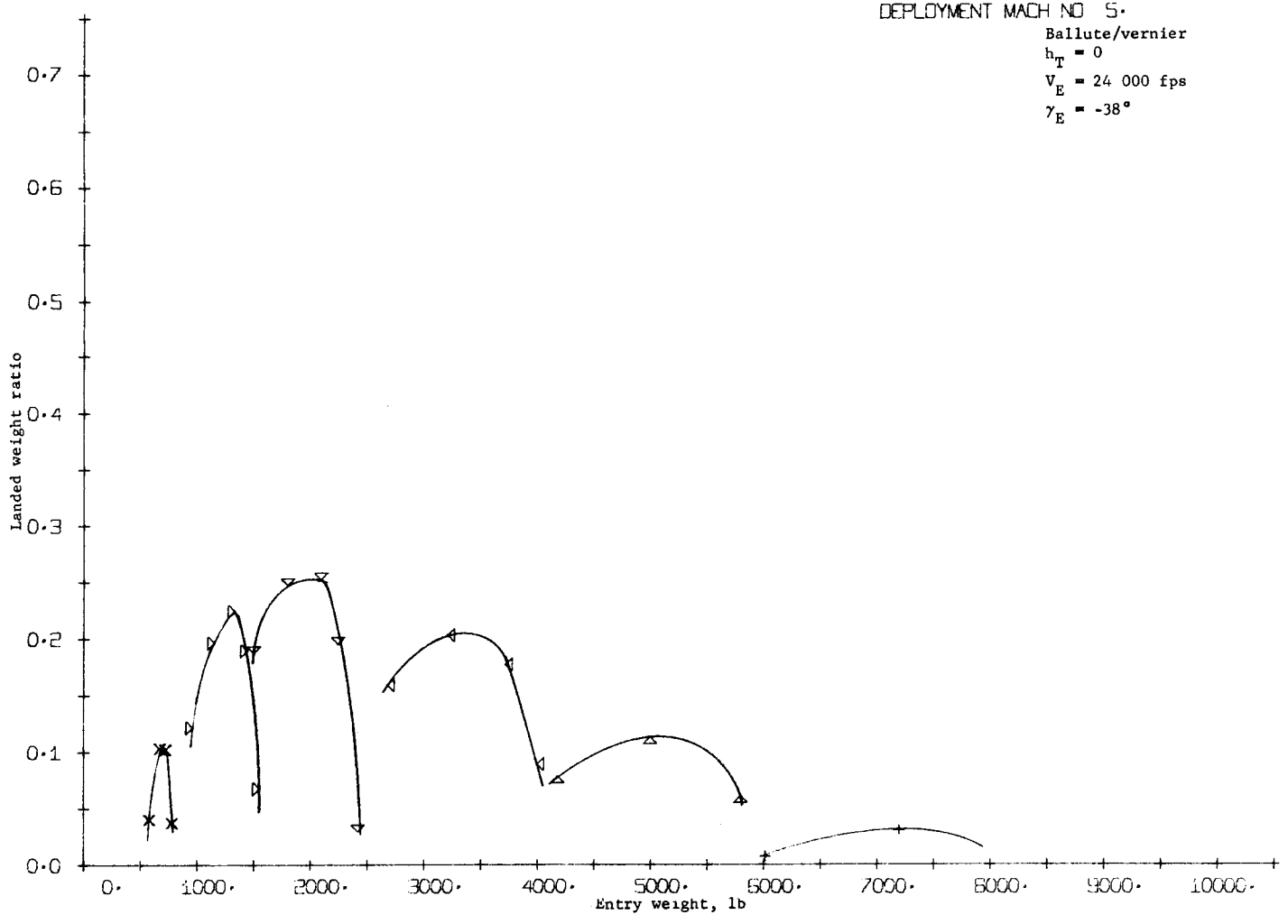

Figure B150.- Terminal Phase System Performance

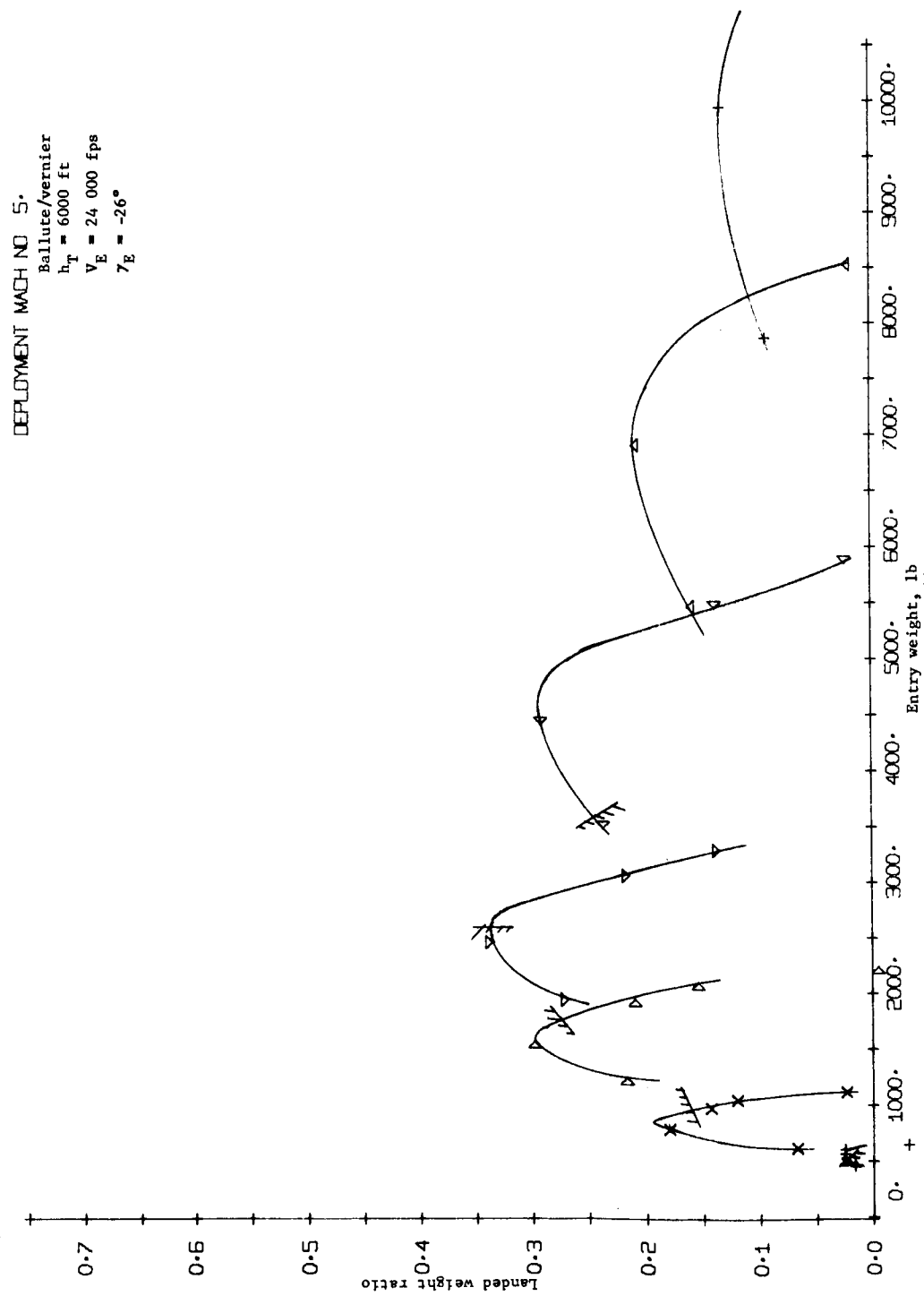

Figure B151.- Terminal Phase System Performance

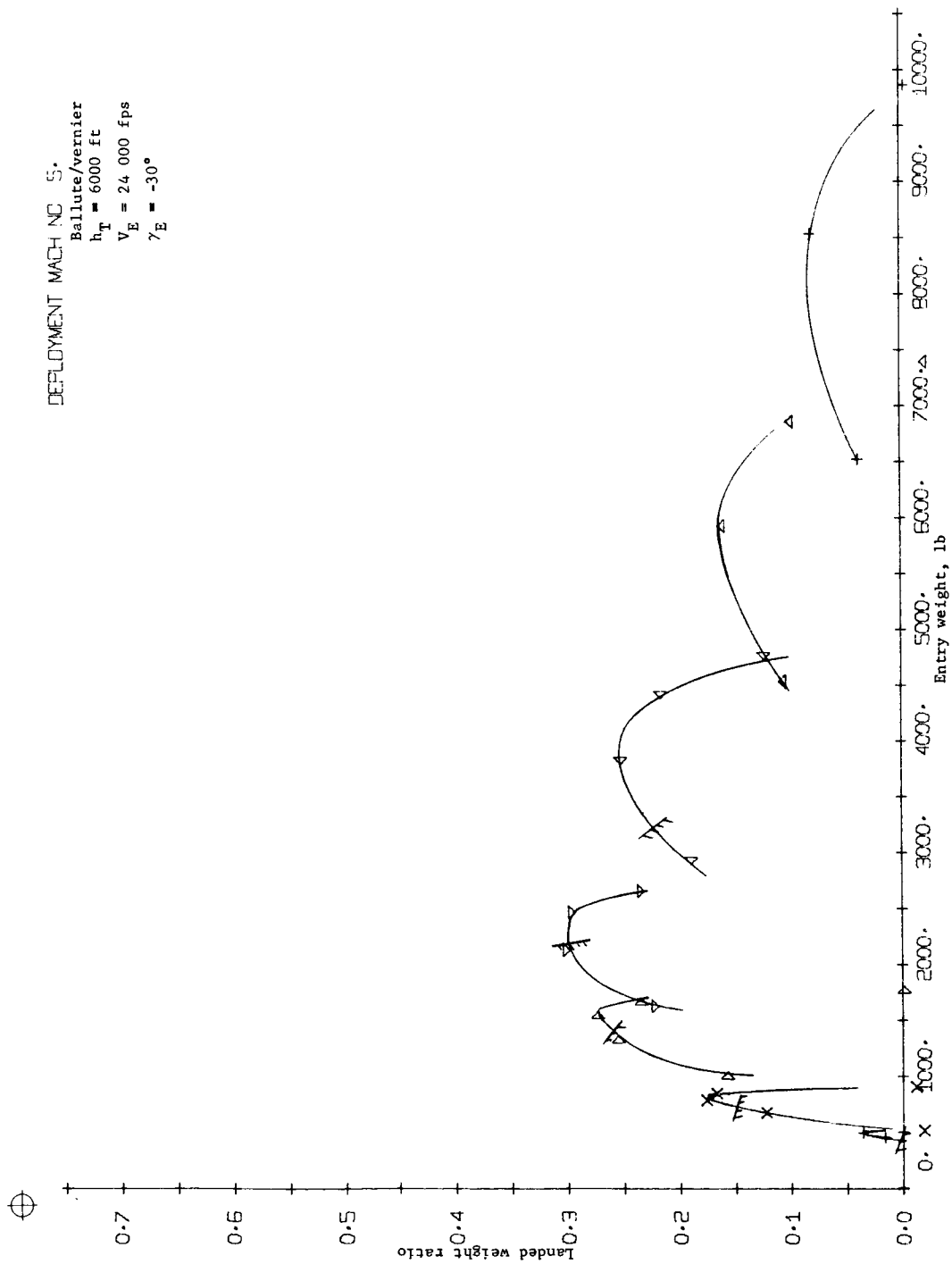

Figure B152.- Terminal Phase System Performance

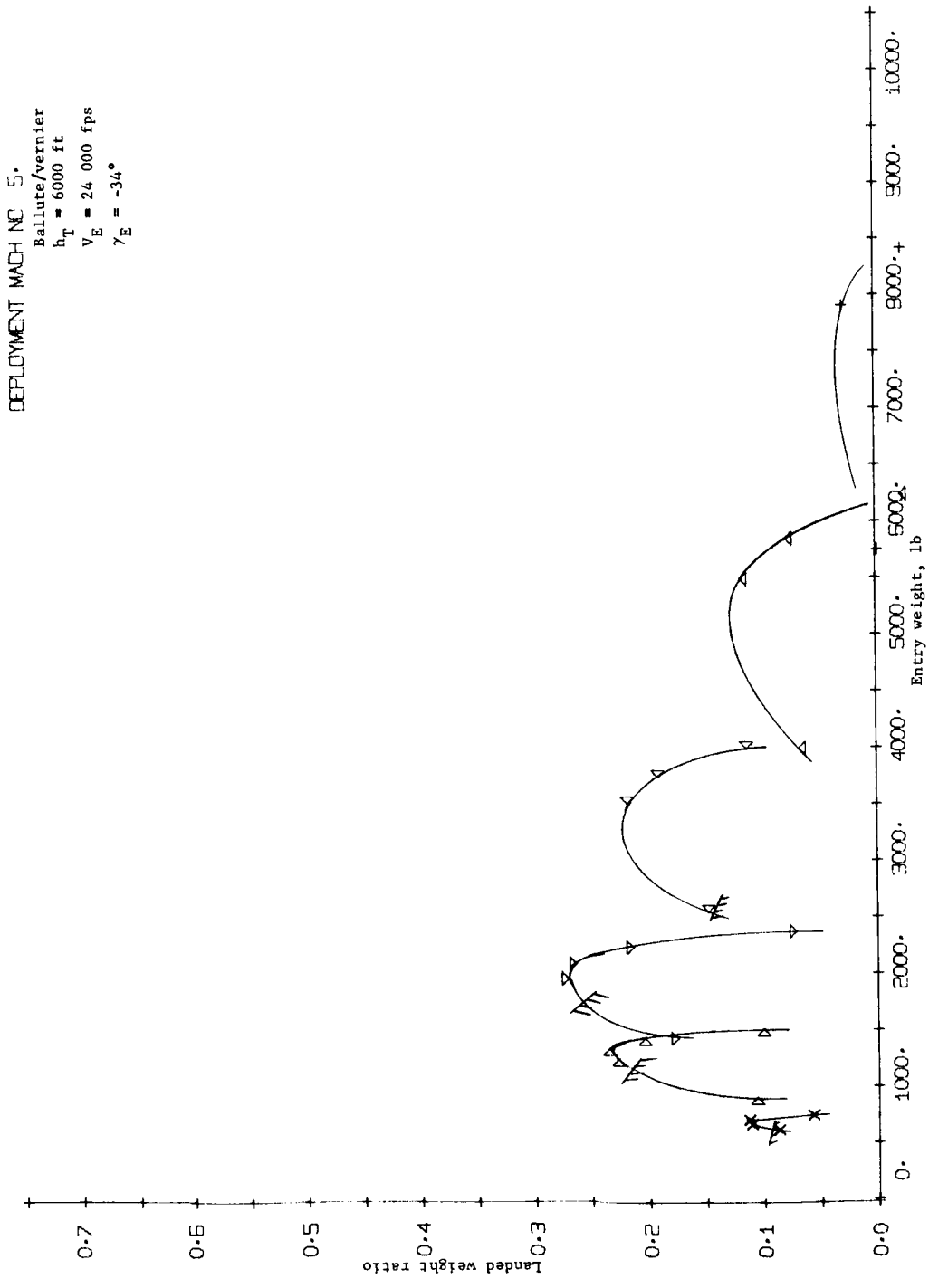

Figure B153.- Terminal Phase System Performance

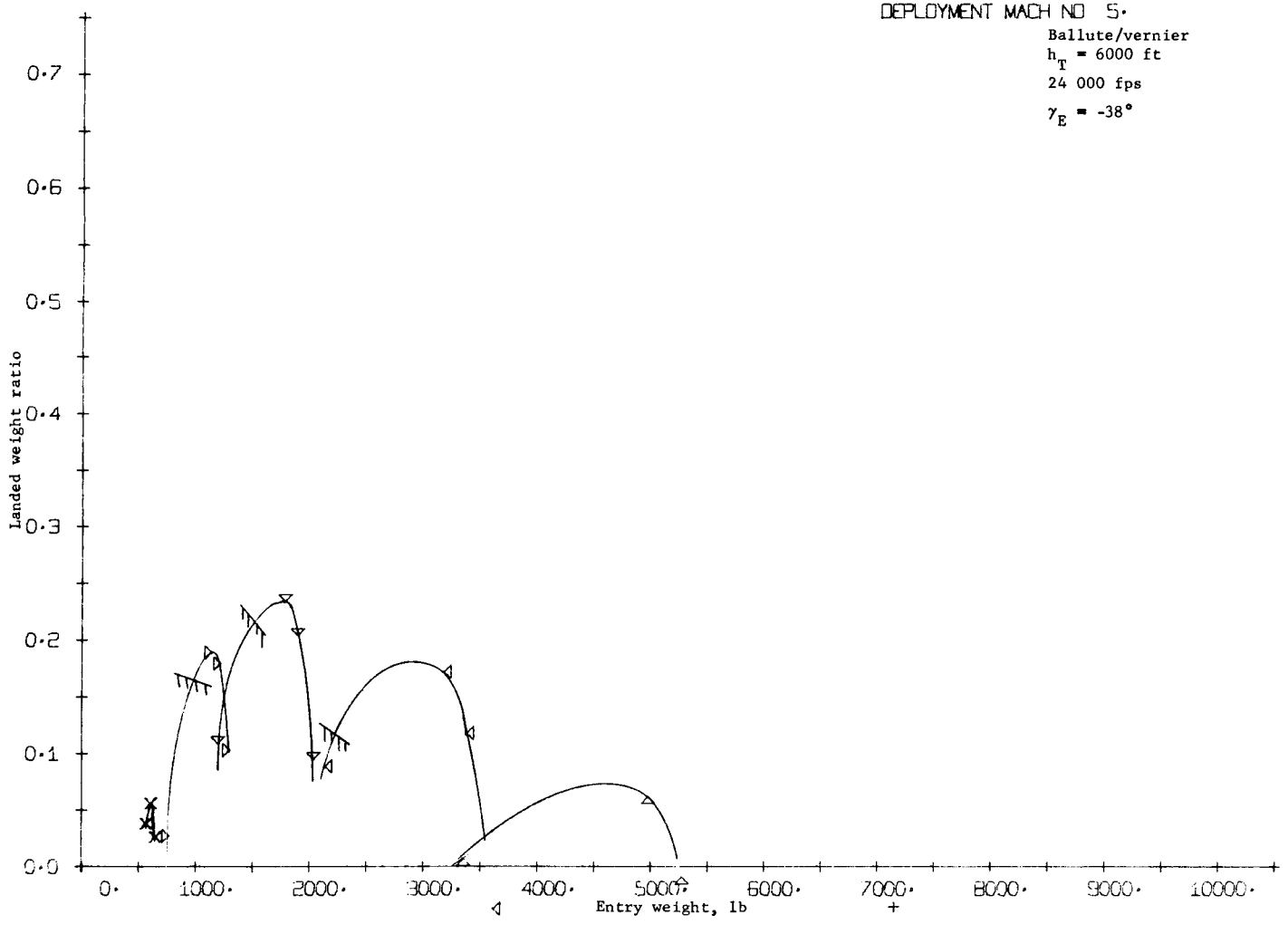

Figure B154.- Terminal Phase System Performance

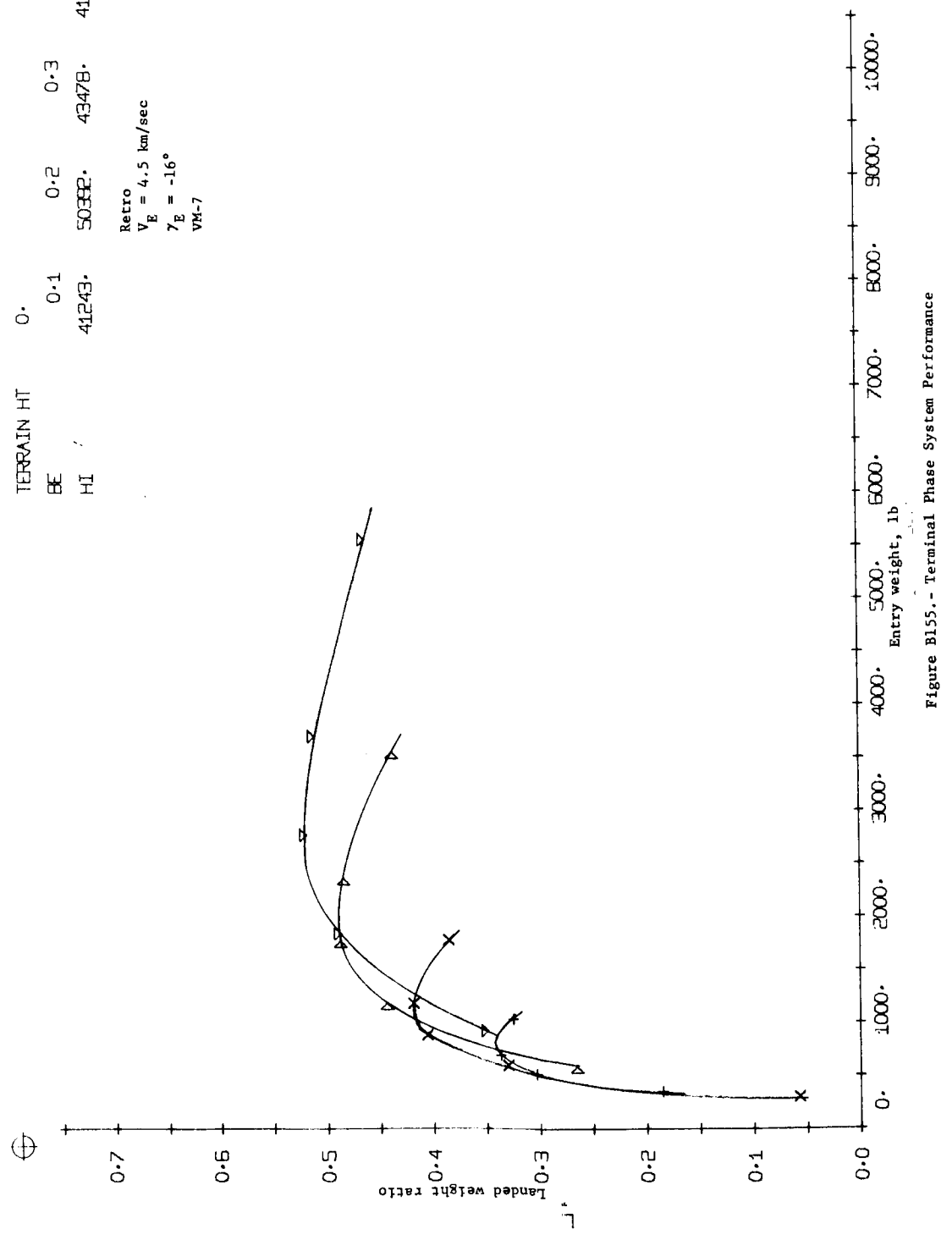

Figure B155.- Terminal Phase System Performance

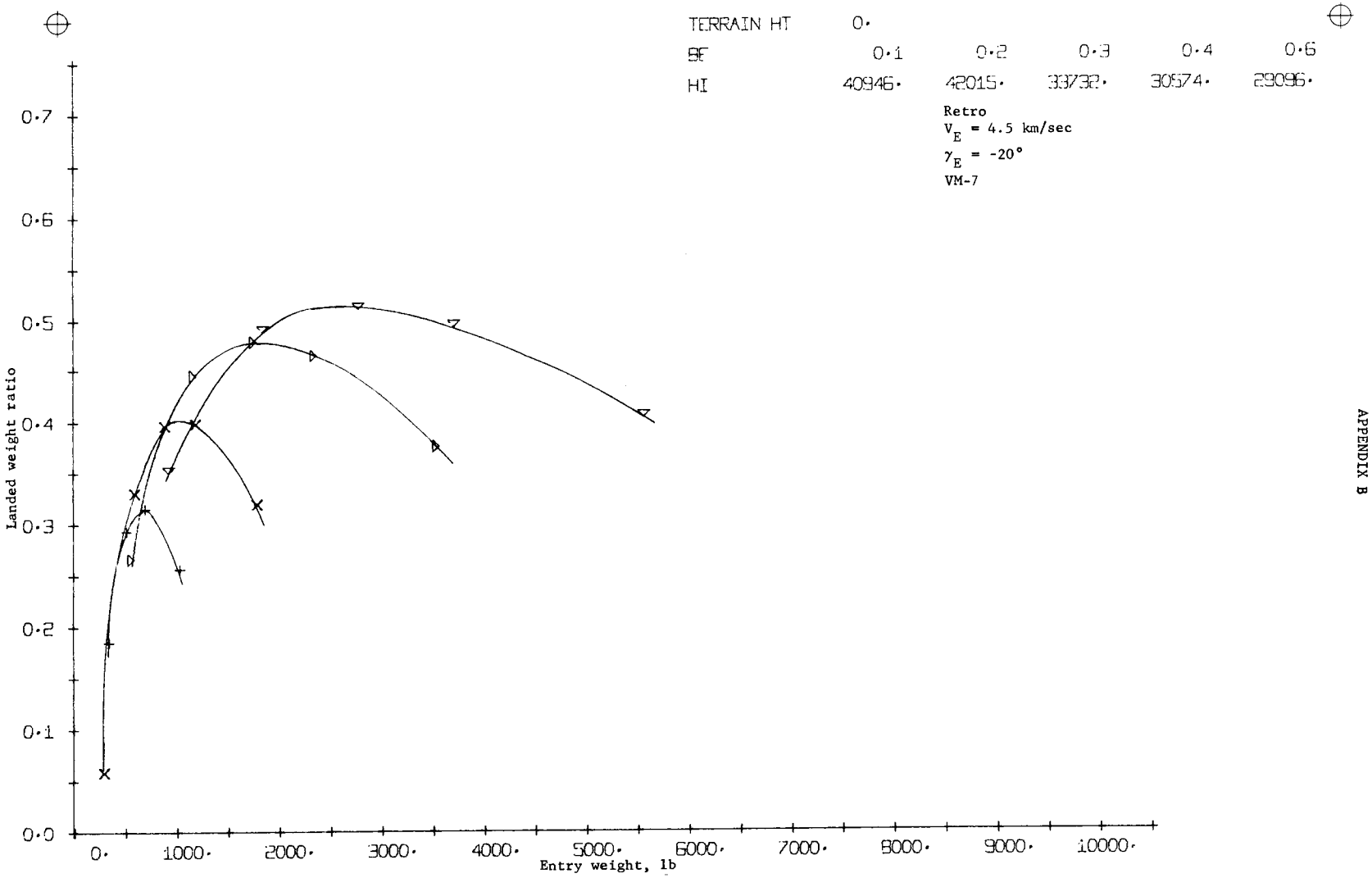

Figure B156.- Terminal Phase System Performance

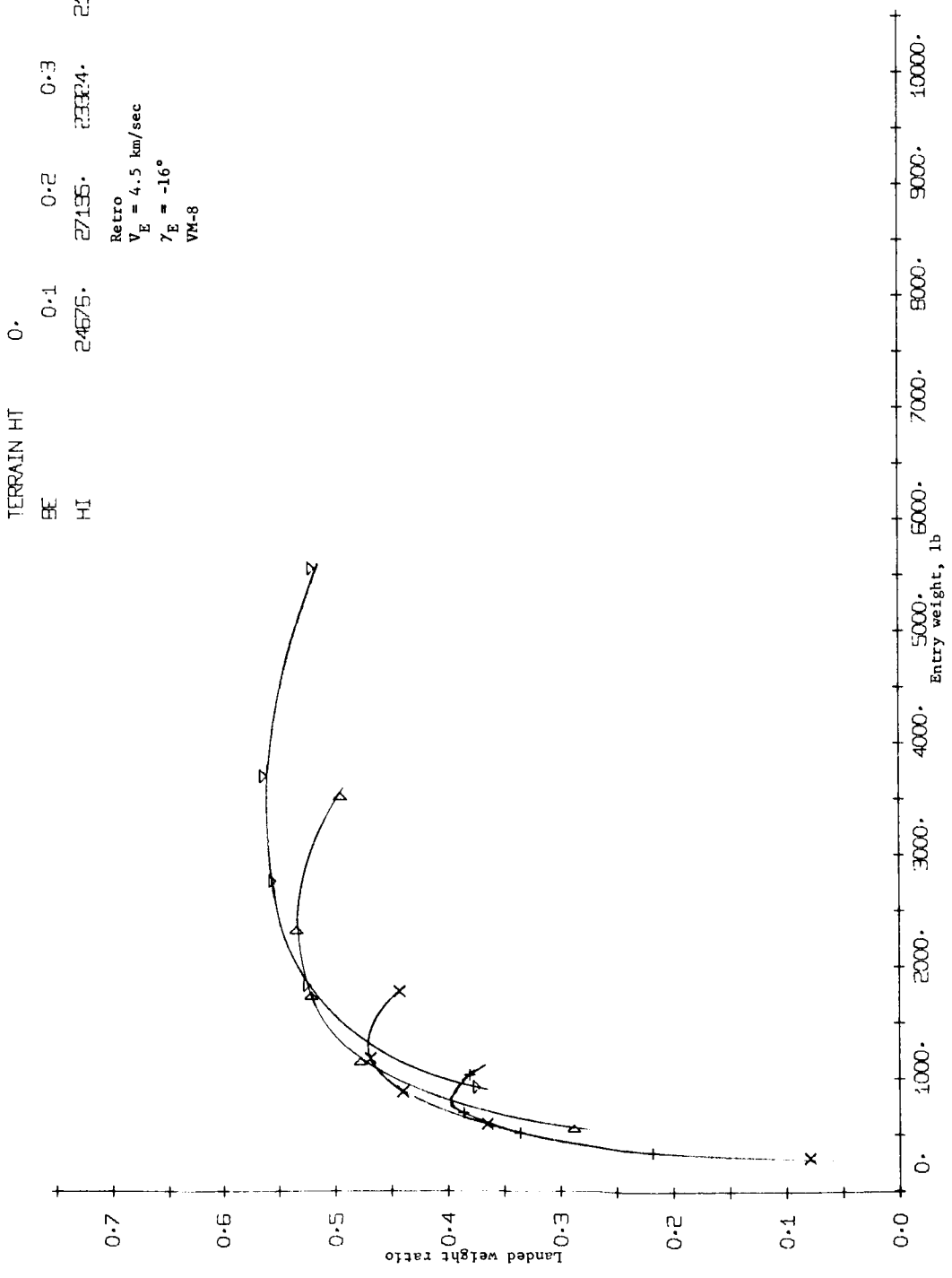

Figure B157.- Terminal Phase System Performance

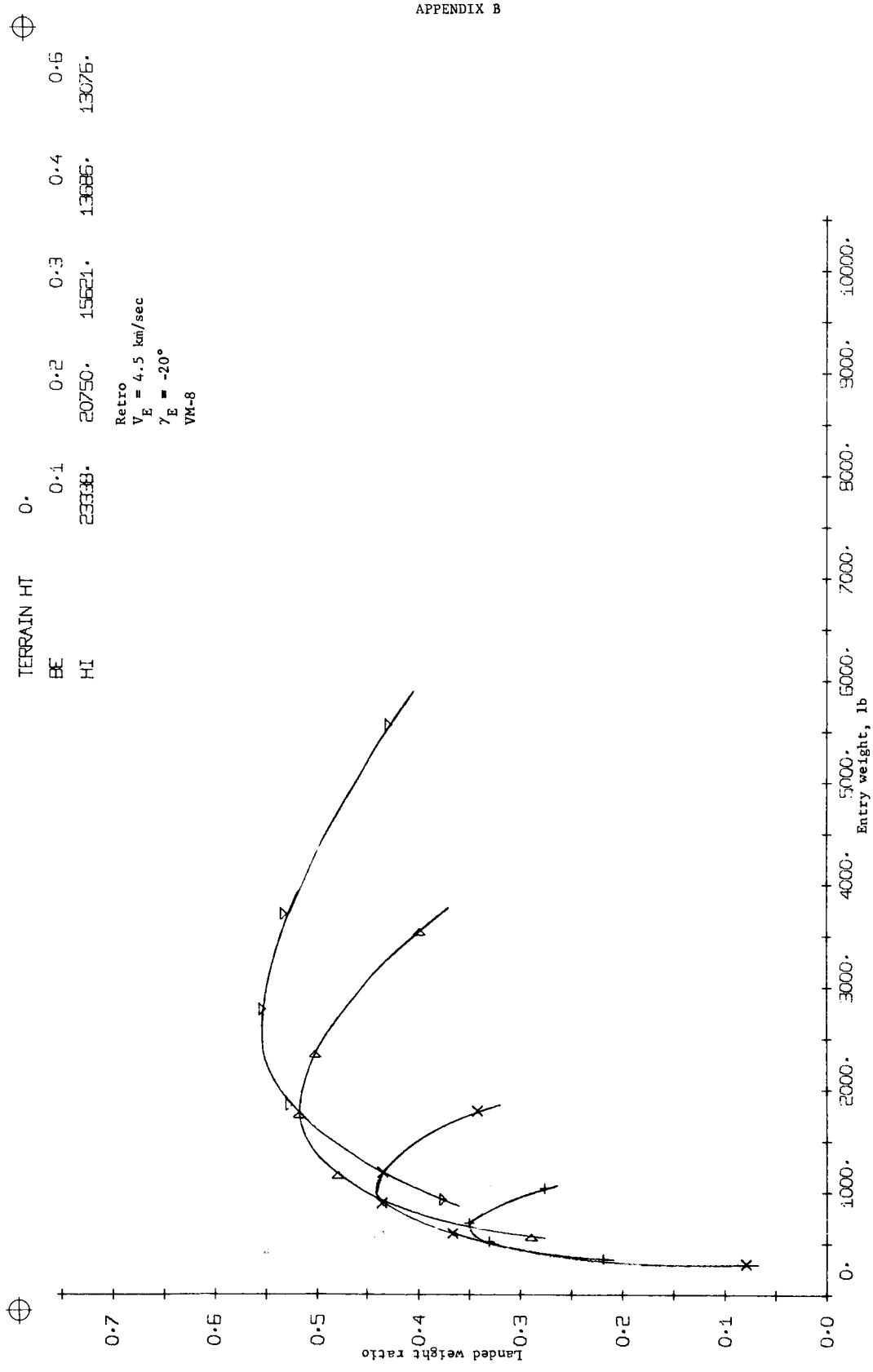

Figure B158.- Terminal Phase System Performance

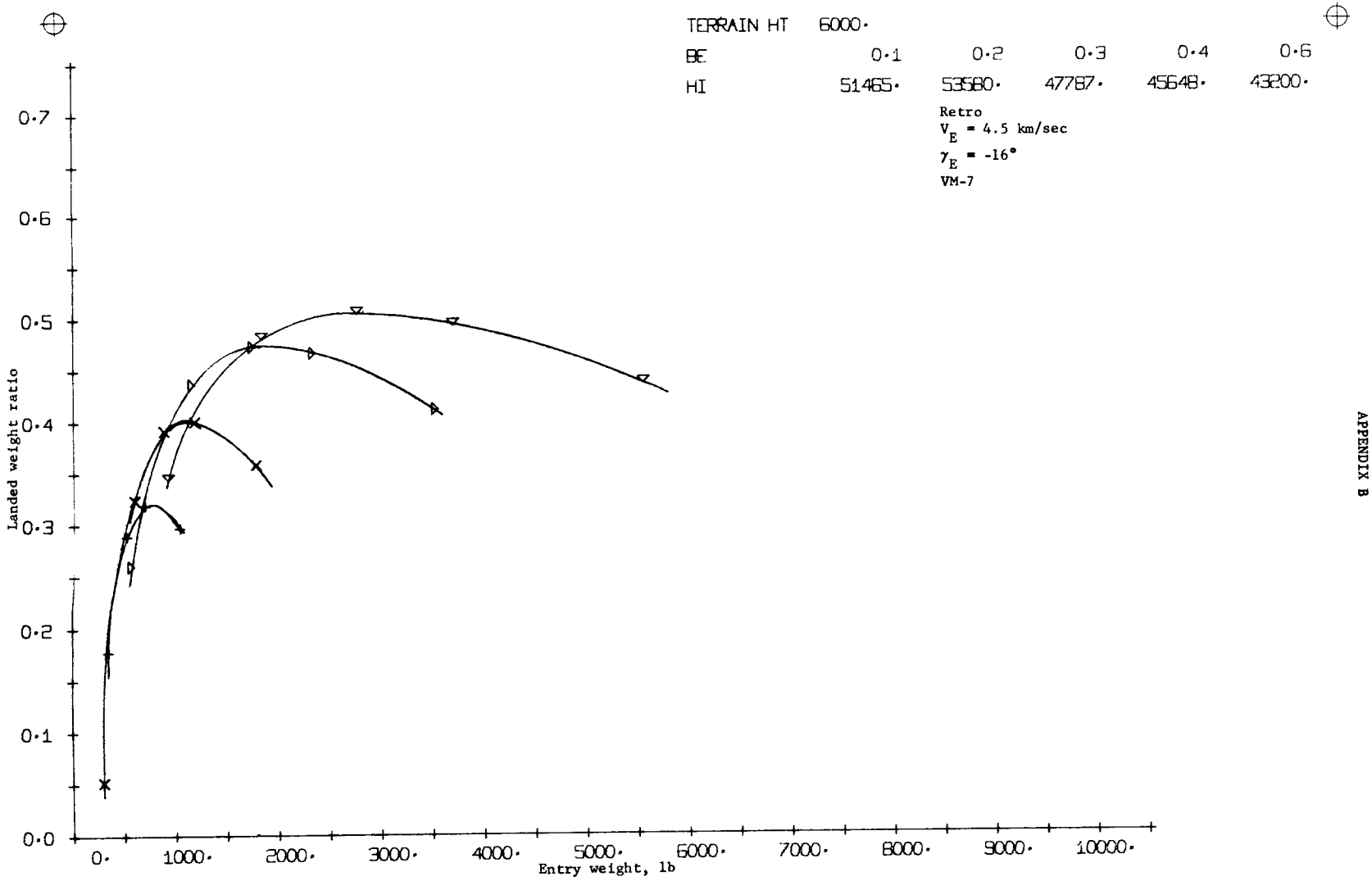

Figure B159.- Terminal Phase System Performance

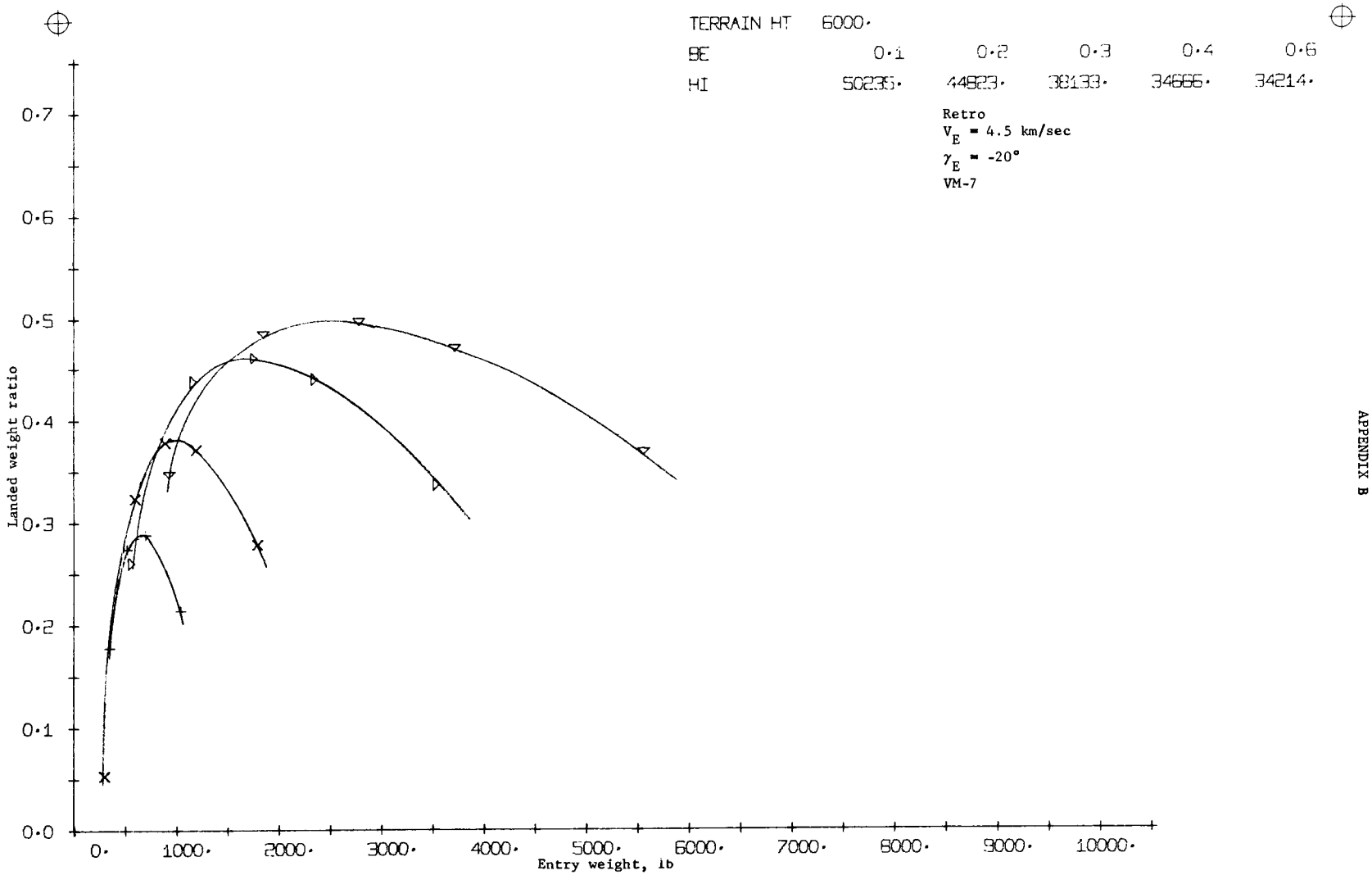

Figure B160.- Terminal Phase System Performance

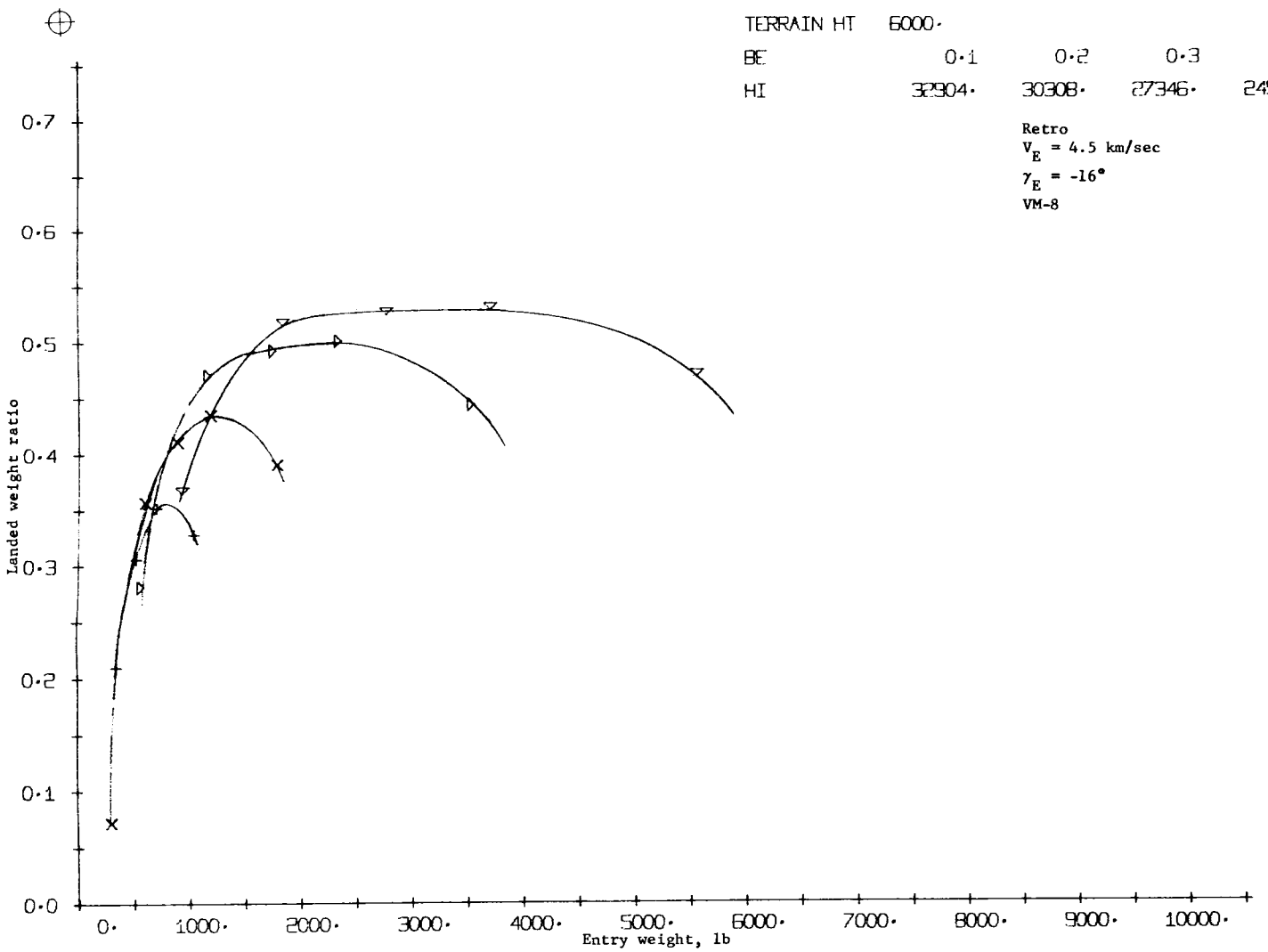

Figure B161.- Terminal Phase System Performance

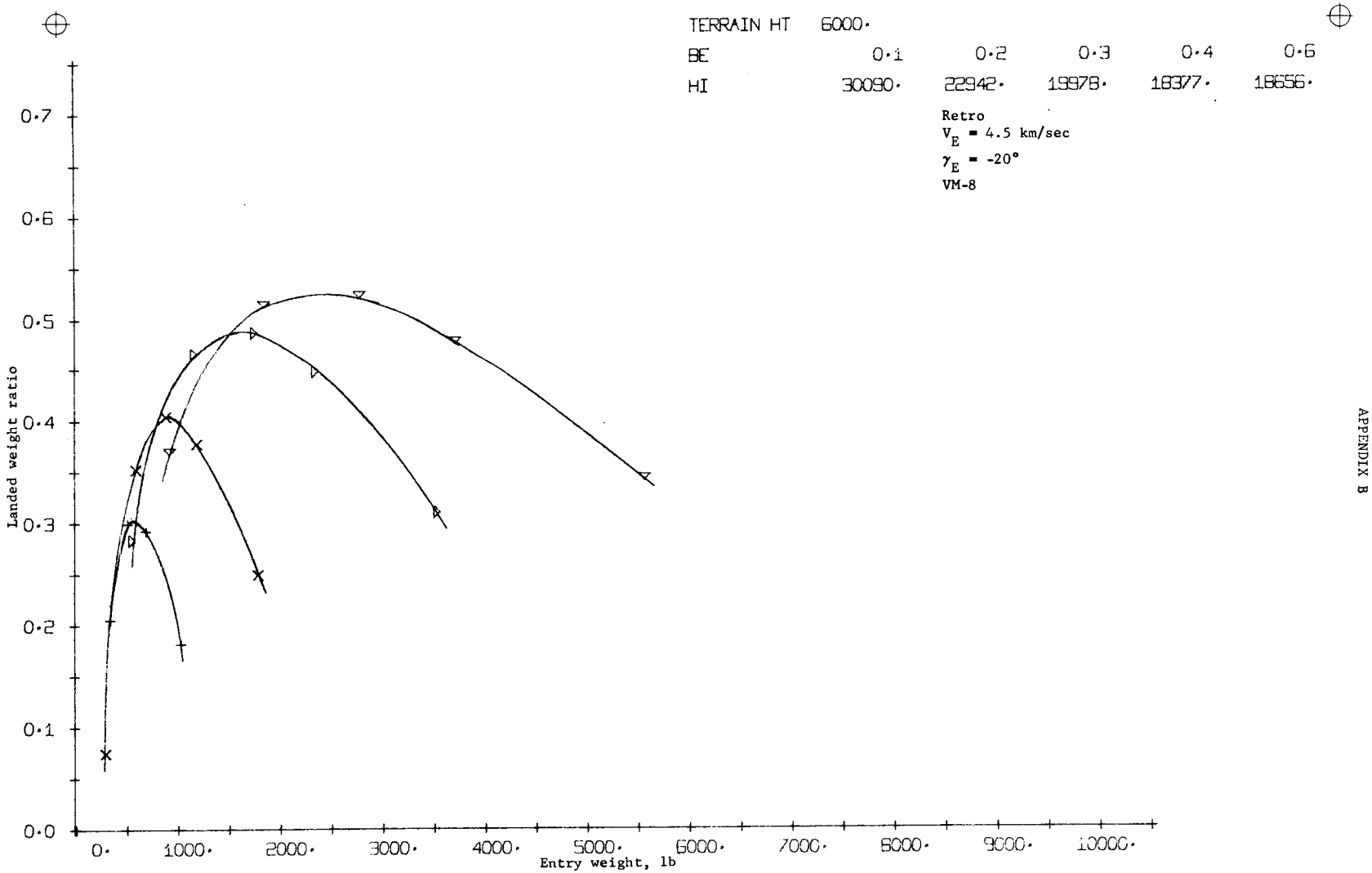

Figure B162.- Terminal Phase System Performance

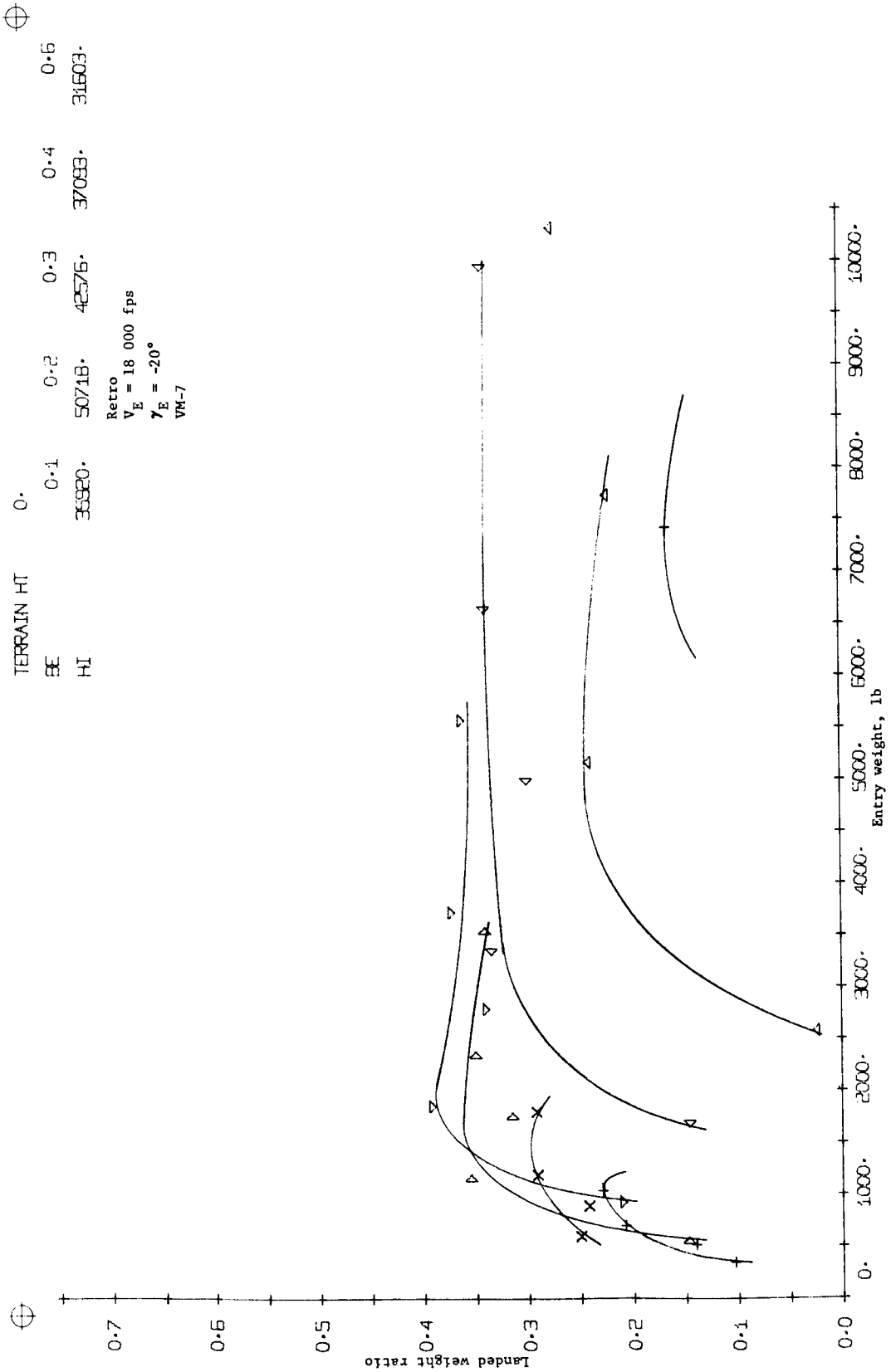

Figure B163.- Terminal Phase System Performance

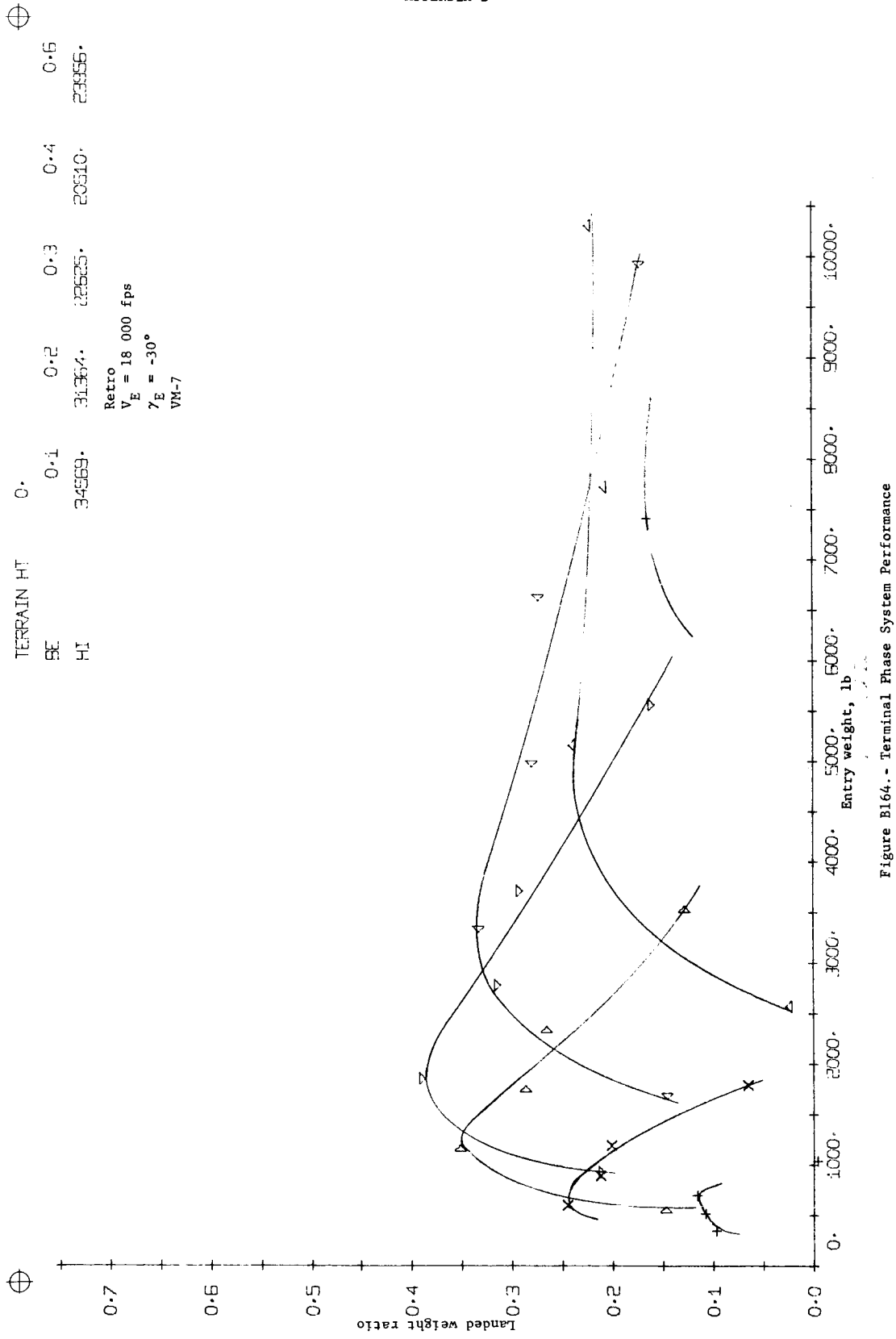

Figure B164.- Terminal Phase System Performance

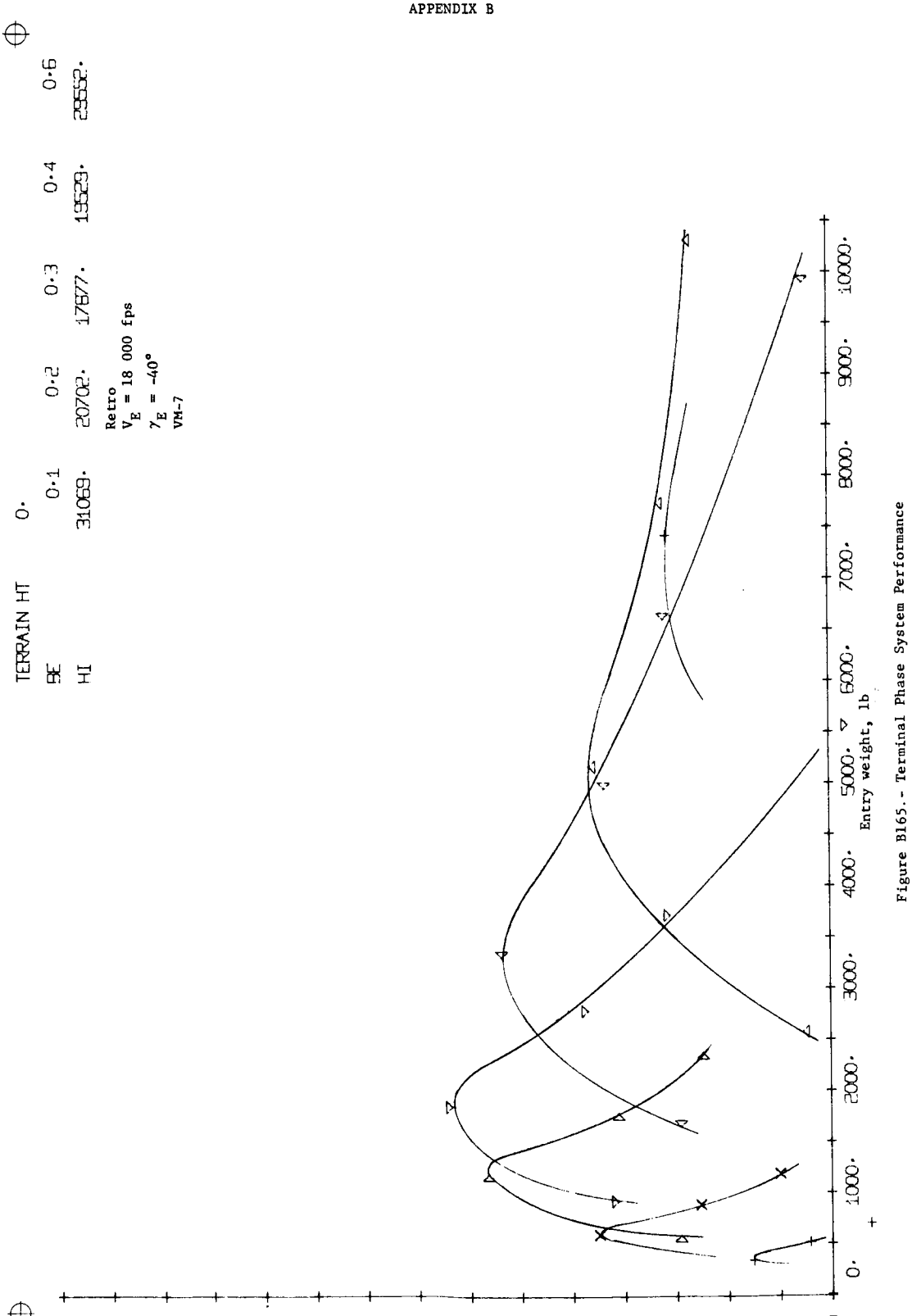

Figure B165.- Terminal Phase System Performance

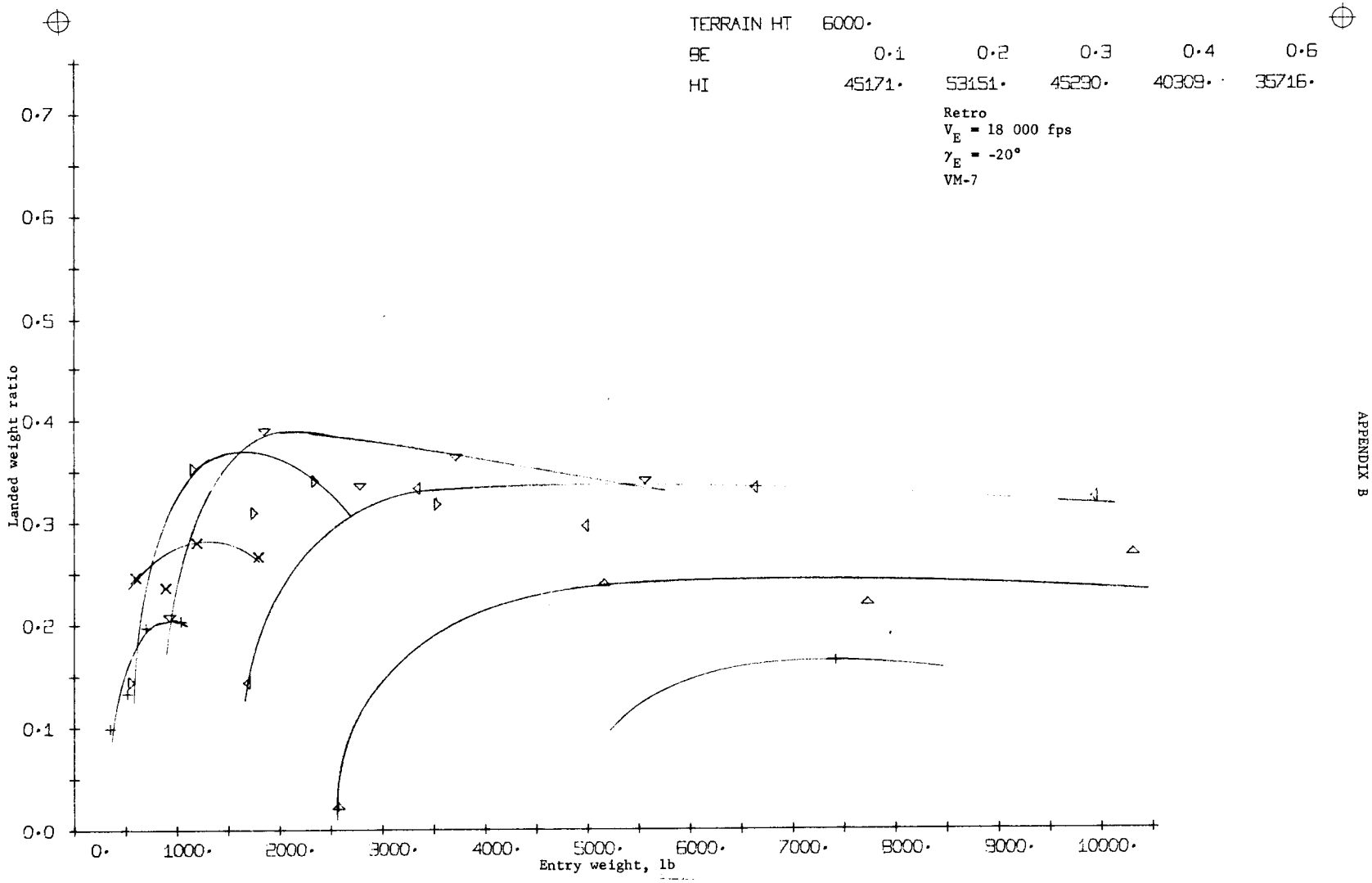

Figure B166.- Terminal Phase System Performance

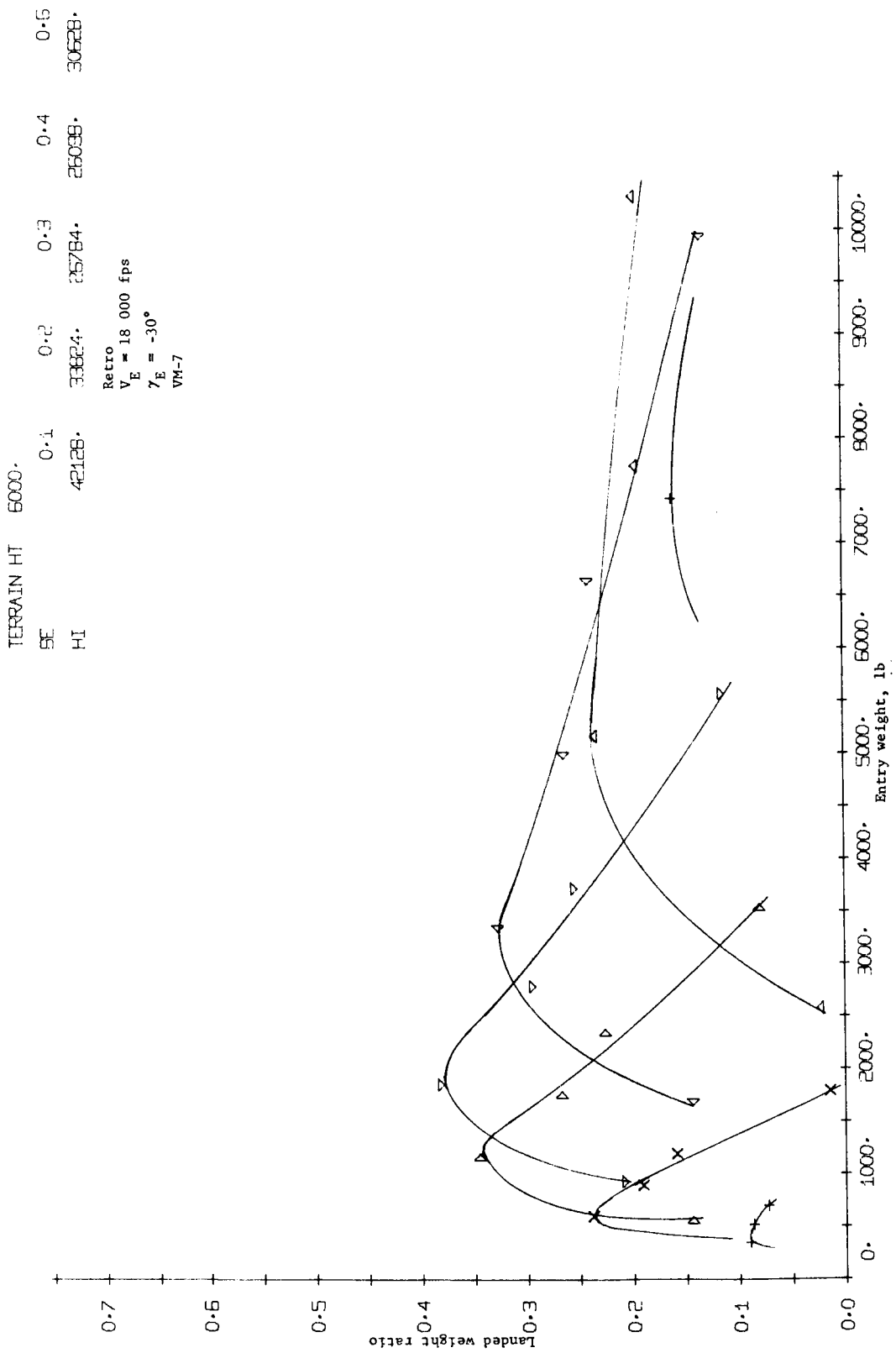

Figure B167.- Terminal Phase System Performance

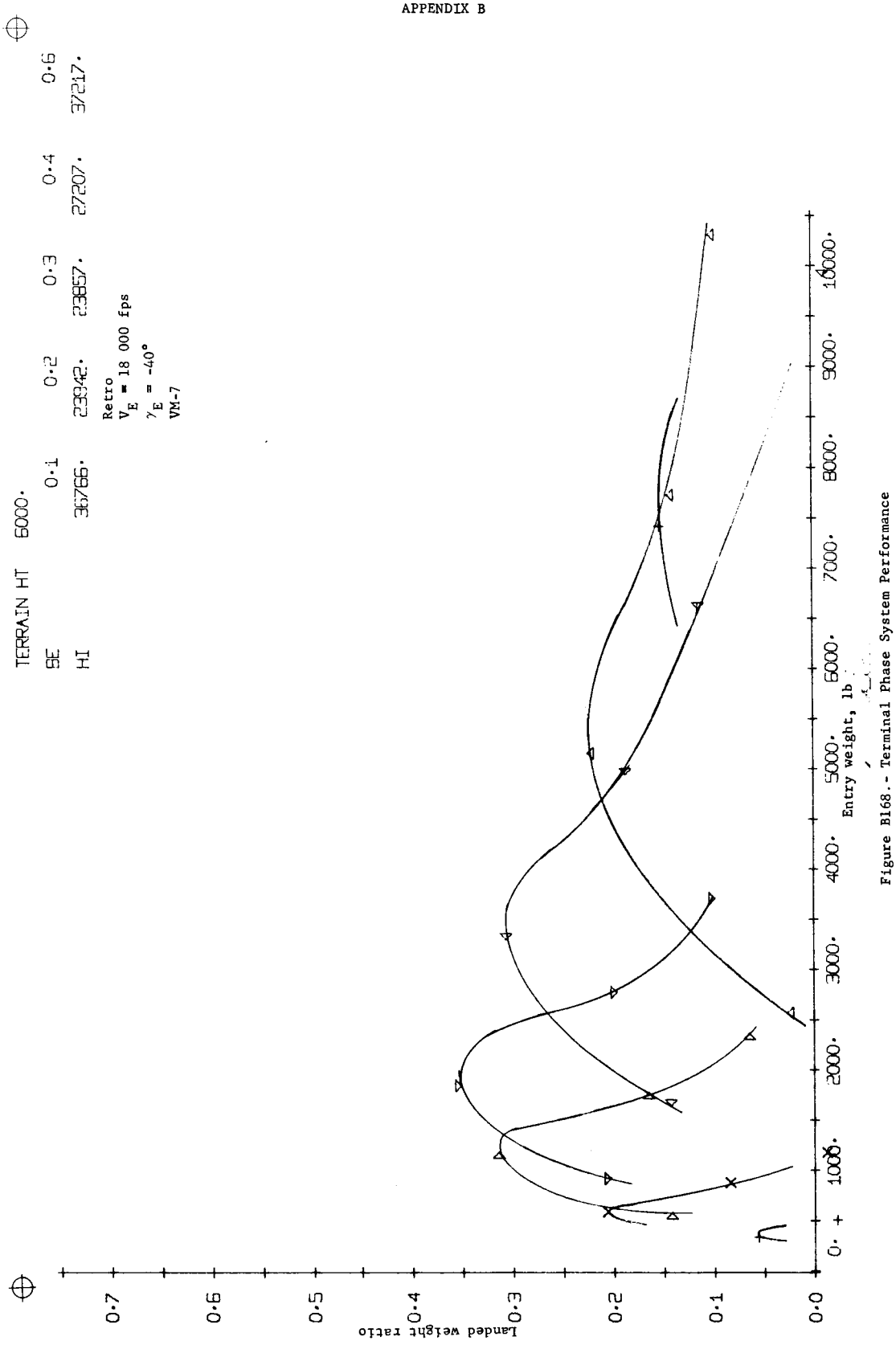

Figure B168.- Terminal Phase System Performance

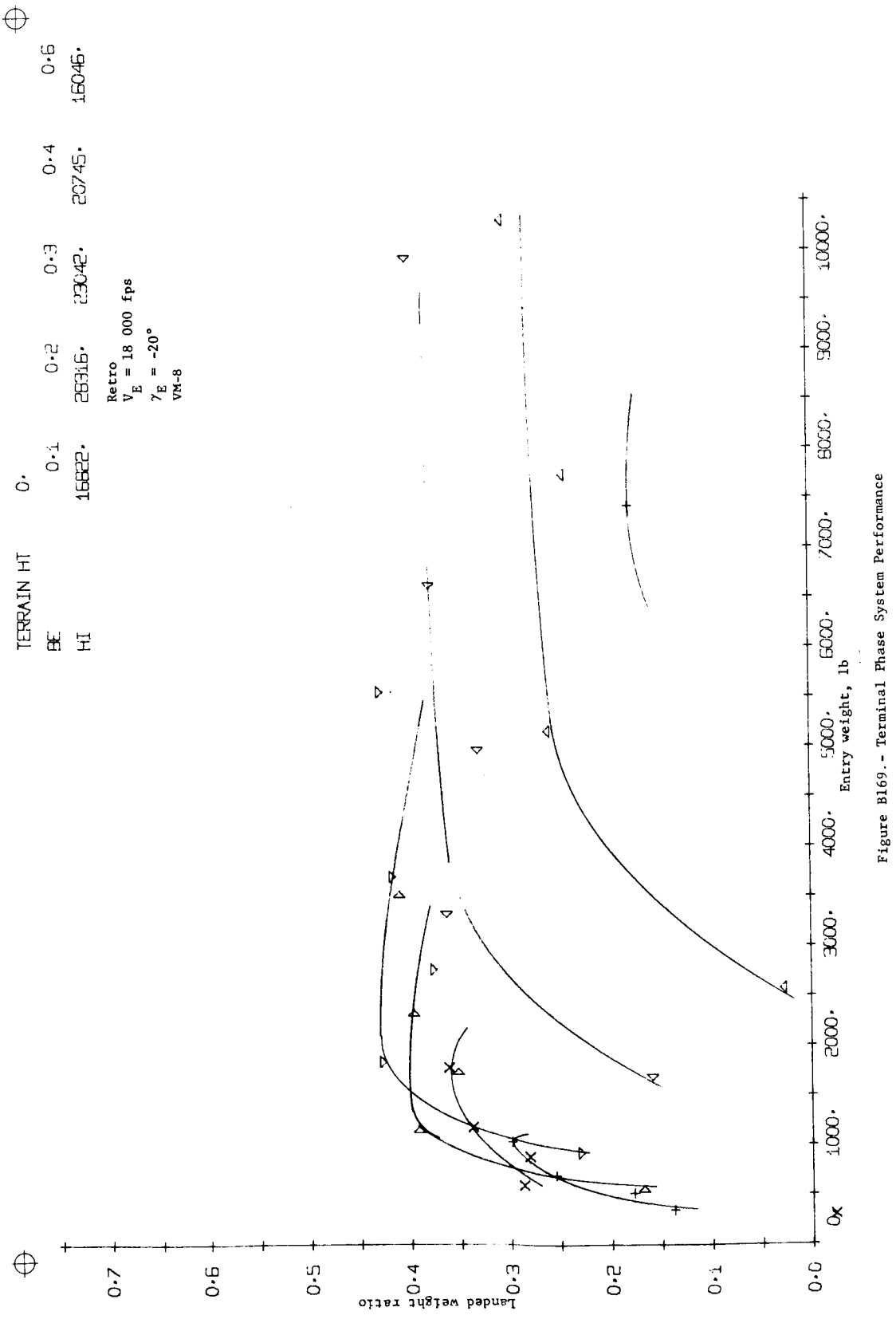

Figure B169.- Terminal Phase System Performance

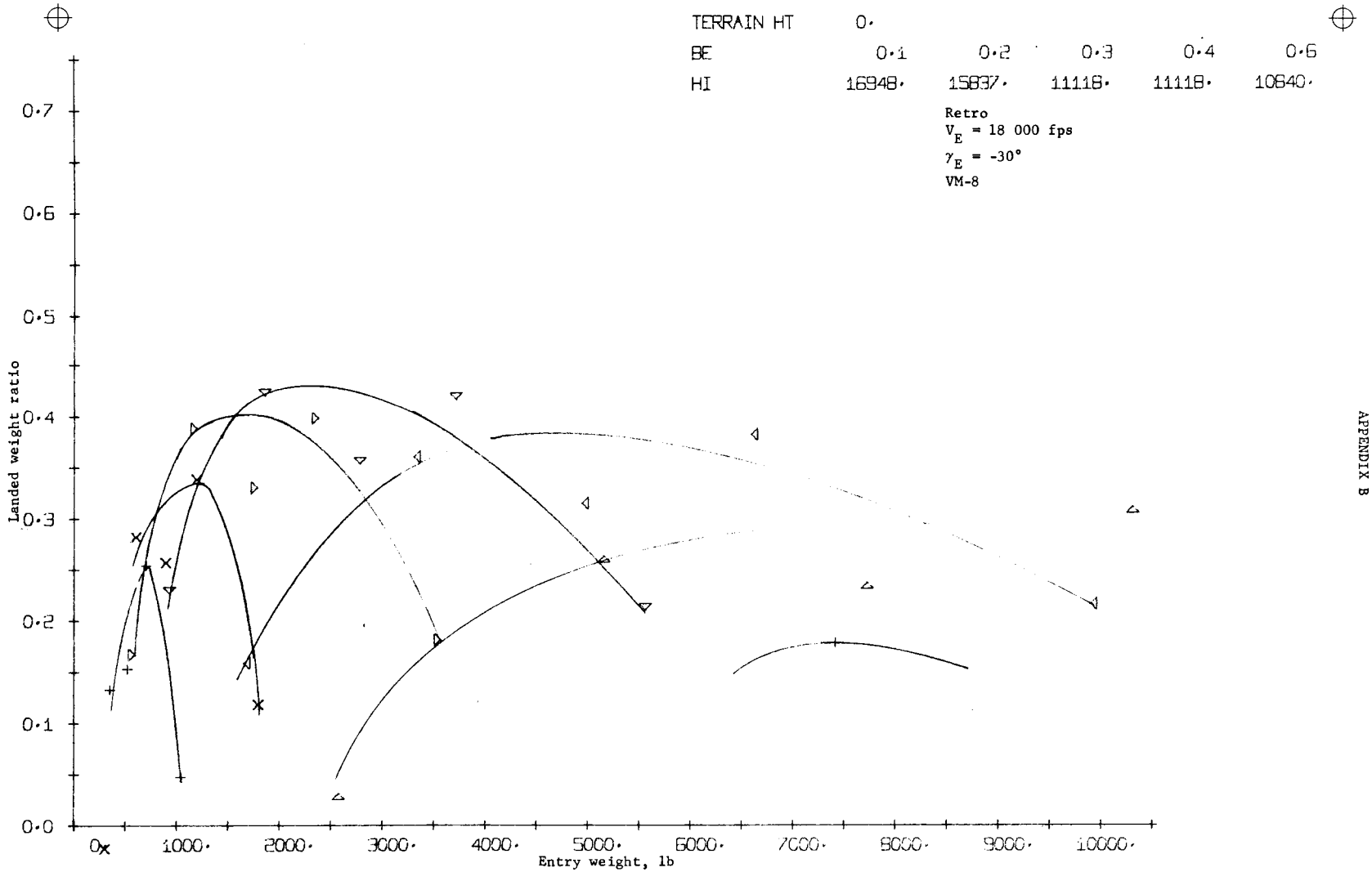

Figure B170.- Terminal Phase System Performance

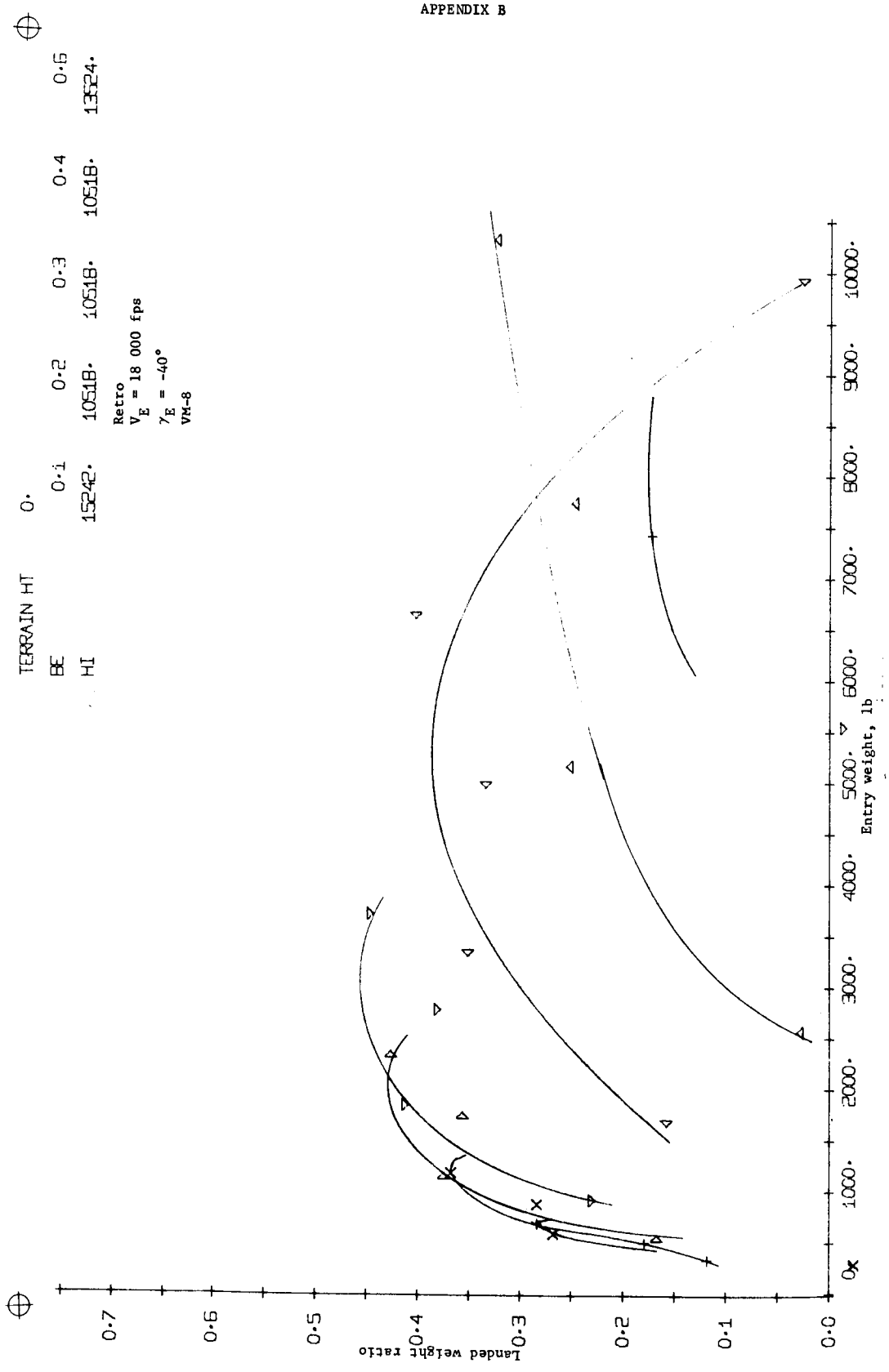

Figure B171.- Terminal Phase System Performance

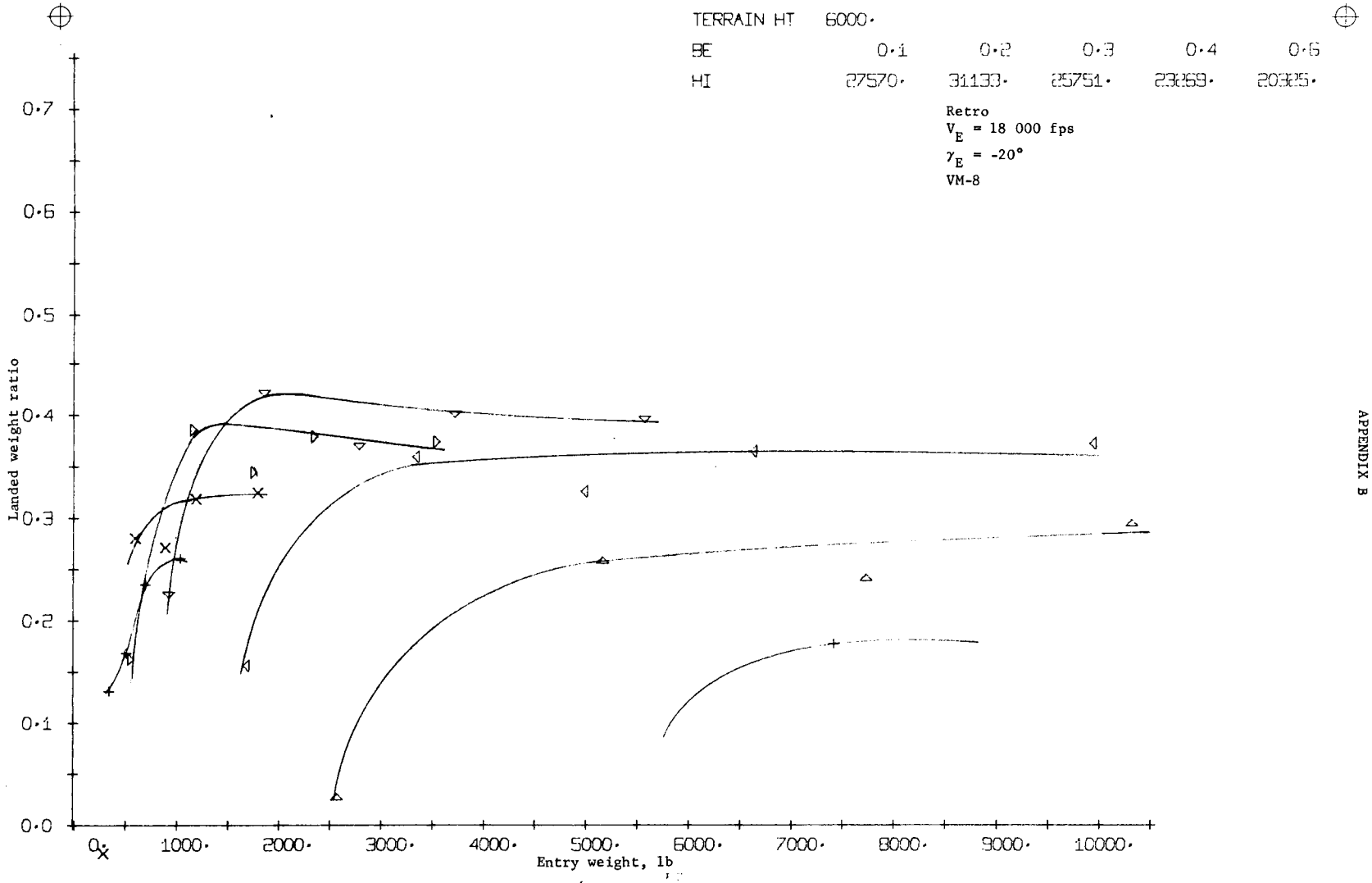

Figure B172.- Terminal Phase System Performance

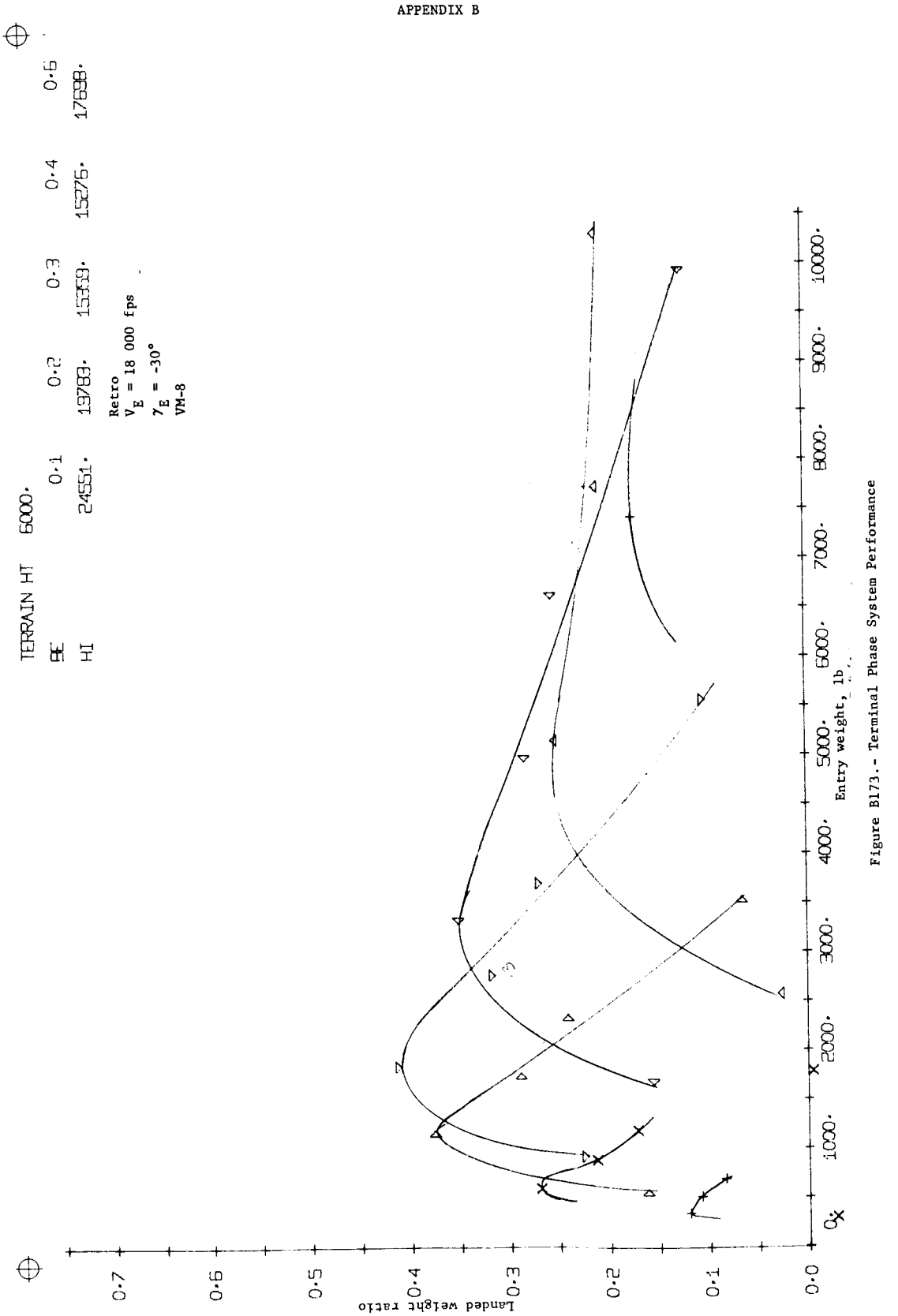

Figure B173.- Terminal Phase System Performance

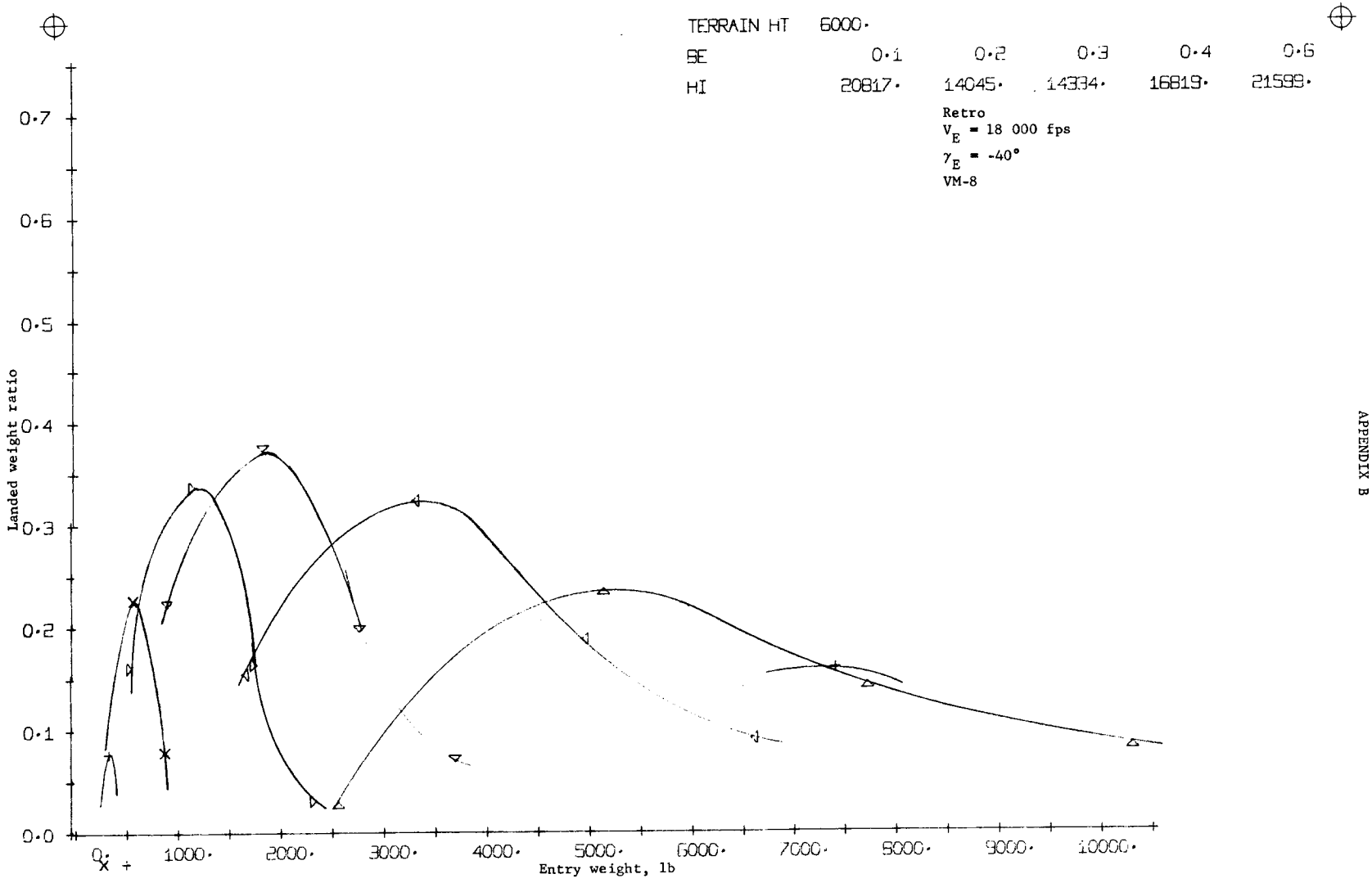

Figure B174.- Terminal Phase System Performance

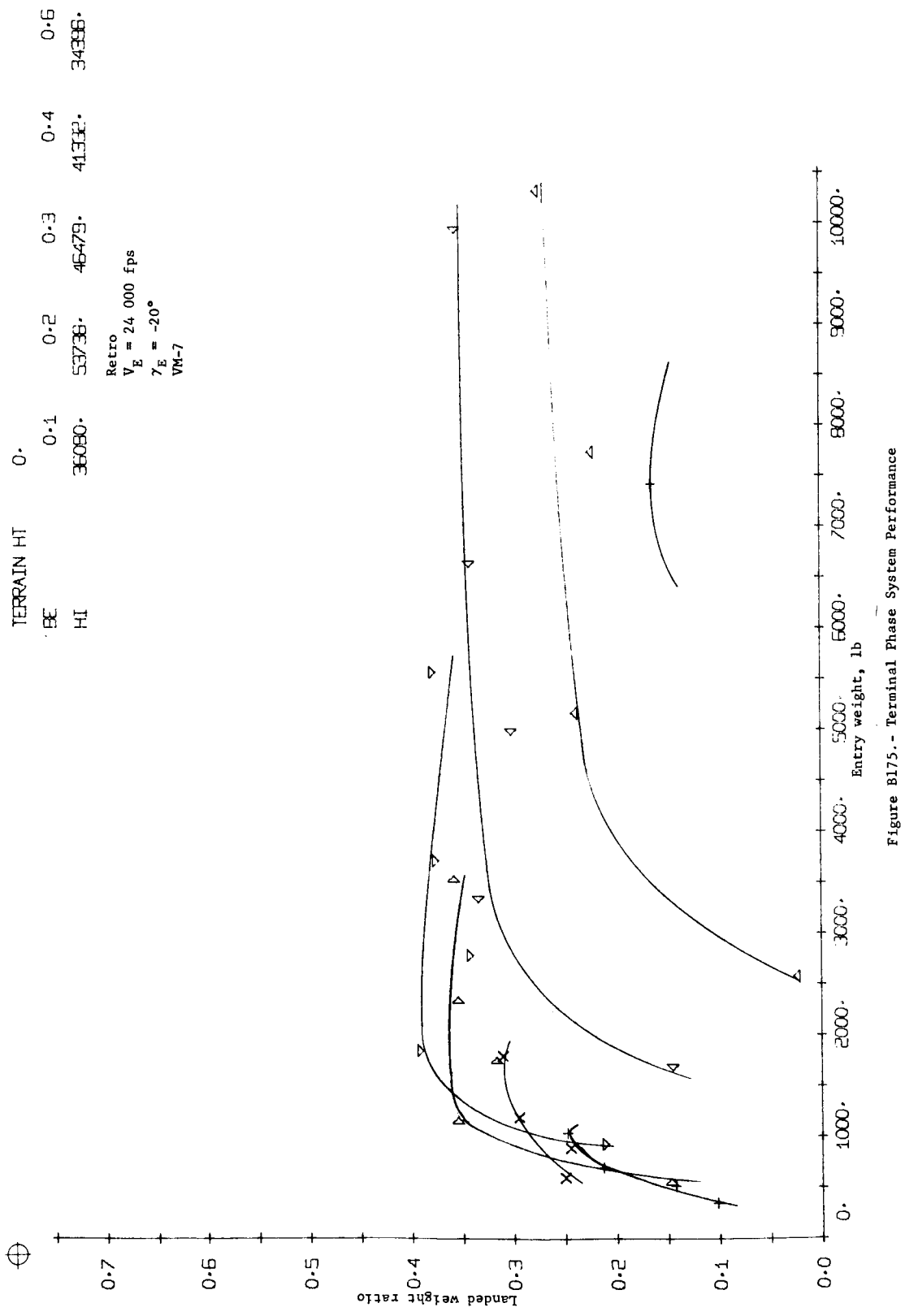

Figure B175.- Terminal Phase System Performance

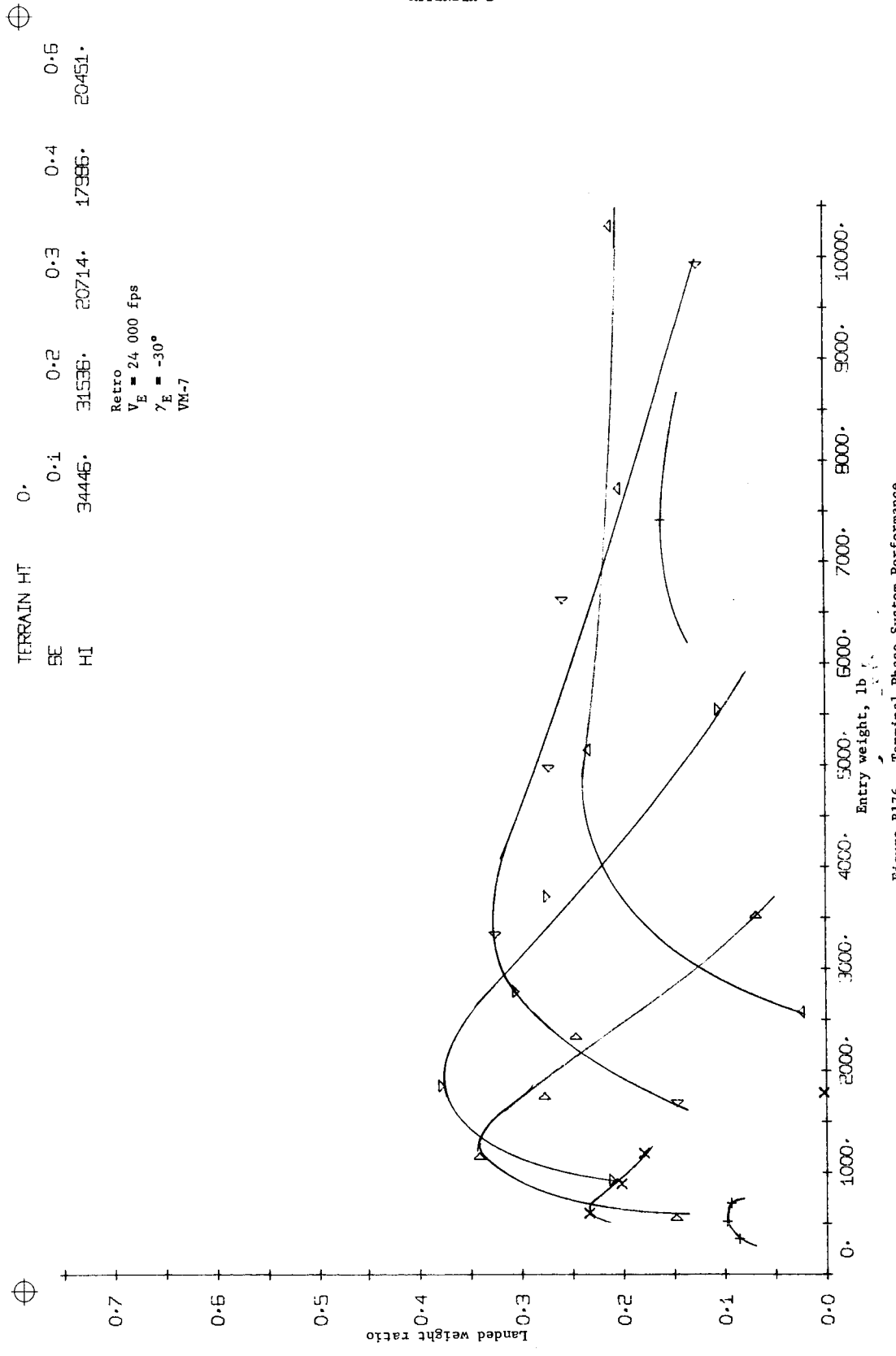

Figure B176.- Terminal Phase System Performance

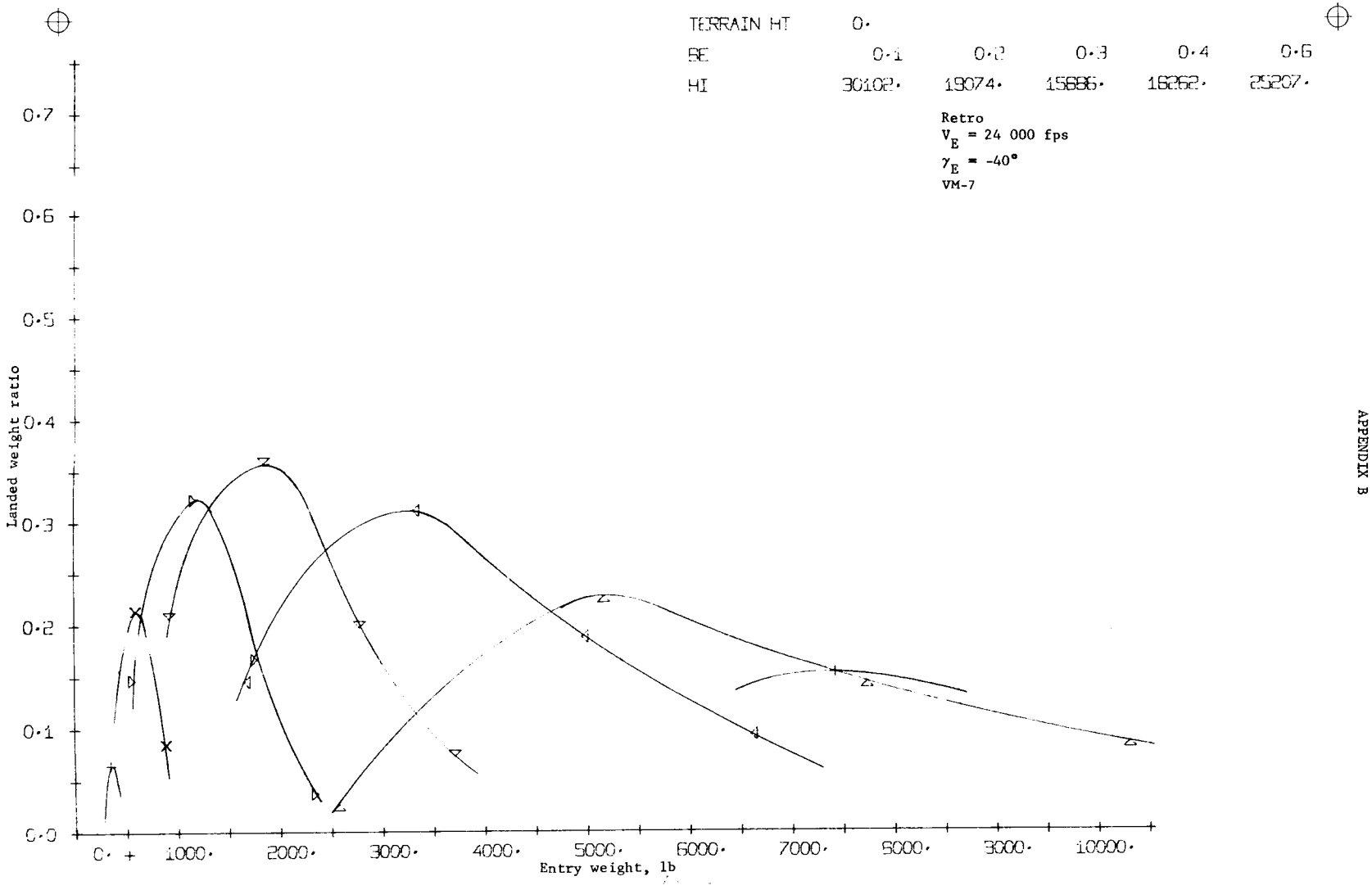

Figure B177.- Terminal Phase System Performance

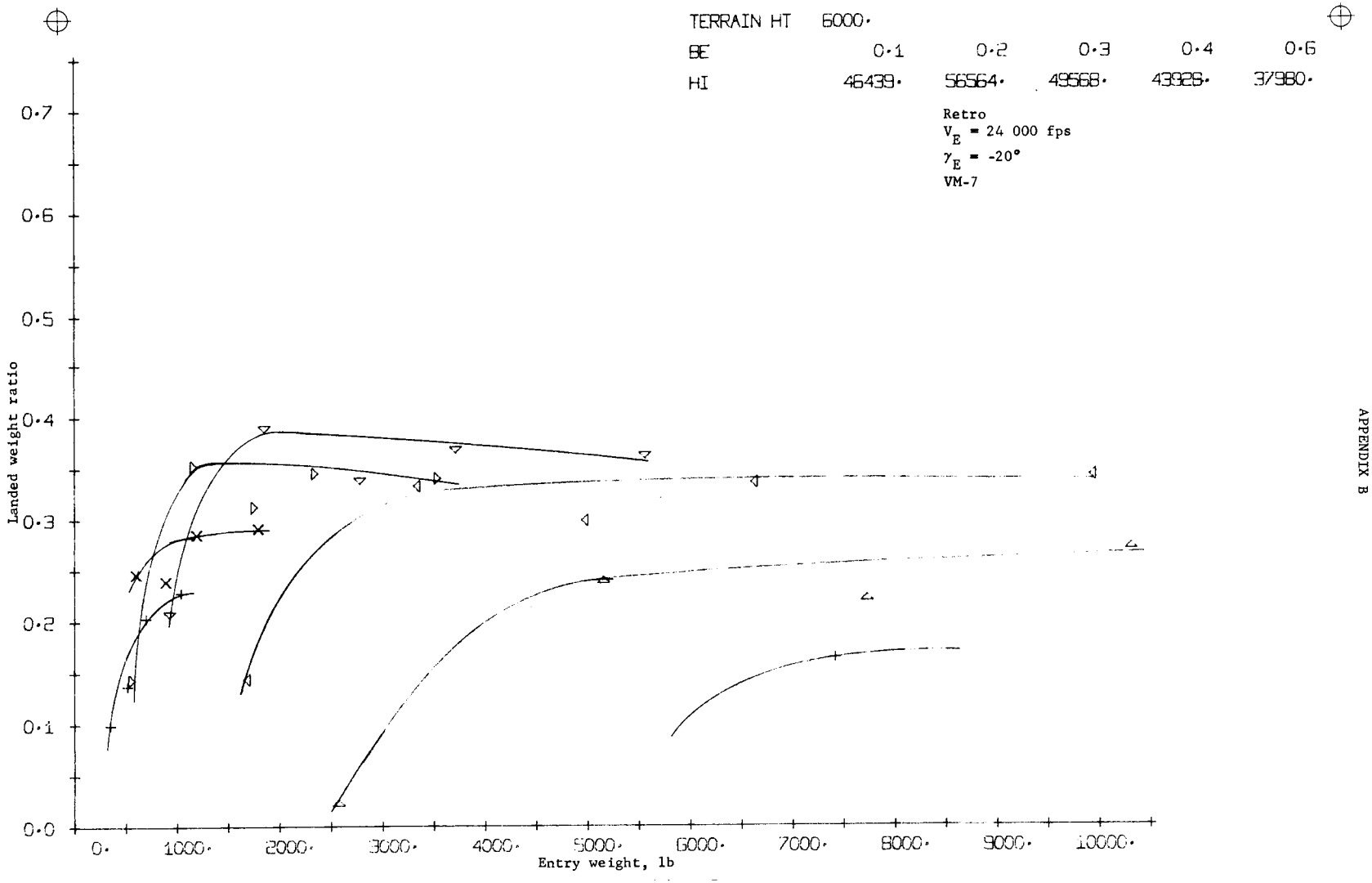

Figure B178.- Terminal Phase System Performance

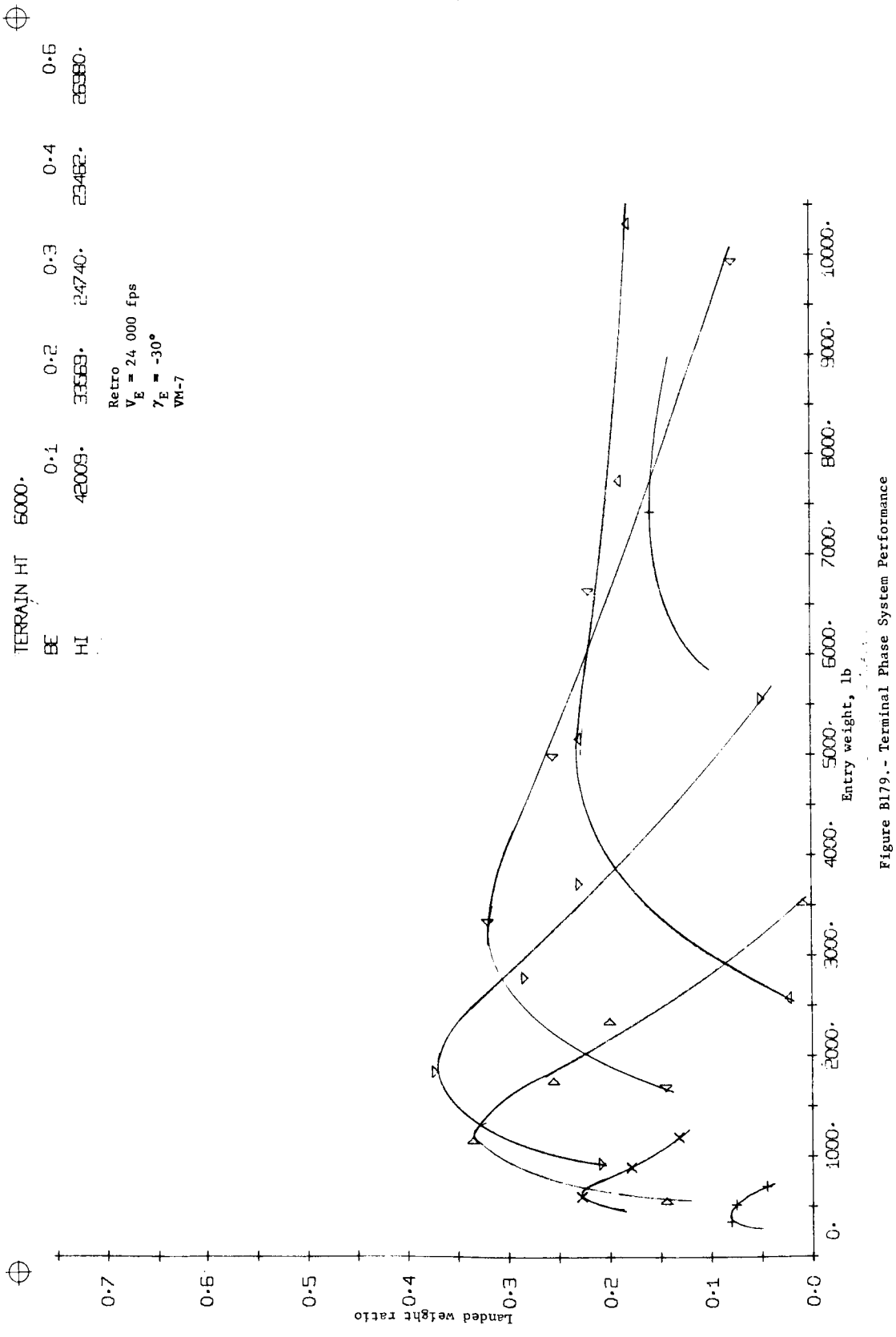

Figure B179.- Terminal Phase System Performance

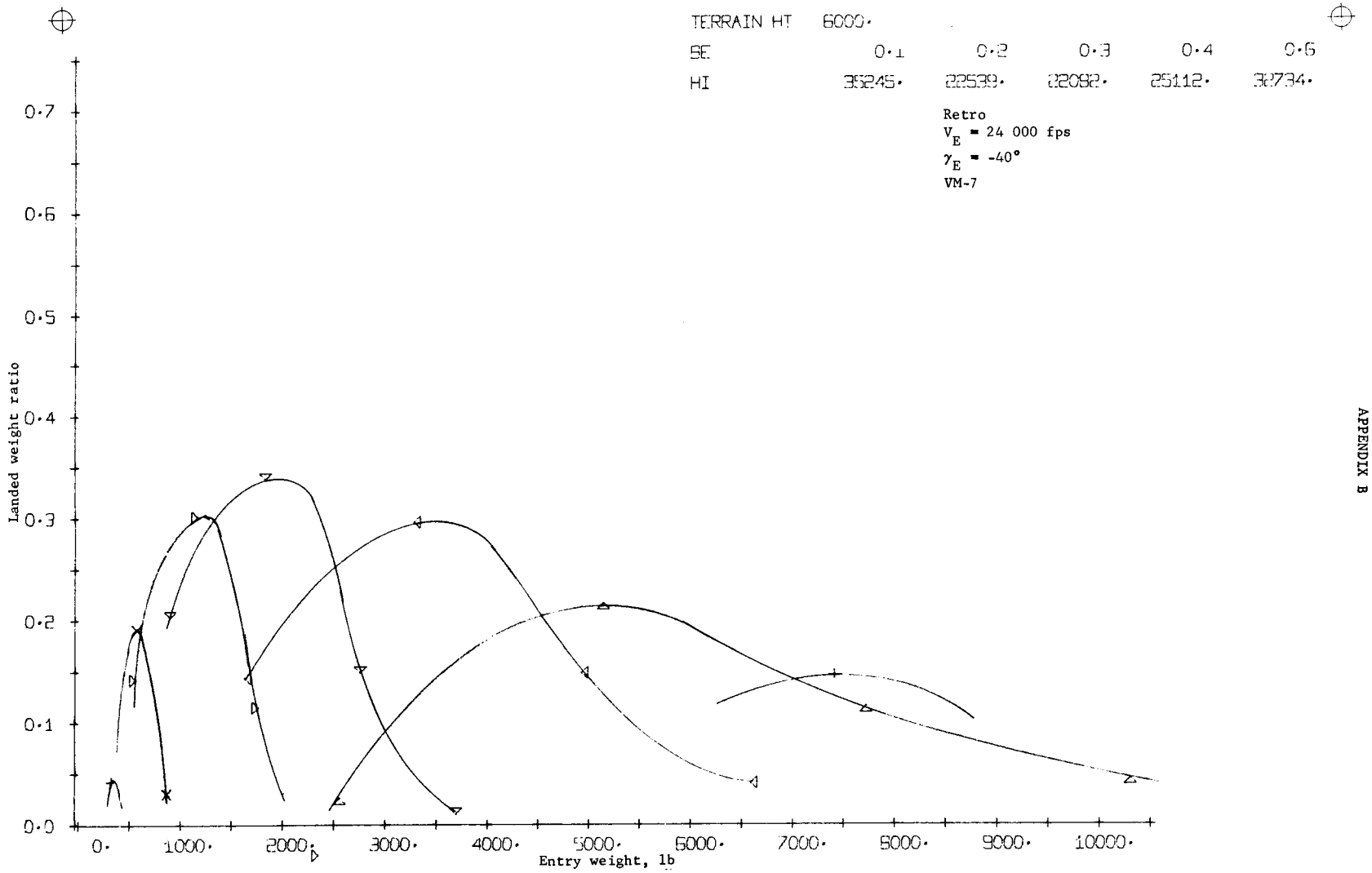

Figure B180.- Terminal Phase System Performance

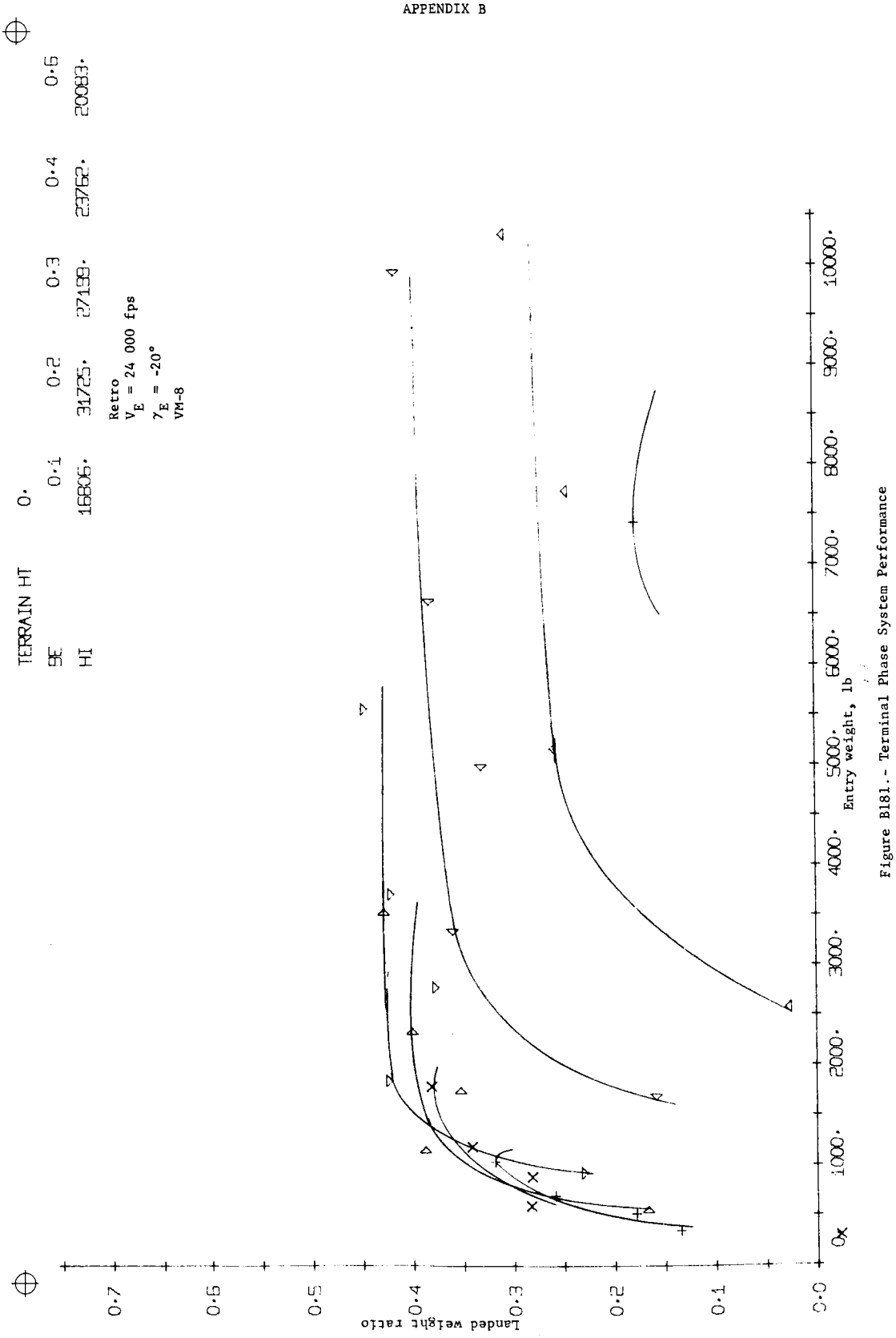

Figure B181.- Terminal Phase System Performance

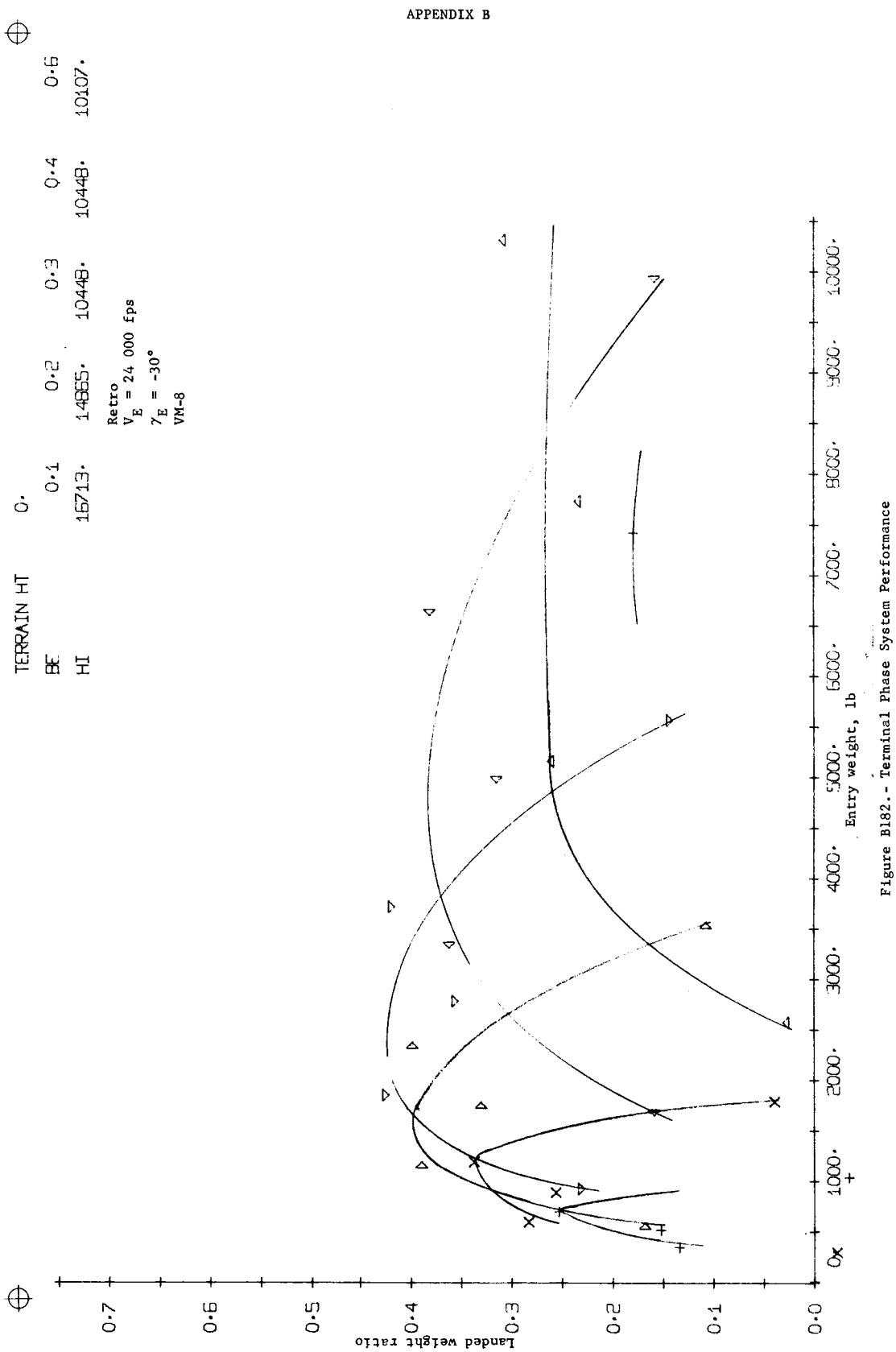

Figure B182.- Terminal Phase System Performance

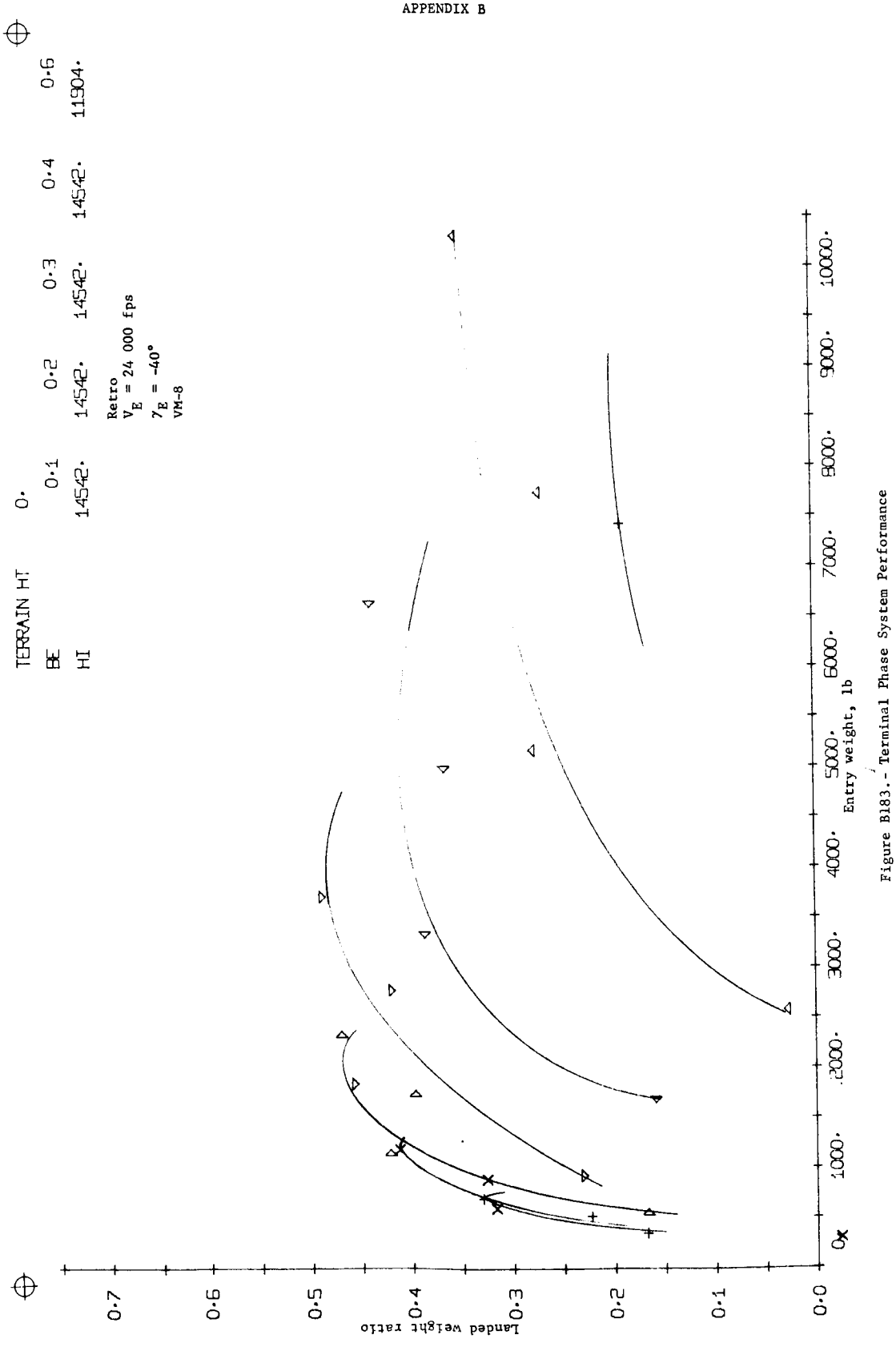

Figure B183.- Terminal Phase System Performance

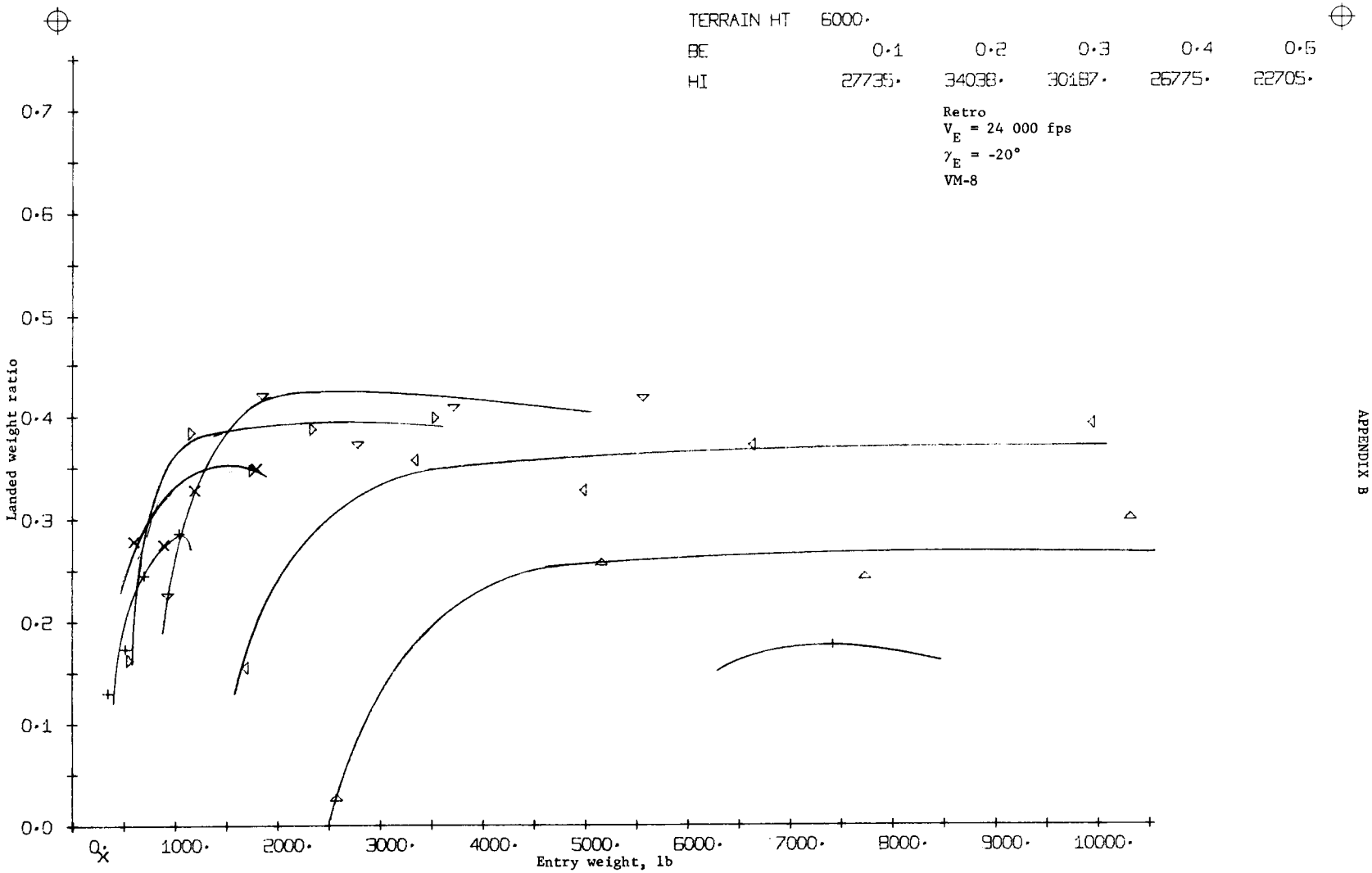

Figure B184.- Terminal Phase System Performance

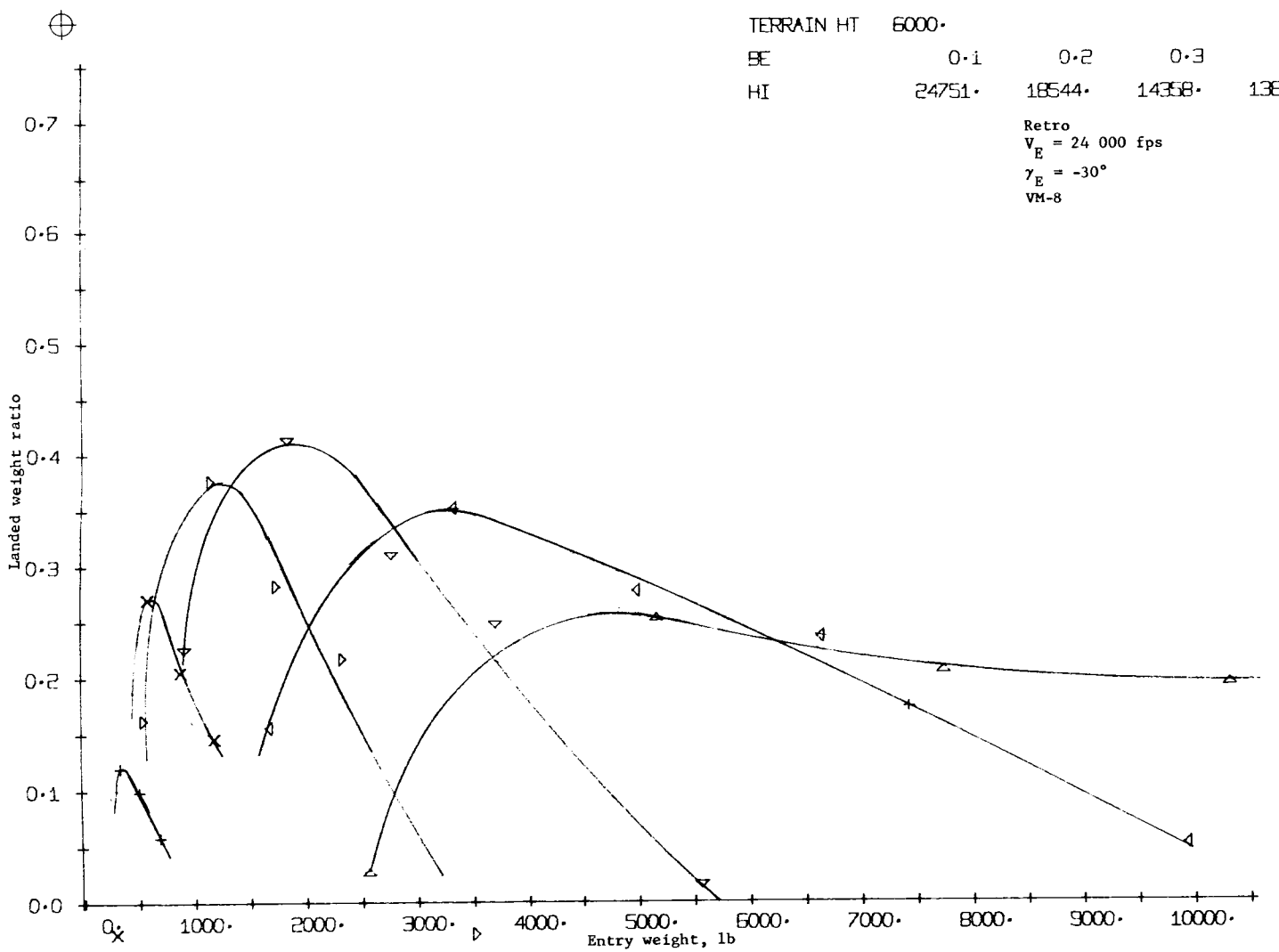

Figure B185.- Terminal Phase System Performance

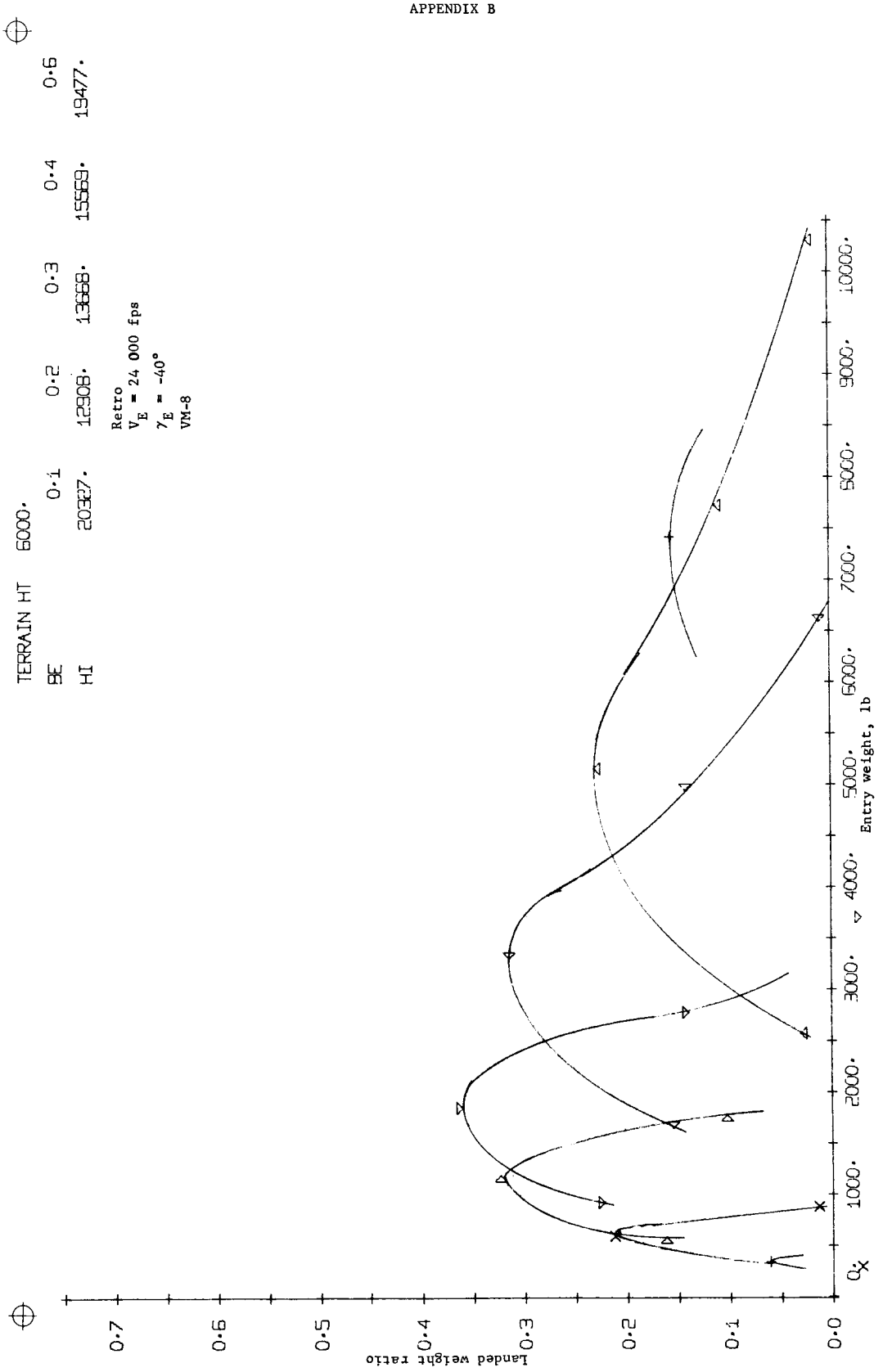

Figure B186.- Terminal Phase System Performance

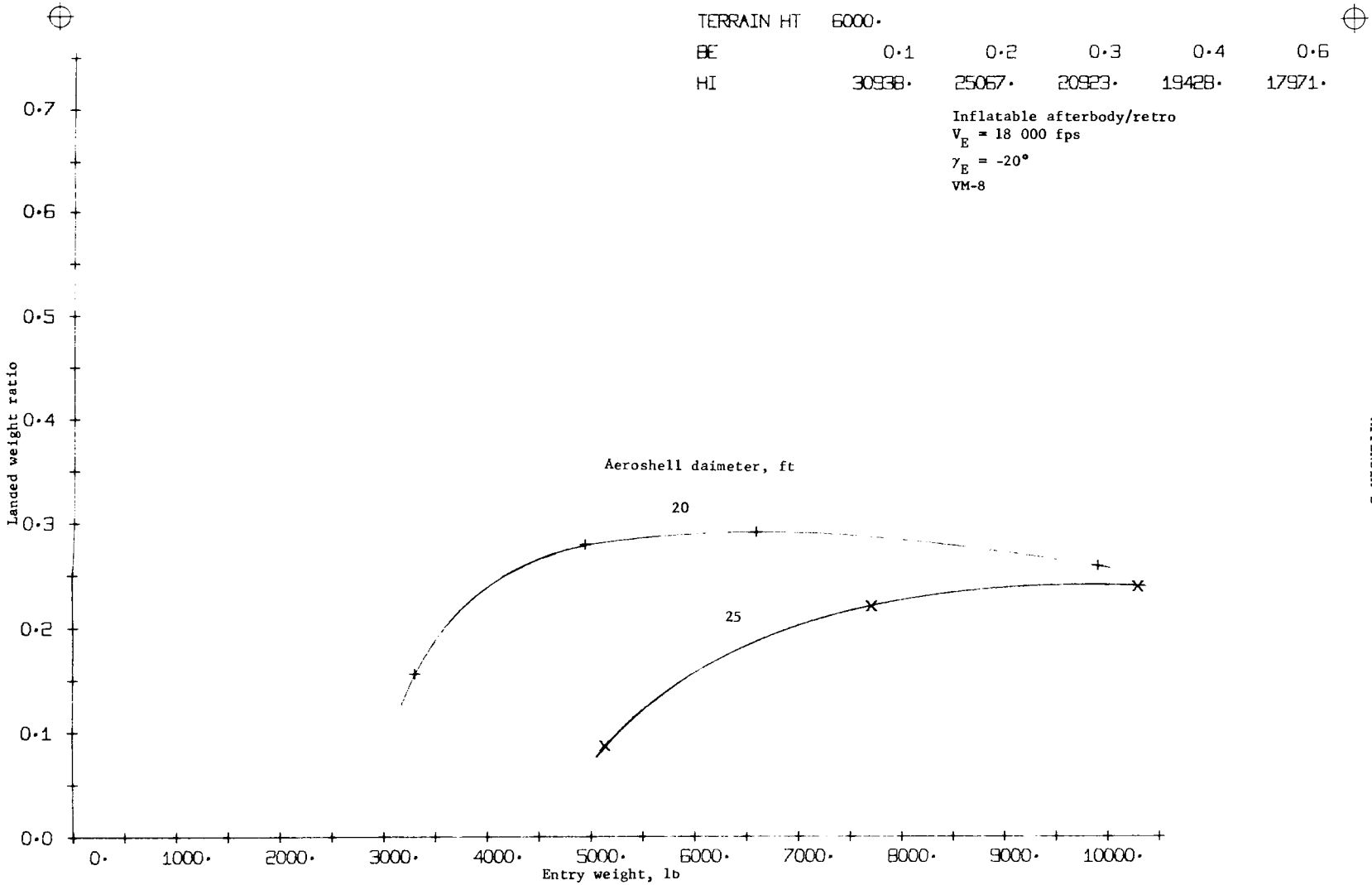

Figure B187.- Terminal Phase System Performance

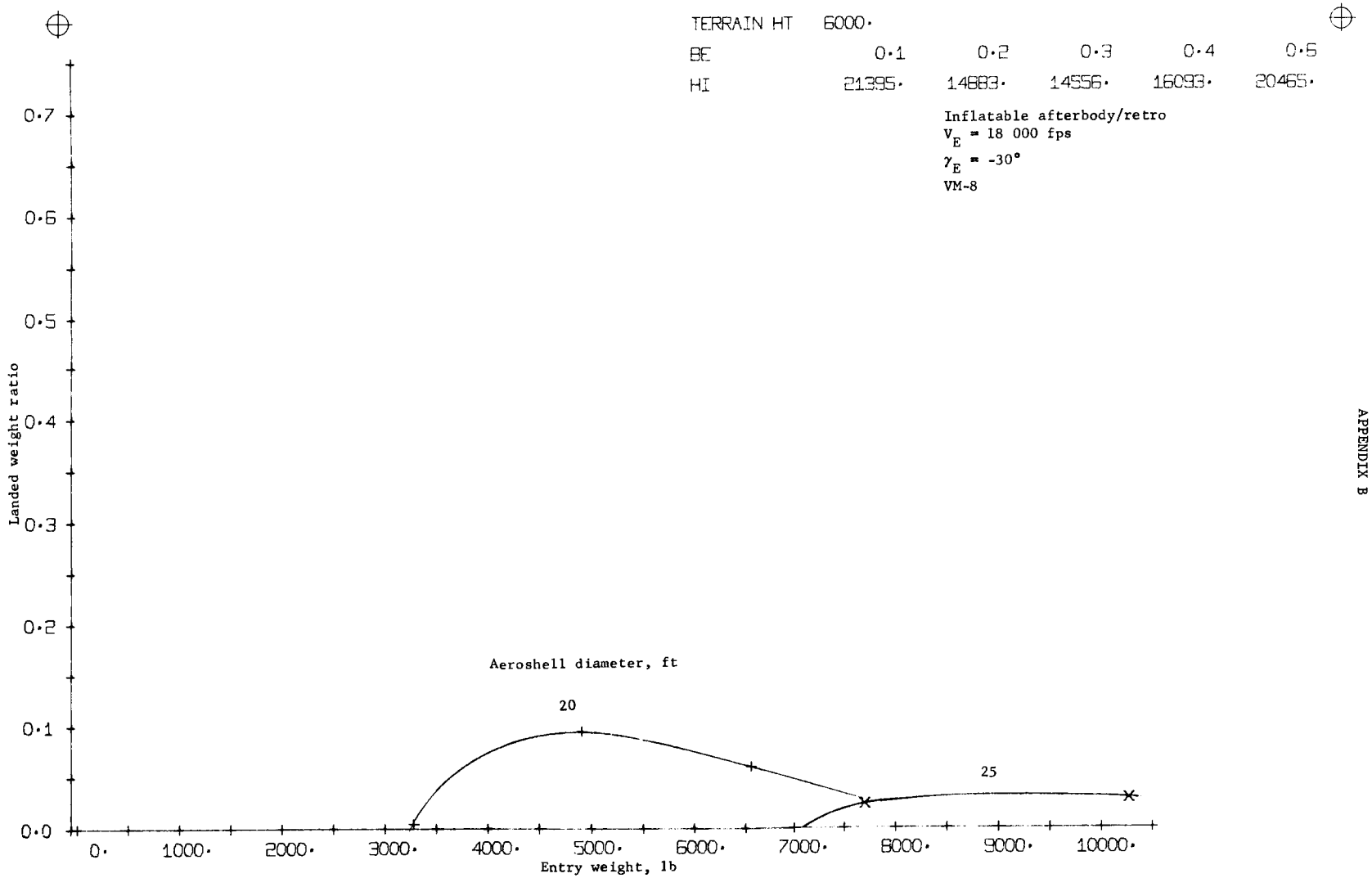

Figure B188.- Terminal Phase System Performance

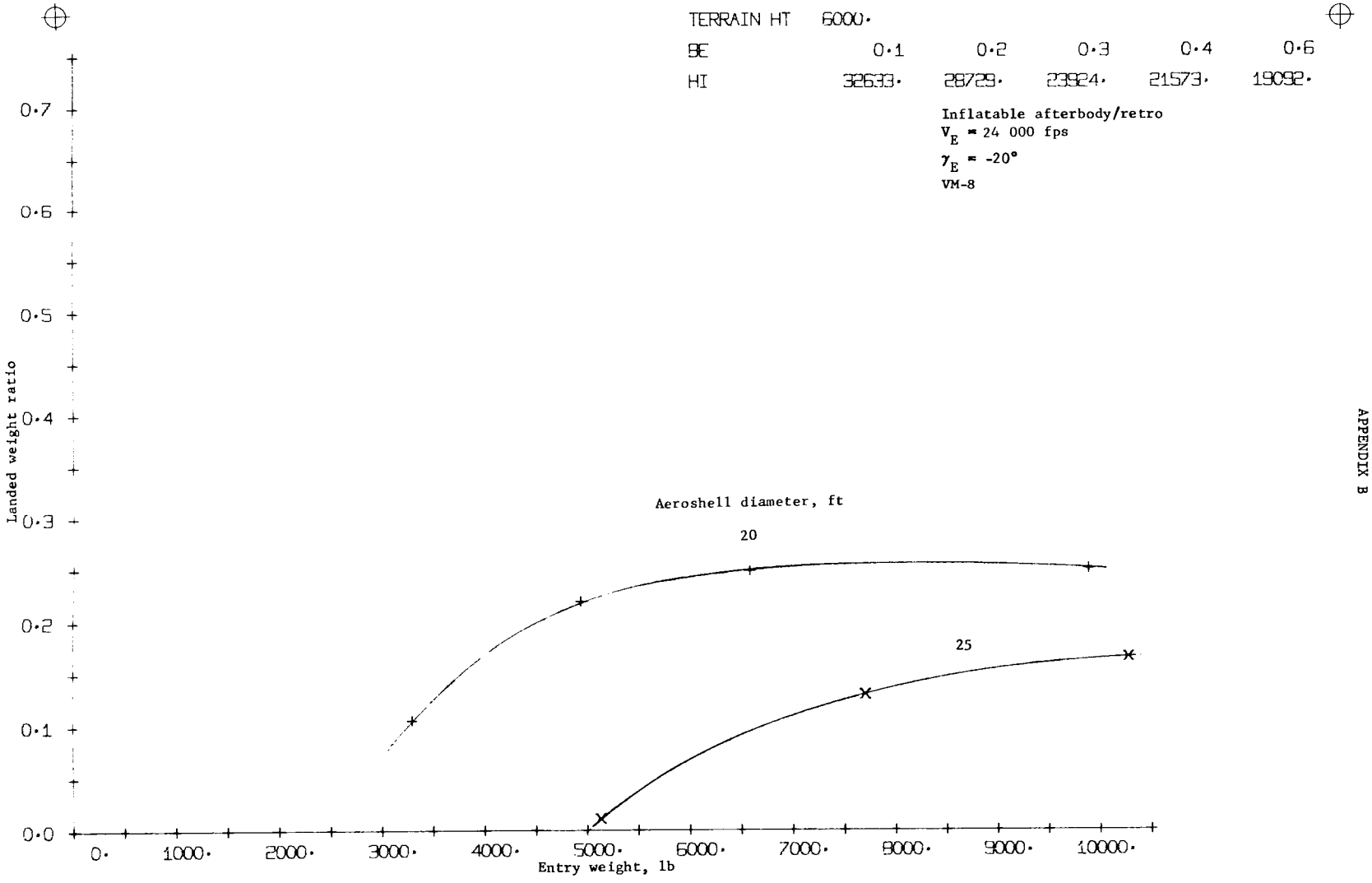

Figure B189.- Terminal Phase System Performance

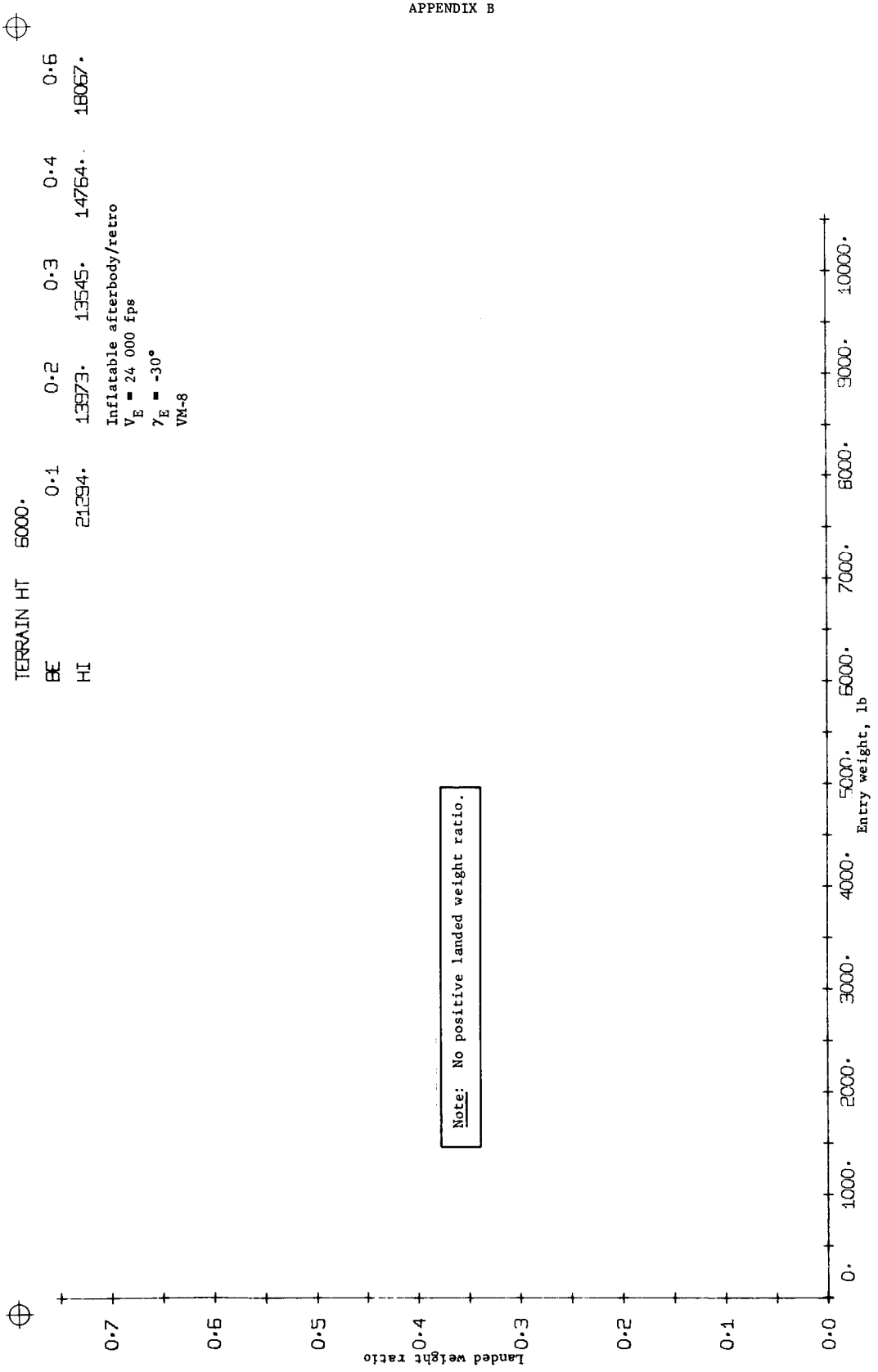

Figure B190.- Terminal Phase System Performance

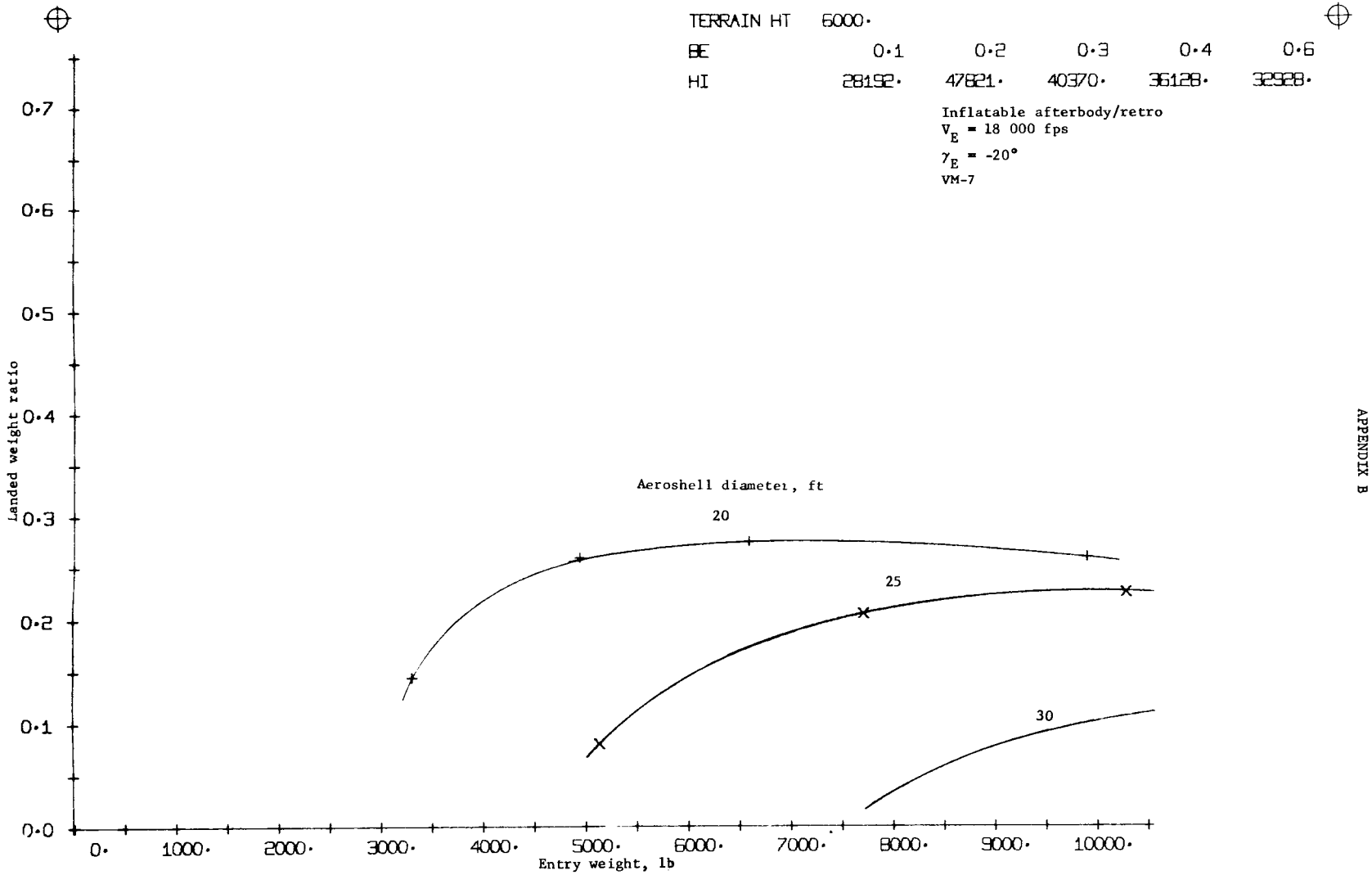

Figure B191.- Terminal Phase System Performance

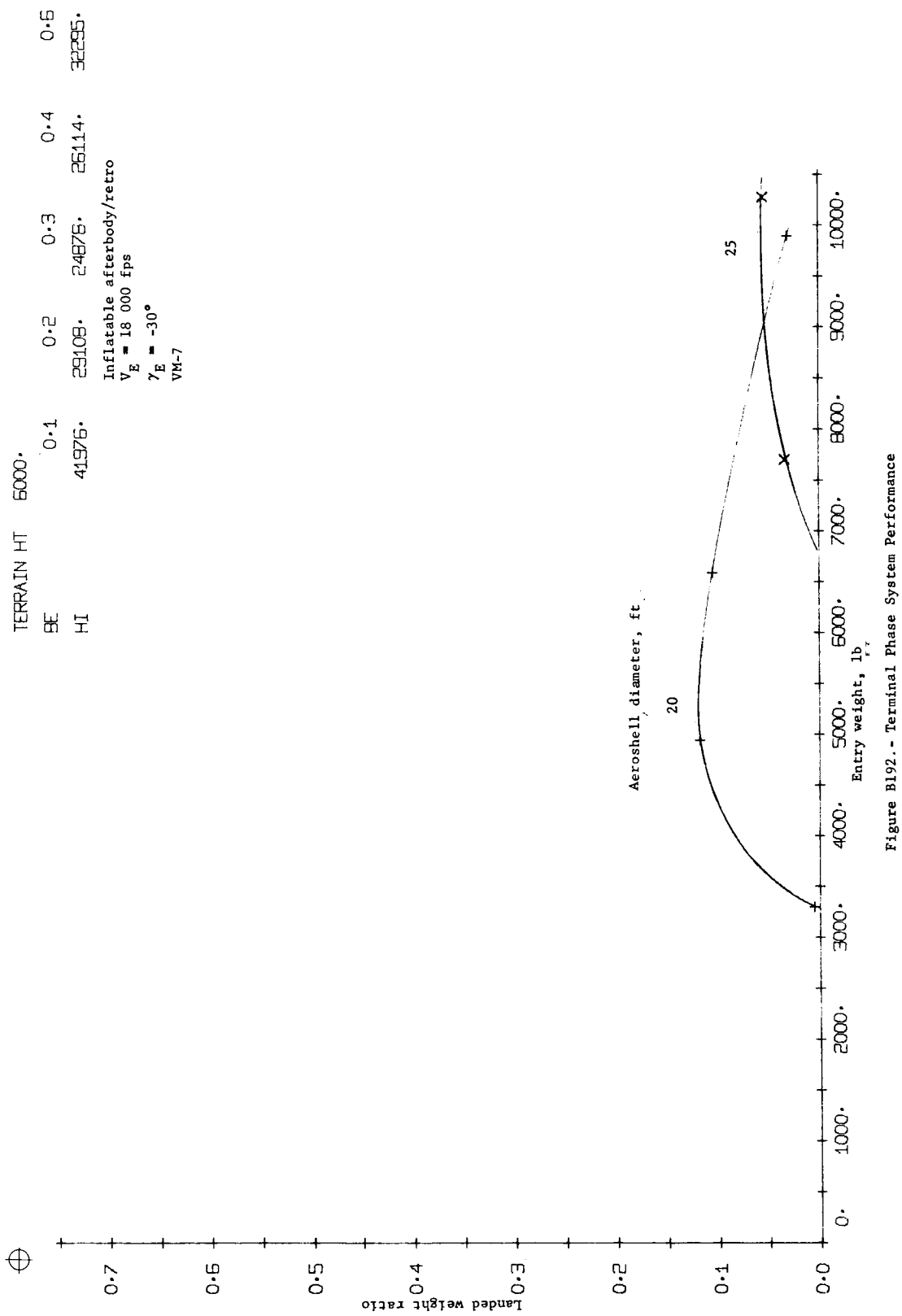

Figure B192.- Terminal Phase System Performance

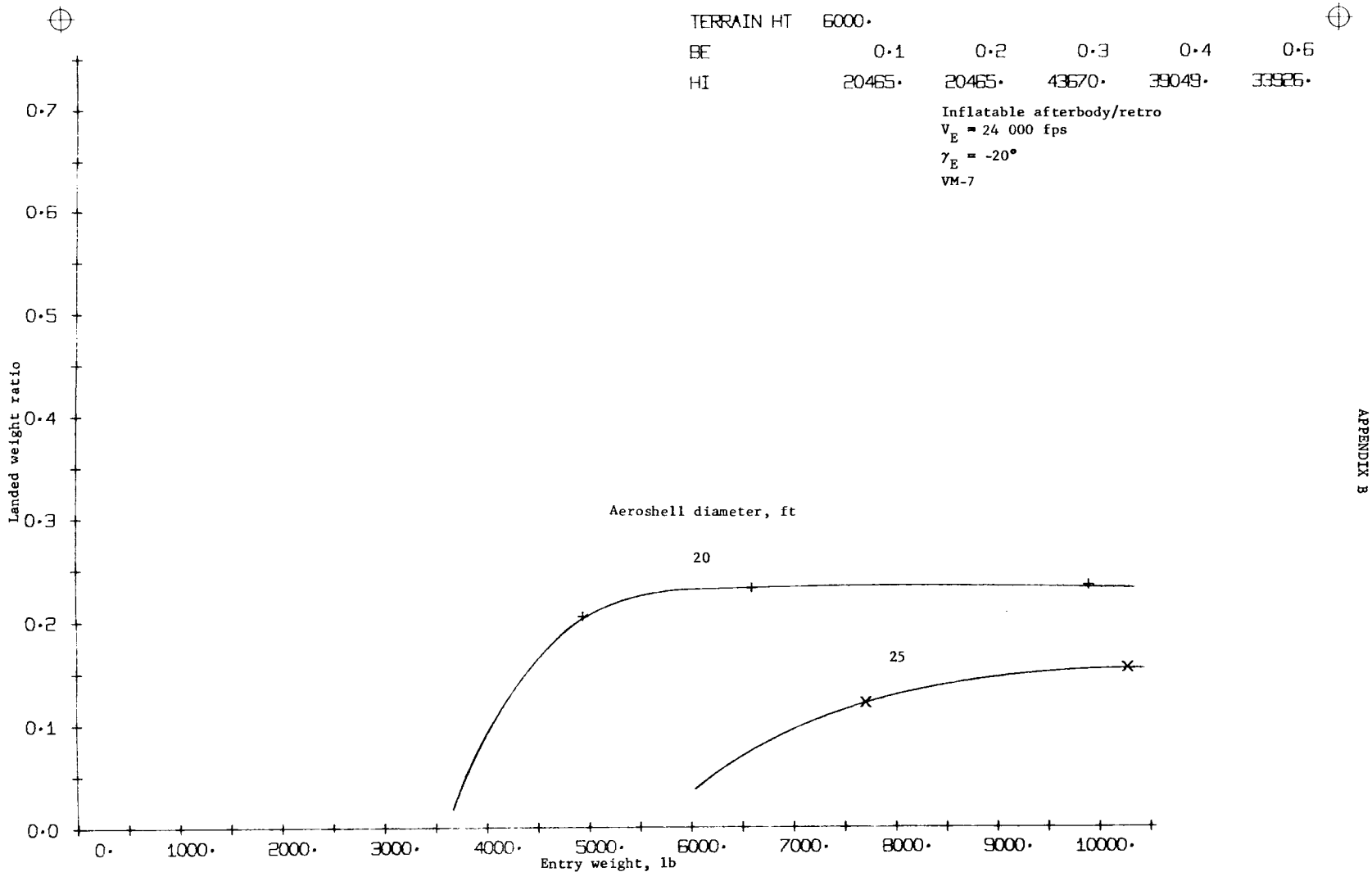

Figure B193.- Terminal Phase System Performance

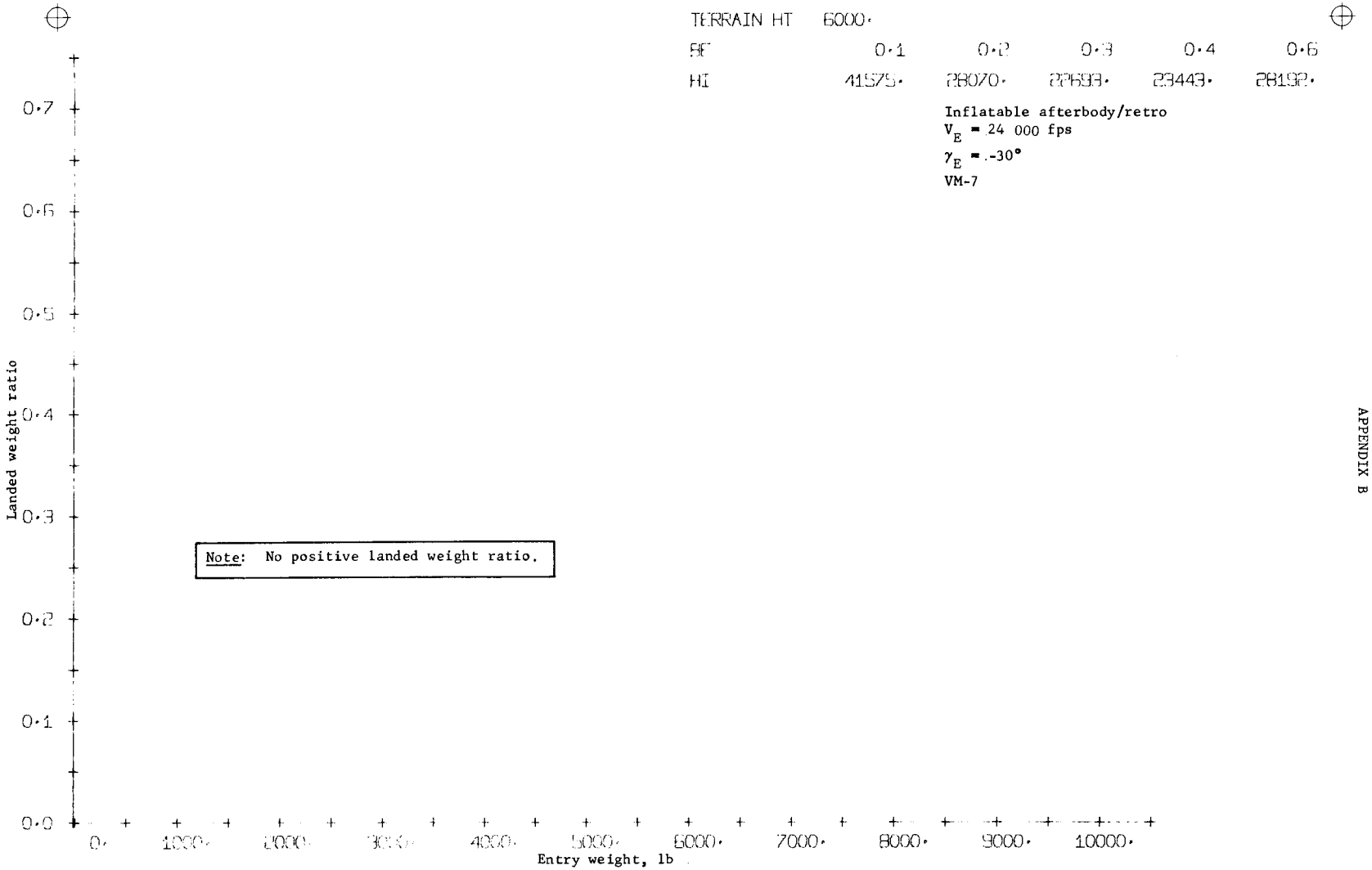

Figure B194.- Terminal Phase System Performance

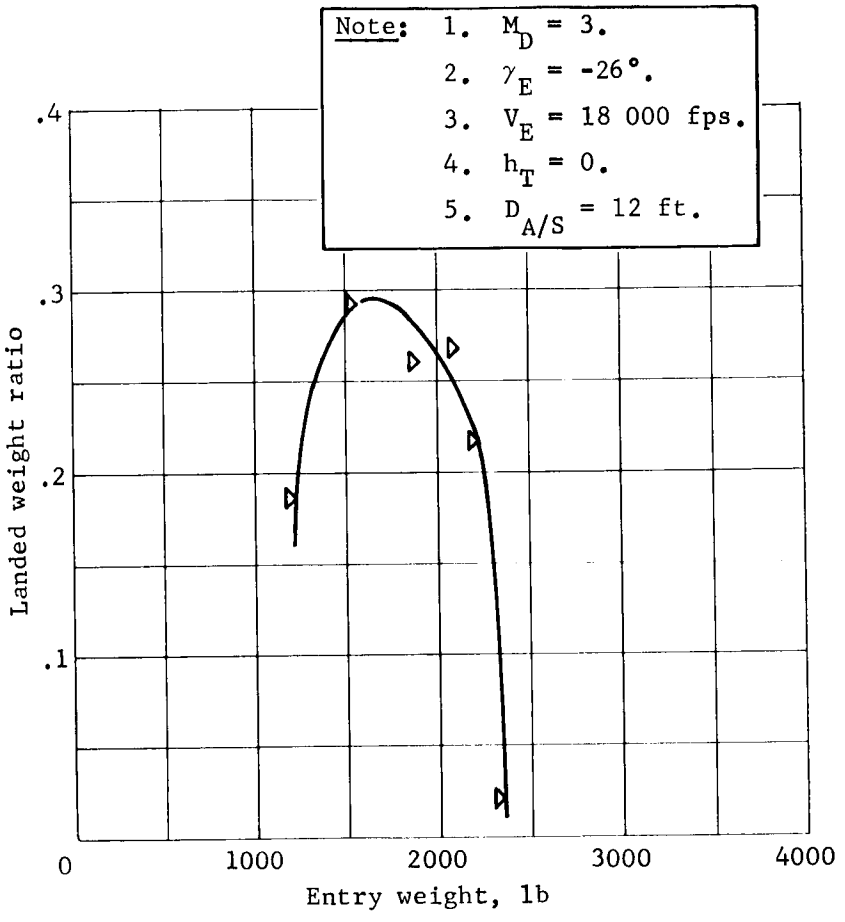

Figure B195.- Ablator Weight Discontinuity Example

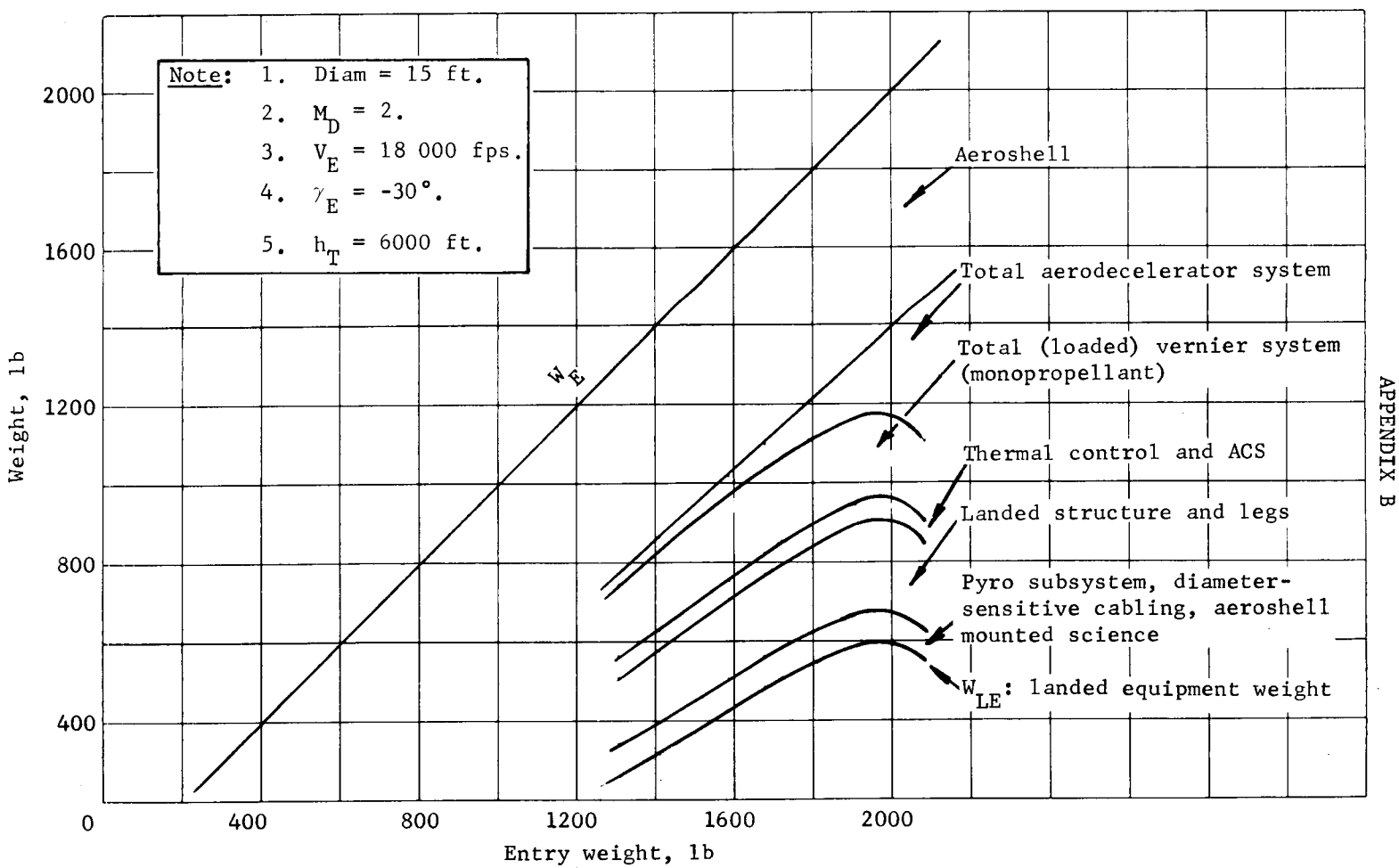

Figure B197.- Landed Equipment Weight

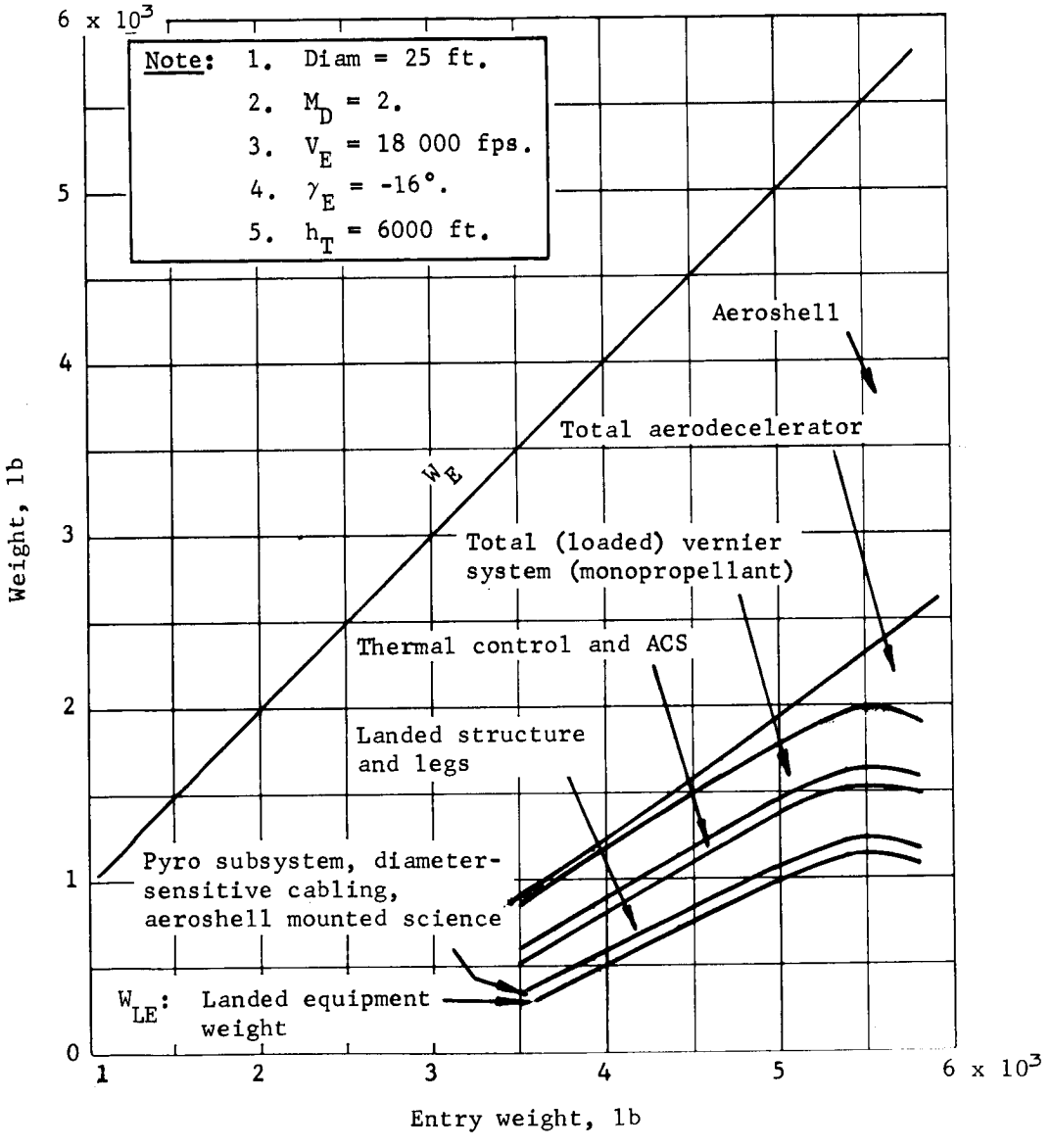

Figure B198.- Landed Equipment Weight

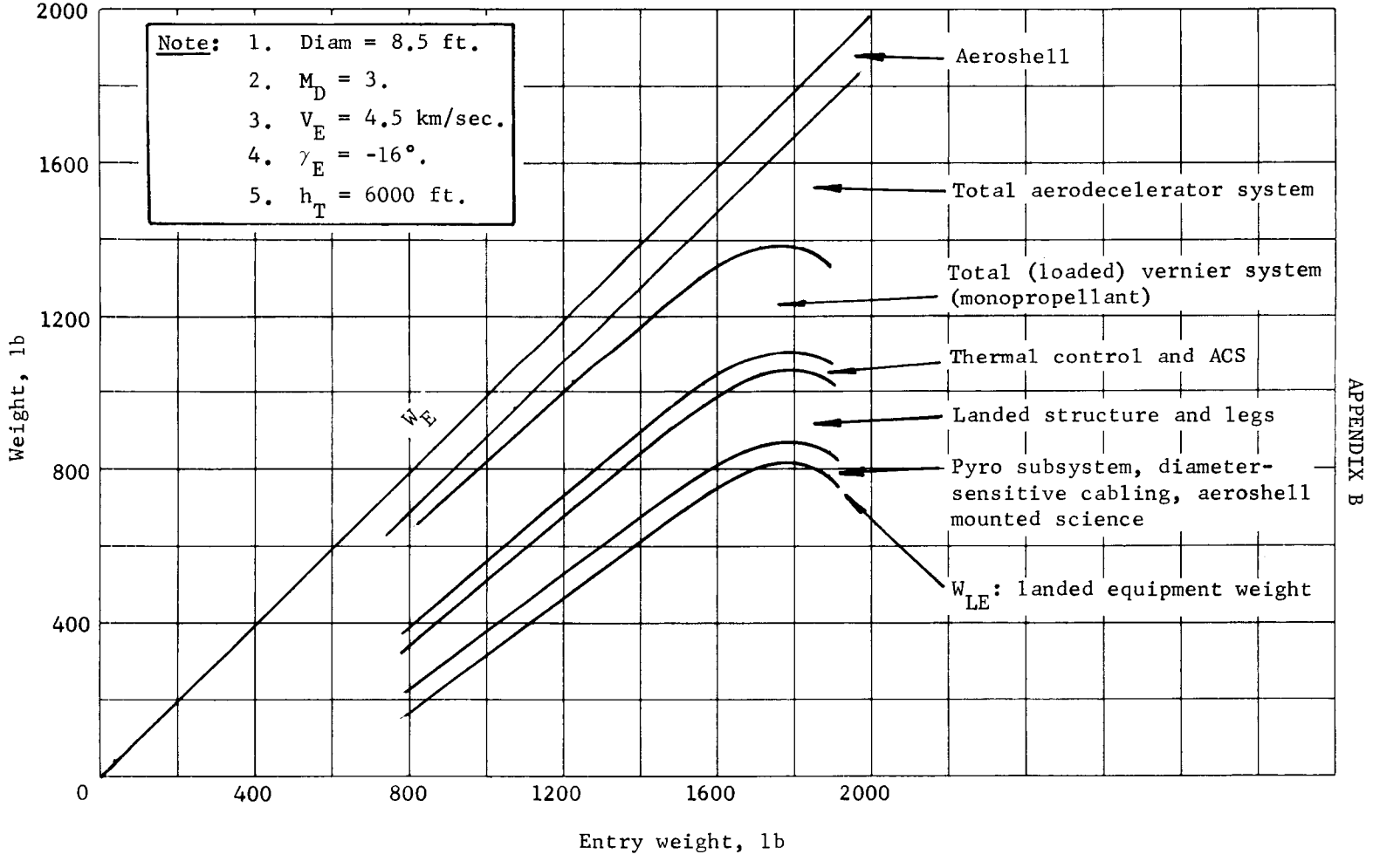

Figure B199.- Landed Equipment Weight

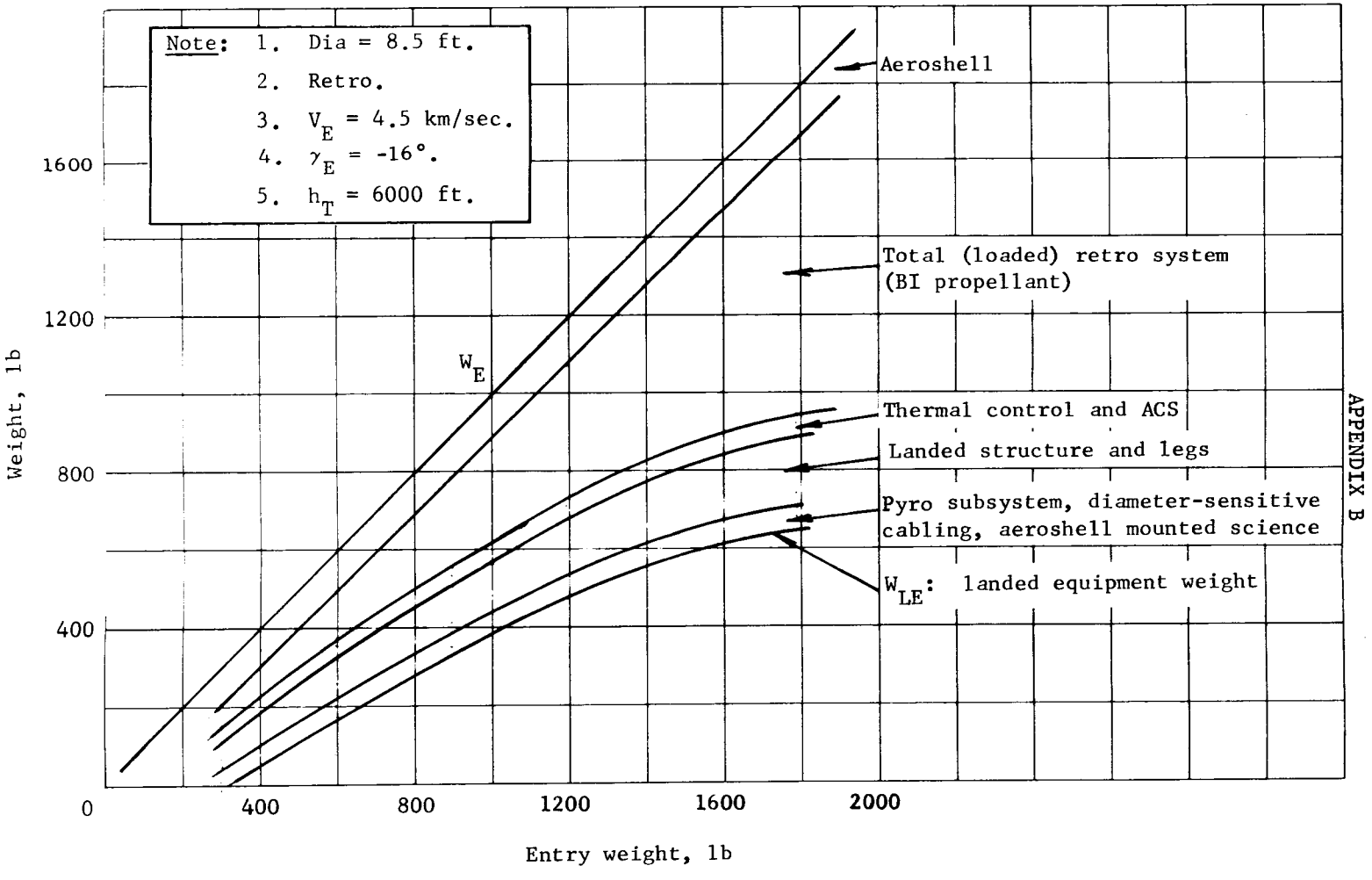

Figure B200.- Landed Equipment Weight

APPENDIX B

Data Analysis

The data shown in figure B201 is a reproduction of figure B99. These data are converted to W_{LE} versus W_E in figure B202. Three specific contours are identified on the figures. The first is maximum W_{LE} for each diameter. This contour is the maximum system performance for any given diameter. The second contour is really the envelope of the curves. The contour describes the maximum W_{LE} for any given W_E. The price paid for using this contour is increased aeroshell diameter (i.e., minimum ballistic coefficient). The third contour lies between the first two and is a locus of maximum W_{LE}/W_E ratio for any given diameter. This contour is one that defines the most efficient system in terms of maximum pounds on the ground per pound entry for any given diameter. These three contours are referred to as maximum W_{LE} contour, maximum W_{LE} envelope, and maximum W_{LE}/W_E ratio contour, respectively.

Plots of maximum W_{LE} and W_E versus aeroshell diameter for the orbit mode aerodecelerators are shown in figures B203 to B210. These figures are crossplots of the peaks of curves similar to figure B202. They show the maximum landed equipment weight and the required entry weight for a particular diameter. For instance, from figures B205 and B206 for a diameter of 10 ft and $\gamma_E = -18°$, the maximum landed equipment weight is 740 lb. The entry weight for this condition is 1650 lb.

Plots of landed equipment weight and entry weight versus aeroshell diameter at $(W_{LE}/W_E)_{max.}$ for orbit mode aerodecelerators are shown in figures B211 thru B216. These figures are crossplots of the peaks of curves similar to figure B201. Similar data for the direct mode are shown in figures B217 thru B232.

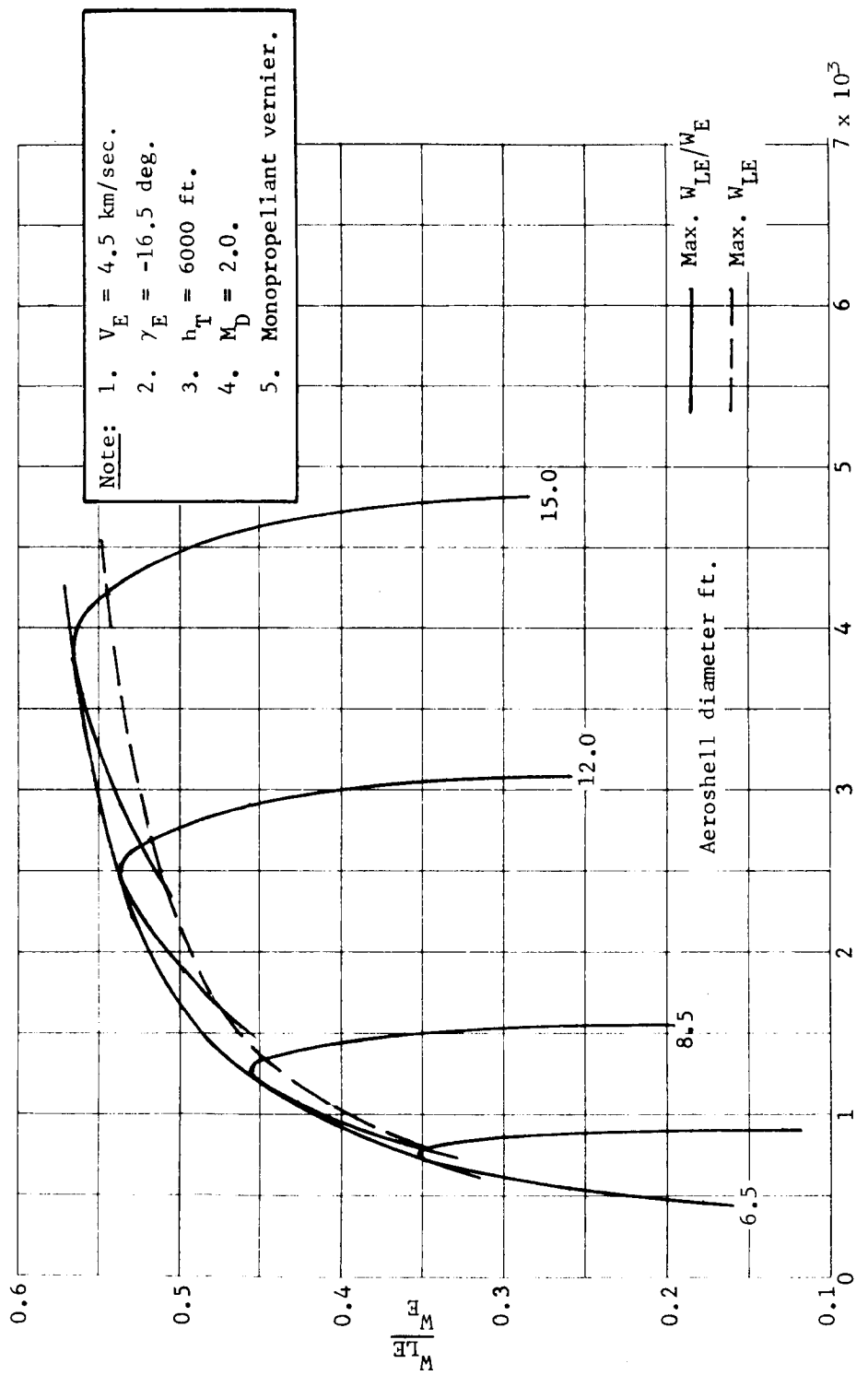

Figure B201.- Aerodecelerator Performance, Entry from Orbit

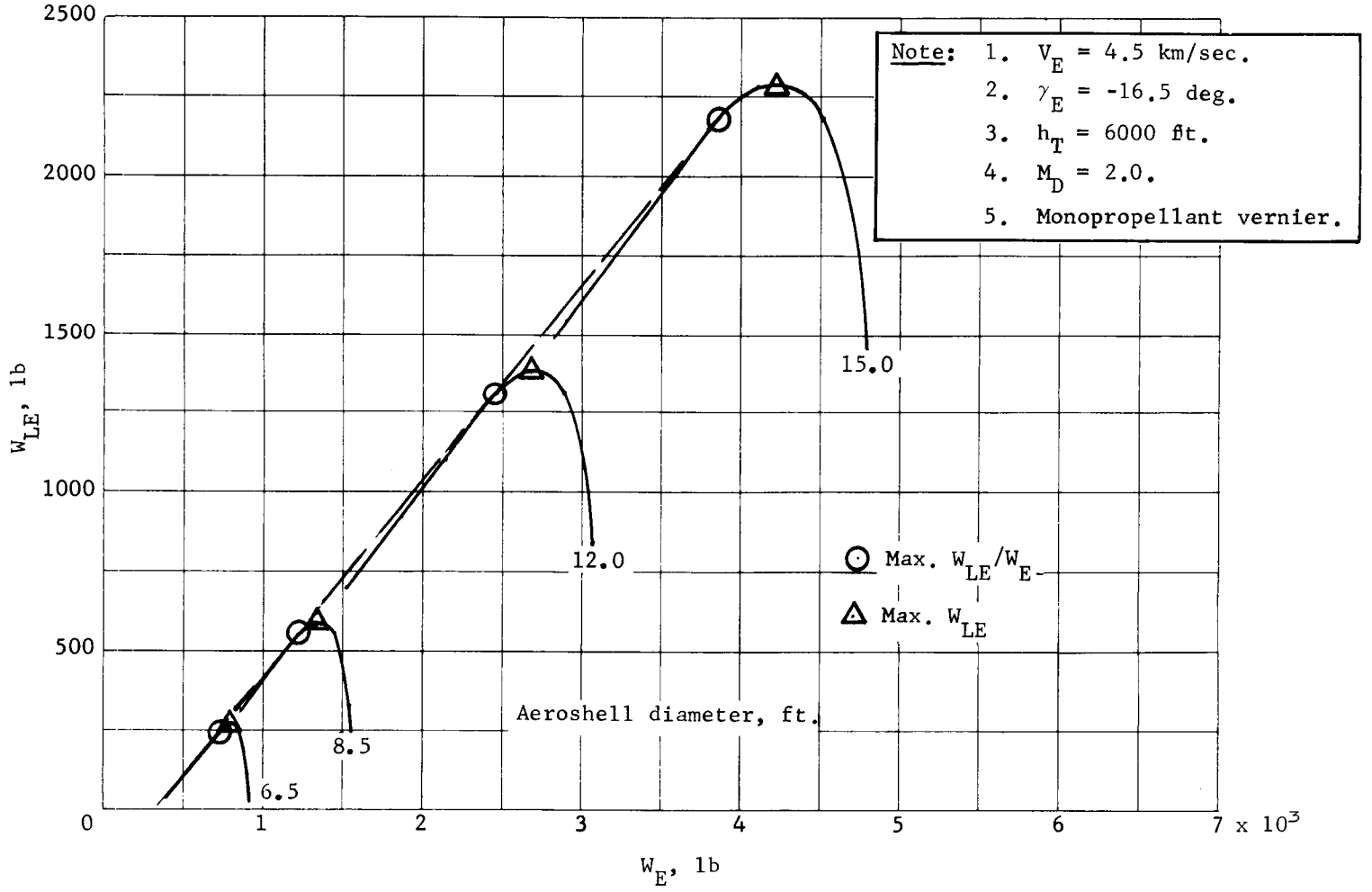

Figure B202.- Aerodecelerator Performance, Entry from Orbit

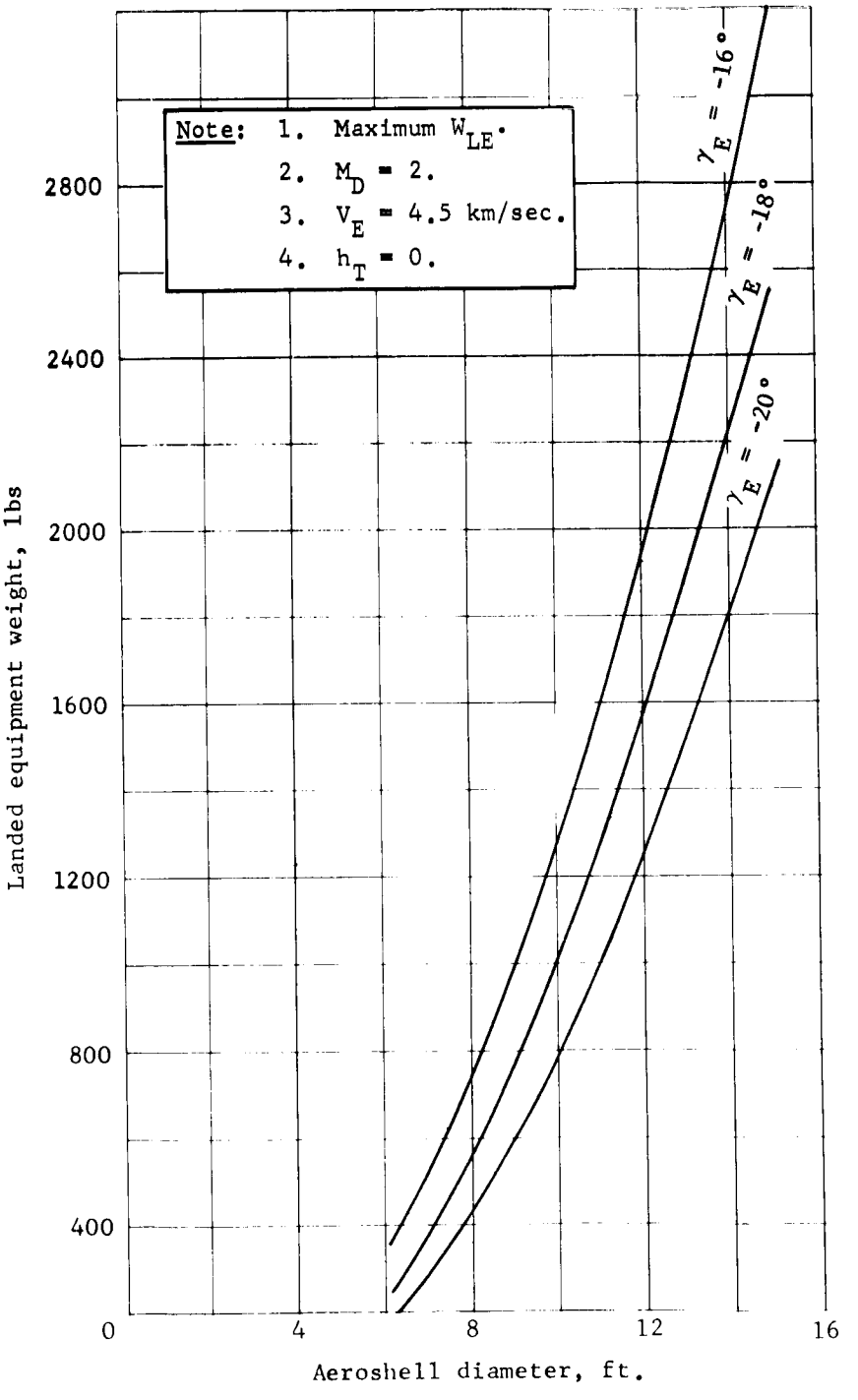

Figure B203.- W_{LE} Versus Aeroshell Diameter for Orbit Mode Aerodecelerators

APPENDIX B

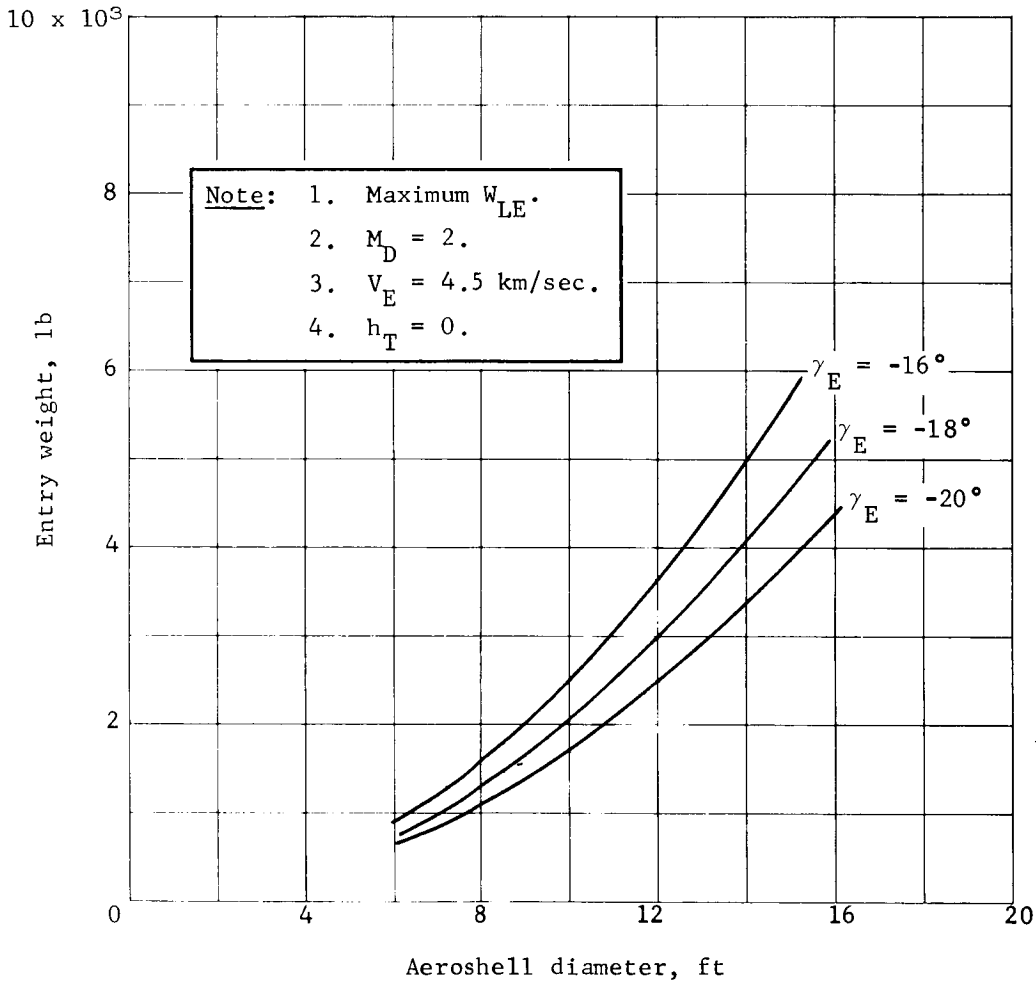

Figure B204.- W_E versus Aeroshell Diameter for Orbit Mode Aerodecelerators

APPENDIX B

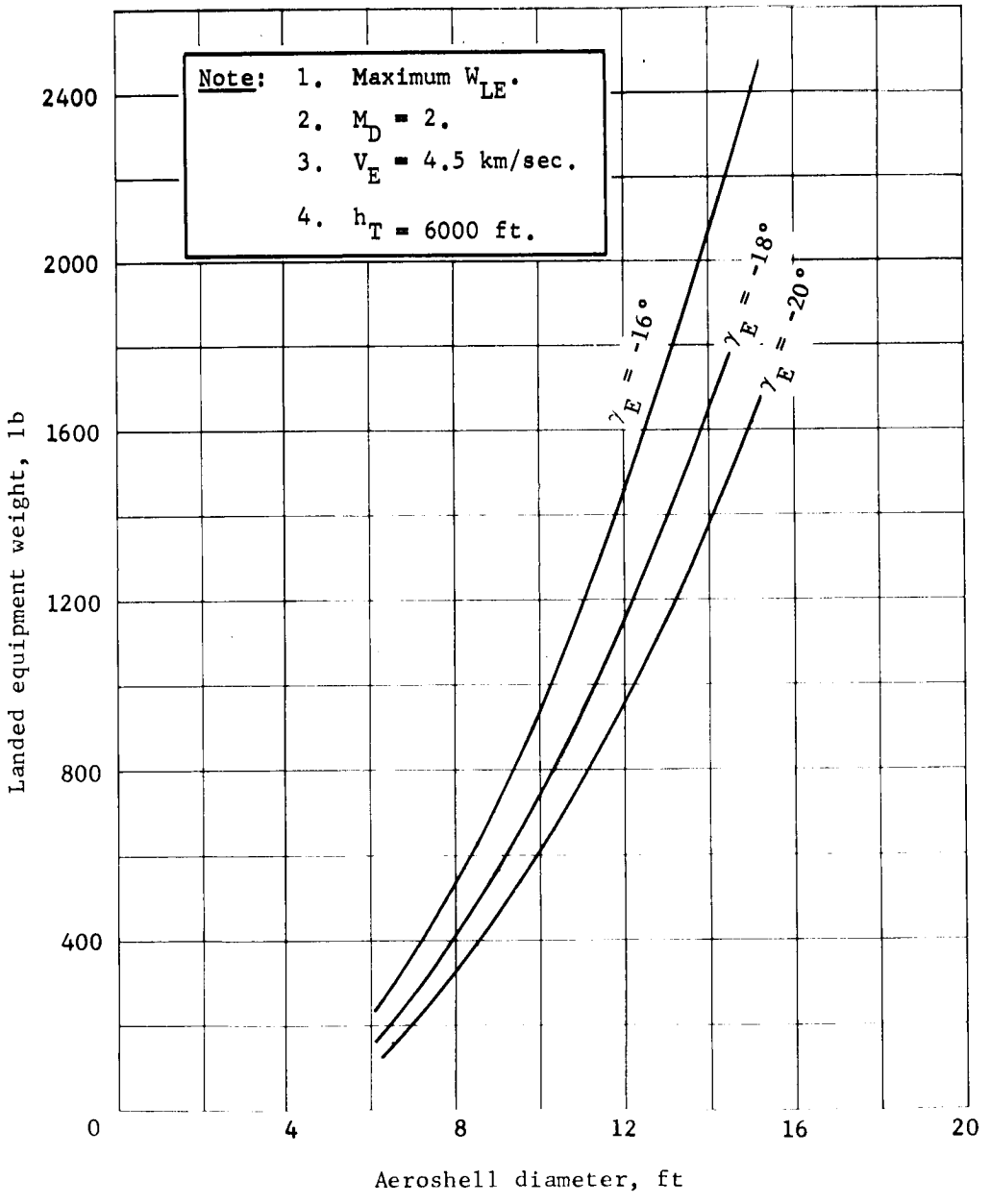

Figure B205.- W_{LE} versus Aeroshell Diameter for Orbit Mode Aerodecelerators

APPENDIX B

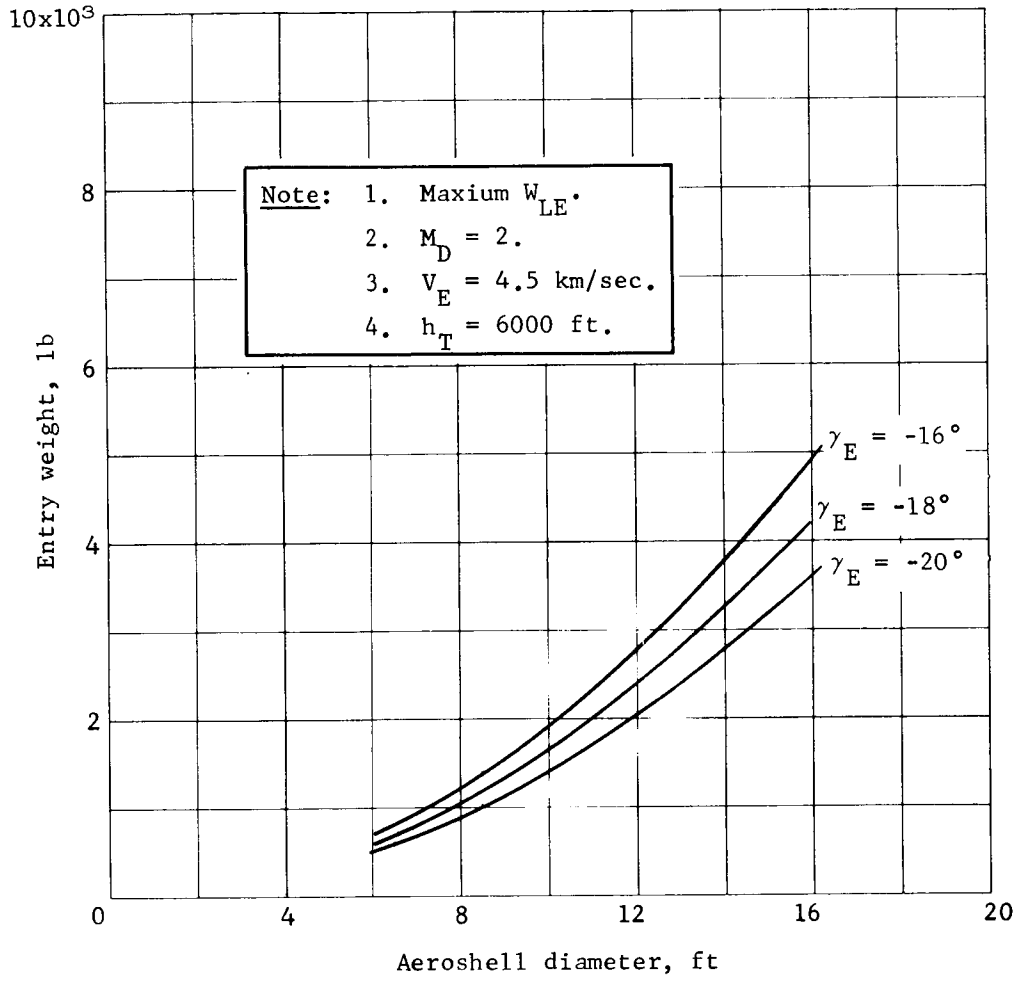

Figure B206.- W_E versus Aeroshell Diameter for Orbit Mode Aerodecelerators

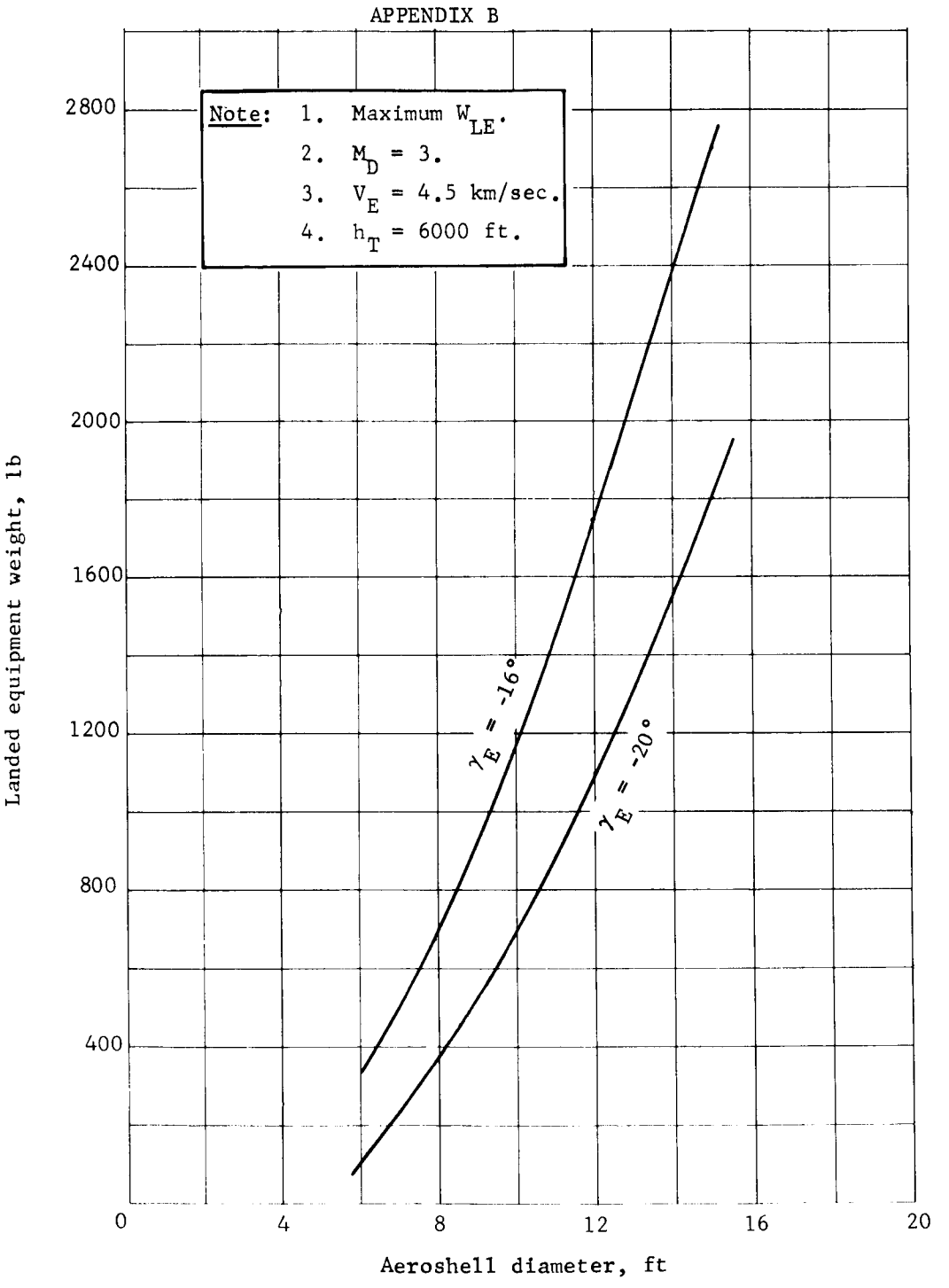

Figure B207.- W_{LE} versus Aeroshell Diameter for Orbit Mode Aerodecelerators

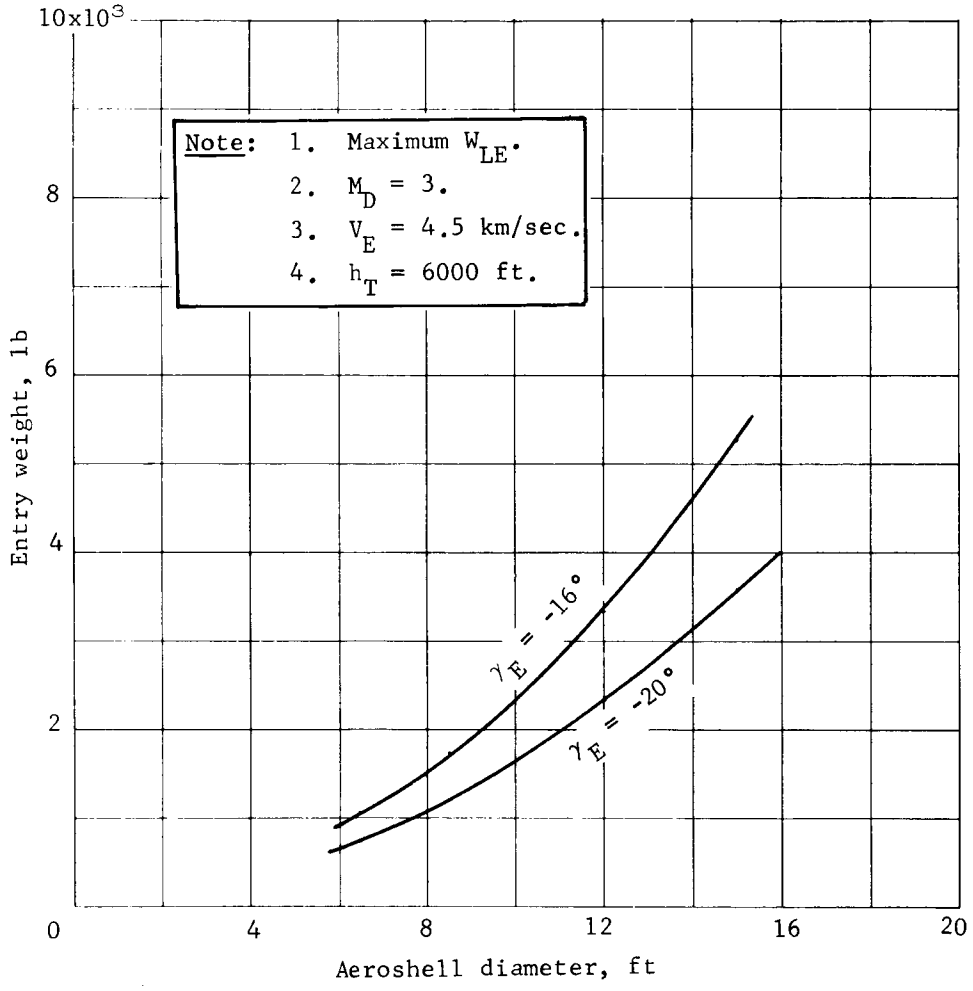

Figure B208.- W_E versus Aeroshell Diameter for Orbit Mode Aerodecelerators

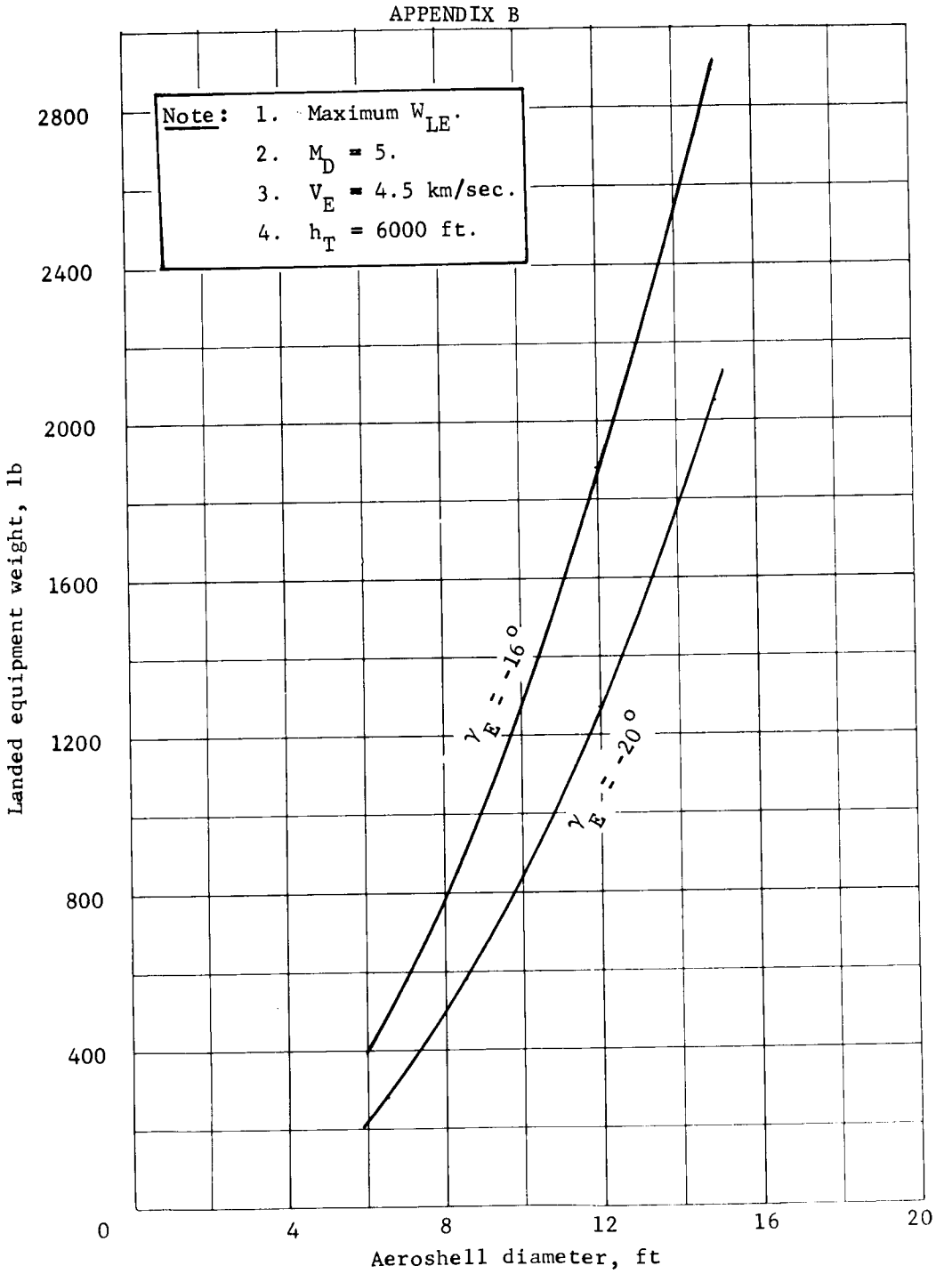

Figure B209.- W_{LE} versus Aeroshell Diameter for Orbit Mode Aerodecelerators

APPENDIX B

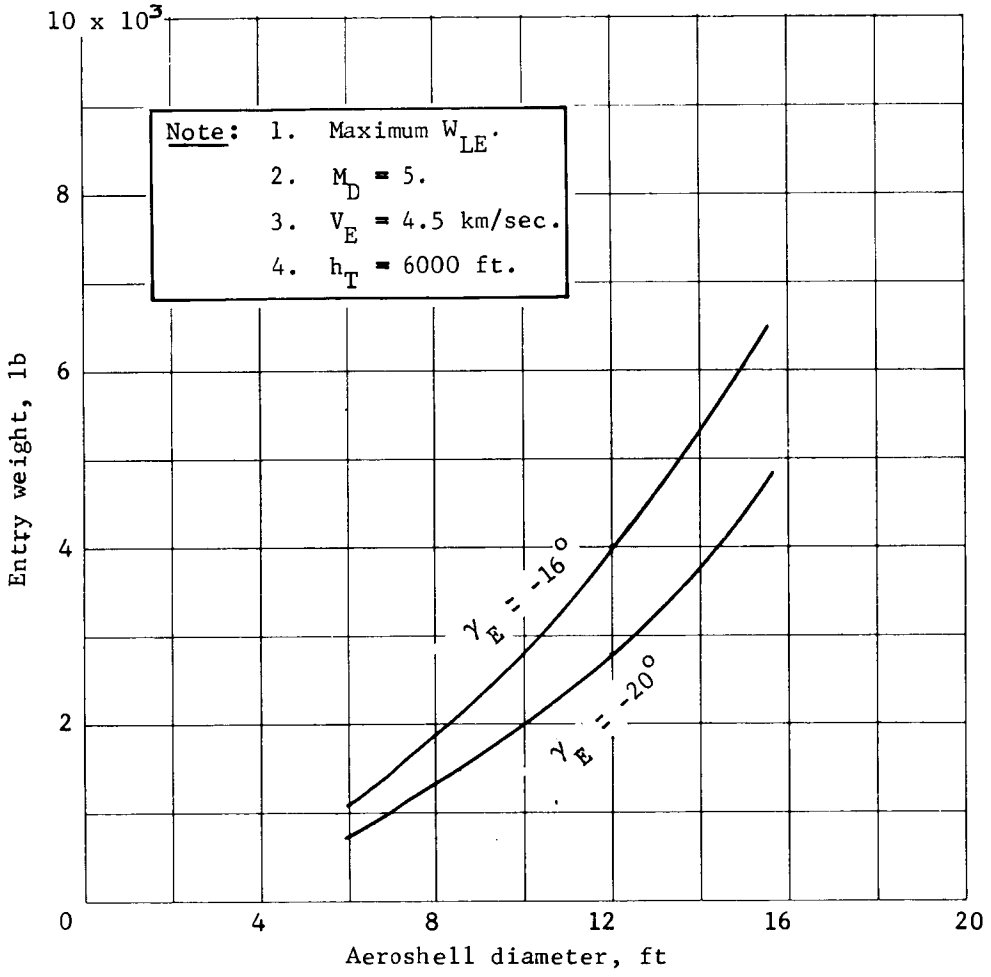

Figure B210.- W_E versus Aeroshell Diameter for Orbit Mode Aerodecelerators

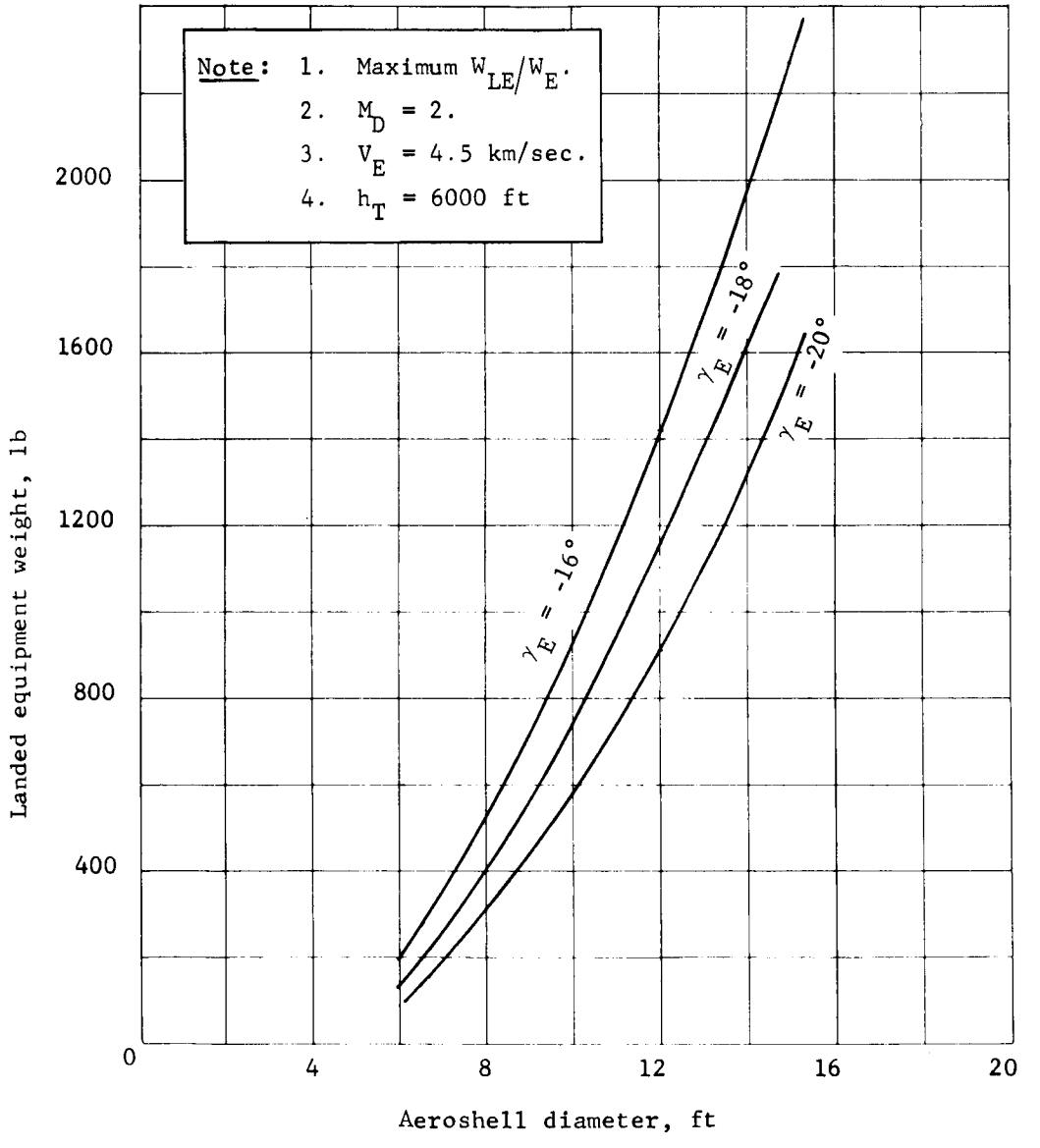

Figure B211.- W_{LE} versus Aeroshell Diameter for Orbit Mode Aerodecelerators

APPENDIX B

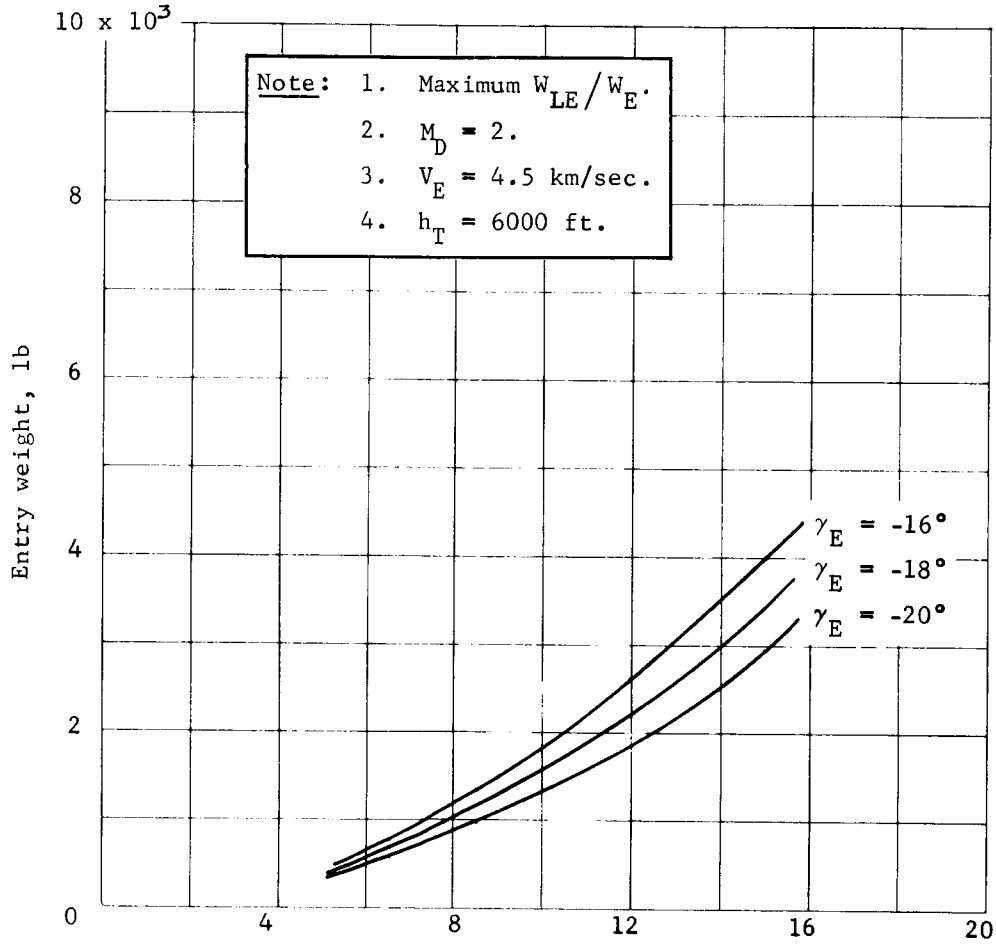

Figure B212.- W_E versus Aeroshell Diameter for Orbit Mode Aerodecelerators

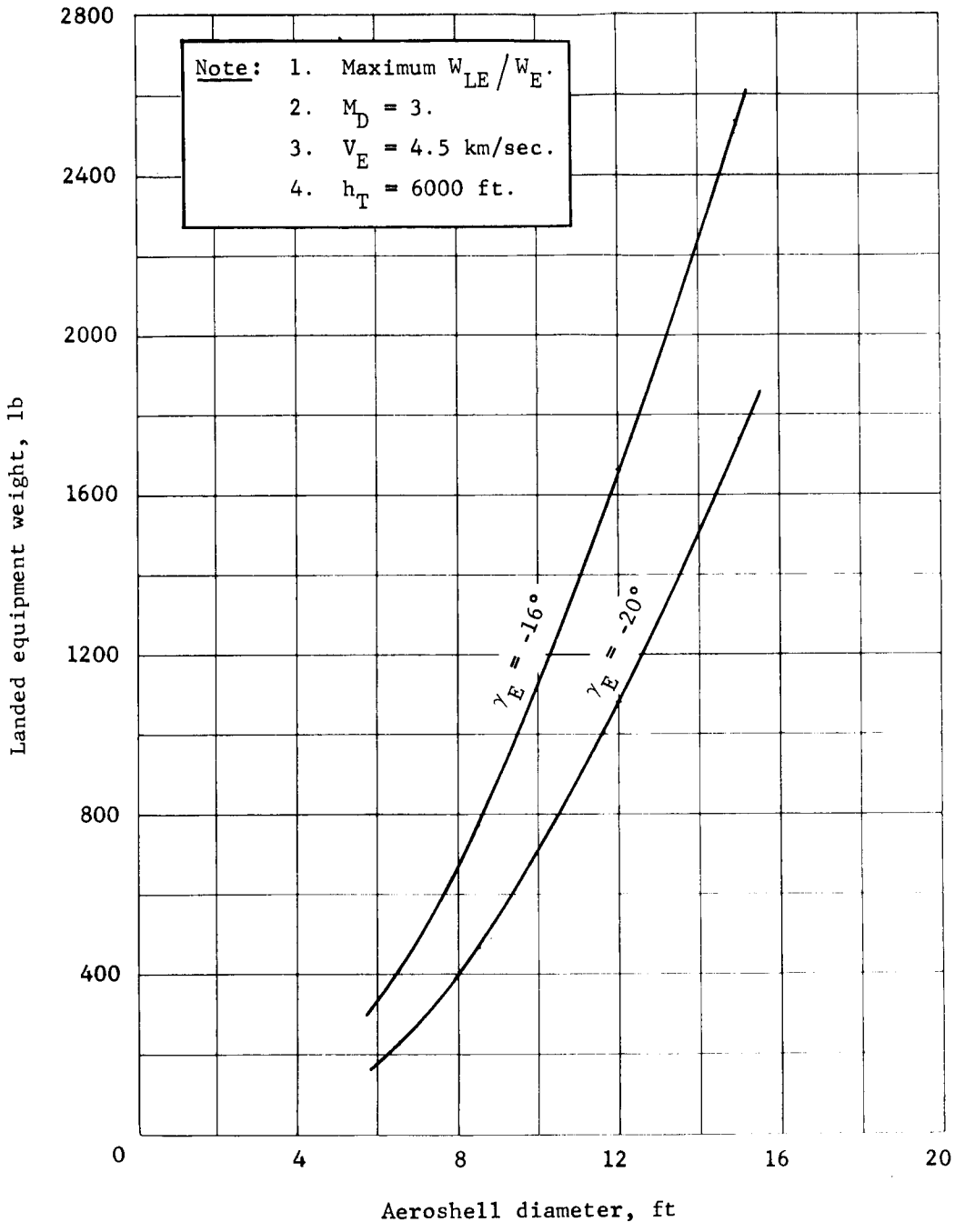

Figure B213.- W_{LE} versus Aeroshell Diameter for Orbit Mode Aerodecelerators

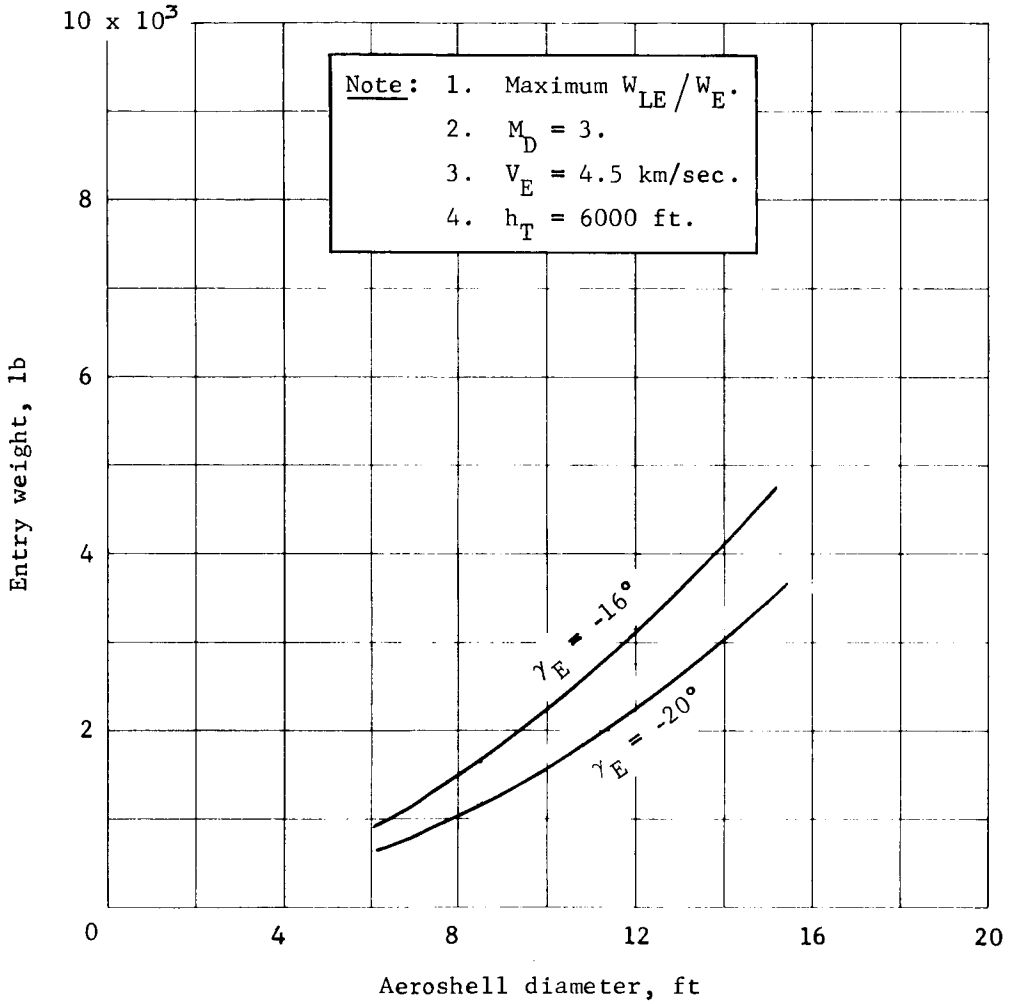

Figure B214.- W_E versus Aeroshell Diameter for Orbit Mode Aerodecelerators

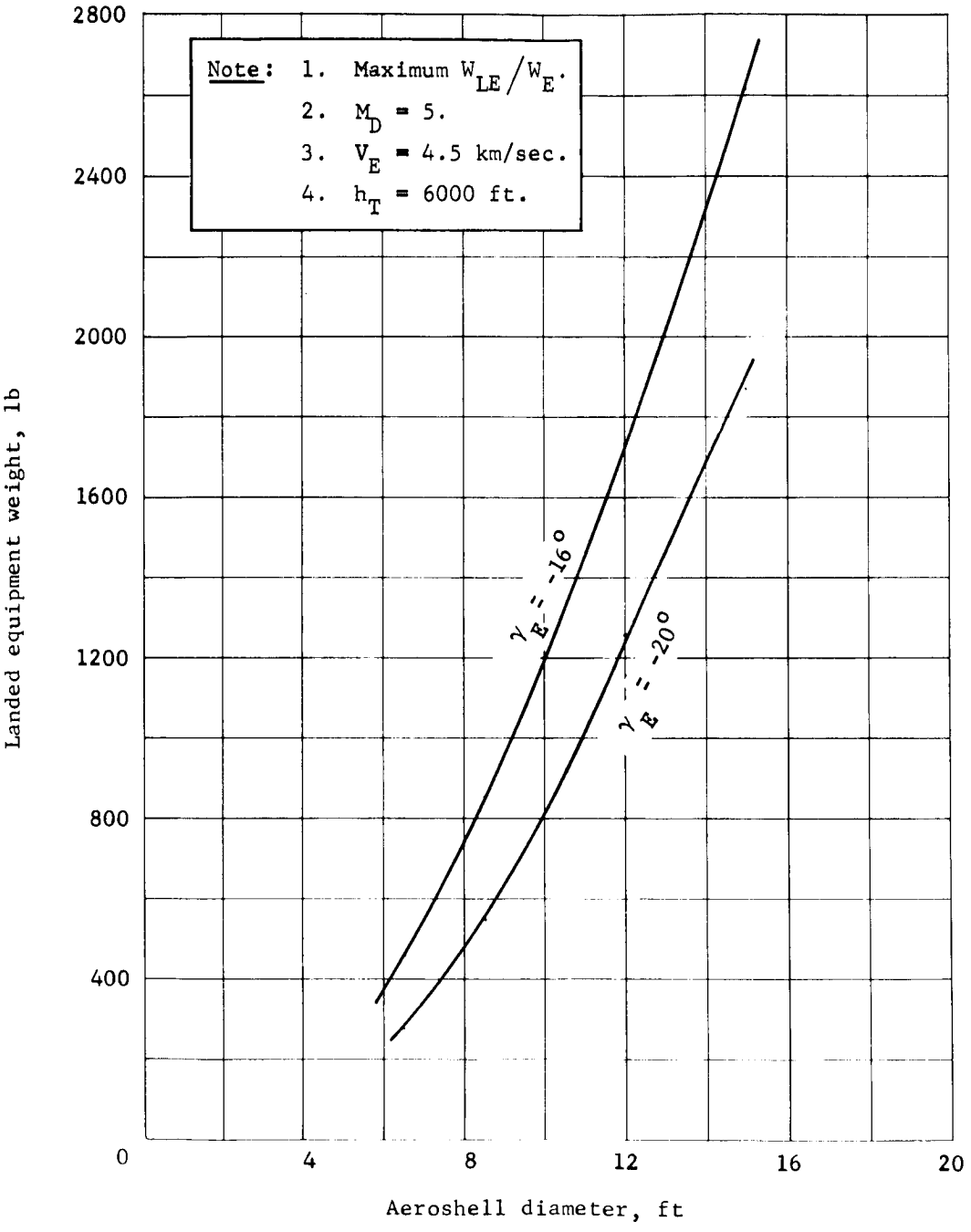

Figure B215.- W_{LE} versus Aeroshell Diameter for Orbit Mode Aerodecelerators

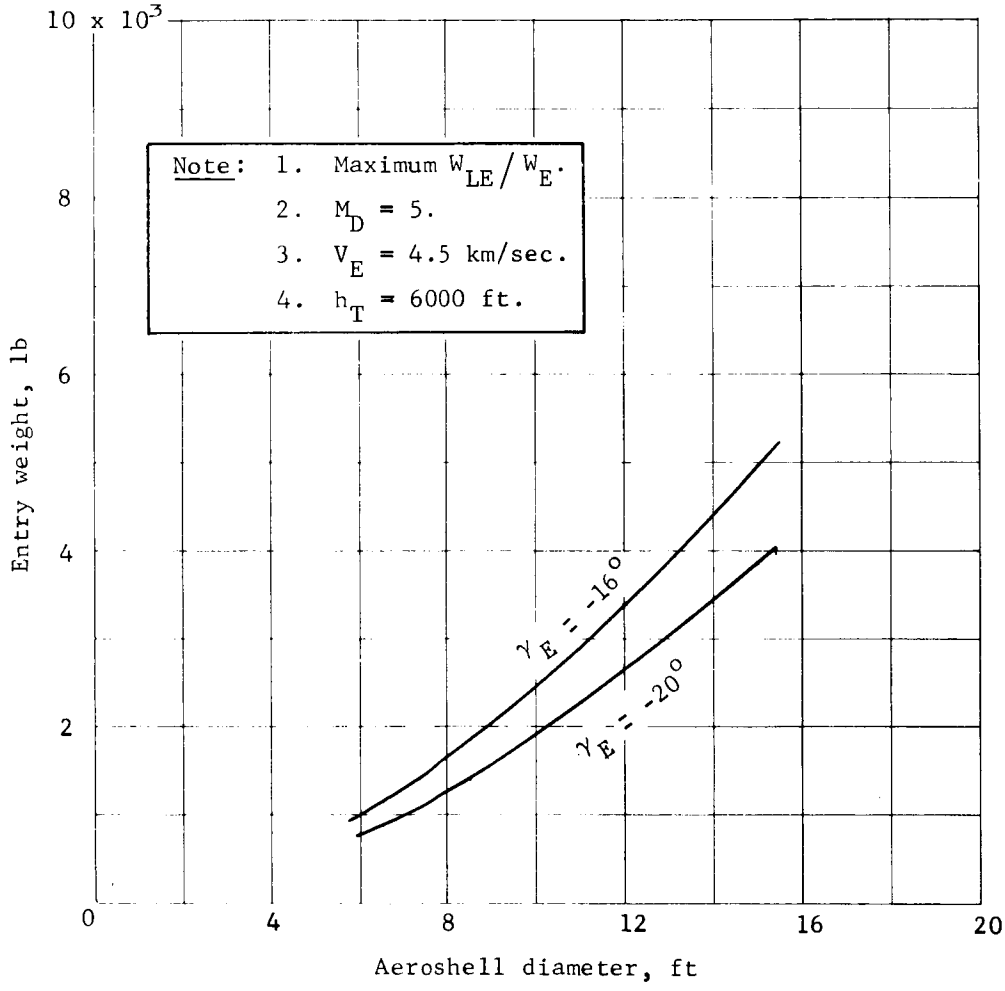

Figure B216.- W_E versus Aeroshell Diameter for Orbit Mode Aerodecelerators

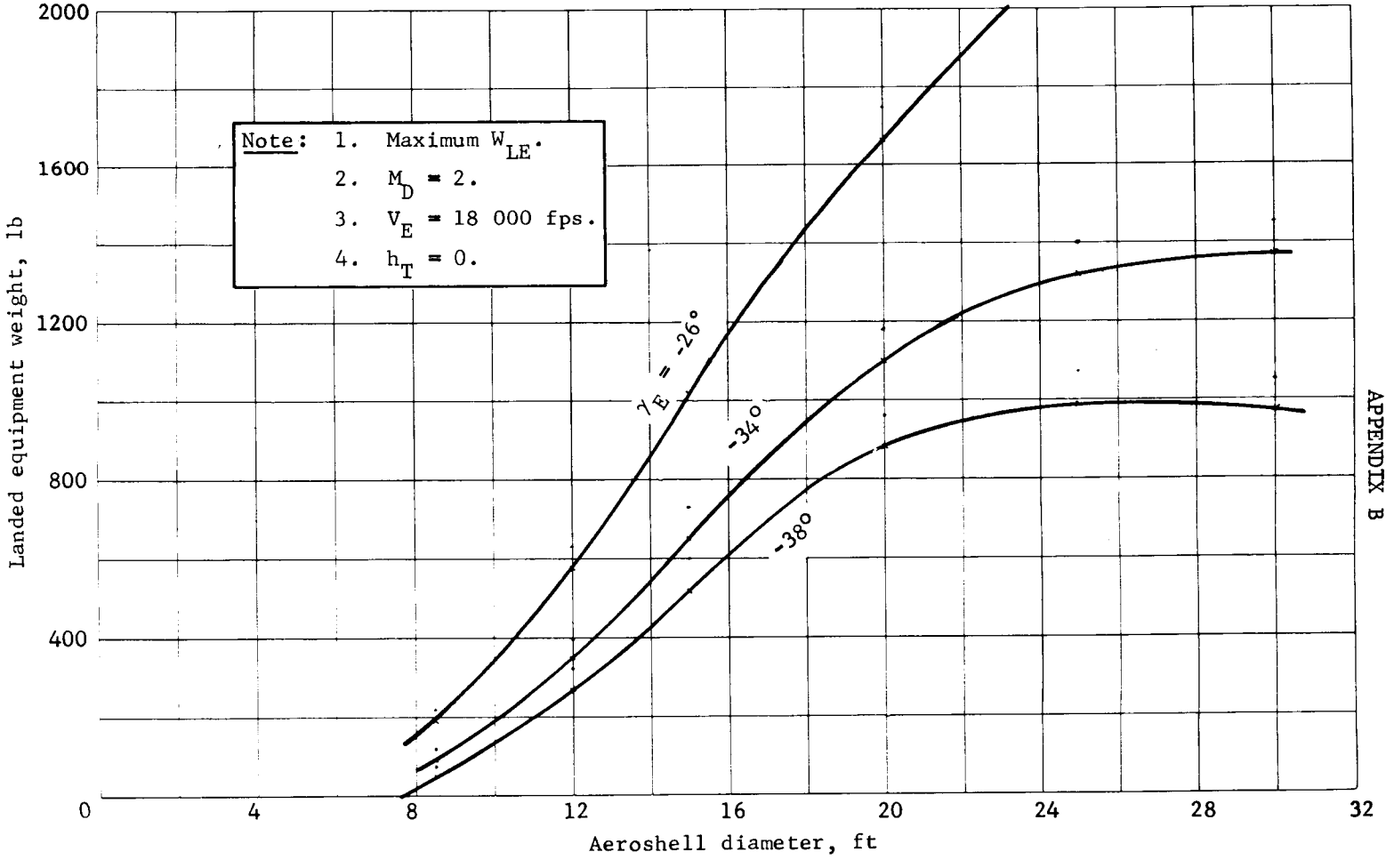

Figure B217.- W_{LE} versus Aeroshell Diameter for Direct Mode

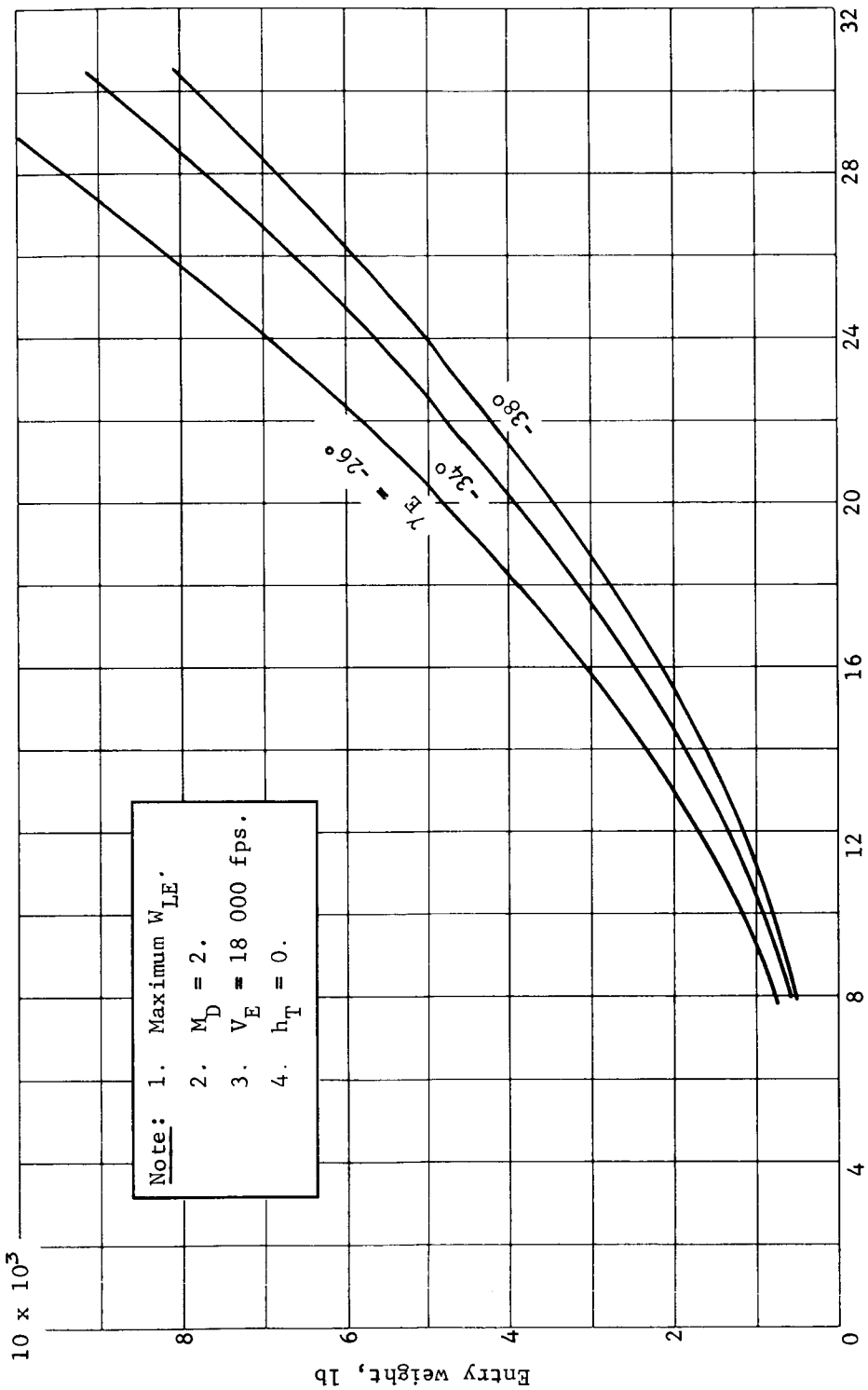

Figure B218.- W_E versus Aeroshell Diameter for Direct Mode

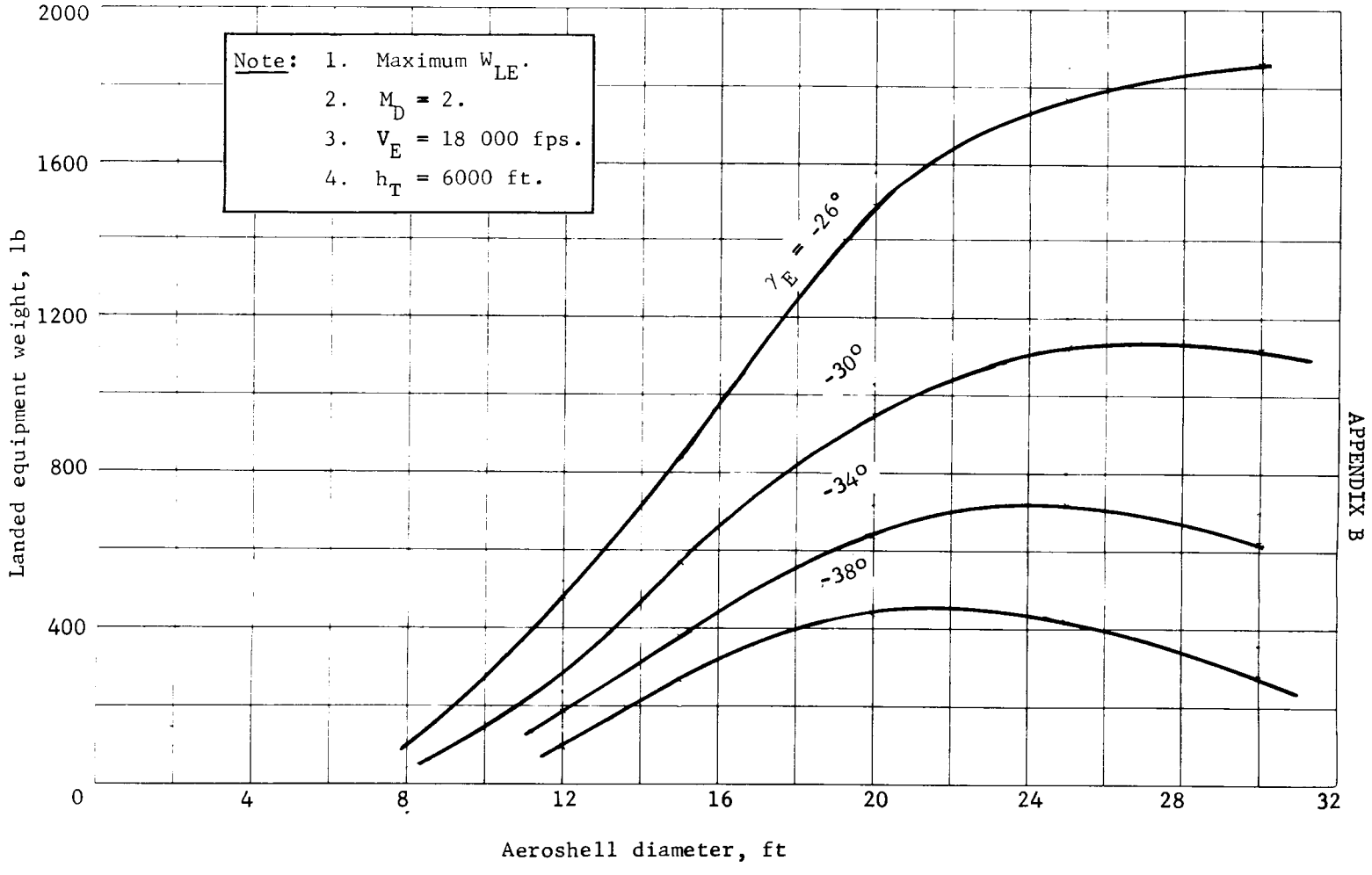

Figure B219.- W_{LE} versus Aeroshell Diameter for Direct Mode

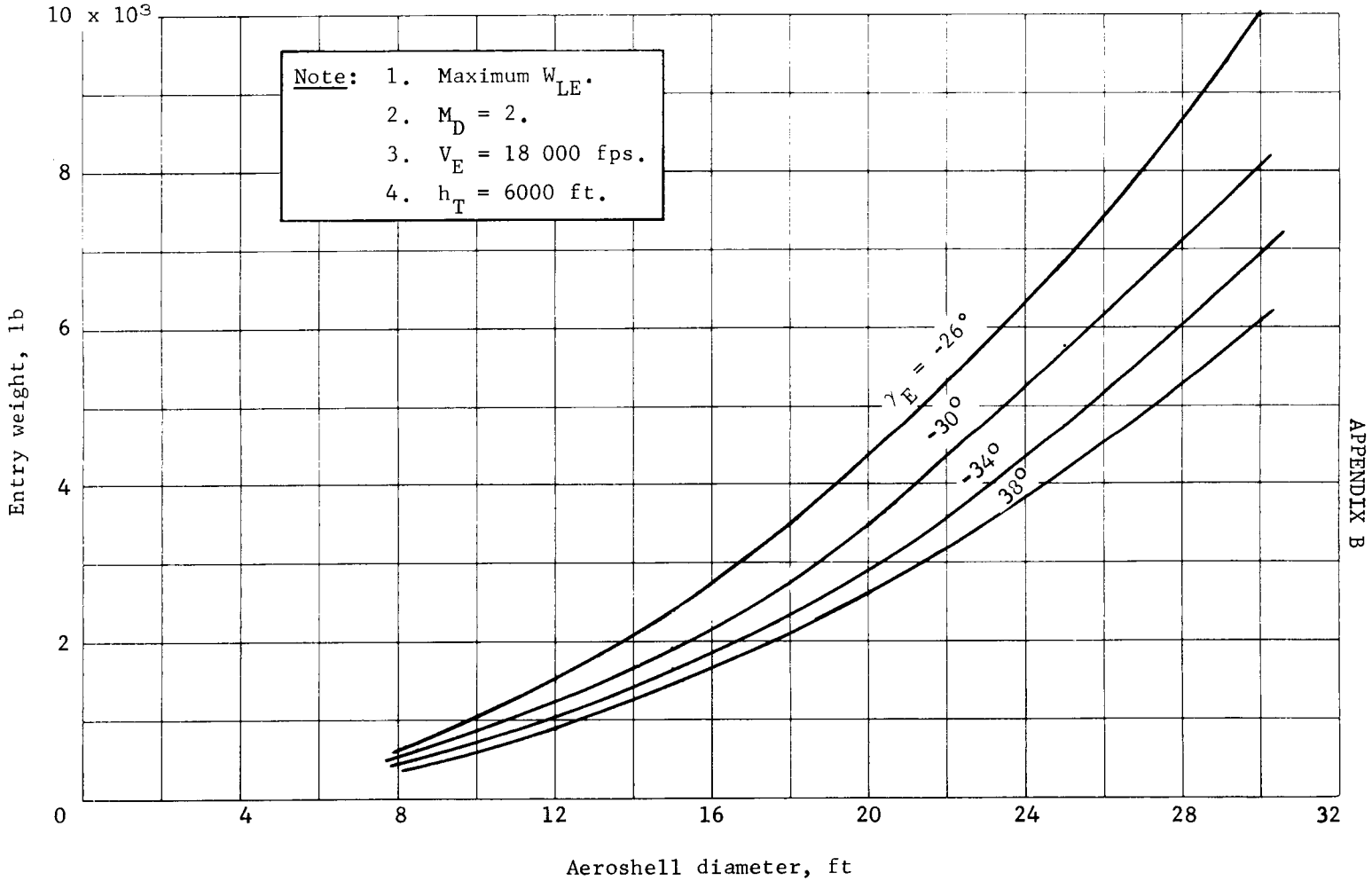

Figure B220.- W_E versus Aeroshell Diameter for Direct Mode

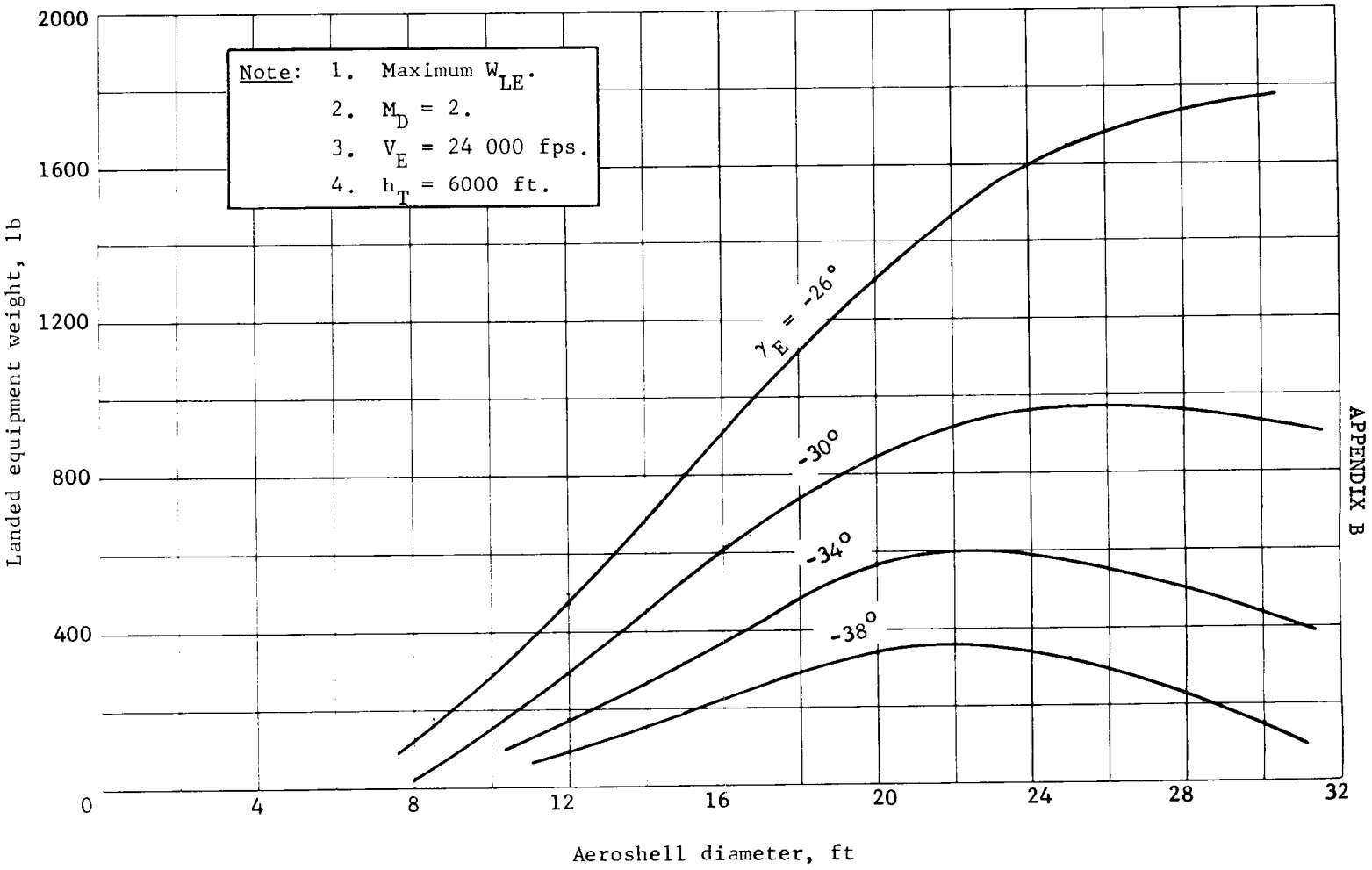

Figure B221.- W_{LE} versus Aeroshell Diameter for Direct Mode

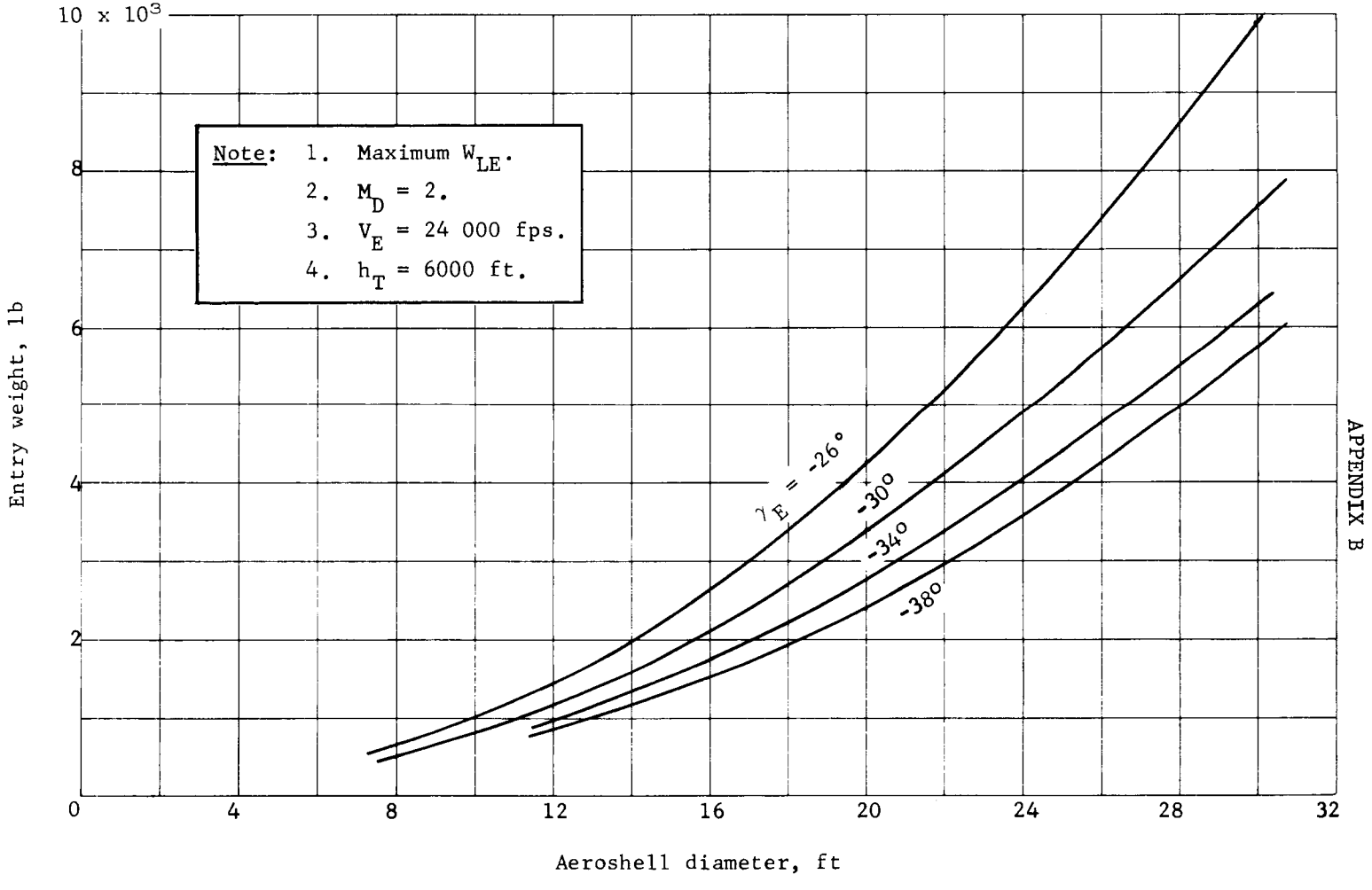

Figure B222.- W_E versus Aeroshell Diameter for Direct Mode

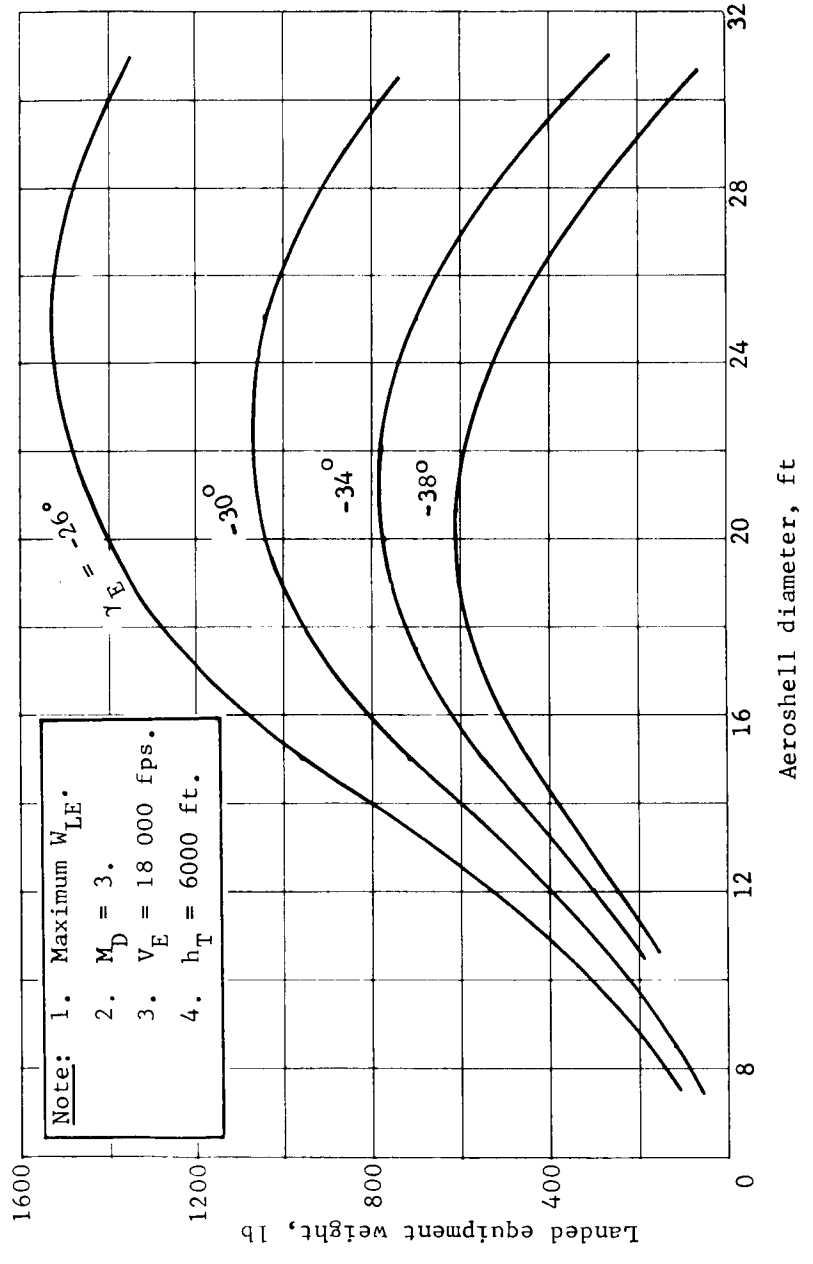

Figure B223.- W_{LE} versus Aeroshell Diameter for Direct Mode

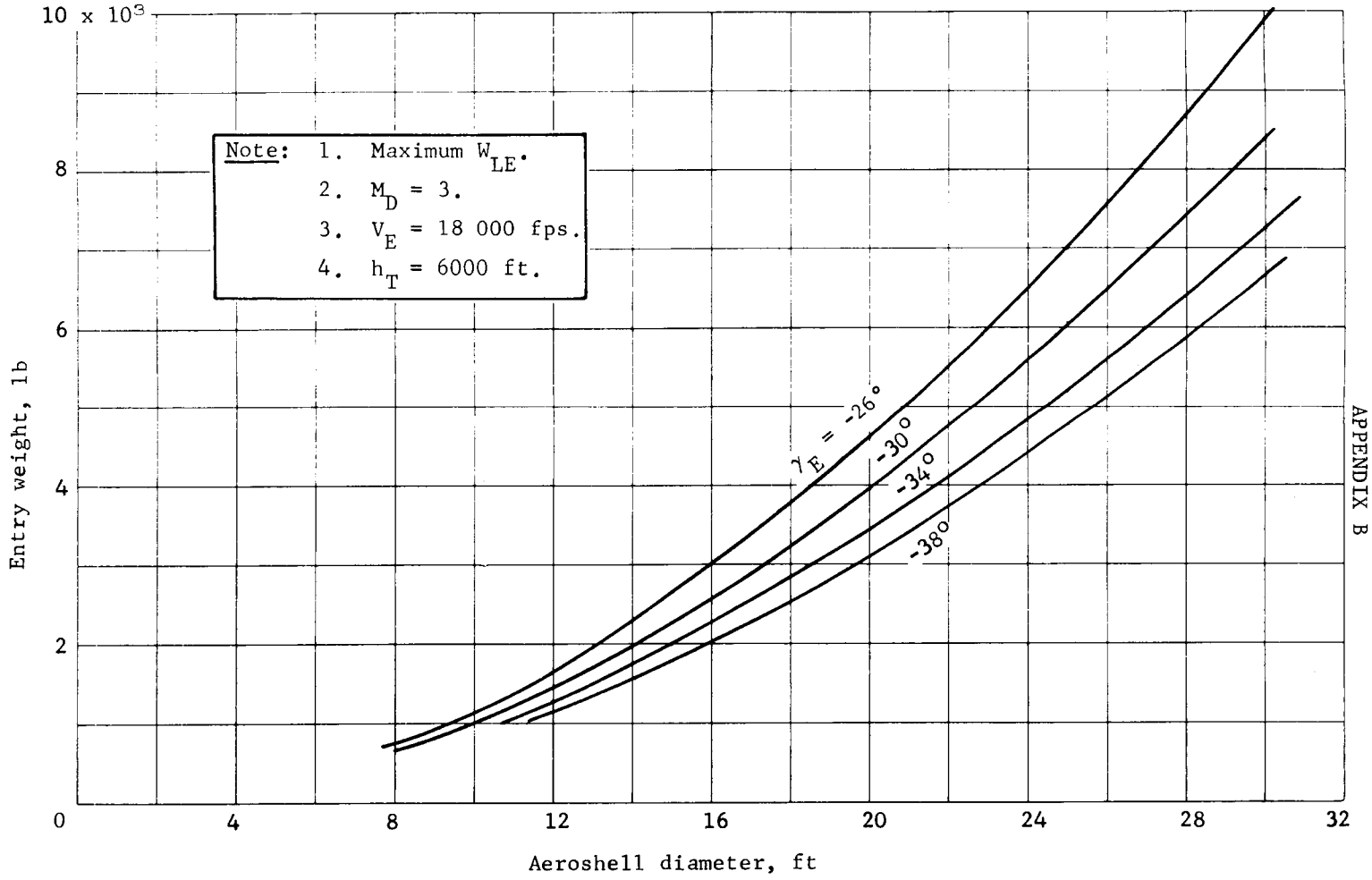

Figure B224.- W_E versus Aeroshell Diameter for Direct Mode

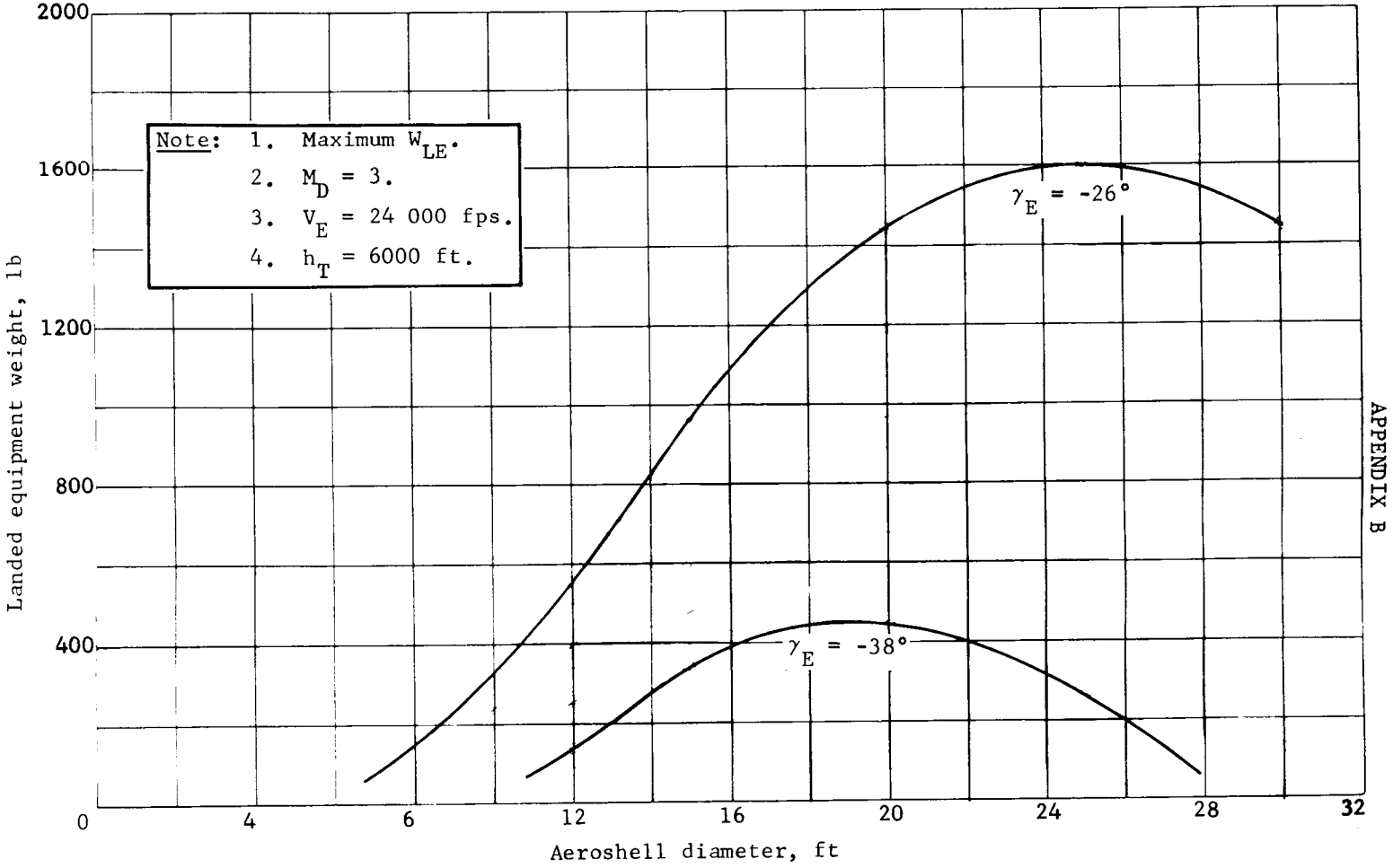

Figure B225.- W_{LE} versus Aeroshell Diameter for Direct Mode

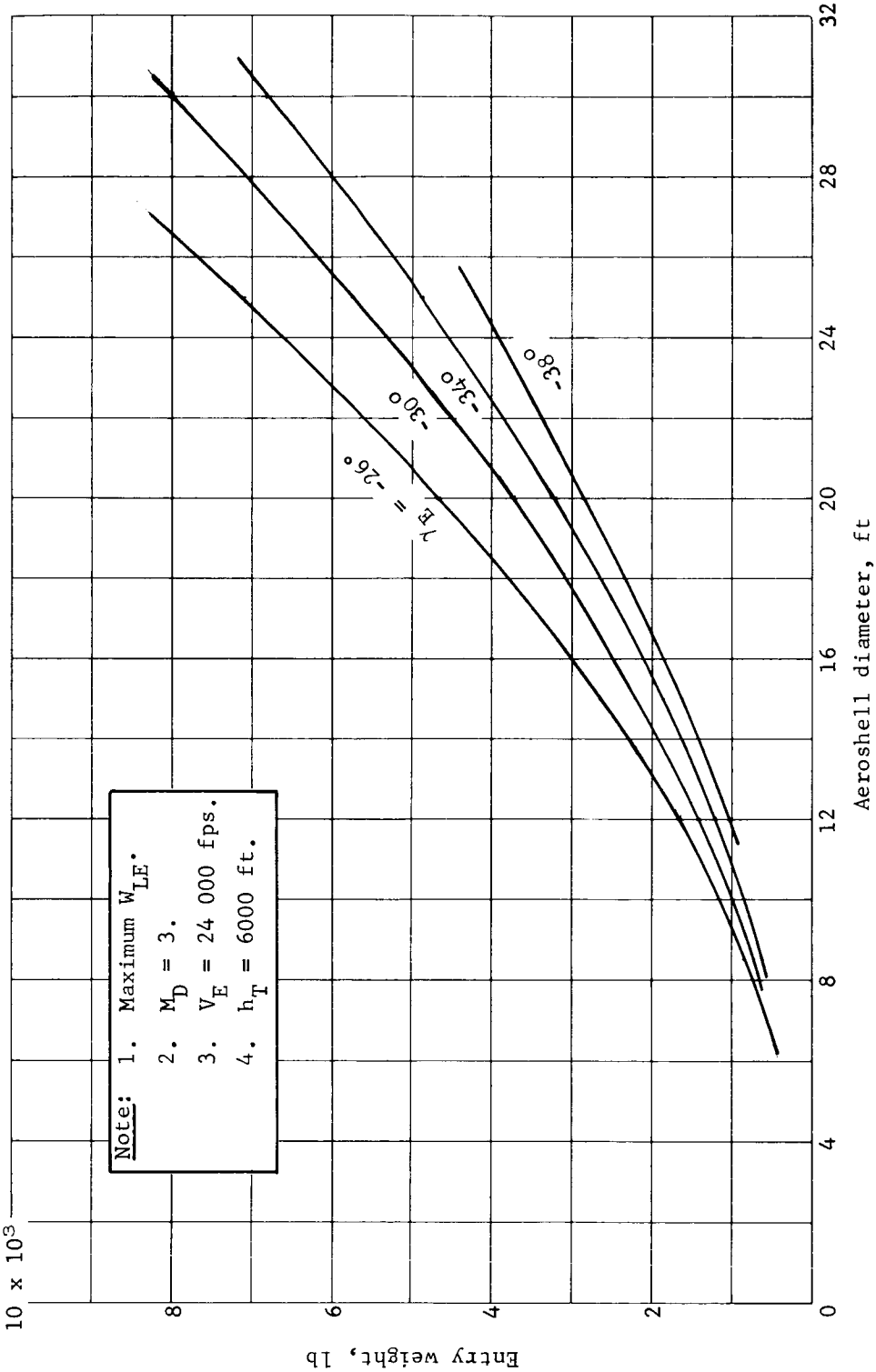

Figure B226.- W_E versus Aeroshell Diameter for Direct Mode

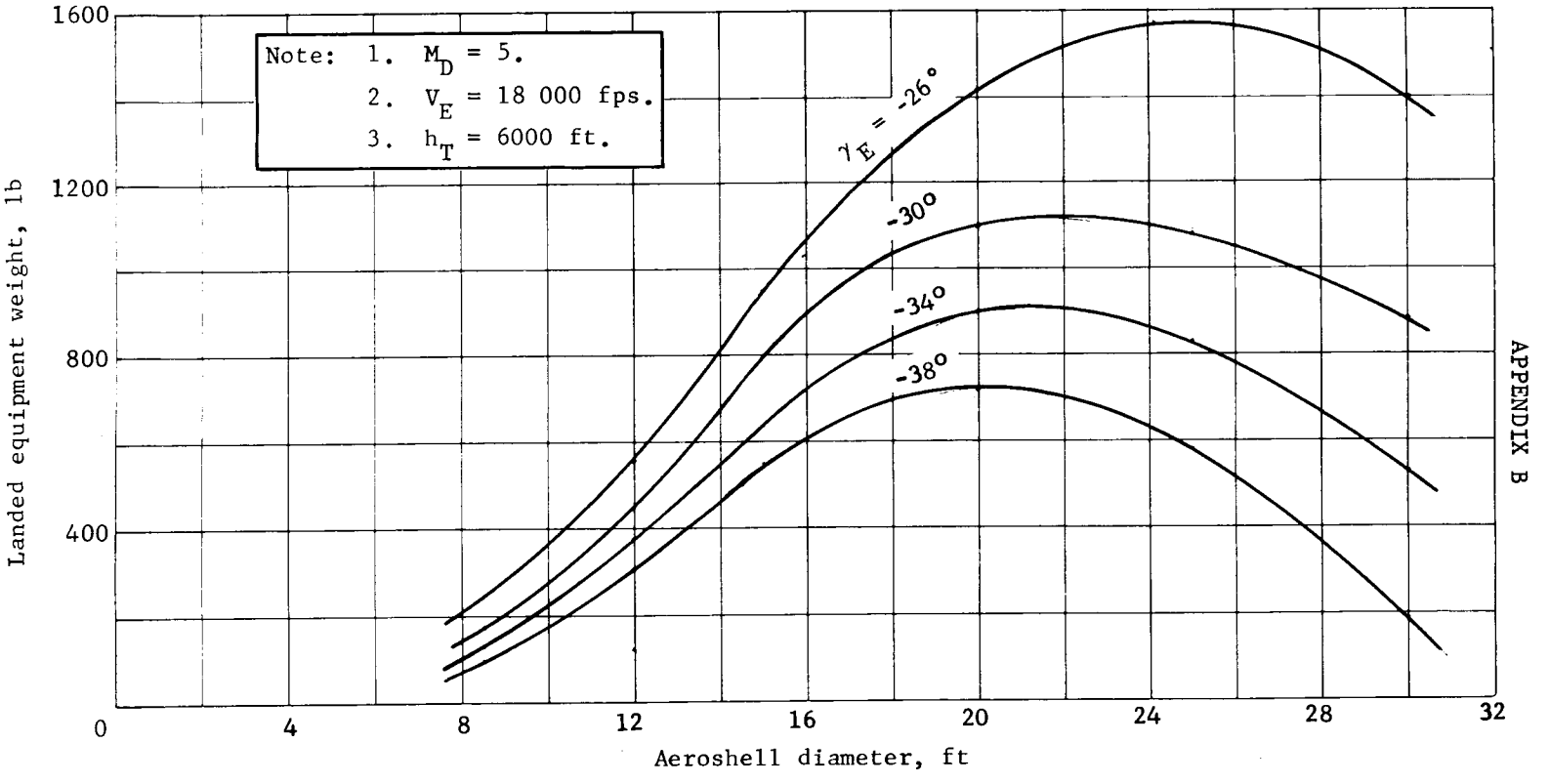

Figure B227.- W_{LE} versus Aeroshell Diameter for Direct Mode

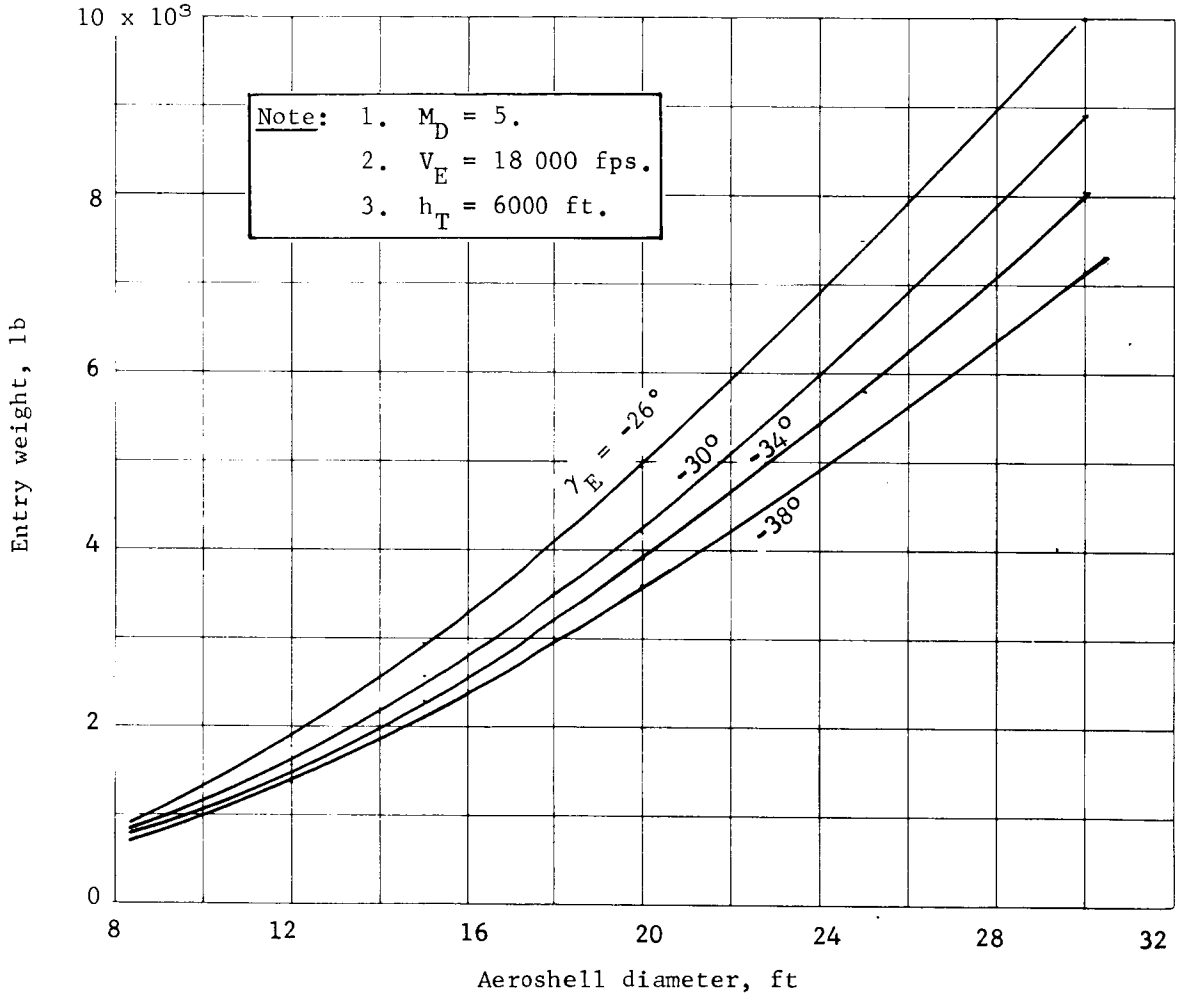

Figure B228.- W_E versus Aeroshell Diameter for Direct Mode

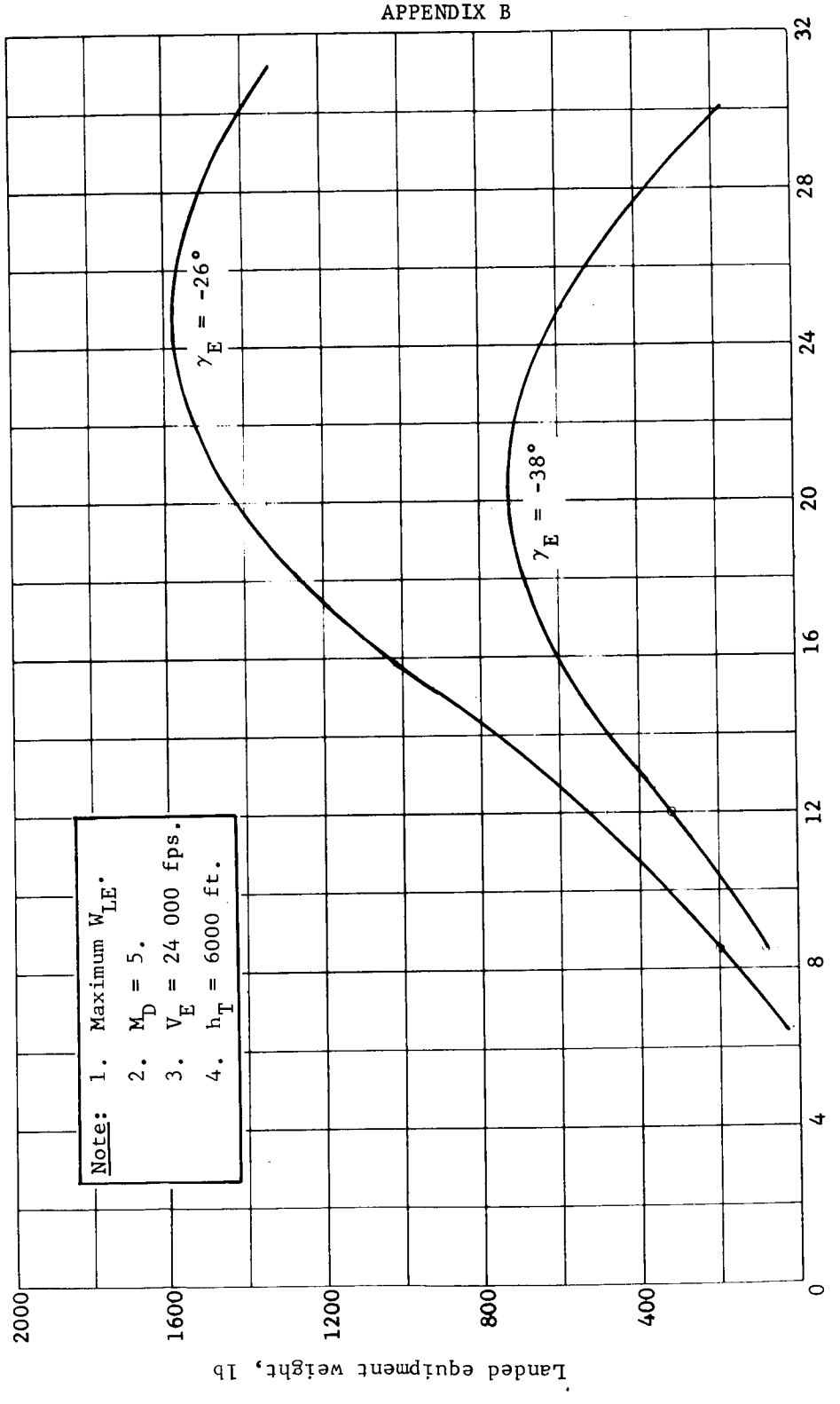

Figure B229.- W_{LE} versus Aeroshell Diameter for Direct Mode

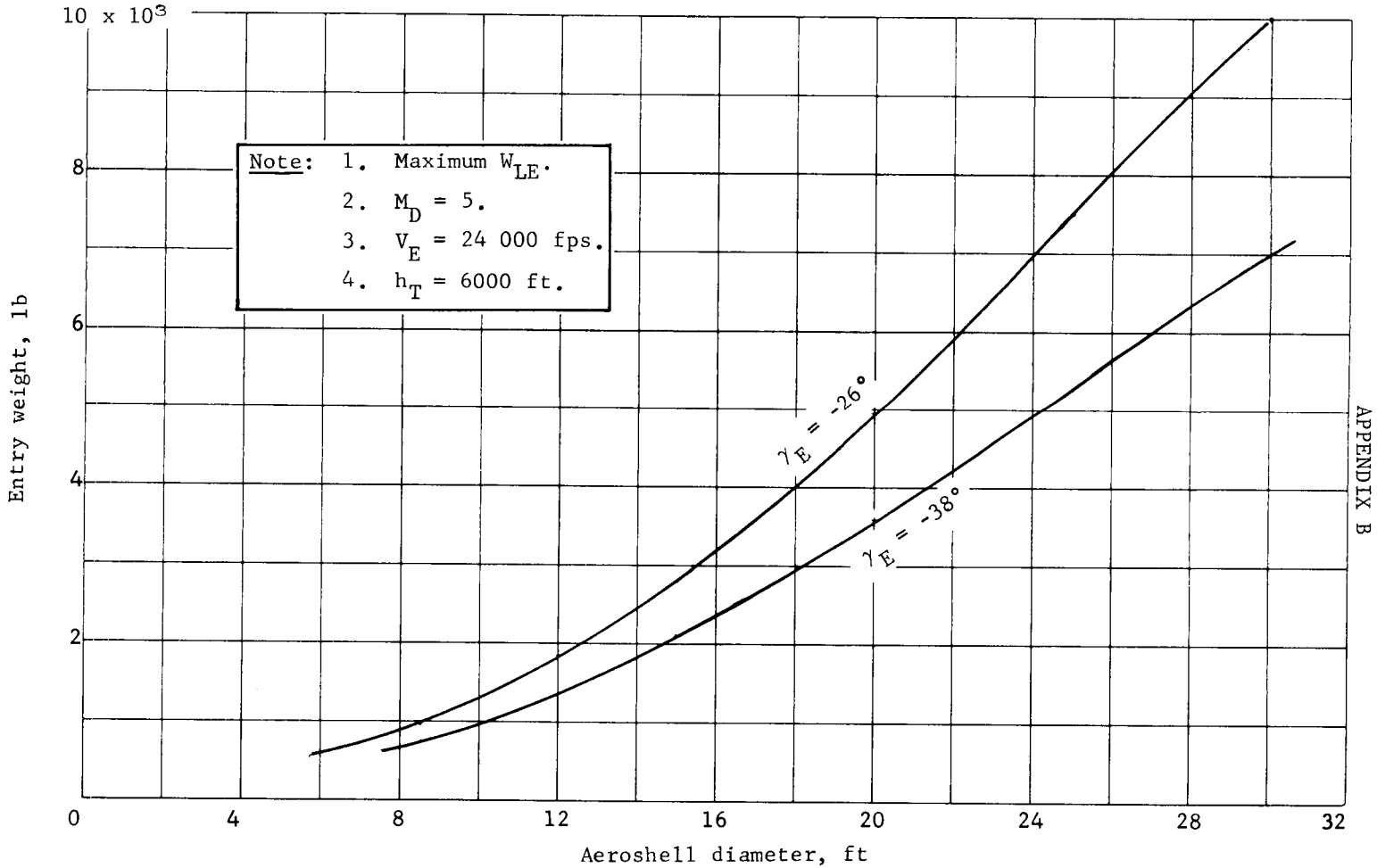

Figure B230.- W_E versus Aeroshell Diameter for Direct Mode

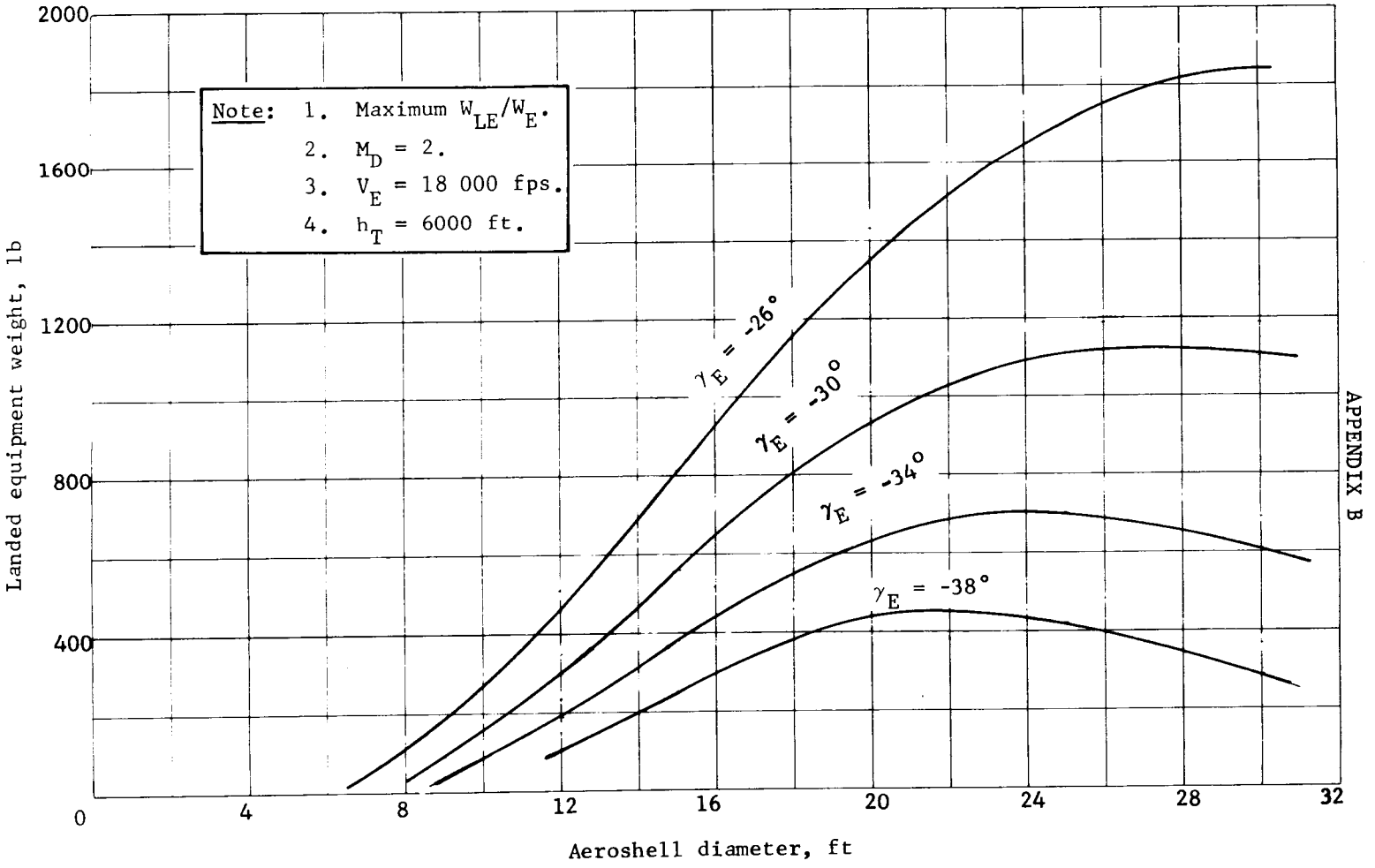

Figure B231.- W_{LE} versus Aeroshell Diameter for Direct Mode

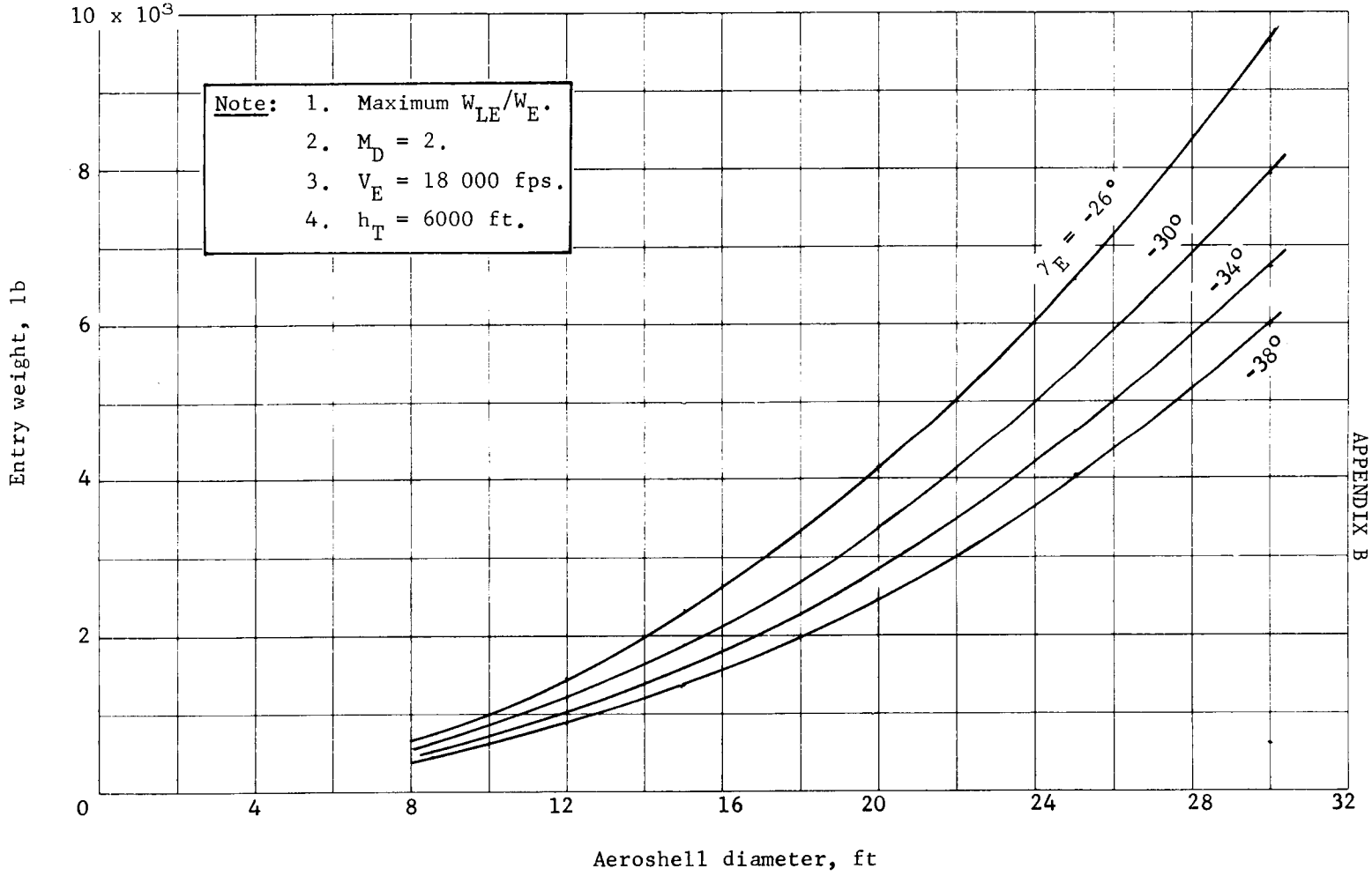

Figure B232.- W_E versus Aeroshell Diameter for Direct Mode

APPENDIX B

Figures B233 and B234 show the effect of terrain height on maximum landed equipment weight. For the orbit mode and a 12-ft diameter aeroshell in figure B233, a zero terrain height yields about 250 to 400 lb more payload than h_T = 6000 ft. The difderence in payload is more pronounced at γ_E = -16° than γ_E = -20°. For the direct mode in figure B234, the difference in payload at 12-ft diameter is about 100 to 200 lb. Notice the higher γ_E of -38° shows the greater difference in payload. The effect of entry angle on maximum landed equipment weight is shown by many of the preceding figures. It shows that increasing entry angle is a powerful factor in decreasing landed equipment. This conclusion could be considered true of all conditions both orbital and direct. However, figure B234 shows that increasing terrain height is also an important factor in reducing landed equipment weight and must be considered in design studies. Another parameter to be considered is entry velocity. For the small range of entry velocities for the orbit mode (14 000 to 16 000 fps), that effect is small. The effect of entry velocity for the direct mode is shown in figure B235. The figure shows that for aeroshell diameters greater than 12 ft an entry velocity of 18 000 fps yields landed equipment weights about 200 lb greater than for 24 000 fps.

Plots of landed equipment weight and entry versus aeroshell diameter for the single-stage retro are shown in figures B236 thru B241. Curves of constant thrust to initial mass and B_E have been plotted. The landed equipment weights should be considered a maximum for the particular F/M_o shown. Plots of the F/M_o used in weight calculations for each aeroshell diameters are shown in figures B242 thru B245.

Figure B246 compares the retro with flaps and the inflatable afterbody/retro at V_E = 18 000 fps and γ_E = -30°. It may be seen that the flaps have a clear advantage over the inflatable afterbodies. This is also true at other entry conditions.

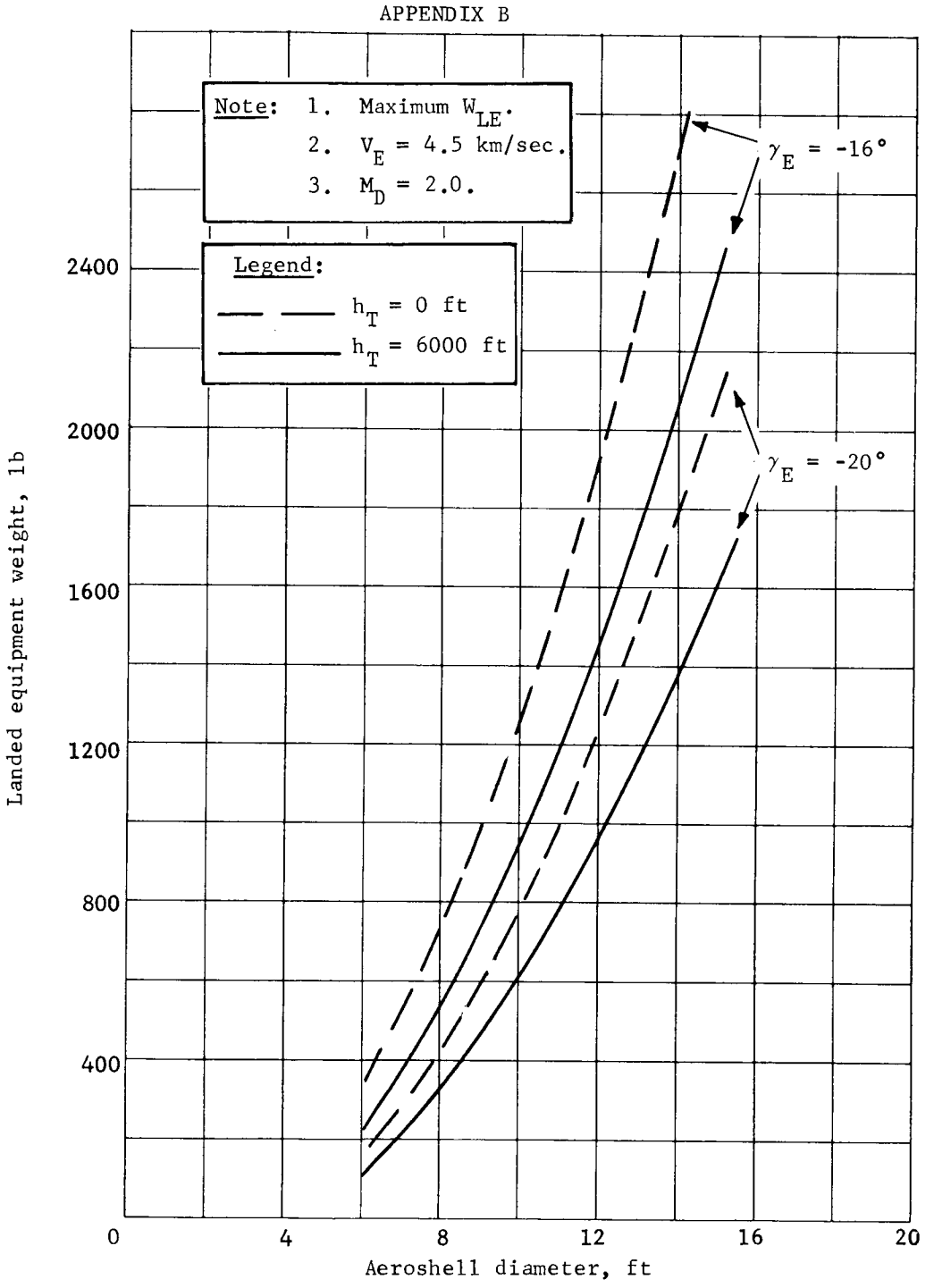

Figure B233.- Effect of Terrain Height

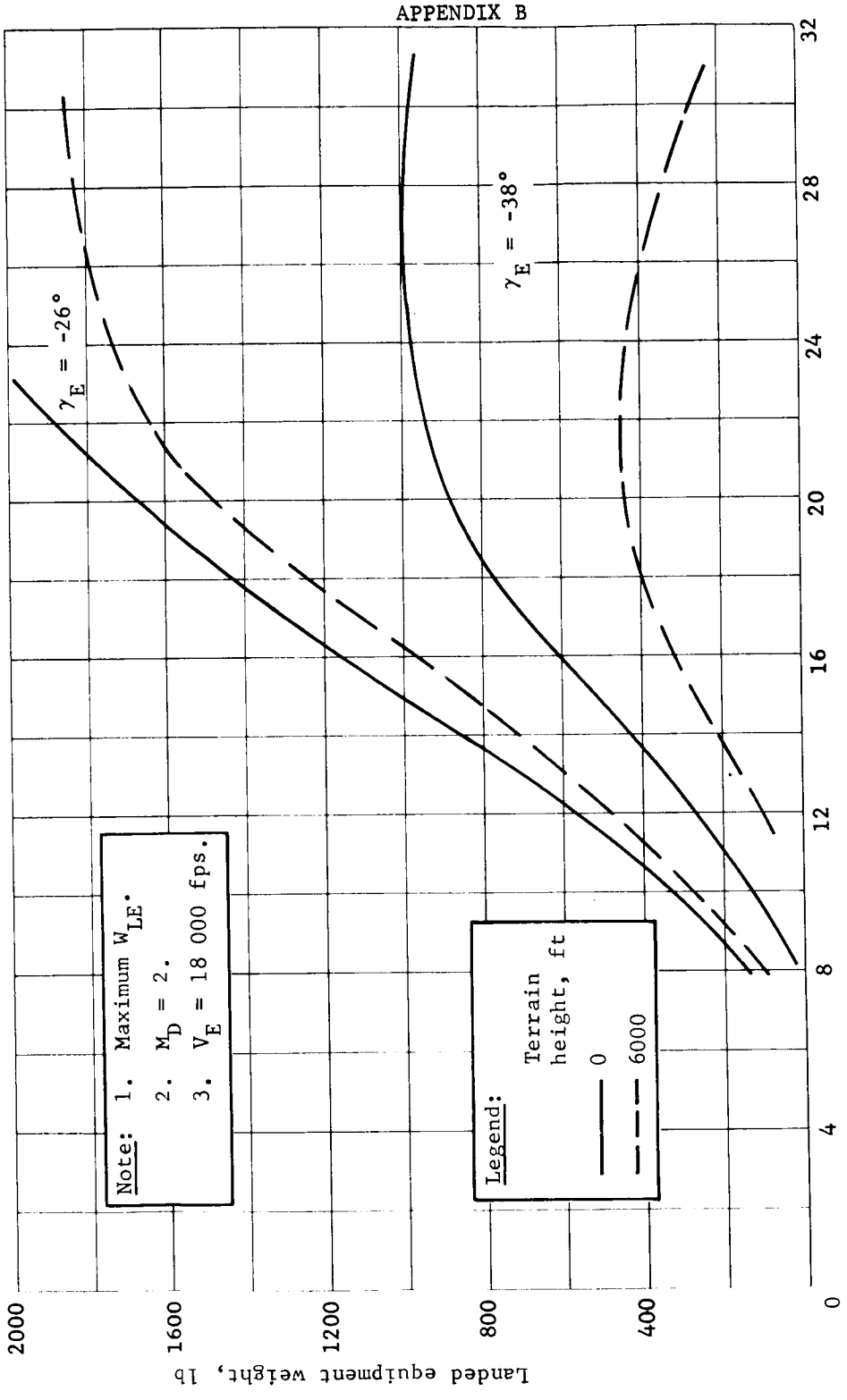

Figure B234.- Effect of Terrain Height

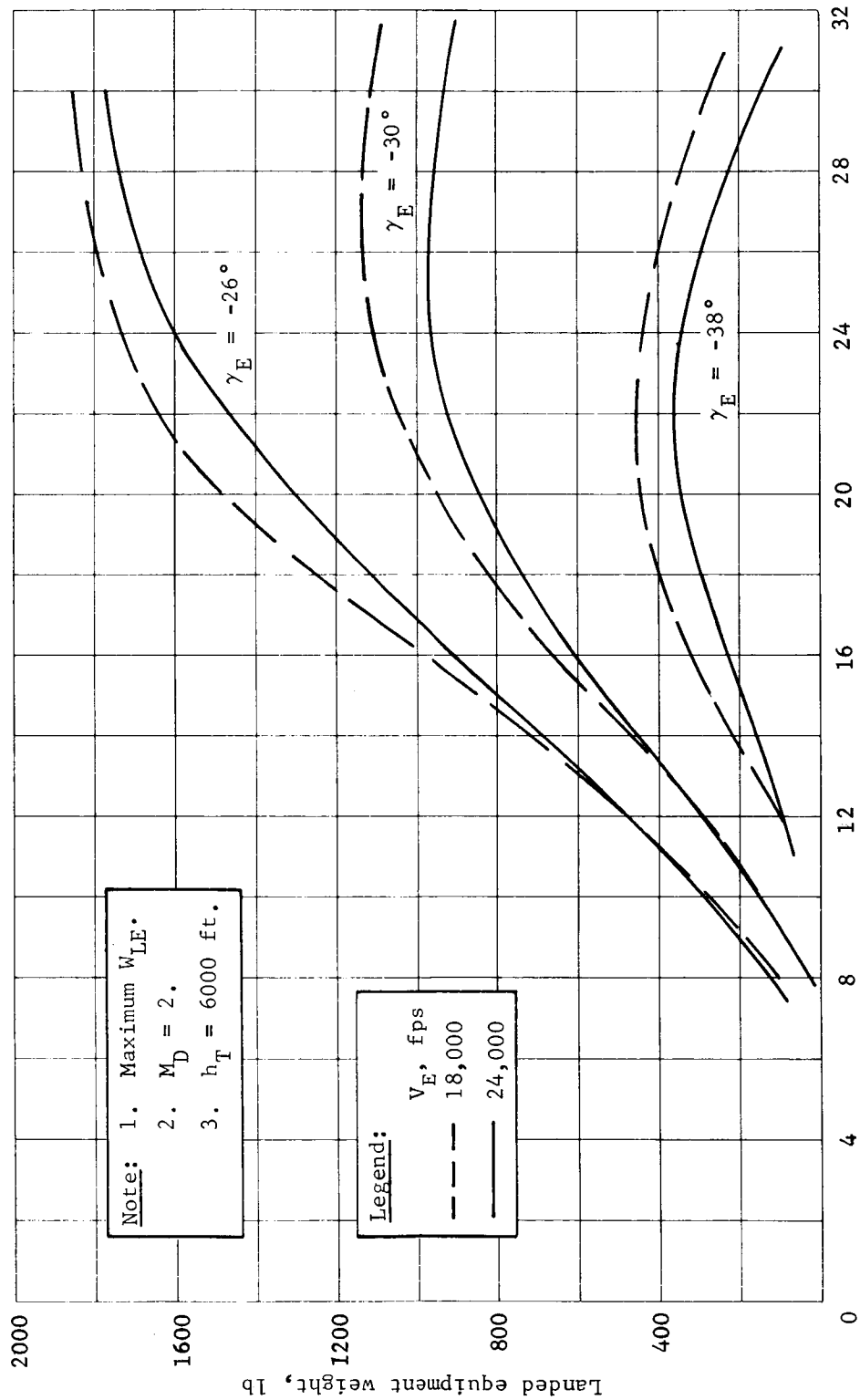

Figure B235.- Effect of Entry Velocity

APPENDIX B

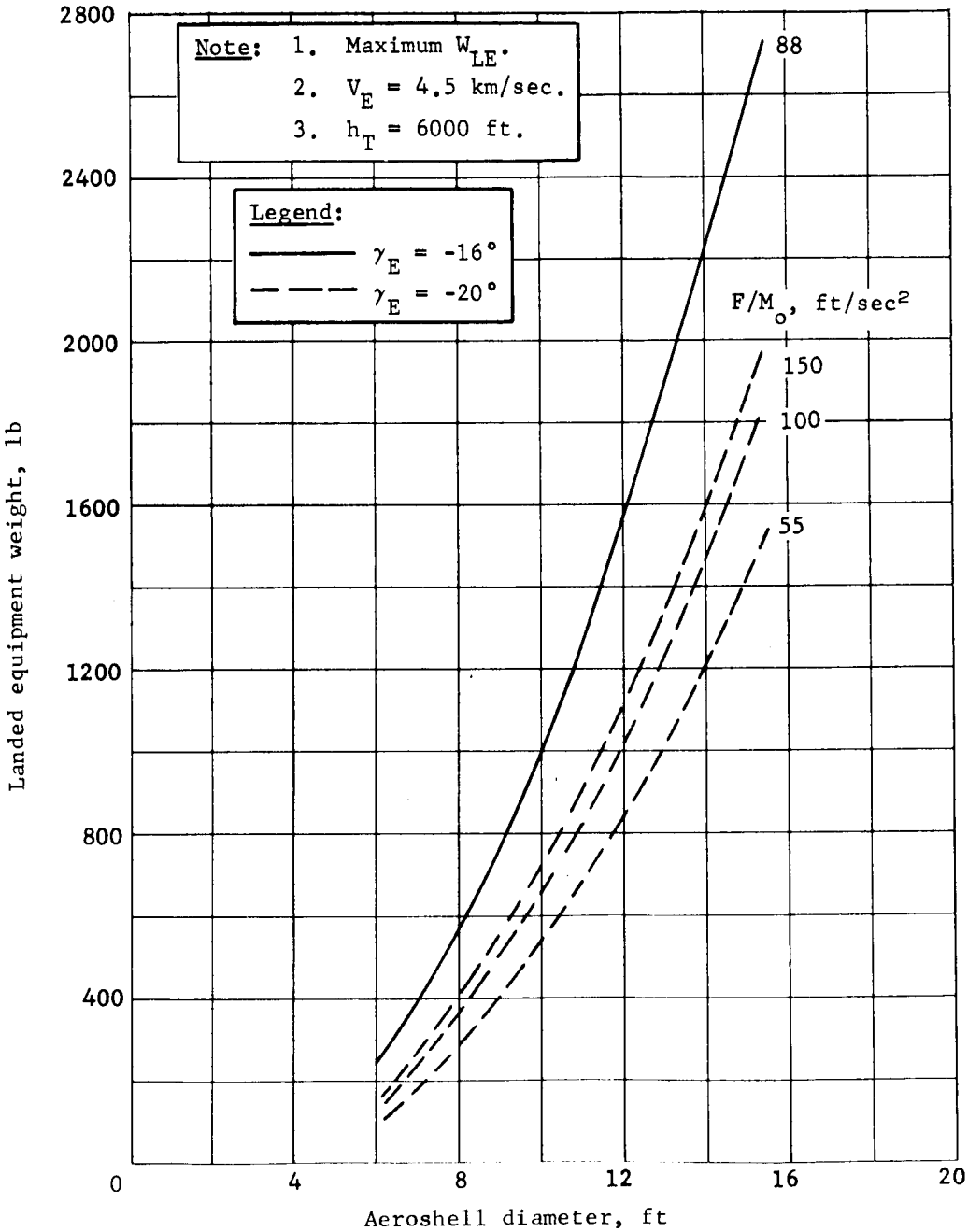

Figure B236.- Retrodecelerator, Entry from Orbit

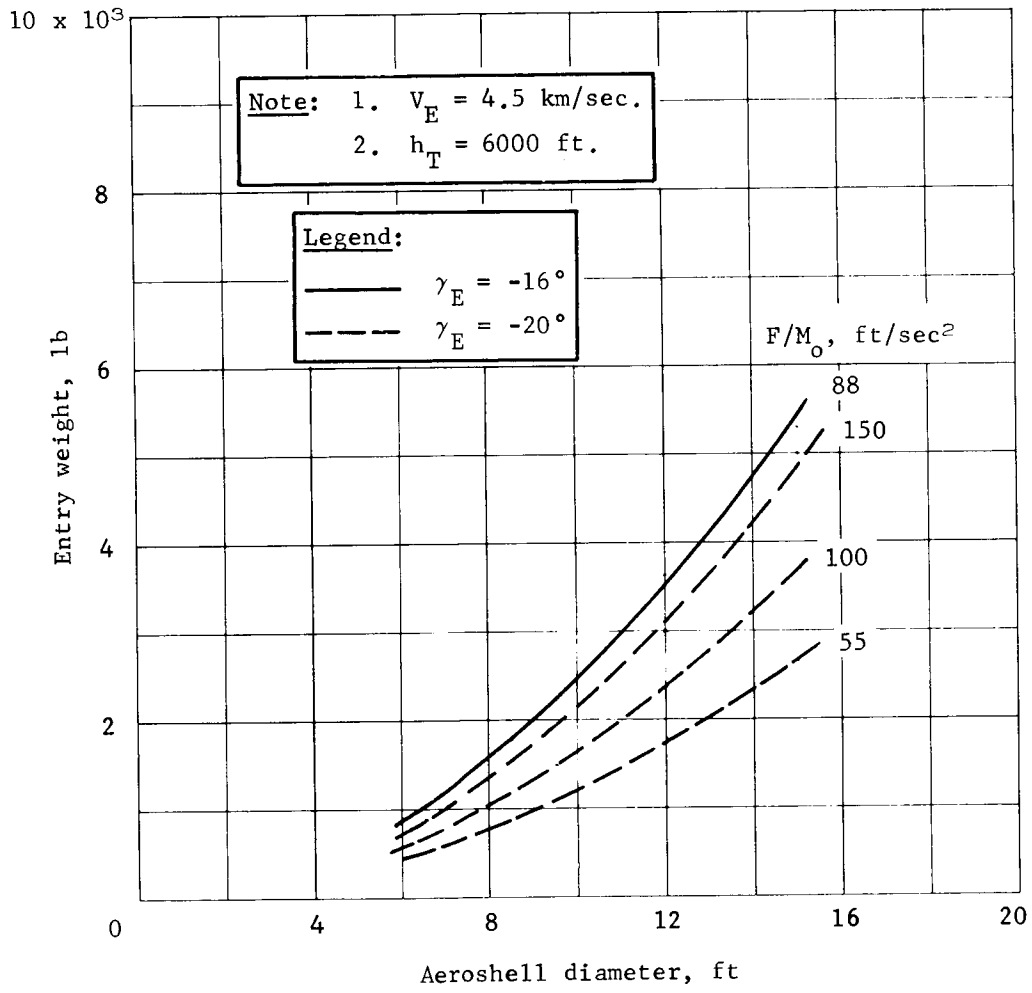

Figure B237.- Retrodecelerator, Entry from Orbit

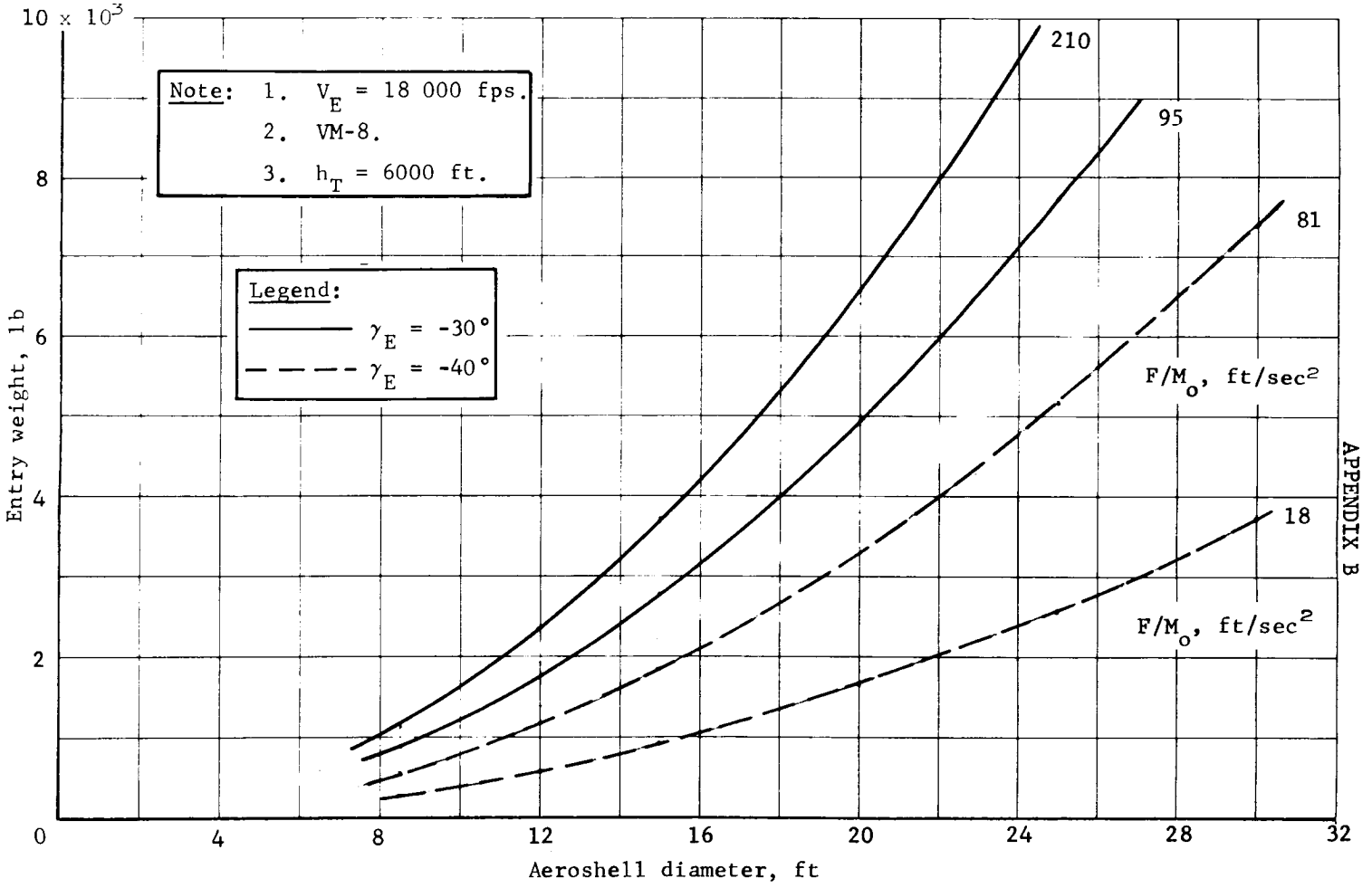

Figure B238.- Retrodecelerator, Direct Entry

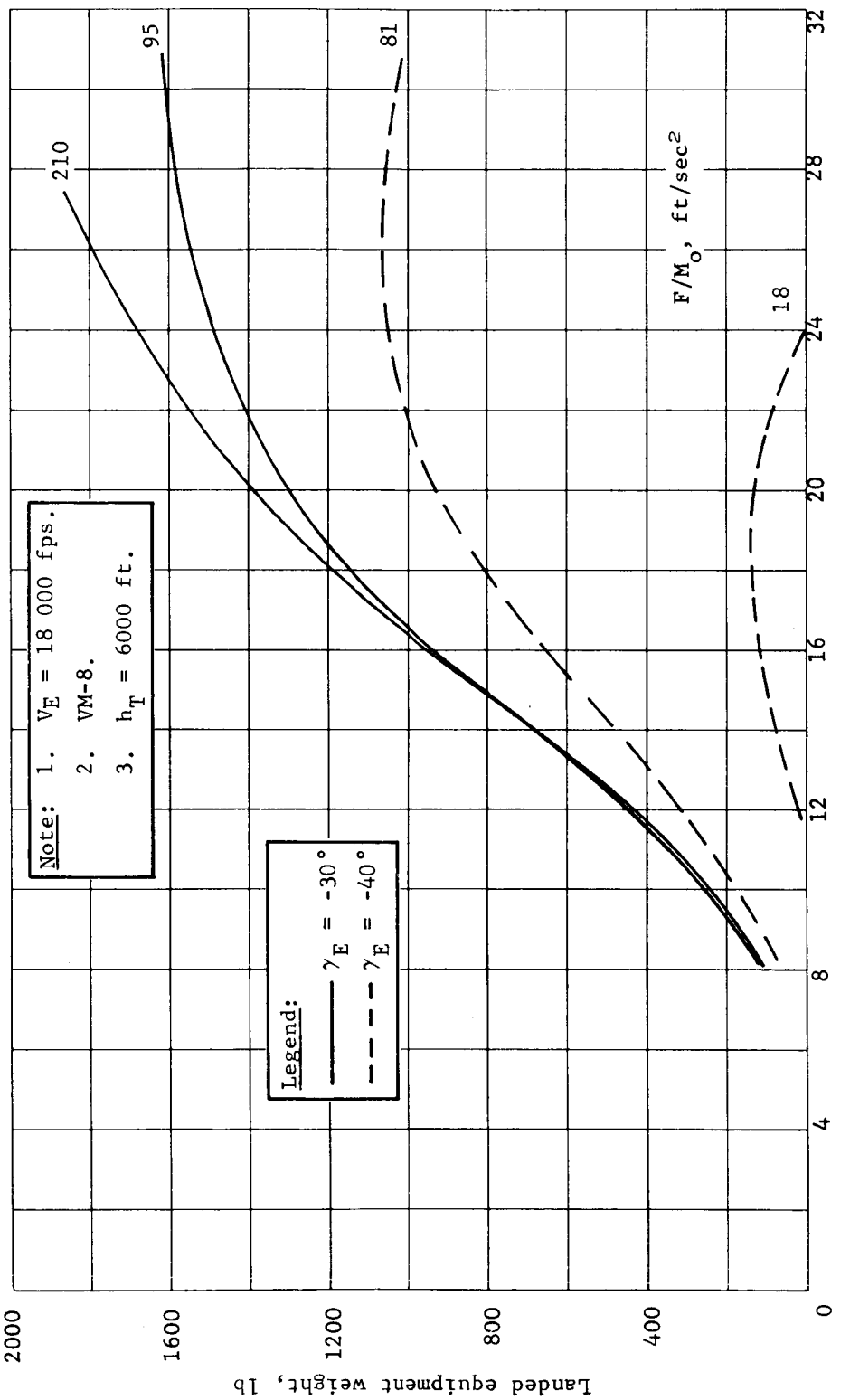

Figure B239.- Retrodecelerator, Direct Entry

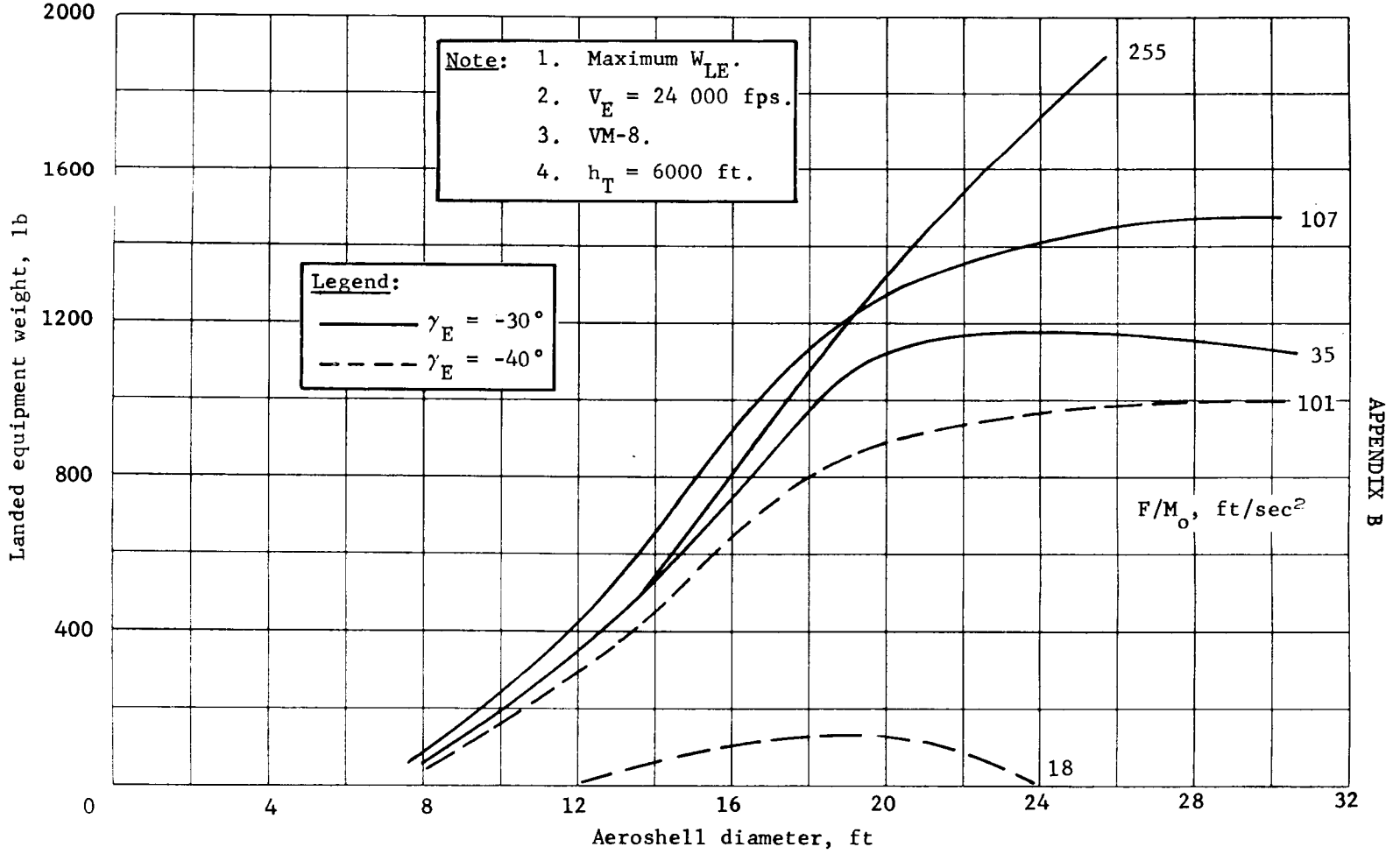

Figure B240.- Retrodecelerator, Direct Entry

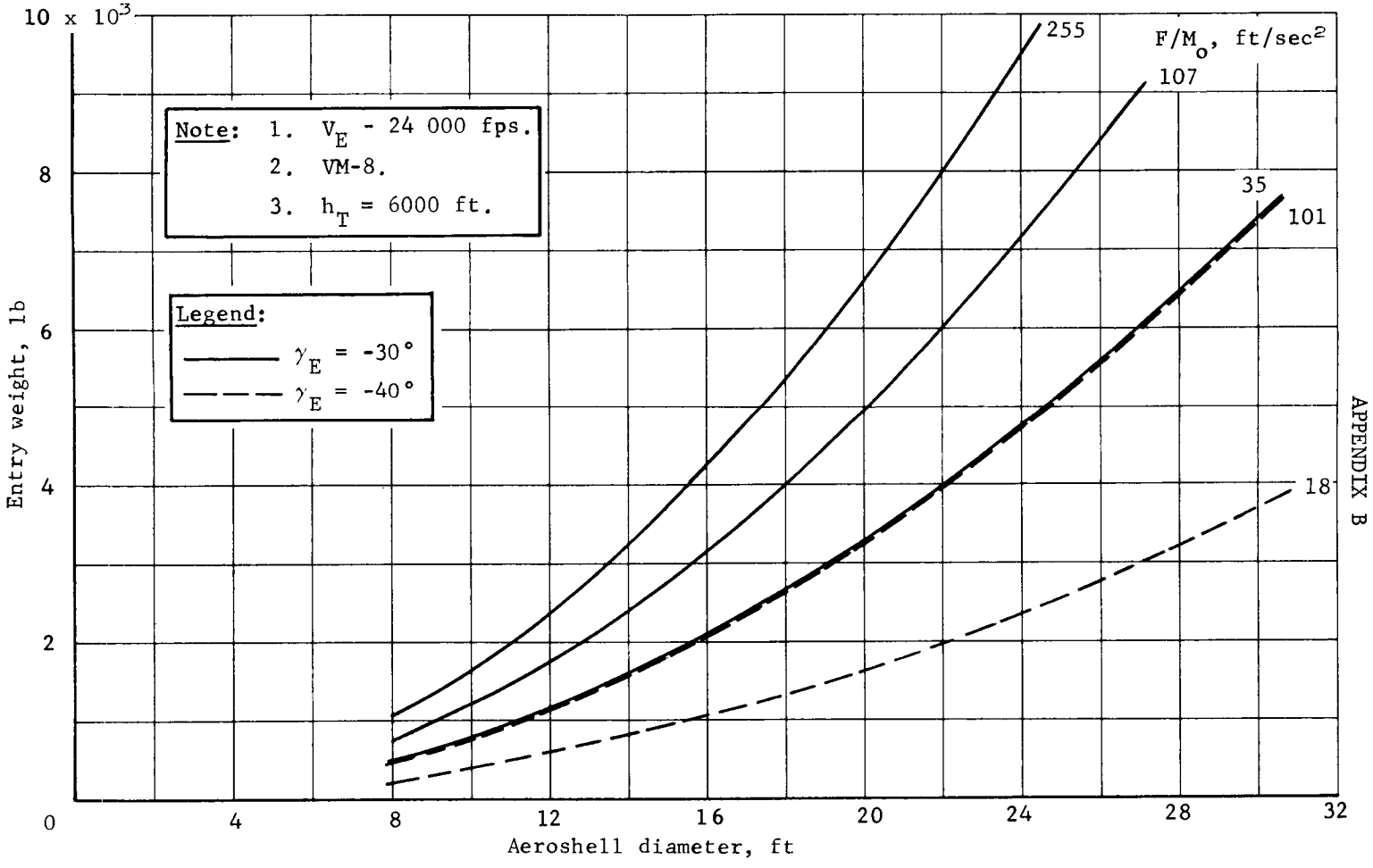

Figure B241.- Retrodecelerator, Direct Entry

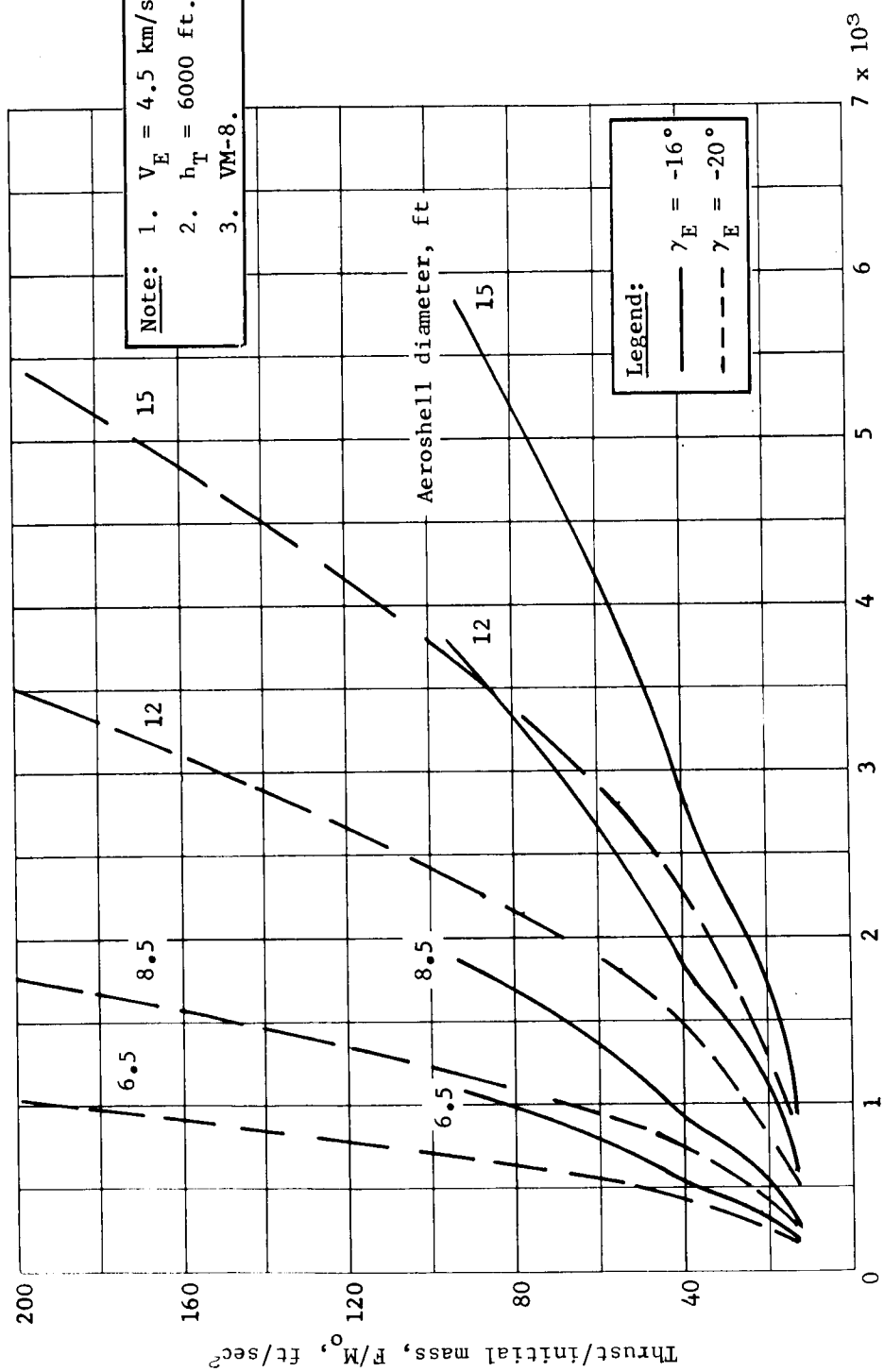

Figure B242.- Retrothrust/Initial Mass

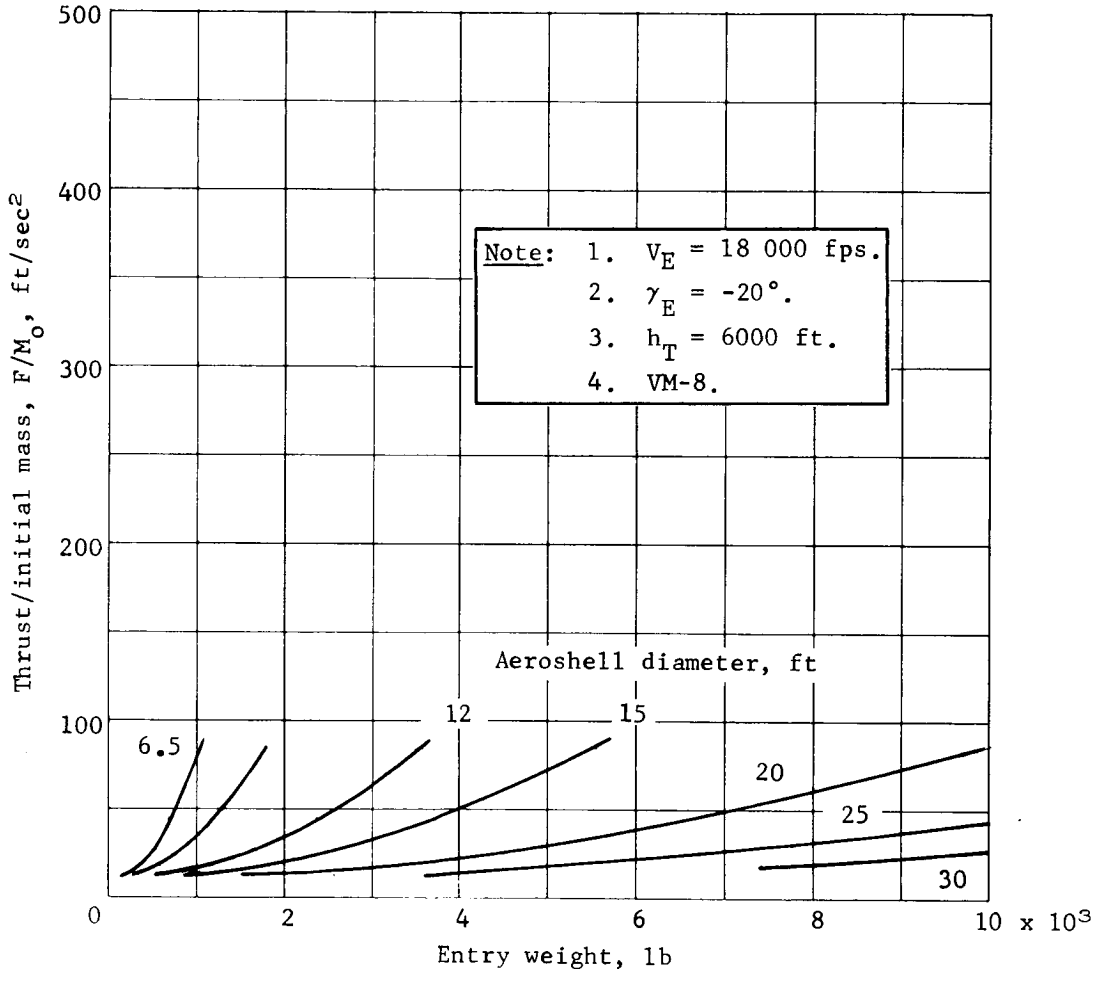

Figure B243.- Retrothrust/Initial Mass

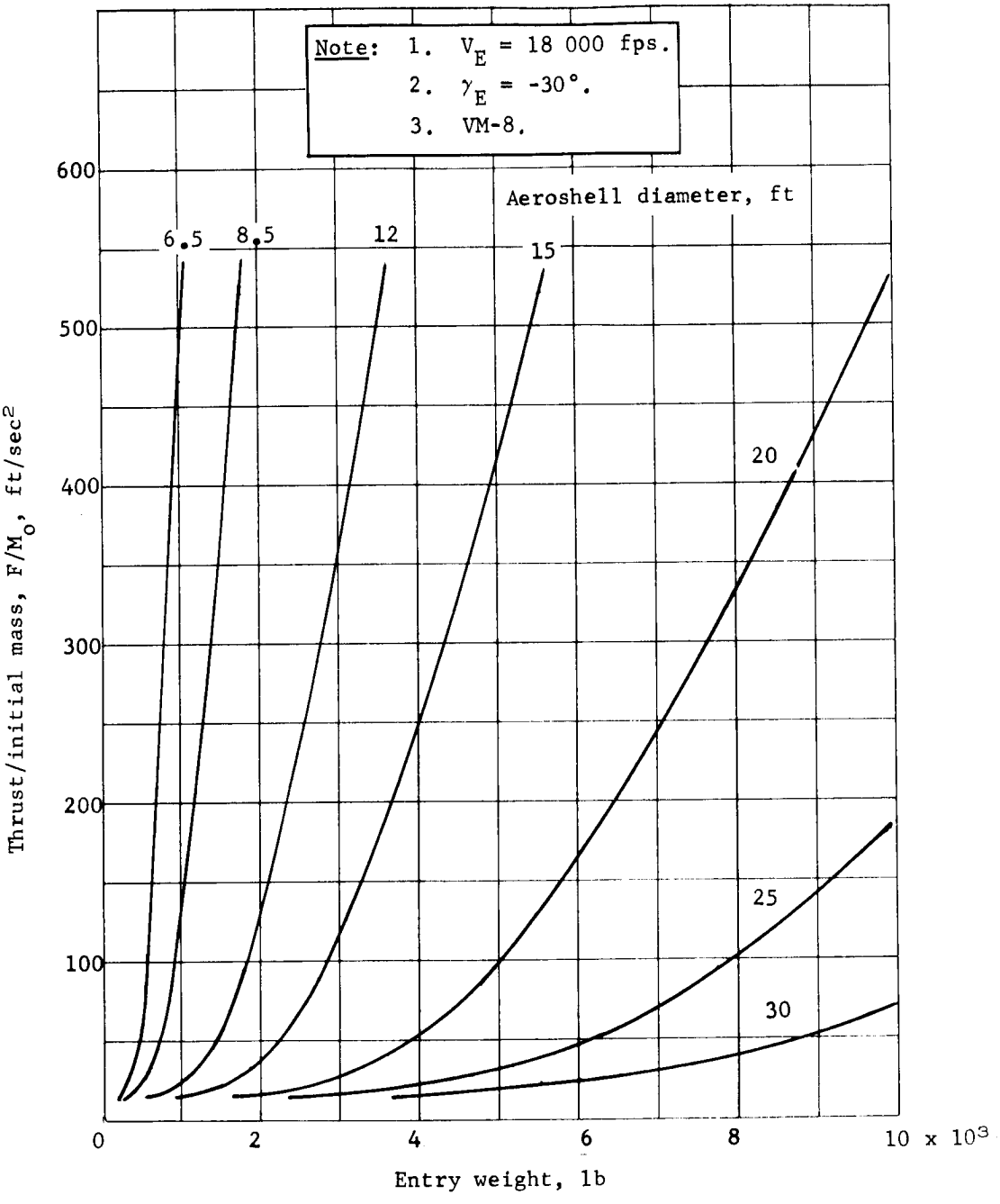

Figure B244.- Retrothrust/Initial Mass

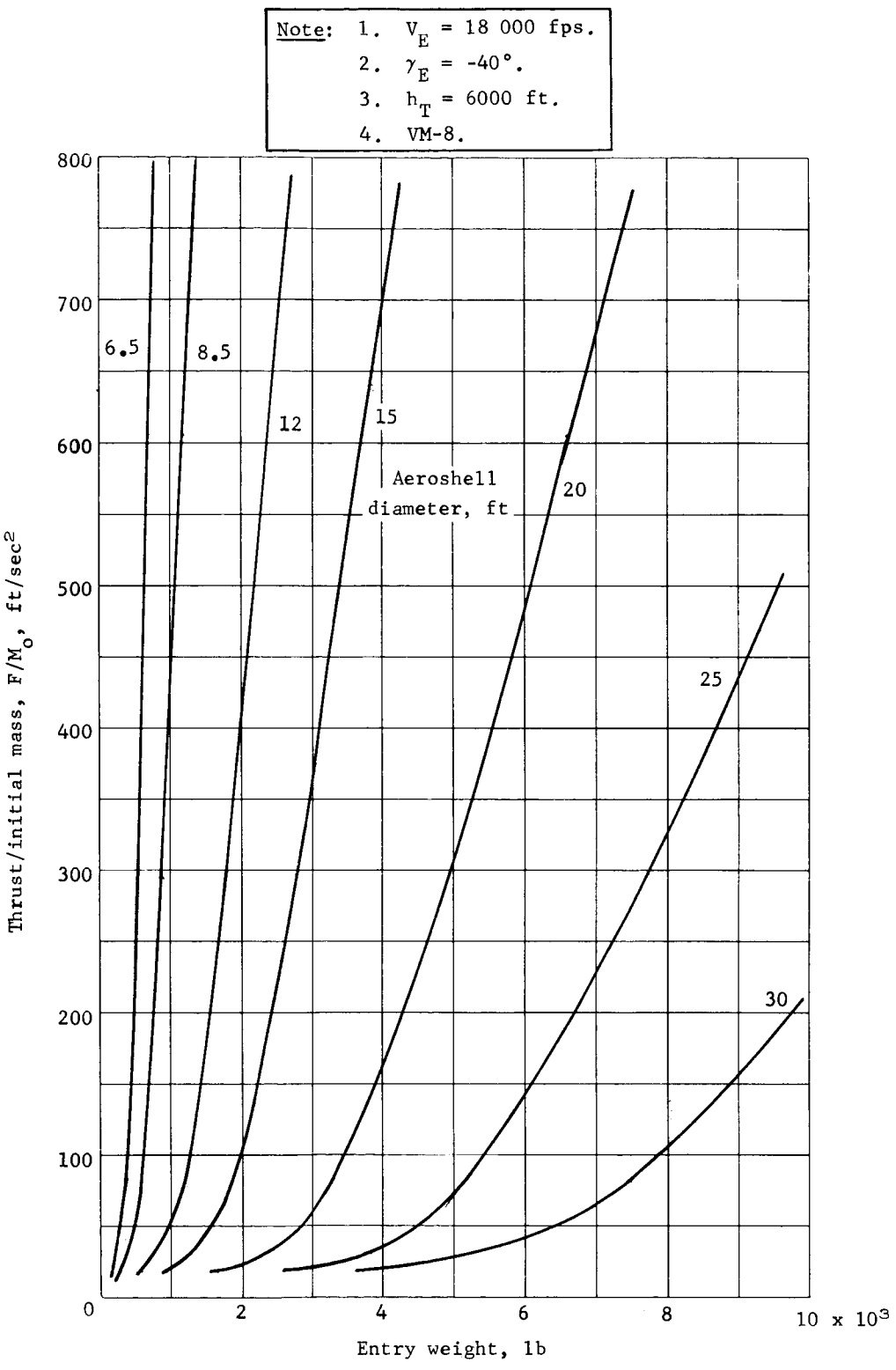

Figure B245.- Retrothrust/Initial Mass

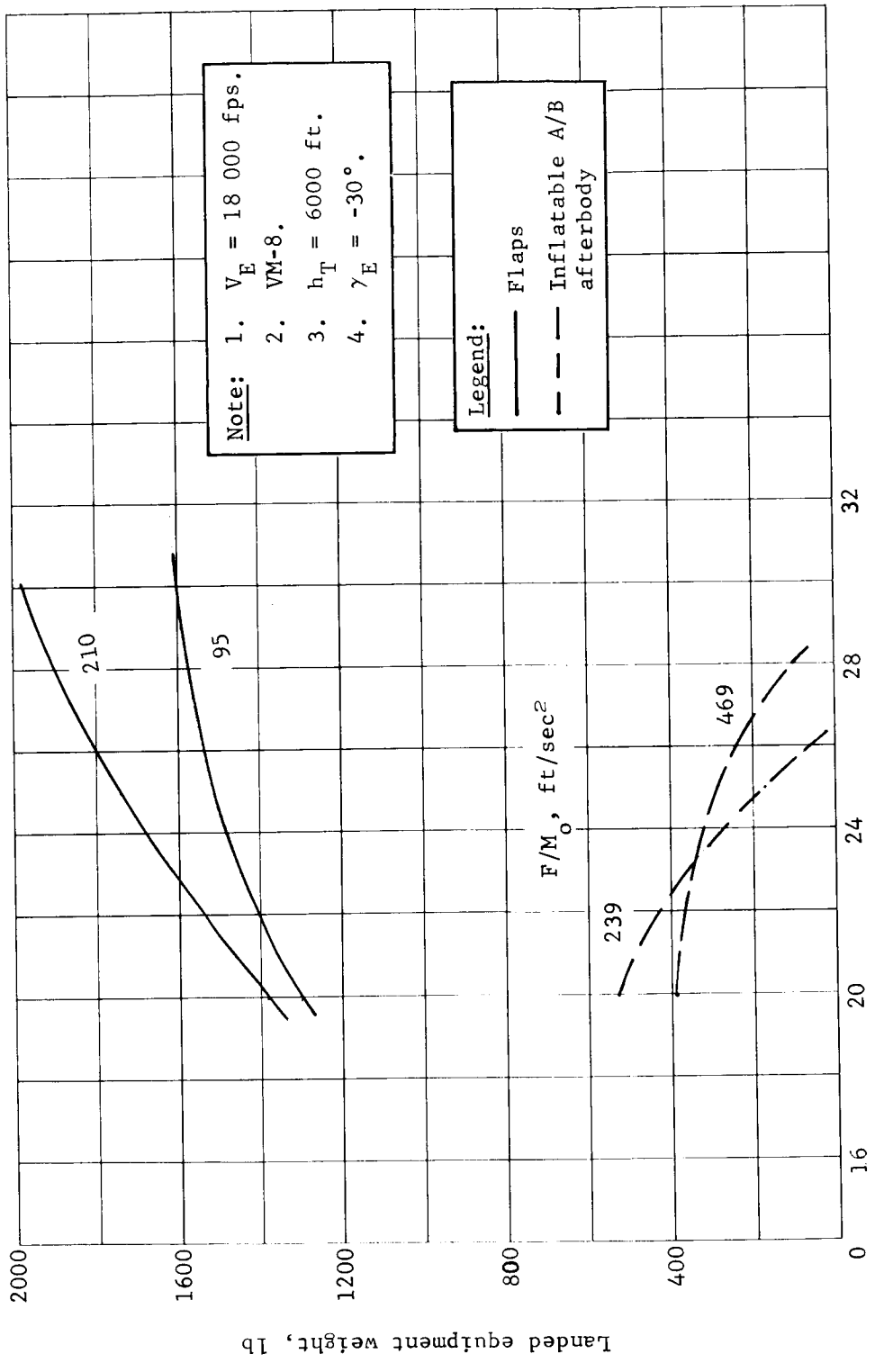

Figure B246.- Comparison of Flaps and Inflatable Afterbodies

APPENDIX B

A conservative design requires margin to account for weight uncertainties. To define this effect, the delivery system weight $W_E - W_{LE}$ is increased by 10%. Curves of W_{LE} versus W_E with and without this 10% margin are shown in figures B247 thru B256 for the orbital parachute system. Consider, as an example, $\gamma_E = -16°$ and $h_T = 0$ in figures B247 and B248. A landed equipment weight of 1000 lb requires at least a 9-ft aeroshell, while a 9.5-ft aeroshell is required with a 10% margin. Entry weight needed goes up from 2050 to 2250 lb. Conversely, a 9-ft aeroshell without margin yields 1000 lb landed equipment weight, but only 900 lb with a 10% margin. Plots of the corrected maximum landed equipment weights versus aeroshell diameter and entry flightpath angle are shown in figures B257 thru B260. These plots can be used for design purposes to provide margin. Another means of achieving a margin is by using the left-hand slope of the diameter curves discussed earlier in this section. This W_{LE} versus W_E slope is somewhat off the maximum W_{LE} and achieves a similar margin to that just discussed. Figures B261 thru B265 show these slopes for orbit and direct modes for aerodecelerators and retros. Figure B265 shows a decreasing slope and, therefore, decreasing landed equipment weight with increasing entry angle for the retro. This trend also holds true for the aerodecelerators. Increasing deployment Mach numbers also have decreased slopes. A comparison of monopropellant and bipropellant verniers is made in figures B261 and B262. They show the bipropellant to be superior in amount of landed equipment weight.

Figure B266 shows the retro/parachute/vernier system performance for $\gamma_E = -20°$ and $-30°$, $V_E = 24\,000$ fps, $h_T = 6000$ ft for an 8.5-ft diameter aeroshell. Figure B267 shows the two-stage retro for the same conditions less $\gamma_E = -20°$. The boundary shown is where the system fails to decelerate to zero velocity at the surface. Also shown is the single-stage retro and the parachute system. For a comparable thrust-to-weight ratio, the single-stage retro yields the highest landed equipment weight. However, the two-stage retro has a larger growth potential.

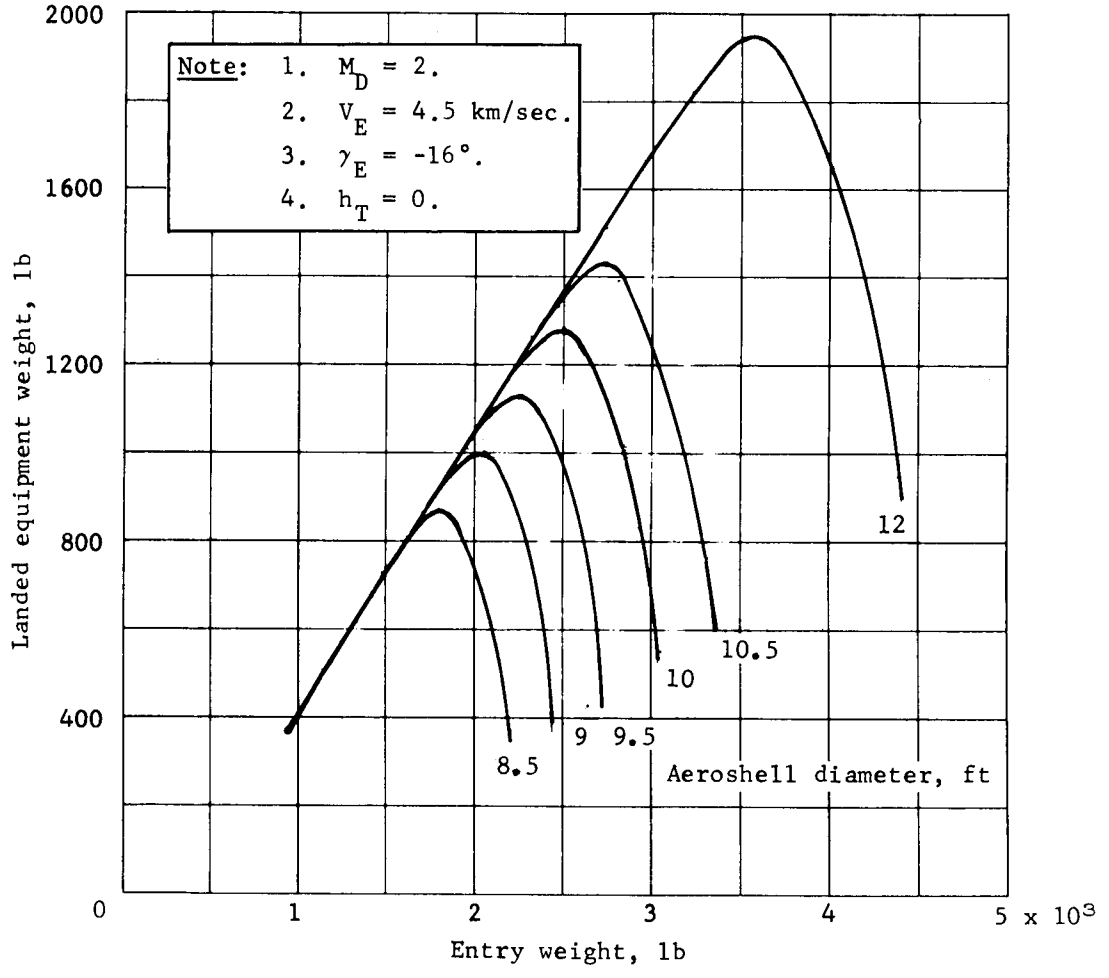

Figure B247.- W_{LE} versus W_E without Margin

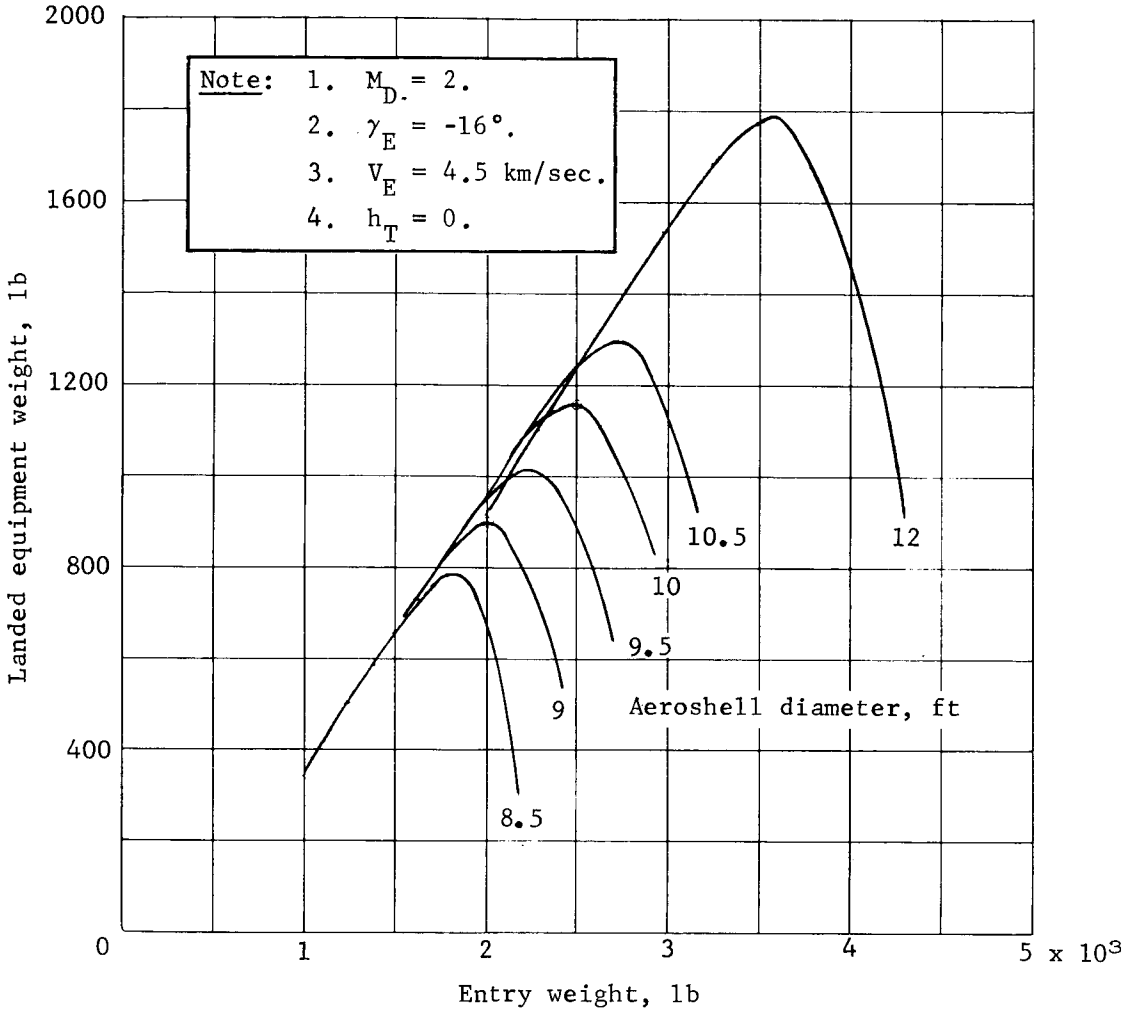

Figure B248.- W_{LE} versus W_E with Margin

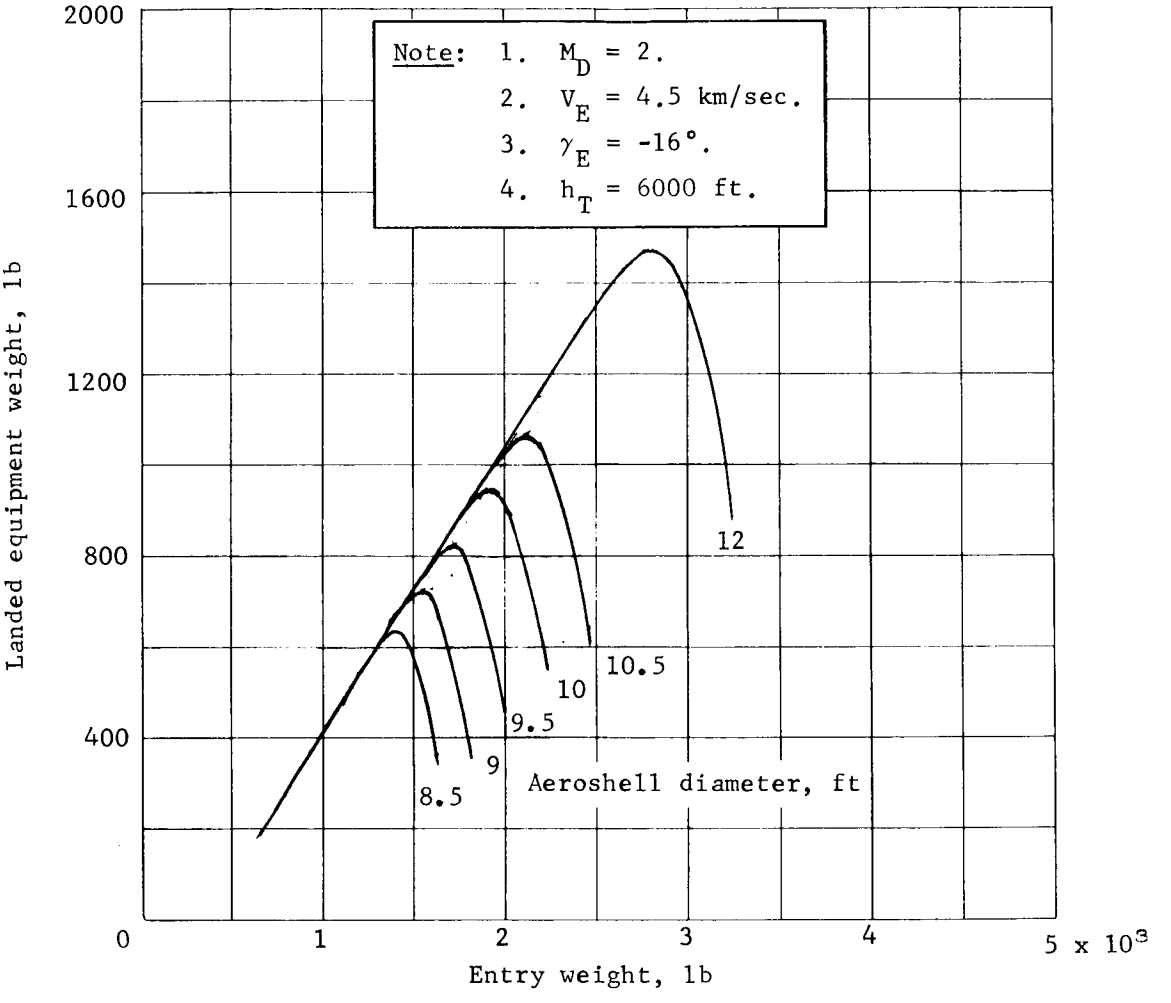

Figure B249.- W_{LE} versus W_E without Margin

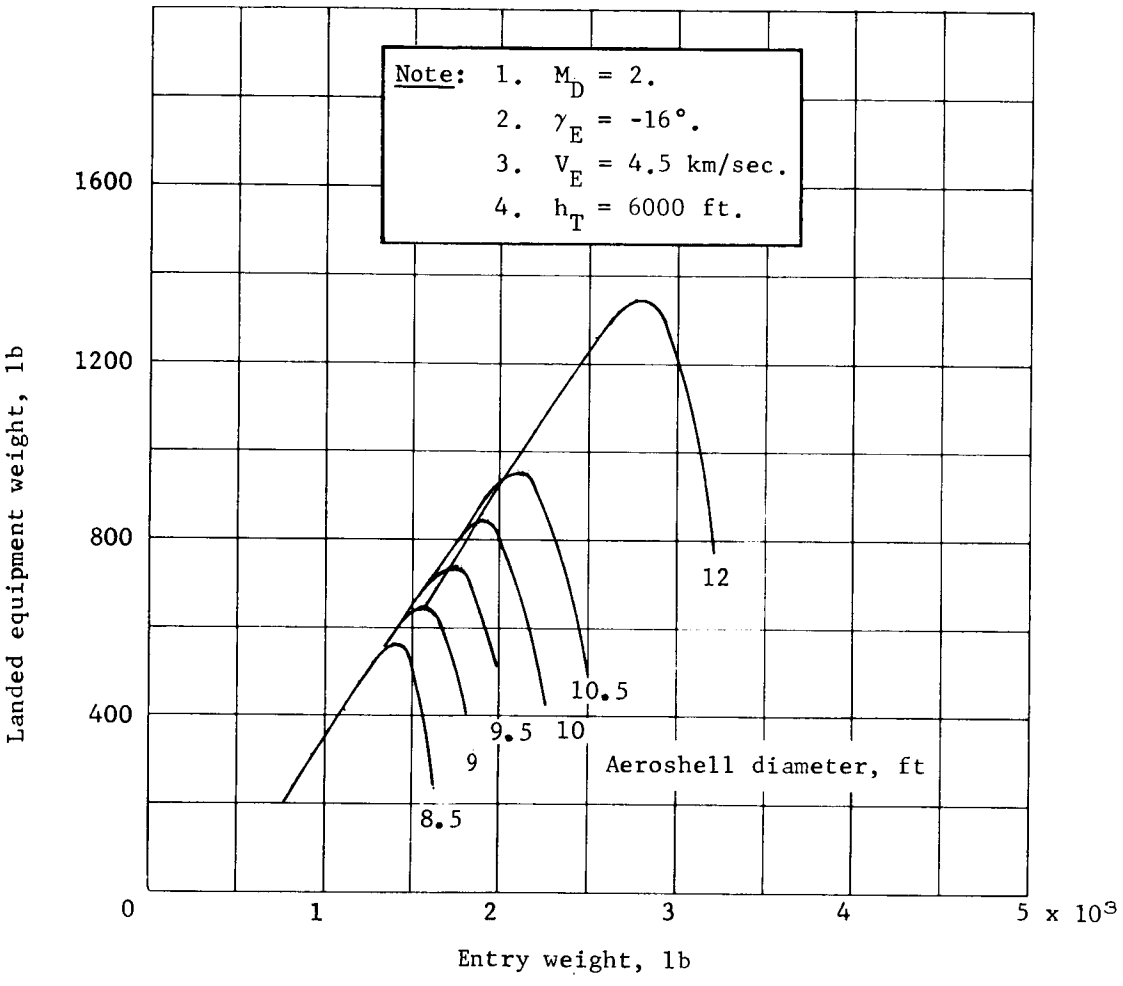

Figure B250.- W_{LE} versus W_E with Margin

APPENDIX B

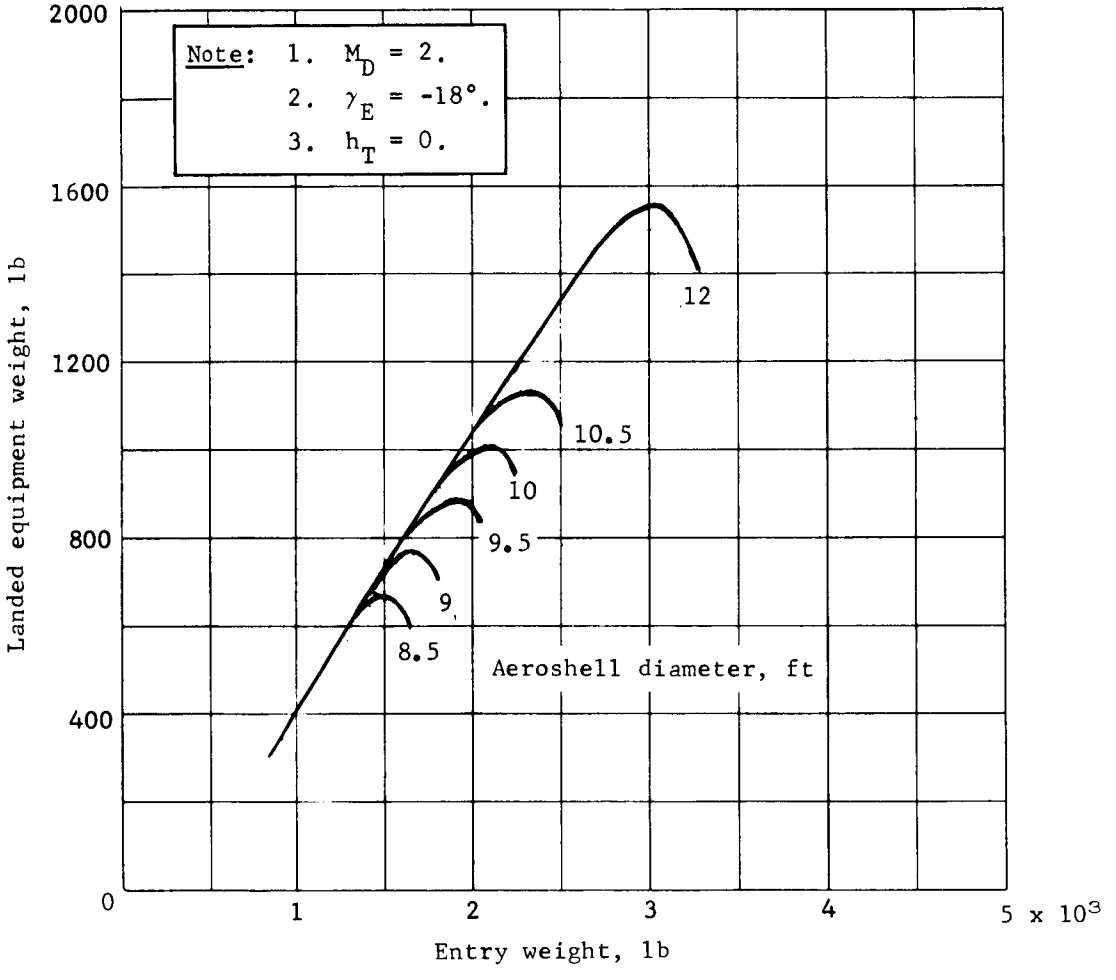

Figure B251.- W_{LE} versus W_E without Margin

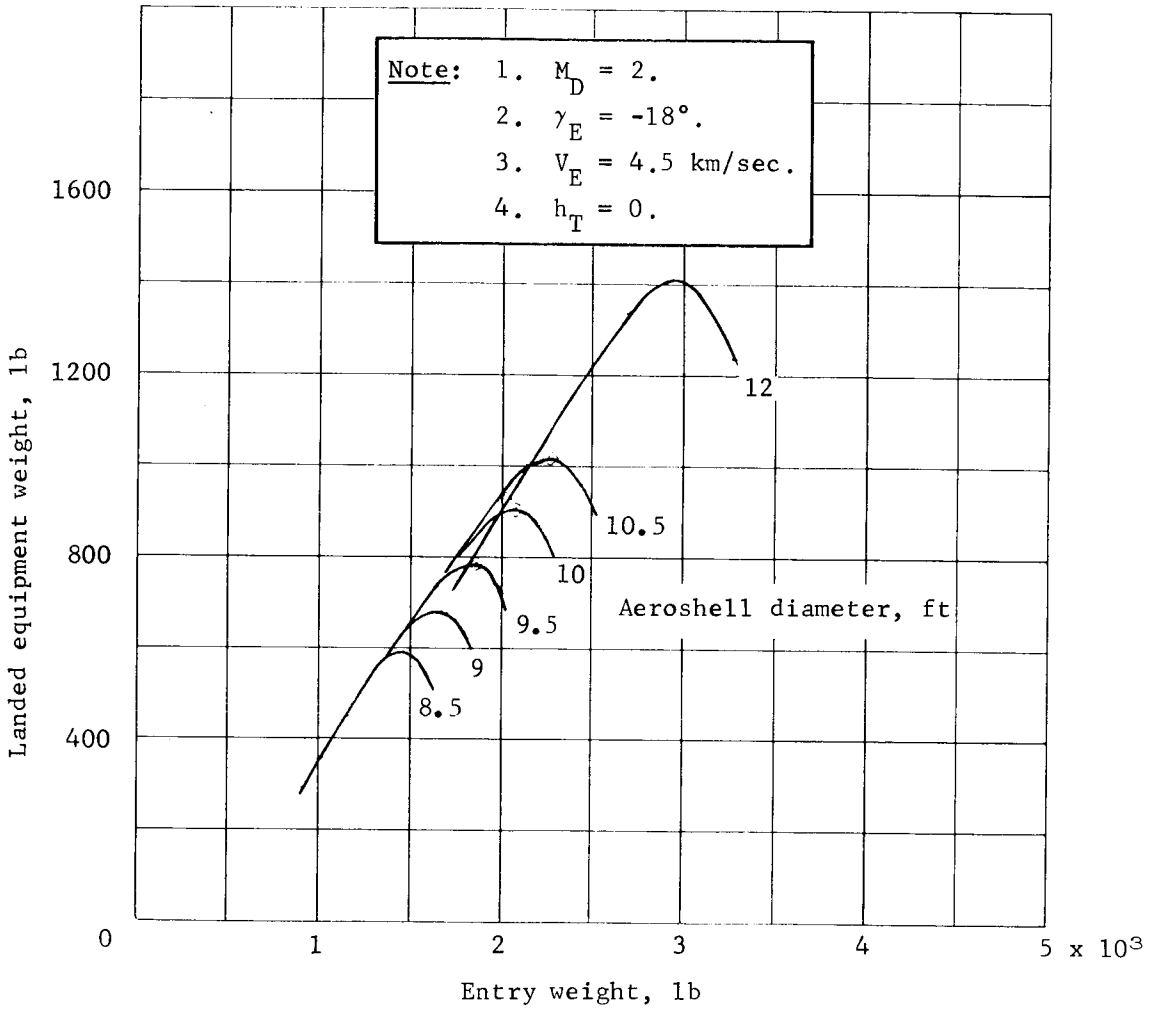

Figure B252.- W_{LE} versus W_E with Margin

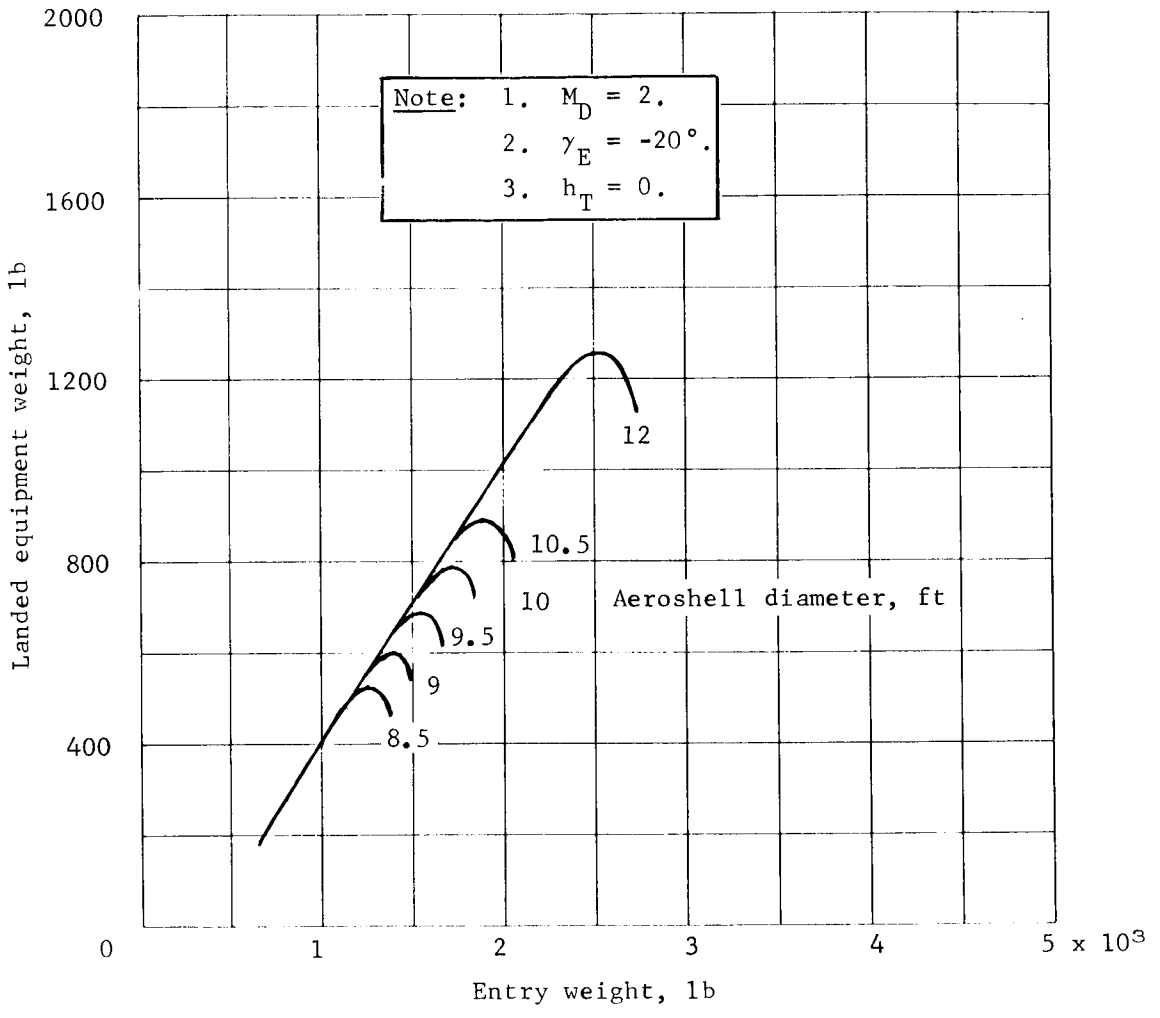

Figure B253.- W_{LE} versus W_E without Margin

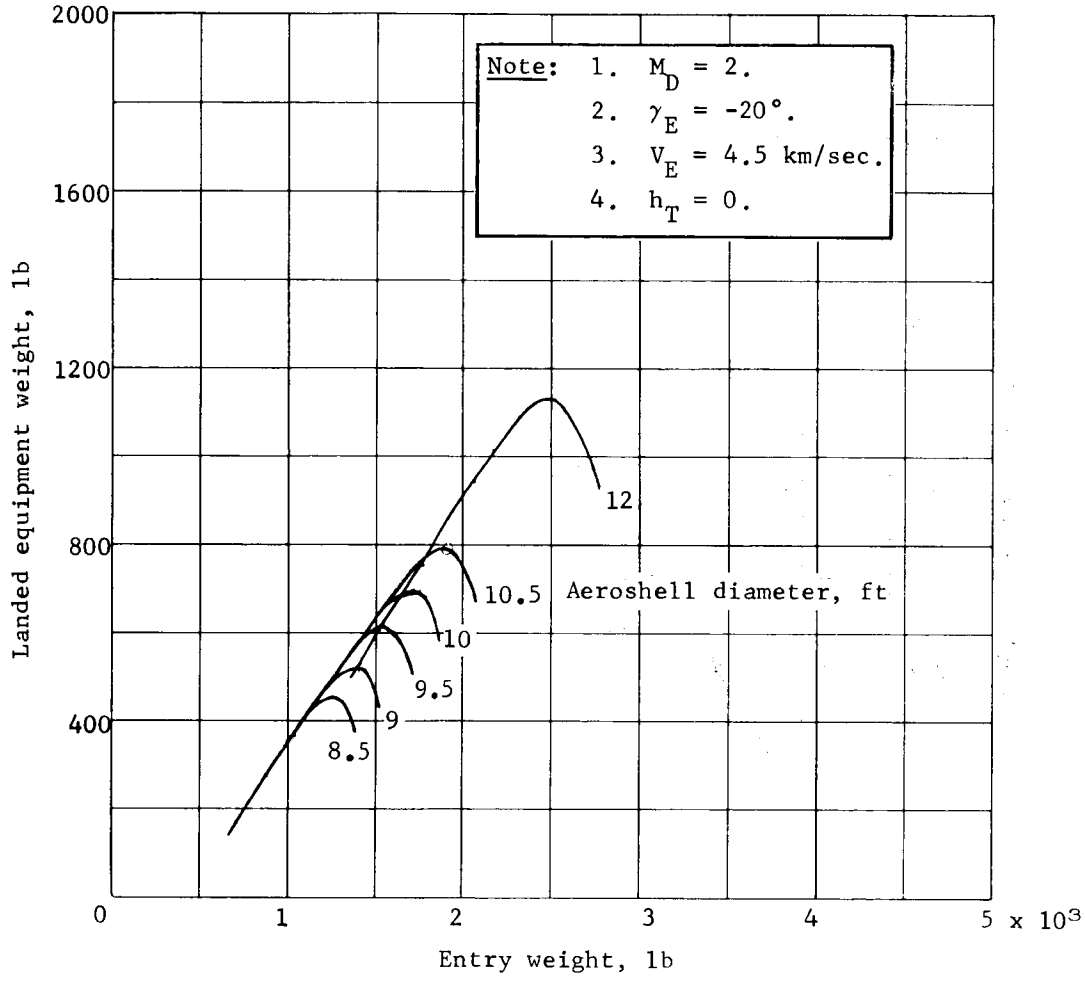

Figure B254.- W_{LE} versus W_E with Margin

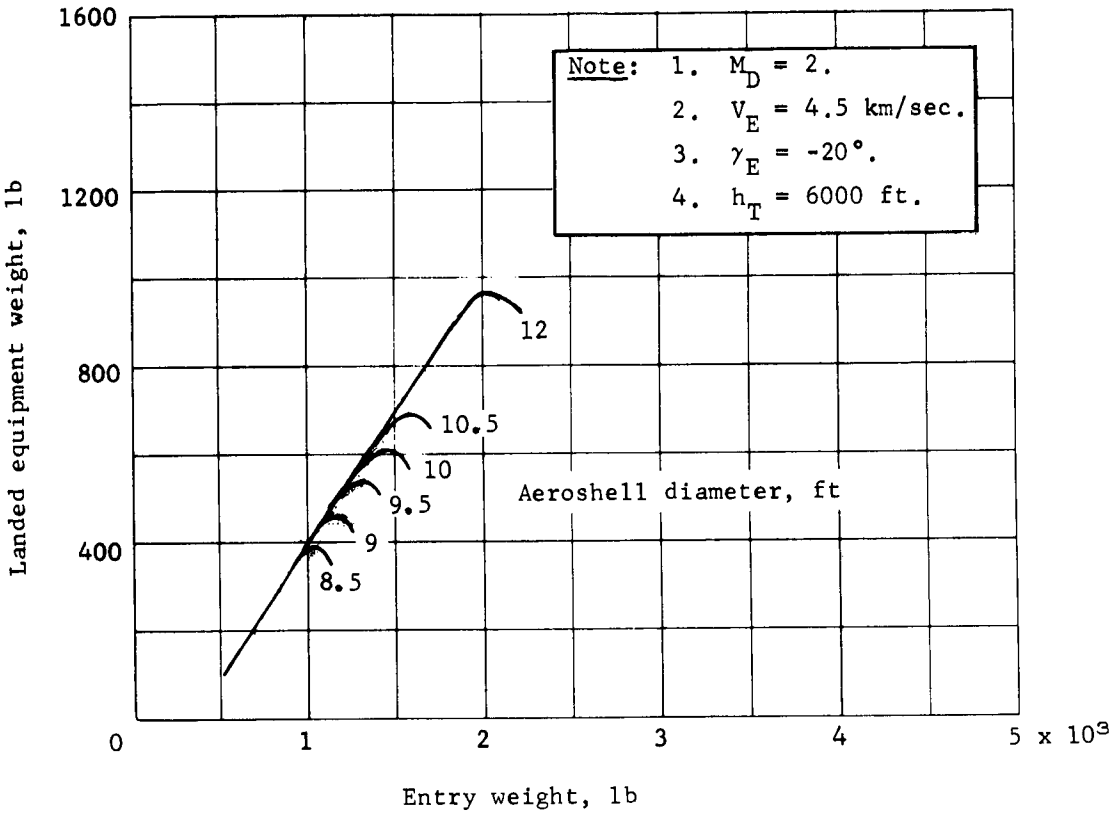

Figure B255.- W_{LE} versus W_E without Margin

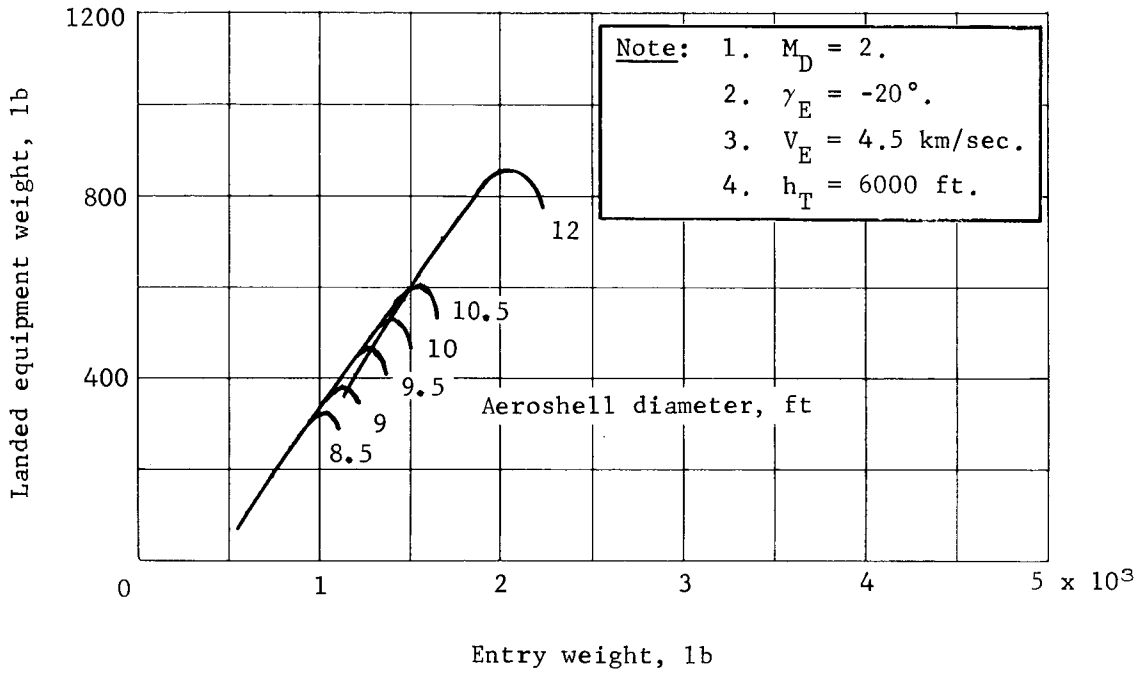

Figure B256.- W_{LE} versus W_E with Margin

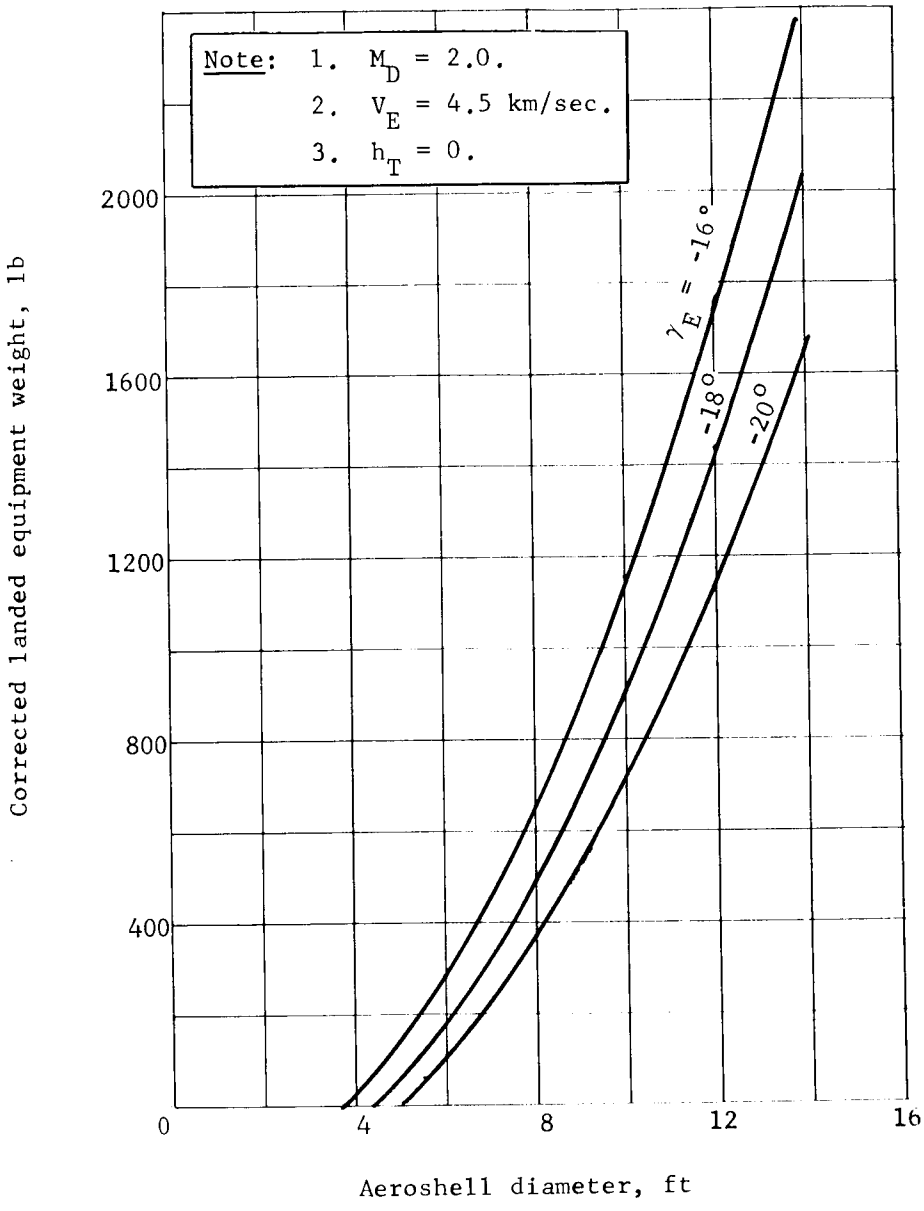

Figure B257.- Maximum W_{LE}, 10% Margin

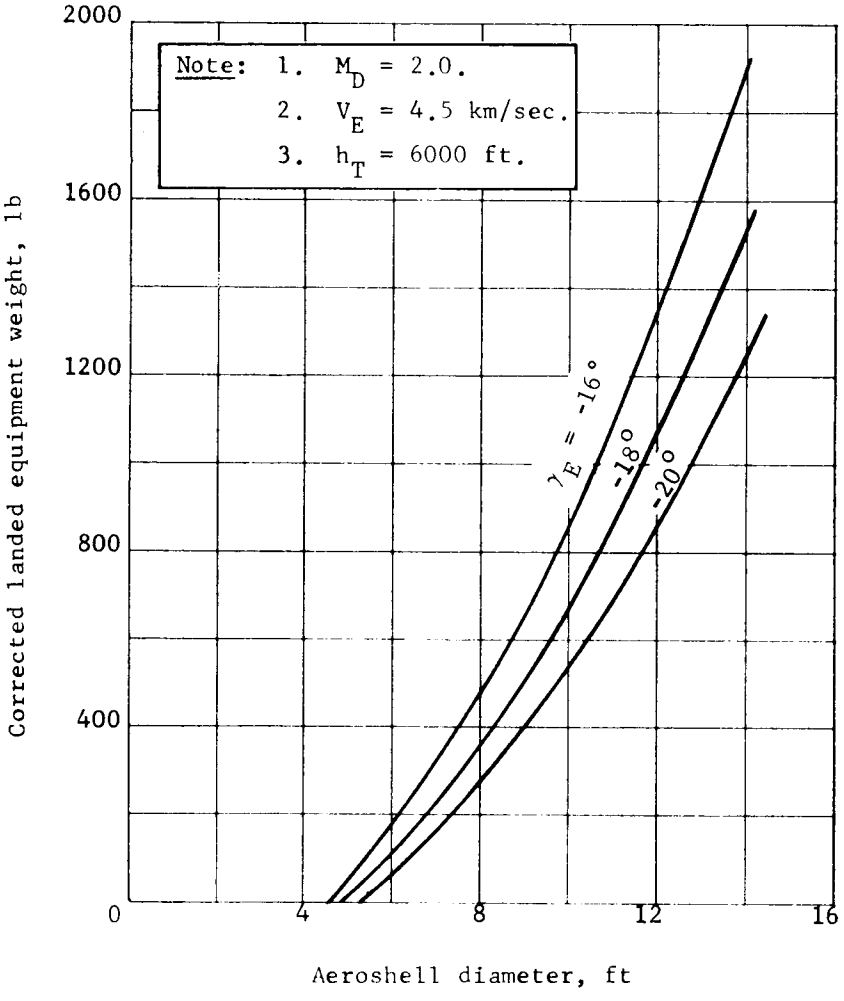

Figure B258.- Maximum W_{LE}, 10% Margin

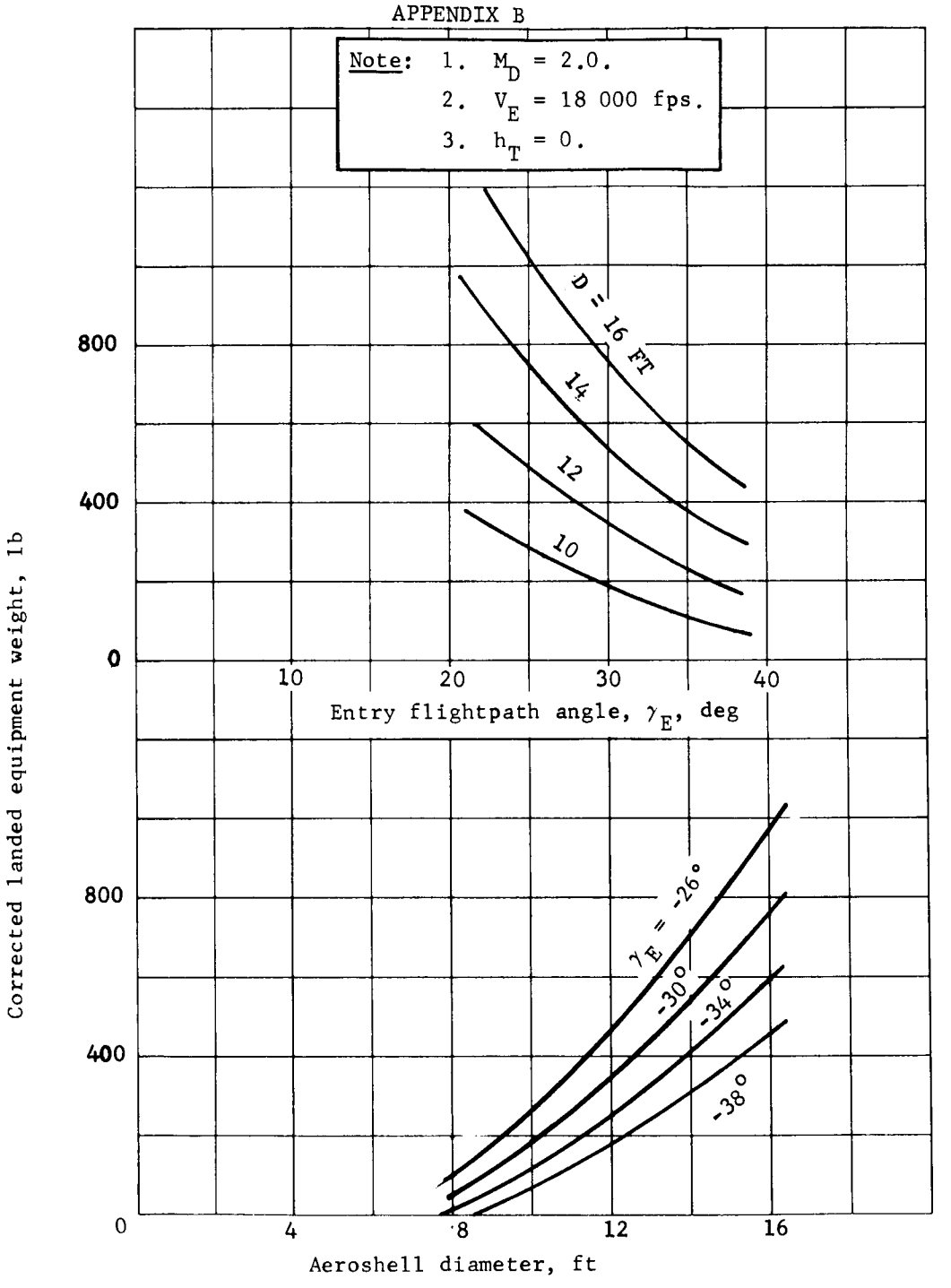

Figure B259.- Maximum W_{LE}, 10% Margin

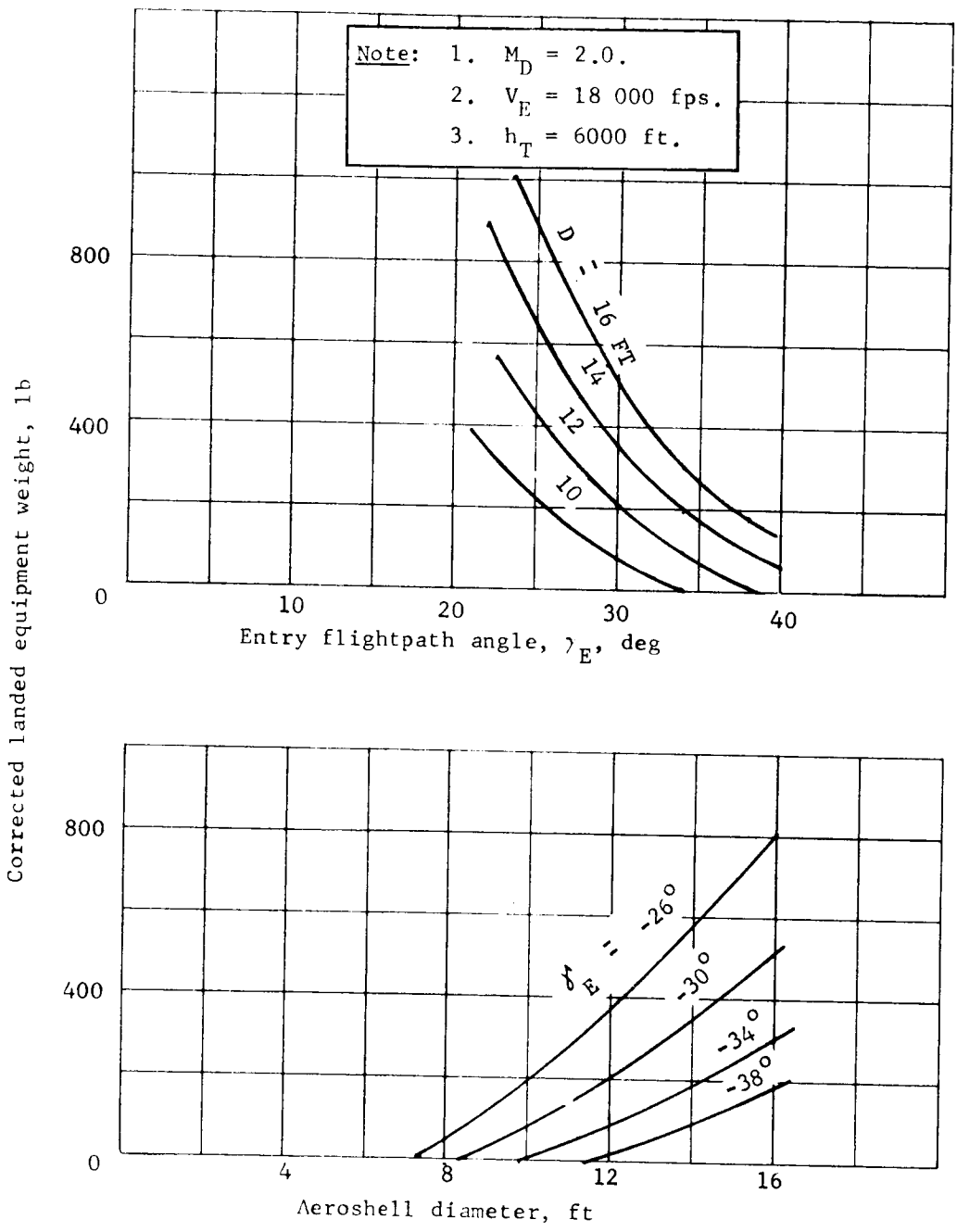

Figure B260.- Maximum W_{LE}, 10% Margin

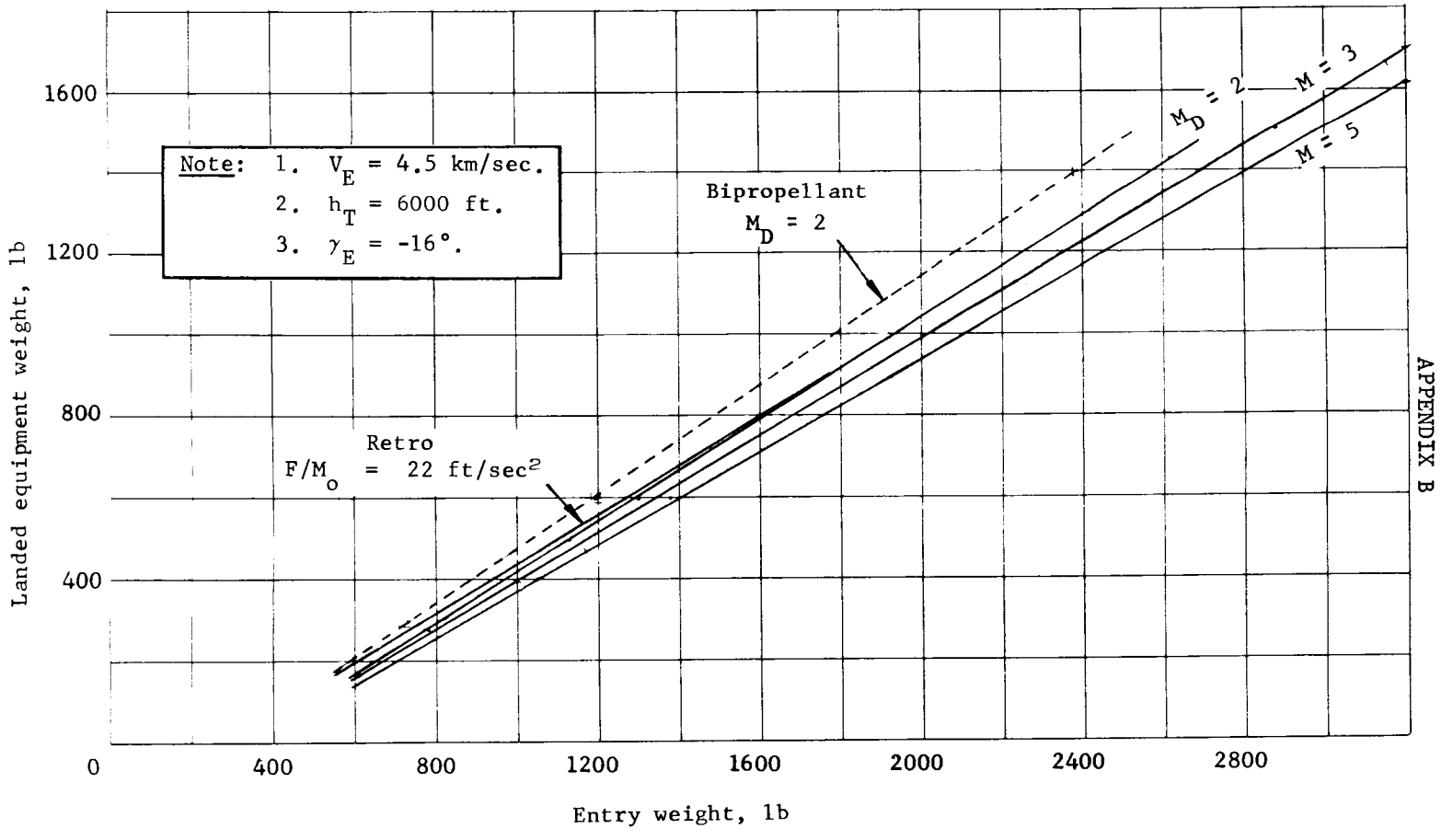

Figure B261.- Comparison of Monopropellant and Bipropellant Verniers

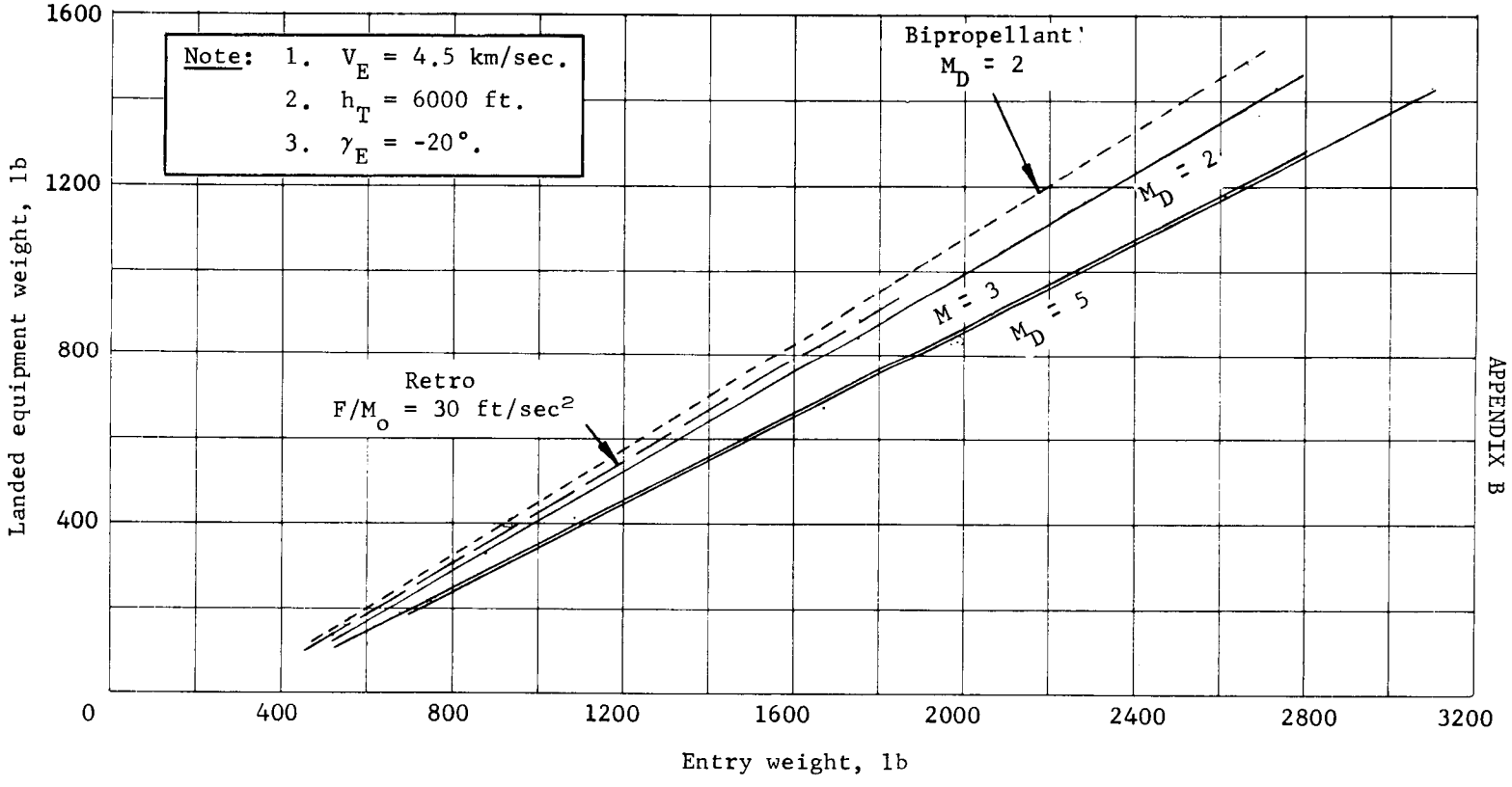

Figure B262.- Maximum W_{LE} Envelope

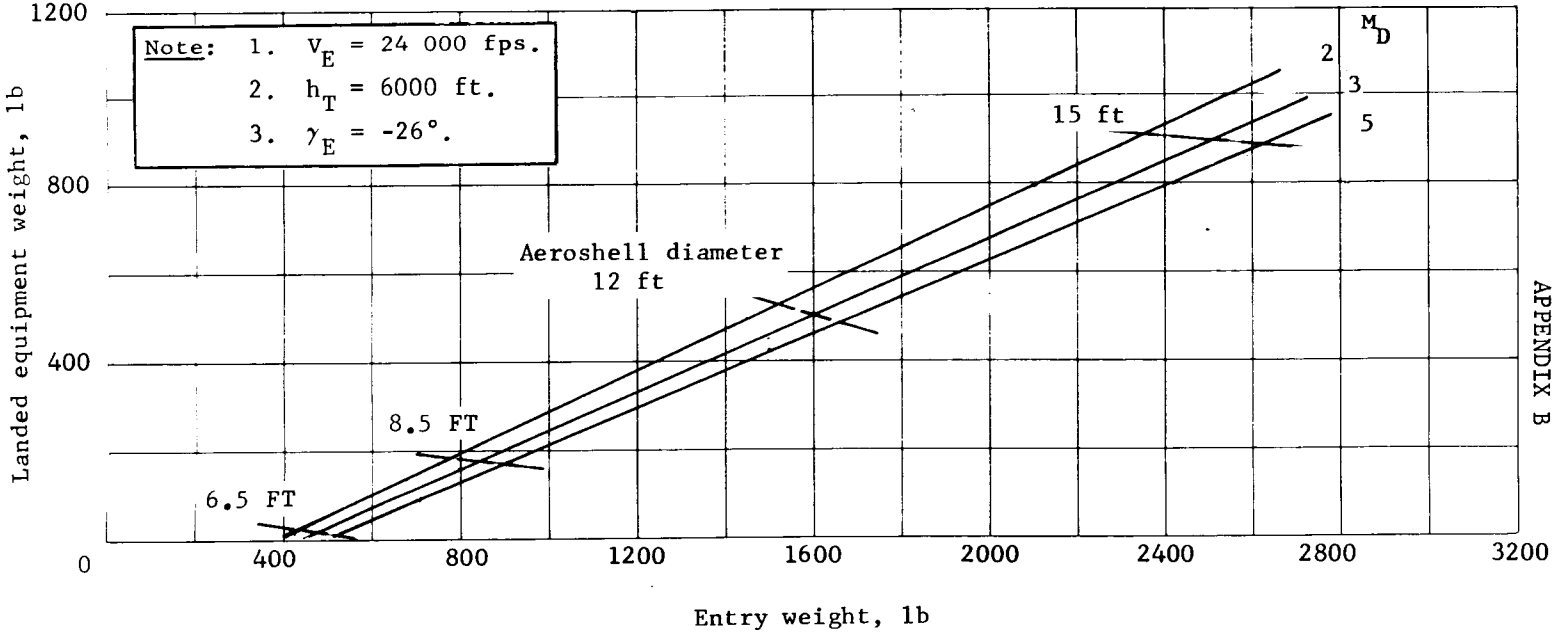

Figure B263.- Aerodecelerator W_{LE} Envelope

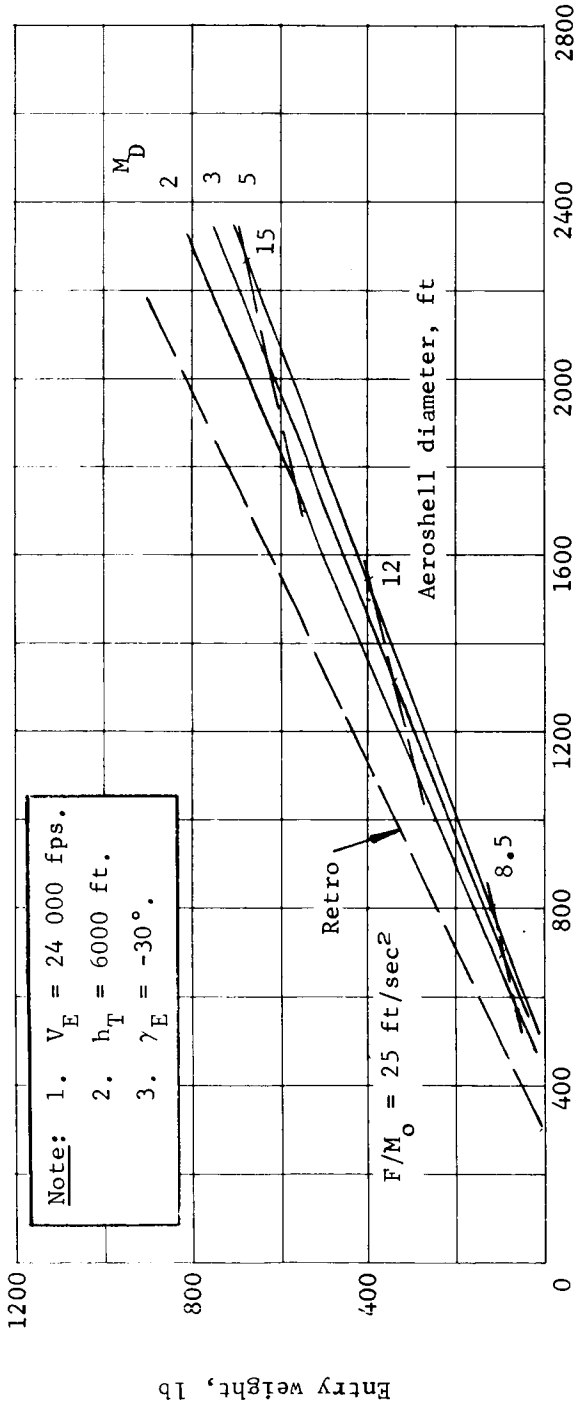

Figure B264.- Retro W_{LE} Envelope

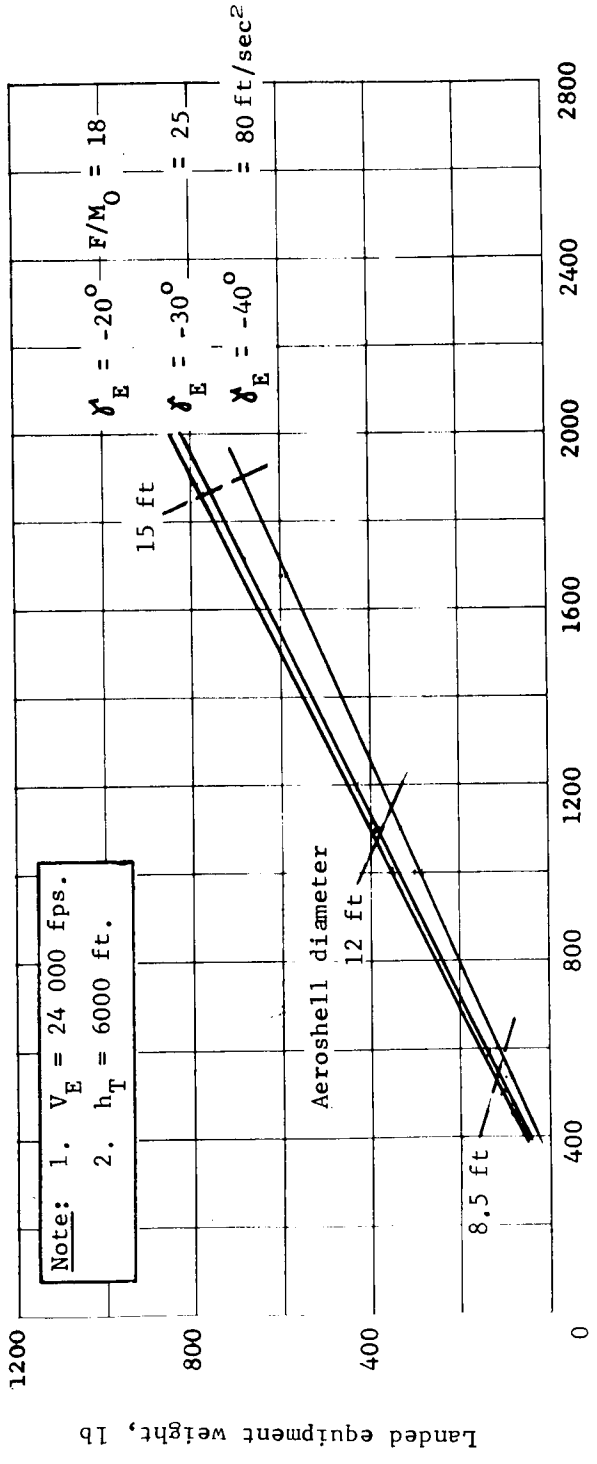

Figure B265.- Retro W_{LE} Envelope

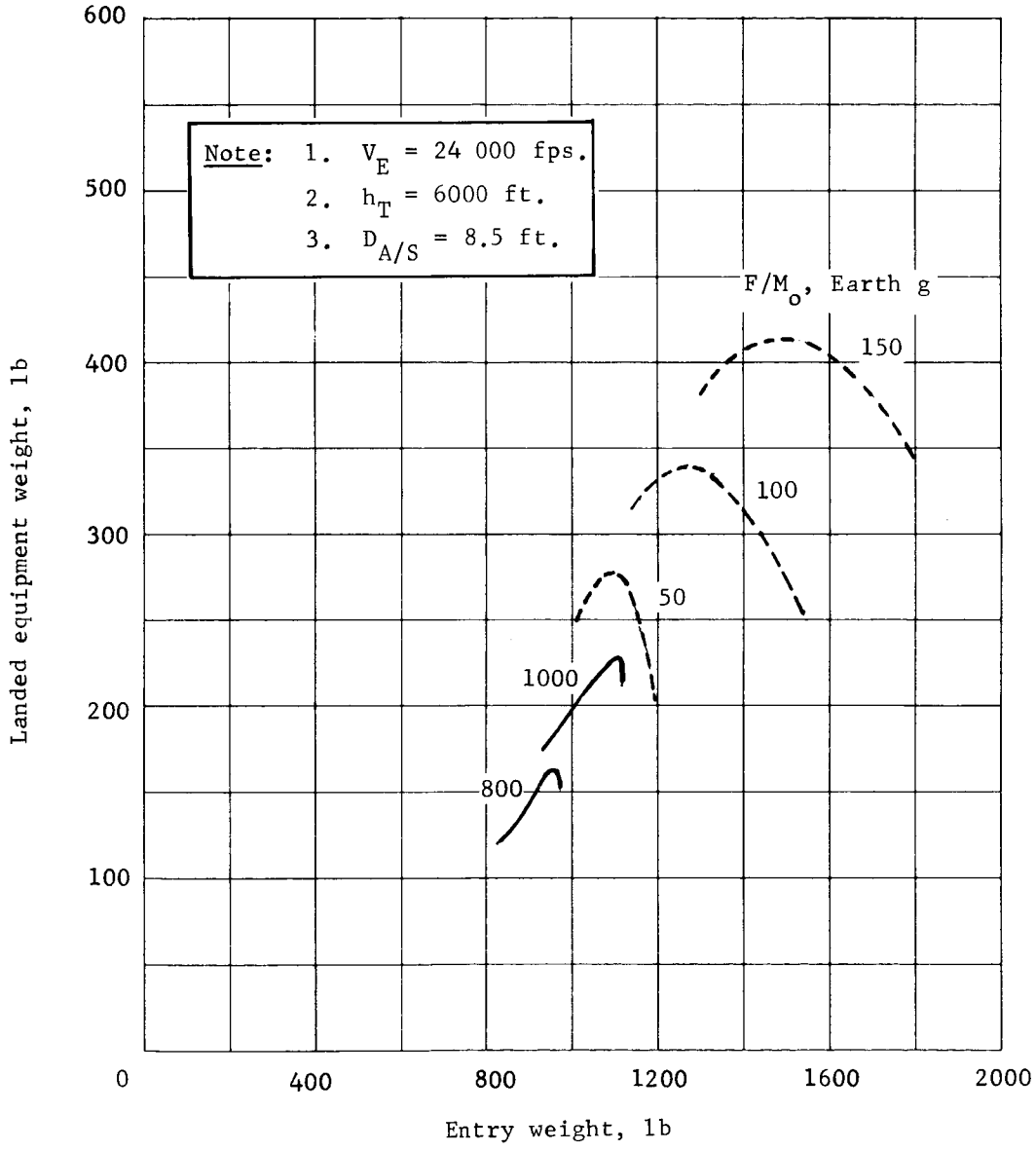

Figure B266.- Retro/Parachute/Vernier System

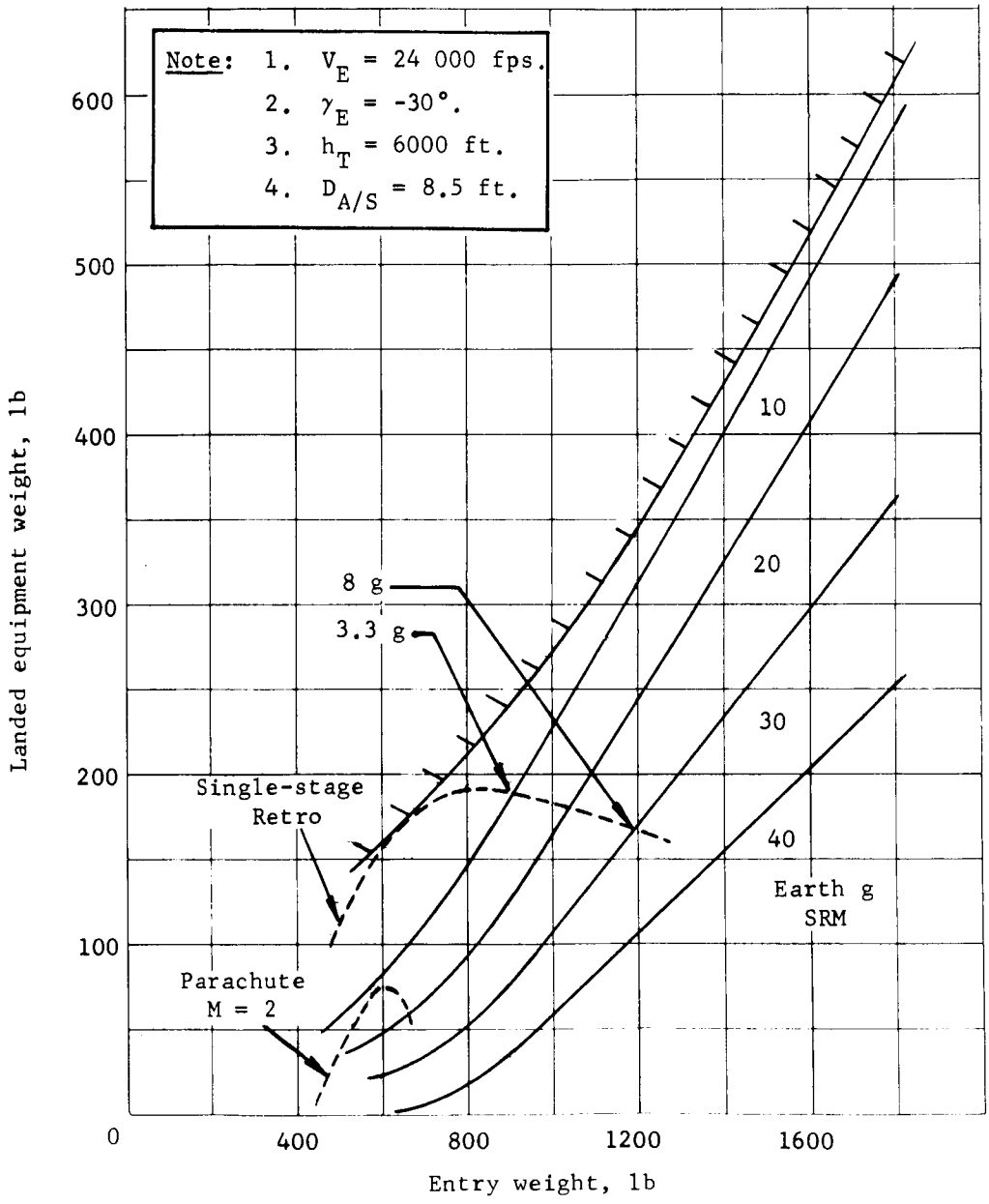

Figure B267.- Two-Stage Retro Performance

APPENDIX B

A comparison of the terminal phase systems (subsonic parachute/vernier, ballute/vernier, all-retro) may be made on the basis of several parameters for both orbit and direct modes. In general, the parameters of interest are landed equipment weight, entry weight, aeroshell diameter, and entry flightpath angle. The comparison is made at a constant terrain height (6000 ft); the effect of varying terrain height was shown earlier. Figures B268 and B269 compare maximum landed equipment weight versus aeroshell diameter for orbit $(V_E = 4.5 \text{ km/sec})$ and direct $(V_E = 18\ 000 \text{ fps})$ modes, respectively. Representative maximum and minimum entry flightpath angles are included: $\gamma_E = -20°$ (orbit) and -38° (direct), $\gamma_E = -16°$ (orbit) and -26° (direct). Comparison is made between parachute/vernier $(M_D = 2)$, ballute/vernier $(M_D = 3,5)$, and the all-retro decelerator systems. The retro system thrust to initial mass is approximately 100 ft/sec^2. These figures are composites of earlier data and are used an an example of the types of comparison leading to the summary charts.

The terminal phase systems capabilities are summarized as a function of assumptions. The basic W_{LE} capability is shown in figures B270 and B271 for fixed diameters of 8.5 and 15.0 ft. The data are based on the maximum W_{LE} contour and, therefore, represent maximum W_{LE} for the given diameters. The data shown in figure B270 for the 8.5-ft diameter compare the orbit and direct modes for the various systems. Both entry weight and W_{LE} are shown as well as the sensitivity of both of these parameters to entry flightpath angle. For the orbit mode, the Mach 5 ballute provides the highest performance per diemeter, but also has the greatest entry weight. The retro system is slightly better than the $M_D = 2.0$ parachute system. The direct mode data show the same trends, except the retro system is relatively better. None of the direct mode performance is acceptable at a diameter of 8.5 ft. Similar data are shown in figure B271 for a 15-ft diameter. The orbit mode data show high performance capability with the same characteristics across systems as was exhibited for the 8.5-ft diameter data. The direct mode data, for a γ_E maximum of -24 to -26°, show acceptable performance, with the retro system showing the best performance capability.

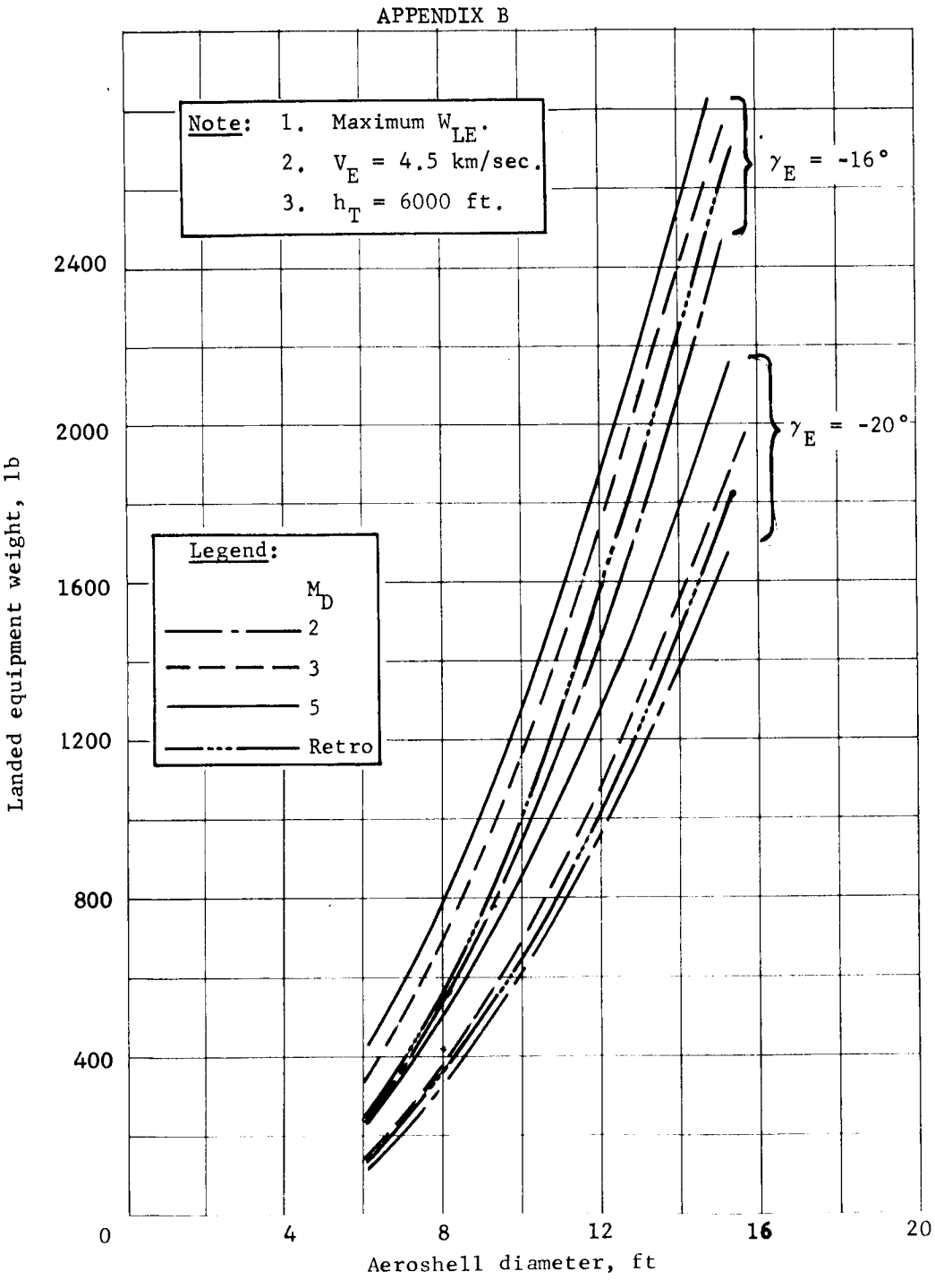

Figure B268.- Effect of Deployment Mach Number

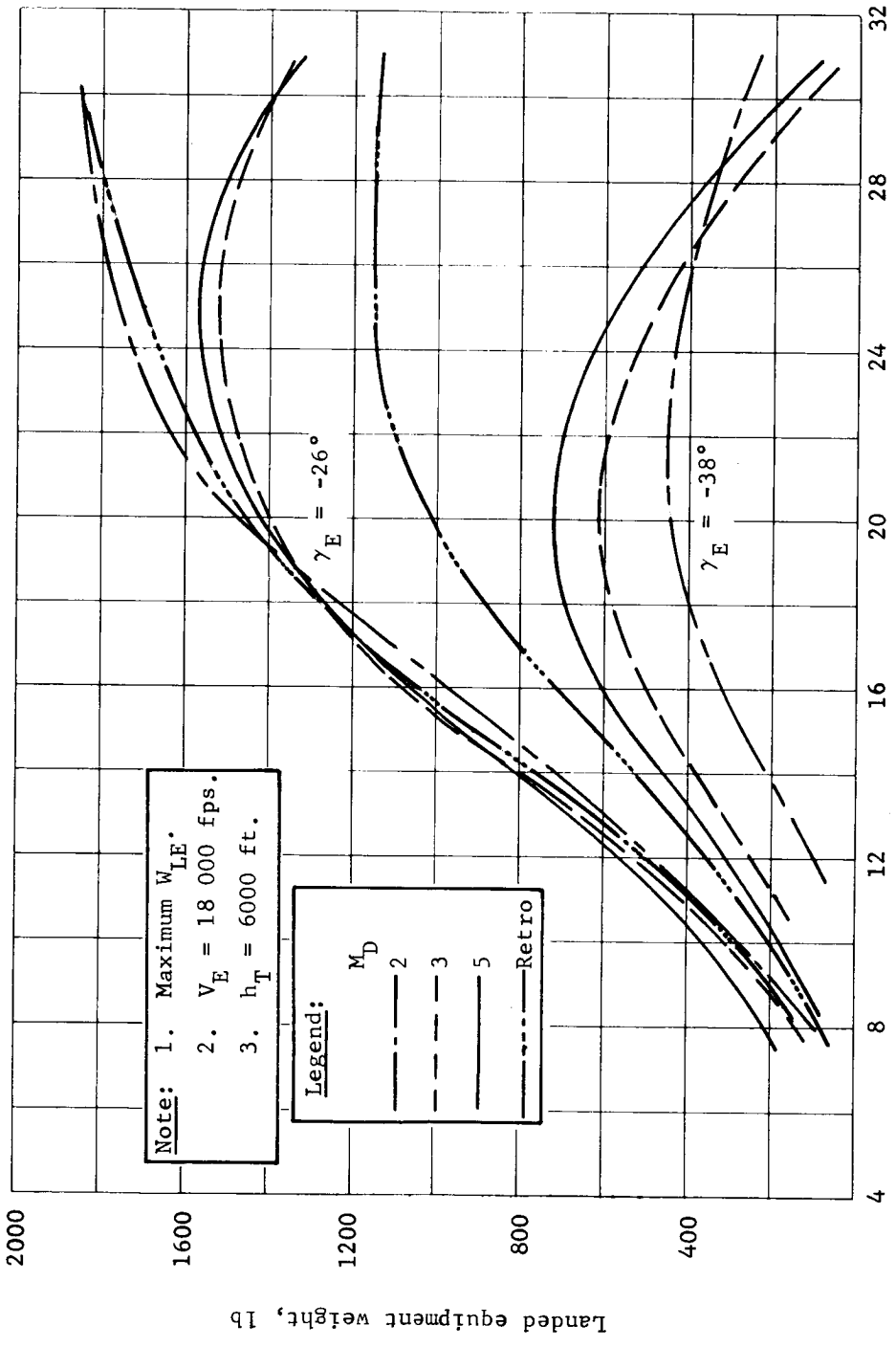

Figure B269.- Effect of Deployment Mach Number

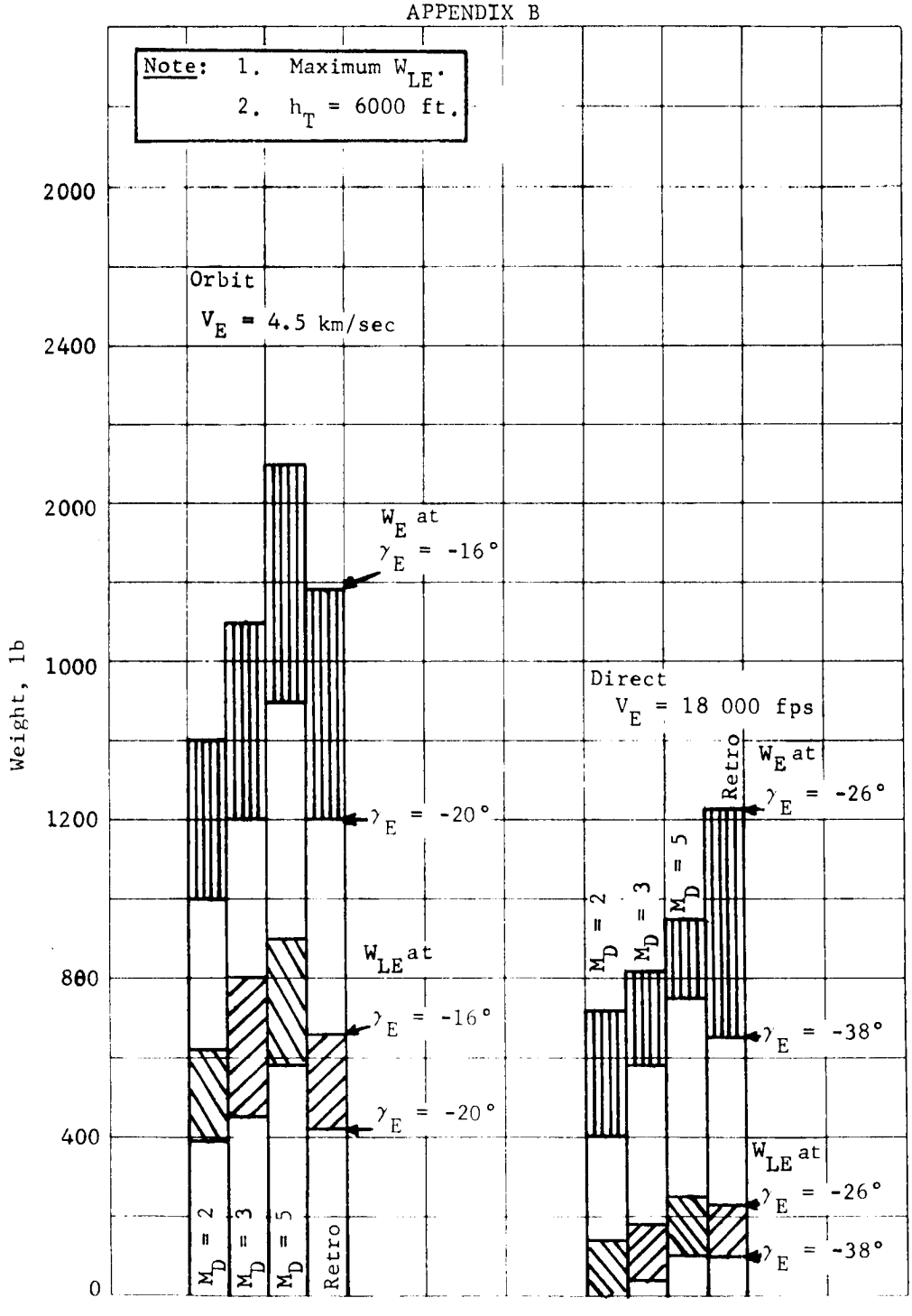

Figure B270.- Terminal Phase Summary, Aeroshell Diameter = 8.5 ft

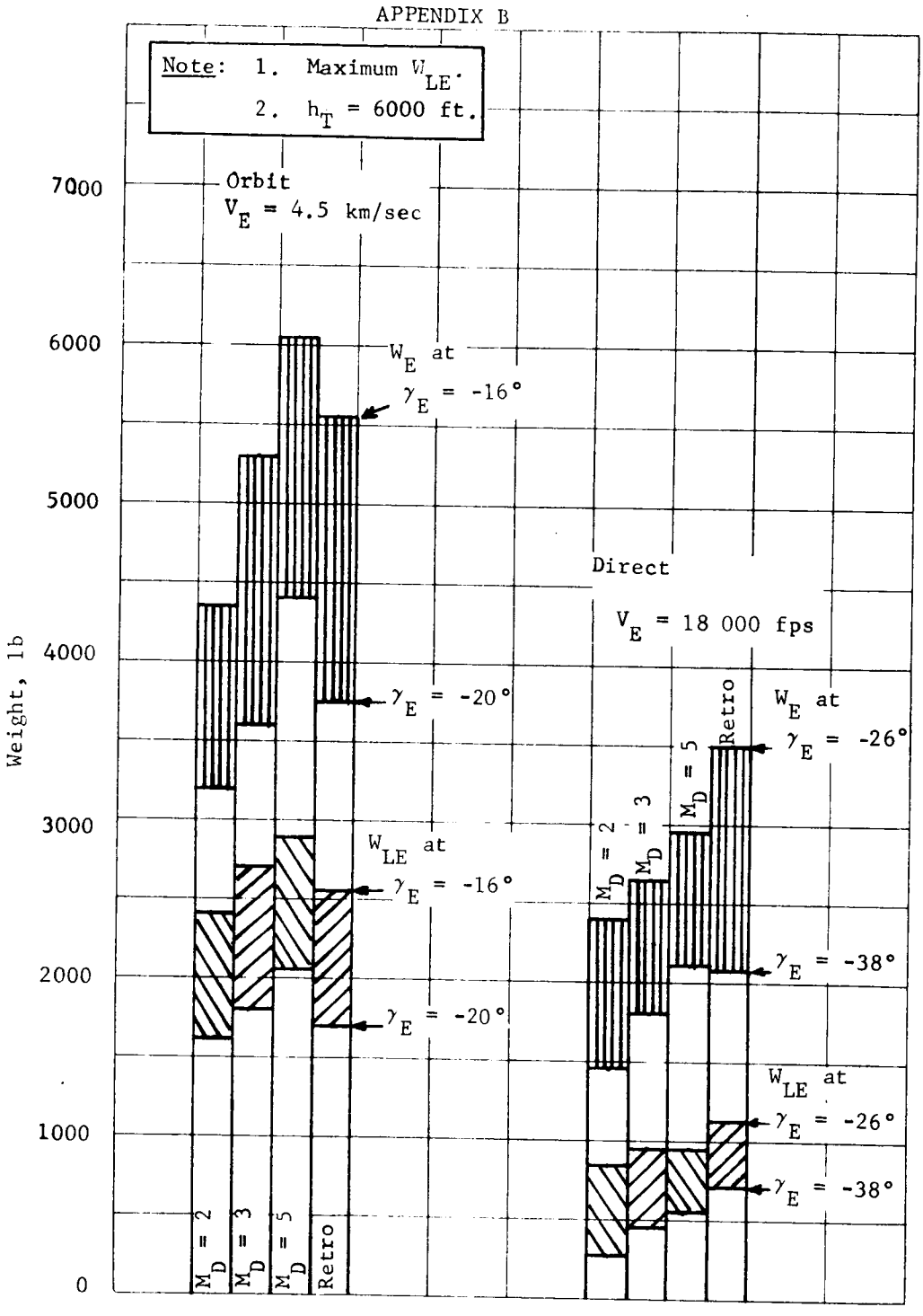

Figure B271.- Terminal Phase Summary, Aeroshell Diameter = 15 ft

It is clear from these data that any of the systems can deliver useful payloads (W_{LE}) in the 600-lb class with diameters in the 8.5 to 15.0-ft range. Generally, the ballute performance is superior for the orbit mode, while all-retro systems are most favorable for the direct mode. At fixed diameter, the orbit mode provides the greatest W_{LE} and continues to provide maximum pounds on the ground per pound entry weight.

The second comparison is made on the basis of fixed landed equipment weight of W_{LE} = 600 lb. This is summarized in figure B272 in terms of minimum required entry weight. Once again, the sensitivity to entry flightpath angle is indicated by the shaded portion of the bars. For the orbit mode, the M_D = 2.0 parachute case requires the lighest entry weight with the all-retro system a close second. For the direct mode, all of the required entry weights are greater than for the orbit mode, with the retro system requiring the smallest entry weight. The retro system data as presented, are somewhat deceiving relative to its apparent insensitivity to γ_E. In reality, the data presented earlier show that the variation in γ_E require a wide variation in required thrust-to-weight ratio.

The required aeroshell diameters for the above comparison are shown in figure B273. For the orbit mode, the M_D = 2.0 parachute system requires the greatest diameter of the aerodecelerator systems, with the all-retro system requiring the greatest diameter. Once again, the retro data can be somewhat misleading because the data are based on using the minimum useful thrust-to-weight ratio. There is a tradeoff between thrust level and diameter. For the direct mode, the required diameters are all greater than those for the orbit mode with the M_D = 2.0 parachute system requiring the largest diameter. Again, assuming $-\gamma_E$ maximum of 18° for the orbit mode and 26° for the direct mode, the corresponding diameter ranges are 8.1 to 9.5 ft for the orbit mode aerodecelerators and 12.3 to 13.6 ft for the direct mode. These data correspond to the case of landing 600 lb of W_{LE} at the lowest entry weight, W_{LE}, without regard to aeroshell diameter.

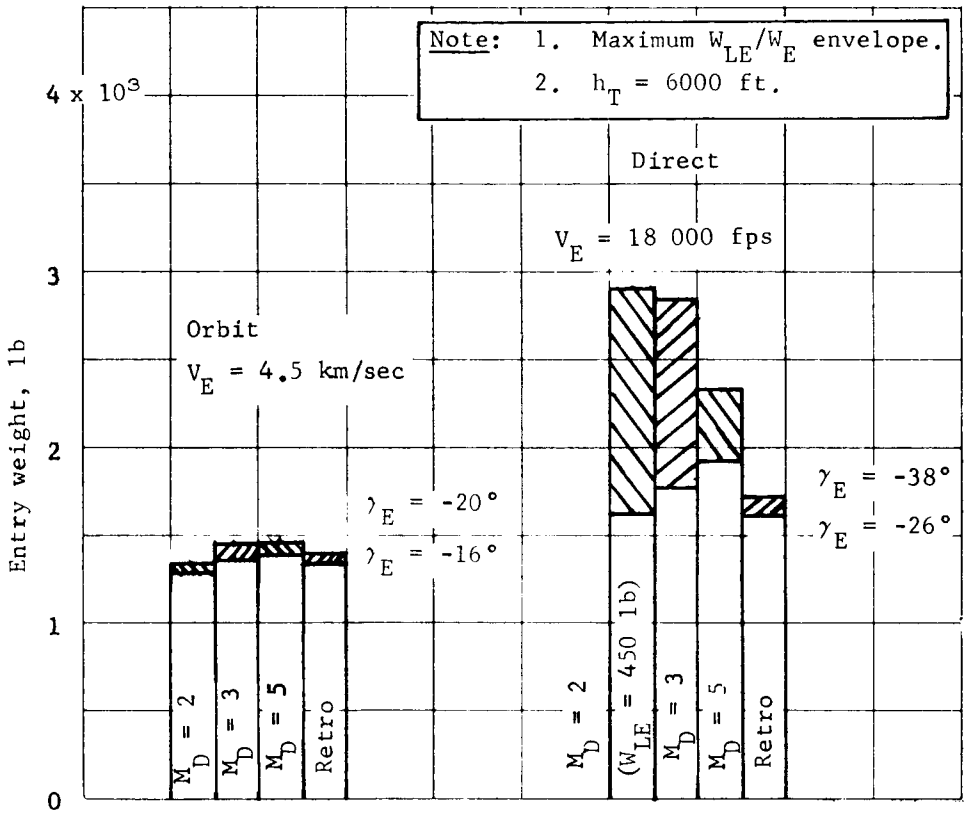

Figure B272.- Terminal Phase Summary, Landed Equipment Weight = 600 lb

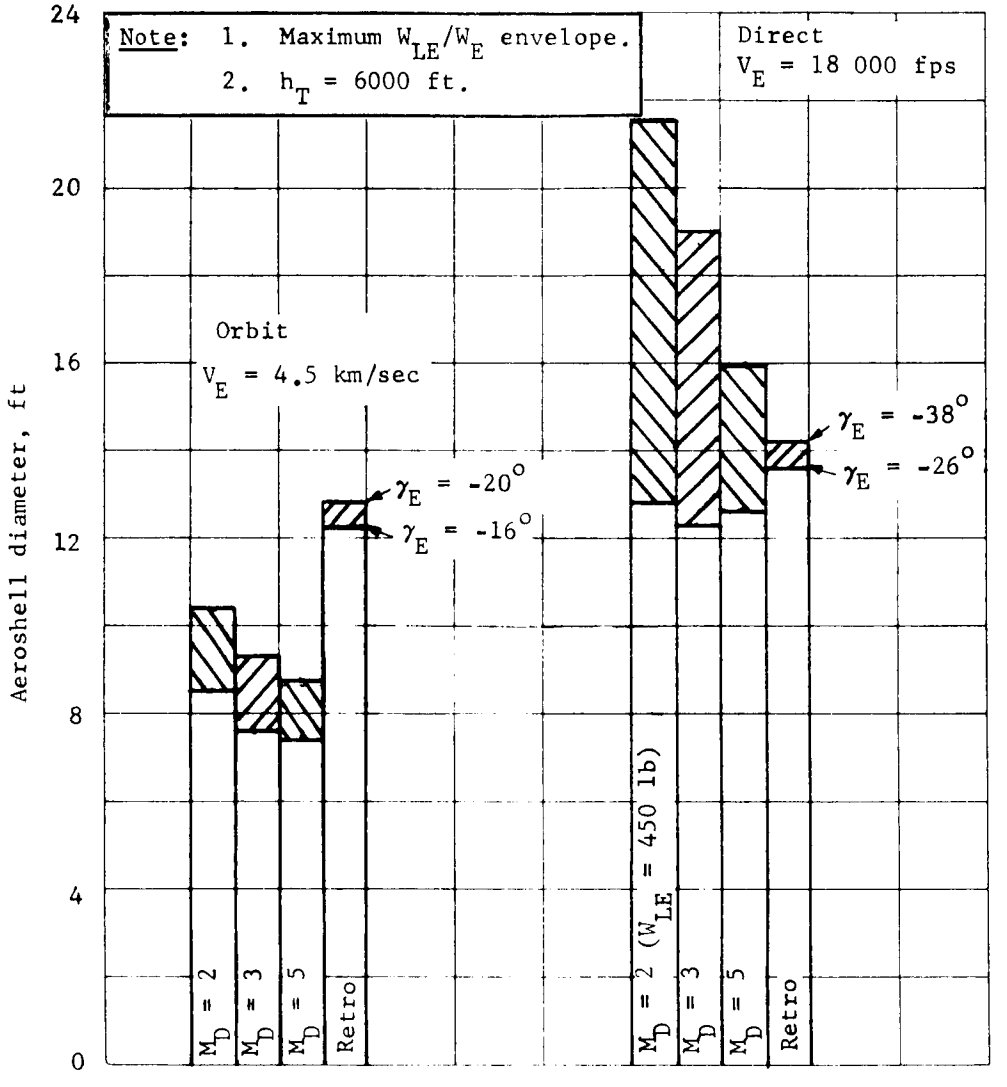

Figure B273.- Terminal Phase Summary, Landed Equipment Weight = 600 lb

APPENDIX B

The final comparison made here is on the basis of a fixed entry system weight of 1500 lb. The maximum allowable landed weight for the systems and mission modes is shown in figure B274. The efficiency of the $M_D = 2.0$ parachute is once again apparent in providing the greatest pound on the ground per pound entry for the orbit mode, while the all-retro system is best for the direct mode. The corresponding required diameters are shown in figure B275. Once again, the orbit mode diameters are smaller than the direct mode cases with the $M_D = 2.0$ requiring the largest diameters.

The variations in these results are only indicative of the kinds of tradeoffs that can be made. A generalization that can be drawn from the analysis is that the $M_D = 2.0$ parachute is best when compared on the basis of pounds on the ground per pound entry. The supersonic ballutes provide the maximum pounds on the ground per foot of aeroshell diameter. The all-retro systems are always competitive, but care must be taken in their evaluation to consider their high sensitivity to required thrust-to-weight ratios.

Before concluding this summary discussion of the data, some mention is made on the degree of conservatism implied in the analysis from a mission profile viewpoint. There are two aspects to this question discussed here. The first, that all of the results presented above are based on the following:

1) The VM-8 atmosphere plus design terrain height define the altitude mark to trigger aerodecelerator deployment;

2) The VM-7 atmosphere in combination with 220-fps horizontal wind design the aerodecelerator size and vernier propellant requirements. The VM-8 atmosphere defines the deployment, design dynamic pressure;

3) The 3σ steepest entry flightpath angle is used in conjunction with 3σ orbit or approach trajectory emphemris uncertainty.

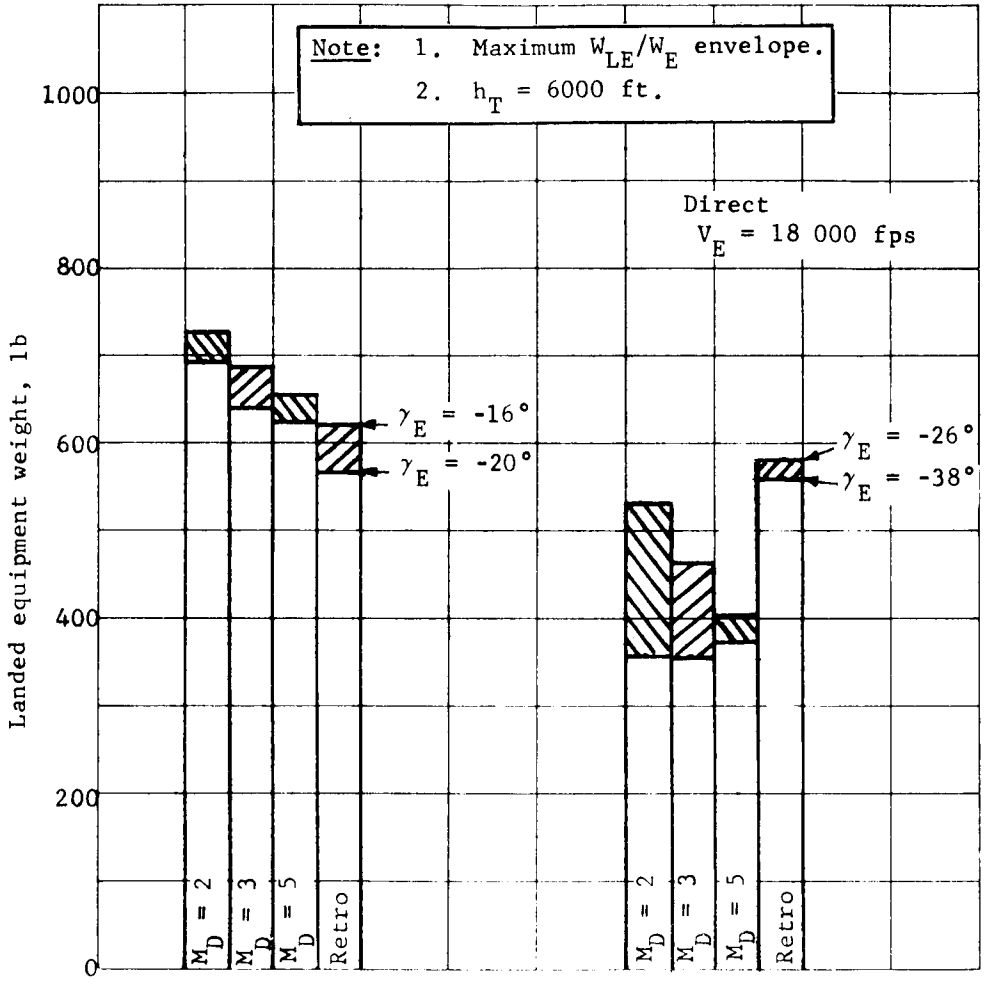

Figure B274.- Terminal Phase Summary, Entry Weight = 1500 lb

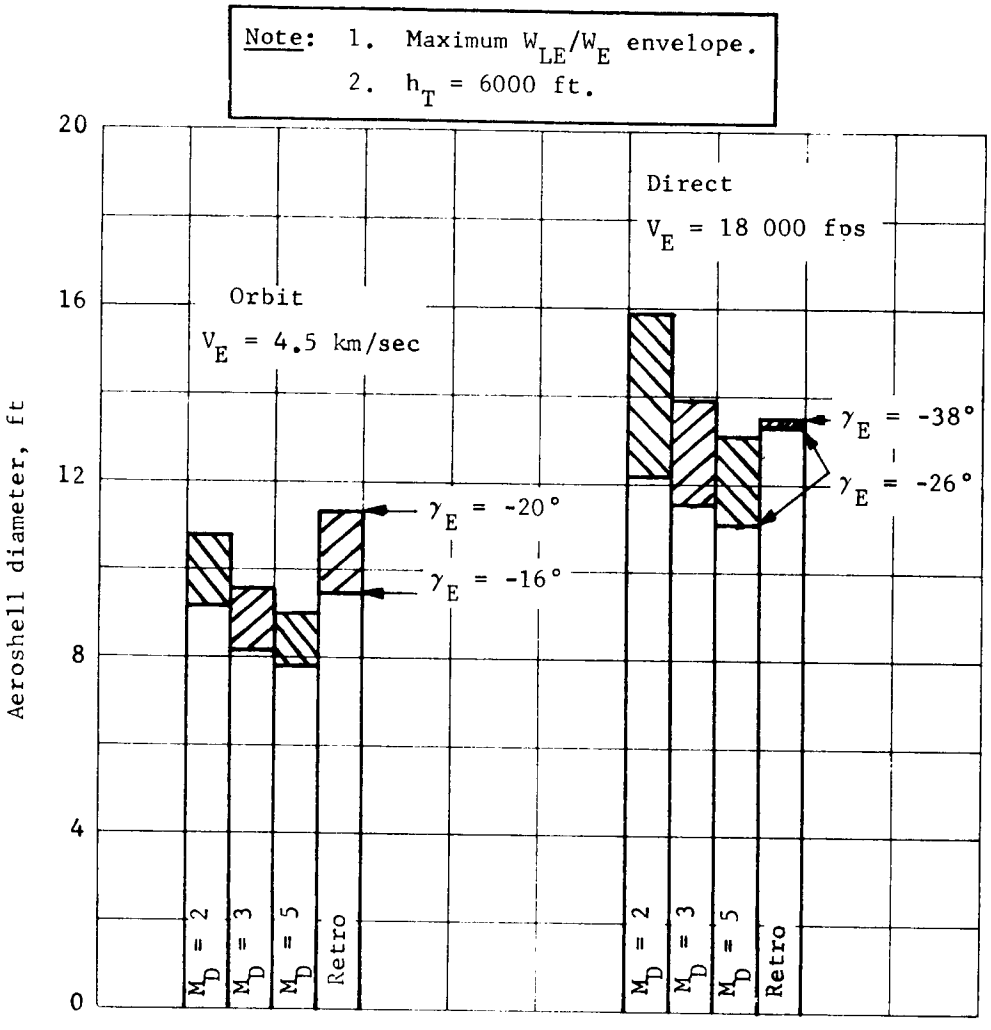

Figure B275.- Terminal Phase Summary, Entry Weight = 1500 lb

All of these things must occur simultaneously. These constraints really fall into two categories from a design viewpoint. The first is that the worst entry flightpath angle and atmosphere are assumed in direct combination. The system might still work if either one or the other is worse than expected. The second category is the definition of altitude mark for aerodecelerator deployment. This must be based on an assumed design terrain height and worst atmosphere. If the terrain height is higher than assumed, the probability of successful landing is low. An altitude mark must be set before flight, and there is less inherent adaptability in the system to cope with surprises. Even so, the combination of events that must occur simultaneously that have been assumed in this analysis should reflect as some degree of conservation in the results.

The second aspect of conservatism that has been partially investigated here is the uncertainty in the weight equations discussed earlier (10% weight margins).

The maximum performance characteristics of the various terminal phase systems and launch vehicles (in terms of capsule system weight) are compared for fixed aeroshell diameters of 8.5 and 15.0 ft, fixed landed equipment weight of W_{LE} = 600 lb and fixed entry weight of W_E = 1500 lb. As in the previous summary type (bar) charts, the constant diameter data are based on maximum W_{LE} for a given diameter. They, therefore, result in the best diameter at a cost of increased entry weight. The fixed W_{LE} comparisons are based on the maximum W_{LE} per pound entry weight. They result in the most efficient system from an entry weight veiwpoint at a cost of increased (nonoptimum) aeroshell diameter.

The 8.5-ft diameter condition is summarized in figure B276. These data show the range of total capsule system weight as a function of γ_E (highest values on bars correspond to shallowest γ_E). The corresponding W_{LE} are also shown on the bars for reference. The scale up the middle of the chart shows the performance capability of the various launch vehicles. It is clear from figure B276 that all of the orbit mode cases require the Titan IIIC/Centaur launch vehicle but with considerable launch vehicle margin. The high deployment Mach number aerodecelerator has the most W_{LE} performance capability. The direct mode performance requirements fall into the Titan IIIF/Stretched Transtage capability, but have negligible landed weight capability in all cases.

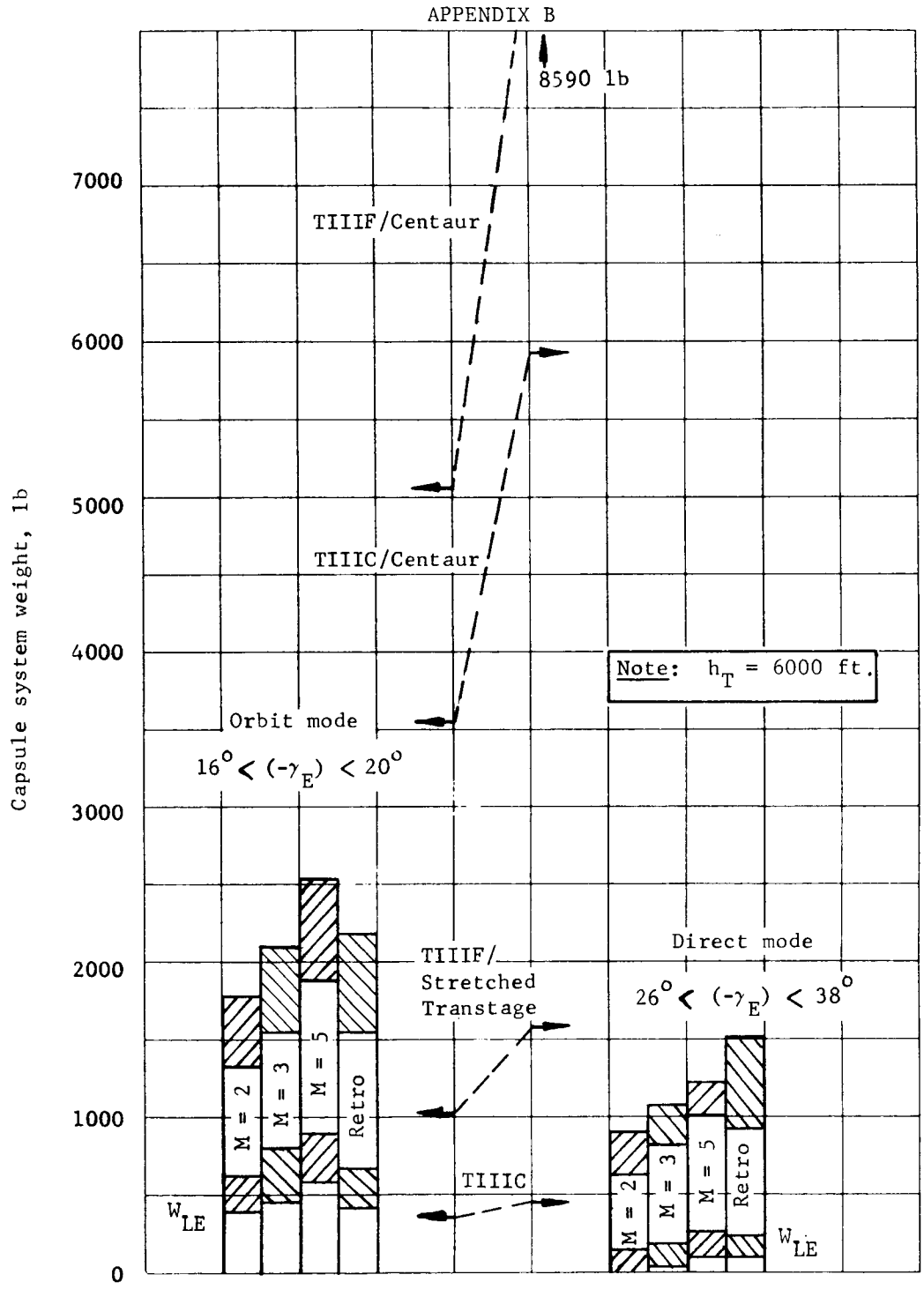

Figure B276.- Performance Summary, Aeroshell Diameter = 8.5 ft

Similar data for the 15-ft diameter aeroshell are shown in figure B277. The orbit mode W_{LE} is large, but unfortunately the total capsule system weight exceeds even the Titan IIIF/Centaur capability.

The direct mode performance requirements clearly fall within the Titan IIIC/Centaur range, with the corresponding W_{LE} comparable to that obtained with the 8.5-ft diameter orbit mode. Again, the Titan IIIC/Centaur is the launch vehicle on this basis and again, with large launch vehicle margin. For the direct mode, the all-retro terminal phase system is the best performer.

The next comparison shown in figure B278 is made on the basis of fixed landed equipment weight of 600 lb. In this case, the highest capsule system weight corresponds to the steepest entry flightpath angle. The data show lowest total system weight for the orbit mode with the $M_D = 2.0$ parachute is the best of the terminal phase systems. The diameters for these cases are given on figure B273. The performance requirements for all of the systems and both modes fall into the Titan IIIC/Centaur capability with large launch vehicle margins.

The final comparison, shown in figure B279, is on the basis of fixed entry weight of 1500 lb. On this basis, the total system weights are generally comparable with the $M_D = 2.0$ parachute and landed equipment weight for the orbit mode. The most competitive configuration for the direct mode is the all-retro system. The diameters are shown in figure B275.

It is clear from these comparisons that the tradeoff between aeroshell diameter, landed equipment weight, and total capsule system weight can be made in many ways. However, the following generalizations can be made:

1) Orbit mode - The $M_D = 2.0$ parachute is most efficient from a weight viewpoint, while the ballutes are favored from an aeroshell diameter viewpoint;

2) Direct mode - The same generalization relative to aerodecelerators is true here, but the all-retro system is competitive. The all-retro system is sensitive to thrust-to-weight ratios (throttling requirements go up). Relative to ballutes versus $M_D = 2.0$ parachutes, the latter are generally preferred on the basis of more straightforward packaging and release considerations;

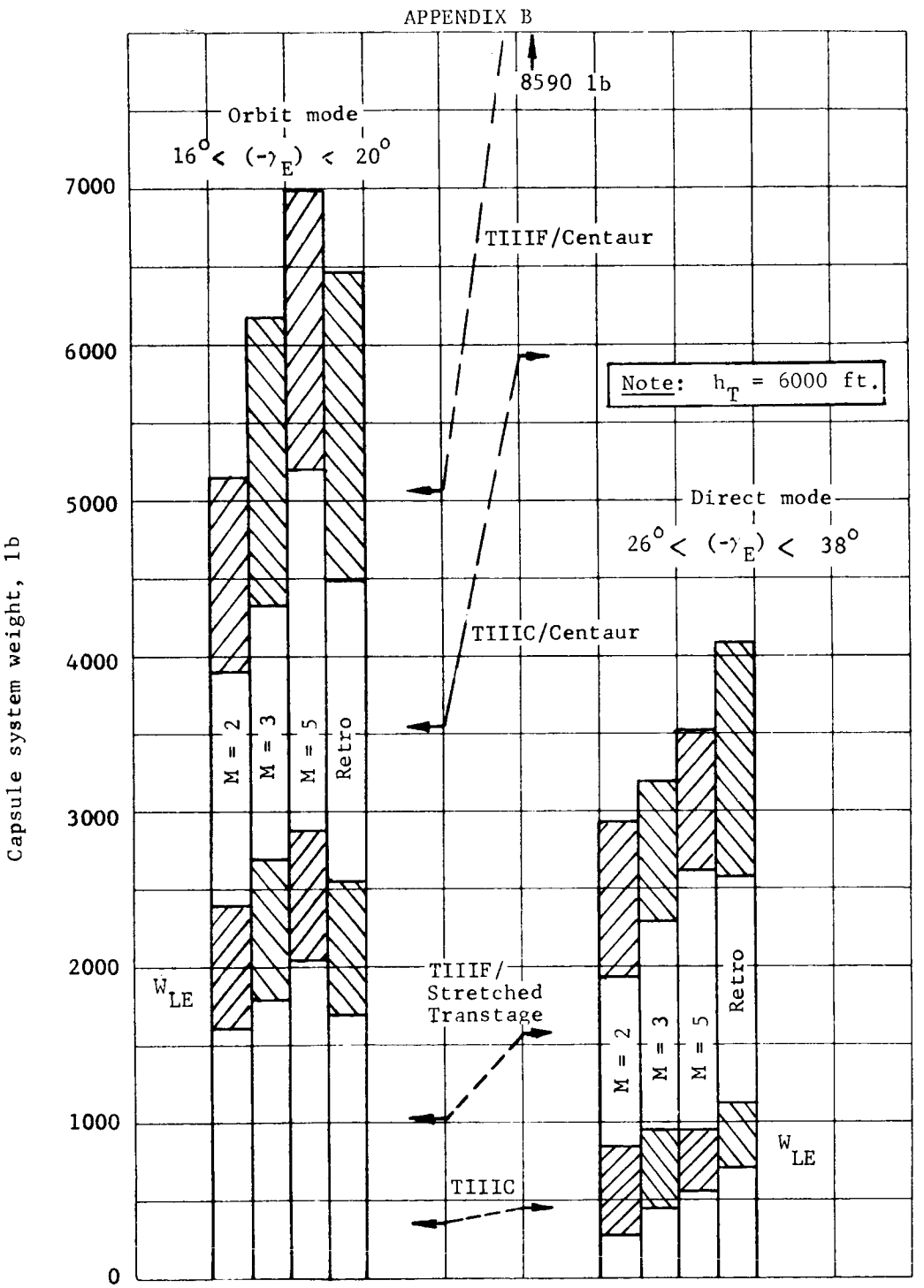

Figure B277.- Performance Summary, Aeroshell Diameter = 15 ft

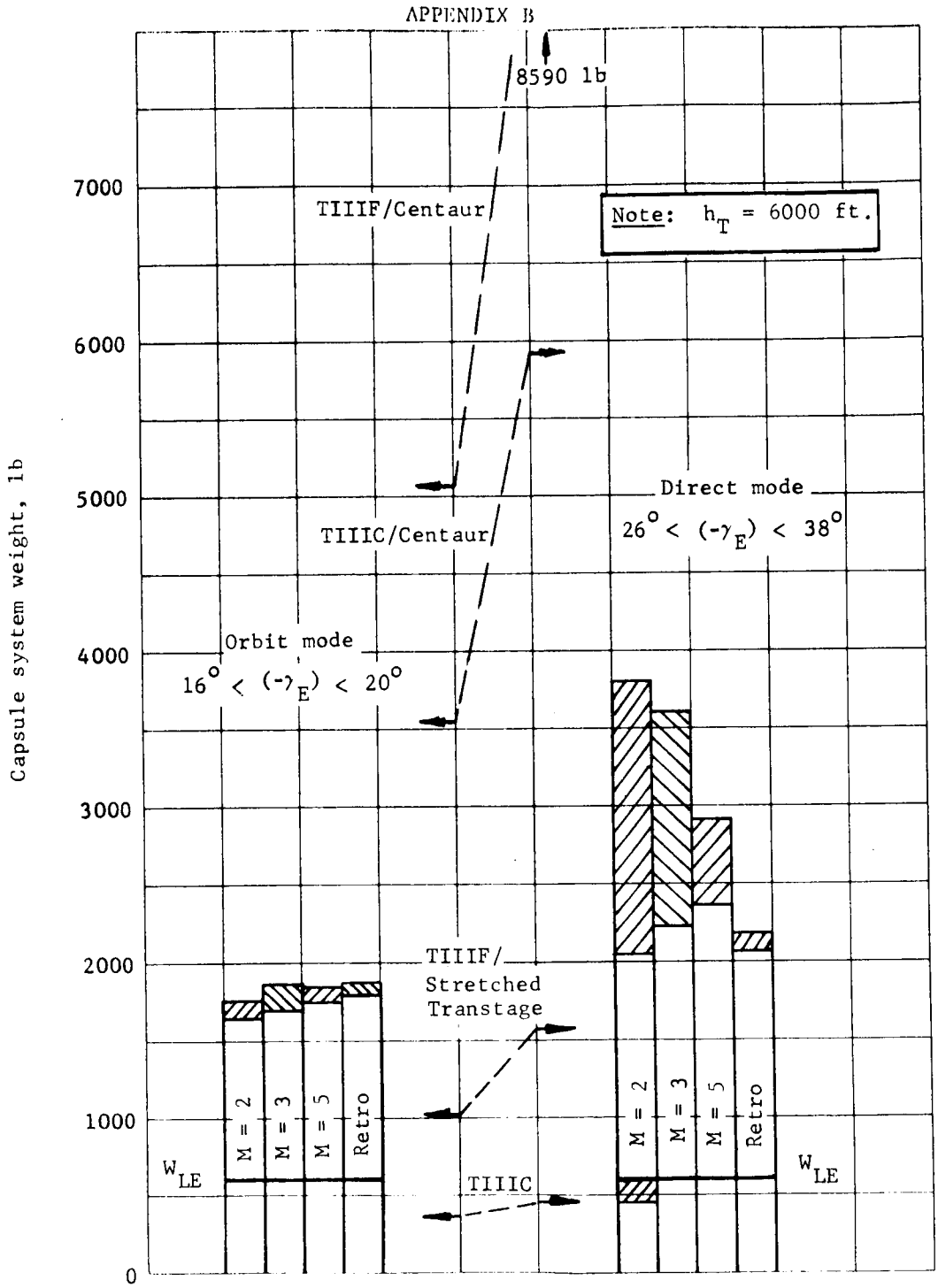

Figure B278.- Performance Summary, W_{LE} = 600 lb

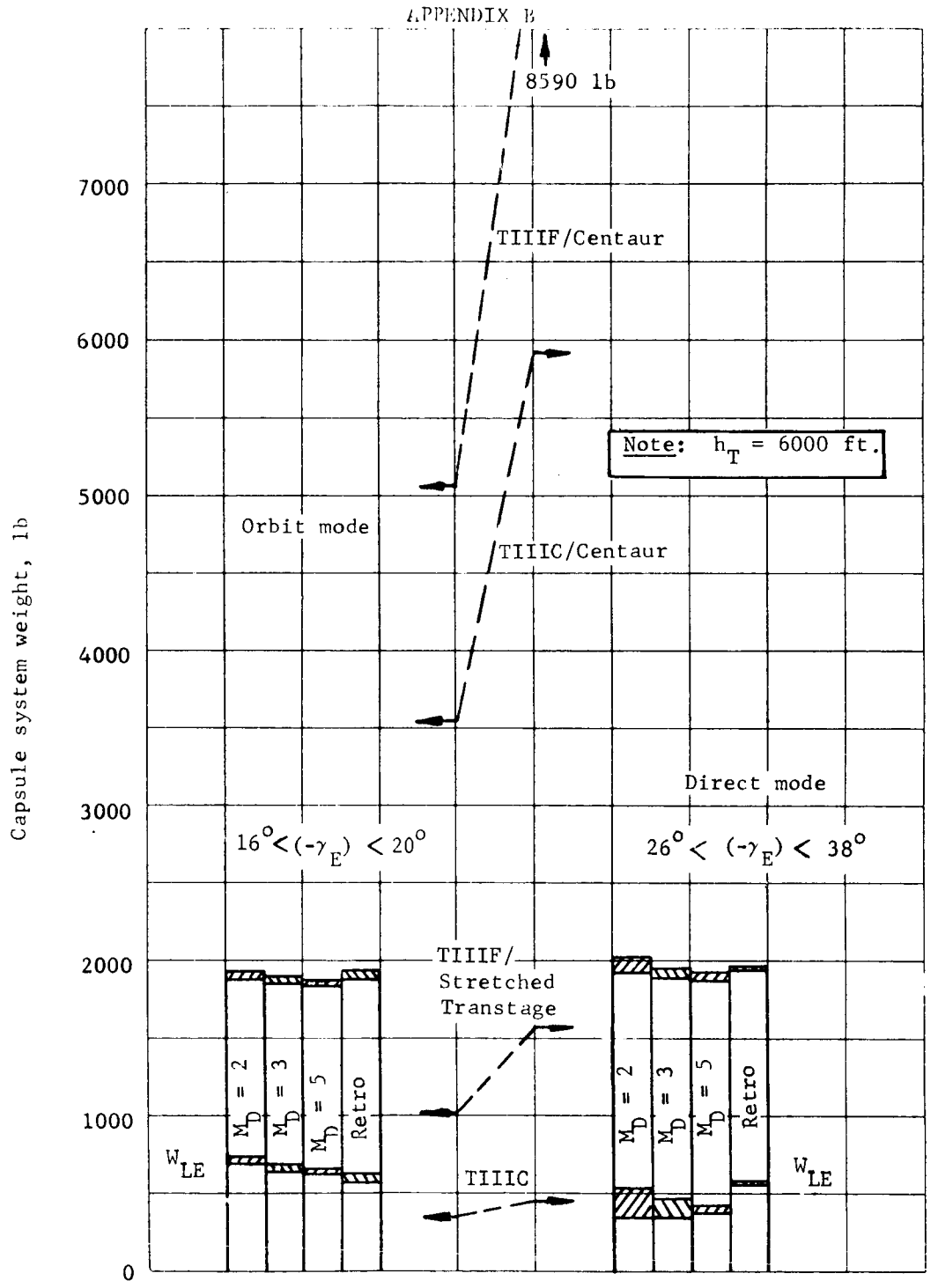

Figure B279.- Performance Summary, W_E = 1500 lb

3) Direct vs. orbit mode - Both modes require the Titan IIIC/Centaur launch vehicle. On this basis, the greater inherent flexibility and adaptability of the orbit mode makes it the more desirable.